AD-A186 493 UNITED STATES AIR FORCE RESEARCH INITIATION PROGRAM 1/ 8
1985 TECHNICAL REPORT VOLUME 3(U) UNIVERSAL ENERGY
SYSTEMS INC DAYTON OH R C DARRAH APR 87
UNCLASSIFIED AFOSR-TR-87-1719 F49620-85-C-0013 F/G 15/3 NL

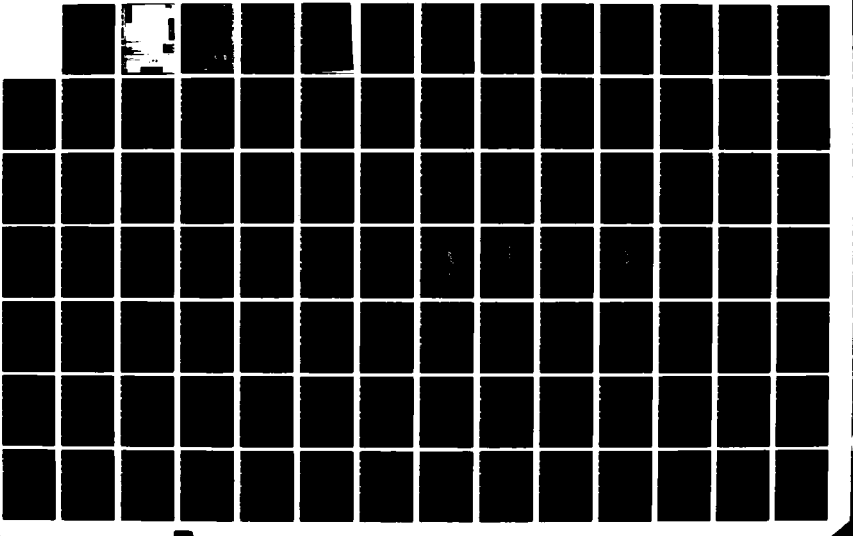

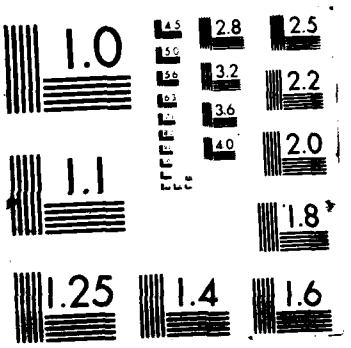
1.0
1.1
1.25
1.4
1.6
1.8
2.0
2.2
2.5
2.8
3.2
3.6
4.0
4.5
5.0
5.6
6.3
7.1
8.0
9.0
10.0

RESEARCH INITIATION PROGRAM

CONDUCTED BY
UNIVERSAL ENERGY SYSTEMS
U.E.S.

1987

FINAL TECHNICAL REPORT

VOLUME 3 OF 3

RODNEY C. DARRAH
PROGRAM DIRECTOR, UES

SUSAN K. ESPY
PROGRAM ADMINISTRATOR, UES

MAJ. RICHARD KOPPA
PROGRAM MANAGER, AFOSR

UNCLASSIFIED
SECURITY CLASSIFICATION OF THIS PAGE

REPORT DOCUMENTATION PAGE

Form Approved
OMB No. 0704-0188

1a. REPORT SECURITY CLASSIFICATION UNCLASSIFIED	1b. RESTRICTIVE MARKINGS
2a. SECURITY CLASSIFICATION AUTHORITY	3. DISTRIBUTION/AVAILABILITY OF REPORT Approved for public release; distribution unlimited.
2b. DECLASSIFICATION/DOWNGRADING SCHEDULE	
4. PERFORMING ORGANIZATION REPORT NUMBER(S)	5. MONITORING ORGANIZATION REPORT NUMBER(S) AFOSR-TR- 87-1715
6a. NAME OF PERFORMING ORGANIZATION UNIVERSAL ENERGY SYSTEMS INC.	6b. OFFICE SYMBOL (If applicable)
	7a. NAME OF MONITORING ORGANIZATION Air Force Office of Scientific Research/XO
6c. ADDRESS (City, State, and ZIP Code) 4401 Dayton Xenia Rd Dayton OH 45432	7b. ADDRESS (City, State, and ZIP Code) Building 410 Bolling AFB DC 20332
8a. NAME OF FUNDING/SPONSORING ORGANIZATION AFOSR	8b. OFFICE SYMBOL (If applicable) XOT
	9. PROCUREMENT INSTRUMENT IDENTIFICATION NUMBER F49620-85-C-0013
8c. ADDRESS (City, State, and ZIP Code) Building 410 Bolling AFB, DC 20332	10. SOURCE OF FUNDING NUMBERS

PROGRAM ELEMENT NO.	PROJECT NO.	TASK NO	WORK UNIT ACCESSION NO
61102F	3396	D5	

11. TITLE (Include Security Classification)
USAF Research Initiation Program Volume 3

12. PERSONAL AUTHOR(S)
Program Director Rodney C. Darrah

13a. TYPE OF REPORT	13b. TIME COVERED	14. DATE OF REPORT (Year, Month, Day)	15. PAGE COUNT
Interim	FROM _____ TO _____	April 1987	

16. SUPPLEMENTARY NOTATION

17. COSATI CODES			18. SUBJECT TERMS (Continue on reverse if necessary and identify by block number)
FIELD	GROUP	SUB-GROUP	

19. ABSTRACT (Continue on reverse if necessary and identify by block number)

(SEE REVERSE)

20 DISTRIBUTION/AVAILABILITY OF ABSTRACT ☒ UNCLASSIFIED/UNLIMITED ☐ SAME AS RPT ☐ DTIC USERS	21. ABSTRACT SECURITY CLASSIFICATION UNCLASSIFIED
22a NAME OF RESPONSIBLE INDIVIDUAL Richard Kopka, Major, Program Manager	22b. TELEPHONE (Include Area Code) (202) 767-4971 / 22c. OFFICE SYMBOL XOT

DD Form 1473, JUN 86 Previous editions are obsolete. SECURITY CLASSIFICATION OF THIS PAGE

INTRODUCTION

Research Initiation Program - 1985

AFOSR has provided funding for follow-on research efforts for the participants in the Summer Faculty Research Program. Initially this program was conducted by AFOSR and popularly known as the Mini-Grant Program. Since 1983 the program has been conducted by the Summer Faculty Research Program (SFRP) contractor and is now called the Research Initiation Program (RIP). Funding is provided to establish RIP awards to about half the number of participants in the SFRP.

Participants in the 1985 SFRP competed for funding under the 1985 RIP. Participants submitted cost and technical proposals to the contractor by 1 November 1985, following their participation in the 1985 SFRP.

Evaluation of these proposals was made by the contractor. Evaluation criteria consisted of:

1. Technical Excellence of the proposal
2. Continuation of the SFRP effort
3. Cost sharing by the University

The list of proposals selected for award was forwarded to AFOSR for approval of funding. Those approved by AFOSR were funded for research efforts to be completed by 31 December 1986.

The following summarizes the events for the evaluation of proposals and award of funding under the RIP.

A. Rip proposals were submitted to the contractor by 1 November 1985. The proposals were limited to $20,000 plus cost sharing by the universities. The universities were encouraged to cost share since this is an effort to establish a long term effort between the Air Force and the university.

B. Proposals were evaluated on the criteria listed above and the final award approval was given by AFOSR after consultation with the Air Force Laboratories.

C. Subcontracts were negotiated with the universities. The period of performance of the subcontract was between October 1985 and December 1986.

Copies of the Final Reports are presented in Volumes I through III of the 1985 Research Initiation Program Report. There were a total of 82 RIP awards made under the 1985 program.

UNITED STATES AIR FORCE

1985 RESEARCH INITIATION PROGRAM

Conducted by

UNIVERSAL ENERGY SYSTEMS, INC.

under

USAF Contract Number F49620-85-C-0013

RESEARCH REPORTS

VOLUME III OF III

Submitted to

Air Force Office of Scientific Research

Bolling Air Force Base

Washington, DC

By

Universal Energy Systems, Inc.

April 1987

INTRODUCTION

Research Initiation Program - 1985

AFOSR has provided funding for follow-on research efforts for the participants in the Summer Faculty Research Program. Initially this program was conducted by AFOSR and popularly known as the Mini-Grant Program. Since 1983 the program has been conducted by the Summer Faculty Research Program (SFRP) contractor and is now called the Research Initiation Program (RIP). Funding is provided to establish RIP awards to about half the number of participants in the SFRP.

Participants in the 1985 SFRP competed for funding under the 1985 RIP. Participants submitted cost and technical proposals to the contractor by 1 November 1985, following their participation in the 1985 SFRP.

Evaluation of these proposals was made by the contractor. Evaluation criteria consisted of:

1. Technical Excellence of the proposal
2. Continuation of the SFRP effort
3. Cost sharing by the University

The list of proposals selected for award was forwarded to AFOSR for approval of funding. Those approved by AFOSR were funded for research efforts to be completed by 31 December 1986.

The following summarizes the events for the evaluation of proposals and award of funding under the RIP.

A. Rip proposals were submitted to the contractor by 1 November 1985. The proposals were limited to $20,000 plus cost sharing by the universities. The universities were encouraged to cost share since this is an effort to establish a long term effort between the Air Force and the university.

B. Proposals were evaluated on the criteria listed above and the final award approval was given by AFOSR after consultation with the Air Force Laboratories.

C. Subcontracts were negotiated with the universities. The period of performance of the subcontract was between October 1985 and December 1986.

Copies of the Final Reports are presented in Volumes I through III of the 1985 Research Initiation Program Report. There were a total of 82 RIP awards made under the 1985 program.

MINI-GRANT RESEARCH REPORTS

1985 RESEARCH INITIATION PROGRAM

Technical Report Number	Title and Mini-Grant No.	Professor
Volume I		
1	Individual Differences in Abilities, Learning, and Cognitive Processes 760-OMG-027	Dr. Phillip L. Ackerman
2	Maximum Voluntary Hand Grip Torque for Circular Electrical Connectors 760-OMG-068	Dr. Samuel Adams
3	Temperature Dependence of Ion-Molecule Association Reactions: Halide Ion Addition Reactions 760-OMG-105	Dr. Lucia Badcock
4	Report Not Received In Time. Will Be Provided When Available. 760-OMG-095	Dr. Richard Bertrand
5	Metaphor and Machines: A New Look at Case Theory 760-OMG-031	Dr. Peter J. Binkert
6	Speech Produced at Various Acceleration Levels 760-OMG-033	Dr. Zinny S. Bond
7	Creating Projected Images 760-OMG-001	Dr. Kevin W. Bowyer
8	Computer-Based Instruction: Effect of Cognitive Style, Instructional Format, and Subject-Matter Content 760-OMG-085	Dr. Linda J. Buehner
9	Nonlinear Feedback Controls for Two-Link Robotic Manipulators 760-OMG-097	Dr. Connie K. Carrington

1245s

1985-86 MINI GRANT PROGRAM

Sponsored by the

AIR FORCE OFFICE OF SCIENTIFIC RESEARCH

Conducted by the

UNIVERSAL ENERGY SYSTEMS, INC.

FINAL REPORT

INDOOR RADON POLLUTION

Prepared by:	Ralph W. Sheets
Academic Rank:	Professor
Department and University:	Department of Chemistry, Southwest Missouri State University Research
Location:	Southwest Missouri State University, Springfield, Missouri

Date of Contract:	January 2, 1986-December 31, 1986
Date of Report:	March 15, 1987
Contract No.:	F49620-85-C-0013/SB5851-0360
Subcontract No.:	S-760-OMG-032
Principal Investigator:	Ralph W. Sheets
Ref:	OSURF Proposal No. 21583-55-00

INDOOR RADON POLLUTION

by

Ralph W. Sheets

ABSTRACT

Indoor air pollution from radon and its daughter decay products is a significant health problem to those who live and work in buildings with higher than average concentrations. Studies were carried out to determine the range and distribution of radon and its daughters in southwest Missouri, and to develop some understanding about how distribution of radon and its daughters is affected by differential pressures, temperatures, and humidities within a building. Difficulties were encountered in using the Eberline working level monitoring system, but measurements of radon daughters were supplemented by grab sampling of radon in southwest Missouri buildings. A total of 143 measurements on 51 buildings in southwest Missouri showed indoor radon concentrations of 0.10 to 14.3 pCi/l. Only 3 of the 51 buildings (6%) had concentrations greater than 4 pCi/l in areas where people live or work. Multiple regression analysis on data collected in the basement and first floor of a two story house showed that changes in working levels in the basement and on the first floor are weakly, but significantly, correlated: both increase or decrease together. The working levels are also correlated with ventilation conditions in the house. The working level in the basement shows a direct correlation with temperature differentials between the first floor and basement: when the first floor is warmer than the basement, working level in the basement increases; when the living room is cooler, basement working level decreases.

I. INTRODUCTION

Indoor air pollution from radon and its daughter decay products is a significant health problem for the general population (1,2,3). Radon-222 is a radioactive gas formed by the decay of radium-226. The main source of atmospheric radon is the decay of radium in rocks and soils, although there are other sources such as groundwater, natural gas, volcanic gases, and combustion of coal (3,4). Radon decays with a 3.82 day half-life to form a series of short-lived (half-lives less than 30 minutes) radioactive daughter elements: polonium-218, lead-214, bismuth-214, and polonium-214. These daughters are potent lung carcinogens (5).

Radon is chemically unreactive, and inhaled radon is exhaled essentially without effect (6). The daughters, however, are charged species, many of which attach themselves to particulates in the air. When inhaled, either in the unattached or attached forms, these may be deposited in the lungs where they cause damage to living cells (6). Unattached daughters are preferentially deposited in the upper passages of the respiratory tract where lung cancers are known to develop among uranium miners exposed to airborne radon (7). Thus the major health effect associated with radon is thought to be production of lung cancers by radon decay daughters, especially the unattached fraction.

The concentration of outdoor radon over the contiguous United States is estimated to be about 0.25 pCi/l (4). Diffusion of radon into buildings from the soil underneath often results in indoor concentrations much higher than the outdoor levels. Typical concentrations in the U.S. average 0.2 to 4 pCi/l (3), but some indoor concentrations have been found to exceed the OSHA standard for radon in uranium mines (about 66 pCi/l) (1). The Environmental Protection Agency estimates that from

about 5,000 to 20,000 lung cancer deaths a year in the U.S. may be attributed to radon and has established a maximum safe lifetime exposure limit of 0.02 working level (WL), or about 4 picoCuries/liter of air (pCi/l). (8). It is expected that the increase in numbers of tight, energy-efficient houses in recent years will increase the exposure of occupants to radon daughters.

The radon pollution problem is of particular importance to the United States Air Force Occupational and Environmental Health Laboratory. Not only are USAF personnel around the world exposed to normal radon daughter concentrations in areas where they live and work, but there are a number of sites and installations where, it may be speculated, there is special concern. These areas include airplane graveyards, underground missile silos, and hardened USAF installations in areas such as Colorado, where soil concentrations of radium are known to be high.

In order to asess the seriousness of indoor radon daughter pollution with respect both to the general public and to USAF personnel, many more studies need to be carried out. Even the extent of radon daughter pollution is unknown. Although measurements have been made on thousands of houses in the U.S., for example, there are still entire states for which no values have been reported. Behavior of indoor radon is not well characterized. Concentrations are known to vary not only with time of day and story above ground, but with geographic and meterological conditions (4). Outdoor radon has been shown to vary seasonally, but apparently few measurements of seasonal variation of indoor background levels have yet been reported (4). Finally, much remains to be

understood about how distribution of radon in multistory buildings is affected by differences in pressure, humidity, and temperature.

It has been recommended (3) that studies of indoor radon and radon daughter concentrations be carried out to determine the range and distribution of radon and its daughters in buildings, and to understand the behavior of radon and its daughters in buildings.

The project described in this paper was carried out to contribute to this effort.

II. OBJECTIVES OF THE RESEARCH EFFORT

A. The original objectives of the research effort were:

a) to determine the range and distribution of radon and its decay products in buildings in southwest Missouri; and

b) to develop some understanding about how the distribution of radon and its daughters is affected by differential pressures, temperatures, and humidities within buildings.

In pursuit of these objectives, the following goals were selected:

1. A Survey of Indoor Radon Daughters in Southwest Missouri --It was decided that twenty buildings, including both residences and office buildings in the Springfield, Missouri area would be surveyed to determine typical radon daughter levels. In buildings chosen to represent a variety of locations and types, radon daughter concentrations were to be continuously monitored over a 24-hour period. In this way it was hoped to identify buildings with elevated levels of radon.

2. Measurement of Diurnal and Seasonal Variations of Indoor Levels -One residence was to be selected for continued periodic measurement of radon daughter working levels. It was planned that once a week during the entire research period, working levels in the residence would be

continuously monitored for a 24-hour period. The residence was to be one in which normal living activities were to be carried out under a variety of ventilation conditions.

3. Investigation of the Influence of Pressure-, Humidity-, and Temperature-Differentials Within a Building on Radon Daughter Distribution --In a selected multistory residence, concentration of radon daughters in the basement and a room on the main floor were to be simultaneously monitored for continuous periods of several days. At the same time, the air temperatures, barometric pressures, and relative humidities of the two areas were to be continuously monitored. It was hoped that comparison of data from these two areas would reveal whether or not there is a symmetry in the growth and decline of daughter concentrations as air is transferred between floors, and whether or not periods of daughter growth and decline coincide with intrastructure difference. in temperature, pressure, and humidity.

It was planned that all measurements of radon daughters would be made using an Eberline radon working level monitoring system. Such a system was acquired and tested. In use, unfortunately, the microcomputerized Eberline system (consisting of one working level readout unit and two working level monitors) proved to be extremely unreliable and erratic. During an entire 9-month period of attempted use, the system operated satisfactorily for fewer than 30 days. (See Appendix.) As a result, the intended goals of this project had to be considerably modified. Measurements of seasonal variation of radon daughters were deleted and studies of the effects of pressure, temperature, and humidity differentials were abbreviated. On the

other hand , it was possible to greatly expand the radon survey in southwest Missouri by making use of Lucas grab sampling for radon gas (9) to supplement the relatively few measurements of radon daughters.

B. Revised Goals of Research Effort

The revised goals of this study were:

1. Evaluation of the Eberline Working Level Monitoring System Under Field Conditions --This would include calibration of system, intercomparison of working level monitors, and comparison of working level monitor measurements with measurements made using a modified Tsivoglou method.

2. Investigation of Influence of Pressure-, Temperature-, and Humidity-Differentials Within a Building on Radon Daughter Distribution -This would require multiple regression analysis of data obtained through simultaneous measurements of radon daughters, pressures, temperatures, and humidities in two different locations within a building.

3. A Survey Of Indoor Radon Levels in Southwest Missouri --This would include measurements of radon gas in approximately 50 buildings to supplement the few measurements of radon daughters obtained in the Springfield, Missouri area.

Experimental procedures and results pertaining to each of these three goals are discussed below in Sections III, IV, and V, respectively.

III. EVALUATION OF EBERLINE WORKING LEVEL MONITORING SYSTEM UNDER FIELD CONDITIONS

A. Apparatus

Continuous monitoring of radon decay daughters was carried out with an Eberline radon working level monitoring system consisting of two portable battery operated CMOS-microcomputer monitors (Model WLM-1-A) and a programmable readout unit (Model WLR-1-A). The monitors can operate unattended for up to one week, continuously drawing air from the environment and collecting radon daughters on a filter. Alpha emissions from the daughters are measured using a silicon diffused junction detector. The alpha counts are stored for preprogrammed intervals of 1 to 60 minutes. The data points, along with parameters used for taking data, are transferred to the readout unit. Calculations and data printout are performed by the readout unit. The system has a stated detection limit of 0.00002 WL (working level) and an upper limit of 100 WL. Field testing of the system by Eberline scientists showed that calibration with an electroplated alpha source gave the same results (within + or - 16%) as calibration in a radon chamber. The coefficient of variation between monitoring units was within 10%. It was also shown that measurements made with the Eberline system gave woking level values comparable to those obtained by a modified Tsivoglou and a modified Kusnetz technique (10).

During the present investigation, simultaneous measurements from two WLM-1's (#306 and #372) were compared with each other and with measurements made using Thomas' three-interval count method. For the latter measurements, the sampling system consisted of a Ludlum Model 2200 battery operated scaler; a Ludlum Model 182 radon flask counter; a

Gast pump with a free air displacement of 113 l/min; a Lab Crest Scientific Model 100 H Century flowmeter; Millipore 0.80 micron cellulose ester filters; and alpha phosphor-on-Mylar discs (William B. Johnson and Associates, Research Park, Montville, NJ).

B. Measurement Techniques

The Eberline system uses an integrated gross alpha counting approach. In use, a WLM (monitor unit) is connected to the WLR (readout unit) and the following parameters are entered: WLM number; a location code; sampling interval (1 to 60 minutes); sample quantity (1 to 200 data points); tail interval (1 to 60 minutes); tail quantity (0 to 200 points); and start time. The tail interval is the length of time for each data point taken during decay of filter activity after sampling is complete and the pump is turned off. From the decay behavior during the tail interval, the program determines whether thoron (Rn-220) is present along with radon (Rn-222).

The following description of the working level monitor is taken from Eberline's Technical Manual (11):

The working level monitor provides the functions of sample collection and data storage. It is microcomputer based and battery powered. Extensive use of CMOS circuitry provides sampling periods of up to one week. The data collection parameters are input via the working level readout unit. These parameters are used by the WLM to collect an operator selected number of data points over the sample period. These data points are stored in memory until retrieved by the WLR. Air is drawn through a membrane filter by a small pump. The flow rate of the pump is controlled by the microcomputer. Radon daughters are collected on this filter and their decay is detected by a silicon

diffused junction alpha detector. The detector signal is amplified and threshold discriminated. The output from the discriminator is counted by the microcomputer. Start-up initiates a time interval clock in the microcomputer which is used to sense a preset sample period starting time. At a time of one time interval plus one second prior to the start time,the WLM begins by taking a background measurement. After measurement is complete the start time occurs, and the microcomputer turns the pump on and the WLM counts the activity on the filter paper for the total time period specified by the parameters input by the operator. The time of each interval and number of intervals specified determine the total period. A total count value for each interval is stored. At the end of the sampling period, the pump is turned off and activity on the filter paper is allowed to decay. This decay, or tail period, is counted for four hours. The tail data and count value are stored. In addition, if specified in the parameters, counts for individual tail intervals may be stored. The readout unit then includes the four hour tail counts in the working level calculation and corrects for thoron contribution by half-life evaluation. The background measurement aids in qualifying the data validity by proving the counting system is not noisy. When the WLM has completed its sample period and tail data collection, it turns off all power except to the microcomputer. It then goes into a low-power operating mode to preserve data for long periods after data collecion.

The comparison method used was a technique developed by Thomas (12) for determination of the radon daughters RaA(polonium-218), RaB(lead-214), and RaC(bismuth-214). Air is drawn through a filter for a specified time and the total alpha disintegrations in three selected

time intervals are counted. The equations relating air concentrations of the daughters to the interval counts are:

$$C2 = (0.1698G(2,5) - 0.0820G(6,20) + 0.0775G(21,30) - 0.0566R)/VE \quad (1)$$

$$C3 = (0.0012G(2,5) - 0.0206G(6,20) + 0.0491G(21,30) - 0.1575R)/VE \quad (2)$$

$$C4 = (-0.0225G(2,5) + 0.0332G(6,20) - 0.0377G(21,30) - 0.0576R)/VE \quad (3)$$

where C2 is RaA concentration, pCi/l; C3 is RaB concentration, pCi/l; C4 is RaC concentration, pCi/l; V is sampling flow rate, l/min; E is the counter efficiency, cpm/dpm; G(x,y) is the gross number of alpha counts from x to y minutes after end of sampling; R is background counting rate, cpm; and the sampling time is 5 minutes.

From these concentrations, the potential alpha energy concentration (PAEC), in working level units, may be calculated:

$$PAEC = 0.0010256(C2) + 0.0050624(C3) + 0.0037247(C4) \quad (4)$$

The experimental procedure for determination of radon daughter concentrations and PAEC's is as follows: A 0.45 millimicrom filter is placed face down on an alpha phosphor-on-Mylar disc. This is placed in intimate contact with the photomultiplier tube in a Ludlum radon flask counter and counted with a Ludlum scaler for 30 minutes. Typical background rates are 0.02 to 0.03 cpm. The filter is connected to a Gast pump metered with a calibrated rotameter. Air is drawn through the filter at a constant rate for exactly 5 minutes. The filter is removed and transferred face down to the counting chamber. After 2 minutes from the end of the sampling, gross alpha counts are recorded until the end of the fifth minute. Counts are subsequently recorded

for the 6-20 and the 21-30 minute intervals. Concentrations of radon daughters and PAEC's are calculated using a Hewlett-Packard 15C calculator, or an Apple II computer, and Equations (1) - (4).

C. Calibration of Instruments

The Eberline system was calibrated according to instructions in the Working Level Monitor Technical Manual (11). Counting efficiencies of both the Eberline monitor and the Ludlum radon counter were determined by comparison with an electroplated Thorium-230 alpha source which is NBS traceable.

Air flow rates were measured with a rotameter which had been calibrated with a soap bubble flowmeter for standard conditions. The rotameter was then calibrated with a filter in place by measuring the pressure drop across the filter and calculating a flow rate corrected to standard conditions.

D. Field Measurements: Results and Discussion

Two WLM's (Nos. 306 and 372) were calibrated, programmed to count for 24 1-hour periods, and placed side by side in the laboratory. At the end of 24 hours, the printout showed an average working level as measured by No. 372 of 0.00121 +/- 5.77%. Individual hourly averages ranged from 0.000435 to 0.00167 WL. The 24-hour average as measured by No. 306 was 0.186 +/- 0.55%, with hourly averages ranging from 0.000350 to 1.46 WL. Comparison of printouts showed that values measured by No. 306 correlated well with those measured by No. 372 (differences less than 20%) for the first 20 hours. They then increased rapidly until, for the 24th hour, No. 306 reported 1.46 WL while No. 372 reported 0.00111 WL. Repeated tests of

this kind showed that No. 306 behaved unpredictably, sometimes reporting values as great as 4000 times the corresponding values reported by No. 372.

The performance of WLM No. 372 was checked by comparison with PAEC measurements carried out by the Thomas method (12). The two methods gave results which agreed reasonably well, with values measured by No. 372 being in the range of 0.88 to 1.36 times the corresponding values measured by Thomas' method (at an ambient working level of about 0.001).

After WLM No. 306 had been repaired by Eberline, comparative tests of the two WLM's showed better agreement over extended periods of time. As an example, side-by-side measurements by the two instruments for 168 consecutive 30-minute periods yielded an average of 0.00106 WL for No. 372 and 0.00116 WL for No. 306. In general, hourly working levels measured by the two monitors increased and decreased in the same order, although occasionally one value increased while the other decreased. Differences between two corresponding values were as small as zero and as great as 100%. Figure 1 shows typical plots for WLM's 306 and 372 measuring 30-minute averages over a 24-hour period. When counts were averaged over 60-minute periods, agreement between the two curves was somewhat better.

During the three-week period succeeding the test shown in Figure 1, WLM No. 306 appeared to function properly. The experiments described in Section IV below were carried out during this time.

After about three weeks, comparative tests indicated that No. 306 was again operating erratically. The monitor was returned to Eberline and eventually replaced with WLM No. 325.

In the meantime, WLM No. 372 began displaying apparent erratic behavior and was returned to Eberline. Subsequent tests at the factory failed to disclose any malfunctioning of No. 372, and it was suspected that the problem concerned the readout unit, WLR No. 161.

By the end of the grant period, the Eberline Working Level Monitoring system was completely inoperable (see Appendix). The entire system performed satisfactorily for a total period of less than one month during the nine-month period of testing and evaluation.

Figure 1. Comparison of WLM #306 and #372

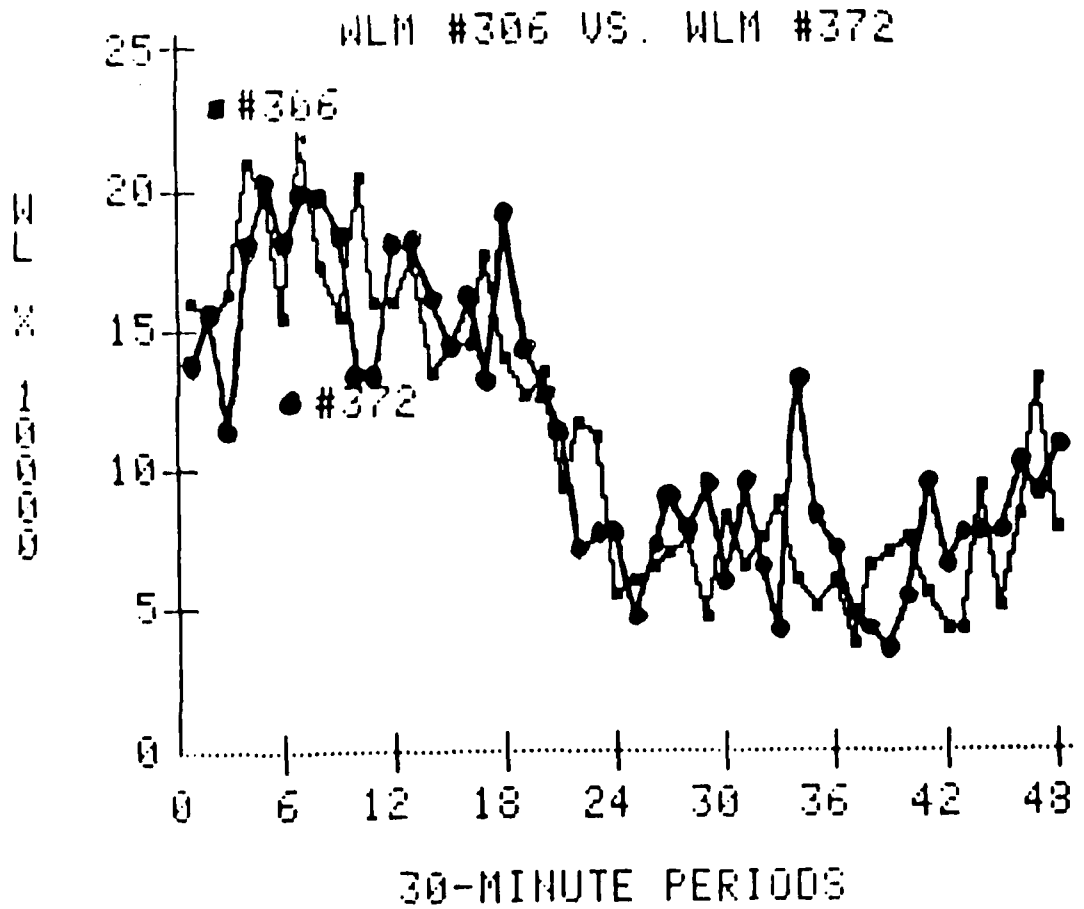

IV. INVESTIGATION OF THE INFLUENCE OF PRESSURE-, TEMPERATURE-, AND HUMIDITY-DIFFERENTIALS WITHIN A BUILDING ON RADON DAUGHTER DISTRUBUTION

A. Introduction

In multistory houses, radon concentrations are usually greatest at the lowest levels and decrease in upper stories (4). There is some evidence which suggests that transport of air between floors can account for radon concentration changes that are too rapid for air exchange dilution (13). Thus measurements of radon concentrations in a basement indicated that rapid growth or decline of radon often coincided with variations in temperature differences between the main floor and basement. In other studies, indoor radon concentrations have been found to vary inversely with barometric pressure, with the rate of change of pressure being more important than the actual value (2). Additionally, since radon is soluble in water, it may be supposed that humidity changes can affect indoor radon and radon daughter concentrations. In order to investigate whether air movement between floors due to pressue, humidity, or temperature differences has a significant effect on radon distribution, the following experiment was carried out.

In a residence which had previously been found to have radon in the range of 0.26-3.58 pCi/l and PAEC in the range of 0.0005-0.020 WL, concentrations of radon daughters in the basement and in the living room above the basement were simultaneously monitored continuously for several days. At the same time, the air temperatures, barometric pressures, and relative humidities of the two areas were continuously recorded. Measurements were made under a variety of ventilation of conditions. Multiple regression analysis was then used to find

correlations between changes in daughter concentrations, on the one hand, and temperature-, pressure-, and humidity-differentials, on the other.

B. Experimental Procedures

Radon daughter concentrations were measured by the Eberline radon working level monitoring system described in Section III above. Temperature and humidity measurements were made with Cole-Parmer hygrothermographs. These instruments are spring-wound, chart-drive recorders which operate over a temperature range of -10 to +50 deg. C and a humidity range of 0 to 100% RH. Pressure measurements were made with Cole-Parmer recording aneroid barographs. These instruments measure and record pressures over a range of 940 to 1045 millibars with a sensitivity of +/- 0.2 MB.

Concentrations of indoor radon were measured for comparison with WL values. These measurements were made by the Lucas grab sampling technique (9) described in Section V below. Air samples were collected in evacuated Lucas flasks and counted in a Ludlum Model 182 radon flask counter connected to a Ludlum Model 2200 scaler.

Multiple regression analysis was carried out on an IBM 4341 mainframe computer using the base SAS (Statistical Analysis System) software package.

The experiment was carried out in the following manner: The test residence is a frame, two-story house with a half-basement which connects with a half crawl space through open vents. The living room is on the first floor directly above the basement. The only entrance to the basement is a door opening into the kitchen, which is on the first floor directly above the crawl space, and which does not directly

open into the living room. When this basement door is closed, the most likely route for radon from the basement to the living room is diffusion through the forced-air duct system and through the living room floor. Previous measurements of radon by the Lucas grab sample method had shown radon levels ranging from 1.85 to 3.58 pCi/l in the basement, 0.26 to 1.20 pCi/l in the first floor living room, and 0.93 to 1.43 pCi/l in a second story bedroom (see Table 1). Measurement of working level at 2100 hours on 4/6/86 showed PAEC = 0.0103 WL in the basement and 0.00232 WL in the living room. Thus it appears that both radon and radon daughter concentrations in the basement averaged about 4 times the concentrations in the living room throughout the month of April, 1986, during which time the house was closed nd heated.

WLM's 306 and 372 were programmed to count from 0000 hours on Wednesday, June 4, 1986 to 2400 hours on Monday, June 9, 1986 - a total of 144 consecutive 60-minute periods. No. 306 was placed in the basement of the test residence at a height of 2 feet above the cement floor. No. 372 was placed in the living room directly above No. 306 at a height of 2 ft above the carpeted hardwood floor. Recording hygrothermographs and barographs were placed in the same two locations.

The test residence was occupied by a family of three, and normal living activities were carried out during the 6-day period. Outdoor temperatures ranged from 20 to 30 deg C during the period, and rain was noted on two of the six days. No heating or cooling devices were in operation in the house during this period, and temperature was controlled by opening and closing windows and doors. A log was kept of times when the house was opened and closed. When one of these events occurred, the front and back doors (east and west sides, respectively)

Table 1. Measurements of Radon in Test Residence

		Rn (pCi/l)			
Date	Time	Crawl Space	Basement	1st Floor	2nd Floor
3/30/86	0620	-	2.94	-	-
3/31/86	0604	-	1.97	-	-
4/1/86	0558	-	1.92	0.32	-
4/2/86	0600	-	2.31	0.62	-
4/5/86	2238	-	2.79	0.58	-
4/14/86	0700	-	2.55	0.26	-
4/14/86	2100	-	-	0.57	-
4/15/86	1718	-	-	-	0.94
4/15/86	2330	-	2.41	1.20	-
4/16/86	1620	-	3.58	0.52	-
4/17/86	2130	-	2.12	-	-
4/18/86	1220	-	2.45	-	-
4/18/86	1850	2.61	2.99	-	-
4/19/86	2139	-	2.34	-	-
4/20/86	1235	-	1.85	-	-
5/2/86	1655	-	-	-	1.07
5/3/86	0855	-	-	-	0.93
5/3/86	2335	-	-	0.48	1.43

together with 1st floor windows on the north and south sides were opened or closed on the same schedule. Second story windows on the east and west sides of the house were also opened and closed on this schedule. The only door to the basement was kept closed at all times except to enter or leave this space.

At the end of the 6-day sampling period, hourly averages for WL's were printed out and placed in a computer file along with corresponding pressures, temperatures, and relative humidities for the two sampling areas. This file was then subjected to multiple regression analysis to try to identify relationships and dependencies among the several variables.

C. Results and Discussion

A Working Level (WL) is defined as the total alpha activity of short-lived radon daughters in secular equilibrium with 100 pCi/l of radon. Radon gas entering a house necessarily leaves some of its daughters (which are solid particles) behind because of the filtering action of soil and other materials through which it passes. This filtered radon would require 3-4 hours for a new secular equilibrium to be reached (14). Since the turnover time for air in a room of a typical house is one air change per hour (ACH) or greater (15), it is unlikely that equilibrium between radon and its daughters is ever reached indoors. Therefore, instead of the radon/WL ratio being 100:1, it is higher, depending on the degree of equilibrium attained. Past experience has led some investigators to assume a 50% equilibrium state and to expect a Rn/WL ratio of about 200.

Sporadic grab sampling of radon in the test house during the sampling period indicated that the Rn/WL ratio in the basement averaged

about 400:1, and in the living room, about 330:1. This would correspond to about 25% and 30% equilibrium in the respective areas. In view of the fact that %equilibrium values decrease as ACH increases, these values seem reasonable for an older (more than 35 years), somewhat drafty house such as the test residence.

Figure 2 shows a plot of hourly WL's in the basement (WLB) versus WL's in the living room (WLL) for the first three days. It is apparent that there is a rough symmetry between the two curves, wuth the WLL always being less than the WLB. Over the 6-day period the WLB ranged between 0.0042 and 0.0195 WL, with an average value of 0.0109 WL for the 144 hours. Values for the WLL ranged from 0.0006 to 0.0047 WL, with an average of 0.00138 WL. The ratio of WLL/WLB ranged from 0.03 to 0.32 with an average value of 0.13. The ratio was smaller (0.12) when the house was open and larger (0.16) when closed (Table 2).

It is not immediately clear what kind of correspondence should be expected between working levels in the living room and basement of the test house. The largest source of indoor radon is thought to be infiltration of soil radon (15). Meteorological conditions (moisture, temperature, wind, and atmospheric pressure) are said to affect both radon exhalation and air infiltration (15). Nero and associates (16) found that, contrary to their expectation, there is little correlation between radon concentrations and ventilation rates in houses they examined. They concluded that radon is drawn into a house by micropressue differences inside and outside the house. These pressure differences are assumed to be caused by winds and by unequal indoor and outdoor pressures due to a "chimney" or "stack" effect (16)

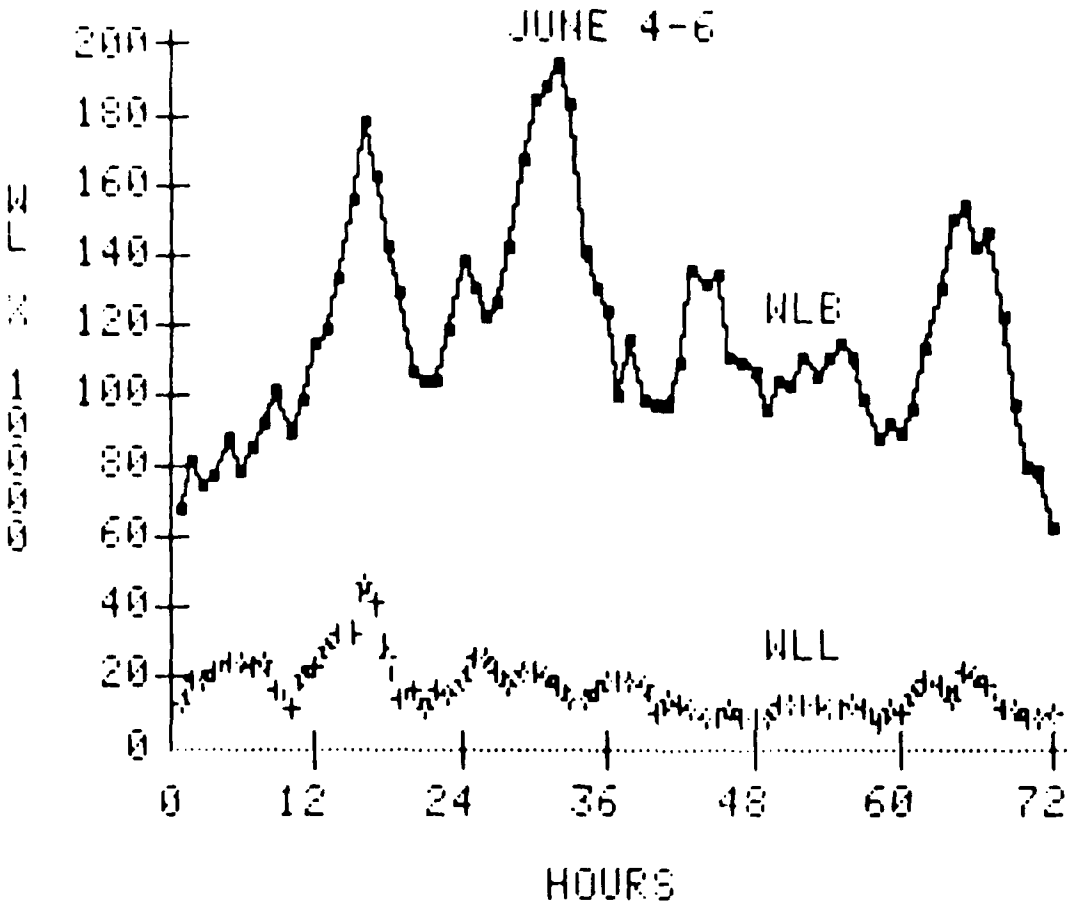
JUNE 4-6
200
180
160
140
120
100
80
60
40
20
0
FLOW X 1000
NLB
NLL
0
12
24
36
48
60
72
HOURS

Table 2. Values for Radon Daughters in Test Residence

Period Measured	June 4-9 (144 hours)
Windows Open	57 hours total
Windows Closed	37 hours total
Avg WL in Basement	0.0109 WL
Avg WL in Living Room	0.00138 WL
Ratio WLL/WLB	
Range	0.03 to 0.32
Average	0.13
Windows Closed	0.16
Windows Open	0.12
Equilibrium between	
radon and daughters	
In Basement	25% equilibrium
In Living Room	30% equilibrium

In considering how radon is transferred from the basement to the living room of the test house, the following parameters seem important:

a) Ventilation: Opening of windows and doors should cause a decrease in living room radon; closing the house should result in a buildup in the living room. Radon levels in the basement should increase and decrease in the same manner.

b) Temperature Differentials: When the air temperature of the living room is higher than that of the basement, one might expect a "thermal inversion" effect. This would prevent cooler basement air from carrying radon through the living room floor into the warmer air. As a result, radon should build up in the basement faster than in the living room. Conversely, when th living room is cooler than the basement, transfer of air from the warmer to the cooler area should result in a decrease of radon in the basement and an increase in the living room.

On the other hand, when the living room is warmer than the basement, the less dense living room air creates a micropressure differential (chimney effect) which draws soil radon into the basement. Both lines of reasoning indicate that radon levels in the basement should increase when temperature of the living room (TLR) minus the temperature of the basement (TB) is a positive number.

c) Pressure and Pressure Differentials: Decreases in atmospheric pressure are expected to cause an increase in release of soil radon and a resulting increase in basement levels. When the pressure in the living room is less than that in the basement, the chimney effect should result in increased radon being drawn into the basement and, presumably into the living room.

d) Humidity Differentials: Since humid air is less dense than dry air, the same arguments made above concerning temperature differentials should apply here (i.e., a buildup of basement radon is expected when the relative humidity of the living room is greater than that of the basement).

In summary, some plausible expectations concerning radon levels in the test house are:

1. Radon concentrations in the basement and living room will increase in periods when the house is closed, and decrease when it is open.

2. Radon levels in the basement will increase when the living room is warmer than the basement, and decrease when the living room is cooler. Radon levels in the living room will show the inverse behavior.

3. Radon concentrations in the basement will increase during periods of decreasing atmospheric pressure, and decrease during periods of increasing pressure.

4. Radon levels in the basement will increase when the relative humidity of the living room is greater than that of the basement.

5. The major influence on radon levels in both the living room and basement will be micropressure differences inside and outside the house. Because of this, and in spite of the fact that the other parameters affect basement and living room radon levels in different ways, radon concentrations in the living room will be generally proportional to concentrations in the basement.

Testing of these expectations in the present study was complicated by several factors. First, no attempt was made to monitor winds and inside-outside pressure differentials. (This was, in fact, not one of

the goals of the research). Second, The test residence had a second story which was not monitored. Some of the factors which influence transfer of radon between the basement and living room would affect transfer between the living room and second floor. Third, since this study measured working level (radon daughters) and not radon gas, allowance had to be made for the fact that some time is required for secular equilibrium, or partial secular equilibrium, to be reached. This means that maximum working level is not necessarily reached at the same time that the maximum radon concentration is attained. Correlation is complicated then by the fact that influences which have an immediate effect on the radon concentration will appear to have a delayed effect on the working level.

The present study yielded results that are in agreement with some of the above enumerated expectations. Examination of Figure 2 seems to confirm that the WLL is roughly proportional to the WLB, generally rising and falling at about the same time. When vertical lines are drawn on the plot to show periods in which the house was closed (X) or open (O) (Figure 3), it is seen that working levels in both the basement and living room did generally increase during closed periods and decrease during open periods. The correlation is far from perfect, however, indicating that other factors are influencing the WL's.

Figure 4 shows the plot with vertical lines drawn to indicate periods when the living room was warmer than the basement (+) or cooler than the basement (-). This plot gives support to the suggestion that WL's in the basement increase during (+) periods and decrease during (-) periods.

Figure 3. Test Residence Open = O; Closed = X

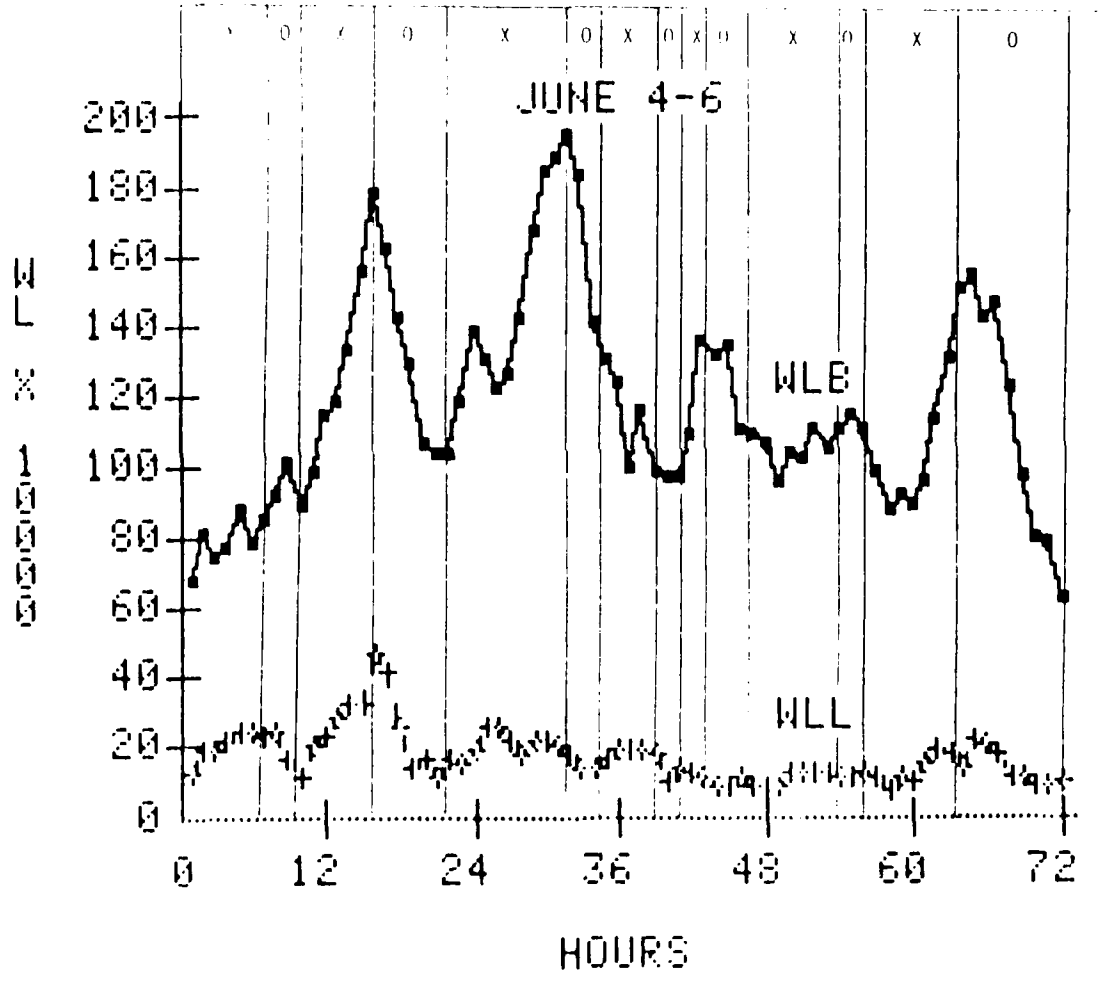

Figure 4. Test Residence Living Room Warmer = +; Living Room Cooler = -

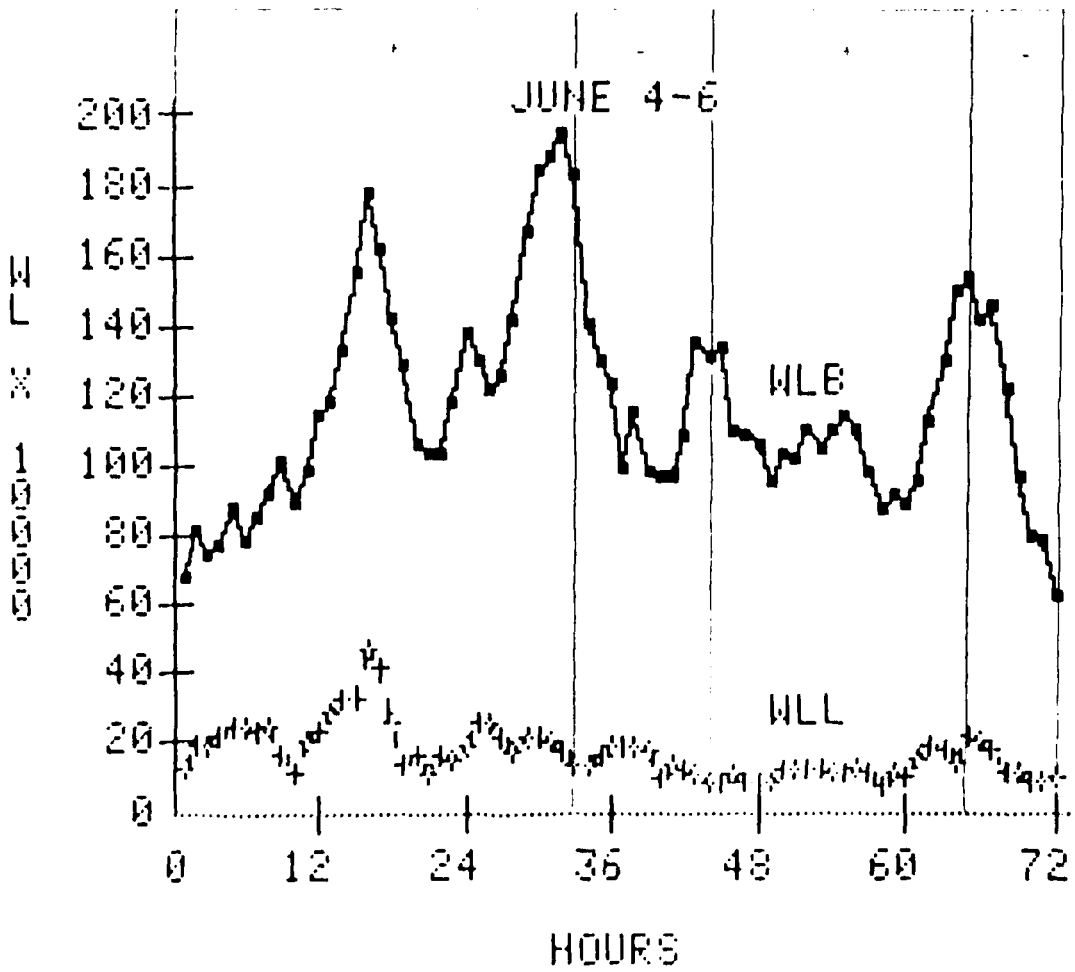

Interpretations such as these drawn from observing time-series plots tend to be subjective and arbitrary. To remove some of the subjectivity and arbitrariness, it was decided to subject the data to multiple correlation analysis. It was hoped that statistical analysis would reveal unambiguously significant relationships between WL's and the other variables.

The data set was broken into sets, with the June 4-6 data being subjected to computer analysis. The derived multiple correlation equations were then applied to the June 7-9 data to see if they fit as well as they fit the data from which they were generated. A number of models were examined to determine correlations between the WLB, or WLL, and various combinations of temperatures, humidities, atmospheric pressures, and ventilation conditions.

Multiple correlation equations were obtained which had rather high correlation coefficients (adjusted R-square values of 0.8-0.9) and in which all beta coefficients were significant at the 0.0001 level. Use of the Durbin-Watson statistic showed, however, that errors in measurements of WL's are strongly autocorrelated (d = 0.7-0.8). Presence of autocorrelation in time-series data such as collected in the present study is not surprising. It is clear that one of the main factors determining the value of a working level measurement in a given hour is the value it had in the previous hour. (Or, other things being equal, if a WL is high in one hourly period, it will also be high in the next hourly period.) When autocorrelation is present, the residual error estimate is inflated and tests on the parameters are ess able to reject the null hypothesis. This means that the values of the correlation coefficients are questionable.

It was decided to try to eliminate autocorrelation by using, not the hourly working levels themselves, but changes in the working level from hour to hour. Models were tested to establish the dependence of hourly changes in the basement working level (CWLB) on the following variables: hourly change in living room working level (CWLL); ratio of WLB/WLL (RWL); hourly change in atmospheric pressure (CP); change in basement temperature (CTB); change in liing room temperature (CTL); changes in relative humidity in basement and living room (CHB and CHL); ratio of basement temperature to living room temperature (RT); ratio of basement humidity to living room humidity (RH); ventilation conditions (OC = +1 for closed house; OC = -1 for open); temperature differentials (THC = +1 if warmer in living room; THC = -1 if cooler); and relative humidity differentials (HWD = +1 if more humid in living room; HWD = -1 if less humid). In addition, several of the independent variables were lagged. For example, in some models CP1 or CP2 (hourly changes in pressure one hour or two hours, respectively, before the measured change in basement working level were used in place of CP. This was an attempt to account for the fact that changes in WL are expected to lag behind corresponding changes in parent radon concentrations.

No significant relationship could be established between most of these variable and the CWLB. The best fit was obtained for the model with CWLB a function of OC1 (working level in the basement decreasing one hour after house was opened, increasing one hour after house was closed) and THC (working level in basement increasing during periods when living room was warmer than basement, decreasing when living room was cooler than basement). Although the multiple correlation coefficient is not high (adjusted R-square = 0.26), both OC1 and THC

are significantly correlated to CWLB (0.01 significance level). Furthermore, analysis shows very little collinearity among the variables, and the absence of autocorrelation (d = 1.702) (See Table 3).

Although the variables are not strongly correlated, they are significantly correlated, and the multiple regression equation has some predictive capability. Figure 5 shows a plot of measured CWLB's for June 4-6 versus CWLB's predicted by Eqn (5). Figure 6 shows corresponding plots for the control set of data, June 7-9.

The best fit obtained for hourly changes in the living room working level (CWLL) was for a model with CWLL a function of CWLB (living room working level increasing or decreasing as basement working level increases or decreases) and OC (living room working level decreasing when house is opened, increasing when house is closed). For this model adjusted R-square is 0.23. The variables CWLB and OC are correlated to CWLL at the 0.05 and 0.01 levels, respectively (See Table 4).

A plot of measured CWLL's versus CWLL's predicted by Eqn (6) is shown for the June 4-6 data in Figure 7.

There appear to be two major reasons why the correlation coefficients are not higher:

1. The most significant influence on both dependent variables (i.e., micropressure differences outside and inside the house) is not included; and

2. Random counting scatter for low numbers of alpha disintegrations affect the apparent direction of change in working level from hour to hour. If counting error is large, one monitor can report an increase in WL while the other reports a decrease in WL

Table 3. Change in Working Level in Basement as a Function of Ventilation Conditions and Temperature Differentials

Multiple Regression Equation:

$$CWLB = -4.84 + 5.66(OCl) + 4.76(THC) \quad (5)$$

Degrees of Freedom:	71
F Value:	13.788
Prob. Greater Than F:	0.001
Adj. R-Square:	0.2648

Variable	Prob. Greater T	STZD Est.	VIF
Intcpt	0.0067	0	0
OCl	0.0008	0.38	1.10
THC	0.0094	0.28	1.10

Durbin-Watson D	1.716
Autocorrelation	0.142

during a given hour, even though both WL's might actually remain unchanged (See Figure 1).

This second reason can also explain why the individual beta coefficients in Eqns (5) and (6) do not show greater significance.

An experiment similar to the one described above had been carried out in the same house during May 28-31, 1986. In this case WLM's No. 306 and 372 weere programmed to count for 96 consecutive 60-minute periods. No. 306 was placed in the crawl space of the test residence, directly on the ground. No. 372 was placed on the floor of the dinig room exactly above No. 306. Pressures, temperatures, and relative humidities of the two areas were monitored, and a log was kept of times when the house was opened and closed.

In this experiment the dining room temperature was greater than the crawl space temperature throughout the 96-hour period, making it impossible to test for a correlation between working levels and temperature differentials. As Figure 8 shows, however, there is a rough proportionality between WL's in the crawl space and in the dining room. Working levels in both areas seem to increase during periods when the house is closed, and decrease when it is opened.

Multiple regression analysis showed that changes in working level in the crawl space (CWLC) are weakly, but significantly correlated with ventilation rates one hour previous (OC1) (R-square = 0.12). Changes in dining room working level (CWLD) are weakly corelated with CWLC and with OC (R-square = 0.19).

Figure 5. Measured CWLB's VS. Predicted CWLB's (Equation 5)

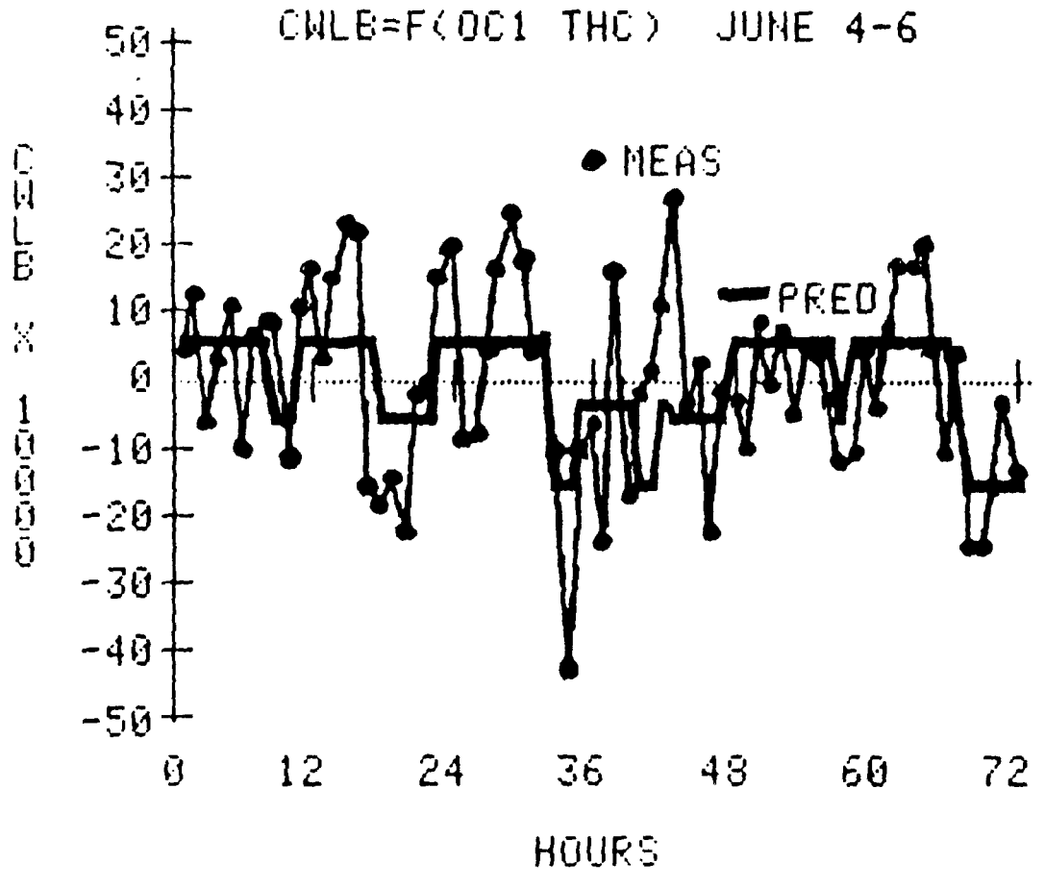

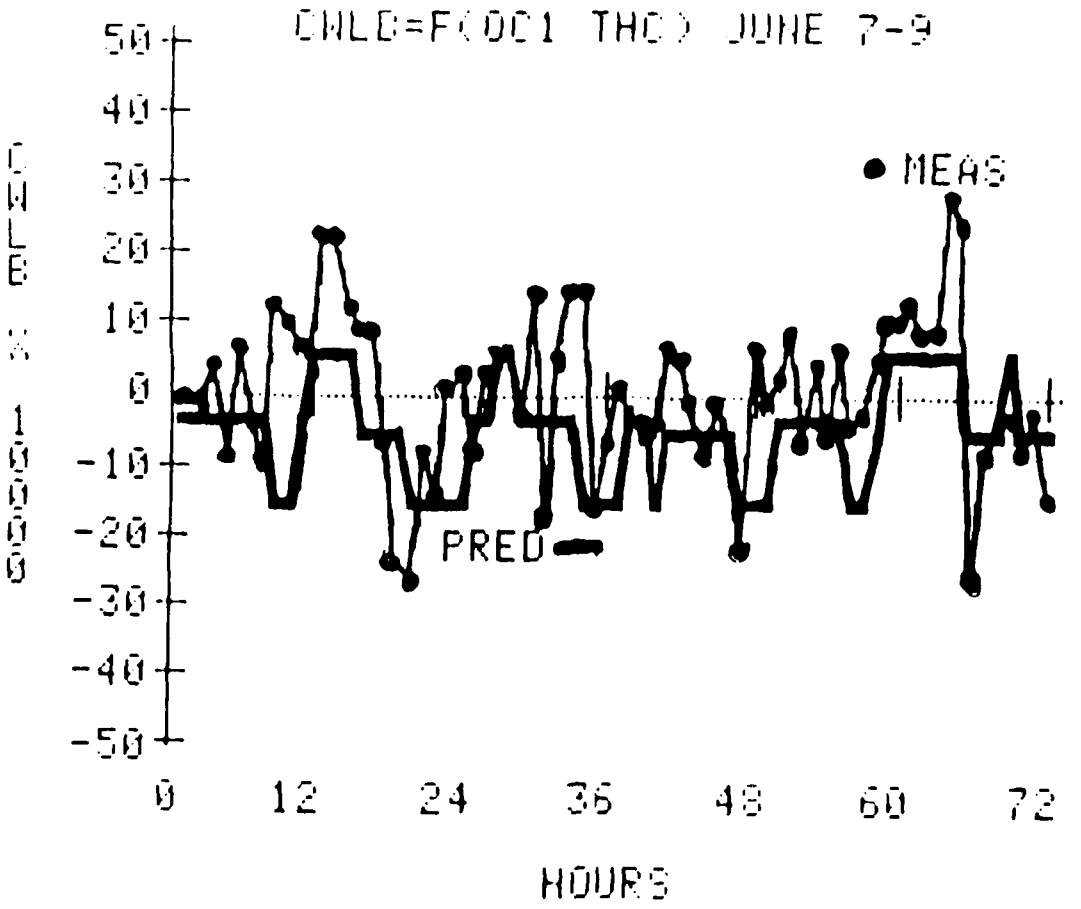
DNLB=F(DC1 THC) JUNE 7-9
DNLB = 1000.0
50
40
30
20
10
0
-10
-20
-30
-40
-50
MEAS
PRED
0
12
24
36
48
60
72
HOURS

Table 4. Change in Working Level in Living Room as a Function of Ventilation Conditions and Change in Working Level in Basement

Multiple Regression Equation

$$CWLL = -0.752 + 0.0725(CWLB) + 1.97(OC) \qquad (6)$$

Degrees of Freedom:	71
F Value:	11.858
Prob. Greater Than F:	0.0001
Adj. R-Square:	0.2342

Variable	Prob. Greater T	Stzd. Est.	VIF
Intcpt	0.1543	0	0
CWLB	0.0478	0.22	1.10
OC	0.0005	0.40	1.10

Durbin-Watson D	2.231
Autocorrelation	-0.118

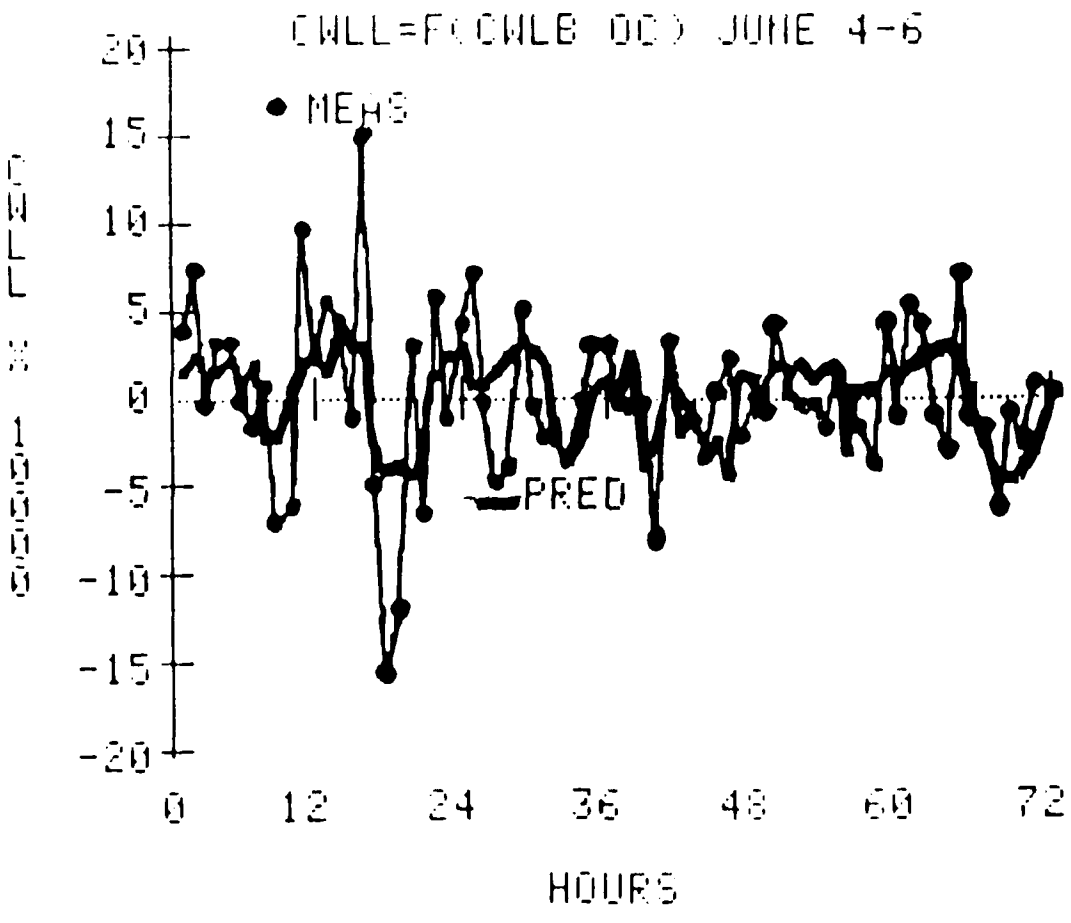
CWLL=F(CWLB OD) JUNE 4-6
MEAS
PRED
20
15
10
5
0
-5
-10
-15
-20
0
12
24
36
48
60
72
HOURS

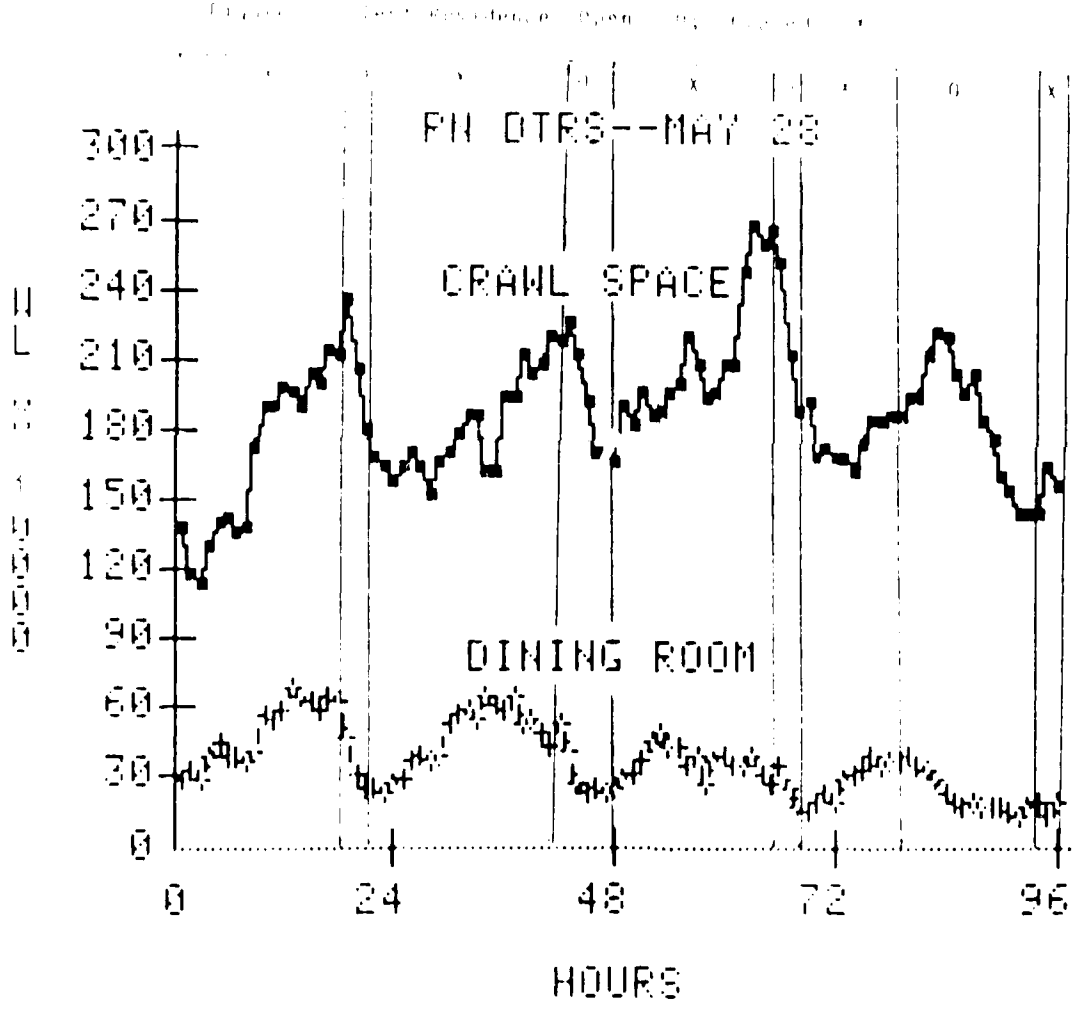
PH DTRS--MAY 28
CRAWL SPACE
DINING ROOM
300
270
240
210
180
150
120
90
60
30
0
0
24
48
72
96
HOURS

Over the 4-day period, working levels in the crawl space ranged between 0.0114 and 0.0267 WL, with an average value of 0.0183 WL. Working levels in the dining room ranged from 0.0013 to 0.0079 WL, with an average of 0.00352 WL. Ratios of WLD/WLC ranged between 0.07 and 0.38, with an average value of 0.19.

D. Conclusions

1. Working levels on the first floor of the test house are proportional to working levels in the basement and crawl space, with first floor levels averaging 10-20% of the working level in the lower areas.

2. Ventilation of the house by opening of doors and windows on the upper levels causes an immediate decrease in working level on the first floor. This is followed by a decrease about one hour later in working level in the basement and crawl space.

3. When temperatures on the first floor are higher than temperatures in the lower areas, there is a buildup of working level in the basement and crawl space.

4. Neither ventilation to the outside nor temperature differentials within the house have as much effect on indoor working levels as do micropressure differences inside and outside the house.

V. A SURVEY OF INDOOR RADON LEVELS IN SOUTHWEST MISSOURI

A. Introduction

In the past few years, measurements on thousands of U.S. homes have found that a large number contain radon at hazardous concentrations (3). It has been estimated that an average indoor radon concentration is 1.2 pCi/l and that approximately 1 million homes have concentrations exceeding 8 pCi/l (16).

Few, if any, measurements of indoor radon in Missouri have yet been reported. This part of the research effort was carried out to determine the magnitude and range of indoor radon concentrations in southwest Missouri. During the 6-month period from March to September, 1986 radon screening measurements were made on 48 residences, schools, and office buildings in Springfield, Missouri, and on 3 residences outside Springfield in southwest Missouri. The findings of this survey are reported below.

B. Experimental Procedures

1. Apparatus

The Lucas alpha-scintillation method (9) was chosen for the measurement of airborne radon. A portable sampling kit was assembled from the following components: Ludlum Model 2200 battery-operated scaler; Ludlum Model 182 radon flask counter; four 100-ml Lucas-type scintillation cells (Rocky Mountain Scientific Glass Blowing Company, Aurora, Colorado). The assembled apparatus weighs approximately 20 pounds and can be hand carried in a standard 8" X 18" X 24" metal instrument case.

The Lucas cell is a cylindrical flask constructed from a Kovar seal. The inner surface is coated with silver-activated zinc sulfide. A quartz window with a transparent tin oxide coating on its inner surface is sealed to one end of the cell. The other end has a stopcock to permit evacuation of the air-tight cell. The cell is placed in a light-tight chamber on the window of a photomultiplier tube, and alpha scintillations produced by radon and its daughters (polonium-218 and polonium-214) are counted. The counting efficiency of such flasks is typically 0.6-0.7 cpm/dpm.

2. Measurement Techniques

Airborne radon concentrations were calculated by the method of Jonassen and Clements (17). This method does not require that secular equilibrium be established between radon and its daughters before counting begins. If the initial sample of radon is free of daughter products at the time it is introduced into the ounting cell, the counting period can start any time after sampling. (If the sample initially consists of a mixture of radon and its daughters, 3-4 hours must be allowed for attainment of equilibrium before ounting begins.)

The equation relating initial radon concentration to number of alpha scintillations in a given time period is:

$$Rn(pCi/l) = C/(2.22)(E)(V)(G) \quad (7)$$

where G = 23904.80625(EXP((-0.0001259)(T1))
EXP((-0.0001259)(T1 + T2)))
-4.50748(EXP((-0.2272)(T1))
-EXP((-0.2272)(T1 + T2)))
-165.5195(EXP((-0/02586)(T1))
-EXP((-0.02586)(T1 + T2)))
+93.65601(EXP((-0.03518)(T1))
-EXP((-0.03518)(T1 + T2))) (7a)

and T1 is the time (minutes) between sample collection and beginning of counting; T2 is the counting interval (minutes); C is the number of net counts in T2 (total counts minus background counts); E is the counter efficiency (cpm/dpm); and V is the volume of the Lucas cell (liters).

These equations were programmed into a Hewlett-Packard 15C handheld calculator so that calculation of a radon concentration requires less than one minute.

The experimental procedure for the determination of airborne radon is as follows: A Lucas cell is flushed several times with nitrogen, evacuated, and counted in a Ludlum radon flask counter. Typical background levels of evacuated flasks are 0.1-0.3 counts per minute. A 0.45 micron Millipore filter is attached to the ball joint of the evacuated cell and the stopcock is opened to obtain a grab sample of air. The stopcock is closed and the time recorded. The sample is stored for three hours to allow secular equilibrium to be reached. The cell is then counted for a period of 2 to 12 hours and the initial radon concentration is calculated using Eqns(7) and (7a). The counting times were selected so that counting errors averaged +/- about 20% standard deviation or less.

3. Testing and Verification of Instruments and Methods

The radon counting apparatus was calibrated by interlaboratory comparison using a standard test cell which had been calibrated at the Randam Corporation laboratory. Efficiency of the apparatus was found to be about 0.64 cpm/dpm.

Experiments were carried out to determine the sensitivity and reproducibility of the apparatus. For environmentally significant radon concentrations (down to about 1 pCi/l), the counting rate is likely to be small. As an example, for a counter efficiency of 0.64 and a Lucas cell of 100 ml volume, the number of counts produced by 1 pCi/l of radon in equilibrium with its two alpha-emitting daughters can be calculated as

1 pCi/l X 0.100 L X 3(2.22 dpm/pCi) X 0.64 cpm/dpm = 0.43 cpm. Statistical fluctuations are large at such counting rates, although precision can be improved by using longer counting intervals. The minimum detectable activity is related to the background count. Calculation of representative minimum detectable concentrations of airborne radon showed that sensitivity is low for short counting times and increases with longer counting intervals. Experiments showed that for radon concentrations of about 0.02 to 4 pCi/l, counting intervals of 2 to 12 hours give calculated percent errors of about 20% or less.

C. Survey Results and Discussion

Measurements of indoor radon concentrations were carried out using the apparatus described above. A total of 24 measurements taken in 16 office buildings, churches, and schools in Springfield, Missouri showed values ranging from ().3() t;o 7.15 pCi/l, with only one measurement being greater than 4 pCi/l (Table 5).

Seventeen measurements on 8 multistory houses in Springfield had radon levels ranging between 0.33 and 5.84 pCi/l, with three of the house having more than 4 pCi/l of radon (Table 6).

Table 7 shows results of 16 measurements on 8 Springfield single-story houses which had basements. Values ranged from 0.28 to 3.87 pCi/l, and none was greater than 4 pCi/l. On the other hand, 24 measurements on 8 Springfield houses without basements (Table 8) yielded values ranging from less than .2 up to 14.3 pCi/l (the highest value measured in this study). Four houses had radon levels greater than 4 pCi/l, but all were in crawl spaces.

TABLE 5. INDOOR RADON MEASUREMENTS IN 16 OFFICE BUILDINGS CHURCHES AND SCHOOLS

LOCATION	NUMBER	RADON (pCi/L) RANGE	GEOMETRIC MEAN	No. > 4 pCi/L
BASEMENTS	12	0.38-7.15	1.06	1
UPPER FLOORS	12	0.30-2.15	0.61	0
ALL BUILDINGS	16	0.30-7.15		1

TABLE 6. INDOOR RADON MEASUREMENTS IN 8 SPRINGFIELD, MISSOURI, MULTISTORY HOUSES

LOCATION	NUMBER	RADON (pCi/L) RANGE	GEOMETRIC MEAN	No. > 4 pCi/L
CRAWL SPACE	1	2.61-4.65	-	1
BASEMENT	7	0.81-5.74	2.48	2
1ST FLOORS	6	0.33-3.48	0.80	0
2ND FLOORS	3	1.23-5.84	2.39	1
ALL HOUSES	8	0.33-5.84		3

TABLE 7. INDOOR RADON MEASUREMENTS ON 8 SPRINGFIELD, MISSOURI SINGLE-STORY HOUSES WITH BASEMENTS

LOCATION	NUMBER	RADON (pCi/L) RANGE	GEOMETRIC MEAN	No. > 4 pCi/L
BASEMENTS	8	0.53-3.87	1.54	0
1ST FLOORS	8	0.28-3.86	0.81	0
ALL HOUSES	8	0.28-3.87		0

TABLE 8. INDOOR RADON MEASUREMENTS ON 16 SPRINGFIELD, MISSOURI SINGLE-STORY HOUSES WITHOUT BASEMENTS

LOCATION	NUMBER	RADON (pCi/L) RANGE	GEOMETRIC MEAN	No. >4 pCi/L
CRAWL SPACE	8	0.27-14.3	2.68	4
1ST FLOOR	16	0.10-2.59	0.73	0
ALL HOUSES	16	0.10-14.3		4

Only three houses outside Springfield were measured (Table 9). Radon values ranged from 0.24 to 4.80 pCi/l in the three houses, and one had radon in a living area at levels greater than 4 pCi/l.

Table 10 summarizes indoor radon data obtained on all residences in southwest Missouri. In general, radon concentrations were found to be highest in basements and lowest on first floors, with second floors having intermediate values.

A summary of all indoor radon measurements is shown in Table 11. Only three houses had radon levels greater than 4 pCi/l in areas which were being used as living quarters. This represents about 6% of the 51 buildings measured.

VI. RECOMMENDATIONS AND PLANS FOR FUTURE INVESTIGATIONS

The Eberline Instrument Corporation believes that it has now modified the WLR-1-A so that the working level monitoring system wil give reliable, accurate, reproducible results (private communication). Once the modified system has been field-tested, it will be used to continue investigating the influence of temperature differentials within a building on radon daughter distribution. Measurements will also be made in the laboratory on a simulated multistory house in which temperatures and humidities in different parts of the "house" will be controlled and varied. Also, a method needs to be developed for dealing with autocorrelation in working level measurements without introducing noise from random counting errors. This line of investigation will be pursued further.

TABLE 9. INDOOR RADON MEASUREMENTS ON 3 SOUTHWEST MISSOURI HOUSES OUTSIDE SPRINGFIELD

SITE	RADON (PCI/L) RANGE	AVERAGE	NO. >4 PCI/L
NIXA, MISSOURI	0.24-0.75	0.50	0
BRANSON, MISSOURI	3.99-4.80	4.40	1
DOUGLAS COUNTY, MO.	0.32-1.58	0.95	0

TABLE 10. SUMMARY OF INDOOR RADON IN RESIDENCES, S.W. MISSOURI

NO. BASEMENTS MEASURED:	15
NO MEASUREMENTS MADE:	30
RANGE OF VALUES:	0.53-5.74
NO. 1ST FLOORS MEASURED:	33
NO. MEASUREMENTS MADE:	55
RANGE OF VALUES:	0.10-4.80
NO. 2ND FLOORS MEASURED:	3
NO. MEASUREMENTS MADE:	7
RANGE OF VALUES:	0.33-5.84

TABLE 11. SUMMARY OF INDOOR RADON MEASUREMENTS, S.W. MISSOURI

NO. BUILDINGS MEASURED:	51
NO. MEASUREMENTS MADE:	143
RANGE OF VALUES (PCI/L):	0.10-14.3
NO. BUILDINGS > 4 PCI/L:	9 = 18%
NO. LIVING QUARTERS > 4 PCI/L:	3 = 6%

The present investigator also intends to work on development of a method which will permit continuous determination of the unattached fraction of daughters within a house. This will be done by replacing the filter paper on a WLM-1-A monitor with a 60-mesh wire screen, so that only charged, unattached daughters will be removed from the ambient and counted. Simultaneous sampling with a modified and an unmodified filter will allow determination of the unattached fraction of daughters, as well as their total concentrations.

Finally, screening of buildings for radon and radon daughters will continue in southwest Missouri. One of the objectives of this survey will be to determine whether houses built on the Northview shale outcroppings which occur in parts of southwest Missouri have higher radon levels than do houses built on the more prevalent limestone soil.

ACKNOWLEDGEMENTS

Research described in this report was sponsored by the Air Force Office of Scientific Research, Bolling AFB, DC, under Contract No. F49620-85-C-0013/SB5851-0360, Subcontract No. S-760-OMG-032. The author would also like to acknowledge support of the Southwest Missouri State University Foundation. Professor Doris E. Files, Department of Economics, Southwest Missouri State University, deserves special thanks for discussions and advice concerning the multiple regression procedures. Finally, the author thanks Lori Outzs and Sarah Thompson for their help in collecting some of the data used in this report.

Some of the results in this report were discussed in papers presented at the 1986 Annual Meeting of the Missouri Academy of Science and at the 21st Midwest Regional Meeting of the American Chemical Society.

REFERENCES

1. Hillman, B., Environmental Science and Technology , Volume 17, 1983, pp. 469A-472A.

2. National Council on Radiation Protection and Measurements, Exposure From the Uranium Series With Emphasis on Radon and its Daughters, NCRP Report No. 77 , National Council on Radiation Protection and Measurements, Washington, D.C., 1984.

3. Nero, A.V., "Indoor Radiation Exposures from 222-Rn and its Daughters: A View of the Issue," Health Physics , Volume 45, 1983, pp.277-288.

4. Gesell, T.F., "Background Atmospheric 222-Rn Concentrations Outdoors and Indoors: A Review," Health Physics , Volume 45, 1983, pp. 289-302.

5. Lundin, F.E., J.K. Wagoner, and V.E. Archer, Radon Daughter Exposure and Respiratory Cancer: Quantitative and Temporal Aspects , United States Public Health Service, Washington, D.C., 1971.

6. The Land and Water Resources Center, Radon in Water and Air, Health Risks and Control Measures, Resource Highlight , University of Maine, Orono, Maine, 1983.

7. Chamberlain, A.C. and E.D. Dyson British Journal of Radiobiology , Volume 29, 1956, p. 317.

8. Environmental Protection Agency, A Citizen's Guide to Radon , Washington D.C., 1986, p. 7.

9. Lucas, H.F., "Improved Low-Level Alpha-Scintillation Counter for Radon," Review of Scientific Instruments , Volume 28, 1957, pp. 680-683.

10. Downard, T.R., F.L. Geiger, and J.R. Millard, "Field Evaluation of

Eberline's Radon Daughter Working Level Monitor," Unpublished document No. IP-70, Eberline Instrument Division, Santa Fe, New Mexico, 1984.

11. Eberline Instrument Division of Thermo Electron Corporation, Working Level Monitor Technical Manual , Santa Fe, New Mexico, 1986.

12. Thomas, J.W., "Measurement of Radon Daughters in Air," Health Physics , Volume 23, 1972, pp. 783-789.

13. Moschandreas, D.J., and H.E. Rector, Radon and Aldehyde Concentrations in the Indoor Environment , Lawerence Berkeley Laboratory Report LBL-12590, Berkeley, California, 1981.

14. Evans, R.B., "Engineer's Guide to the Elementary Behavior of Radon Daughters," Health Physics , Volume 17, 1969, p.229.

15. Mueller Associates, Inc., Indoor Air Quality Environmental Information Handbook: Radon , U.S. Department of Commerce DE86-005006, National Technical Information Service, Washington, D.C., 1986.

16. Nero, A.V., Jr., "The Indoor Radon Story," Technology Review , Volume 89, 1986, pp. 28-40.

17. Jonassen, N., and W.E. Clements, "Determination of Radon-222 Concentrations by an Integrated Count Method," Health Physics , Volume 27, 1974, pp. 347-351.

USAF/UES Research Initiation Program

Sponsored by the
Air Force Office of Scientific Research

Conducted by
Universal Energy Systems, Inc

Final Report

Reliability of Systems with Random Transfer of Control

Kyle Siegrist
Department of Mathematics and Statistics
University of Alabama in Huntsville
Huntsville, Alabma 35899
(205) 895-6470

Rome Air Development Center
Systems Reliability and Engineering Branch
Reliability and Maintainability Techniques Section
Griffiss Air Force Base, New York 13441

June 30, 1986

Contract No F49620-85-C-0013
Subcontract No S 760 OMG 013

Reliability of Systems with Random Transfer of Control

Summary and Conclusions

The research described in this report was conducted under the Research Initiation Program sponsored by the Air Force Office of Scientific Research and conducted by Universal Energy Systems, Inc. (Contract No. F49620-85-C-0013, Subcontract No S-760OMG-013). The research was a continuation of work begun at the Systems Reliability and Engineering Branch of the Rome Air Developnment Center, Griffiss, AFB, NY during the Summer of 1985 under the USAF/UES Summer Faculty Research Program.

The research concerns the reliability of systems (software, hardware, or combined systems) which can be decomposed into a finite number of modules with control of the system randomly transferred among the modules. Thus, the model treated here differs from classical network reliability models which assume that all modules or states are active at all times. The report is divided into three parts.

In the first part, it is assumed that control of the system is transferred among the modules according to a Markov process. Each module has an associated reliability which gives the probability that the module will operate correctly when called and will transfer control successfully when finished. It is also assumed that the system has a terminal module which corresponds to mission success. The reliability of the system is defined to be the probability that the system reaches the terminal module without

failing and it studied in terms of the module reliabilities and the transition probabilities. Improved methods of predicting system reliability, allocating module reliability, and determining module sensitivity are developed which take advantage of the network structure of the system. A measure of inherent sensitivity is developed which is based on the transition probabilities alone and which can be used to estimate the sensitivity of the modules before their reliabilities are known. Special branching and sequential systems are studied in detail. The first part is an improvement of the report issued at the end of the USAF/UES Summer Faculty Research Program.

In the second part, it is again assumed that control of the system is transferred among the modules according to a Markov process, and that each module has an associated reliability. However, it is assumed that the system does not have a terminal module; rather the system operates continuously until it fails. The mean number of transitions until failure is used as a measure of system reliability and is studied in terms of the module reliabilities and the transition probabilities. As in the first part, methods of predicting system reliability, allocating module reliability, and determining module sensitivity are developed. Special branching and sequential systems are studied in detail. The techniques and results in the second part parallel those in the first part.

In the third part, general systems with random transfer of control are studied. It is assumed that the transfer of control among the modules is caused by external inputs and is random only becaused the inputs are unknown. Specifically, it is assumed that

the input sequence is a stochastic process and that, when an input is received, the system goes to a new state which is a deterministic function of the old state and the input. Thus, the state sequence is a stochastic process which is driven by the input sequence. A reliability framework is imposed on the model by assuming that for each state of the system there is a set of inputs which would cause the system to fail if it is in that state. It is shown that if the inputs are statistically independent, then the state sequence is a Markov chain and hence either the model of the first part or the second part applies (depending on whether there are terminal states). However, the assumption of statistically independent inputs is unrealistic. It is shown that if the inputs are correlated then the state sequence may not satisfy the Markov property and hence the application of the models in the first two parts is questionable. It is also shown that if the input sequence is a Markov process (a more realistic assumption) then the joint state-input sequence is also a Markov processs. In theory, system reliability could be studied in terms of the joint process, but this would involve knowning the transition probabilities of the input sequence and this information is unlikely to be available in practice.

In conclusion, the Markov chain models studied in the first two parts are mathematically well developed and can yield quite explicit results. However, there are mathematically compelling reasons to question the assumption of Markov transfer of control for systems whose transitions are driven by correlated inputs. Hence the Markov models should be used with care. In addition, more study is needed to understand the stochastic behavior of such systems.

Part I
Reliability of Systems with Markov Transfer of Control and with Terminal States

Introduction

This part considers a model, originally proposed by Cheung [1], for software systems which can be decomposed into a finite number of functionally independent modules. There are two main assumptions. First, it assumed that control of the system is transferred among the modules according to a Markov chain. The Markov property means that given knowledge of the module in control at any given time, the future behavior of the system is conditionally independent of the past behavior. Second, it is assumed that the system has a terminal module corresponding to mission success. That is, ideally the system will eventually complete its task successfully and enter the terminal state.

The terminal module will be denoted by T and the remaining (transient) modules by the integers 1, 2, ..., n. Thus, the dynamics of the ideal system are described by a Markov chain with state space {1, 2, ..., n, T} and transition matrix P. That is, P_{ij} is the probability that control will next be passed to module j, given that module i has control. Since T is absorbing, $P_{TT} = 1$. All other states eventually lead to T. Usually the system will have a designated initial module.

Next it is assumed that each of the transient modules 1, 2, ..., n is failure prone. Specifically, module i has an associated reliability R_i which is the probability that the module will operate

correctly when called and will transfer control successfully when finished. Equivalently, the system has probability $1-R_i$ of failing each time it enters state i. Mathematically, the imperfect system is modeled by adding an absorbing state F (failure) and by modifying the transition probabilities appropriately. Specifically, the imperfect system is described by a Markov chain with state space {1, 2, ..., n, T, F} and transition probability matrix $\hat{P}$ given as follows

$$\hat{P}_{ij} = R_i P_{ij} \text{ for } i = 1, \ldots, n \text{ and } j = 1, \ldots, n, T;$$

$$\hat{P}_{iF} = 1-R_i \text{ for } i = 1, \ldots, n;$$

$$\hat{P}_{TT} = 1, \hat{P}_{FF} = 1.$$

Thus, the dynamics of the imperfect system are completely described by the module reliability function R and the ideal transition matrix P, since this description is equivalent to specifying the transition matrix $\hat{P}$ of the imperfect system. Note that T and F are absorbing states and that the transient states 1, 2, ..., n lead to T and F.

System reliability is defined to be the probability that the system eventually completes its task successfully without failing. Mathematically, this is simply the probability that the Markov chain for the imperfect system is eventually absorbed into T rather than F. The purpose of the model is the study of system reliability in terms of the module reliabilities and the ideal transition probabilities.

Cheung [1] developed a method of computing system reliability

and a method of computing the sensitivity of system reliability with respect to a given module reliability. These methods are satisfactory for numerical results, but are not well suited for obtaining explicit analytical results. In this paper, alternative methods will be developed which can lead to such explicit results. In addition, a measure of "inherent" sensitivity will be developed which depends only on the ideal transition probabilities. A simple method of allocating module reliability to meet a given system reliability demand will be given. Finally, these methods will be applied to general branching and sequential systems.

As noted above, one of the main assumptions of the model is the existence of a terminal state corresponding to mission success. However, there are systems which have no such natural terminal state, systems which run more or less continuously (until failure). For such systems, a better model is the semi-Markov model of Littlewood [5] with mean time to failure as the measure of reliability. Another, simpler approach is to consider a discrete Markov chain as described here, except without an absorbing terminal state and with the mean number of transitions until failure as the measure of reliability. This model will be treated in Part II.

System Reliability

For each transient state $i = 1, 2, \ldots, n$ let ρ_i denote the probabiltiy that the Markov chain for the imperfect system, starting in state i, is eventually absorbed into T (i.e., the probability that the system eventually completes its task successfully). Thus ρ is

the system reliability function.

The method of computing ρ given in [1] will be reviewed briefly. It is based on a standard method of computing absorption probabilities for a Markov chain; a derivation may be found in [2].

Let $\hat{Q}$ denote the restriction of the transition matrix $\hat{P}$ of the imperfect system to the transient states 1, 2, ..., n. Note that $\hat{Q}_{ij} = R_i Q_{ij}$ where Q is the restriction of the transition matrix P of the ideal system to the transient states. The matrix

$$\sum_{k=0}^{\infty} \hat{Q}^k = (I - \hat{Q})^{-1} \qquad (1)$$

is called the potential matrix of the imperfect system; its ij value gives the expected number of visits to j by the imperfect system starting in state i. Of course, similar remarks apply to the potential matrix of the ideal system, obtained by replacing $\hat{Q}$ with Q in (1).

For each transient state i, let $G_i = \hat{P}_{iT} = R_i P_{iT}$ denote the probability of going to the terminal state T from state i in one step for the imperfect system. Using the notation of matrix multiplication,

$$\rho = (I - \hat{Q})^{-1} G$$

In particular, if state i is the initial state, then the system reliability is

$$\rho_i = \sum_{j=1}^{n} (I - \hat{Q})^{-1}_{ij} G_j.$$

Another method of computing system reliability will now be

given. Suppose that the initial state is i. Let j be any specified transient state (j may be i). Then a simple application of the Markov property shows that

$$\rho_i = A_{ij} + B_{ij}\rho_j \tag{2}$$

where A_{ij} is the probability, starting in state i, of eventually reaching the terminal state T without reaching state j first and where B_{ij} is the probability, starting in state i, of eventually reaching state j. If i = j, "reaching state j" should be interpreted as "returning to state j" in which case we obtain from (2)

$$\rho_j = A_{jj}/(1-B_{jj}).$$

Substituting this result back into (2) gives the desired result:

$$\rho_i = A_{ij} + B_{ij}A_{jj}/(1-B_{jj}) \tag{3}$$

Each of these quantities is defined in terms of the imperfect system. Schematically, Equation 3 is represented in Figure 1 below where the wavy lines indicate that these are not necessarily one step transitions. Indeed many transitions may be involved.

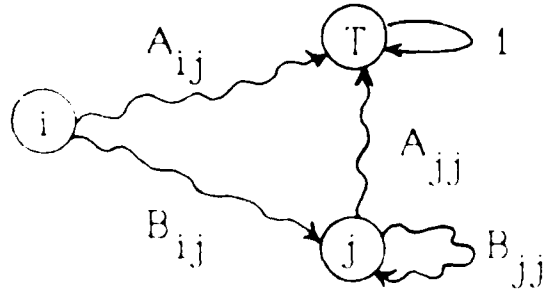

Figure 1. Schematic Representation of Equation 3.

From the Markov property, the matrices A and B are related to the basic data R and P according to the following systems of equations:

$$A_{ij} = R_i P_{iT} + \sum_{k \neq j} R_i P_{ik} A_{kj}; \tag{4}$$

$$B_{ij} = R_i P_{ij} + \sum_{k \neq j} R_i P_{ik} B_{kj}. \tag{5}$$

Moreover, $B_{ij}/(1-B_{jj})$ is the same as $(I-\hat{Q})^{-1}_{ij}$, namely the expected number of visits to state j for the imperfect system starting in state i.

The method of using Equation 3 for computing system reliability is important for two reasons. First, it may turn out that for some state j (such as a state which acts as a central control), the quantities A_{ij}, B_{ij}, A_{jj}, B_{jj} can be computed explicitly in terms of the ideal transition probabilities and the state reliabilities. Second, of the four quantities in (3) only two, A_{jj} and B_{jj} depend on R_j, the reliability of state j. Specifically note from (4) and (5) that if $i \neq j$, then A_{ij} and B_{ij} do not depend on R_j. If $i = j$, (4) and (5) give

$$A_{jj} = R_j[P_{jT} + \sum_{k \neq j} P_{jk} A_{kj}],$$

$$B_{jj} = R_j[P_{jj} + \sum_{k \neq j} P_{jk} B_{kj}].$$

Letting $\tilde{A}_{jj} = P_{jT} + \sum_{k \neq j} P_{jk} A_{kj}$ and $\tilde{B}_{jj} = P_{jj} + \sum_{k \neq j} P_{jk} B_{kj}$, we see that (3) can be rewritten in the form

$$P_i = A_{ij} + B_{ij} R_j \tilde{A}_{jj} / (1 - R_j \tilde{B}_{jj}) \tag{6}$$

where $\tilde{A}_{jj}$, $\tilde{B}_{jj}$, and (if $i \neq j$), A_{ij}, B_{ij} are independent of R_j. Thus, Equation 6 allows us to isolate the effect of the reliability of state j on total system reliability and will be important in the sensitivity and allocation problems to be considered next.

Sensitivity

Suppose that state i is the initial state. The *sensitivity* of any transient state j is defined to be $\partial\rho_i/\partial R_j$ the partial derivative of system reliability with respect to the reliability of state j. This quantity is a measure of how sensitive system reliability ρ_i will be to small changes in the reliability R_j of state j.

In [1] various determinant expansions were used to obtain a formula for the sensitivity of a state. Another method of computing sensitivity, which is better for analytic purposes, can be obtained from (6). If $i \neq j$, then

$$\partial\rho_i/\partial R_j = B_{ij}\tilde{A}_{jj}/(1-R_j\tilde{B}_{jj})^2 = B_{ij}\tilde{A}_{jj}(1-B_{jj})^2 \qquad (7)$$

and if $i = j$

$$\partial\rho_i/\partial R_i = \tilde{A}_{ii}/(1-R_i\tilde{B}_{ii})^2 - \tilde{A}_{ii}/(1-B_{ii})^2. \qquad (8)$$

The quantity $B_{ij}/(1-B_{jj})$ is the expected number of visits to state j starting in state i for the imperfect system while $1/(1-B_{ii})$ is the expected number of visits to i starting in i. Therefore if a state is visited a large number of times on average, then system reliability will be very sensitive to inaccuracies in the reliability of that state.

The terms A_{ij} and B_{ij} will in general be complicated functions of the state reliabilities and the ideal transition probabilities. It would be helpful to have an inherent measure of the sensitivity of a state which could be obtained from the ideal transition probabilities alone and which could be used before the state reliabilities are measured. Since, hopefully, we anticipate that the state reliabilities will be near 1, a natural measure of the inherent sensitivity of state j is $\partial\rho_i/\partial R_j$ evaluated with $R_k = 1$ for all $k = 1, 2, \ldots, n$. Note that when all state reliabilities are set equal to 1, A_{ij} becomes a_{ij} and B_{ij} becomes b_{ij} where a_{ij} and b_{ij} have the same meanings as A_{ij} and B_{ij} respectively, except relative to the ideal (failure free) system rather than the imperfect system. Also, of course, $\tilde{A}_{jj} = A_{jj} = a_{jj}$ and $\tilde{B}_{jj} = B_{jj} = b_{jj}$. Finally, note that $a_{jj} = 1 - b_{jj}$ since if the ideal system does not return to j, then it must be absorbed into T without reaching j. Therefore, substituting into (7) and (8), we obtain the following expressions for the *inherent sensitivity* of state j, starting in state i, denoted S_{ij}. If $i \neq j$, then

$$S_{ij} = b_{ij}/(1-b_{jj}). \tag{9}$$

If $i = j$, then

$$S_{ii} = 1/(1-b_{ii}). \tag{10}$$

However, the expressions in (9) and (10) represent the expected number of visits to state j, starting in the initial state i for the ideal system. Therefore we also have

$$S_{ij} = (I-Q)^{-1}_{ij}$$

where Q is the restriction of the ideal transition matrix P to the transient states.

In summary, the expected number of visits to state j by the ideal system is a measure of the inherent sensitivity of state j. It will be near the true sensitivity of state j for an imperfect system in which all of the state reliabilities are near 1. Moreover, note that $A_{ij} \leq a_{ij}$ and $B_{ij} \leq b_{ij}$. Therefore a comparison of (7) and (8) with (9) and (10) shows that the inherent sensitivity gives an upper bound on the true sensitivity. Finally, note that a ranking of the states according to inherent sensitivity will be the same as a ranking of the states according to true sensitivity if the state reliabilities are sufficiently close to 1. Examples can be constructed which show that this will not necessarily be true if the state reliabilities are not near 1.

Allocation

In this section we will consider the problem of determining the reliability required by a given state in order to meet a given system reliability demand.

Suppose that state i is the initial state. Consider a fixed transient state j. Solving for R_j in (6) gives

$$R_j = (\rho_i - A_{ij})/(B_{ij}\tilde{A}_{jj} + \tilde{B}_{jj}\rho_i - \tilde{B}_{jj}A_{ij}). \qquad (11)$$

If the system reliability ρ_i is specified, if the ideal transition probabilities are known, and if the state reliabilities for the states other than j are known, then (11) can be used to determine the reliability of state i.

If the ideal transition probabilities are known, but none of the state reliabilities are known (the usual case), then the reliabilities of the states other than j can be set equal to 1 in (11) to give a rough estimate of the reliability needed for state j. But then A_{ij} would become a_{ij} and B_{ij} would become b_{ij} where we recall that a_{ij} and b_{ij} have the same meanings as A_{ij} and B_{ij} respectively, except for the ideal system rather than the imperfect system. However, for the ideal system, $b_{ij} = 1-a_{ij}$. Therefore, substituting into (11) gives

$$R_j = (\rho_i - a_{ij})/(\rho_i - a_{ij} + a_{jj} - \rho_i a_{jj}). \qquad (12)$$

Equation 12 can be used to determine the reliability needed for a given state j in order to achieve a given system reliability ρ_i *assuming that the other states are perfect* (i.e. have reliability 1). Since, of course, the other states will in general not be perfect, (12) should be viewed as a rough estimate only, which can be used to obtain an order-of-magnitude estimate of R_j.

Branching Systems

In this and the following section, two special types of systems will be considered. These systems not only provide examples of the methods of the previous sections, but also are of sufficient

generality and richness of structure to be interesting in their own right.

First a general branching system will be studied which has the ideal transition graph given below:

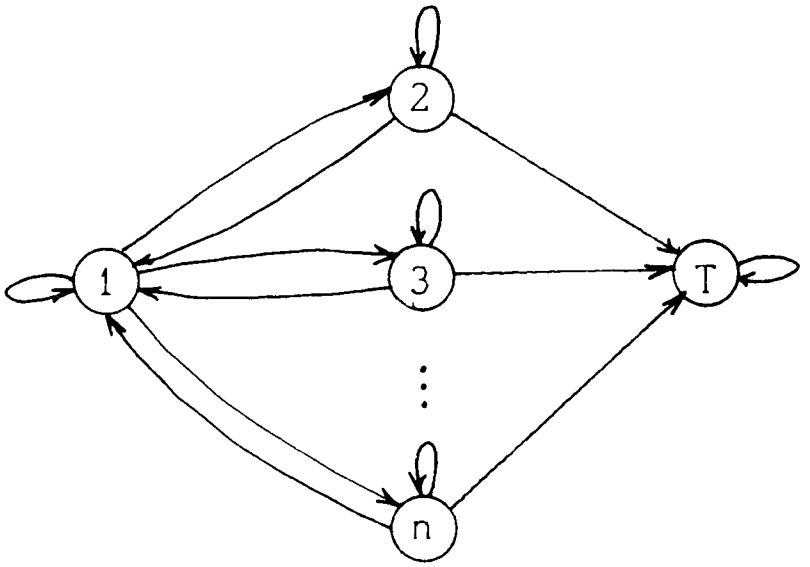

Figure 2. Branching System.

State 1 acts as a central control which may pass control to any of the states 2, ..., n or back to itself or to the terminal state. Each of the branch states 2, ..., n can pass control back to itself, back to the control state 1, or to the terminal state. We assume that the ideal transition matrix P and the state reliability function R are given. State 1 is designated as the initial state.

Equation 3 with i = 1 and j = 1 will be used to compute the system reliability ρ_1 explicitly. Thus

$$\rho_1 = A_{11}/(1-B_{11}). \tag{13}$$

Note that in order to reach T from state 1 without returning to state 1, the system must either go directly to T or to some branch state j, stay at the branch state for some k transitions, and then go to T. It therefore follows that

$$\begin{aligned} A_{11} &= R_1 P_{1T} + \sum_{j=2}^{n} R_1 P_{1j} \sum_{k=0}^{\infty} (R_j P_{jj})^k R_j P_{jT} \\ &= R_1 P_{1T} + \sum_{j=2}^{n} R_1 P_{1j} R_j P_{jT}/(1-R_j P_{jj}). \end{aligned} \tag{14}$$

On the other hand, in order to return to state 1, starting at state 1, the system must either return in one step to state 1 or go to some branch state j, stay at the branch state for some k transitions, and then return to state 1. Thus by a similar argument

$$B_{11} = R_1 P_{11} + \sum_{j=2}^{n} R_1 P_{1j} R_j P_{j1}/(1-R_j P_{jj}). \tag{15}$$

Therefore from (3) the system reliability is given by (13) where where A_{11} and B_{11} are given in (14) and (15) respectively. It would be difficult to obtain this explicit result from the matrix inversion technique of equation of Cheung [1].

The sensitivity of system reliability ρ_1 with respect to the various state reliabilities could now be computed using (13) (15) and standard calculus. However, (9) and (10) will be used to compute the inherent sensitivities. Recall that the advantage of the inherent sensitivity is that it can be computed before the state reliabilities are estimated. Using arguments similar to those for finding ρ_1, the results are

$$S_{11} = \frac{1}{1 - P_{11} - \sum_{j=2}^{n} P_{1j}P_{j1}/(1-P_{jj})};$$

$$S_{1i} = \frac{P_{1i}}{(1-P_{ii})[1 - P_{11} - \sum_{j\neq i} P_{1j}P_{j1}/(1-P_{jj})] - P_{i1}P_{1i}},$$

for $i = 2, \ldots, n$.

Sequential Systems

In this section a sequential system will be considered which has the ideal transition graph given below:

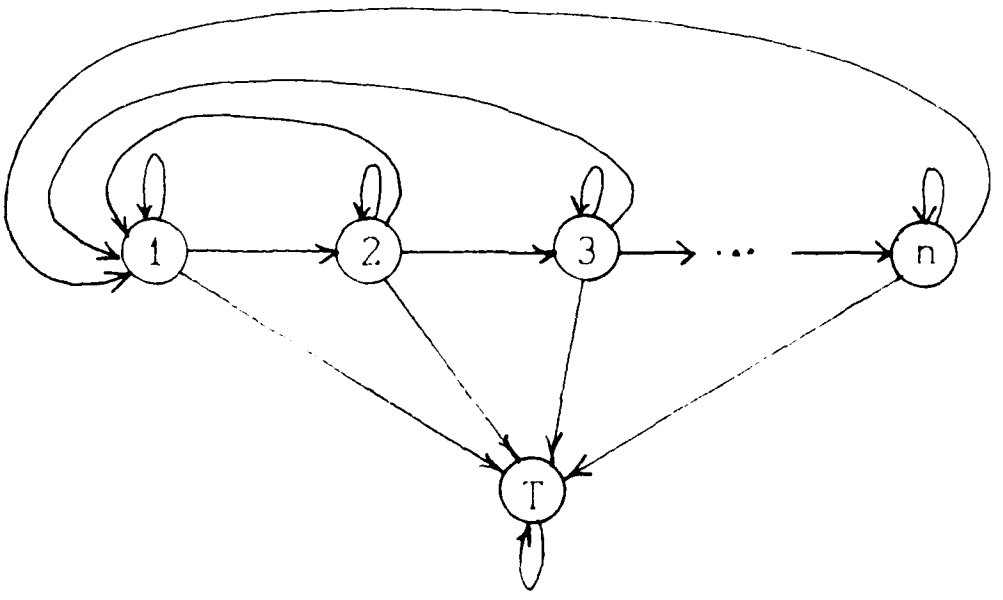

Figure 3. Sequential System.

State 1 is designated as the initial state and we assume that the ideal transition matrix P and the state reliability function R are

known. Note that control tends to pass sequentially from state 1 to state 2, ..., to state n except that, in each state, control can return to that state, go to the initial state 1, or go to the terminal state T.

Equation 3 with i = 1 and j = 1 will be used to compute the system reliability ρ_1 explicitly. From (3),

$$\rho_1 = A_{11}/(1-B_{11}). \tag{16}$$

Note that in order to go from state 1 to state T without returning to state 1, the system must visit states 1, 2, ..., k, T for some state k (with any number of returns to the intermediate states 2, ..., k). It follows with a little work that

$$A_{11} = R_1P_{1T} + \sum_{k=2}^{n} R_1P_{12}\left[\prod_{j=2}^{k-1} R_jP_{jj+1}/(1-R_jP_{jj})\right]R_kP_{kT}/(1-R_kP_{kk}). \tag{17}$$

Similarly, in order to return to state 1, starting at state 1, the system must visit state 1, 2, ..., k, 1 for some state k (with any number of returns to the intermediate states 2, ..., k). Therefore

$$B_{11} = R_1P_{11} + \sum_{k=2}^{n} R_1P_{12}\left[\prod_{j=2}^{k-1} R_jP_{jj+1}/(1-R_jP_{jj})\right]R_kP_{k1}/(1-R_kP_{kk}). \tag{18}$$

Therefore from (3), the system reliability is given by (16) where A_{11} and B_{11} are given in (17) and (18) respectively.

To conclude this section, a numerical example will be considered which was motivated by a radar software system discussed in [7]. The ideal transition graph is given in Figure 4

and the ideal transition probabilities are $P_{11} = 0.8$, $P_{12} = 0.2$, $P_{21} = 0.4$, $P_{22} = 0.4$, $P_{23} = 0.2$, $P_{31} = 0.4$, $P_{33} = 0.4$, $P_{3T} = 0.2$.

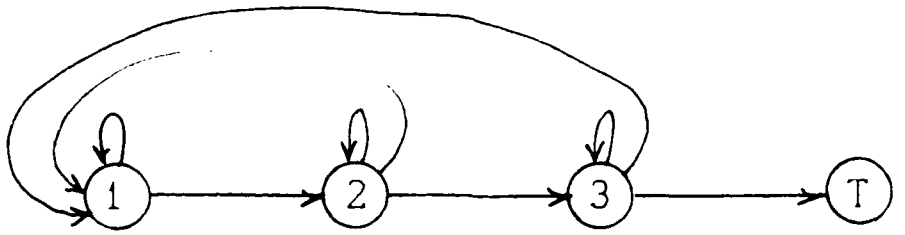

Figure 4. A Sequential System with n = 3.

Note that the system is a special case of the general sequential system. Using (16)-(18) and some algebra, the system reliability (with state 1 as the initial state) is

$$\rho_1 = \frac{.008R_1R_2R_3}{(1-.8R_1)(1-.4R_2)(1-.4R_3)-.08R_1R_2(1-.4R_3)-.016R_1R_2R_3} \qquad (19)$$

where R_1, R_2, and R_3 are the state reliabilities. For example, if $R_1 = R_2 = R_3 = 0.99$ then $\rho_1 = 0.597$.

The inherent sensitivities for this example can be computed form (9) and (10) and the type of arguments that have been used before. The results are $S_{11} = 45$, $S_{12} = 15$, $S_{13} = 5$. Thus, system reliability will be enormously sensitive to changes in the state reliabilities, particularly state 1. For example, if $R_1 = 0.999$, $R_2 = 0.99$, $R_3 = 0.99$ then $\rho_1 = 0.799$ compared with $\rho_1 = 0.597$

when $R_1 = R_2 = R_3 = 0.99$.

Finally, the allocation scheme of described earlier will be applied to this example. Suppose that we want a system reliability of $\rho_1 = 0.9$. Note first that $a_{1j} = 0$ for $j = 2$ and 3. Moreover, $a_{11} = 1/45$, $a_{22} = 1/15$, $a_{33} = 1/5$. Substituting into (12) gives $R_1 = 0.9975$, $R_2 = 0.9926$, $R_3 = 0.9783$. Recall that, for each i, the value of R_i given by the allocation scheme is the reliability needed by state i to achieve $\rho_1 = 0.9$ assuming that the other states are perfect. Thus we need to increase the state reliabilities somewhat for simultaneous allocation. Let $R_1 = 0.9999$, $R_2 = 0.999$, $R_3 = 0.99$. Substituting into (19) gives $\rho_1 = 0.9343$.

Part II
Reliability of Systems with Markov Transfer of Control and without Terminal States

Introduction

This part concerns software/hardware systems which can be decomposed into a finite number of functionally independent modules. The main assumption is that the transfer of control among the modules satisfies the Markov property which implies that the future behavior of the system is conditionally independent of the past behavior, given knowledge of the module in control at the present. Each module is failure prone and has an associated reliability which measures the probability that the module functions correctly when called and transfers control successfully when finished.

In Part I, this model was studied under the additional assumption that the system has a terminal module corresponding to mission success. System reliability was defined to be the probability that the system eventually reaches the terminal module without failing. Methods were developed for predicting system reliability and computing the sensitivity of system reliability with repsect to module reliability. Also, explicit results were obtained for certain types of branching and sequential systems.

There are many systems, however, which have no natural terminal state corresponding to success. Some systems are designed to run for fixed periods of time while others run more or less continuously (until failure). For example, consider a radar system which has software modules corresponding to search,

acquire and track states. Such a system will run continuously until it fails or is shut down for maintenance. It will not do to add a terminal state to such a system artificially, to make it fit the model of Part I, for this can result in misleading or even ridiculous conclusions, as will be shown later.

In this paper, a discrete Markov chain model like the one in Part I will be developed except without the assumption of a terminal state. The mean number of transitions until failure will be the measure of reliability considered. This approach is reminiscient of the continuous time, semi-Markov model for modular software systems which was studied by Littlewood [5] and Laprie [4] with mean time to failure as the measure of reliability. The main difference is that the continuous time model allows a random time spent in each state (but forbids transitions from a state to itself), while the discrete model measures time in discrete units and allows transitions from a state to itself. The continuous time model is more realistic in some ways, but is also harder to work with. Indeed, in [4] and [5], only asymptotic results are tractable. The main advantage of the discrete model is that it is simple to work with and can lead to quite explicit results. Moreover, the discrete model is particularly appropriate for systems in which the transitions corresponds to inputs received at regular time units, for then the mean number of transitions until failure can be converted to the mean time until failure. For systems in which the transitions are driven by inputs received at irregular time units, the mean number of transitions until failure can be multiplied by the mean time between inputs to obtain an

approximation to the mean time until failure.

This part is a sequel to Part I. Methods will be developed for computing the system reliability, the sensitivity of system reliability relative to module reliability, and the module reliability needed to obtain a given system reliability. The results will be applied to general branching and sequential systems.

The Markov Chain Model

The modules (or states) of the system will be denoted 1, 2, ..., n. Usually the system has a designated initial state. The ideal (failure free) system is described by a Markov chain with state space {1, 2, ..., n} and transition matrix P. That is, P_{ij} is the conditional probability that the next state will be j given that the current state is i.

The reliability of state i, denoted R_i, is the probability that state i will function correctly when called and will transfer control successfully when finished. Equivalently, the system will fail with probability $1-R_i$ each time state i is entered.

The imperfect system is modeled by adding an absorbing state F (failure) and modifying the transition probabilities appropriately. Specifically, the imperfect system is described by a Markov chain with state space {1, 2, ..., n, F} and transition matrix $\hat{P}$ given by

$$\hat{P}_{ij} = R_i P_{ij} \quad \text{for } i, j = 1, \ldots, n;$$

$$\hat{P}_{iF} = 1 - R_i \quad \text{for } i = 1, \ldots, n;$$

$$\hat{P}_{FF} = 1.$$

We assume that $R_i < 1$ for each i and hence each of the states 1, 2, ..., n eventually leads to F. State F is absorbing. Note that the dynamics of the imperfect system are completely described by the state reliability function R and the ideal transition matrix P since this description is equivalent to specifying the transition matrix $\hat{P}$ of the imperfect system.

Expected Number of Transitions Until Failure

For $i = 1, 2, \ldots, n$, let M_i denote the mean number of transitions until failure for the imperfect system, starting in state i. If the transitions of the system correspond to inputs received at regular time intervals, then M_i is proportional to the expected time until failure, starting in state i. Two methods of computing the function M will be given.

Let $\hat{Q}$ denote the restriction of the transition matrix $\hat{P}$ of the imperfect system to the (transient) states 1, 2, ..., n. Note that $\hat{Q}_{ij} = R_i P_{ij}$. The matrix

$$\sum_{k=0}^{\infty} \hat{Q}^k = (I-\hat{Q})^{-1}$$

is the potential matrix of the imperfect system. Its ij value gives the expected number of visits to j by the imperfect system starting in state i (for a derivation see [2]). It follows that

$$M_i = \sum_{j=1}^{n} (I-\hat{Q})^{-1}_{ij} \qquad (1)$$

In the notation of matrix multiplication, (1) can be written in the form $M = (I-\hat{Q})^{-1}\mathbf{1}$ where $\mathbf{1}$ denotes the constant function 1 defined

on 1, 2, ..., n.

Equation 1 is the basic method of computing M. It is satisfactory for numerical work, but may not always be best for analytical purposes. Another method will now be developed which can take advantage of the structural properties of the system.

Let i and j be any of the states 1, 2, ..., n. A simple application of the (strong) Markov property shows that

$$M_i = N_{ij} + B_{ij}M_j \tag{2}$$

where N_{ij} is the expected number of transitions until the imperfect system either fails or reaches state j, starting in state i and B_{ij} is the probability that the imperfect system eventually reaches state j, starting in state i. If i = j, "reaches" should be interpreted as "returns to" in which case we obtain from (2)

$$M_j = N_{jj}/(1 - B_{jj}).$$

Substituting this result back into (2) gives the desired result:

$$M_i = N_{ij} + B_{ij}N_{jj}/(1 - B_{jj}). \tag{3}$$

From the Markov property, the matrices N and B are related to the basic data R and P according to the following systems of equations:

$$N_{ij} = 1 + \sum_{k \neq j} R_i P_{ik} N_{kj}; \tag{4}$$

$$B_{ij} = R_i P_{ij} + \sum_{k \neq j} R_i P_{ik} B_{kj}. \tag{5}$$

Moreover $B_{ij}/(1 - B_{jj})$ is the same as $(I - \hat{Q})^{-1}_{ij}$, namely the expected

number of visits to j for the imperfect system starting in state i.

However, the trick to using (3) is finding a state j for which the quantities N_{ij}, N_{jj}, B_{ij} and B_{jj} are easy to compute directly (state i, the initial state, is usually determined from the physical system).

Note that if $R_j = R$ for all j then

$$M_i = 1/(1 - R) \tag{6}$$

for all i since each transition can be viewed as a Bernoulli trial with constant probability R of success and therefore the number of transitions until failure has a geometric distribution. Note also that Equation 6 is completely independent of the ideal transition probabilities and the number of states.

Another advantage of (3) is that it allows us to isolate the effect of the reliability R_j of state j on the system reliability M_i. From (4) and (5) note that if $i = j$ then N_{ij} and B_{ij} do not depend on R_j. If $i = j$, (4) and (5) give

$$N_{jj} = 1 + R_j \sum_{k \neq j} P_{jk} N_{kj},$$

$$B_{jj} = R_j [P_{jj} + \sum_{k \neq j} P_{jk} B_{kj}].$$

Letting $\tilde{N}_{jj} = \sum_{k \neq j} P_{jk} A_{kj}$ and $\tilde{B}_{jj} = P_{jj} + \sum_{k \neq j} P_{jk} B_{kj}$ we see that (3) can be rewritten in the form

$$M_i = N_{ij} + B_{ij}(1 + R_j \tilde{N}_{jj})/(1 - R_j \tilde{B}_{jj}) \tag{7}$$

where $\tilde{N}_{jj}$, $\tilde{B}_{jj}$, and (if $i \neq j$) N_{ij}, B_{ij} are independent of R_j. This representation will be useful in the sensitivity and allocation

problems to be considered next.

Sensitivity

Suppose that state i is the initial state so that M_i, the expected number of transitions until failure, starting in state i, is the measure of system reliability. The sensitivity of M_i with respect to R_j is defined to $\partial M_i/\partial R_j$, the partial derivative of M_i with respect to the reliability of state j. This sensitivity is a measure of how small changes in the reliability of a state effect the expected number of transitions until failure. Sensitivity can be used to determine which states are most critical and can be used to judge the quality of estimates of M_i based on estimates of the R_j, $j = 1, 2, \ldots, n$.

From (7), if $i \neq j$,

$$\partial M_i/\partial R_j = B_{ij}(\tilde{N}_{jj}+\tilde{B}_{jj})/(1-R_j\tilde{B}_{jj})^2$$
$$= B_{ij}(\tilde{N}_{jj}+\tilde{B}_{jj})/(1-B_{jj})^2. \qquad (8)$$

If $i = j$,

$$\partial M_i/\partial R_i = (\tilde{N}_{ii}+\tilde{B}_{ii})/(1-R_i\tilde{B}_{ii})^2 = (\tilde{N}_{ii}+\tilde{B}_{ii})/(1-B_{ii})^2. \qquad (9)$$

As all state reliabilities approach 1, either $B_{jj} \to 1$ or $\tilde{N}_{jj} \to \infty$. In any event, $\partial M_i/\partial R_j \to \infty$ unless $i \neq j$ and $B_{ij} = 0$ (i.e., unless it is impossible to reach state j from the initial state i).

Therefore, when all state reliabilities are near 1, M_i will be extremely sensitive to changes in the state reliabilities. This means that statistical estimates of M_i based on estimates of R_j,

AD-A186 493 UNITED STATES AIR FORCE RESEARCH INITIATION PROGRAM 2/ 8
1985 TECHNICAL REPORT VOLUME 3(U) UNIVERSAL ENERGY
SYSTEMS INC DAYTON OH R C DARRAH APR 87
UNCLASSIFIED AFOSR-TR-87-1719 F49620-85-C-0013 F/G 15/3 NL

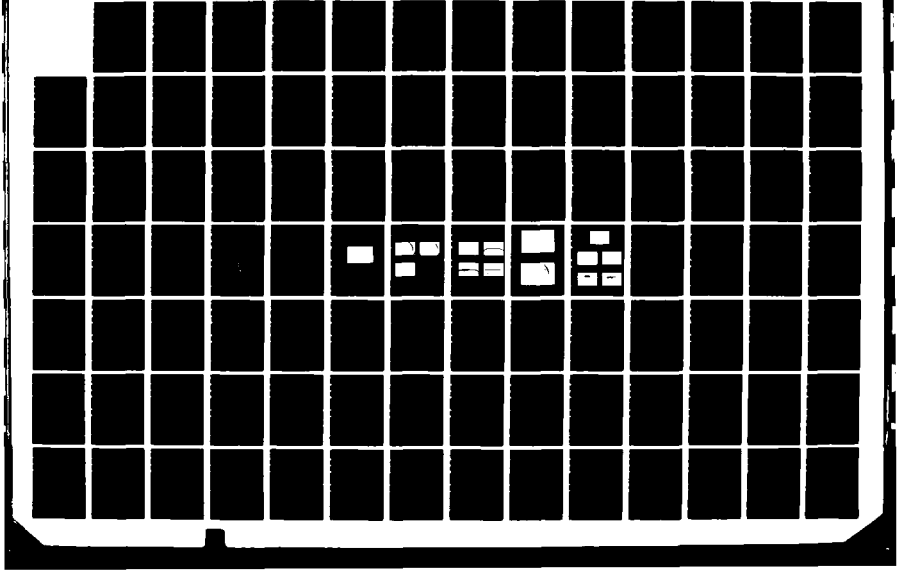

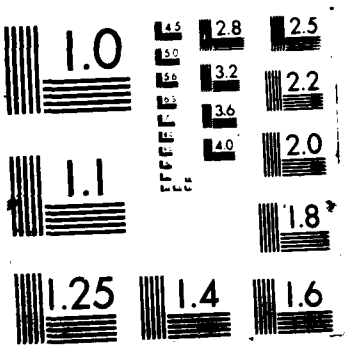
1.0
1.1
1.25
1.4
1.6
1.8
2.0
2.2
2.5
2.8
3.2
3.6
4.0

= 1, 2, ..., n must be used very cautiously.

Allocation

In this section, we will consider the problem of determining the reliability needed for a given state in order to meet a given system reliability demand.

Suppose that state i is the initial state. Let j be any other state. Solving for R_j in (7) gives

$$R_j = (M_i - N_{ij} - B_{ij})/[\tilde{N}_{jj}\tilde{B}_{ij} + \tilde{B}_{jj}(M_i - N_{ij})]. \qquad (10)$$

If M_i is given, if the ideal transition probabilities are known and if the reliabilities of the states other than j are known, then (10) can be used to determine the reliability needed for state j. Note, however, that there is no guarantee that R_j given by (10) is in the interval (0,1). That is, it may not be possible to find a meaningful value of R_j to achieve a given value of M_i.

If none of the state reliabilities are known (the usual case) then (6) can be used to obtain a uniform value $R_j = R$ of the state reliabilities needed to achieve a specified value of M:

$$R = 1 - 1/M. \qquad (11)$$

As noted earlier, this value is independent of the number of states and the ideal transition probabilities.

Branching Systems

In this and the following section, two special types of systems

will be considered. These systems not only serve as examples for the methods of the previous sections, but also are of sufficient generality to be interesting in their own right.

First a general branching system will be studied which has the ideal transition graph given in Figure 1. State 1 acts as a central control which may pass control to any of the states 2, ..., n or back to itself. Each of the branch states 2, ..., n can pass control back to itself or back to the control state 1. We assume that the ideal transition matrix P and the state reliability function R are given. State 1 is designated as the initial state.

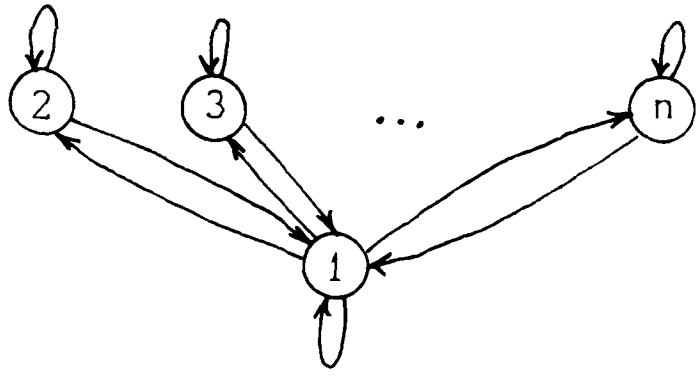

Figure 1. Branching System.

Equation 3 (with i = j = 1) will be used to compute M_1, the expected number of transitions until failure, starting in state 1. Note first that the imperfect system, starting in state 1 will make at least one transition before failure or return to state 1 occurs. Furthermore, if the system moves to branch state j on the first

transition, then on average, the system will make $1/(1-R_jP_{jj})$ transitions until failure or return to state 1 occurs. It follows that

$$N_{11} = 1 + \sum_{j=2}^{n} R_1P_{1j}/(1-R_jP_{jj}). \tag{12}$$

On the other hand, the probability that the imperfect system, starting in state 1, will eventually return to state 1 is

$$B_{11} = R_1P_{11} + \sum_{j=2}^{n} R_1P_{1j}R_jP_{j1}/(1-R_jP_{jj}). \tag{13}$$

Therefore from (3),

$$M_1 = N_{11}/(1-B_{11}) \tag{14}$$

where N_{11} and B_{11} are given in (12) and (13) respectively.

The sensitivity $\partial M_1/\partial R_j$ can be computed using (12)-(14) and standard calculus or using (8) and (9).

Sequential Systems

In this section, a system will be considered which has the ideal transition graph given in Figure 2.

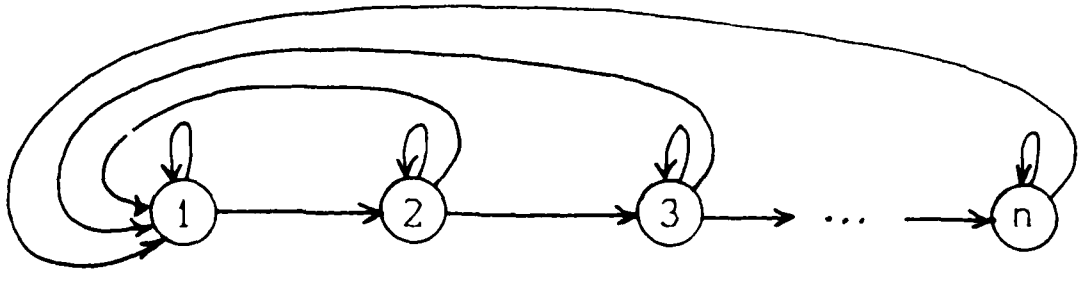

Figure 2. Sequential System.

Note that control tends to pass sequentially from state 1 to state 2, ..., to state n except that in each state, control can return to that state or to state 1. State 1 is the initial state. We assume that ideal transition matrix P and the state reliability function R are known.

Equation 3 with i = j = 1 will be used to compute M_1, the expected number of transitions until failure for the imperfect system starting in state 1. First note that when the system is in a given state i, the expected number of transitions until the system leaves i is $1/(1-R_iP_{ii})$. It follows with a little work that

$$N_{11} = 1 + \sum_{i=2}^{n} R_1P_{12}\left[\prod_{k=2}^{i-1} R_kP_{kk+1}/(1-R_kP_{kk})\right] 1/(1-R_iP_{ii}). \quad (15)$$

(By convention, products over vacuous index sets are 1.) By a similar argument, the probability of eventual return to state 1, starting in state 1 for the imperfect system is

$$B_{11} = R_1P_{11} + \sum_{i=2}^{n} R_1P_{12}\left[\prod_{k=2}^{i-1} R_kP_{kk+1}/(1-R_kP_{kk})\right]R_iP_{i1}/(1-R_iP_{ii}) \quad (16)$$

From (3), the expected number of transitions until failure for the imperfect system starting in state 1 is

$$M_1 = N_{11}/(1-B_{11}) \quad (17)$$

where N_{11} and B_{11} are given by (15) and (16) respectively.

Finally, a numerical example in the special case n = 3 will be

considered. The ideal transition graph is given in Figure 3 (without the dotted lines).

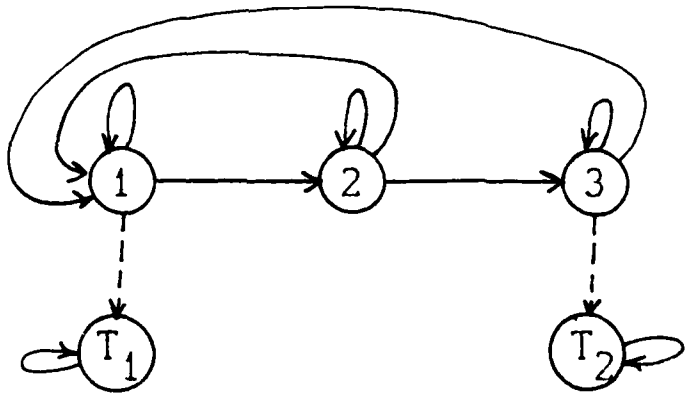

Figure 3. A Sequential System with n = 3.

The ideal transition probabilities are

$$P_{11} = 0.8,\ P_{12} = 0.2,\ P_{21} = 0.4,\ P_{22} = 0.4$$
$$P_{23} = 0.2,\ P_{31} = 0.5,\ P_{33} = 0.5 \qquad (18)$$

Using (15)-(17) and some algebra we find that

$$M_1 = \qquad (19)$$

$$\frac{(1-0.4R_2)(1-0.5R_3)+0.2R_1(1-0.5R_3)+0.04R_1R_2}{(1-0.8R_1)(1-0.4R_2)(1-0.5R_3)-0.08R_1R_2(1-0.5R_3)-0.02R_1R_2R_3)}$$

For example, if $R_1 = 0.999$, $R_2 = 0.99$, and $R_3 = 0.99$ then $M_1 \simeq 260$.

The sensitivity of M_1 with respect to the various state reliabilities can be computed from (19) and standard calculus or from (8) and (9). With the values of R_1, R_2, and R_3 given

above, $\partial M_1/\partial R_1 \simeq 46{,}051$, $\partial M_1/\partial R_2 \simeq 15{,}309$, and $\partial M_1/\partial R_3 \simeq 5968$. Clearly the system reliability is enormously sensitive to changes in the module reliabilities. For example, if R_1 is decreased form 0.999 to 0.99 (all other values the same), M_1 decreases to 100.

If the state reliabilities are unknown, the allocation scheme of Equation 11 can be used to find the reliabilities needed to achieve a given value of M. For example, if M is to be 500 then we need $R_i = 1 - 1/500 = 0.998$ for each i.

Finally, we will show in the context of this numerical example, that misleading results can occur if a terminal state is added to a system artifically to make it fit the model of Part I. Suppose first that terminal state T_1 is added to the system as shown in Figure 3. The transition probabilities in (18) are modified by letting $P_{11} = 0.795$, $P_{12} = 0.195$, and $P_{1T_1} = 0.01$ (all other values are the same). Suppose that $R_1 = R_2 = R_3 = 0.99$. Then from Part I, the system reliability (defined to be the probability that the system reaches terminal state T_1 before failing) is approximately 0.41. Next suppose that T_2 (instead of T_1) is added to the system as a terminal state. The transition probabilities in (18) are modified by letting $P_{31} = 0.495$, $P_{33} = 0.495$, $P_{3T_2} = 0.01$ (all other values in (18) are the same). As before, let $R_1 = R_2 = R_3 = 0.99$. Then the system reliability (probability of absorption into T_2) is approximately 0.08.

Thus, although the two systems superficially seem quite similar (in terms of the numerical values of the transition probabilities),

their reliabilities, as measured by the model in Part I, are drastically different. The reason of course, is the difference in the location of the terminal state relative to the initial state.

Part III

General Systems with Random Transfer of Control

Introduction

In this part, we will consider a software system which can be decomposed into a finite number of modules or states as in the first two parts. We will assume that external inputs enter the system and cause it to change states. The change of state for a *known* input is assumed to be deterministic, however the input stream is generally unknown and hence will be modeled by a stochastic process. Thus, the successive states of the system also form a stochastic process which is driven by the random input stream. Unlike the first two parts, however, the state process is not assumed to be Markov. Rather, we are interested in what properties must be true of the input process in order for the state process to be Markov. Also we will consider the joint state-input process.

Mathematical Model

Let S deonote the state space of the system. We assume that S is a finite set which can be identified with {1, 2, ..., n} for some n. Let I denote the input space. We will allow I to be a general (measurable) space. Let H: $S \times I \to S$ denote the state transition function. That is, H is a function from the set of state-input pairs into the set of states; if the system is in state $x \in S$ and receives input $u \in I$ then the system move to state H(x,u). Therefore, given the input stream $u_0, u_1, \ldots$ the system moves successively through

the states x_0 (the initial state), $x_1 = H(x_0,u_0)$, $x_2 = H(x_1,u_1) = H(H(x_0,u_0),u_1)$, ...

Now suppose that the input stream is random. That is, the successive inputs U_0, U_1, U_2, ...form a stochastic process on a probability space (Ω,F,P). Then the sequence of states X_0, X_1, X_2, ... forms a stochastic process induced by the input process: X_0 is the initial state and

$$X_{n+1} = H(X_n,U_n) \text{ for } n = 0, 1, 2, \ldots$$

It is clear that the probability distribution of the state process is completely determined by X_0, H and the probability distribution of the input process .

Mathematical models similar to the one described here, only in the context of learning theory, have been studied by Norman [6].

The Markov Property

In general, the state process is not a Markov chain, in spite of the fact that the next state of the system is a deterministic function of the current state and input. The reason for this is possibility that the input process may be correlated in such a way that the Markov property does not hold for the state process. Recall that the Markov property means that the future behavior is independent of the past behavior, given the present state.

A simple example may help to illustrate the problem. Suppose that the state space S consists of two states, denoted x and y. Suppose the the input space consists of two inputs, 0 and 1. The state transition function H is given as follows:

$$H(x,0) = x,\ H(y,0) = y,$$
$$H(x,1) = y,\ H(y,1) = x.$$

Thus, if input 0 is received, the system remains in its same state while if input 1 is received, the system changes to the other state. Suppose that $U_0 = 0$ with probability 1/2 and $U_0 = 1$ with probability 1/2 and that $U_n = U_0$ for $n = 1, 2, \ldots$ Finally, suppose that $X_0 = x$. If the history $X_0 = x$, $X_1 = x$, $X_2 = x$ is observed then U_0 must have been 0 and therefore X_3 will be x with probability 1. On the other hand, if only $X_2 = x$ is observed, then no information is gained about U_0 (if $U_0 = 0$, the sequence would be $X_0 = x$, $X_1 = x$, $X_2 = x$; if $U_0 = 1$, the sequence would be $X_0 = x$, $X_1 = y$, $X_2 = x$). Hence in this case, X_3 will be x with probability 1/2 and will be y with probability 1/2. Therefore, knowledge of X_0, X_1, X_2 is not equivalent to knowledge of X_2 in terms of predicting X_3 and hence the Markov property is not satisfied.

We will now show that if the input sequence is independent, then the state sequence is a Markov chain. To prove this, suppose that U_0, U_1, ... are independent and that U_n has probability measure μ_n on I. Then

$$P[X_{n+1} = y \mid X_0 = x_0, X_1 = x_1, \ldots, X_n = x_n]$$

$$= P[H(X_n,U_n) = y \mid X_0 = x_0, H(X_0,U_0) = x_1, \ldots, H(X_{n-1},U_{n-1}) = x_n]$$

$$= P[H(x_n,U_n) = y \mid X_0 = x_0, H(x_0,U_0) = x_1, \ldots, H(x_{n-1},U_{n-1}) = x_n]$$

$$= P[H(x_n,U_n) = y]$$

since U_n is independent of $U_0, \ldots, U_{n-1}$. By a similar argument,

$$P[X_{n+1} = y \mid X_n = x_n] = P[H(x_n, U_n) = y]$$

Therefore the state sequence $X_0, X_1, \ldots$ is a Markov chain with one step transition probabilities at time n given by

$$P[X_{n+1} = y \mid X_n = x] = \mu_n\{u \in I: \ H(x,u) = y\}.$$

Note that this chain is not time homogeneous (stationary) in general. However, if the inputs are independent and identically distributed with common probability measure μ on I then the state sequence is a time homogeneous Markov chain with one step transition probabilities given by

$$P[X_{n+1} = y \mid X_n = x] = \mu\{u \in I: \ H(x,u) = y\}.$$

Also, of course, if the transition function H is actually independent the inputs ($H(x,u) = H(x)$ for all $u \in I$) then the state sequence is a time homogeneous Markov chain with one step transition probabilities given by

$$P(X_{n+1} = y \mid X_n = x) = 1[H(x), y]$$

where $1[H(x),y] = 1$ if $H(x) = y$ and 0 otherwise.

There do not seem to be any other simple, natural conditions on the input sequence $U_0, U_1, \ldots$ or on the transition function H which will insure that the state sequence $X_0, X_1, \ldots$ is a Markov chain. Moreover, the conditions that the input sequence be statistically independent or that the transition function be indepndent of input

are not likely to be satisfied in reality. Thus it seems unlikely that the state sequence of a real system with random transfer of control will be a Markov chain. However, the methods of Parts I and II may still give useful results. Indeed the central modeling problem is how to decompose the system into states in such a way that the decomposition is useful *and* the Markov property is at least approximately satisfied by the state sequence. More study and tests on *real* systems are needed to resolve this question.

The Joint State-Inpupt Process

We will first show that if the input sequence U_0, U_1, ... is a Markov chain then then the joint state-input sequence (X_0,U_0), (X_1,U_1), ... is also a Markov chain. Specifically, suppose that the input sequence is a time homogeneous Markov chain on the input space I with transition probability kernel Q. Then

$$P[U_{n+1} \in A \mid U_0 = u_0, U_1 = u_1, \ldots, U_n = u_n] = P[U_{n+1} \in A \mid U_n = u_n],$$

for u_0, u_1, ... $\in$ I and A a (measurable) subset of I, and

$$P[U_{n+1} \in A \mid U_n = u] = Q(u,A).$$

Therefore,

$$P[X_{n+1} = y, U_{n+1} \in A \mid X_0 = x_0, U_0 = u_0, \ldots, X_n = x_n, U_n = u_n]$$

$$= P[H(X_n,U_n) = y, U_{n+1} \in A \mid X_0 = x_0, U_0 = u_0, \ldots, X_n = x_n, U_n = u_n]$$

$$= P[H(x_n,u_n) = y, U_{n+1} \in A \mid X_0 = x_0, U_0 = u_0, U_1 = u_1, \ldots, U_n = u_n]$$

$$= P[U_{n+1} \in A \mid U_n = u_n] \mathbf{1}[H(x_n,u_n),y]$$

Therefore (X_0,U_0), (X_1,U_1), ... is a Markov chain with one-step transition probabilities given by

$$P(X_{n+1} = y, U_{n+1} \in A \mid X_n = x, U_n = u) = \mathbf{1}[H(x,u),y]Q(u,A).$$

Although the state process X_0, X_1, ... is not a Markov chain in the usual sense, it is a *Markov chain in a random environment* in the sense of Cogburn (1980). The input process U_0, U_1, ... is the environmental process.

Next we will show that if the input sequence U_0, U_1, ... is a Markov chain, then the joint input-state sequence (U_0,X_1), (U_1,X_2), ... is a Markov chain. As before, suppose that the input sequence U_0, U_1, ... is a time homogeneous Markov chain with transition probability kernel Q. Then

$$P[U_n \in A, X_{n+1} = y \mid U_0 = u_0, X_1 = x_1, \ldots, U_{n-1} = u_{n-1}, X_n = x_n]$$

$$= P[U_n \in A, H(X_n,U_n) = y \mid X_0 = x_0, U_0 = u_0, X_1 = x_1, \ldots, U_{n-1} = u_{n-1}, X_n = x_n]$$

$$= P[U_n \in A, H(x_n,U_n) = y \mid X_0 = x_0, U_0 = u_0, U_1 = u_1, \ldots, U_{n-1} = u_{n-1}]$$

$$= P[U_n \in A, H(x_n,U_n) = y \mid U_{n-1} = u_{n-1}].$$

Therefore, (U_0,X_1), (U_1,X_2), ... is a Markov chain with transition probabilities given by

$$P[U_n \in A, X_{n+1} = y \mid U_{n-1} = u, X_n = x] = Q(u, A \cap \{v \in I: H(x,v) = y\}).$$

Reliability Framework

Suppose now that the system is unreliable because the next state function H is partially incorrect. Specifically suppose that for each state $x \in S$, there exists a (measurable) subset F_x of the input space I such that $H(x,u)$ is incorrect for $u \in F_x$. Thus we are assuming that, depending on the state of the system, there are certain inputs which cause the system to malfunction.

Let $F = \{(x,u): u \in F_x\}$. That is, F is the set in state-input phase space with cross-sections F_x, $x \in S$. We will assume in this section that the input stream U_0, U_1, ... is a Markov chain and therefore so is the joint state-input sequence (X_0,U_0), (X_1,U_1), ...

The reliability of the system is determined by the random variable

$$\tau = \text{Min}\{n: (X_n,U_n) \in F\},$$

the number of transitions until the system fails. That is, τ is the first time that an input is received which causes the system to fail.

There are two natural measures of reliability based on τ:

$$P(\tau = \infty) \text{ and } E(\tau).$$

The first, $P(\tau = \infty)$, is the probability that the system never

fails. This measure of reliability would be useful, for example, if the system eventually reaches one of a number of terminal states which represent terminal answers or decisions. This is the point of view of Part I, assuming that the state process is Markov.

The second, $E(\tau)$, is the expected time until failure. This measure of reliability would be appropriate for systems which run continuously and eventually fail with probability one. This is the point of view of Part II, assuming that the state process is Markov.

There are standard methods for computing $P(\tau = \infty)$ and $E(\tau)$ in terms of the transition probabilities of the joint state-input process (X_0,U_0), (X_1,U_1), ... (see, for example, [2]). Unfortunately, the transition probabilities of the joint state-input process depend of the transition probabilities of the input process, and these are unlikely to be available in practice.

Suppose that the inputs U_0, U_1, ... are independent and identically distributed with common probability measure μ on I. Then, as shown earlier, the state sequence X_0, X_1, ... is a Markov chain with transition probabilities given by

$$P(x,y) = \mu\{u \in I:\ H(x,u) = y\}.$$

In this setting, the system fits the models of Parts I and II, with the reliability of state $x \in S$ given by

$$R_x = \mu(F_x).$$

References

[1] Cheung, RC, "A User-Oriented Software Reliability Model," *IEEE Transactions on Software Engineering*, Vol SE-6, No 2, March, 1980.

[2] Cinlar, E, *Introduction to Stochastic Processes*, Prentice Hall, Englewood Cliffs, New Jersey, 1975.

[3] Cogburn, R, "Markov Chains in Random Environments: the Case of Markovian Environments," *The Annals of Probability*, Vol 8, No 5, October, 1980.

[4] Laprie, JC, "Dependability Evaluation of Software Systems in Operation," *IEEE Transactions on Software Engineering*, Vol SE-10, No 6, November, 1984.

[5] Littlewood, B, "Software Reliability Model for Modular Program Structure," *IEEE Transaction on Reliability*, Vol R-28, No 3, August, 1979.

[6] Norman, NF *Markov Processes and Learning Models*, Academic Press, New York, 1972.

[7] Soistman, EC and Ragsdale, KB, "Combined Hardware Software Reliability Prediction Methodology," Vol II, Rome Air Development Center Contract Report OR 18-173, December, 1984.

1986 USAF-UES RESEARCH INITIATION GRANT

Sponsored by the

AIR FORCE OFFICE OF SCIENTIFIC RESEARCH

Conducted by the

UNIVERSAL ENERGY SYSTEMS, INC.

FINAL REPORT

ADVANCED PROPELLANT FORMULATIONS: APPLICATION OF NEW SYNTHETIC STRATEGIES TO USEFUL AND ENERGETIC INTERMEDIATES

Prepared by:	Ricardo A. Silva
Academic Rank:	Professor of Chemistry
Department and University:	Department of Chemistry California State University, Northridge

Date:	15 January 1987
Contract No:	F49620-85-C-0013/SB5851-0360
Subcontract No:	S-760-OMG-066/Dr. Ricardo Silva, Principal Investigator (Ref. CSUN #F-85-545)

ACKNOWLEDGMENT

The author thanks the Air Force Systems Command, the Air Force Office of Scientific Research, and the Universal Energy Systems Inc., for providing the opportunity to explore the chemistry described in this report through a Research Initiation Grant.

Thanks are especially due to Dr. Robert Chapman, RPL Edwards AFB for the many hours he has spent consulting with us during various phases of this work and to Mr. Stuart Dimock whose skill in the library and the laboratory contributed so much to this report.

ADVANCED PROPELLANT FORMULATIONS: APPLICATION OF NEW SYNTHETIC STRATEGIES TO USEFUL AND ENERGETIC INTERMEDIATES

by

Dr. Ricardo A Silva

ABSTRACT

This report describes work undertaken to apply new synthetic methodologies for the synthesis of reactive intermediates capable of transformation to components curently in use in solid propellant formulations.

The report describes efforts made to consolidate and establish optimum reaction conditions for a number of key intermediates in the synthetic scheme as well as investigations of alternate approaches which show considerable promise. Much of the work originally envisaged is not complete and our preliminary results have uncovered a whole new arena for fruitful study. Recommendations regarding further studies in thisarea are described as well as the possible extension to other molecular targets of potentially greater importance for the formulation of new energetic propellants.

I. INTRODUCTION

This report focusses on efforts originally initiated during the tenure of an AFOSR Summer Faculty Fellowship at the Rocket Propulsion Laboratory at Edwards AFB. That work was the subject of a Final Report submitted to the AFOSR via Universal Energy Systems, Inc.,dated 30 September, 1985 and frequent reference will be made to this document.

In the earlier report[1], the rationale for selecting certain molecular entities was provided and in this work we decided to focus our attention primarily on the particular system represented by 1 since the material was readily available, reasonably inexpensive and was a system in which we had some practical experience. Substrate 1 was also attractive because it was easily amenable to analysis by our detection techniques (infrared and nuclear magnetic resonance spectroscopy)

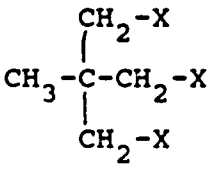

1

a. X = OH b. X = Br

c. X = NH_2 d. X = OSO_2CF_3

e. X = NCO f. X = $OSO_2C_6H_5$

g. X = OSO_2CH_3 h. X = N_3

II. OBJECTIVES

At the outset it was decided to explore the synthesis of the various derivatives of 1 so as to delineate the most favorable experimental parameters for each. This would then allow us to approach the target 1e from converging pathways and to decide which of these schemes would be the most efficient and practical. Earlier wehad synthesized 1d from the alcohol and in this work we would investigate methods of improving the yield by varying reaction conditions and the kind of base employed. The conversion of 1d to 1e would then be attempted.

In a parallel effort we would seek to optimize the synthesis of 1b and 1c and then to uncover the best methodology to proceed to 1e

III. RESULTS AND DISCUSSION

In the case of the tri-triflate 1d, the thermal sensitivity of this compound made it difficult to isolate and to handle. Consequently our studies had to include its preparation at low temperature immediately prior to attempted conversion to the target. We obtained the maximum yields by the procedure described earlier for the triflate[1]. In spite of continued efforts we could not improve on this procedure. In the course of our investigation, we varied the reaction temperature, reagent concentrations and the nature of added base. Lietrature reports[2] indicated that 2,6-dialkylpyridines might be better than pyridine

itself but this did not prove to be the case in our hands. The conversion of 1d to 1e was attempted with tetra-alkyl ammonium isocyanates but as before we could not find any trace of alklyl isocyanates (by IR analysis). A limited attempt to perform this reaction with sodium azide was also unsuccessful. We had hoped that the use of macrocyclic ethers as complexing agents would prove successful but time constraints prevented us from exploring this further.

We reproduce here the relevant spectroscopic details for compound 1d.

Infrared Spectrum: Significant bands near 1425, 1235-1200, 1141 and 957 cm^{-1}

NMR Spectrum(δ): ^{1}H: 1.26 (s, 1H); 4.47 (s, 2H)

^{13}C: 15.5, 40.5, 74.4, 118.5

^{19}F: 74.5, 78.5

In our parallel experiments we needed to have fairly substantial amounts of starting materials at hand since this strategy promised to be more amenable to large scale production. In addition, there were a larger number of variations possible between these various intermediates and to investigate each of these would require a good supply of materials. Accordingly we have prepared substantial quantities of 1b, 1c and 1h for further studies. Efficient routes to compounds 1f and 1g have also been developed and we are now poised to extend studies on these intermediates. Our initial attempts to effect one step conversions of 1f and 1g

to 1h in high yield were not too promising. Reaction of both of these with sodium azide in a variety of solvents including diglyme and diethylene glycol did not yield useful quantities of the azide. However, we were able to obtain 1h in acceptable yields from 1f by choosing the solvent, reaction conditions and work-up procedure very carefully.

In addition we were able to synthesize quantities of 1c which could be used to generate the target molecule by reaction with phosgene. Though we did not attempt this process, it has been carried out by our collaborators in modest yield[3].

Of greater significance are our preliminary results on attempts to convert 1h to the target 1e by use of the Staudinger Reaction and variants thereof[4]. This reaction is illustrated below.

$$R\text{-}N_3 \longrightarrow \underset{2}{R\text{-}N{=}P(C_6H_5)_3} \longrightarrow R\text{-}NCO + (C_6H_5)_3PO$$

This route shows great promise in that it allows for a one pot conversion of 1h to our target and eliminates a number of intermediates. There are two undesirable side reactions associated with this reaction and they are the intramolecular cyclization of product and the intermolecular reaction of product isocyanate with intermediate 2 to form carbodiimides. The geometry of our intermediate material precludes the intramolecular process and we hope to prevent intermolecular reaction by employing high dilution techniques.

We have begun the study of this route and the reaction of substrate 1h with triphenylphosphine and subsequently with carbon

dioxide is complete in a matter of minutes at ambient temperatures. The identifiable products include the expected triphenylphosphine oxide and a mixture containing bands in the infrared absorption spectrum which correspond to isocyanate and carbodiimide. There is no sign of any residual azide absorption. We think that these results show promise and there is every indication that we will be able to suppress the unwanted intermolecular formation of carbodiimide. We wish to continue this study to ascertain the best conditions for conversion to our target molecule.

IV. CONCLUSIONS AND RECOMMENDATIONS

This work has explored a variety of reagents and reaction conditions for effecting the synthesis of the target molecule, 1e, from materials which we have made readily available. Though we have not yet developed a simple high yield process to the target, our results indicate that there is a high probability that this can be done.

Our recommendations include continuing the two parallel schemes in order to optimize the conditions necessary for the synthesis of 1e and thence to other more energetic materials exemplified by 3, 4 and 5.

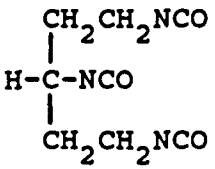

3.

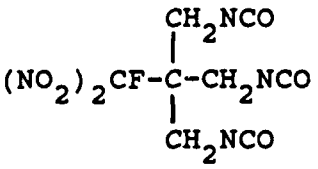

4.

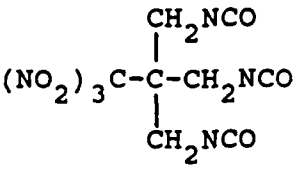

5.

Our preliminary literature survey indicates that all of these are attainable synthetic goals.

BIBLIOGRAPHY

1. R.A.Silva, Final Report, AFOSR, 30 Sept. 1985; S. Dimock, Final Report, AFOSR, 1985.
2. H.C.Brown, B.Kanner, J.Amer.Chem.Soc.,1953, 75, 3965; 1966, 88, 986; P.J.Stang, W. Treptow, Synthesis, 1980, 283.
3. R.Chapman, RPL Edwards AFB, private communication.
4. H.Staudinger, J.Meyer, Helv.Chim.Acta, 1919,2, 635; H. Staudinger, E. Hauser, ibid.,1921, 4, 861; G. Singh, H. Zimmer, Organomet.Chem.Revs.,1967, 2, 279; P. Molina, M. Alajaran, A. Argues, Synthesis, 1982, 596; M.P. Ponomarchuk, L.S. Sologub, L.F. Kasokhim, V.P. Kukhar, Zh.Obshch.Khim., 1985, 55, 1725.

1986 USAF MINI-GRANT

Sponsored by the

AIR FORCE OFFICE OF SCIENTIFIC RESEARCH

Conducted by

UNIVERSAL ENERGY SYSTEMS, INC.

FINAL REPORT

STUDIES ON COMBUSTION OF LIQUID FUEL SPRAYS IN STAGNATION FLOWS

Prepared By:	Dr. S. H. Sohrab
Academic Rank:	Assistant Professor
Department:	Department of Mechanical Engineering
University:	Northwestern University
Research Location:	Department of Mechanical Engineering Northwestern University Evanston, Illinois
USAF Researcher:	Mr. Michael Powell Rocket Propulsion Laboratory Edwards AFB, California

Subcontract No.: S-760-OMG-069

STUDIES ON COMBUSTION OF LIQUID FUEL SPRAYS IN STAGNATION FLOWS

T. H. LIN and S. H. SOHRAB

Department of Mechanical and Nuclear Engineering
Northwestern University
Evanston, Illinois 60201

ABSTRACT

The report introduces studies on steady combustion of polydispersed sprays of liquid fuels in the stagnation-point flows. The burner assembly is designed to produce polydispersed sprays of the fuels within the background of gaseous combustible or oxidizing mixtures. Thus, steady combustion of these fuels within a planar flame adjacent to the boundary layer near a quartz plate can be studied. Using the laser sheet lighting for photography, the flow field as well as droplet size and distribution throughout the pre- and post-flame regions maybe investigated. The general characteristics of the spray burner system are first examined using water droplets in air. It is found that sprays of water in methane/air mixture result in a homogeneous soot formation region downstream of the lean methane flames. In addition, photographs of burning kerosene droplets as they pass through planar lean methane/air flames are presented. Also, preliminary observations concerning combustion of ethyl-alcohol, methyl-alcohol, heptane and octane sprays in lean methane/air mixtures are discussed. The potential application of the experimental model to future studies of the structure, extinction and stability of poly and monodispersed spray combustion is emphasized.

Introduction

Combustion processes in sprays of liquid hydrocarbon fuels are of central significance to the understanding of gas turbine engines and liquid rockets. In addition, spray combustion has diverse application in industrial boilers, furnaces, diesel engines, and fuel-injected spark ignition engines. Although problems of solid propellant rockets have been extensively studied, liquid rockets and the associated stability problems remain to be resolved. Here, the simultaneous presence of the two phases further complicate the homogeneous chemically reacting flow and the resulting interactions between flow/flame/droplet greatly enrich the physical phenomena.

Most studies of spray phenomena have been concerned with combustion of free or suspended single droplets. Even though such studies are significant for fundamental understanding of droplet burning they are only partly helpful in description of spray combustion. Because of the complex interaction between droplets, the results of tests on single droplet or those considering an array of droplets cannot be readily extended to the turbulent spray combustion which often involve dense sprays. In spite of their wide applications, relatively few studies on spray combustion have been reported. Early theoretical study of sprays was initiated by Williams [1,2] who introduced statistical formulation of the spray problem. More recently, the application of large activation energy matched asymptotic technique to spray combustion has been initiated [3].

Early experimental works on sprays were primarily of qualitative nature providing some rudimentary understanding [4]. More recently, combustion of monodispersed sprays was investigated in Wilson-cloud chamber type apparatus [5,6]. Here, by sudden expansion of the saturated vapor of the fuel, a cloud of small droplets were generated. The spherical propagation of flame through

such drops were thus studied. Also, propagation of flames in bunsen type inverted cone flames have been reported [7,8]. Here, by measuring the cone angle the flame propagation speed could be approximately deduced. The propagation of planar flames in sprays passing through tubes have also been studied [9]. More recent works concerning application of laser diagnostic techniques to spray combustion studies have been reviewed by Chigier [10]. These works on spray have greatly contributed to our knowledge of spray combustion. Among other observations, the thicker reaction zones with either smooth or corrugated flame surfaces have been observed. Also, the propagation speed of the flame front through such poly or mono dispersed sprays have been determined [5-9].

Although the above mentioned studies have provided much needed insight into spray combustion, the complete modeling of actual spray has not been fully possible in these models. This is primarily caused by either the absence of flow nonuniformity or the unsteady nature of such studies. For example, spherical propagation of flame in the cloud chamber [5,6] is basically unsteady such that accurate investigations of flame structure becomes difficult. Also, the inverted cone studies [8] involve complex fluid mechanics of entrainment and the associated lack of control of the mixing shear layers. Finally, the planar flame propagation is one dimensional. However, it is well established that in actual turbulent spray combustion fields, flames always encounter velocity gradients and therefore are under stretching or compression as discussed by Karlovitz [11].

In view of the fact that the spray combustion in most applications including liquid rockets is fully turbulent, inclusion of flame stretch is quite significant. Therefore, in a recent investigation [12], studies of the spray of liquid hydrocarbon fuels were considered within the stagnation flow

configuration, where the rate of stretch can be systematically controlled. Application of stagnation flow configuration to the study of flame extinction has a relatively long history [13]. More recent works, among others, have considered the application of stagnation point flow [14] and counterflow [15,16] configurations to the study of combustion of gaseous fuels.

In this experimental work, the feasibility of the proposed model and its limitations are first explored. This will be followed by the discussion of sprays in non-reactive cold flows. Next, the characteristics of sprays of liquid fuels are discussed and for this preliminary study, we will consider kerosene, ethyl- and methyl-alcohol, heptane and octane as representative hydrocarbon fuels. The choice is motivated by the relevance to liquid rocket fuels as well as the ease for future comparisons of flame speeds with existing data obtained by previous studies mentioned earlier.

Experimental

The burner system is composed of a quartz contoured nozzle with 38 mm exit diameter and 7 to 1 area ratio, a flat quartz plate and a liquid fuel atomizer. In Fig. 1 the schematic of the stagnation flow spray burner assembly is shown. Air and gaseous fuel are metered by conventional rotameter and premixed in the lower chamber of the burner as shown in Fig. 1. The combustible mixture enters the 102 mm diameter extension tube containing glass beads producing uniform velocity profile within the tube. A liquid fuel atomizer is situated in the center of the extension tube as shown in Fig. 1.

Two different types of atomizers with fundamentally different working mechanisms are considered. The first type is a high-pressure liquid fuel atomizer such as used in conventional oil spray burners. Here, atomization is accomplished by passage of high pressure liquid through a small orifice of

special geometry. The liquid was introduced to atomizer from a 1 liter storage tank pressurized by nitrogen using a pressure regulator. The nozzle was designed to operate at 100 psig under a constant flow rate of 0.85 gallons per hour (GPH). Thus, changing the liquid fuel flow rate was only possible through reduction in liquid back pressure which would necessitate operation away from the optimum design pressure. Also, the rated capacity, 0.85 GPH, is an order of magnitude in excess of the required flow rates of the fuels. Such atomizer had to be used because of the limitations in the lowest possible flow achievable in this type of atomizer. The divergent angle of the spray cone was 80 degrees.

The second type of atomizer employs ultra-sonic vibration of a specially designed nozzle using piezo-electric crystals for liquid atomization. This atomizer produces droplets 20-50 μm in size with negligible axial momentum. For this atomizer the liquid fuel was fed into the nozzle by gravity, maintaining a desired level of liquid fuel at all times. The ultra-sonic atomizer produced a narrower jet, about 40 degrees spray angle, with little unatomized liquid flow.

The atomized droplets are in part entrained by the methane/air mixture. In passing through the contoured nozzle, a uniform-velocity polydispersed spray is formed at the exit plane of the nozzle. This flow subsequently impinges on a flat quartz plate located at a specified and fixed height above the nozzle rim. As shown in Fig. 1, a ring of cooling water with small water jets surrounds the nozzle for cooling the rim as well as the exhaust system. A fuel drain pipe is provided for droplets which may accumulate within the glass bead region. An exhaust system is surrounding the nozzle, Fig. 1, to prevent the upward motion of the hot products of combustion and also for removal of these gases from the laboratory. The quartz plate provides for the

observation and photography of the spray from the top. Since some drops can survive through reaction zone and will impinge on the hot quartz plate, the thermal shock property of silica is essential. The observations through the transparent window allow for better monitoring of droplet motion, evaporation and combustion after the reaction zone. The system is capable of providing a stable flat flame of any gaseous fuel with the simultaneous possibility of introducing droplets of any other liquid fuel into the flow field.

A schematic drawing of the spray in stagnation flow is shown in Fig. 2 where z and r refer to the axial and radial directions. For observation and evaluation of size of the droplets, a sheet of Argon-ion laser light, 1-2 mm thick, is produced by passing the laser beam through a cylindrical lens. The light sheet can then be oriented either parallel or perpendicular to the axis of the spray jet. This will allow for observation of droplet streamlines as well as the droplet diameters, respectively, at any axial and radial location within the flow field.

Sprays in Nonreactive Flows

To explore the general features of the sprays in stagnation flows, the spray of water droplets in air are considered first. Figure 3 shows the direct photograph of the streamlines which is obtained when water droplets are illuminated by laser sheet light passing through the jet centerline parallel to the axial direction. Unless otherwise specified, the ultra-sonic nozzle is used in these tests. The faint opposing streamlines above the stagnation plane are the reflections of the lower streamlines in the transparent quartz plate. The bright intense line is the front edge of the thick, 15 mm, quartz plate.

A most interesting feature of the flow field shown in Fig. 3 is the

boundary layer adjacent to the quartz plate. As is to be expected for stagnation-point flows, the thickness of the boundary layer is constant. The streamlines are seen to primarily deflect and produce curves which are asymptotic to the boundary layer. The uniform spacing between these streamlines also reflects the uniformity of droplet distribution in the spray. These water droplets are anticipated to be in 20-50 μm range based on suggestions of atomizer manufacturer. Some occasional, and relatively brighter, streamlines are also identifiable, see Fig. 3, which do not diverge as much and cross the boundary layer and impinge on the plate. These are believed to belong to the few larger droplets with too much inertia which do not follow the gas flow. We can also identify these larger droplets in the presence of flames to be discussed later.

In Fig. 4, a series of photographs taken from the top view through the quartz plate are shown. Here, the laser light is a horizontal, planar sheet which is perpendicular to the axis of symmetry at different axial positions. The top view is therefore dependent on the thickness of the laser sheet light, as well as the axial position and the exposure times used in photography. We note that near the nozzle rim streamlines are vertical, Fig. 3, and the top view will show the initial drop size, Fig. 4a. Near the boundary layer, on the other hand, the drops are diverging and will produce radial streamlines, see Fig. 4b, which diverge from the jet axis of symmetry.

If the direct photographs from the top views are sufficiently magnified, the size and distribution of the drops at various axial positions along the spray can be investigated. An example of such a process is shown in Figs. 4c-4d, which are preliminary results obtained by magnification of the central portion of the spray shown in Fig. 4a. Thus, Fig. 4d is obtained by magnifying Fig. 4c using a conventional microfiche system. In these

preliminary examples the potential of the technique is clearly demonstrated. This is quite useful, since the droplet characteristics, before reaching a flame and after passage through the flame, can be examined.

Sprays in Reactive Flows

In the following, combustion of polydispersed droplets of methyl- and ethyl-alcohol, kerosene, heptane and octane within the background of lean methane/air mixture have been considered. The experiments involve the establishment of a homogeneous lean methane/air flame first. Next, droplets of the above fuels are introduced into the flow field and burn as they enter the planar methane flame. Therefore, the methane flame acts as an ignition source for the sprays. The fuel droplets are made visible by the laser light scattering.

Before considering liquid fuels however, the characteristics of the lean methane/air flames as droplets of water are introduced in the flow was examined. Thus, the modifications of the otherwise homogeneous reaction zone as a result of the effects of inhomogenities, drop vaporization in the absence of chemical reaction, could be examined. In Fig. 5a, the direct photograph of the initial lean methane/air flames is shown. In the presence of water droplets, Fig. 5b, a homogeneous region of soot formation appears on the downstream side of the flame. This is quite interesting, since the methane flame is actually fuel lean and not easily susceptible to soot formation. This phenomena is clearly related to the cooling effects caused by water evaporation in these hot post-flame regions. Figures 5c and 5d are direct photographs of methane/air flames with the water drops which are illuminated respectively upstream and downstream of the reaction zone. The reduced number of visible lines in Fig. 5d reflects the fact that many of the smaller water

drops actually vaporized in passage through the flame. Finally, comparison of Fig. 5a with Figs. 5b-5d show that the flame thickness increases as the water droplets are added to the gaseous stream.

For sprays of combustible fuels, basically, two distinguishable burning modes were observed depending on the volatility of the liquid fuels. For less volatile fuels with large heat of vaporization, such as kerosene, methyl- or ethyl-alcohol, droplets remained intact until they closely approached the methane flame. Here, droplet evaporation and combustion occur primarily near and downstream of the methane flame. For volatile fuels such as heptane and octane, on the other hand, droplet evaporation occurs immediately after atomization. Thus, these fuels produce appreciable vapor which subsequently burns within the methane flame.

In Fig. 6, direct photographs of methane/air flames in the presence of droplets of methyl-alcohol are shown. The side view of this burning configuration, Fig. 6a, shows that no soot is observed in the presence of methanol sprays. However, the thickness of the original methane/air flame was seen to increase when methanol droplets were added. The top view shown in Fig. 6b corresponds to the horizontal laser light at axial position 5 mm below the flame sheet. Therefore, the small droplets shown in Fig. 6b are pre-flame droplets. The characteristics of ethyl-alcohol sprays were quite similar to those observed for methyl-alcohol. This result clearly shows that droplet size can be studied without much interference from the flame radiation.

A series of photographs showing various stages as increasingly more droplets of kerosene are added to the methane/air mixture are shown in Fig. 7. It is noted that for these tests with kerosene, the high pressure atomizer rather than the ultra-sonic atomizer is used. As a result, the droplets are expected to be larger for this situation. First, the planar methane flame of

Fig. 7a changes and anchors on the nozzle rim as shown in Fig. 7b as a result of the change in mixture composition which approach towards stoichiometric condition as the kerosene is added. A trace of yellow color due to formation of soot follows the individual kerosene drops as they burn downstream of the methane flame. For large quantities of droplets, the soot formation is quite large, see Fig. 7e, as expected for these exceedingly rich burning conditions.

Another observation in Fig. 7 is the gradual thickening of the reaction zone as kerosene is added to methane/air mixture. This agrees with the earlier observations [5,6] of the reaction zones in sprays as compared to homogeneous gaseous mixtures. Also, variation of the flame position with respect to the stagnation plane is detected which is an indication of the change in the flame propagation speed. Indeed, the value of the axial velocity at the upstream edge of the preheat zone is defined as the stretched flame propagation speed. It is also noted that as more droplets of kerosene are added, the methane flow rate can be substantially reduced while maintaining steady burning.

For heptane and octane sprays when using the high pressure atomizer, the flames were found to be highly corrugated and unstable [12]. This is caused by the rapid evaporation of the droplets and the subsequent mixture composition nonuniformities. Moreover, the flames of these sprays showed highly cellular structures under chaotic motion. This is expected for rich mixtures of these fuels and is the manifestation of the diffusional-thermal instability discussed by Sivashinsky [17]. It is believed that the generation of more uniform droplets by the new ultra-sonic atomizer will help in obtaining flat, but not necessarily smooth, flames of these fuels.

Concluding Remarks

The present report represents the first investigation of the combustion of liquid fuel sprays in the stagnation flow configuration. The complete description of all of the implications of the present experimental model is quite extensive and will encompass almost every aspect of the field of spray combustion. In what follows certain general and immediate application of the experimental system will be outlined and their relevance to the broad topic of turbulent spray combustion will be emphasized. The objective of the studies described herein is to help in closer modeling and improved understanding of the combustion proceses within turbulent sprays such as in liquid rocket engines.

To begin with, the position of flames within the stagnation flow will provide for immediate evaluation of the flame propagation speeds in poly or mono dispersed sprays under varying rates of stretch. The extrapolation to zero rate of stretch will then give the precise value of the laminar flame propagation speed in the spray. Here, the flame propagation speed is defined as the value of the axial velocity at the upstream edge of the preheat zone. It is noted that since flame surfaces within turbulent sprays always undergo stretching, the provision for systematic variation of the stretch rate by the model is significant.

Another important feature of the present model is that it provides a steady and planar flame within the spray, thus allowing for accurate diagnostic evaluation of the flame structure. Therefore, both pre- and post-flame processes can be investigated. Furthermore, the phenomena of flame extinction due to variations in droplet size, droplet number density or rate of stretch can be studied. The knowledge of flame extinction is important since it determines whether or not a flame sheet will undergo local extinction

within the turbulent spray. Also, determination of the temperature profile across the planar flame will provide much needed information concerning the structure of the reaction zone.

Since the fuel droplets scatter laser light, determination of the droplet velocity with laser doppler velocimetry is readily accomplished without the need for seeding the flow field with particulates. Also, using the laser sheet lighting, the trajectory, size and distribution of droplets can be determined through photography and cinematography. Therefore, the actual history of evaporation and combustion of the droplets can be studied. Since velocities after the planar flame increase by many folds due to sudden expansion, the motion of droplets are expected to be accelerated. Knowledge of the droplet history and possible break-up through such severe velocity and temperature gradients is important to the understanding of spray combustion.

In addition, the experimental model can be used to evaluate the burning characteristics of sprays under systematic variation in the phase of the fuel. Using a liquid vaporizer, the fuel can be introduced either as droplet or as vapor premixed with air. Since the reaction zone is governed by gas phase combustion, depending on the overall fuel/air ratio, an optimum burning regime can thus be identified. Also, combustion of any liquid fuel within the background of another gaseous fuel and oxidizer mixture can be analyzed. Indeed, the results presented herein on combustion of kerosene droplets within lean methane/air mixture represent such situation. The potential implication of an optimization procedure when the characteristics of the liquid and gaseous fuels are judiciously chosen could be far reaching and in need of further exploration.

As was mentioned earlier, in rich sprays of heptane and octane, the flame surfaces were observed to assume cellular structure. Thus, the present model

is an excellent vehicle for the study of the well known flame instability phenomena in turbulent spray combustion. The understanding of the methods for suppression or judicious enhancement of such instabilities [18] is also relevant to the understanding of liquid rocket combustion. Finally, the study of counterflow diffusion flames of two sprays can be performed. Here, the structure of a diffusion flame supported by counterflowing sprays of oxidizer and fuel within the background gaseous nitrogen will be considered. Studies on interactive combustion of premixed flames introduced earlier [19,20] can also be extended to sprays in the counterflow configuration.

In view of the above considerations, the diverse applications of the proposed model to the study of spray combustion is apparent. The present report established the feasibility of the model. Although the above mentioned topics are quite diverse in nature, they can all be viewed within a global framework aimed at modeling turbulent spray combustion.

Acknowledgements

This research was sponsored by The Air Force Office of Scientific Research/AFSC, United States Air Force, under contract F49620-85-C-0013SB5851-0360. The work was in part performed at Air Force Rocket Propulsion Laboratory (AFRPL) under AFOSR/Universal Energy Systems Subcontract S-760-OMG-069.

One of the authors (SHS) expresses his deep appreciation to Mr. Michael Powell of AFRPL for his help and support. Also, the assistance of Mr. Ranney Adams of the Combustion Research Laboratory and the hospitality of the personnel at the AFRPL are kindly appreciated.

References

1. Williams, F. A.: 8th Symposium (International) on Combustion, Williams and Wilkins Co., Baltimore, MD, 1962.

2. Williams, F. A.: Combustion Theory, Addison Wesley, Reading, MA, 1965.

3. Lin, T. H.: An Asymptotic Analysis of Flame Propagation in Dilute Sprays, Master's Thesis, Northwestern University (1984).

4. Wolfhard, H. G. and Parker, W. G.: Evaporation Processes in a Burning Spray, J. Inst. Petrol. 35, 118 (1949).

5. Hayashi, S. and Kumagai, S.: Flame Propagation in Fuel Droplet-Vapor-Air Mixtures, 15th Symposium (International) on Combustion, The Combustion Institute, p. 445, 1974.

6. Hayashi, S., Kumagai, S. and Sakai, T.: Propagation Velocity and Structure of Flames in Droplet-Vapor-Air Mixtures, Combust. Sci. Tech. 15, 169 (1976).

7. Mizutani, Y. and Nakajima, A.: Combustion of Fuel Vapor-Drop-Air Systems: Part I - Open Burner Flames, Combust. Flame 21, 343 (1973).

8. Polymeropoulos, C. E. and Das, S.: The Effect of Droplet Size on the Burning Velocity of Kerosene-Air Sprays, Combust. Flame 25, 247 (1975).

9. Ballal, D. R. and Lefebvre, A. H.: Flame Propagation in Heterogeneous Mixtures of Fuel Droplets, Fuel Vapor and Air, 18th Symposium (International) on Combustion, The Combustion Institute, p. 321, 1981.

10. Chigier, N.: Group Combustion Models and Laser Diagnostic Methods in Sprays: A Review, Combust. Flame 51, 127 (1983).

11. Karlovitz, B., Denniston, D. W., Knapschaefer, D. H. and Wells, F. E.: Studies in Turbulent Flames, 4th Symposium (International) on Combustion, Williams and Wilkins, Baltimore, MD, p. 613, 1953.

12. Sohrab, S. H.: Studies on Combustion of Liquid Fuel Sprays in Stagnation Flows, AFOSR/UES Final Report, AFRPL, September 1985.

13. Potter, A. E., Jr., Heimel, S. and Butler, J. N.: 8th Symposium (International) on Combustion, Williams and Wilkins Co., Baltimore, MD, p. 1027, 1962.

14. Sohrab, S. H. and Williams, F. A.: Extinction of Diffusion Flames Adjacent to Flat Surfaces of Burning Polymers, J. of Polymer Science, Polymer Chemistry Edition, 19, 2955 (1981).

15. Tsuji, H. and Yamaoka, I.: First Specialist Meeting (Int.) of The Combustion Institute, Tome I, Bordeaux, p. 111, 1981.

16. Tsuji, H. and Yamaoka, I.: 19th Symposium (International) on Combustion, The Combustion Institute, p. 1533, 1982.

17. Sivashinsky, G. I.: On a Distorted Flame as a Hydrodynamic Discontinuity, Acta Astronautica 3, 889 (1976).

18. Sohrab, S. H. and Chao, B. H.: Influences of Upstream Versus Downstream Heat Loss/Gain on Stability of Premixed Flames, Combust. Sci. Tech. 38, 245 (1984).

19. Sohrab, S. H., Ye, Z. Y. and Law, C. K.: An Experimental Investigation on Flame Interaction and the Existence of Negative Flame Speeds, 20th Symposium (International) on Combustion, The Combustion Institute, p. 1957, 1984.

20. Sohrab, S. H., Ye, Z. Y. and Law, C. K.: Theory of Interactive Combustion of Counterflow Premixed Flames, Combust. Sci. Tech. 45, 27 (1985).

Figure Captions

Figure 1. Schematic of stagnation flow spray burner.

Figure 2. Stagnation-point spray flowfield.

Figure 3. Direct photograph of streamlines in nonreactive spray of water drops in air.

Figure 4. Direct photographs showing top views of water sprays illuminated with laser sheet lighting.

Figure 5. Direct photographs of CH_4/air flames in presence of water droplets (a) Pure CH_4/air flame (b) CH_4/air flame with water drops (c) CH_4/air flames with water drops under pre-flame illumination. (d) CH_4/air flame with water drops and post-flame illumination.

Figure 6. Direct photographs of CH_4/air flames with methyl-alcohol drops (a) side view (b) top view with laser sheet lighting.

Figure 7. Direct photographs of CH_4/air flames as increasingly more drops of kerosene are introduced into the flow.

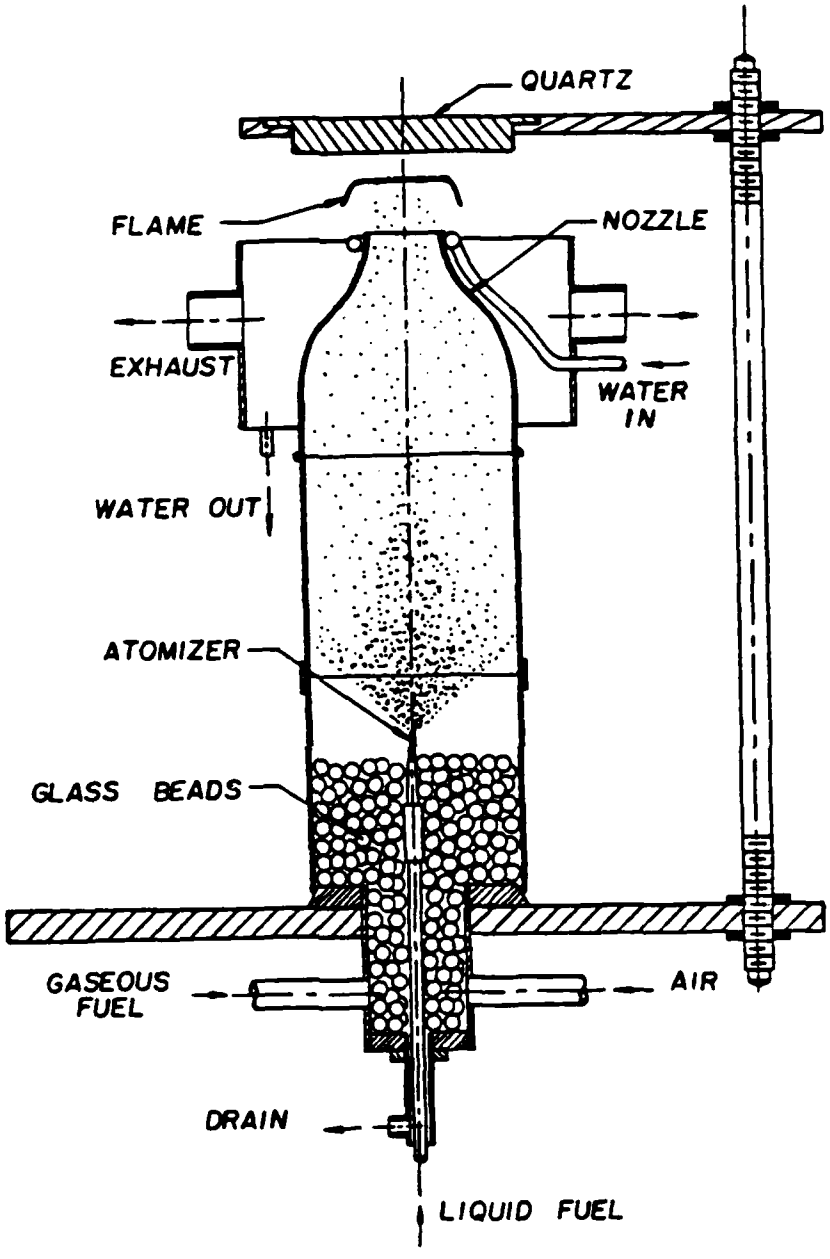
QUARTZ
FLAME
NOZZLE
EXHAUST
WATER IN
WATER OUT
ATOMIZER
GLASS BEADS
GASEOUS FUEL
AIR
DRAIN
LIQUID FUEL

Figure 1

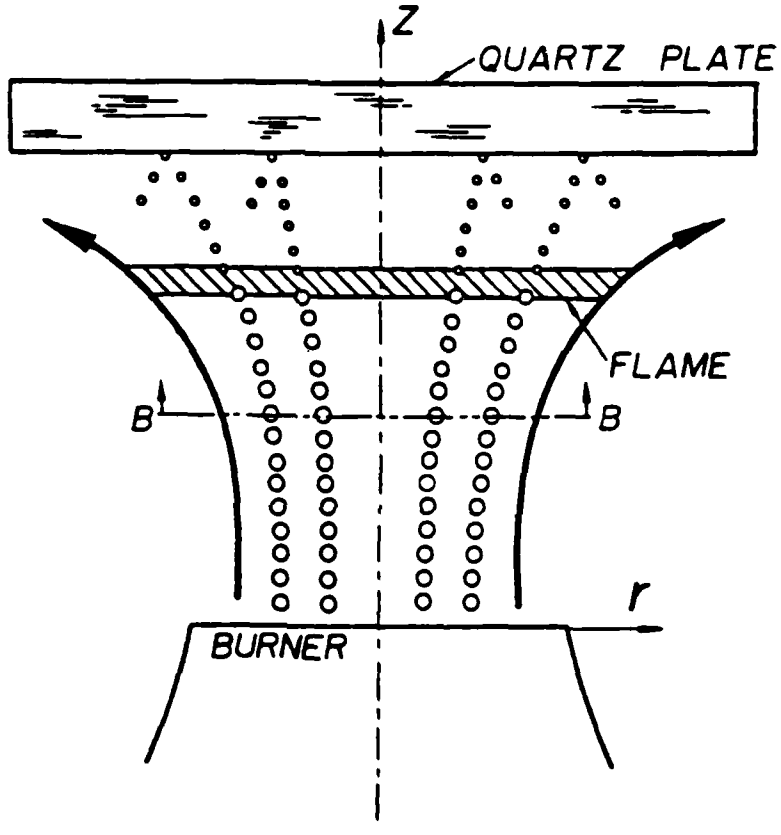

Figure 2

Figure 3

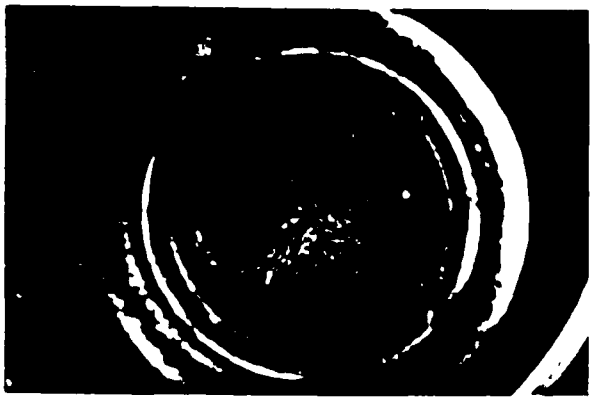

a

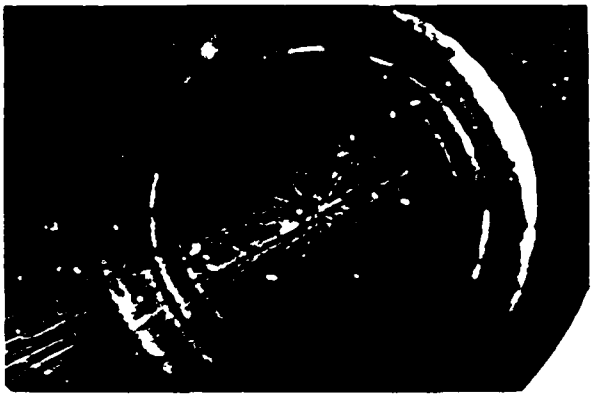

b

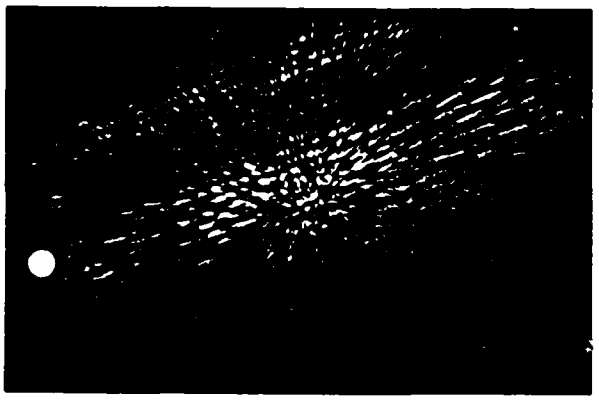

c

d

Figure 4

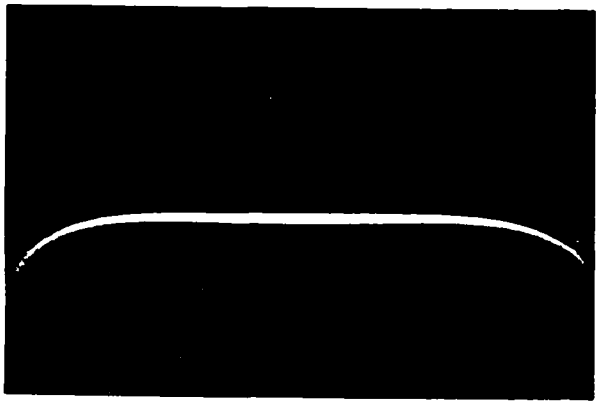

a

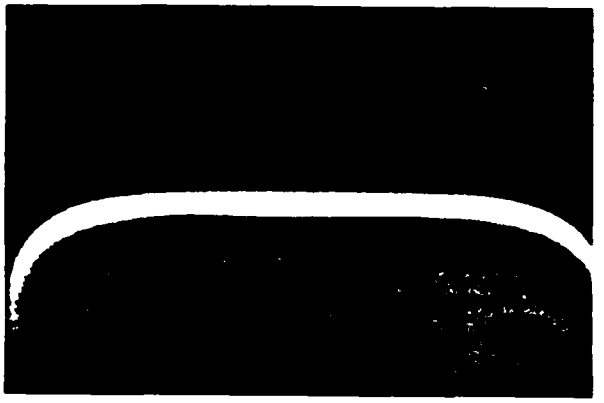

b

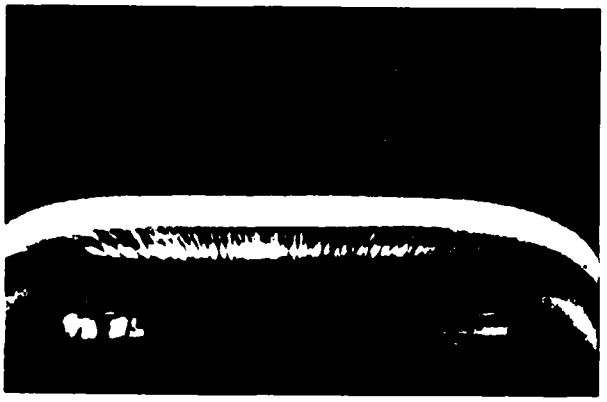

c

d

Figure 5

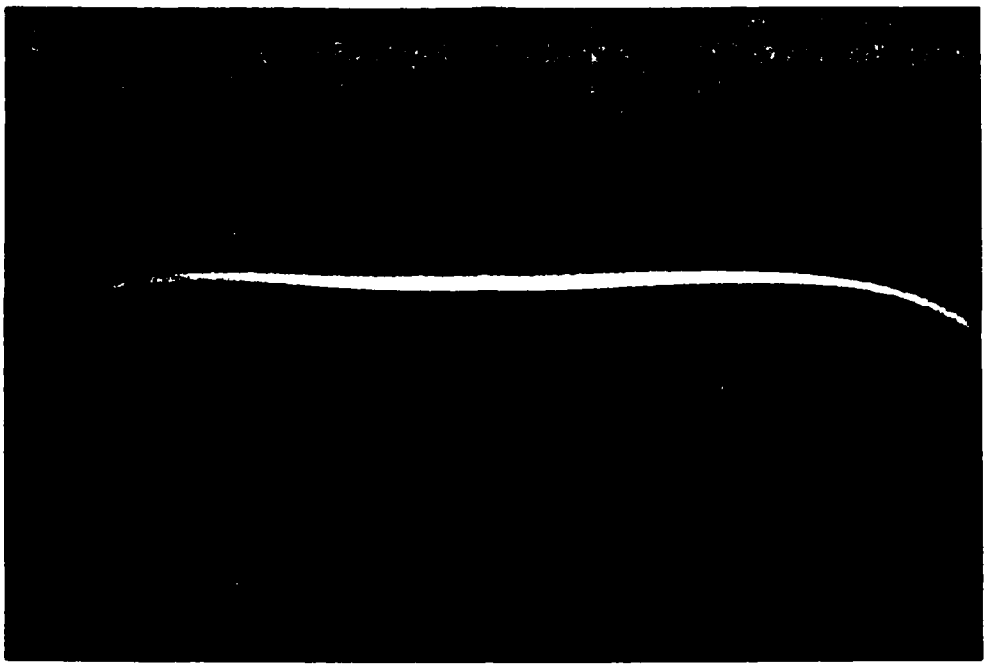

(a)

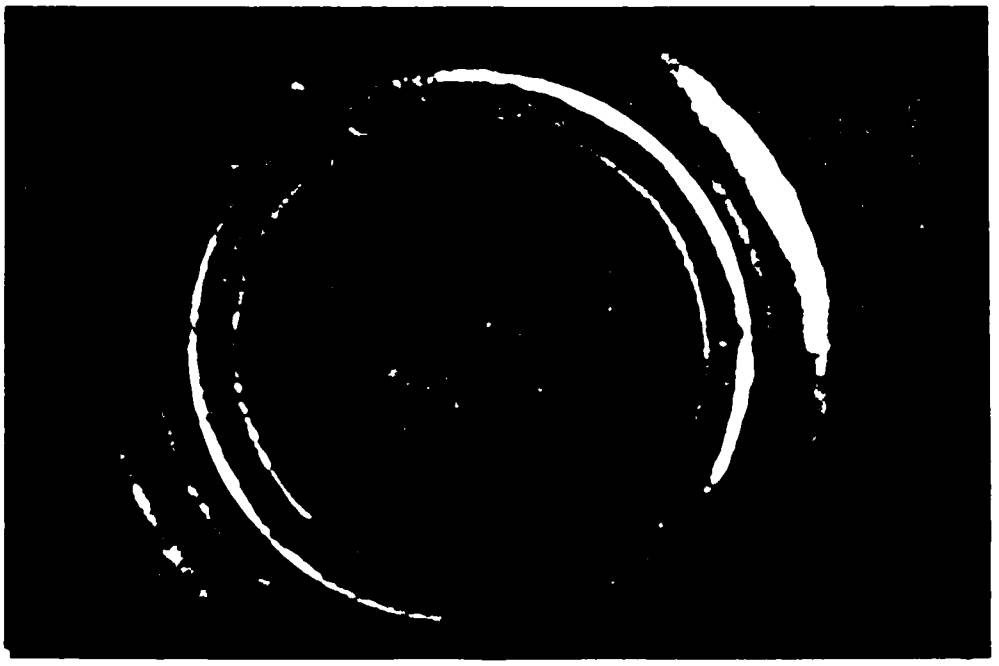

Figure 6

(b)

a

b

c

d

e

Figure 7

1986 USAF-UES RIP GRANT

Sponsored by the

AIR FORCE OFFICE OF SCIENTIFIC RESEARCH

Conducted by the

UNIVERSAL ENERGY SYSTEMS, INC.

FINAL REPORT

MONITORING ENVIRONMENTAL QUALITY BY METABOLITE ANALYSIS

Prepared by: Richard Stebbins, Ph.D.

Academic Rank: Associate Professor

Department and University: Department of Chemistry, University of Southern Maine

Research Location: University of Southern Maine, Portland, Maine

Date: Jan. 1, 1986 - Dec. 31, 1986

Contract No: F49620-85-C-0013/SB8551-0360

Subcontract No: S-760-OM6-082

Monitoring Environmental Quality by Metabolite Analysis

by

Richard G. Stebbins

ABSTRACT

The USAF has an interest in determining the extent of its responsibility for environmental damage caused by its more heavily used products such as JP-4 jet fuel, insecticides, plane deicer and AFFF foam. The transient nature of the toxic components of these products in the environment makes specific chemical monitoring of suspected spills problematic. Bluegills were seperately exposed to Malathion and JP-4 jet fuel, while golden shiners were seperately exposed to Malathion, JP-4, plane deicer and AFFF foam. The livers and guts of the bluegills and the guts of the shiners were analyzed for the toxic components of these formulations and the suspected metabolites of these components. These analyses and the feasibility of using such analyses to monitor environmental quality are discussed.

INTRODUCTION

The USAF has an interest in determining the extent of its responsibility for environmental damage caused by its activities, and in complying with EPA, NIOSH, OSHA and other governmental regulations. Some of the more widely used Air Force materials with pollution potential include jet fuel, deicer, the pesticides Malathion and Aqueous Fire Fighting Foam (AFFF). Spills and leakage of these materials are detrimental to the aquatic environment as evidenced by fish kills and other stress to the aquatic ecosystem. Such problems can result in major regulatory, financial and public relations problems for the Air Force.

One method of confirming a spill in an aquatic environment is chemical analysis of the water or fish tissue for the specific chemical. For chemicals which rapidly decompose or for spills into fast moving waters, detection of the primary pollutant can be extremely difficult. One approach to this problem is analysis for metabolites associated with the pollutant rather than the primary pollutant itself. Detection of specific metabolites or elevated levels of such metabolites would constitute proof of the presence of the primary pollutant.

Much work has been done in the last 25 years to trace the metabolic pathways of different species. A large percentage of this work has been done on rodents in an effort to more fully understand the metabolism of the human body. Work on biodegradation studies is much less extensive when one considers the large number of chemicals that we, as a ...

The main objective of this study was to determine the repetitive [illegible] using natural [illegible] to mimic explosive or ballistic impact to the primary occupants (Crew Test Dummy, CTD) in a right seated and AFRF fire fighting team. The rest of the study are presented in four chapters, one for each material studied. Each chapter includes an introduction, an experimental section, the results of this experimentation, a short summary of results and a list of appropriate journal references.

MALATHION

INTRODUCTION

Malathion is a heavily used organophosphorous pesticide (1) the structure and mass spectrogram of which are shown in Fig. 1a. It is used by commerical agricultural concerns, by those interested in residential lawn and garden care, and by companies specializing in mosquito control. This heavy use makes it a rather common environmental pollutant. Both the behavorial (2) and physiological (3,4) effects of this compound to piscine species have been noted.

Analysis of this pesticide and assessment of its impact on the aquatic environment are complicated by the fact that Malathion breaks down (hydrolyzes) in water and is also metabolized by aquatic organisms (5,6,7,8). Fig. 2a shows the structure of some of the more common metabolic and hydrolytic products of Malathion. DMTP and DMOTP have been identified as metabolic products in mammals (6,7) while MCA, DCA and Malaoxon have been identified as metabolic products of mammals and some species of saltwater fish (1,3,6,7). No literature references identifying the metabolic pathways of Malathion in fresh water fish were found. Since MCA, DCA and Malaoxon have already been identified as metabolic

products in salt water fish, it seemed reasonable to search for these metabolites in fresh water species.

EXPERIMENTAL:

Materials: Boron trifluoride 14% in methanol (Varian), N-methyl-N'-nitro-N-nitrosoguanadine (97%, Aldrich), Malathion, Malaoxon, the dicarboxylic acid of Malathion (DCA), the 1-ethylmonocarboxylic acid of Malthion (MCA), the dimethyl ester of DCA and the methyl ester of the 1-ethyl MCA (supplied by American Cyanamid of Princeton, N.J.) were all used without further purification. All were refrigerated between uses. The solvents hexane, methanol, diethyl ether, ethyl acetate and acetonitrile were all Baker resi-analyzed or the equivalent.

Instrumentation: Chromatograms were obtained using a Varian 3700 gas chromatograph with a ^{63}Ni electron capture detector and a 2M x 1/8" glass column packed with a 4% OV-101 + 6% OV-210 on 80/100 mesh Gas Chrom Q. The temperature of the injection port, column and detector were 200°, 200°, and 300° C respectively. The carrier gas was grade 5 nitrogen (Airco) with a flow rate of 24 cc/min. A Varian 4270 integrator recorded and quantified the chromatographic response. Gc mass spectograms were obtained on an HP 5840A/HP5987-MS/HP 100-DS system with a 25 meter SE-54 capillary column. The carrier gas was helium flowing at 1 cc/min. Ionizing voltage was 70 ev in the electron impact mode with the source temperature at 200° F. Runs were temperature programmed from 38° F-290° F at 6° F per minute. Occasionally an HP 3761 A-

gc/ms. A mass selective detector HP 5970 B data system was used under identical gc conditions as listed above.

Analytical Methods: Standard solutions of Malathion and related compounds (about 10 ppm) were prepared by serial dilutions from stock solutions of the pure compounds dissolved in hexane. It was found that these standard solutions decompose slowly as a function of time even when refrigerated and must be replaced periodically. All standard solutions were refrigerated between uses. Triplicate analysis of Malathion in water was performed on 125 cc samples collected and stored in glass bottles with teflon-coated screw tops. The samples were refrigerated and processed within 24 hours of collection. All glassware used in the analysis, including the collection bottles, was cleaned in accordance with EPA method 608 and rinsed three times with resi-analyzed hexane. Each sample was acidified with 1 ml of HCl and extracted with 25, 15, and 10 ml portions of 15% diethylether/hexane v/v. The combined volumes were dried over anhydrous sodium sulfate until ready for gc analysis.

Duplicate analysis of Malathion in tissue was performed on freshly sacrificed fish. At sacrifice, the appropriate tissue was immediately collected (within 20 minutes) and ground for 15 minutes with a 5 ml portion of 15% diethylether/hexane in an all glass tissue grinder (Lurex Mfg. Co.). The extract was poured into a glass collection tube and a second 5 ml portion of tissue solvent was ground for an additional 10 minutes. This extract was combined with the first, refrigerated and dried over

anhydrous sodium sulfate until analysis. Each sample was air evaporated to 1.0 ml and eluted on a Florisil column prepared according to EPA micro method for the determination of organochlorine pesticides in animal tissue. The sample was eluted with 10 ml of hexane and 10 ml of 1% methanol hexane v/v. The eluates were discarded and further elution with a second 10 ml portion of 1% methanol hexane was performed. This eluate, containing Malathion, was air evaporated to 1 ml and stored over sodium sulfate until gc analysis. Elution with a further 15 ml portion of methanol yielded the fraction containing Malaoxon. It too was evaporated to 1 ml before analysis.

Methylation of standard solutions of IDA and MPA was accomplished by reaction with BF_3, methanol and by reaction with diazomethane. For the former method, 1 ml of freshly opened BF_3 /MeOH was added to about 50 mg of compound dissolved in dry acetonitrile/diethyl ether in a clear dry glass flask. The contents were heated to 60° C for 40 minutes, and allowed to cool. Two ml of water and 2 ml of saturated sodium sulfate were added to the flask, and the mixture was extracted 3 times with 5 ml portions of 15% diethylether/hexane V/V. The extracts were combined, evaporated to 1 ml under a stream of nitrogen and stored over anhydrous sodium sulfate until ready for analysis. The times and temperatures were varied widely to attempt to improve the efficiency of this procedure.

Diazomethane was generated using an Aldrich Diazald apparatus according to the procedure of Aldrich Technical Information

Bulletin #AL-132. Derivatization of standard solutions of DCA and MCA was accomplished by adding 1 ml of the final 1:1 methanol diazomethane to about 50 mg of crystalline dicamba in a acetonitrile diethyl ether in a clean dry glass flask. The resulting solution was allowed to react for 2 minutes at room temperature, and the excess diazomethane was purged by bubbling dry nitrogen through the solution for 10 minutes. The resulting solution was evaporated to 0.5 ml with nitrogen and immediately chromatographed.

Duplicate analysis of Malathion breakdown products in water was accomplished on 125 ml samples. Each sample was extracted with 25,15 and 10 ml portions of 15% diethylether hexane V/V to rid the sample of Malathion. The sample was then extracted with 15,10 and 10 ml portions of 50/50 V/V acetonitrile/diethylether. These latter extracts were combined, evaporated to dryness under N_2 gas and derivatized with diazomethane as described above.

Triplicate analysis of Malathion metabolites was performed on freshly sacrificed fish tissue. At sacrifice, the appropriate tissue was immediately collected (within 10 minutes) and ground for 10 minutes with a 5 ml portion of 50-50 acetonitrile-diethylether V/V in an all-glass tissue grinder (Lurex Mfg. Co.). The resulting mixture was centrifuged and the supernatent liquid transferred to another flask. The remaining tissue was ground again for 10 minutes with a second 5 ml portion of solvent, centrifuged, and combined with the first 5 ml of liquid. The combined extracts were evaporated to 1.0 ml and cleaned up with

the sample was placed on the Florosil column and eluted as above; and diesters of the carboxylic acid were eluted in the 2nd 1% methanol-hexane fraction.

The other half of the sample was evaporated to dryness under nitrogen and derivatized with diazomethane as above. The derivatized sample was placed on a Florosil column and eluted as above. The 2nd 1% methanol-hexane fraction contained the derivatized MCA and DCA.

Fish: For exposure to Malathion, both bluegills (L. Macrochirus) and golden shiners (N. Crvataleucas) were used. Four groups of bluegills were obtained, the first from a commercial hatchery in Poteet, Texas and the last three from a commercial hatchery in LaVernia, Texas. The shiners were obtained from Carroll Cutting of Standish Maine. Three fish each comprised the control and exposed group. The bluegills were housed in 20 l glass aquaria containing 14 l of dechlorinated, gently aerated water at 76-78° F and pH = 7.2. The shiners were housed in similar aquaria and water at 71-74° F. The pH of the water was 7.10 before adding the fish and 7.70 upon completion of the exposure.

For both groups, Malathion was added to the water prior to introduction of the fish such that the initial concentration of Malathion was 110 ppt for the bluegills and 107 ppt for the shiners. Because Malathion hydrolyzes in water, additional malathion was added once a day to return the concentration to its original value. The fish were not fed during the exposure

At that time, both groups of fish were sacrificed and their livers and gut intestinal tracts removed. All fish parts were ground and processed as above as soon after death as possible.

RESULTS AND DISCUSSION:

Standard solutions of Malathion, Malaoxon and the methylated derivatives of possible metabolites were chromatographed under the conditions specified in the experimental section. Retention times, sensitivities and the minimum detection limits associated with the compounds are given in Table 1a.

Because of the wide range of values reported in the literature associated with the rate of hydrolysis of Malathion, it was necessary to make an independent measurement of this value. A solution of 150 ppb Malathion in deionized water at pH equal 7.00 and 25° was allowed to stand open to the atmosphere. An aliquot was taken every two days and analyzed for Malthion. A plot of the natural log of the chromatographic response as a function of time is given in Fig. 3a. Linear least squares analysis of these data give a half-life = 1.79 ± 0.06 weeks for the first order breakdown of Malathion. The correlation coefficient for the regression was R= -0.9914. When the experiment was repeated under the same conditions but with breathing air sparged through the system at 14 cc min half-life = 0.10 ± 0.02 weeks. These results suggest that Malathion is oxidized and that hydrolysis rate is dependent on the sparging rate as well as the size and geometry of the

aquaria. Further work supported the well-established ideas that the rate of hydrolysis increased as the pH increased, and that certain cations, notably Cu^{++} and Al^{+++} catalyze the rate of hydrolysis (8,11).

Since the hydrolysis products of Malathion are different in acidic or basic solutions (11), and since the natural waters in which the fish were housed were basic, identification of hydrolysis products was accomplished at pH=8.00 and 11.46. Natural water was adjusted to these pH values by addition of small amounts of NaOH. After sitting open to the atmosphere at the pH of interest for a week, the solutions were analysed for the hydrolysis products. In order to accomplish this, extracted water samples were derivatized so that MCA and DCA were chromatographable.

Methylation of standard solutions of MCA and DCA with BF_3/ methanol resulted in none of the methyl esters of these compounds, but did yield the methyl ester of DMDTP (RT = 5.36 min. on the packed glass column and confirmed by gc/ms on a separate column). Methylation with diazomethane yielded the monomethyl ester of MCA and the dimethyl ester of DCA respectively, but never in quantitative yield. Twenty-six % of the MCA was converted while only five % of the DCA was converted.Since these latter compounds are of primary interest furtner samples were methylated with diazomethane.

Analysis of water at pH=8.00 gave no evidence of DCA or MCA but did give evidence of DMDTP (RT = 5.36 min.) and the phosphorodithioic acid, O,O - dimethyl ester (the [illegible] ester

analysis of the fish containing [illegible] at a minimum [illegible] of the derivatized extract [illegible] the gas chromatograph and the [illegible] and ratio of the fluorescence [illegible] gas chromatograph of the methyl ester of MCA, [illegible] and the heptafluorobutyric acid ester of prostaglandin $F_{2\alpha}$. Fig. 7 is a chromatogram of the derivatized and nonderivatized extract of this sample.

Golden shiners (N. Crysteleucas) were exposed for [illegible] water containing 137 ppb Malathion at a pH of 7.02 and a temperature of 23° C. The pH of the water rose during the exposure to 7.16 and the Malathion was held at a constant level by daily addition of small amounts of the substance. Analysis of liver after 96 hrs (both for the shiners and the bluegills of the previous summer) was positive for Malathion. Analysis of liver for metabolites was negative. Analysis of the gut tissue gave positive evidence of MCA. Fig.7a shows a chromatogram of the derivatized gut extract of an exposed fish vs a control. Table 2a shows the results of the analysis. The three combined gut samples yield an average MCA level of $7.11 \times 10^{-4} \pm$ [illegible] % ppm. No IDA was found. Since MCA was not a hydrolysis product of the [illegible] or [illegible] it can safely be assumed that the product identified is metabolic in origin and not simply ingested from the water.

Summary

1. The rate of [illegible] of Malathion in water at 23 degrees

and pH = 7.0 was found to be $t_{1/2}$ = 1.79 ± .08 weeks.

2) The rate of hydrolysis increased as the temperature, the stirring rate and the concentration of certain metal ions was increased.

3) The hydrolysis products in basic natural water were identified and found to vary with pH.

4) Malathion, but not its metabolites was identified in the livers of exposed fish.

5) MCA was identified in the gut of exposed fish and it is of metabolic origin.

Table 1a

Chromatographic Characteristics of Organophosphorous Compounds.[a]

Compound	RT (min)	SEN (R/pg)[b]	MDL (pg)[c]
Malathion	12.90	112	38
MCA (4-ethyl-1-methyl)	10.86	228	18
DCA (dimethyl)	9.10	926	4.4
Malaoxon	13.02		

a) Obtained on a 2M x 1/8" glass column packed with 4% OV-101 + 6% OV-210 on 80/100 mesh Gas Chrome Q. Column T=200°. The detector is an ECD.

b) Integrator response units per picogram

c) Minimum detector limits on picograms

Table 2a

Analysis of N Crystoleucas (Golden Shiners) Upon Exposure to Malathion.

Sample	Tissue Mass (mg)	Metabolites (Ng)[a]	Ng/g tissue
Liver Controls			
1	50.5	ND	
2	111.8	ND	
Exposed Livers			
D1	96.7	ND	
D2	111.9	ND	
D3	108.0	ND	
Gut Controls			
G1	176.4	ND	
G2	38.3	ND	
Exposed Gut			
GD1	158.2	MCA (116)	7.33×10^2
GD2	150.8	MCA (96)	6.36×10^2
GD3	174.2	MCA (133)	7.63×10^2

a) ND means not detected

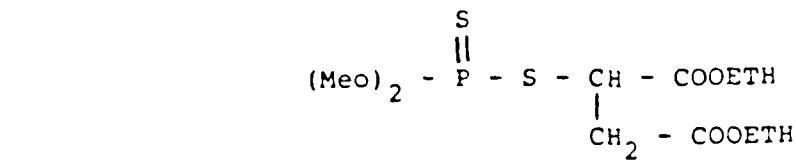

MALATHION (I)

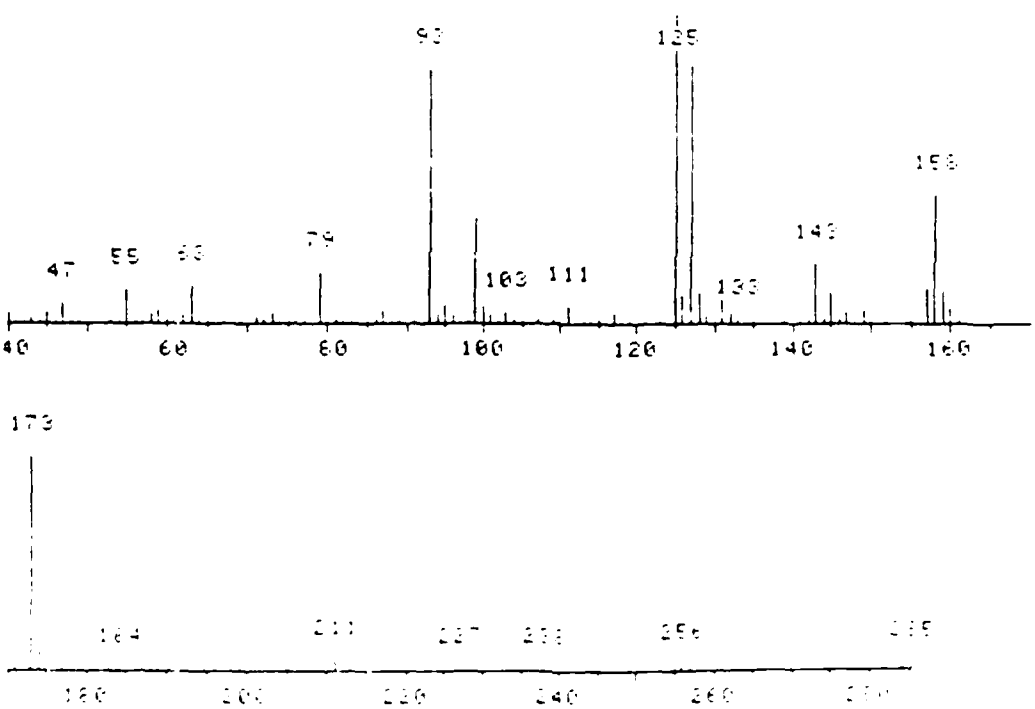

Fig. 1a. Malathion and its mass spectrogram.

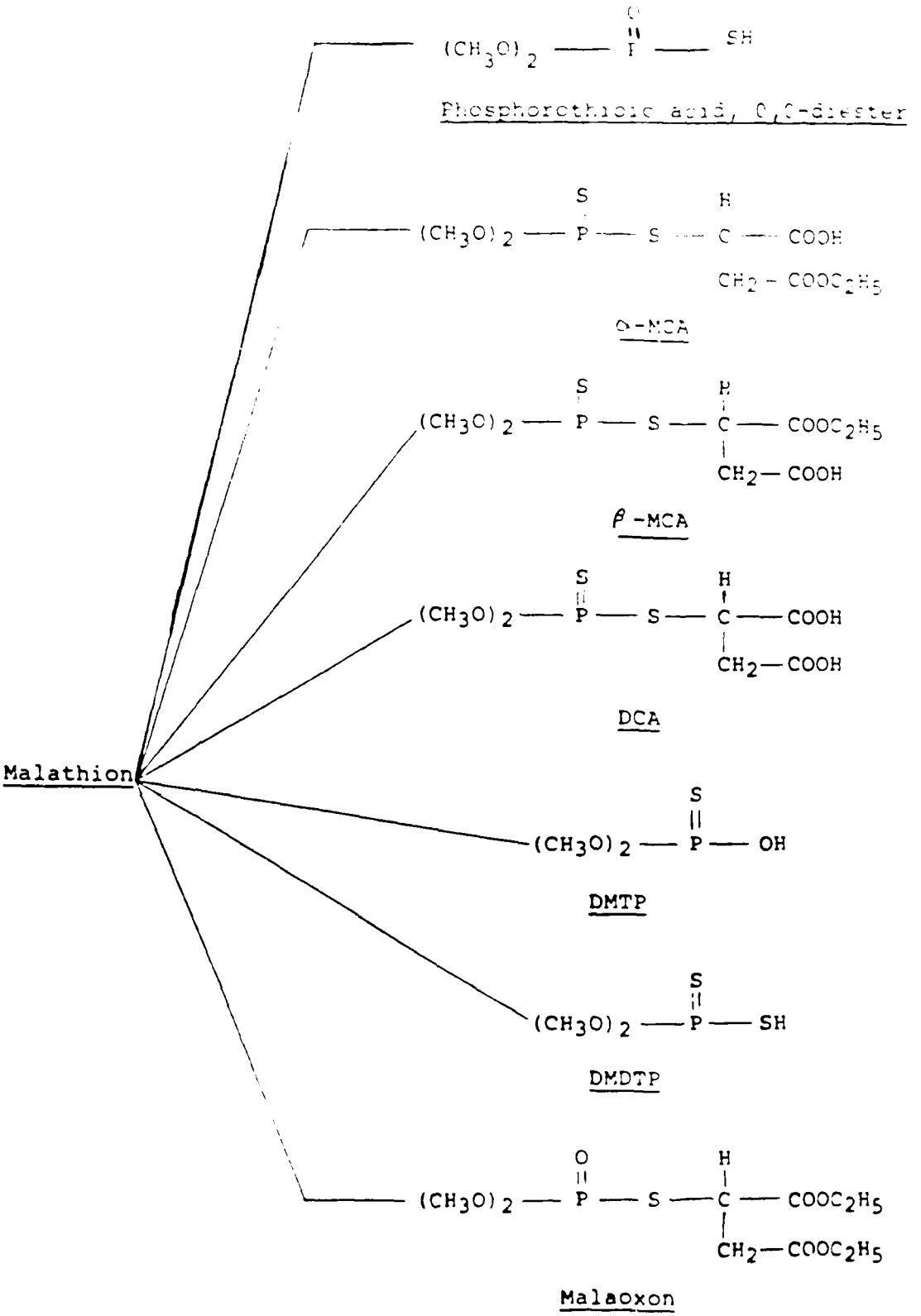

Fig. 2a. Metabolic and hydrolytic products of Malathion.

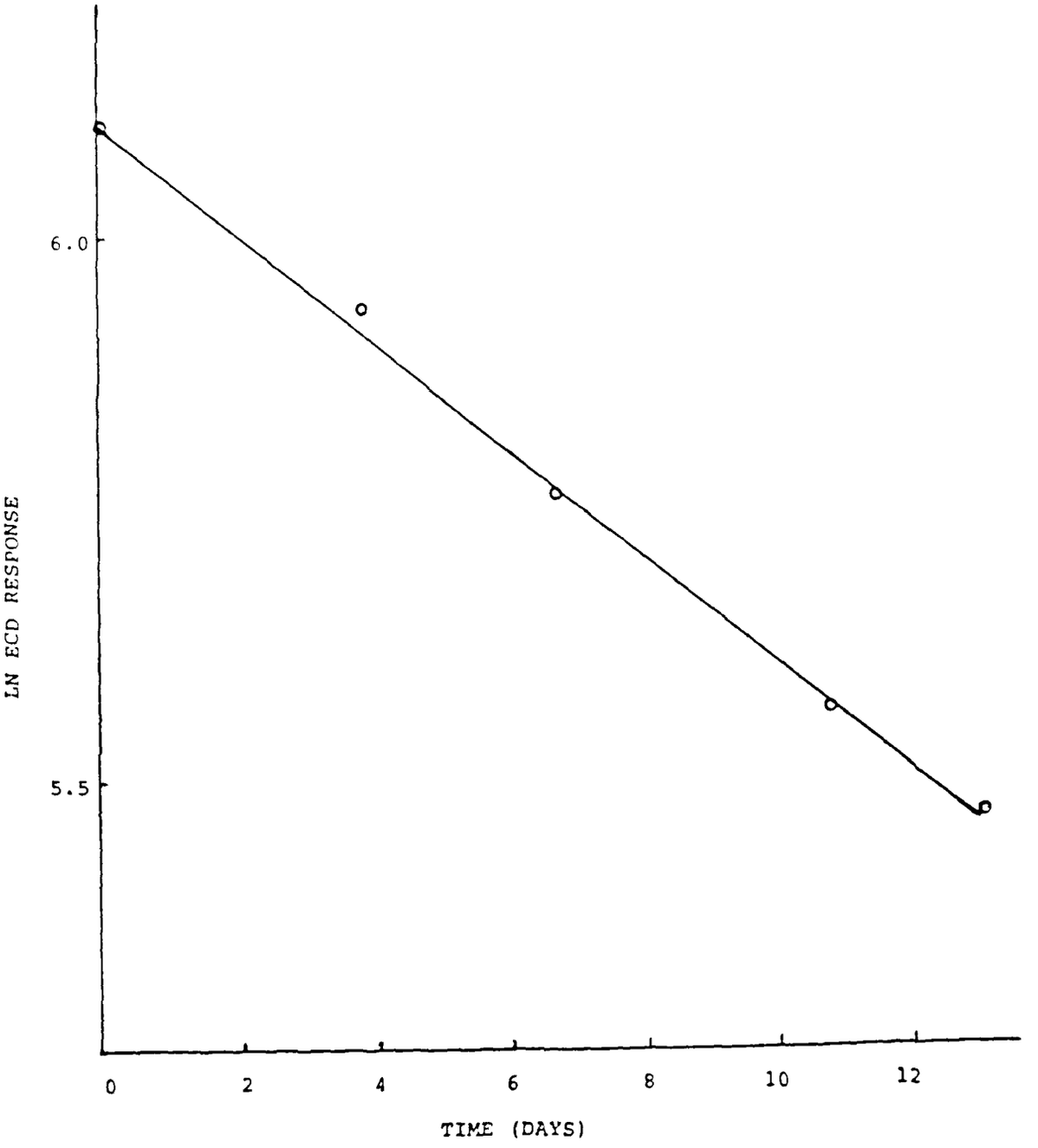

Fig. 3a. Ln of response vs. time for the breakdown of Malathion in deionized water at 25°C and pH = 7.0.

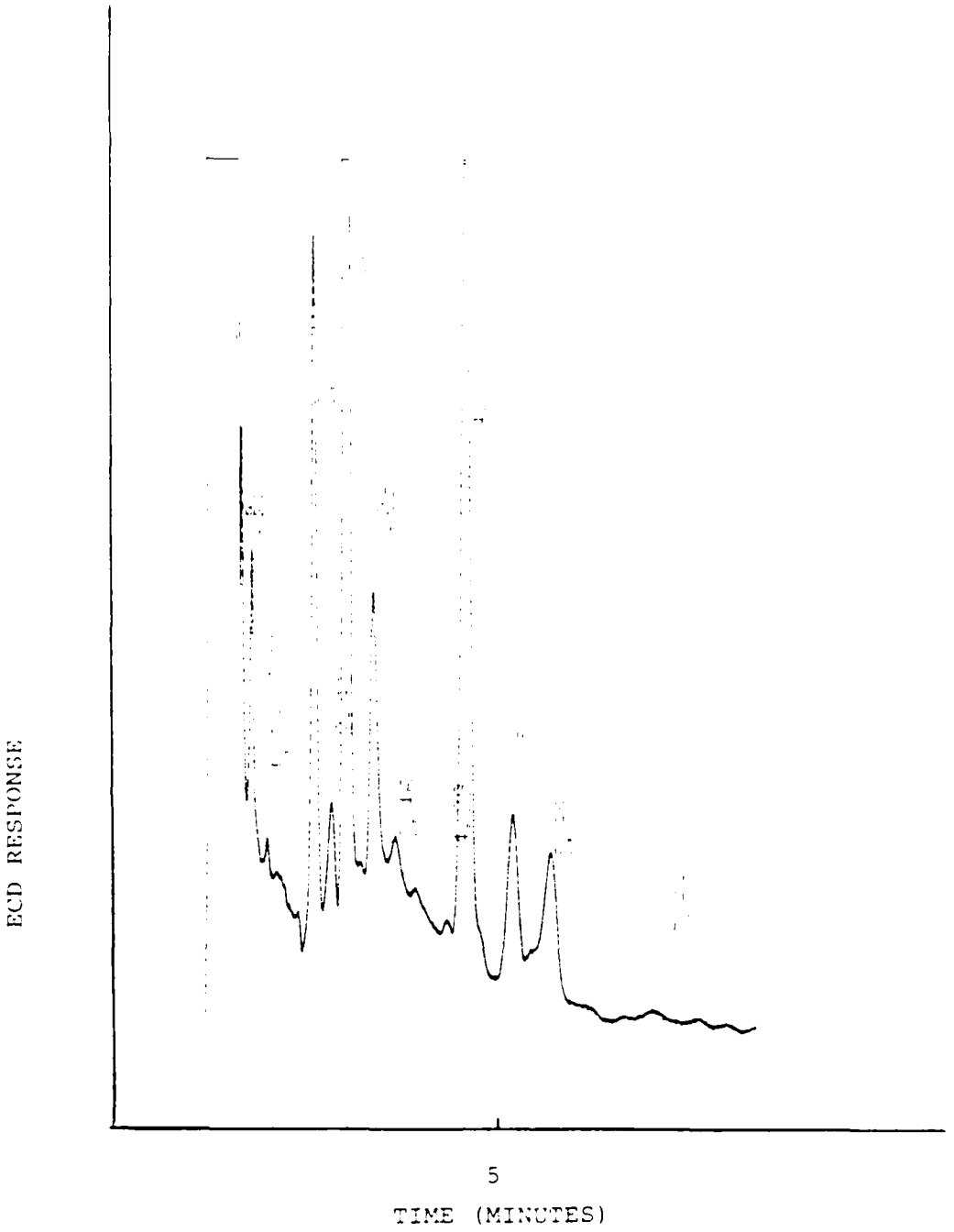

Fig. 4a. Chromatogram of pH = 8.00 water derivatized extract

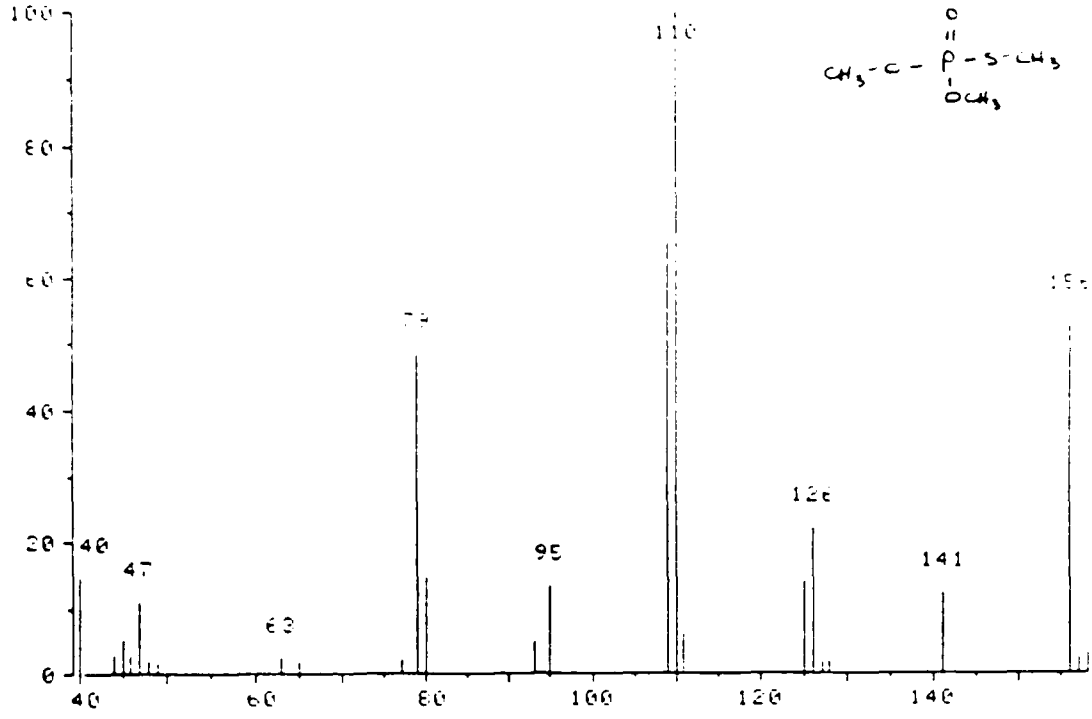

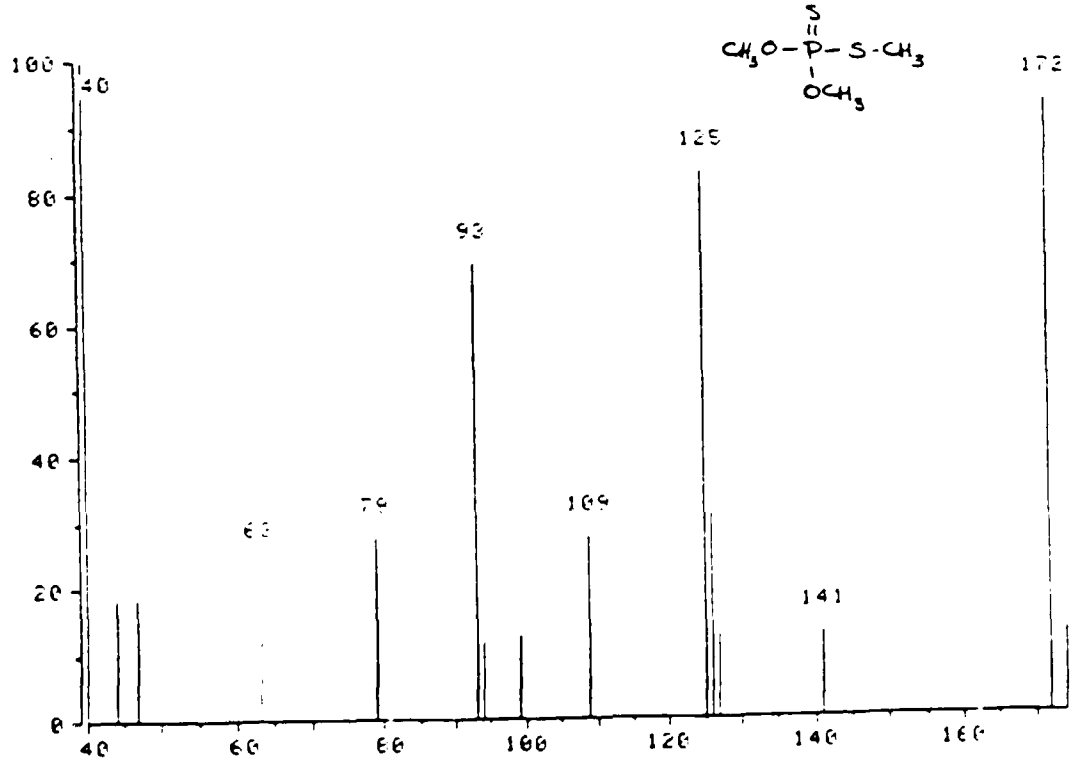

Fig. 5a. Mass spectrograms of hydrolysis products of Malathion

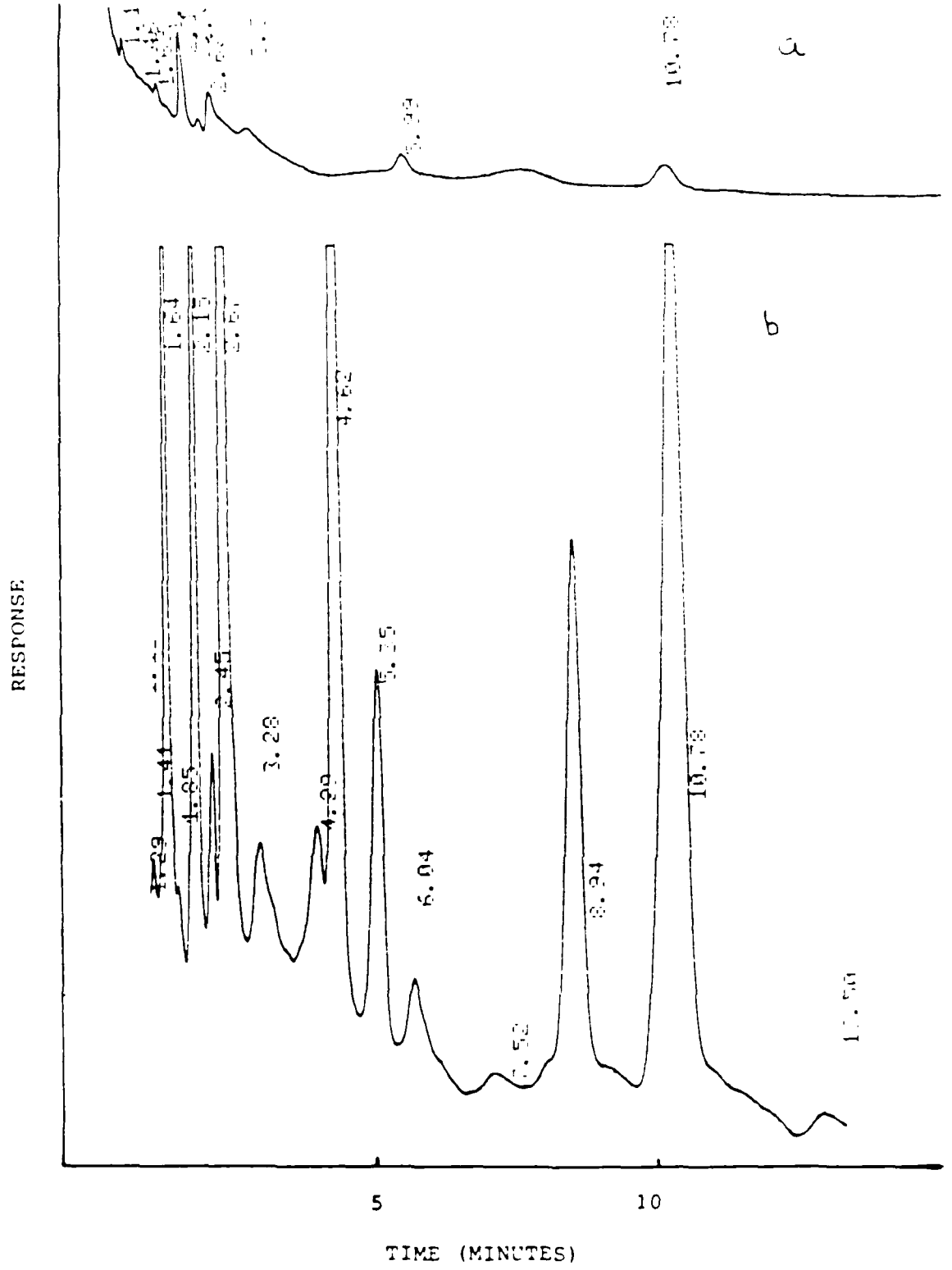

Fig. 6a. Chromatograms of (a) acetonitrile-diethylether extract (pH=11.46) (b) derivatized acetonitrile-diethylether water extract (pH=11.46).

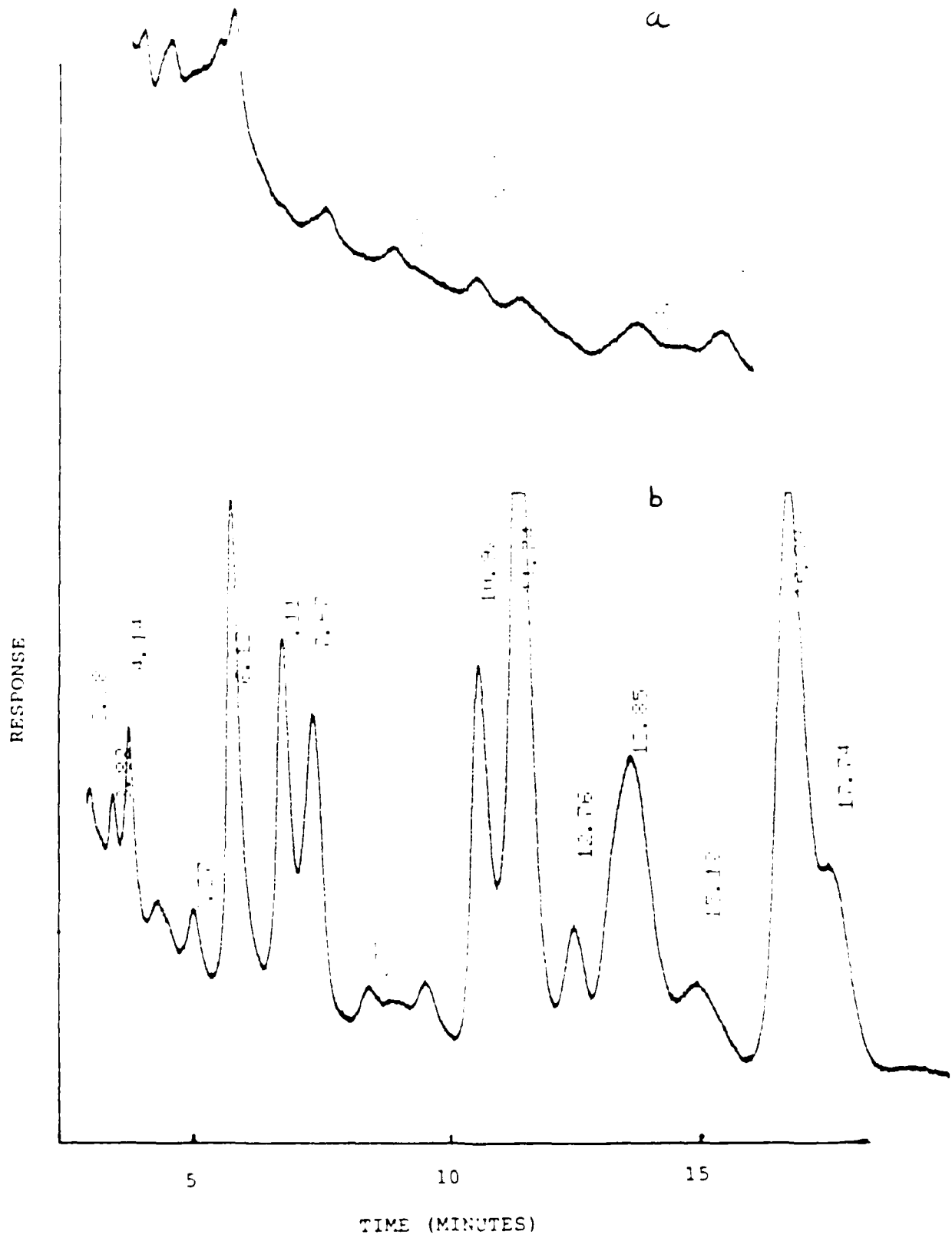

Fig. 7a. Chromatogram of (a) fish gut control, not exposed to Malathion (b) fish gut exposed to 137 ppm Malathion

References

1 [illegible]

2 Henry, M.J. and Anderson, [illegible]

3 Cook, B.H., Moore, J.D. and Lothrop, [illegible]

4 Murphy, E., Proceedings of the Society for Experimental Biology and Medicine 142, 382-386.

5 Casarett and Doull: Toxicology, 2nd Ed. Macmillan Pub. Co. Inc., N.Y. 1986

6 Bradway, D.E. and Shattk, T.M., J. Agric. Food Chemistry, 23, 1342-1344 (1975).

7 Shattk, T.M. and Enos, H.F., J. Agric. Food Chemistry, 17, 1188-1189 (1969).

8 Kadoum, A.M., J. Agric. Food Chemistry, 17, 1178-1180 (1969).

9 Chapman, R.A. and Cole, C.M., J. Environ. Sci. Health, B17 5, 487-504 (1982).

10 Chapman, R.A. and Harris, C., J. Environ. Sci. Health, B19 4+5, 397-407 (1984).

11 Bender, M.E., Water Research, 3, 561 (1969).

JP-4 JET FUEL

Introduction

JP-4 is a common aviation fuel containing a complex mixture of hydrocarbons, both aliphatic and aromatic (1). Aromatics comprise about 10% by weight of the total fuel. The toxicity of the monocyclic aromatics such as benzene, toluene and the xylenes has been recognized (2,3,4,5). Work on different possible metabolites of these compounds was done by the author in the summer of 1985. It was found that these aromatics were quickly volatilized from fish exposure tanks upon sparging with air. Thus, exposure of fish to these aromatics was of short duration and the possibility of identifying metabolites of these compounds was small.

Some work has been done on identification of metabolic products of double ring aromatics (naphthalenics) in fish. Most of this work has focused on the identification of naphthalenic metabolites after injection or force feeding of fish with naphthalenic containing solutions or food (6-12). However, one group did study the accumulation of naphthalenics in cutthroat and steelhead trout after exposure to the water soluble fraction of Prudhoe Bay crude oil in flowing sea water (13). Further, one group identified the metabolic products of naphthalene in 3 species of marine fish after exposure of these fish to the water soluble fraction of solutions containing naphthalene (14). After review of the cited literature, identification of the major

conjugated metabolites of napathalenics seemed to [illegible] ... of ... [illegible] ... The napththalenic hydroxylated metab... [illegible] ... identified by other groups was 1,2-naphtha-ereni... [illegible] ... (See Fig. 1).

EXPERIMENTAL

Materials: Naphthalene and toluene (Baker Analyzed Reagent), acetonitrile (E.M. Science Pesticide Analyzed), methanol, hexane, diethylether (Baker resi-analyzed), Florosil PR grade (60-100 Mesh, Attech), anhydrous sodium sulfate (Mallinckrodt Analytical Reagent), tetramethylammonium hydroxide 14% in methanol (Varian), N-heptafluorobutyryl imidazole reagent (Attech), α-methyl-2-naphthalene methanol and 6-amino-2-naphthol (both Aldrich), 1-naphthol, 2-naphthol, 1,3 dimethylnaphthalene, 1-methylnaphthalene, 1-ethylnaphthalene, 2-methylnaphthalene, 1,2-naphthoquinone, 1-naphthylamine, [illegible] (Chemical Service 98%), 1,8-naphthalenediol (Chem Service 98%) and N-methyl-N-trimethylsilyltrifluoroacetamide (Aldrich) were all used without further purification. Ultrapure hydrogen (Matheson [illegible]) was passed through a gas purifying cartridge (Alltech) before entering the chromatograph. Ultrapure hydrogen and zero breathing air (Airco) were used for the FID detector. Two different types of [illegible] were used, one being [illegible] ... [illegible] ... [illegible] ... [illegible] ... [illegible] ... [illegible] ... [illegible] ...

Mass spectrograms were obtained on a [illegible] with a [illegible] mass selective detector. The chromatograph column was a [illegible] 12.5M x 2mm cross-linked dimethyl silicone gum column. The carrier gas was helium flowing at 1.5 cc/min. The injection port was at 250°C and each run was temperature programmed in the [illegible]

[illegible] were [illegible] with [illegible] appropriate solvent terpene, and [illegible] of terpene [illegible]

[illegible] was refrigerated [illegible]

[illegible]

[illegible] The resulting [illegible] was heated [illegible] [illegible] water [illegible] ml of water was added [illegible] extracted with 2 ml of toluene. The resulting [illegible] was stored over anhydrous sodium sulfate until ready for analysis.

[illegible] columns were prepared by placing a [illegible] in the tip of a Chromaflex column [illegible]. The column was packed with 1.0 gm of Florisil which was previously activated at 1200° F. Granular sodium sulfate (1.0 gm) was then added to the top of the column. The column was washed with 50 ml of nanograde hexane followed by 50 ml of nanograde methanol and then dried overnight at 130° C in an oven. The columns were cooled to room temperature and prewet with [illegible] of the sample.

[illegible] minutes of heat and [illegible]

[illegible] these species of

[illegible] exposure. Under the same conditions

[illegible] uptake of naphthalenics was not

[illegible] and 2-methylnaphthalene were

[illegible] at trace levels.

[illegible] the difference in the

[illegible] was used with the bluegills

[illegible] differences in the

[illegible] these species of

[illegible] of naphthalenic hydrocarbons was not

[illegible] sacrificed

[illegible] to the water

[illegible]

unfeasable. 6-Amino-2-naphthol was confirmed as a metabolite in the gut of the 24 hour group of fish. Confirmation was established by chromatographing the gut extract, then a standard solution containing the 6-amino-2-naphthol, and last, the original gut extract spiked with the 6-amino-2-naphthol. Growth of the peak at 20.65 minutes (Fig. 4b) associated with 6-amino-2-naphthol confirmed this compound as a metabolite. This same procedure was repeated on a 10M-methyl silicone column with the same results. It should be noted that although the peak of interest was distinct on the plot, its area was below the discriminator level set on the integrator and therefore no quantitative estimate of concentration was available. Since the estimated sensitivity of the FID is greater that that of the HP gc-ms by about a factor of 10 (even in the gc-ms SIM mode) we were unable to reconfirm this compound by gc-ms.

No 6-amino-2-naphthol was observed in the 5 hour or 96 hour fish. This implies that the uptake, storage and metabolism of this compound leads to a maximum concentration of the naphthol betweeen the first and forth day of exposure, followed by slow depletion.

SUMMARY

1) JP-4 jet fuel contains a small amount of naphthalene and related compounds including trace amounts of 1-aminonaphthalene.

2) Substantial amounts of unmetabolized naphthalenics were identified in the gut of bluegills, but only traces were found in the gut of shiners.

3) 8-Amino-2-naphthol was identified as a metabolite in the gut of golden shiners.

Table 1b

Chromatographic Parameters of Aromatic Compounds [a,b]

Compound	Retention Time (Min)	Response/Picogram
Toluene	3.87	
P-Xylene	4.32	
M-Xylene	4.39	
O-Xylene	4.65	
Naphthalene	8.00	34.4
2-Methylnaphthalene	8.54	37.4
1-Methylnaphthalene	8.74	37.2
1,3-Dimethylnaphthalene	9.27	60.3
1-Aminonaphthalene	14.34	36.6

[a]FID response at highest sensitivity

[b]Obtained on a 30M x. 22mm ID DB wax column with a flowrate of 1.48cc/min N_2 carrier gas.

Table 2b

Some Individual Components of JP-4 Jet Fuel

Compounds	Weight % of compound in fuel
Toluene	3.62
p-Xylene	.90
m-Xylene	.56
o-Xylene	.85
Naphthalene	.22
2-Methylnaphthalene	.32
1-Methylnaphthalene	.17
1,3-Dimethylnaphthalene	.17

Table 3b

Chromatographic Parameters of Possible Naphthalenic Metabolites[2]

Compound	Retention Time	Response/Picogram
∝-Methanol-2-naphthalenemethanol	10.87	18.1
1-Naphthol	17.54	20.7
1,5-Naphthalenediol	17.74	.6
2-Naphthol	18.70	19.4
8-Amino-2-naphthol	36.03	14.7

a) Obtained on a 30Mx.22 mm ID DB Wax column with a flowrate of 1.48 cc/min N_2 carrier gas

Table 4b

Mass Spectral Peaks Associated With Naphthalenic Compounds

Compounds	Mass[a]
1-naphthol	144, 115, 116
2-naphthol	144, 115, 116
1,2-naphthalenediol, 1,2-dihydro	116,115, 149, 118, 162
1,2-naphthoquinone	130, 102, 50, 51
1,4-naphthoquinone	158, 104, 102, 130
8-Amino-2-naphthol	143, 115, 116

[a] Intensities of peaks decrease from first to last.

Table 5b

96 Hour Uptake of Naphthalenic Compounds in Bluegills (gut)[a,b]

Compound	R
Naphthalene	4×10^4
1-Methylnaphthalene	38.8
2-Methylnaphthalene	38.0
1-Methylnaphthalene	19.6
1,2-Dimethylnaphthalene	15.1
1,4-Dimethylnaphthalene	17.0

[a] Response ratio of doped fish to undoped controls

[b] The response is in counts by a mass selective detector of a mass spectrometer.

Table 6:

Retention Times of α-Aminonaphthalene and 4-Amino-1-naphthol Standards

Compound	RT (MIN) 30M—DBWAX	RT (MIN) 25-DB-1	RT (MIN) 10M—Methyl Silicone
α-Aminonaphthalene	14.34	15.54	8.44
4-Amino-1-naphthol	36.03	19.98	11.42

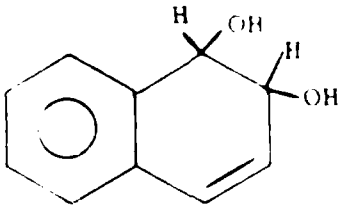

1,2-Naphthalenediol, 1,2-dihydro (I)

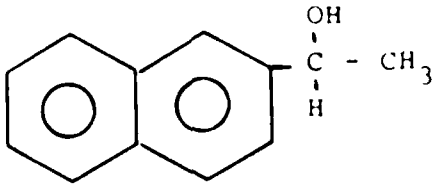

∝ -Methyl-2-naphthylenemethanol (II)

Fig. 1b. Structural formulae of some possible naphthalenic metabolites.

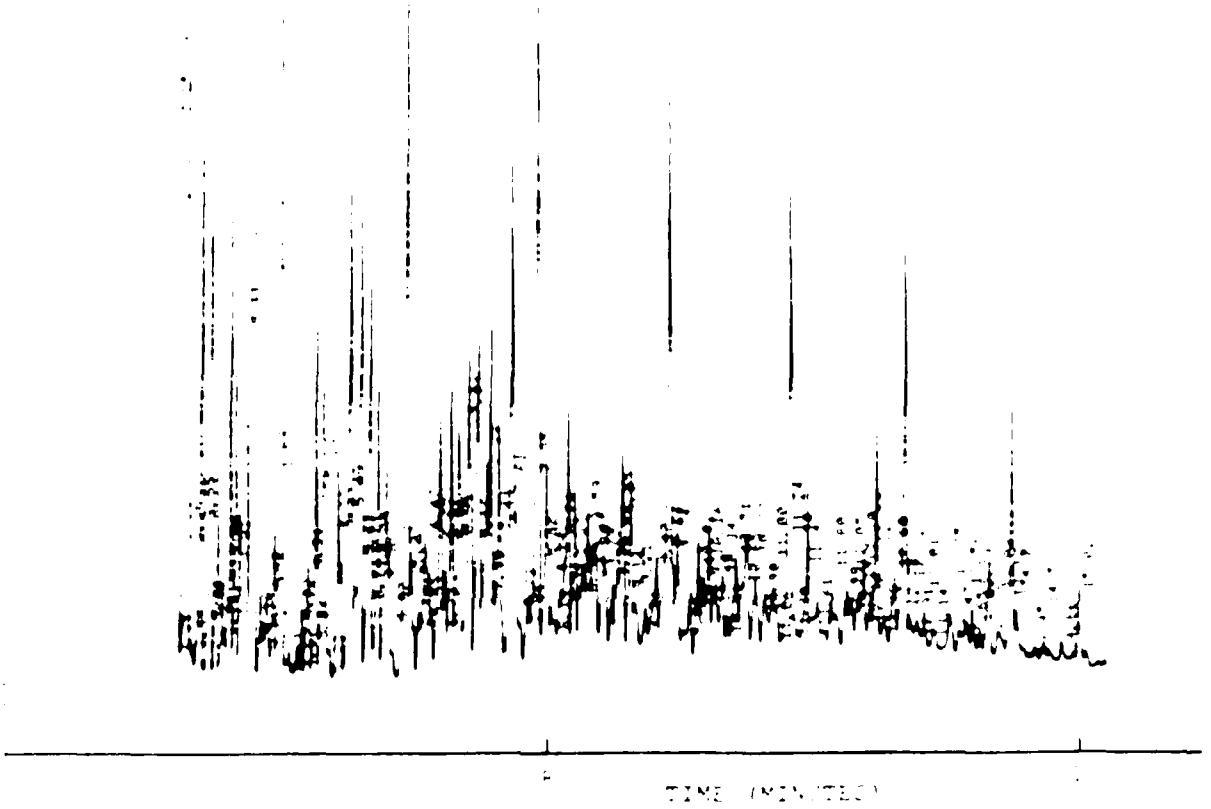
TIME (MINUTES)

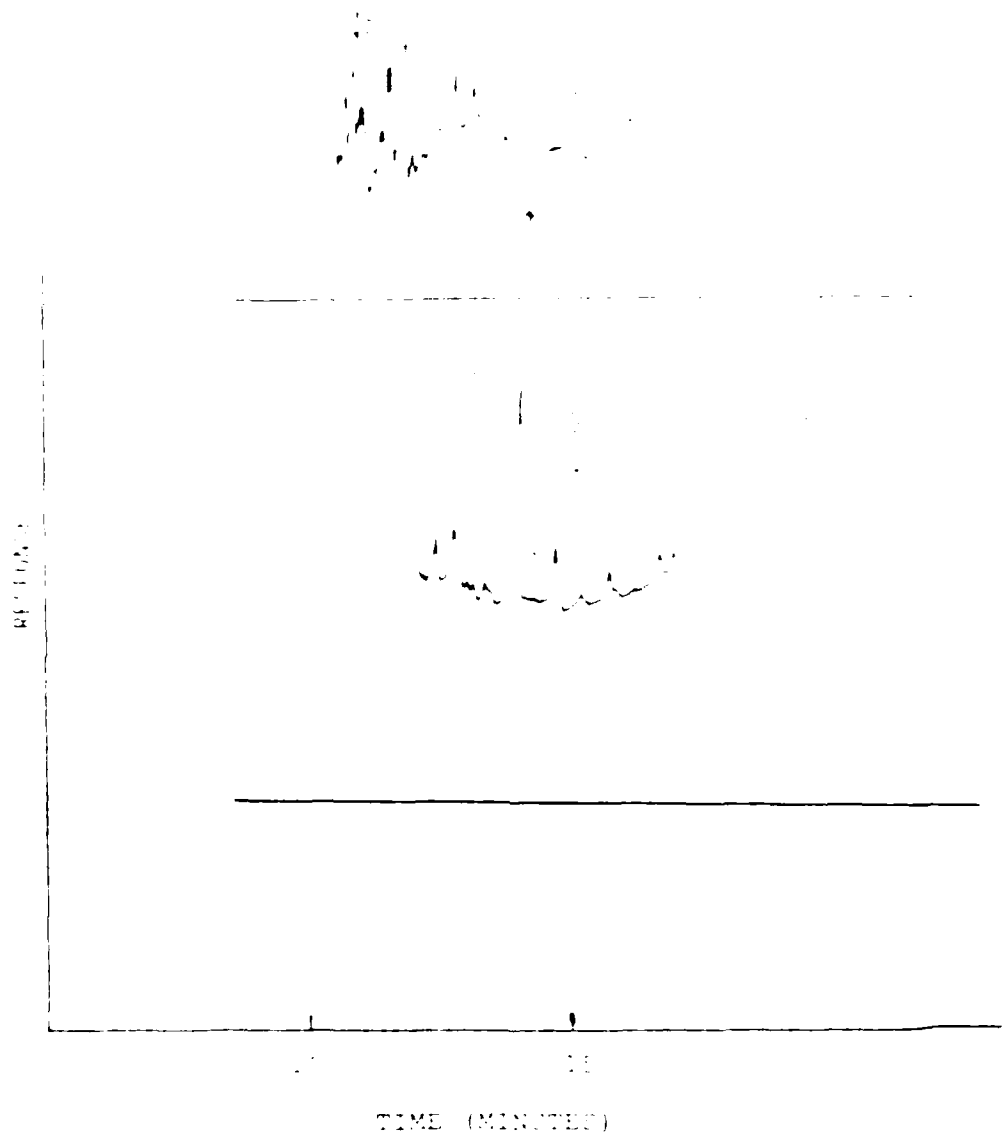

Fig. 3a. Chromatographic response of (a) JT-4 jet fuel (b) JT-4 jet fuel doped with 1-Aminonaphthalene

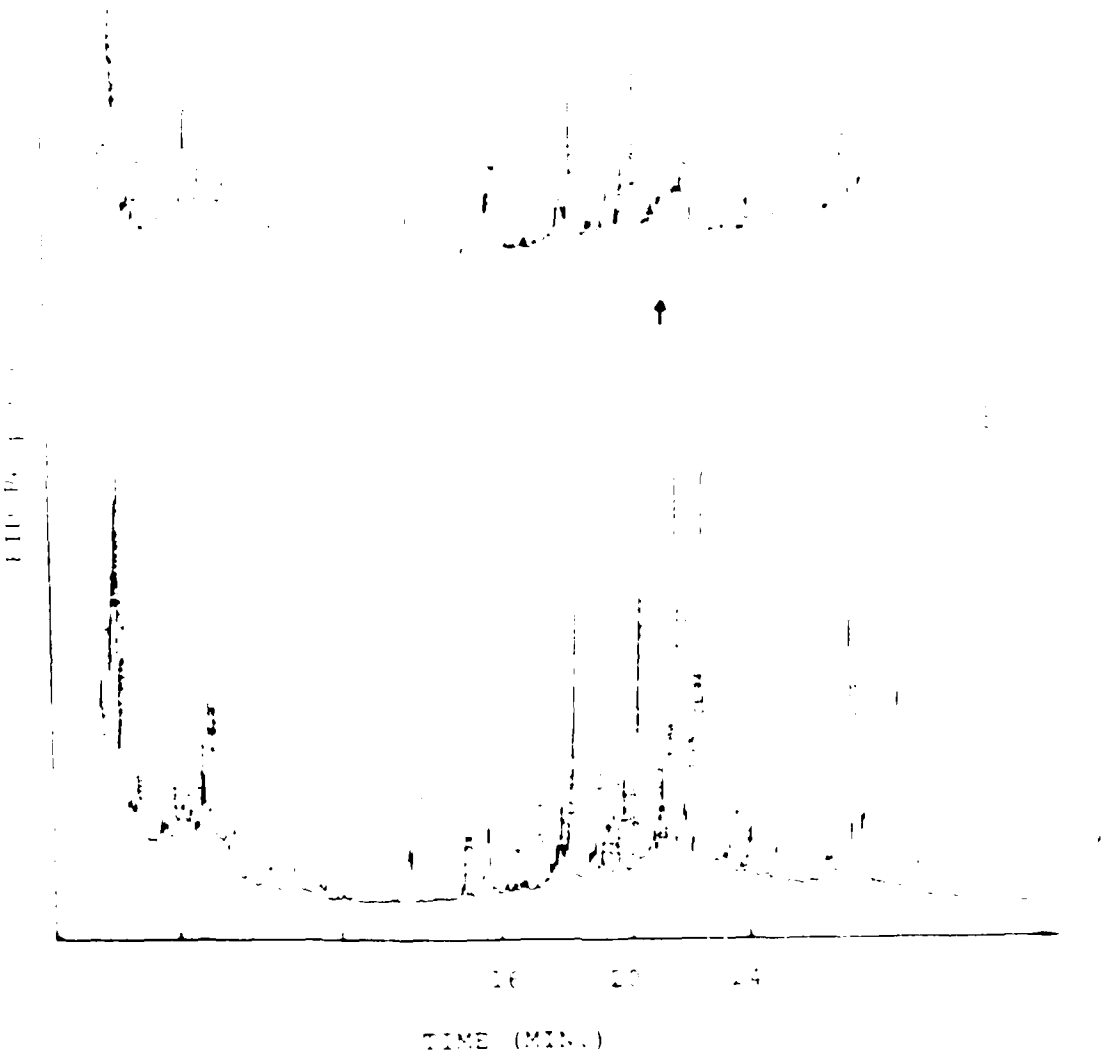

Fig. 48. Chromatographic response of (a) gut extract of fish exposed to JP-4 (b) the sample of (a) spiked with 6-amino-1-naphthol. The peak at 20.65 min. was identified as 6-amino-1-naphthol.

AD-A186 493 UNITED STATES AIR FORCE RESEARCH INITIATION PROGRAM 3/ 8
1985 TECHNICAL REPORT VOLUME 3(U) UNIVERSAL ENERGY
SYSTEMS INC DAYTON OH R C DARRAH APR 87
UNCLASSIFIED AFOSR-TR-87-1719 F49620-85-C-0013 F/G 15/3 NL

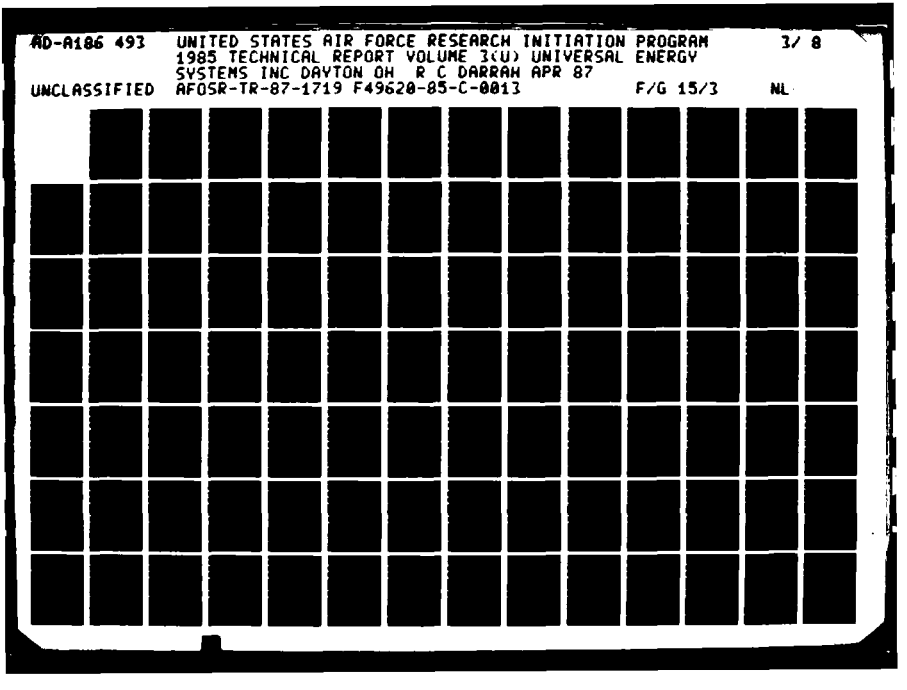

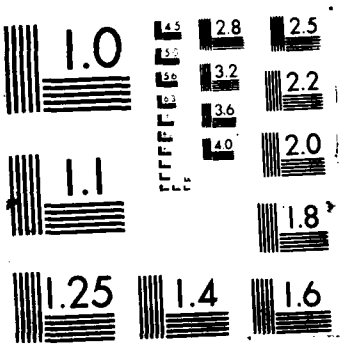
1.0
1.1
1.25
1.4
1.6
1.8
2.0
2.2
2.5
2.8
3.2
3.6
4.0

DEICER

INTRODUCTION

Plane deicer has several different formulations, the major component always being ethylene glycol(see the Hazardous Materials Information Sheets for those formulations used by the Air Force). Identification of metabolities of ethylene glycol in mammals (1-4) and in bacteria (5) has been previously accomplished. However, no work on the metabolism of ethylene glycol in piscene species was found. In 1961 Gessner established that unmetabolized ethylene glycol, along with oxalic acid were found in the urine of rabbits exposed to ethylene glycol, while glycoaldehyde and glycolic acid were identified as metabolites in various tissues of the same subjects (1). Bove observed the same metabolites plus glyoxylic acid in rats(2). McChesney et.al. found ethylene glycol, glyoxylic acid and oxalic acid in the urine of rats and monkeys (3). Arena also reported these findings (4). Willets identified glycolate as a metabolite of a Flavobacteria species(5) and DeBont identified proprionate as a bacterial metabolite of 1,2-propanediol (6).

Although the metabolism of ethylene glycol in fish may be quite different than in mammals and bacteria, it was decided that those metabolites identified in mammals would be good starting point in the search for piscene metabolites. Fig. 1c shows the structures of ethylene glycol and its possible metabolites. Fig.

2c shows the structures of the derivatized (methylated) metabolites.

EXPERIMENTAL

Materials: Ethylene glycol (99+),N-methyl-N-nitro-N'-nitrosoguanidine, glycoaldehyde dimer (95%), glycolic acid (95%), glyoxylic acid (95%), oxalic acid (anhydrous 99 +) and methylmethoxyacetate (99+), all Aldrich, were used without further purification. 1,2-Dimethoxyethane (98+), dimethyloxalate (98+) methoxyacetic acid (98+), all Chem Service, and methyl glyoxalate (98+) from Fluka were also used without purification. The plane deicer was obtained from Loring Air Force Base and had a composition obtained from its Hazardous Material Information Sheet of 66.3% ethylene glycol and 33.7% non-aqueous, unidentified materials.

Instrumentation: All chromatograms were obtained using a Varian 3700 gas chromatograph with 4270 electronic integrator and a flame ionization detector(FID). The column was a 30Mx.22mm DB-WAX FSOT capillary column used in the splitless mode. The temperatures of the injection port and the detector were 240° C and 300° C respectively. The oven was temperature programmed at 40° C, 1/min.-10° /min.-200° C, 15 minutes. The nitrogen flow rate was 1.39 cc/min with a linear velocity of 26.7 cm/sec. Gc-mass spectrograms were obtained on an HP-5890 gc with a 5970 mass selective detector. The chromatographic column was an HP 12.5Mx.2mm crosslinked dimethylsilicone capillary column. The carrier gas was helium flowing at 1.5 cc/min. The injection port

was 210° C and each run was temperature programmed in the splitless mode from 40° to 200° at 10° /minute.

Analytical Methods: Stock solutions of each of the compounds were prepared by weighing the appropriate masses of each into 10 ml volumetric flasks and diluting to the mark with methanol. A chromatographic standard containing most of the compounds was prepared by pipeting 1 ml portions of each stock solution into a volumetric flask and diluting to the mark (the concentration of each component in the resulting solution was about 5.0×10^{-3} M). The chromatographic standard was refrigerated between uses and replaced periodically.

Florosil columns were prepared by placing a loose plug of glass wool in the tip of a chromaflex column (Kontes #42100 22-7mm). The column was packed with 1.6 gm of Florosil previously activated at 1200° F. Granular sodium sulfate 1.6 gm was then added to the top of the column. The column was washed with 50 ml of nanograde hexane followed by 50 ml of nanograde methanol and then dried overnight at 130° in an oven. The columns were cooled to room temperature and pre-wet with 1 ml of hexane prior to elution of the sample.

Duplicate analysis of ethylene glycol and its possible metabolites in tissue was performed on freshly sacrificed golden shiners. At sacrifice, the appropriate tissue, liver or gut, was collected within 2½ minutes of death and ground for 15 minutes with a 5 ml portion of methanol in an all-glass Pyrex 19 x 15 tissue grinder. The liquid was decanted into a glass collection

tube and a second 5 ml portion of solvent added. This solution was ground for an additional 10 minutes and the liquid extract combined with the first.

The sample was divided into two equal portions. The first was evaporated to dryness under a gentle stream of nitrogen and derivatized with diazomethane. The resulting solution was evaporated to 0.5 ml placed on a Florosil column and eluted with 12 ml hexane (fraction 1) and 12 ml methanol (fraction 2). The second fraction was evaporated to 1 ml and stored in Teflon-stoppered glass vials until ready for analysis.

The second half was evaporated to 0.5 ml, placed on a Florosil column and eluted as above. The second fraction was collected and evaporated with nitrogen to 1 ml and stored in Teflon-stoppered glass vials until ready for analysis.

Fish: Golden shiners (N. Crystoleucas) were used in this study. Four groups of golden shiners were supplied by Carroll Cutting from a private lake in Standish, Maine, while two groups were supplied by Mcgraw's bait ponds in Clinton, Maine. Each group was acclimatized for at least a week in a 40 gallon tank with water from the pond of origin before experiments were performed. Fish (groups of three) were exposed to plane deicer by placing them in a 14 l aquarium with an ethylene glycol concentration of 5 ppm. At 10 ppm a significant number of fish expired during the 96 hour time-span of the experiment. Simultaneously, control groups of three were placed in similar aquaria without deicer. Groups of exposed fish, both exposed and controls were sacrificed at 24 and

96 hours.

RESULTS AND DISCUSSION

Table 1c gives the retention times and sensitivities to an FID detector of ethylene glycol and its possible metabolites (both derivatized and underivatized). Table 2c gives the mass spectral data associated with these compounds. Upon exposure to plane deicer at 5 ppm, uptake of ethylene glycol was observed in the gut of sets of fish sacrificed at 24 hours and 96 hours. Fig.1c compares the chromatograms of gut extract from fish exposed to plane deicer for 96 hours with that of a control. The peak at 11.86 minutes is identified as ethylene glycol. The concentration of ethylene glycol is greater in the 96 hour fish than in the 24 hour fish by a factor of two. Identification of the ethylene glycol was confirmed by gc-ms.

Of the metabolites, no glycoaldehyde was observed either in the gc or gc-ms. Glycolic acid and dimethyl oxalate (derivatized oxalic acid) were observed by gc at retention times of 9.02 and 9.12 minutes respectively and reconfirmed by gc/ms, but these species were common to both the exposed fish and control groups and thus could not be said to have originated from the ethylene glycol of the plane deicer.

SUMMARY

1) Unmetabolized ethylene glycol was identified in the gut of shiners exposed to plane deicer.

2) The concentration of ethylene glycol was greater in 96-hour fish than in 24-hour fish.

3) Glycolic acid and oxalic acid were identified in the gut of shiners exposed to plane deicer but were also found in the control fish.

4) No metabolites were identified that could unambiguously be said to come from ethylene glycol.

Table 1c

Chromatographic Parameters of Ethylene Glycol-Related Compounds

Compound	RT (MIN)	Response/Picog
Non-methylated		
Glycoaldehyde	8.39	5.35×10^{-2}
Glycolic acid	9.10	1.45×10^{-1}
Ethylene glycol	12.10	6.69×10^{-1}
Methylated		
1,2-Dimethoxyethane	6.32	4.28×10^{-3}
Methyl Methoxyacetate	6.46	8.75×10^{-1}
Dimethyloxalate	9.12	5.99×10^{-1}
Methoxyacetic acid	15.12	4.44×10^{-1}

a) Obtained on a 30M x .22 mm DB-Wax capillary column in the splitless mode. Temperature programed at 40°-1 minute, 10°/min, 200°-15 minutes. The response is in integrator response units.

Table 2c

Mass Spectral Data Associated With Ethylene Glycol-related Compounds

Compound	Mass	% of Parent Peak
Ethylene Glycol	31	1.00
	33	.28
	43	.11
	42	.04
	62	.03
Glycolic Acid	75	1.00
	31	.52
	45	.34
	43	.25
	47	.23
Glycoaldehyde	31	1.00
	29	.68
	32	.39
	30	.08
	42	.06
	60	.05

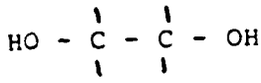

ETHYLENE GLYCOL

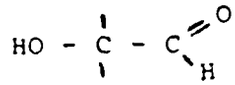

GLYCOALDEHYDE

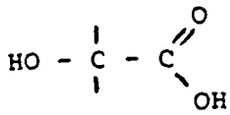

GLYCOLIC ACID

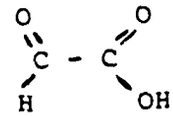

GLYOXYLIC ACID

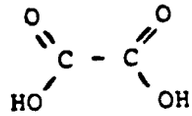

OXALIC ACID

Fig. 1c. Ethylene glycol and possible metabolites.

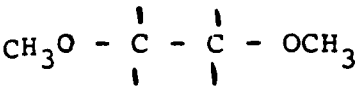

1,2 - DIMETHOXYETHANE

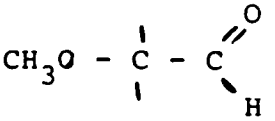

METHOXYACETALDEHYDE

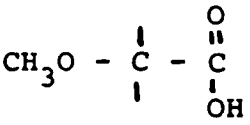

METHOXYACETIC ACID

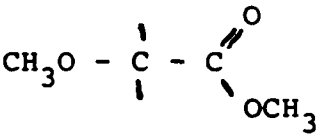

METHYL METHOXYACETATE

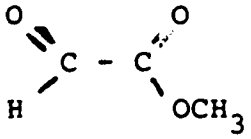

METHYL GLYOXALATE

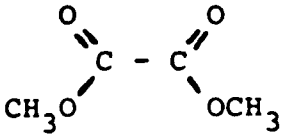

DIMETHYL OXALATE

Fig. 2c. Methylated metabolites of ethylene glycol

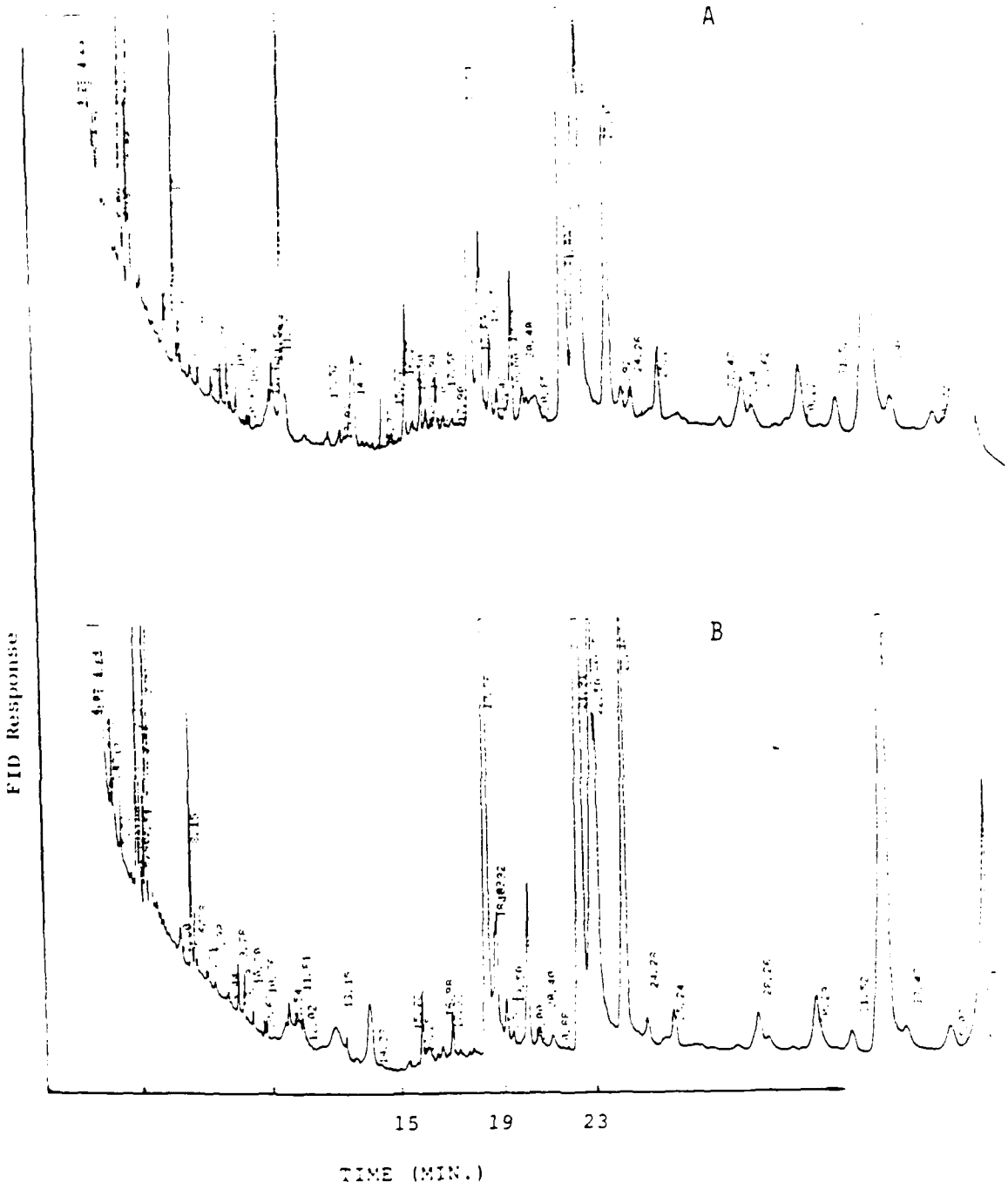

Fig. 3d. Chromatographic response of (a) gut extract from a fish exposed to 5 ppm ethylene glycol in deicer (b) a control fish.

References

(1) Gessner, P.K., Park, D.V. and Williams, R.T., Biochem. J., 74, 1-5 (1960).

(2) Bove, K.E., Am. J. Clin. Path., 45, 46-50 (1966).

(3) McChesney, E.W., Goldberg, L., Parek, C.K., Russel, J.C. and Min, B.H., Fd Cosmet. Toxicol., 9, 21-38 (1971).

(4) Arena, J.M.: Poisoning, Toxicology-Symptoms-Treatment, 4th Ed., Charles C. Thomas Pub. Co., Springfield, Ill., 1979.

(5) Willetts, A, Biochimica et Biophysica Acta, 677, 194-199 (1981).

(6) Debont, J. A. M., Van Dijken, J. P. and Van Ginkel, K.G., Biochimica et Biophysica Acta, 714, 465-470 (1982).

AFFF FOAM

INTRODUCTION

AFFF is a commercial aqueous film-forming foam used by the Air Force to fight fires. The Hazardous Materials Information Sheet on this product states that it is a 6% solution of the MMM product Light Water (FC206) in water. The major non-aqueous component of AFFF is diethylene glycol monobutylether (Butyl Carbitol or 2-(2-butoxyethoxy) ethanol) at about 1.6% by weight. Extensive literature work including computer searches of various databases yielded no information about identification of metabolites of this compound in any biological system. However, the urine of rats was found to contain n-butoxyacetic acid as a metabolite of the analagous compound Butyl Cellusolve (1). Other work identified methoxyacetic acid and ethoxyacetic acid as metabolites of ethylene glycol monomethyl ether and ethylene glycol monoethyl ether respectively in primary testicular cell cultures (2). Since these were the only data available, it was decided to look for the analogous 2-(2-butoxy ethoxy) acetic acid as well as a number of other related or at least possible compounds. Fig. 1d shows the structures of Butyl Carbitol and some possible metabolites. It does not show the methylated metabolites.

EXPERIMENTAL

Materials: Butyl Carbitol (99+), Butyl Cellusolve (99+), 1-butanol (99+) and ethlene glycol (99+, all Aldrich, were used without further purification. The AFFF fire fighting foam was obtained from Loring Air Force Base and had a composition obtained from its Hazardous Material Information Sheet of 1.6% Butyl Carbitol, 0.1% fluorocarbon and a host of trace constituents.

Instrumentation: All chromatograms were obtained using a Varian 3700 gas chromatograph with 4270 electronic integrator and a flame ionization detector (FID). The column was a 30Mx.20mm DB-WAX FSOT capillary column used in the splitless mode. The temperatures of the injection port and the detector were 240° C and 300° C respectively. The oven was temperature programmed at 40° C, 1 min. -10° /min.- 200° C, 15 minutes. The flow rate was 1.39 cc/min with a linear velocity of 26.7 cm/sec.

Gc-mass spectrograms were obtained on an HP-5890 gc with a 5970 mass selective detector. The chromatographic column was J&W 30Mx.22mm DB-WAX FSOT capillary column used in the splitless mode. The carrier gas was helium with a flow rate of 1.5 cc/min. The injector port and the detector were 240° C and 300° C respectively and the column was temperature programmed at 40° C, 1 min.-10° /min. - 200° C, 15 min.

Analytical Methods: Stock solutions of each of the compounds were prepared by weighing the appropriate masses of each into 10 ml volumetric flasks and diluting to the mark with solvent. A chromatographic standard with most of the compounds was prepared by pipeting 1 ml portions of each stock solution into a volumetric

[illegible] and diluting to the mark (the concentration of each component in the resulting solutions was about 5.0×10^{-3} M). This standard was refrigerated between uses and replaced periodically.

Florosil columns were prepared by placing a loose plug of glass wool in the tip of a chromaflex column (Kontes #42100 22-7mm). The column was packed with 1.6 gm of Florosil which was previously activated at 1200° F. Granular sodium sulfate (1.6 gm) was then added to the top of the column. The column was washed with 50 ml of nanograd hexane followed by 50 ml of nanograde methanol and then dried overnight at 130° C in an oven. The columns were cooled to room temperature and pre-wet with 10 ml of hexane prior to elution of the sample.

Each stock solution (0.3 ml) was separately placed on a Florosil column and eluted with 12 ml of hexane (fraction 1), 12 ml of methanol (fraction 2) and a second 12 ml of methanol (fraction 3). The resulting fractions were chromatographed and those fractions containing the compounds identified.

Duplicate analysis of Butyl Carbitol and its possible metabolites in tissue was performed on freshly sacrificed golden shiners. At sacrifice, the appropriate tissue, liver or gut, was collected within 20 minutes of death and ground for 15 minutes with a 5 ml portion of methanol in an all-glass Pyrex 19 x 150 tissue grinder. The extract was decanted into a glass collection tube and a second 5 ml portion of tissue/solvent ground for an additional 10 minutes. This extract was combined with the first.

The sample was divided into two equal portions. The first was evaporated to dryness under a gentle stream of nitrogen and derivatized with diazomethane. The resulting solution was evaporated to 0.5 mL, placed on a Florosil column and eluted with 12 ml hexane (fraction 1) and 12 ml methanol (fraction 2). The second fraction, containing the compounds of interest, was evaporated to 1 mL and stored in Teflon-stoppered glass vials until ready for analysis.

The second half was evaporated to 0.5 ml, placed on a Florosil column and eluted as above. The second fraction was collected and evaporated with nitrogen to 1 ml and stored in Teflon-stoppered glass vials until ready for analysis.

Fish: Golden shiners (*N. Crystoleucas*) were used in this study. Four groups of golden shiners were supplied by Carroll Cutting from a private lake in Standish, Maine, while two groups were supplied by Mcgraw's bait ponds in Clinton, Maine. Each group was acclimatized for at least a week in a 40 gallon tank with water from the pond of origin before experiments were performed. Fish (groups of three) were exposed to Butyl Cartitol by placing them in a 14 l aquarium with a Butyl Carbitol concentration of 5 ppm. Simultaneously, control groups of three were placed in similar aquaria without deicer. Groups of fish, both exposed and controlled, were sacrificed at 96 hours.

RESULTS AND DISCUSSION

Table 1d gives the retention times of Butyl Carbitol and some of its possible metabolites. Samples of Butyl Cellusolve, n-butanol and ethylene glycol were commercially available, but 2-butoxyacetic acid and 2-(2-butoxyethoxy) acetic acid were unavailable. Table 2d gives mass spectral data associated with the compounds of Table 1d. Upon exposure to 5 ppm Butyl Carbitol, uptake of this compound was observed in the gut of fish sacrificed at 96 and 264 hours. Fig. 2d compares the chromatogram of gut extract from 96-hour exposure to Butyl Carbitol with that of a control. The peak at 14.93 minutes has been identified as Butyl Carbitol.

Comparison of the exposed and control fish chromatograms leads to the conclusion that either there is no accumulation of metabolites in the gut, or that they are present in such low concentrations as to be undetectable. Analysis by gc-ms gave similar results.

SUMMARY

1. Unmetabolized Butyl carbitol was identified in the gut of shiners exposed to this compound.

2. No metabolites of Butyl Carbitol were identified in the gut of exposed shiners.

Table 1d

Chromatographic Parameters of Butyl Carbitol-related Compounds[a]

Compound	Retention Time (min)
N-Butanol	6.00
Ethylene glycol	12.79
Butyl Cellusolve	9.82
Butyl Carbitol	14.93

[a]Obtained on a 30M x .22mm DB-Wax capillary column in the splitless mode. Temperature programmed 0°- minute, 10°/minute, 200°-15 minutes.

Table 2d

Mass Spectral Data Associated Wi... Butyl Carbitol-related Compounds

Compound	Mass	% Parent Peak
N-Butanol	27	.97
	31	1.00
	41	1.00
	43	.97
	56	1.00
Butyl Cellusolve	41	1.00
	45	1.00
	57	1.00
	31	.83
	87	.47
	75	.21
Butyl Carbitol	45	1.00
	57	.99
	41	.58
	75	.24
	87	.15
Ethylene Glycol	31	1.00
	33	.28
	43	.11
	42	.04
	62	.03

$CH_3CH_2CH_2CH_2-O-CH_2CH_2-O-CH_2CH_2-OH$

2-(2-BUTOXYETHOXY)ETHANOL

BUTYL CARBITOL

$CH_3CH_2CH_2CH_2-O-CH_2CH_2-O-CH_2COOH$

2-(2-BUTOXYETHOXY) ACETIC ACID

$CH_3CH_2CH_2CH_2-O-CH_2CH_2OH$

n-BUTOXYETHANOL (BUTYL CELLOSOLVE)

$CH_3CH_2CH_2CH_2-O-CH_2COOH$

n-BUTOXYACETIC ACID

$CH_3CH_2CH_2CH_2OH$

n-BUTANOL

$HO-CH_2CH_2-OH$

ETHYLENE GLYCOL

Fig. 14. Butyl Carbitol and some possible metabolites

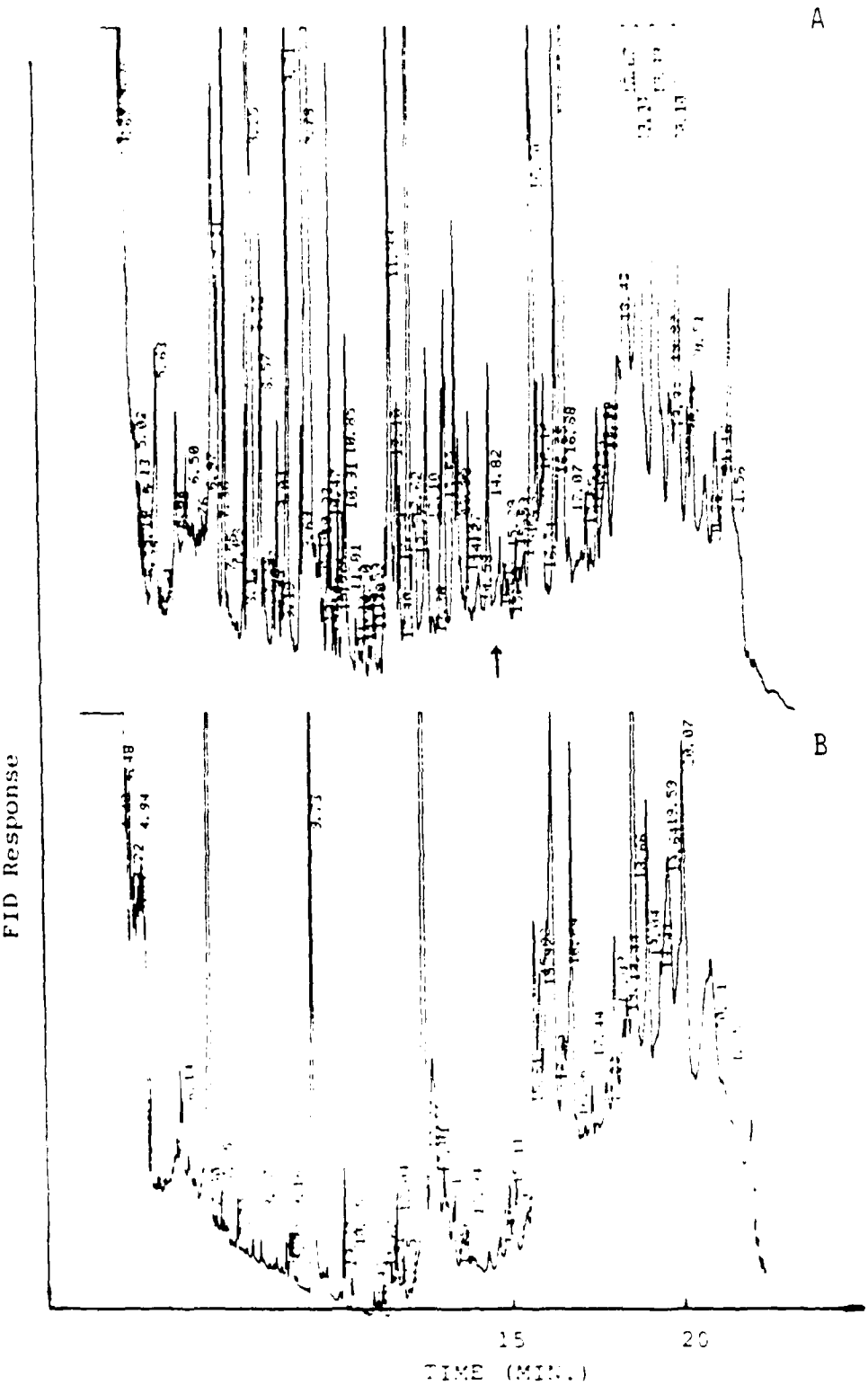

Fig. 2d. Chromatographic response of (a) gut extract from fish exposed to 5 ppm Butyl Carbitol (b) control fish

References

(1) Jonsson, A.K., and Steen, Goran, Acta Pharmacol. et Toxicol., 42 354-356, (1978).

(2) Gray, T.J.B., Moss, E.J., Cressy, D.M. and Gangolli, S.D., Toxicology and Applied Pharmachology, 79, 490-501, (1985).

CONCLUSIONS

1) Metabolites of Malathion and JP-4 jet fuel were identified in the guts of bluegills and golden shiners respectively. Therefore, it was possible to monitor environmental incidents associated with these materials by metabolite analysis.

2) MCA (we could not distinguish between the two isomers) was the most useful metabolite of Malathion to monitor, while 8-amino-2-naphthol was the most useful metabolite of JP-4 jet fuel to monitor.

3) Metabolites of plane deicer and AFFF foam were not identified in the guts of shiners, although uptake of ethylene glycol and Butyl Cartitol was observed.

4) Although it was possible to identify and even quantify results associated with metabolites of Malathion and JP-4, at this time several factors mitigate against using these analytical methods to monitor environmental incidents associated with these materials. Namely:

   a) Rapid deterioration of tissue following death or freezing makes sampling problematic. Only freshly sacrificed or recently killed fish are useful.

   b) The hydrolysis of Malathion, both path and rate, are dependent on a number of variables including temperature, pH and the concentration of different metal ions. Since a possible hydrolysis product is MCA, each natural water system would have to be tested for this compound to insure that any MCA found in the gut was of metabolic origin.

   c) Analysis of MCA requires derivatization with diazomethane, a compound which is both explosive and mutagenic.

   d) Although 8-amino-2-naphthol was identified as a metabolite of 1-amino-naphthalene (a trace component of JP-4) the concentrations of both were so small that it was difficult to see them even with the most sensitive instrumentation.

   e) The rate of metabolism of each compound has not been thoroughly studied at this time and is probably species dependent. Therefore, the time of exposure necessary to see metabolites in various tissues is not certain. It is believed

that the rate of metabolism of xenobiotics in fish is almost 1/10 that of mammals. This means that it is probably easier to detect the unmetabolized parent than a metabolite of that parent.

ACKNOWLEDGEMENTS

The author is most appreciative for the funding of this RIP project by the Air Force System Command, the Air Force Office of Scientific Research, and Universal Energy Systems. More specifically, I would like to thank Maj. Thomas Doane, Chief, Ecology Function, for initiating and providing direction for this project. In addition, the following were instrumental in the completion of the project.

1. The University of Southern Maine for funding and support.

2. Robert Anderegg, Ph.D. for the gc-m specs associated with the Malathion study.

3. Carroll Cutting for supplying the project with several loads of shiners.

4. Cristina Olsen for helping to prepare the tables and final manuscript.

5. Gary Mabbott, Ph.D. and Colby College for use of, and advice about their HP gc-ms.

6. Mike Reynolds for his work on the rate of hydrolysis of Malathion.

7. Therese Roy for her dedicated efforts on all experimental aspects of the work.

8. Linda Thompson for her experimental work on jet fuel and deicer.

9. My colleagues in Chemistry for moral support and occasional technical advice.

1985-86 USAF-UES Research Initiation in Science and Engineering Program

Sponsored by the

AIR FORCE OFFICE OF SCIENTIFIC RESEARCH

Conducted by the

UNIVERSAL ENERGY SYSTEMS, INC.

FINAL REPORT - PART I

Use of Two Simple, Micro-based Models in Analysis of Geotechnical Test Data

Prepared by:	Dr. B.W. Stewart
Academic Rank:	Assistant Professor
Department and	Department of Mechanical and Industrial Engineering
University	University of Cincinnati
Research Location:	University of Cincinnati, Cincinnati, Ohio
USAF Research:	Capt. W.A. Kitch

Date:	March 31, 1987
Contract No.:	F49620-85-C-0013/SB5851-0369
Contract Amount:	$19,995
Contract Duration:	Jan. 2, 1986 - Dec. 31, 1986

Section I. Summary of the Project Goals

The insitu testing of geological material by blast loading is an extremely complicated problem in which many unknowns are present. Ambiguities in the source and site characterizations as well as the normal experimental uncertainties may make any empirical material model inferred from the data highly questionable. As the goal of such testing is a mechanical model of the medium valid throughout a large range of strains, and strain rates, it is important to minimize the effect of these uncertainties.

One of several unanswered questions dealing with source characterization is that of the source efficiency factor.[1] This factor relates the effectiveness in producing ground motion of a discrete cylindrical source array to that of a continuously distributed planar source with the same areal charge density. It is not known what effect charge diameter and charge spacing have upon this factor but currently a value between 65-70% is used in calculations, irrespective of source microgeometry. It is not known what type and magnitudes of errors this might introduce. In this report we will examine: a) the dependence of the efficiency factor upon both the source microgeometry, and b) the dependence of the efficiency factor upon the mechanical properties of the medium separating the charges.

Another largely unaddressed question is the effect of dispersion [2][3] upon ground motion testing. The effects of dispersion and material attenuation can look similar when analyzing ground motion data. If the effects of dispersion are not properly accounted for, any material models obtained empirically will have extremely limited applicability. Since one goal of

blast-induced ground motion testing is the verification and improvement of mechanical soil models, the treatment of dispersion is important. In addition, this phenomenon may be even more important, in some instances, to the survivability of protective structures than material attenuation but seemingly receives little attention.

The effects of dispersion in geotechnical testing will be examined in this report. Understanding dispersion in earth materials is essential to the proper interpretation of the data obtained from this testing and therefore to the mechanical models derived from this data. A simple micromechanical model which still incorporates the most fundamental properties of actual soils will be used to derive a dispersion relation for stress waves propagating therein. This dispersion relation will be used to predict the evolution of the pulse shape.

Generally the effect of dispersion, even in the case that the soil does not absorb energy from the pulse, is to flatten the pulse as it propagates. This is because the longer wavelength components of the pulse travel faster than the shorter wavelength components. Thus the sharp initial pulse of Figure 1a decays (still without loss of energy) into the pulse of Figure 1b after some period of time.

Even though the various energy loss mechanisms will be ignored in this approach, the applicability of the result can be readily seen. In regions where the pulse is very sharply defined (Figure 1) the response of the medium is both nonlinear and strain rate dependent. In these regions accurate soil models (including energy losses) must therefore model both

(a)

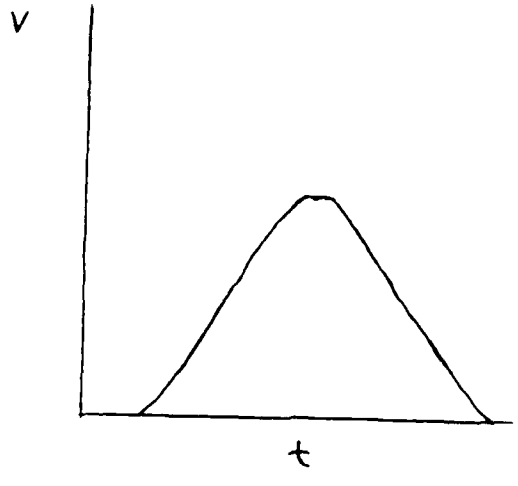

(b)

Figure 1

of frequency dependent attenuation are found in multiple scattering effects from random occlusions in the medium, viscoelastic effects, certain friction models, etc. A variation of this use of moments in the analysis can enable the researcher to determine the nature of certain types of simple non-linearities in the medium by simply analyzing the data, i.e. without the construction of an explicit soil model. This program could be an important addition to the currently employed tools of analysis.

Section II. The Efficiency Factor

A. Outline of Approach

In the examination of the effect of the microgeometry upon the efficiency factor, we will possibly use two different approaches. Both are based upon the facts that the medium separating the charges gives rise to the efficiency factor itself.

When an explosive source is detonated, there is an initial stage lasting approximately 10 ms during which the rapid burning of the charge causes elastic/plastic waves to propagate from the borehole into the surrounding medium. The second stage, lasting approximately 100 ms, involves the expansion of the high pressure gas which was generated by the detonation of the charge. The explosive by-products then do work on the surrounding medium through the expansion process and simultaneously initiate elastic/plastic waves. The characteristics (intensity, temporal profile, etc.) of the waves generated in stage one are strongly dependent only upon the detonation process itself. The thermal characteristics of the

surrounding medium are unimportant in this stage mainly due to the time interval involved. However, the same possibly may not be said for stage two as its duration is roughly ten times that of stage one. We will accordingly concentrate our attention on the processes involved in stage two.

Method A is a thermodynamic approach. In the continuous case, after the detonation we have a "void" containing only hot gases, by-products of the detonation itself. In the discrete source case, we would have soil material as well present. Whatever portion of the total energy of the explosion (assumed to be equal in both cases) that doesn't go into the internal energy of the matter in the "void" will be present as energy in a stress wave. The presence of soil matter will increase the internal energy and decrease the energy available to produce ground motions. The only material parameters in the calculations would be the specific heat, thermal diffusivity, and mass density of the soil.

Method B is an attenuation based approach. The medium near to the sources is in the hydrodynamic region. It is well known how stress waves attenuate with distance in viscous fluids.[5] Discrete arrays have a larger <u>average distance per unit charge</u> from a given observation point than do continuous source arrays. One would therefore expect a greater attenuation in discrete arrays. This effect can be calculated quantitatively with the effective (hydrodynamic region) soil viscosity and the size of the hydrodynamic zone as the only unknowns.

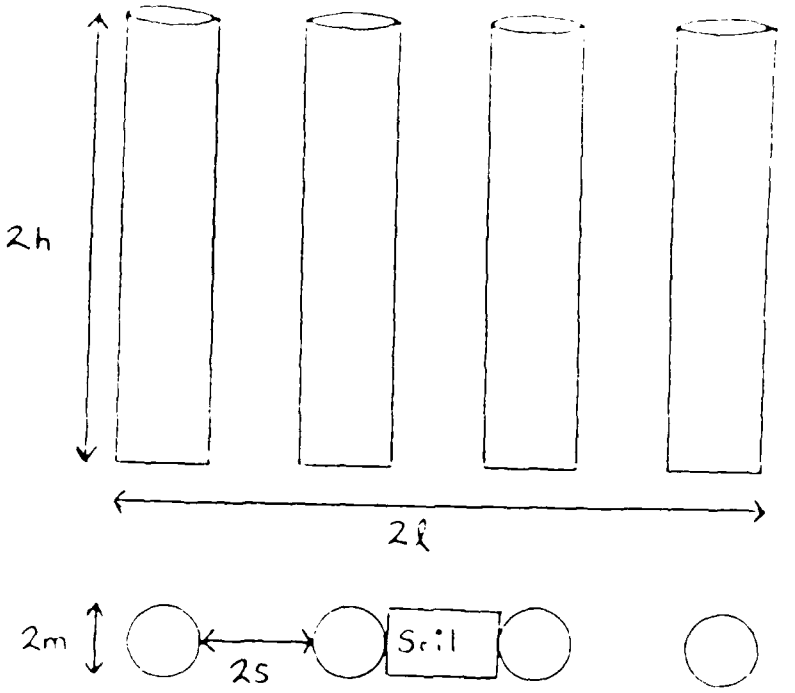

Figure 2

then:

$$M_{soil} = \rho_{soil}\ 8smh\ (N-1) \qquad (1)$$

where N is the number of sources. We assume that the total source yields, Y, are the same in both the continuous and discrete array. The first law of thermodynamics in the continuous case is then:

$$U_1 - U_2 + Y = {}_1W_2 \qquad (2)$$

where U refers to the internal energy of the contents of the cylinder and ${}_1W_2$ is the work done by the expanding gases.

In the discrete case, heat from the by-products will be transferred to the soil, lowering the temperature and pressure of the gas and resulting in a decrease in work done. An estimate of the decrease of the temperature of the explosive by-products can be easily found.

We can see that the neglection of heat transfer between the by-products and the surrounding soil is justified as follows.

The thermal diffusion depth is a measure of how far heat penetrates into a medium in a given time interval. It is defined to be:

$$d = 2\sqrt{\alpha\ \Delta\ \tau}$$

Where α is the thermal diffusivity of the medium and $\Delta\tau$ is the time interval. For soil this is an extremely small quantity:

$$d \sim 1.4 \times 10^{-7} m$$

Thus only the immediate region surrounding the sources will be affected. Since this depth is so small that curvature effects are negligible we can approximate the problem by a semi-infinite planar medium with a sudden temperature difference applied to the surface. We will use the mean temperature for the by-products in our temperature difference calculation and then treat the by-product temperature as constant. This value is

$$T_m = .718\ T_{bpo}$$

we make use of the solution found by Schneider (See Ref. 7 for further details). Employing

$$h = 200\ w/m^2\text{-}^\circ c$$

$$k = .52\ w/m\text{-}^\circ c$$

$$\alpha = 1.4 \times 10^{-7}\ m^2/s$$

$$\tau = .1\ sec$$

we arrive at a temperature profile within the surrounding soil (where x is measured from the soil/by-product interface in co-moving co-ordinates) of

$$\frac{T(x)-T_0}{T_m - T_0} = .06 \exp\left[- (2.3575)\ 2\frac{x}{\sqrt{\alpha\tau}} \right]$$

The total energy absorbed is found by multiplying the above by $(\rho Ac)_{soil}$ and integrating. Then

Q_L = heat loss by the by-products

$$= (\rho Ac)_{soil}(.0509\sqrt{\alpha\tau})(T_m - T_0)$$

For the Thompson-Ho array $A = 2.55\ m^2$, then using

$$c = 1.84\ KJ/Kg\text{-}^{o}K$$

$$\rho = 2050\ Kg/m^3$$

we have

$$Q_L = .058\ (.718\ T_{bpo} - T_o)$$

This represents less than .02% (not 2%) of the initial energy of the by-products. Therefore, we can safely neglect the heat loss to the soil at the interface. However, considerable mixing between the soil remaining inside the cavity and the by-products. This mixing results in a much greater heat loss to the soil due to the much larger effective exposure area of the soil remaining in the cavity. (For example, it is well known that the same mass of ice when crushed is much more effective at absorbing heat than when in large blocks).

Our model is based on the following set of assumptions:

1) We assume the volume of the soil between the sources in the discrete array is made up (after "fragmentation" by the blast) of a gaussian distribution of sizes of spherical particles:

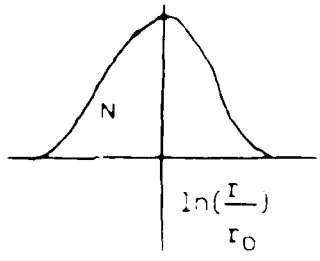

The spherical assumption allows us to determine the effective surface area of the particles. In order to fix our distribution, we will assume

that the mode radius is known (r_o). We further assume that the effective spread, a_o, of the Gaussian distribution is also known. The number of particles with a given radius is then given by

$$N = N_o \exp\left[-\frac{\alpha^2}{a_o^2}\right]$$

where $$\alpha = \ln\left[\frac{r}{r_o}\right]$$

In order to fix N_o, we require that the total volume given by

$$V_{total} = \int_{-\infty}^{\infty} N(\alpha)V(\alpha)d\alpha;\ V(\alpha) = \frac{4\pi}{3} r^3 = \frac{4\pi}{3} r_o^3\ e^{3\alpha}$$

is equal to that of the "mixing" soil in the actual array. Then

$$V_{total} = N_o \int_{-\infty}^{\infty} \exp\left[-\frac{\alpha^2}{a_o^2}\right]\ \frac{4\pi}{3} r_o^3\ e^{3\alpha}\ d\alpha$$

Then

$$V_{total} = \frac{4\pi^{3/2}\ r_o^3}{3}\ N_o\ e^{\frac{9}{4} a_o^2}$$

or $$N_o = \frac{3V_{total}}{4\pi^{3/2}\ r_o^3}\ e^{9/4\ a_o^2}$$

We will assume that V_{total} is constant during the expansion process. We can now relate the effective mixing area to the total volume:

$$A_{eff} = \int_{-\infty}^{\infty} N(\alpha)A(\alpha)d\alpha$$

$$A(\alpha) = 4\pi r^2 = 4\pi r_o^2\ e^{2\alpha}$$

then

$$A_{eff} = \frac{3V_{total}}{r_o}\ \exp\left[-\frac{5}{4} a_o^2\right]$$

The procedure leading to eqn. (3) is still valid for estimation of "mixing" heat transfer as long as the typical size of the soil particle is larger than the thermal penetration depth, $D \sim 1\times10^{-4}$m. Let the gaussian spread go to zero (all particles of the same size) and the average size be equal to 1×10^{-3}m. This estimation is appropriate for granular media. (For a medium with some degree of consolidation, a_o can be 2-3 and heat transfer will be unimportant).

Then

$$A_{eff} = (3\times10^{3}m^{-1})\ V_{total}$$

$$= 7.1585\times10^{3}m^{2} \text{ for the Thomsen-Wu case.}$$

This value can be substituted into equation (3) for an estimate of the energy lost to the soil contained within the expanding cavity through mixing:

$$Q_L = 146.5\ (.718\ T_{bpo}-T_o)$$

The efficiency of the array can be expressed as

$$\eta = 1 - \frac{Q_L}{Y} = 1 - \frac{146.5(.718T_{bpo}-T_o)}{(mc_v)_{bp}(T_{bpo}-T_o)}$$

$$= 1 - \frac{162.77}{1.746\times10^{3}} \left[\frac{.718T_{bpo}-T_o}{T_{bpo}-T_o}\right]$$

$$= 1 - .0932 \left[\frac{.718T_{bpo}-T_o}{T_{bpo}-T_o}\right]$$

Then $\eta > 93\%$ for a mixing model with the assumed distribution of particle sizes in the Thomsen-Wu geometry.

Then for this case the by-products lose less than 7% of the internal

energy to the soil. Thomsen and Wu (Ref. 1) arrived at an efficiency factor, empirically, for this array of 62%. Obviously, the efficiency factor is affected to some degree by this thermodynamic mechanism but, it isn't the dominant effect. We refine this approach and present an alternative model (valid when the "semi-infinite solid" assumption is not valid) in Section D. In the next section we examine another possible explanation.

C. The Viscous Fluid Model

It has been determined previously (Ref. 8) that geometric (i.e., source arrangement, spacing, diameter, etc.) effects alone are insufficient to completely explain the mechanism behind the factor which relates the relative ability to produce ground motion for discrete and continuous source arrays. In the last section it was determined that a simple thermodynamic model allowing heat transfer to the portion of soil which remains in the expanding cavity is also inadequate to solely model the effect. Here we present an additional mechanism, first touched on in (Ref. 8), which provides an effective means of efficiency factor prediction for a wide range of spacings, as well as array aspect ratios.

The model advocated here is based on the observation that in the immediate vicinity of the array, the stresses induced by the blast exceed the shear strength of the soil. In this region, the "hydrodynamic zone," the soil reacts to the propagating shock wave more as a viscous fluid than as a solid. Then the approach here will be to model both the continuous and discrete arrays as being embedded in a viscous fluid. The effect of the viscosity is to attenuate the shock wave as it propagates in the hydrodynamic zone over and above the omnipresent geometric attenuation. This attenuation is strongly frequency dependent, another feature the model shares with observation (Ref. 9). When the peak stress is attenuated to a point below the shear strength of the soil, we assume the hydrodynamic zone ends. By comparing a certain potential function, constructed in each case, at the end of the hydrodynamic zone, we are in effect comparing the potential to

induce ground motion in each case. The attenuation experienced by the stress wave in the two cases, discrete array and continuous source, is different, as the average distance each source element undergoes attenuation is different in each case. This result gives rise to the efficiency factor.

In order to illustrate the difference in average distance in each of the two source types, consider the figures below.

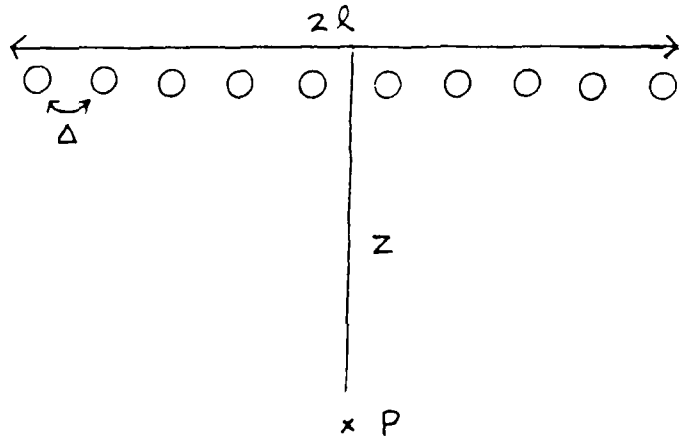

Figure 3

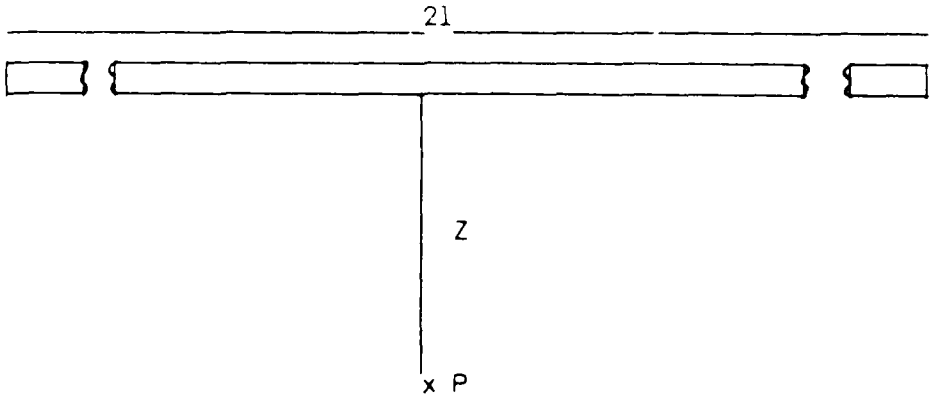

Figure 4

We calculate the average distance to the point P (assumed to be on the boundary of the hydrodynamic zone) in each case. For this purpose, we assume our sources to be one dimensional, i.e. no height nor thickness. The distance Z is assumed to be the same in each case. The volume of the hydrodynamic zone should be equal in each case although edge effects should make the contour near the edges a little different. At the midpoint any differences should be very small.

In the discrete case:

$$R^{D}_{ave} = \frac{\sum n_i r_i}{\sum n_i}$$

where $$r_i = \left[Z^2 + (i\Delta)^2 \right]^{\frac{1}{2}}$$

The spacing, Δ, is related to the array length and total number of sources, N, by

$$\Delta = \frac{2l}{(N-1)}$$

Then
$$R^D_{ave} = \frac{Z + 2\sum_{i=1}^{N} \left[Z^2 + \left(\frac{2li}{(N-1)^2}\right)^2 \right]^{\frac{1}{2}}}{N}$$

or
$$R^D_{ave}/l = \frac{\frac{Z}{l} + 2\sum_{i=1}^{\frac{N-1}{2}} \left[\frac{Z^2}{l^2} + \left(\frac{2i}{(N-1)^2}\right)^2 \right]^{\frac{1}{2}}}{N}$$

and in the continuous case

$$R^C_{ave} = \frac{1}{2l} \int_{-l}^{l} \left[Z^2 + x'^2 \right]^{\frac{1}{2}} dx'$$

which can be integrated to yield

$$R^C_{ave}/l = \frac{1}{2} \left\{ \frac{Z^2}{l^2} \ln \left[\frac{1 + \sqrt{1 + Z^2/l^2}}{Z/l} \right] + \left[1 + \frac{Z^2}{l^2} \right]^{\frac{1}{2}} \right\}$$

A companion is presented in Table 1 for various values of Z/l and N.

(Recall Z is the midline distance to be end of the hydrodynamic zone.)

	Z/l		
	.1	.5	.9
N 3	1.36	1.23	1.13
5	1.21	1.12	1.07
7	1.15	1.08	1.04
9	1.11	1.06	1.03
11	1.09	1.05	1.03

Table 1. R^D_{ave} / R^C_{ave}

Z/l	R^C_{ave}/l
.1	.5174849
.5	.7394715
.9	1.060591

Table 2. R^C_{ave}

A crude method of determining the relative influence at this average distance upon the relative ability for producing ground motion in each case can be found by approximating the exact (within the assumptions previously listed) expression for the potentials:

$$\Phi = \int_{-\infty}^{\infty} \rho(x') \frac{\exp\left\{-\Gamma 1 \left[\frac{Z^2}{1^2} + \frac{X'^2}{1^2}\right]^{\frac{1}{2}}\right\}}{\left[\frac{Z^2}{1^2} + \frac{X'^2}{1^2}\right]^{\frac{1}{2}}} dx'$$

where $$\rho(x') = \frac{2}{N} \sum_{i=1}^{\frac{N-1}{2}} \delta\left(X'^2 - \frac{(2i)^2}{(N-1)^2}\right) + \frac{\delta(x')}{N}$$

in the discrete case, and

$$\rho(x') = 1 \quad -1 \leq X' \leq 1$$

$$= 0 \quad |X'| > 1$$

in the continuous case.

Our approximation is (only for purposes of illustration!)

$$1\ \Phi^C \approx \frac{e^{-(\Gamma 1)\, R^C_{ave}/1}}{(R^C_{ave}/1)}$$, in the continuous case

and

$$1\ \Phi^D \approx \frac{e^{-\Gamma 1\, (R^D_{ave}/1)}}{(R^D_{ave}/1)}$$, in the discrete case.

then

$$\frac{\Phi^D}{\Phi^C} \approx \frac{R^C_{ave}}{R^D_{ave}} \cdot \exp\left[- \Gamma 1 \cdot \left(\frac{R^C}{1}\right) \left\{ \frac{R^D}{R^C} - 1 \right\} \right]$$

As a concrete example, suppose N = 3 and $\frac{Z}{1} = .5$.

Then from Tables 1 and 2

then

$$\frac{\Phi^D}{\Phi^C} \approx \frac{1}{1.23} \exp \left[- \Gamma 1 (.7394715) \{.23\} \right]$$

$$\approx \frac{\exp[-\Gamma 1 (.17)]}{1.23} \approx .81 * \exp \left[- \Gamma 1 (.17) \right]$$

Furthermore, suppose that $\Gamma 1 \approx 2$

then

$$\frac{\Phi^D}{\Phi^C} \approx 58\%$$

The model we present is one in which the source (either discrete or continuous) is embedded in a finite, isotropic viscous fluid medium. The viscous fluid is surrounded by an infinite elastic medium. The extent of the viscous medium depends upon the yield of the source and the shear strength of the soil. We use the viscous fluid medium in order to model the pulse attenuation induced in the hydrodynamic zone. This approach has been recently used (Ref. 9) with another objective in mind. Using this model, we will compare the "attenuated potentials" of the two source types.

We form the following potential function.(+)

$$\Phi_A = \int dx' \int dy' \int dz' \rho(x',y',z') \frac{\exp\left[(iK-\alpha)\{(x'-x)^2+(y'-y)^2+(z'-z)^2\}^{\frac{1}{2}}\right]}{\left[(x'-x)^2+(y'-y)^2+(z'-z)^2\right]^{\frac{1}{2}}} \qquad [4]$$

where the region of integration includes all space. Here the observation point is given by (x,y,z) and the source point by (x',y',z'). K is the wave number of the particular spectral component under consideration, $\rho(x',y',z')$ is the source charge density, and α is the (frequency dependent) attenuation factor. Implicitly assumed in eqn. (4) is the concept of superposition of both spectral components (in the Fourier analysis) and of the sources themselves.

If the source is such that the thickness (measured in the z-direction) is much smaller than the height (y-direction) or the length (x-direction), then we can approximate the source by an infinitely thin plane. Then

$$\rho(x',y',z') = \delta(z')\rho(x',y')$$

Substitution into (4) and integration over z' yields:

$$\Phi_A = \int dx' \int dy' \rho(x',y') \frac{e^{(iK-\alpha)\left[(x'-x)^2+(y'-y)^2+z^2\right]^{\frac{1}{2}}}}{\left[(x'-x)^2+(y'-y)^2+z^2\right]^{\frac{1}{2}}}$$

(+) For background on eqn. (4), See Ref. 8).

Furthermore, we assume that $\rho(x',y') = \{\theta(y'+m) -$

$- \theta(y'-m)\}\ \{\theta(x'+1) - \theta(x'-1)\}\ \sigma_0$,

where σ_0 = constant and is a measure of the areal charge density.

then

$$\Phi_A = \sigma_0 \int_{-m}^{m} dy' \int_{-1}^{1} dx' \ \frac{e^{(iK-\alpha)\left[(x'-x)^2+(y'-y)^2+z^2\right]^{\frac{1}{2}}}}{\left[(x'-x)^2+(y'-y)^2+z^2\right]^{\frac{1}{2}}}$$

Change of variables (Assume $l \geq m$)

Let $\epsilon - 1 = \frac{l}{m}$ aspect ratio; $\beta' = \frac{x'}{l}$; $\beta = \frac{x}{l}$; $\eta' = \frac{y'}{m}$; $\eta = \frac{y}{m}$; $R = \frac{z}{l}$

Then the argument of the exponent may be written as

$$(iK-\alpha)\left[\, l^2(\beta'-\beta)^2+m^2(\eta'-\eta)^2+z^2 \,\right]^{\frac{1}{2}} =$$

$$(iK-\alpha)l\left[(\beta'-\beta)^2+ \frac{m^2}{l^2}(\eta'-\eta)^2 + \frac{z^2}{l^2}\right]^{\frac{1}{2}}$$

$$= \Gamma\left[(\beta'-\beta)^2+\epsilon^2(\eta'-\eta)^2+R^2\right]^{\frac{1}{2}}$$

where $\Gamma = (iK-\alpha)l$. We will assume an observation point at the midline $x=y=0$. Then, also, $\beta=\eta=0$ and: $\Phi_A = \sigma_0 m \int_{-1}^{1} d\eta' \int_{1}^{1} d\beta' \ \frac{e^{-\Gamma\left[\beta'^2+\epsilon^2\eta'^2+R^2\right]^{\frac{1}{2}}}}{\left[\beta'^2+\epsilon^2\eta'^2+R^2\right]^{\frac{1}{2}}}$

Exploiting the symmetry about $\eta', \beta' = 0$

$$\Phi_A = 4\sigma_0 m \int_{0}^{1} d\eta' \int_{0}^{1} d\beta' \ \frac{\exp\{-\Gamma\left[\beta'^2+\epsilon^2\eta'^2+R^2\right]^{\frac{1}{2}}\}}{\left[\beta'^2+\epsilon^2\eta'^2+R^2\right]^{\frac{1}{2}}} \qquad [5]$$

The expression above is not integrable in closed form. Our approach will be to integrate it numerically for specific choices of the aspect

ratio, ϵ, attenuation factor Γ, and midline distance, R. We will then compare the results obtained for the discrete array and the continuous source cases. (The discrete array expression will consist of a sum of terms like eqn. (5) with appropriately chosen limits and parameters). Tables 3 and 4 indicate the results obtained.

Table 3

Efficiency factor for aspect ratio = 1, $\bar{\Gamma}$m = .5 for various numbers of source elements and hydrodynamic zones sizes.

Efficiency Factor	Number of Sources	$\frac{Z}{M}$
93.2	5	.1
90.6	5	.5
93.6	5	1.0
93.4	7	.1
93.5	7	.5
95.7	7	1.0
95.1	11	.1
96.0	11	.5
97.4	11	1.0

Table 4

Efficiency factor for aspect ratio = 1, $\bar{\Gamma}$m = 1 for various numbers of source elements and hydrodynamic zones sizes.

Efficiency Factor	Number of Sources	$\frac{Z}{M}$
92.9	5	.1
88.4	5	.5
91.5	5	1.0
92.6	7	.1
92.0	7	.5
94.2	7	1.0
94.3	11	.1
95.0	11	.5
96.5	11	1.0

A calculation was also performed for the Thomsen-Wu array (aspect ratio = 1.43), neglecting thermodynamic effects, for various values of $\bar{\Gamma}$m,

z/m. (Recall these values are related to the medium properties). Conservative choices were made and Table 5 presents the results.

Table 5

Efficiency Factor for the Thomsen-Wu array (aspect ratio = 1.43, number of source elements = 11) for various medium properties.

Efficiency Factor	Z/m	Γ_m
96.98%	1	1
93.2%	.5	2
93%	.25	2
94.58%	1	2
94.98%	.5	1

The table presents higher values of Γ_m than does Tables 3 or 4. This is because for $\Gamma_m < 1$ the efficiency factor is not strongly dependent upon aspect ratio. Therefore Tables 3 and 4 are relatively accurate for the Thomsen-Wu array if $\Gamma_m < 1$.

We curve-fit the results for an aspect ratio of one for a variety of number sources and hydrodynamic zone sizes. The results are given in eqns. (6) and (7). (We recommend linear interpolation for Γ_m between those listed).

$$Eff = A_0 + A_1 \left(\frac{z}{m}\right) + A_2 \left(\frac{z}{m}\right)^2$$

where

$$\Gamma_m = .5 \quad \begin{cases} A_0 = 101.5236 - 2.057655N + .1323648N^2 \\ A_1 = -75.12608 + 16.27323N - .8429415N^2 \\ A_2 = 58.30522 - 11.91516N + .6063844N^2 \end{cases} \qquad (6)$$

$$\text{For } \Gamma = 1 \quad \begin{cases} A_0 = 106.9969 - 3.431175N + .206119N^2 \\ A_1 = -108.1394 + 22.9988N - 1.189518N^2 \\ A_2 = 81.36503 - 16.66584N + .8541222N^2 \end{cases}$$

We will return to this result in the latter portion of the next section.

As can be seen from the tables, the calculations done for a variety of attenuation factors (as it is unknown what exact value should be used) and for a variety of hydrodynamic zone sizes indicate that for constant array length, and for $N \geq 7$ the efficiency factor, predicted solely on this mechanism, is approximately 90%. Thus this approach alone is also seemingly insufficient to account for the calculated value of Thomsen and Wu.

D. Suggested Approach to Efficiency Factor Estimation

We have seen that for arrays consisting of more than seven (or so) members the viscous fluid model (alone) predicts an efficiency factor of 90%. We have also argued that the efficiency factors predicted by a thermodynamic model are on the order of 95%. What then is the basis of the Thomsen-Wu result of 62%? The Thomsen-Wu result is empirically obtained, for a specific array by comparing the results of calculations (with realistic soil models) involving a 1-D continuous source and a 2-D discrete array. Undoubtedly we have dimensional, thermodynamic, and "soil viscosity," effects involved here. The comparison of 1-D to 2-D arrays by itself will introduce an efficiency factor of about 80% near to the source due only to geometric effects (Ref. 8). The net efficiency factor a Thomsen-Wu calculation would (almost certainly) predict if they had compared 2-D sources (continuous vs. discrete array) should be approximately 80%. This value is close to that predicted here for the Thomsen-Wu array using both the viscous soil fluid and the thermodynamic model. (As they are independent effects, the efficiency factor of a model which includes both effects is simply the product of the separate efficiency factors). We therefore believe an accurate prediction of the efficiency factor can be made from test to test by a synthesis of the two models. In this section, we expand on our thermodynamic model in order to lay the groundwork for efficiency factor prediction in the case that the thermal diffusion depth is on the order of the soil particle size and indicate the procedure for implementation.

Our alternate thermodynamic model is based upon the following set of assumptions. This approach is valid when r_o (the mean particle size) is on the order of the thermal penetration depth.

i) the volume-time relationship is a power law relationship. It is the same in both the continuous source and discrete array. We will use the expansion exponent found in Ref. (10).

ii) the explosive by-products behave as an ideal gas with constant specific heats.

iii) the lumped heat capacity approach to transient heat transfer calculation is valid. The Biot number varies linearly with soil particle size.

iv) the <u>product</u> formed by the convection coefficient and the exposed surface area of the expanding volume is constant.

Operating under the assumptions above, we can see that the rate of heat transfer in this case will be given by

$$\dot{Q} = hA\,(T_{bp} - T_s)$$

where: $s = \frac{1}{2} \times$ the source spacing

d = discrete source radius

$l = \frac{1}{2}$ the array length

Before we continue with the development of the model let us consider the limitations imposed by our assumptions. The by-products can be modeled

more accurately using the JWL equation of state but again, this is a higher order effect. Assumption (iii) is reasonably accurate, however, the accuracy of assumption (iv) is in doubt. The convection coefficient is a function of by-product velocity. There undoubtedly exists a relationship as well between the exposed surface of the cavity and the by-product velocity. A rough calculation, using a convection coefficient dependence upon velocity obtained from a specialist, Ref. (11), yields $hA \tilde{\propto} \tau^{n-.7}$ where n is the expansion law parameter. From (10), n=.86. The product hA is therefore not a strong function of time but is is not a constant either. A more accurate, i.e. numerical, calculation could be done, at a later date, with the incorporation of the JWL equation of state, a non-constant hA, etc. (In fact, if the expansion rate were known very accurately, a more complex numerical approach might yield soil material properties at high strain rates).

An energy balance done on the explosive by-products yeilds the evolution equation

$$(mc_v)_{bp} \frac{dT_{bp}}{d\tau} = hA\,(T_s - T_{bp}) - P\frac{dV}{d\tau} \qquad (\star)$$

, where: the subscript "bp" refers to the explosive by-products

the subscript "s" refers to the soil contained in the source cavity.

P is the by-product pressure

V is the cavity volume.

Likewise, an energy balance on the soil yields

$$(mc_v)_s \frac{dT_s}{d\tau} = hA\,(T_{bp} - T_s)$$

When the ideal gas law, used to replace P , and the assumed expansion law

$$\frac{V}{V_o} = \left(\frac{\tau}{\tau_o}\right)^n \qquad ; \quad \tau_o = .01 \text{ sec.}$$

are inserted into eqn. (★) we obtain

$$\dot{T}_{bp} = K_1 (T_s - T_{bp}) + \frac{K_2}{\tau} T_{bp} \tag{8}$$

and

$$\dot{T}_s = K_3 (T_{bp} - T_s) \tag{9}$$

where: $\dot{} = \frac{d}{d\tau}$

$$K_1 = \frac{hA}{(mc_v)_{bp}}$$

$$K_2 = (1 - \frac{c_p}{c_v})_{bp} n$$

$$K_3 = \frac{hA}{(mc)_s}$$

These equations can be decoupled to yield

$$\ddot{T}_{bp} + (K_3 + K_1 - \frac{K_2}{\tau}) \dot{T}_{bp} + (\frac{K_2}{\tau^2} - \frac{K_3 K_2}{\tau}) T_{bp} = 0 \tag{10}$$

$$\ddot{T}_s + (K_3 + K_1 - \frac{K_2}{\tau}) \dot{T}_s - \frac{K_3 K_2}{\tau} T_s = 0 \tag{11}$$

The most accurate approach (short of integrating the non-lumped capacity equations) would be to integrate (numerically) the above and use to calculate the heat lost, by calculating $T_s(\tau)$ from eqn. (11) with the initial condition $T_s \ (\tau=\tau_o) = T_o$. The heat lost by the by-products to the

soil is gained as internal energy (neglecting thermal expansion of the soil) by the soil.

Thus

$$|Q_1| = (mc)_S \left[T_S\,(\tau=\tau_f) - T_0 \right]$$

The efficiency is then

$$\eta = 1 - \frac{|Q_1|}{U_{bp}(\tau=\tau_0)} = 1 - \frac{|Q_1|}{(mc_v)_{bp}\left[\tau_{bpo} - \tau_0\right]}$$

We have used T_0 as the reference temperature instead of T = ØK as this is the <u>useful</u> energy.

We will take the Frobenius approach to the solution of eqn. (11). We form a trial solution

$$T_S = \tau^R \sum_{n=0}^{\infty} a_n \tau^n$$

then

$$\dot{T}_S = \sum_{n=0}^{\infty} a_n (n+R) \tau^{n+R-1}$$

and

$$\ddot{T}_S = \sum_{n=0}^{\infty} a_n (n+R)(R+n-1) \tau^{n+R-2}$$

Substituting into eqn. (11) yields:

$$\sum_{n=0}^{\infty} a_n(n+R)(n+R-1)\,\tau^{n-2} + (K_3+K_1-\frac{K_2}{\tau}) \sum_{n=0}^{\infty} a_n(n+R)\tau^{n-1} - \frac{K_3K_2}{\tau} \sum_{n=0}^{\infty} a_n\tau^{n-1}$$

Requiring the sum of the coefficients of each power of τ to vanish yields

for the indicial equation

$$R=0,\ R=K_2+1$$

and for the recursion relation for the coefficients a_n:

$$a_{n+1} = -a_n \left[\frac{(K_3+K_1)(n+R) - K_3K_2}{(R+n+1)(R+n)-K_2(R+n+1)} \right]$$

Then the general solution is

$$T_s = \sum_{n=0}^{\infty} \{ {}^{0}a_n \tau^n + {}^{1+K_2}a_n \tau^{n+1+K_2} \}$$

Subject to the conditions

$$T_s\ (\tau=\tau_0) = T_0$$

.

$$T_s\ (\tau=\tau_0) = K_3\ (T_{bpo} - T_0)$$

where

$${}^{0}a_{n+1} = -{}^{0}a_n \left[\frac{(K_3 + K_1)n-K_3K_2}{(n+1)\ (n-K_2)} \right]$$

$${}^{1+K_2}a_{n+1} = -{}^{1+K_2}a_n \left[\frac{(n+1)(K_3+K_1)+K_2K_1}{(n+1)\ (n+2+K_2)} \right]$$

In order to employ the Frobenius series, one needs only to determine the coefficients a_n numerically to the accuracy desired. An alternative approach is to numerically integrate equations (10), (11). Since the alternative approach will be required only in very few circumstances, we did not proceed further.

The efficiency of a discrete area containing only thermodynamic effects can be found from

$$\eta_{th} = 1 - ABCDE$$

where

A = Ratio of soil volume to source volume

$= \frac{V_{soil}}{V_{source}}$, where V_{soil} is the volume of soil contained between sources in the array

$B = \frac{(\rho c)_{soil}}{(\rho c_v)_{bp}}$ = Ratio of soil density times specific heat to the density of explosive times specific heat of the by-products

$C = \frac{.718 T_{bpo} - T_o}{T_{bpo} - T_o}$

$D = \frac{.18067 \times 10^{-4} m}{r_o}$, with r_o measured in meters.

$E = \exp\left[- \frac{5}{4} a_o^2 \right]$, where a_o is the measure of the "spread" of the Gaussian distribution of soil particle sizes. For perfect uniformity, $a_o = 0$.

Using reasonably uniform values for factors B,C,D,E

$$\eta_{th} = 1 - .03 \frac{V_{soil}}{V_{source}} \qquad (12)$$

The above expression will be reasonably accurate for nonconsolidated granular media. Notice that the array microgeometry is what is important for a given explosive and soil medium. The above expression is also limited to

cases where

$$V_{soil} \leq 7.24\ V_{source}$$

This limitation arises from our basic assumption that the soil was dispersed by the blast and remained inside the expanding cavity afterward. As the assumed power law expansion rate yields a final cavity volume to initial source volume ratio of 7.24, the soil volume used in equation (12) can have an upper bound of only 7.24 V_{source}. Then

$$78\% \leq \eta_{th} \leq 100\%$$

As previously mentioned in arriving at the 62% efficiency factor (discrete array to continuous source), Thomsen and Wu compared the (numerically calculated) ground motion predicted for a 2-D discrete array to that predicted in a 1-D continuous source of the same length. Using our viscous fluid model we numerically integrated eqn. (5) and its 1-D (ie, for a line source) counterpart for a variety of hydrodynamic zone sizes and attenuation factors. The results were then curve-fit to yield:

$$\text{Relative efficiency} = a\ (\frac{z}{l})^b$$

where $a = .903 - .095\Gamma l$

$b = .233 + .058\Gamma l$

l = array or source half length

z = midline distance to end of hydrodynamic zone

Γ = attentuation factor

and

possible source of error in relating source strength to resultant ground motion can be controlled. We will return to specific recommendations in a latter section.

Section III. Recommendations

In this section we summarize the results of the previous section and make specific recommendations concerning use of those results. We have seen that all heat transfer between the explosive by-products and the soil at the boundary of the cavity can be neglected but that if, the average size of the soil particles that remain within the cavity is small enough, heat transfer here can't be neglected. This should be considered especially for granular media. A more realistic set of size distribution parameters for the Gaussian function used here could be experimentally determined if needed or a different distribution function itself could be employed. Unless the medium has a larger thermal diffusivity than the value used in our analysis, we don't believe that the additional effort will be worthwhile for efficiency factor calculational purposes. Experimental soil fragmentation studies however, may provide insight into the microscopic mechanisms involved in explosive loading.

In this light we recommend that for almost all applications the relationships presented in Section II-D concerning thermodynamic losses be used. Other values for the specific heat and density of the soil and the density of the explosive could be used in the expressions previously developed to improve the accuracy if applicable.

The losses associated with attenuation in the hydrodynamic zone may

$$\text{Relative efficiency} = \frac{\text{Efficiency of 2-D continuous source}}{\text{Efficiency of 1-D continuous source}}$$

Then, as an example, for a conservative set of values:

$$\Gamma 1 = .5$$

$$\frac{z}{1} = .5$$

the relative efficiency is about 72%. If these values were to be valid in the Thomsen-Wu case, then the relative efficiency of a 2-D discrete array to a 2-D continuous source would be

$$\frac{62\%}{72\%} = \text{"True" 2-D efficiency factor}$$

$$= 86\% \qquad (13)$$

Returning for the moment to the two sample calculations done in the previous two sections. We estimated that the efficiency factor based on a (solely) thermodynamic approach was approximately .93 (or higher). Using a representative figure from Table 3,4, or 5 gives an efficiency factor neglecting the thermodynamics of approximately .94. The efficiency factor taking these two independent loss mechanisms into effect should be the product of them or

$$\eta_{total} = .87 \text{ or } 87\%$$

This is strikingly close to the "true" efficiency factor (after accounting for the dimensional effects) predicted by the Thomsen-Wu computer calculation. We can conclude that the methods introduced in the current and two previous sections will be useful in predicting the efficiency factor from case-to-case based on the array microgeometry. By their implementation, a

10. Allen, R.T. and Zerkle, J.E., Ground Motion Predictions for the CARES MP-2 Event, Report No. PT-U83-0622, Pacifica Technology, Del Mar, California, Sept. 1983.

11. Behbahani, A., Private communication.

12. Stump, B.W., Body Force Equivalence of Finite High-Explosive Simulators, Report #AFWL-TR-83-123 Air Force Weapons Lab, April, 1984.

II. APPROACH: (Continued)

Given the above medium properties and assuming a harmonically time-dependent source (this causes no difficulty as any time dependence can be formed by an appropriate Fourier analysis) the governing wave equations are (6):

$$(\nabla^2 + K_1^2)\,\phi = f(\bar{x}') \tag{1}$$

$$(\nabla^2 + K_2^2)\,\psi = g(\bar{x}') \tag{2}$$

where: ϕ, ψ are the dilatational and shear potentials, respectively.

K_1, K_2 are the wave numbers for the dilatational and shear waves. In this form dispersion effects can be incorporated.

$f(\vec{x}')$, $g(\vec{x}')$ are the source geometry factors.

The shear and dilatational potentials are related to the displacements U_r, U_z in cylindrical co-ordinates by

$$U_z = \frac{\partial \phi}{\partial z} - \frac{\partial^2 \psi}{\partial r^2} - \frac{1}{r}\,\frac{\partial \psi}{\partial r} \tag{3}$$

$$U_r = \frac{\partial \phi}{\partial r} + \frac{\partial^2 \psi}{\partial z \partial r} \tag{4}$$

II. APPROACH: (Continued)

We are concerned with the radial displacement at the midline (z=0) of the explosive source array. By symmetry:

$$U_r\ (z=0) = \frac{\partial \phi}{\partial r} \tag{5}$$

Thus the quantity of interest will be $\frac{\partial \phi}{\partial r}$.

The solution to equation (1) is well-known to be (5) (See Appendix B):

(6)

$$\phi = \int_{-\infty}^{\infty} dx' \int_{-\infty}^{\infty} dy' \int_{-\infty}^{\infty} dz' \ \frac{f(x',y',z')\exp\{iK[(x'-x)^2+(y'-y)^2+(z'-z)^2]^{\frac{1}{2}}\}}{[(x'-x)^2 + (y'-y)^2 + (z'-z)^2]^{\frac{1}{2}}}$$

Where ' refers to the source co-ordinate. Unprimed quantities are observation point co-ordinates. Implicit in the solution, eqn. (6), is the concept of superposition of waveforms. Some previous work (1) seems to indicate that in the absence of air blast, linear superposition is reasonably accurate.

Our problem then is to integrate eqn. (6) either analytically or numerically for various explosive source geometries, i.e., for various $f(\bar{x}')$. A comparison of the geometric attenuation of various types of source configurations will then be made in order to determine the regions of equivalence. In this manner we will examine the different scaling regions.

III. RESULTS

We examined recently proposed scaling region criteria. These criteria were obtained by trial and error. We sought to either validate or modify the scaling regions as needed. Calculations are contained in the appendices. The interested reader is referred there for the details. Our work indicated new scaling regions, not determined by the work previously done probably due to the lack of data in these regions.

The results of the research seem to indicate that there may be two spherical scaling regions, each with possibly different scaling laws. The field is quasi-static (i.e., the wave number k has little effect) in the region $kR<1$. For the "typical" array (recall large k components are rapidly attenuated by the medium), this quasi-static region includes the three regions proposed by Drake.

It is in the region $kR>1$ (the "radiation zone") that the behavior (i.e., the distance dependence) of the field, although still spherical in nature, changes from that in the quasi-static region. Spherical behavior in the quasi-static region is indicated by a R^{-2} dependence.

III. RESULTS: (Continued)

In the radiation zone spherical behavior is indicated by a R^{-1} dependence. The different geometric dependence of the two spherical fields seems to suggest that one would have two different scaling laws. This was not investigated further.

In addition, we verified the scaling regions proposed by Drake analytically. This is in effect a validation of our approach, as well, since the data also closely fits our results. It also would seem to strengthen support for use of the Drake(2,3) regions over those advanced previously by Higgins(4).

IV. CONCLUSIONS:

In summary, the major results of the research were in: a) validating empirically obtained scaling region criteria by a totally independent, analytical method; and b) establishing the usefulness and appropriateness of the analytical approach when dealing with geometric questions in this field of research.

Further research might center around investigating the possible existence of the second spherical region, mentioned previously, and the development of an appropriate scaling law valid within it. If such a region does have a different scaling law, one would expect data taken at the larger distances to deviate somewhat from the presently used scaling rule.

ACKNOWLEDGMENTS

I would like to acknowledge the assistance of Capt. W.A. Kitch of the AFWL/NTED Division at Kirtland AFB for aiding in preliminary research and also for beneficial discussions as the work progressed. Mr. Jeff Fischer of the University of Cincinnati also provided excellent support in handling the numerical computations involved. Finally, the sponsorship of the Air Force Systems Command, Air Force Office of Scientific Research, and the Air Force Weapons Laboratory is greatly appreciated.

APPENDIX - REFERENCES

1. Bratton, J.L., Dzwilewski, P.T., and Phillips, J.S., "Multiple Burst Ground Shock Environments," Technical Report No. AFWL-TR-81-144, Science Applications, Inc., Albuquerque, New Mexico, March 1982.

2. Drake, J.L., "Consistent Scaling of DIHEST Ground Motions," Applied Research Associates, Inc., Albuquerque, New Mexico, August 1984.

3. Drake, J.L., and Higgins, C.J., "A Method for Scaling Explosion-Produced Ground Motion From Various Buried Source configurations," Response of Geologic Materials to Blast Loading and Impact, ASME, New York, New York, June 1985, pp. 119-132.

4. Higgins, C.J., Johnson, R.L., and Triandafilidis, G.E., "The Simulation of Earthquake - Like Ground Motion with High Explosives," Report No. CE-45(78) NSF-507-1 on NSF Grant ENG 75-21580, The University of New Mexico, Albuquerque, New Mexico, July 1978.

5. Jackson, J.D., Classical Electrodynamics, New York, New York, John Wiley and Sons, Inc., 1975.

6. Lee, T.M., "Surface Vibration of a Semi-Infinite Viscoelastic Medium," Proc. Int. Symposium on Wave Propagation and Dynamic Properties of Earth Materials, Univ. of New Mexico, Albuquerque, New mexico, August 1967, pp. 123-138.

Appendix A

A-I. The Governing Equation - The Inhomogenous Helmholtz Equation

The evolution of the pressure or shear wave radiating from an explosive source in an elastic media satisfies the scalar wave equation:

$$\nabla^2 \Psi - \frac{1}{c^2} \frac{\partial^2 \Psi}{\partial t^2} = -4\pi f(\vec{x},t) \qquad \text{(A-1.1)}$$

where $f(\vec{x},t)$ is a known source distribution. The factor c is the velocity of propagation in the medium, assumed here to be without dispersion (i.e., $c \neq c(w)$), where w is the frequency of the wave). We consider the simple situation of no boundary surfaces and proceed to remove the explicit time dependence by introducing a Fourier transform with respect to frequency. We suppose that $\Psi(\vec{r},t)$ and $f(\vec{r},t)$ have the Fourier integral representations.

$$\Psi(\vec{r},t) = \frac{1}{2\pi} \int_{-\infty}^{\infty} \Psi(\vec{r},w) e^{-iwt} dw \qquad \text{(A-1.2)}$$

$$f(\vec{r},t) = \frac{1}{2\pi} \int_{-\infty}^{\infty} f(\vec{r},w) e^{-iwt} dw \qquad \text{(A-1.3)}$$

When these representations (A-1.2), (A-1.3) are inserted into the wave equation (A-1.1) it is found that the Fourier transform $\Psi(\vec{r},w)$ satisfies the inhomogeneous Helmholtz wave equation

$$(\nabla^2 + K^2) \Psi(\vec{r},w) = -4\pi f(\vec{r},w)$$

A-I. The Governing Equation - The Inhomogenous Helmholtz Equation

for each value of w. Here k(=w/c) is the wave number associated with frequency w. In this form, the restriction of dispersion-free propagation is unnecessary. A priori, any connection between k and w is allowed, although causality imposes some restrictions.

In the case at hand the time dependence of the source will be localized in time (i.e., the source vanishes except in some small interval Δt). However, it is well known that by Fourier analysis we can form such a localized time dependence from a number of sinusoidally varying sources. Thus we lose no generality in considering potentials and sources (localized in space) which vary sinusoidally in time.

In this case:

$$f(\vec{r},t) = \rho(\vec{r})e^{-iwt}$$

$$\Psi(\vec{r},w) = \Psi(\vec{r})e^{-iwt}$$

A-II. The Green's Function Method of Solution of the Inhomogenous Helmholtz Equation

A solution of the equation

$$(\nabla^2 + K^2)\,\Psi(\vec{r}) = -4\pi\rho(\vec{r}) \qquad \text{(A-2.1)}$$

can be constructed from a superposition of the solutions for point sources of unit strength, $\rho(\vec{r})$, if we define $\rho(\vec{r})$ by

$$\rho(\vec{r}) = \iiint \delta(\vec{r}-\vec{r}')\rho(\vec{r}')d^3x' \qquad \text{(A-2.2)}$$

where $\iiint\delta(\vec{r}-\vec{r}')d^3x' = 1$. ($\delta$ is the Dirac delta function.)

Suppose that a solution $G(\vec{r},\vec{r}')$ can be found for the equation

$$(\nabla^2 + K^2)\,G(\vec{r},\vec{r}') = -4\pi\delta(\vec{r}-\vec{r}') \qquad \text{(A-2.3)}$$

Then $\Psi(\vec{r})$, the desired solution of equation (A-2.1), is readily shown to be

$$\Psi(\vec{r}) = \iiint G(\vec{r},\vec{r}')\rho(\vec{r}')d^3x' \qquad \text{(A-2.4)}$$

To verify that equation (A-2.4) is a solution of equation (A-2.1), we utilize equations (A-2.2) and (A-2.3) as follows:

$$(\nabla^2 + K^2)\iiint G(\vec{r},\vec{r}')\rho(\vec{r}')d^3x' =$$

$$= \iiint(\nabla^2 + K^2)G(\vec{r},\vec{r}')\rho(\vec{r}')d^3x'$$

$$= \iiint -4\pi\delta(\vec{r}-\vec{r}')\rho(\vec{r}')d^3x'$$

$$= -4\pi\rho(\vec{r})$$

A-II. The Green's Function Method of Solution of the Inhomogenous Helmholtz Equation - (Continued)

Using the solution to Poisson's equation as an analogy, we find the Green's function for equation (A-2.1) to be

$$G(\vec{r},\vec{r}') = \frac{1}{4\pi} \quad \frac{e^{iK|\vec{r}-\vec{r}'|}}{|\vec{r}-\vec{r}'|}$$

We note that in the limit k -> 0, we have the Poisson equation.

Appendix B

B-I. Source Configurations

The following source configuration were examined:

a) single spherical source

b) single cylindrical source

c) continuous planar source - both rectangular and circular

d) planar source composed of an array of discrete cylindrical sources. (We examined the case of even number of sources as well as odd number of sources.)

B-II. Solutions

The solutions to the wave equation appropriate to the above source configurations are:

a) Spherical source - $\Phi_{,R} \alpha \frac{e^{iKR}}{iKR^2} \{iKR-1\}$ (B-2.1)

b) Cylindrical source - $\Phi_{,R} \alpha N_0(KR)$ (B-2.2)

for R> radius of cylinder where N_0 is the Neumann function of order o.

c) Continuous rectangular source -

(2l = length; 2m = width)

i) Near zone - $\Phi_{,R} \alpha \tan^{-1}\left[\frac{ml}{R(m^2+l^2+R^2)^{\frac{1}{2}}}\right]$ (B-2.3)

B.II. Solutions - (Continued)

ii) Intermediate and Far Zones -

$$\Phi,_R \alpha \int_0^{1m}\int_0^{} e^{iK\left[x'^2+y'^2+R^2\right]^{\frac{1}{2}}} \qquad \text{(B-2.4)}$$

$$\left\{ \frac{i\,KR}{\left[x'^2+y'^2+R^2\right]} - \frac{R}{\left[x'^2+y'^2+R^2\right]^{3/2}} \right\} dx'dy'$$

continuous circular source - radius = a

$$\Phi,_R \alpha \frac{R}{(R^2+a^2)^{\frac{1}{2}}} e^{iKR\left[R^2+a^2\right]^{\frac{1}{2}}} - e^{iKR} \qquad \text{(B-2.5)}$$

d) Discrete rectangular source - (here we examined only the near zone as the intermediate and far zones are as in cii) above.) Here 2s is the array member width and 2δ is the array member spacing.

i) even source

$$\Phi,_R \alpha \text{ const.} + \frac{2}{\pi} \sum_{n=1}^{\infty} \frac{1}{n} \sin\left(\frac{n\pi}{1+\beta}\right) \cos n\pi \exp\left[-\frac{4\pi nR}{S+\delta}\right] \qquad \text{(B-2.6)}$$

ii) odd source

$$\Phi,_R \alpha \text{ const.} + \frac{2}{\pi} \sum_{n=1}^{\infty} \frac{1}{n} \sin\left(\frac{n\pi}{1+\beta}\right) \exp\left[-\frac{4\pi nR}{S+\delta}\right] \qquad \text{(B-2.7)}$$

where $\beta = \frac{\delta}{S}$

Appendix C

C-I. Scaling Considerations

The comparison of the "exact" (numerical integration of eqn. (6)) solution with the various analytical approximations (B-2.3), (B-2.4) indicates that for a certain range of R the continuously distributed planar source is a good approximation to the exact solution. On the other hand, for another range of R the static periodically distributed planar model is relatively accurate. We shall call this "transition" value of R, R_T. With these two analytical models in hand, we can examine scaling region definitions.

The approach will be to expand the two models in their regions of accuracy and to compare the behavior of these models with that of the single spherical source, the infinitely long cylindrical source, and the infinite planar source (the "ideal" sources). The scaling regions will then be chosen as those in which the dominant field behavior is that of one of these ideal sources.

In order to indicate our procedure, we will use the static example. The static solution is relatively accurate for $R < R_T$. For all but those arrays with large ($\alpha > 3$) aspect

C-I. Scaling Considerations - (Continued)

ratios, this value is greater than R = 1. Then, one can see that the static calculation is practically the only calculation necessary in order to determine scaling regions (with the exception of the possible second spherical region).

In the static case the quantity of interest, $\Phi_{,R}$ is given by:

$$\Phi_{,R} \alpha \tan^{-1}\left[-\frac{ml}{R(m^2+l^2+R^2)^{\frac{1}{2}}}\right]$$

In order to examine the dominant field behavior, we expand the above using

$$\tan^{-1}X = X - \frac{1}{3}X^3 + \ldots \qquad X^2<1$$

$$\tan^{-1}X = \frac{\pi}{2} - \frac{1}{X} + \frac{1}{3X^3} - \ldots \qquad X^2>1$$

Case #1: $R < m < l$

Then $$\Phi_{,R} \alpha \frac{\pi}{2} - \frac{R(m^2+l^2+R^2)^{\frac{1}{2}}}{ml} + \ldots$$

C-I. Scaling Considerations - (Continued)

This is planar behavior as the leading term is a constant.

Case #2: $m \leq R < 1$

Then $$\Phi_{,R} \alpha \frac{m}{R} \left\{1 - \frac{R^2}{2l^2} - \ldots \right\}$$

This is cylindrical behavior as the leading term has a single inverse power dependence.

Case #3: $m < 1 \leq R$

Here $$\Phi_{,R} \alpha \frac{ml}{R^2} \left\{1 - \frac{1}{2}\frac{l^2}{R^2} - \frac{1}{2}\frac{m^2}{R^2} + \ldots \right\}$$

This is spherical behavior as the leading term has a inverse square dependence.

Since one would expect scaling laws to change as field behavior changes in given regions, scaling laws should be based on the following break-down of regions:

Planar	$R < m < 1$
Cylindrical	$m \leq R < 1$
Spherical	$m < 1 \leq R$

C-I. Scaling Considerations - (Continued)

It then turns out, quite independently from the method of Drake, that this break-down of regions coincides with that of Drake.

In addition to the regions suggested by Drake, we discovered "inner" scaling regions. "Inner" regions scaling breakdown is of course based on the near field static solutions (B-2.6) and (B-2.7). The examination of the dominant field behavior is a little more complex and the resulting breakdown a little less clear cut.

In the case of both even and odd arrays, the field can be expanded as:

$$\Phi_{,R} \alpha 1 + \frac{2(\beta+1)}{\pi} \sum_{n=1}^{\infty} a_n(P) \left\{ - \frac{1}{1 - \frac{4\pi n\beta R}{(1+\beta)\delta} + \frac{1}{2}\left\{\frac{4\pi n\beta R}{(1+\beta)\delta}\right\}^2} \right\} - \ldots$$

where $a_n(P)$ is equal to one function of n in the odd case and a different function of n in the even case. We will have planar behavior if the constant (=1) in the denominator of the terms in the summation dominates; cylindrical behavior if the term proportional to R dominates; etc. We evaluated the sum numerically for different values of R and compared with expected behavior. The resultant region breakdown for the odd array is:

C-I. Scaling Considerations - (Continued)

$$R/\delta < \frac{1}{4\beta} \qquad \text{Planar Behavior}$$

$$\frac{1}{4\beta} \leq R/\delta < \frac{1+2\beta}{4\beta} \qquad \text{Cylindrical Behavior}$$

Assuming that $m > \frac{1+2\beta}{4\beta}\,\delta$, there is no inner spherical region.

For the even arrays, we have determined that the "best" inner breakdown is:

$$R/\delta < \frac{1}{4} \qquad \text{Cylindrical Behavior}$$

C-II. Other Source Configurations

In the manner of Drake (1), we briefly examine the field behavior of both single spherical and cylindrical sources in addition to circular disc sources. The integrands of the solution (B-2.1) and the solutions (B-2.2) and (B-2.5) can be expanded in the various regions to obtain the dominant field behavior in those regions. The results are:

Spherical source (Radius=a)

$R<a$ Planar behavior

$a \leq R$ Spherical behavior

Cylindrical source (Radius=a)

$R<a$ Planar behavior

$a \leq R<M$ Cylindircal behavior

$M \leq R$ Spherical behavior

Circular disc (Radius=a)

$R<a$ Planar behavior

$a \leq R$ Spherical behavior

Note that the region breakdown for the circular disc could also have been obtained from that of the rectangular planar arrays by setting l=m, with the resulting "disappearance" of the cylindrical region.

APPENDIX - NOTATION

The following symbols are used in this paper:

∇^2 - The Laplacian operator

K - The wave number

ϕ, Ψ - The dilational and shear potentials, respectively

$f(\vec{x}'), g(\vec{x}')$ - The source geometry factors

U_r, U_z - The displacements (cylindrical co-ordinates)

R - The perpendicular distance between the array center and the point of observation

C - The velocity of propagation for a particular mode of wave

w - The wave frequency

$\delta(\vec{r})$ - The Dirac delta function

$\rho(\vec{r})$ - The source density

$G(\vec{r}, \vec{r}')$ - The Green function

$\bar{\Phi}_{,R} \equiv \frac{\partial \bar{\Phi}}{\partial R}$

N_0 - The Neumann function of zero order

α - The array aspect ratio $\alpha = \frac{\text{length}}{\text{width}}$

$2m$ - The width of an array

$2l$ - The length of an array

$2b$ - Array member width

2δ - Array member spacing

R_T - Transition value of R

$\beta \equiv \frac{\delta}{b}$

a - Source radius

TABLE 1

Odd Arrays

$\frac{\varepsilon}{\delta} < R/\delta < \frac{1}{4\beta}$ Planar scaling

$\frac{1}{4\beta} \leq R/\delta < \frac{1+2\beta}{4\beta}$ Cylindrical scaling

$(\frac{1+2\beta}{4\beta})\ \delta \leq R < m$ Planar scaling

$m \leq R < 1$ Cylindrical scaling

$1 \leq R$ Spherical scaling

Even Arrays

$\varepsilon/\delta < R/\delta < \frac{1}{4}$ Cylindrical scaling

$\delta/4 \leq R < m$ Planar scaling

$m \leq R < 1$ Cylindrical scaling

$1 \leq R$ Spherical scaling

ε is the cut-off distance. This is the distance beyond which high frequency components are severely attenuated.

The above assume "natural" ordering, i.e.:

$\varepsilon \leq s \leq \delta \leq m \leq 1$

1986 USAF-UES RESEARCH INITIATION GRANT PROGRAM

Sponsored by the

AIR FORCE OFFICE OF SCIENTIFIC RESEARCH

AND UNIVERSAL ENERGY SYSTEMS, INC.

FINAL TECHNICAL REPORT

THE ROLE OF ANTIOXIDANT NUTRIENTS IN PREVENTING HYPERBARIC OXYGEN DAMAGE TO THE RETINA

Prepared by :	William L. Stone, Ph.D.
Academic Rank:	Associate Professor
Department and University:	Department of Pediatrics and Biomedical Sciences Meharry Medical College
Research Location:	Meharry Medical College
USAF Research:	Col. Richard Henderson, M.D. Armed Forces Institute of Pathology CPL-A, Washington, D.C., 20306-6000

Date:	February 24, 1985
Contract No.:	F49620-85-C-0013/SB5851-0360
Subcontract No.:	S-760-OMG-037

[illegible] THE RETINA

Abstract

Hyperbaric oxygen treatment was found to adversely affect the electroretinograms (ERGs) of rats fed a diet deficient in both vitamin E and selenium (the basal or B diet) or a diet deficient in vitamin E alone (B+Se diet). Both vitamin E and selenium are micronutrients thought to play essential roles in preventing in vivo lipid peroxidation. After 4 wks of hyperbaric oxygen treatment (3.0 ATA of 100 % oxygen, 1.5 hrs per day, 5 day/wk) rats fed the B diet deficient in vitamin E and selenium showed decreased ($p < 0.05$) a-wave amplitudes (85±9 uV, N=11) compared with a-wave amplitudes (151±10 uV, N=21) for rats fed an identical diet but not treated with hyperbaric oxygen. Rats fed a basal diet supplemented with both vitamin E and selenium (the B+E+Se diet) or with vitamin E alone (the B+E diet) showed constant a- and b- wave amplitudes that did not decrease after 15 weeks of hyperbaric oxygen treatment. After 15 weeks of hyperbaric oxygen treatment rats fed the B+Se diet deficient in vitamin E alone showed decreased ($p < 0.01$) a-wave (61±9 uV, N=4) and b-wave (253±23 uV, N=4) amplitudes compared with a-wave (115±7 uV, N=4) and b-wave amplitudes (450±35 uV, N=4) for rats fed the same diet but not treated with hyperbaric oxygen. Vitamin E supplementation alone appear to provide long term protection from hyperbaric oxygen damage to the retina. Dietary deficiencies of both vitamin

[illegible] oxygen.

Quantitative histopathology studies showed that rats fed the vitamin E and selenium deficient diet (the B diet) for 6 wks had necrosis of the retinal outer nuclear cell layer in the temporal region compared with rats fed the same diet but supplemented with vitamin E and selenium (B+E+Se diet). This necrosis of the photoreceptor cells was not, however, influenced by 4 wks of hyperbaric oxygen treatment. Rats fed the vitamin E deficient diet for 17 wks and treated with hyperbaric oxygen for 15 wks also showed a significant ($p < 0.05$) photoreceptor cell necrosis compared with rats fed an identical diet but not treated with hyperbaric oxygen. The retinal pigment epithelium cells were found to have a greater cell height in rats fed the vitamin E deficient diet for 17 wks but this histopathology was not influenced by hyperbaric oxygen treatment for 15 wks.

The livers of rats fed the B diet for 6 wks had significantly higher levels of malondialdehyde (MDA) than rats fed the B+E+Se diet. Hyperbaric oxygen (4 wks) did not, however, increase the levels of liver MDA. The polyunsaturated fatty acid content (PUFA) of whole liver homogenate from rats fed the B or B+E+Se was very similar and unaffected by hyperbaric oxygen treatment (4 wks). Similarly, the PUFA content of rat liver phospholipids was unaffected by diet or hyperbaric oxygen treatment. The plasma of rats fed the B diet for 6 wks and treated with hyperbaric oxygen for 4 wks was significantly higher than

rats fed the identical diet but not treated with hyperbaric oxygen.

BACKGROUND

Hyperbaric oxygen treatment is increasingly being used to treat a variety of clinical disorders and to enhance wound healing. These clinical disorders include gas gangrene, gas embolism, decompression sickness and carbon monoxide poisoning. The therapeutic benefits of long term hyperbaric oxygen treatment are potentially limited by the toxic effects of high oxygen concentration upon the retina, lung and other organs (1-4). Hyperbaric oxygen toxicity is associated with increased lipid peroxidation and increased free radical generation. Vitamin E effectively quenches free radicals generated by lipid peroxidation and selenium (Se) is a cofactor for glutathione peroxidase which detoxifies lipid hydroperoxides or hydrogen peroxide. Rats deficient in vitamin E and/or selenium have been shown to have increased in vivo lipid peroxidation. Humans deficient in vitamin E and/or selenium might be particularly susceptible to hyperbaric oxygen toxicity.

The retina is more sensitive to toxic and environmental disorders than most other tissues. The retina is particularly predisposed to the toxic effects of lipid peroxidation initiated by oxy-radicals. This is because the retina has: a) a very high content of polyunsaturated fatty acids (about 30% 22:6n3) which are very susceptible to lipid peroxidation (5); b) a very high consumption of oxygen, about seven times more per g of tissue than the brain and ; c) the presence of pigments (e.g. retinal) capable of inducing photosensitized oxidation reactions (6).

Retinal lipid peroxidation is likely to be accelerated under conditions of hyperbaric oxygen stress.

In animal models hyperbaric oxygen can cause severe retinal pathology and, in humans, causes loss of visual fields and visual definition (7). The ability of the retina to resist oxidative damage is very dependent upon the functioning of both enzymatic and chemical antioxidant mechanisms (8). Rat retinas normally have very high levels of vitamin E and significant glutathione-S-transferase and glutathione peroxidase activities (8,9). Retinal vitamin E and glutathione peroxidase are decreased to very low levels by nutritional deficiency of vitamin E and selenium, respectively (6,10). Retinal glutathione-S-transferase activity is induced in the absence of dietary vitamin E and selenium (9).

Armstrong, et al. (11), have shown that intravitreal injections of synthetic lipid hydroperoxides into rabbit eyes causes a marked decrease in the a-, b-, and c-wave electroretinogram (ERG) amplitudes. In the absence of any hyperbaric stress, rats fed a basal diet deficient in both vitamin E and selenium (the B diet) for 20 weeks or longer show a decreased a- and b-wave ERG amplitudes (6). The retinal pigment epithelium of rats fed the diet deficient in both vitamin E and selenium also show a large accumulation of fluorescent lipofuscin pigment (10) as well as major ultrastructural alterations (12). Lipofuscin pigment is thought to be a by-product of in vivo lipid peroxidation.

The primary goal of this investigation was to determine if hyperbaric oxygen damage to the retina was accelerated in rats deficient in dietary antioxidant nutrients and inhibited in rats supplemented with antioxidant nutrients. The antioxidant nutrients tested in this study were vitamin E and selenium. Damage to the retina was determined noninvasively by measurement of a- and b- wave ERG amplitudes. Further characterization of retinal damage was made by quantitative histopathology studies.

METHODS

Male, 30 g, inbred Fischer-344 (CDF) rats were obtained from Charles River Breeding Laboratory. The animals were housed in suspended stainless steel, wire-bottomed cages and maintained at 25±2 C and 50% relative humidity. Lighting was on a 6:00 AM to 6:00 PM light period and a 6:00 PM to 6:00 AM dark period (light intensity). Upon arrival in the animal care facility, the rats were fed a normal Purina laboratory chow (Rodent Laboratory Chow 5001, Ralston Purina Co., St. Louis, MO) and water ad libitum for 1 week. The experiment was divided into two phases.

Phase I

In phase one a factorial design was utilized in which rats were randomly assigned to four dietary groups: 1) a basal diet deficient in both vitamin E and selenium but adequate in all other nutrients (the B diet with 24 rats) as proposed by the National Research Council for the Laboratory Rat (13); 2) a basal diet plus vitamin E (the B+E diet) with 8 rats); 3) a basal plus

selenium diet (the B+Se diet with 8 rats); 4) a basal plus vitamin E plus selenium diet (the B+E+Se diet with 24 rats). Vitamin E was provided at a level of 50 mg/kg of diet at 1.1 IU per mg of all-rac-alpha-tocopherol and selenium at a level of 0.4 ppm as sodium selenite. The detailed composition of the basal diet is provided in Table 1.

All dietary supplies were purchased from U.S. Biochemical Co, Cleveland, OH. The Torula-based diets were prepared in 2 kg batches by slowly mixing the constituents to avoid heating, and stored at 4 C. The glass and stainless steel feeders, obtained from Hazelton Systems, Aberdeen, MD, were filled every 2 days and any uneaten food discarded to minimize rancidity. Rats in all the dietary groups were provided with deionized water to which 3 ppm chromium (as CrCl3) was added. Both diet and drinking water were provided ad libitum.

Half the rats from each dietary group were treated with hyperbaric oxygen (HBO) i.e., 3.0 ATA of pure oxygen, 1.5 hr per day, 5 days/week. This treatment began 2 weeks after the start of the dietary regimens. The remaining rats provided a nonHBO control groups to monitor retinal damage that might be due to antioxidant deficiency alone.

At 2, 4, 6, 8, and 17 weeks after the start of the dietary protocols, ERGs were recorded using an aluminized mylar plastic positive electrode placed on the cornea of each rat. This electrode effectively eliminates the possibility of corneal damage. The ground electrode was attached to the rat ear lobe.

A negative pin electrode was inserted under the scalp. We used a ganzfeld (whole field) flash, a Grass photostimulator and a Tektonix model 6512 recording oscilloscope with a 5A22N differential amplifier and a 5B10N time base amplifier. The animals were placed in a dark room for 1 hr before measuring ERGs. About 10 min before recording an ERG, each rat was anesthetized (IM injection) with 0.1 ml of ketamine (50 mg/ml). At least six's a- and b-wave amplitude measurements were made for each eye and the results (at least 12 measurements per rat) averaged.

Phase II

During the phase I rats in the B+HBO group were being depleted of vitamin E and selenium while continuously being treated with HBO. It was reasonable, therefore, to ask whether any retinal damage observed in phase I B+HBO rats actually required long term HBO treatment. Alternatively, there might be critical level of vitamin E and glutathione peroxidase below which retinal damage could occur even with short term HBO treatment. This alternative hypothesis was tested in phase II by treating five rats fed the B diet for six weeks with a short term (3 days) exposure and then recording the ERG amplitudes. In this experiment, the rats would already be depleted of vitamin E and selenium at the time of initial exposure to HBO.

Blood collection and nutritional assessment.

Rats from each dietary group were bled after 3, 7 and 11 weeks on the various diets and plasma vitamin E and plasma glutathione peroxidase (GSHPX) activity measured. Glutathione peroxidase is a selenoenzyme and its activity in rat plasma and red blood cells (RBCs) is a good measure of selenium status. About 1.5 ml of blood was obtained from each rat after cutting (under methoxyfluorane anesthetization) off a small section from the end of the tail. The blood was collected into a 5 ml tube containing EDTA as an anticoagulant and spun at 600xg for 20 min and the plasma and red blood cells (RBCs) separated.

Glutathione peroxidase activity was measured in the individual plasma samples by the coupled method of Paglia and Valentine (14) using cumene hydroperoxide as a substrate. Plasma vitamin E was measured using a slight modification of the spectrofluorometric method of Duggan (15). A 0.5 ml aliquot of plasma was thoroughly mixed with 0.5 ml of distilled water and 1.0 ml of redistilled ethyl alcohol followed by addition of 4.0 ml of redistilled hexane and 1.5 min of vortexing. The fluorescence of the organic phase was measured in a model 111 Turner fluorometer equipped with a UV, T-5 lamp. Interference filters with a 340nm and a 295nm bandpass were used for emission and excitation, respectively (Ditric Optics Inc., MA). A set of DL-alpha-tocopherol standards were run with each set of measurements.

Lipid Peroxidation

Lipid peroxidation has classically been determined by the thiobarbituric acid (TBA) assay which measures the MDA content of biological samples. It is likely, however, that this assay also measures the nonvolatile precursors of MDA as well as endogenous MDA. The thiobarbituric assay has been used by other investigators to estimate the MDA content of animal tissues. We have also used the TBA assay since it provides useful comparative data. Since the amounts of lipid peroxides may be very low in the animal tissues we used the highly sensitive fluorescent assay described by Ohkawa, Ohishi and Yagi (18).

In this assay, 0.2 ml of tissues sample (plasma or liver homogenate) were added to 0.2 ml of 8.1% sodium dodecylsulfate (SDS), 1.5 ml of 20% acetic acid at pH 3.5, 1.5 ml of 0.8% TBA. The mixture was adjusted to 4.0 ml with distilled water, heated at 95 deg C for 60 min with a glass ball condenser. After cooling, 1.0 ml of distilled water and 5.0 ml of n-butanol:pyridine (15:1, v/v) were added and vigorously shaken. After centrifugation at 4000 x g for 10 min the fluorescence of organic layer was measured at 553 nm emmision and 515 nm excitation. Freshly diluted 1,1,3,3-tetramethoxypropane was used as an external standard.

Histopathology

Rats were anesthetized with halothane (Halocarbon Inc.) and then perfused (transcardiac) with isotonic saline (300 ml) followed by 0.075 M Karnofsky's fixative (500 ml). The perfusion pressure was maintained at 90 mm Hg. The eyes were enucleated,

1. We found that the a- and b-wave electroretinogram (ERG) amplitudes for the rats fed the diet supplemented with vitamin E and selenium (B+E+Se diet) or vitamin E alone (B+E diet) were very constant throughout the 17 wk feeding experiment and were unaffected by 15 wks of HBO treatment. Figure 1A and 1B provide the a-wave amplitudes for the B+E group and the B+E+Se after 6 wks (4 wks HBO) and 17 wks (15 wks HBO) of being fed the test diets.

Rats fed the diet deficient in both vitamin E and selenium (B diet) had a- and b-wave amplitudes indistinguishable from the other groups after 4 wks of being fed the diets and the a- and b-wave amplitudes were unaffected by 2 wks of HBO treatment. Figure 1A shows, however, that after 6 wks on the B diet and 4 wks of HBO treatment there was a marked decrease in the a-wave amplitudes of rats fed the B diet and treated with HBO (85 ± 9 uV) compared to the a-wave amplitudes (151 ± 10 uV) of rats fed the identical diet but not treated with HBO (the B+nonHBO group) or compared with the a-wave amplitudes for rats in the B+Se, B+E and B+E+Se groups (with or without HBO treatment). The a-wave amplitudes of rats in B+nonHBO (6 wk diet) were very similar to those recorded for rats in the B+Se, B+E and B+E+Se groups (with or without HBO treatment). Figure 3 shows a typical ERG tracing for rats fed the B diet and either treated or not treated with hyperbaric oxygen.

The b-wave amplitudes of rats fed the B diet for 6 wks and treated with HBO for 4 wks (277 ± 25 uV) was the lowest recorded

treated with HBO. The a-wave amplitudes for this B+3 day HBO group was 130±12 uV (N=6), which was very similar to the a-wave amplitude observed for the age-matched control nonHBO B rats (150±10 uV, N=21) and similar to that observed for B+E+Se, B+E or B+Se rats (HBO or nonHBO) at this time point (see Figure 1A). These data indicate that prolonged HBO treatment, as well as vitamin E and selenium deficiency are required for a significant decrease in a-wave amplitudes.

The b-wave amplitudes for the phase II B+ 3 day HBO rats was 262±61 uV (N=6) which is not significantly different from the 386±26 uV (N=21) observed for the B nonHBO group. It is possible, however, that a greater sample size could have established statistical significance.

Plasma vitamin E and selenium-glutathione peroxidase levels

Table 2 and table 3, respectively, provide the plasma vitamin E levels and the plasma Se-glutathione peroxidase activities for rats in all treatment groups at both 2 and 4 weeks after start of HBO. Rats fed the vitamin E and Se deficient diet had significantly lower ($p < 0.01$) plasma vitamin E and plasma glutathione peroxidase than rats fed the diet supplemented with these micronutrients. This was true at both 2 and 4 weeks.

It is important to note that the levels of vitamin E and the activity of glutathione peroxidase were not influenced by 4 weeks of hyperbaric oxygen treatment. This result is somewhat surprising. We anticipated that hyperbaric oxygen would increase

regions of the retina. The ONL thickness in nasal, central or temporal regions of rats fed the B or the B+E+Se diet was not influenced by hyperbaric oxygen treatment for 4 wks.

Rats fed the B+Se diet for 17 wks and treated with hyperbaric oxygen for 15 wks showed a significant ($P < 0.05$) decrease in the ONL thickness compared with rats fed an identical diet but not treated with hyperbaric oxygen (see Figure 5). Rats in the B+E or the B+E+Se dietary groups all had similar ONL thicknesses which were unaffected by hyperbaric oxygen treatment for 15 wks. The RPE cell height in the central retinal region was found to be increased in rats fed the B+Se diet (17 wks) but hyperbaric oxygen (15 wks) did not influence the RPE cell height. The RPE cell height was very similar in rats fed the B+E and B+E+Se diets (17 wks) and was also not influenced by hyperbaric oxygen treatment (15 wks).

Lipid Peroxidation in Liver and Plasma

The MDA levels in livers from rats fed the B or B+E+Se diet are shown in Figure 6. As expected, livers from rats fed the B diet had higher levels of MDA than livers from rats fed the B+E+Se diet. Surprisingly, rats treated with hyperbaric oxygen (in either the B or the B+E+Se dietary group) had lower levels of MDA than rats not treated with hyperbaric oxygen. This unusual results is discussed in the accompanying paper in more detail. Plasma levels of MDA were higher in rats fed the B diet compared with rats fed the B+E+Se diet (see Figure 7). As expected,

AD-A186 493 UNITED STATES AIR FORCE RESEARCH INITIATION PROGRAM 4/ 8
1985 TECHNICAL REPORT VOLUME 3(U) UNIVERSAL ENERGY
SYSTEMS INC DAYTON OH R C DARRAH APR 87
UNCLASSIFIED AFOSR-TR-87-1719 F49620-85-C-0013 F/G 15/3 NL

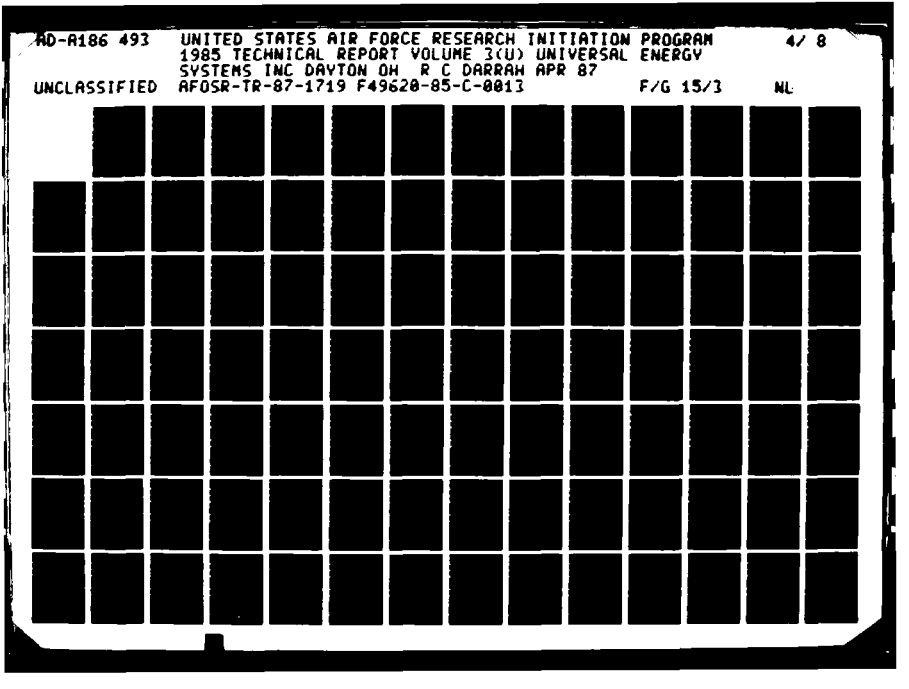

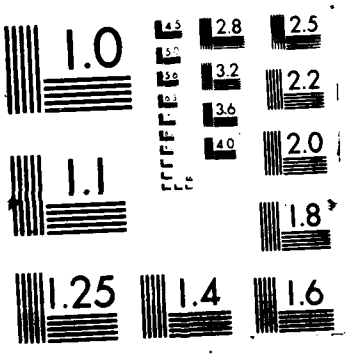
1.0
1.1
1.25
1.4
1.6
1.8
2.0
2.2
2.5
2.8
3.2
3.6
4.0

observed only in the B rats treated with hyperbaric oxygen for 4 wks cannot be readily correlated with photoreceptor necrosis since this necrosis was observed even in the B rats not treated with hyperbaric oxygen. Future electron miscroscopy experiments may shed more light on the specific ultrastructural changes occurring in the B rats treated with hyperbaric oxygen for 4 wks.

Rats fed the B+Se diet for 17 wks and treated with hyperbaric oxygen for 15 wks showed a significant decrease in both the a- and b-wave amplitudes (see Figures 2&2) compared with age-matched rats fed the same diet but not treated with hyperbaric oxygen. The a- and b-wave amplitudes recorded for rats fed (17 wks) the B+E diet or the B+E+Se were similar and unaffected by hyperbaric oxygen treatment (15 wks). Histopathology studies showed photoreceptor cell necrosis only in the central region of retinas from rats fed the B+Se diet (17 wks) and treated with hyperbaric oxygen. The retinal pigment epithelium cell height was increased in rats fed the B+Se diet (17 wks) but this increase was found in both rats treated or not treated with hyperbaric oxygen (15 wks).

Our results clearly indicate that dietary antioxidants play a major role in protecting the retina from damage by hyperbaric oxygen. Vitamin E appears to be more important than selenium but deficiencies of both micronutrients will act synergistically to accelerate retinal damage due to hyperbaric oxygen. Our results do not directly address the potential damage of hyperbaric oxygen to man. Rats, however, are generally considered a species very resistant to oxidative damage

washed three times with 0.2 M cacodylate buffer, post-fixed in 1% osmium tetroxide, dehydrated in graded ethanol and embedded in Epon 812. For each eye the retina was divided along the temporal-nasal line. The resulting superior and inferior blocks were thin-sectioned on a Sorvall 5000 ultramicrotome using a diamond knife and stained with 1% toluidine blue.

Measurements of the retinal pigment epithelial (RPE) layer cell height and the outer nuclear layer (ONL) thickness were conducted using a Zeiss Interactive Digital Analysis System (ZIDAS). The temporal region of the retina was defined as the distance starting from the temporal ora serrata and extending 3000 um towards the center of the retina. Similarly, the nasal region was defined as the distance form the nasal ora serrata and extending 3000 um towards the center of the retina. The central region was defined as the region extending 1500 um from the center of the retina towards the nasal ora serrata and 1500 um from the center of the retina towards the temporal ora serrata, i.e. the central region was 3000 um in length. The mean of ten measurements of ONL and RPE thickness for each field of 300 um was recorded. For any given region (nasal, central or temporal) we averaged the values obtained from ten 300 um fields.

RESULTS

Electroretinograms

The effect of antioxidant deficiency and long term hyperbaric oxygen treatment on rat electroretinograms was studied in phase

for any group but was significantly lower ($p < 0.05$) only when compared to the B+E (with or without HBO) or the B+Se+HBO means (see Figure 2A). All the HBO and nonHBO rats in the B group and an equal number of rats in the B+E+Se were sacrificed for histopathology and biochemical studies at wk 6.

Rats deficient in vitamin E alone (the B+Se group) showed a- and b-wave amplitudes that were similar after 2, 4, 6 and 8 wks on the test diet and were unaffected by hyperbaric oxygen treatment. Furthermore, the a- and b-wave amplitudes at these time points were the same as those recorded for rats supplemented with selenium alone (B+Se) or supplemented with both vitamin E and selenium (B+E+Se). Figure 1A and 2A provide the a-wave and b-wave amplitudes, respectively, for the B+Se group after 6 wks of being fed the test diet. Figure 2A and 2B show that after 17 wks on the test diet, and 15 wks of hyperbaric oxygen treatment, the a-wave (61 ± 9 uV, N=4) and b-wave amplitudes (253 ± 22 uV, N=4) of rats deficient in vitamin E alone (B+Se group) decreased ($p < 0.01$) compared with respect the a-wave (115 ± 7 uV, N=4) and b-waves (451 ± 33 uV, N=4) amplitudes for age-matched rats fed the same diet but not given hyperbaric oxygen treatment. At wk 17, the a-wave and b-wave amplitudes of the B+Se+nonHBO rats were very similar to those observed for the B+E or the B+E+Se rats with or without hyperbaric oxygen treatment.

In phase 2, we examined the effects of a 3-day treatment with hyperbaric oxygen (3.0 ATA of 100% oxygen for 1.5 hr/day) on six rats previously fed the B diet for eight weeks but not previously

vitamin E utilization and therefore increase vitamin E depletion in rats fed the B diet and treated with HBO.

Weight of Experimental Animals

Rats fed the B diet deficient in both vitamin E and selenium for 6 wks, and treated with hyperbaric oxygen (HBO) for 4 wks show a decreased weight and weight gain compared with age-matched rats fed an identical diet but not receiving HBO treatment (see Figure 4). Similarly, rats fed the vitamin E deficient diet and treated with HBO (B+Se+HBO) also showed a reduced weight and weight gain which continued during the 15 wks of HBO treatment. HBO treatment did not appear to be adversely affecting the weight or weight gain of rats fed the vitamin E and selenium supplemented diet (the B+E+Se diet) or the diet supplemented with vitamin E alone (the B+E diet).

Quantitative Histopathology Studies

The thickness of the outer nuclear layer (ONL) and the retinal pigment epithelium (RPE) layer were examined by phase contrast light microscopy. After 6 wks on the experimental diets we found that rats fed the B or the B+E+Se diet had a very similar RPE thickness in the nasal, temporal and central regions of the retina (see Table 4) . Furthermore, the RPE cell height was not influenced by hyperbaric oxygen treatment for 4 wks. The ONL thickness of the nasal region was found to decrease in rats fed the B diet for 6 wks compared with age-matched rats fed the B+E+Se diet. This was not found in the temporal or central

fed the B diet treated with hyperbaric oxygen had higher levels of MDA than B rats not treated with hyperbaric oxygen.

DISCUSSION

Dietary deficiencies of both vitamin E and selenium were found to adversely effect the electrophysiological response of the retina to light. Decreased a-wave and b-wave ERG amplitudes as a result of 4 wks of hyperbaric oxygen treatment were apparent only in rats deficient in both vitamin E and selenium. Rats fed diets deficient in vitamin E alone or selenium alone for 6 wks did not show decreased ERG amplitudes after 4 wks of hyperbaric oxygen treatment. Hafeman and Hoekstra (16) have shown that dietary deficiency of both vitamin E and selenium is much more effective in promoting in vivo lipid peroxidation than dietary deficiency of either vitamin E or selenium alone.

Rats fed the B diet for 6 wks were sacrificed along with some control rats fed the B+E+Se diet. Histopathology studies at this time point failed to show any major alterations in the RPE cell height due to diet, hyperbaric oxygen or the interaction between diet and hyperbaric oxygen. The ONL layer was influenced by diet but not by hyperbaric oxygen and only in the nasal region where there was a small decrease in the ONL thickness of rats fed the B diet. The ONL contains the nuclei for the photoreceptor cells and a decreased ONL layer is indicative of photoreceptor cell necrosis (12). The photoreceptor cells are thought to give rise to the a-wave in the electroretinogram. The decreased a-wave ERG

and have much higher levels of selenium-glutathione peroxidase than humans. Our results strongly suggest that nutritional supplementation of patients with antioxidant nutrients could diminish the oxygen toxicity problems associated with hyperbaric oxygen therapy.

REFERENCES

1) Clark JM, and Fisher AB, Oxygen toxicity and extension of tolerance in oxygen therapy. In: Davis, JC, and Hunt, TK, eds Hyperbaric Oxygen Therapy. Bethesda: Undersea Medical Society, 19--, :61-77.

2) Small, A, New perspectives on hyperoxic pulmonary toxicity-a review. Undersea Biomed Res 1984; 11;1-24.

3) Kappus, K, Sies, H, Toxic drug effects associated with oxygen metabolism: redox cycling and lipid peroxidation. Experientia 1981; 37; 1233-1241.

4) Gable, WD, Townsend, FM (1962) Aerospace Med. 33, 1344.

5) Farnsworth, CC, Stone, WL, and Dratz, EA. (1978) Biochim. Biophys. Acta, 552, 281-293.

6) Stone, WL, Katz, ML, Lurie, M, Marmor, MF and Dratz, EA (1979) Photochem. Photobiol., 29, 725-730.

7) Nichols, C.W. and Lambertson, C.J. (1969) New Engl. J. Med., 281, 25-30.

8) Stone, W.L. and Dratz, E.A. (1982) Exp. Eye Res., 35, 405-412.

9) Stone, WL, and Dratz, EA. Increased glutathione s-transferase activity in antioxidant-deficient rats. Biochim Biophys Acta 1980; 631; 503-506.

10) Katz, ML, Stone, WL, and Dratz, EA. Fluorescent pigment accumulation in retinal pigment epithelium of antioxidant-deficient rats. Invest Ophthalmol 1978; 17; 1049-1058.

11) Armstrong, D, Hiramitsu, T, Gutterridge, J, and Nilsson, SE. Studies on experimentally induced retinal degeneration. 1. Effects of lipid peroxides on electroretinographic activity in the albino rabbit. Exp Eye Res 1982; 35; 157-171.

12) Katz, M.L., Parker, K.R., Handelman, G.J., Bramel, T.L. Dratz, E.A. (1982) Exp. Eye Res., 34, 339-369.

13) National Research Council Publication on Nutrient Requirements of Laboratory Animals, No. 10, p 56, Washington, DC, Nat Acad Sci, 1978.

14) Paglia, DE, and Valentine, WN. Studies on the quantitative and qualitative characterization of erythrocyte glutathione peroxidase. J Lab Clin Med 1967; 70; 158-169.

15) Duggan, DE. Spectrofluorometric determination of tocopherols 1959; 84;116-122.

16) Hafeman, DG and Hoekstra, WG. Lipid peroxidation in vivo during vitamin E and selenium deficiency in the rat as monitored by ethane evolution. J Nutr 1977; 107; 666-672.

17) Jenkinson, SG, Lawrence, RA, Burk, RF and Gregory, PE, Non-selenium-dependent glutathione peroxidase activity in rat lung associated with lung glutathione s-transferase activity and effects of hyperoxia. Toxicol and Applied Pharmacol; 1983; 68; 399-404

18) Ohkawa, H., Ohishi, N., Yagi, K., Assay for lipid peroxides in animal tissues by thiobarbituric acid reaction. Anal. Biochem.;1979;95; 351-358

ACKNOWLEDGEMENTS

The author would like to thank the Air Force System Command, the Air Force Office of Scientific Research and Universal Energy Systems. We also acknowledge the useful discussions with Dr. Howard Davis and Dr. Richard Harris in the Veterinary Pathology Division at Brooks AFB. Capt. Fanton in the Veterinary Services Division is also acknowledged for his role as a consultant in this project.

Table 1. Composition of basal diet.

Ingredient	g/100g
Tourla yeast	36.00
Sucrose	43.05
Corn oil, tocopherol stripped	14.50
Vitamin mix 1	2.20
Mineral mix Draper 2	4.00
L-Methionine	0.25

1. The vitamin mixture provided: (in mg/100 g of diet) ascorbic acid, 99; inositol, 11; choline chloride, 16.5; p-aminobenzoic acid, 11; niacin, 9.9; riboflavin, 2.2; pyridoxine-HCl, 2.2; thiamin HCl, 2.2; calcium pantothenate, 6.6; biotin, 0.05; folic acid, 0.2; vitamin B-12, 0.003. In addition the vitamin mixture contains: (in units /100 g of diet) vitamin A acetate, 1980; calciferol(D3), 220.2.

2. The salt mix provided (in mg/100 g of diet): $CaCO_3$, 654; $CuSO_4.5H_2O$, 0.72; $Ca_3(PO_4)_2$, 1422; Ferric citrate.$3H_2O$, 64; $MnSO_4.H_2O$, 5.5; potassium citrate.H_2O, 946; KI, 0.16; K_2HPO_4, 309; NaCl, 432; $ZnCO_3$, 1.8; and $MgCO_3$, 164.

Table 2

Plasma vitamin E levels (mean±SD) in male Fischer-344 rats fed diets supplemented or deficient in vitamin E and/or selenium and with or without hyperbaric oxygen (HBO) treatment.

diet	treatment	vitamin E ug/ml of plasma	
	time fed diets-	4 wks	6 wks
B	HBO	1.60±0.04a	0.75±0.06a
B	nonHBO	2.0±0.08a	0.84±0.11a
B+E	HBO	5.29±0.50b	5.85±0.21b
B+E	nonHBO	5.40±0.13b	5.95±0.33b
B+Se	HBO	1.45±0.07a	1.15±0.08a
B+Se	nonHBO	1.38±0.12a	1.10±0.14a
B+E+Se	HBO	5.27±0.81b	5.90±0.14b
B+E+Se	nonHBO	5.27±0.91b	5.55±1.77b

ANOVA at wk 4 and wk 6 indicate diet ($P<0.001$) as the only factor influencing plasma vitamin E levels. Means with different letters are significantly different ($P<0.01$ by Duncan's multiple range) at a given time point.

Table 3

Plasma glutathione peroxidase levels (mean±SD) in male Fischer-344 rats fed diets supplemented or deficient in vitamin E and/or selenium and with or without hyperbaric oxygen (HBO) treatment.

diet	treatment	glutathione peroxidase activity, mU/ul of plasma	
	time fed diets-	4 wks	6 wks
B	HBO	3.41±0.59a	1.71±0.63a
B	nonHBO	3.45±1.13a	1.80±0.91a
B+E	HBO	3.53±0.35a	0.93±0.19a
B+E	nonHBO	4.50±0.81a	0.82±0.53a
B+Se	HBO	11.38±1.42b	7.22±1.60b
B+Se	nonHBO	7.38±0.96c	7.75±1.65b
B+E+Se	HBO	10.45±1.31b	8.17±1.57b
B+E+Se	nonHBO	8.90±1.65cb	9.69±2.75b

Milli enzyme units for glutathione peroxidase activity are nanomoles of NADPH oxidized per mim. ANOVA at wk 4 indicated that diet and the interaction between diet and hyperbaric oxygen were significant ($P<0.001$). At wk 6 ANOVA indicated diet as the only significant factor ($P<0.001$). At any time point means with a different letter were significantly ($P<0.001$) different by Duncan's multiple range test.

Table 4

Height of retinal pigment epithelium layer (mean±SD) for male Fischer-344 rats fed diets supplemented and deficient in vitamin E and/or selenium and either treated (HBO) or not treated (nonHBO) with hyperbaric oxygen.

dietary group	RPE cell height (um)		
	nasal	central	temporal
	------ test diets for 6 wks------		
B nonHBO	6.63±0.52	6.86±0.82	5.63±0.60
B HBO	6.00±1.09	6.15±0.95	6.17±0.82
B+E+Se nonHBO	5.76±0.20	5.77±0.52	6.17±0.08
B+E+Se HBO	6.57±0.92	6.52±0.68	5.80±0.36
	------- test diets for 17 wks----		
B+E nonHBO	5.59±0.45	5.85±0.24	5.37±0.70
B+E HBO	5.39±0.31	6.05±0.63	5.90±0.38
B+Se nonHBO	5.20±0.37	6.59±0.11	6.00±0.15
B+Se HBO	5.81±0.69	6.28±0.63	5.78±0.55
B+E+Se nonHBO	5.63±0.50	6.09±0.14	5.32±0.56
B+E+Se HBO	5.88±0.17	5.32±0.26	5.35±0.32

ANOVA indicated that diet (but not hyperbaric oxygen) was a significant factor ($P < 0.035$) at wk 6 for the nasal region. ANOVA also indicated that diet (but not hyperbaric oxygen) was an important factor ar wk 17 in the central region.

Figures 1A and 1B

A-wave amplitudes (base line voltage to trough of electroretinogram) for each dietary group (mean±SEM) after 6 wks (Figure 1A) or 17 wks (Figure 1B) of being fed the test diets. The cross-lined means are the a-waves obtained from the hyperbaric oxygen treated rats (4 wks HBO for Figure 1A and 15 wks HBO for Figure 1B). For Figure 1A and 1B the means with different letters are significantly different at $P < 0.05$ and $P < 0.01$, respectively.

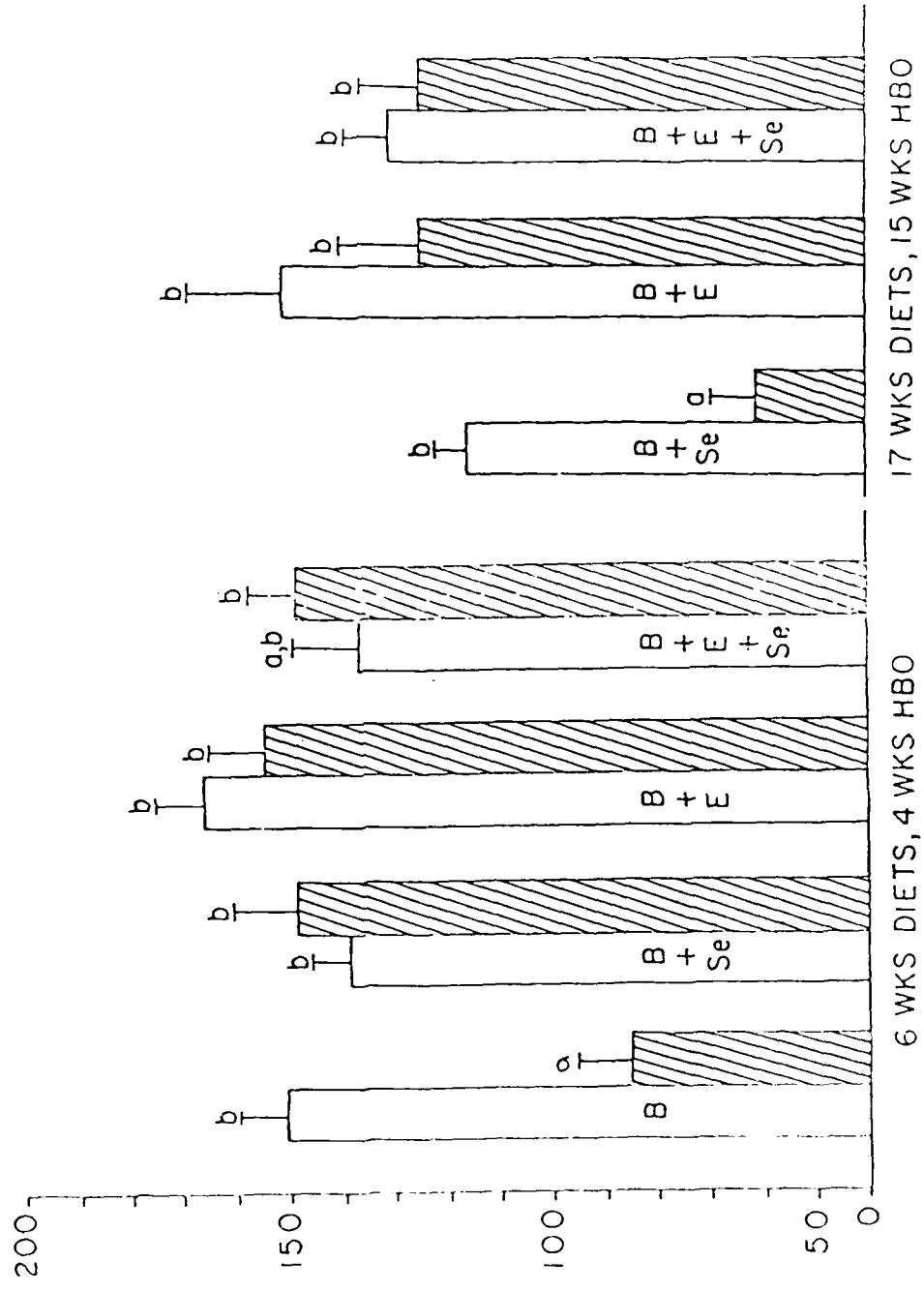
6 WKS DIETS, 4 WKS HBO
17 WKS DIETS, 15 WKS HBO
B
B + Se
B + E
B + E + Se
200
150
100
50
0
A-WAVE AMPLITUDE (μvolts)

Figures 2A and 2B

B-wave amplitudes (from trough to peak of electroretinogram) for each dietary group (mean±SEM) after 6 wks (Figure 2A) or 17 wks (Figure 2B) of being fed the test diets. The cross-lined means are the B-waves obtained from the hyperbaric treated rats (4 wks HBO for Figure 2A and 15 wks HBO for Figure 2B). For Figure 2A and 2B the means with different letters are significantly different at $P < 0.05$ and $P < 0.01$, respectively.

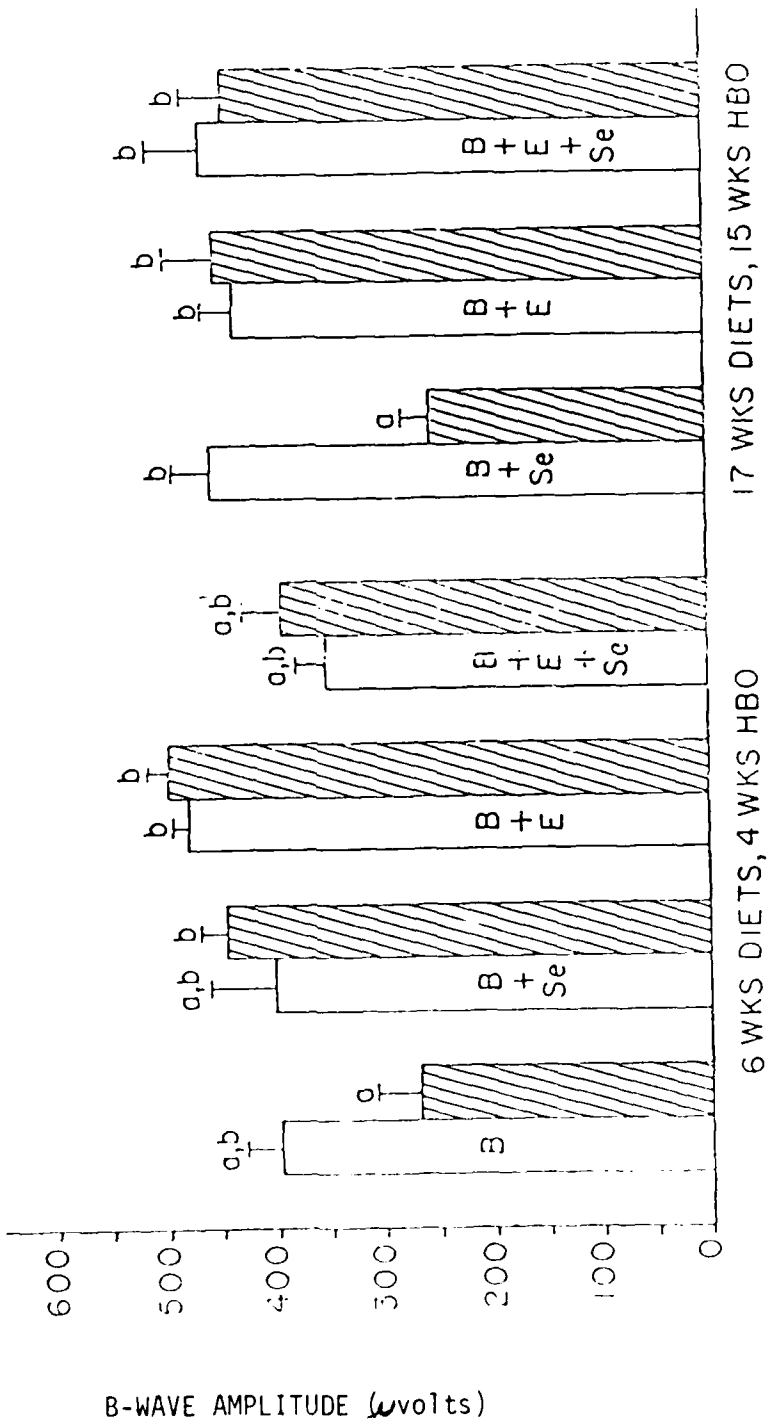
6 WKS DIETS, 4 WKS HBO
17 WKS DIETS, 15 WKS HBO
B
B + Se
B + E
B + E + Sc
B + Se
B + E
B + E + Se
0
100
200
300
400
500
600
B-WAVE AMPLITUDE (μvolts)

Figure 3

Typical electroretinograms obtained from rats fed a vitamin E and selenium deficient diet for 6 wks and either not treated with hyperbaric oxygen (top Figure) or treated with hyperbaric oxygen for 4 wks (bottom Figure) at 3 ATA pure oxygen 1.5 hr/day, 5 days/wk.

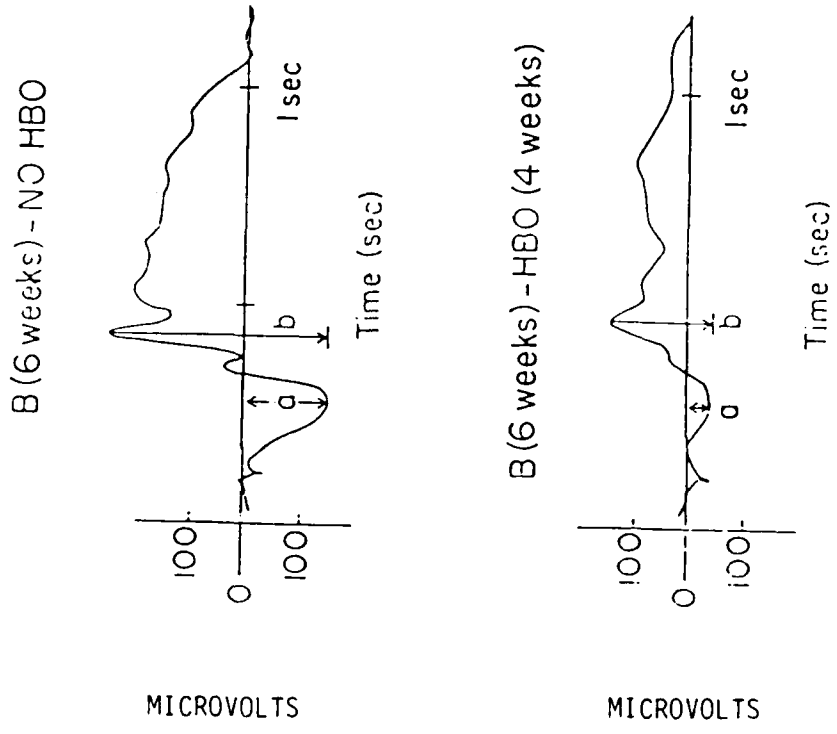
B (6 weeks) - NO HBO
1 sec
b
a
Time (sec)
100
0
100
MICROVOLTS
B (6 weeks) - HBO (4 weeks)
1 sec
b
a
Time (sec)
100
0
100
MICROVOLTS

Figure 4

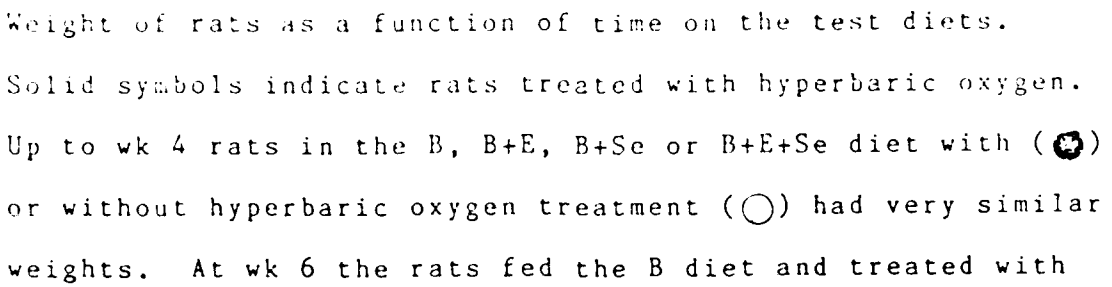

Weight of rats as a function of time on the test diets. Solid symbols indicate rats treated with hyperbaric oxygen. Up to wk 4 rats in the B, B+E, B+Se or B+E+Se diet with (●) or without hyperbaric oxygen treatment (○) had very similar weights. At wk 6 the rats fed the B diet and treated with hyperbaric oxygen had a lower weight ($P < 0.05$) compared with the other diet-treatment groups. At wk 8 rats fed the B+E diet and treated with hyperbaric oxygen (▲) had a lower weight compared with the other diet-treatment groups ($P < 0.05$)

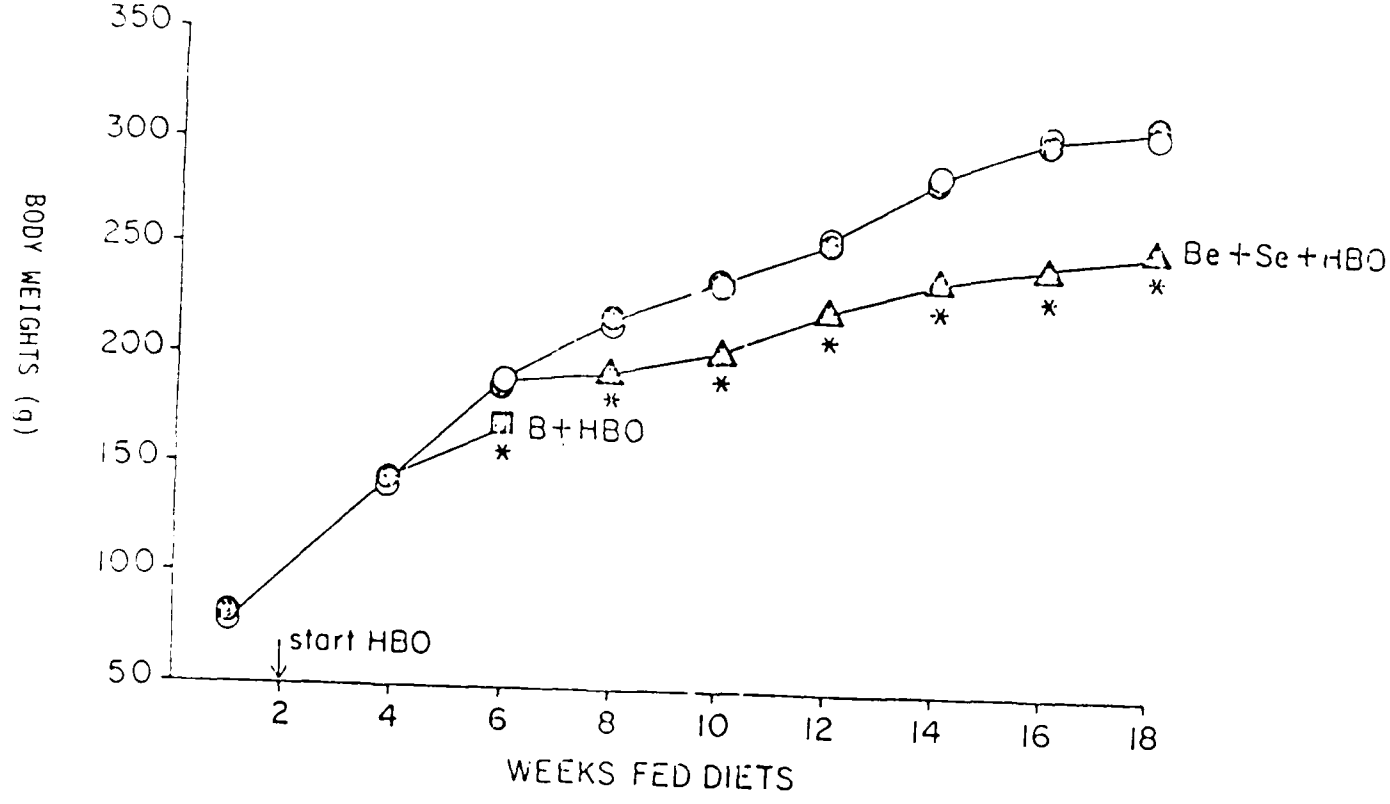
350
300
250
200
150
100
50
BODY WEIGHTS (g)
start HBO
2
4
6
8
10
12
14
16
18
WEEKS FED DIETS
B+HBO
Be+Se+HBO

Figure 5

Height of the outer nuclear layer (Mean±SD) for rats fed diets deficient or supplemented with vitamin E and/or selenium and treated (HBO) or not treated (nonHBO) with hyperbaric oxygen. Means with different letters are significantly different ($P < 0.05$).

ANOVA
Treatment

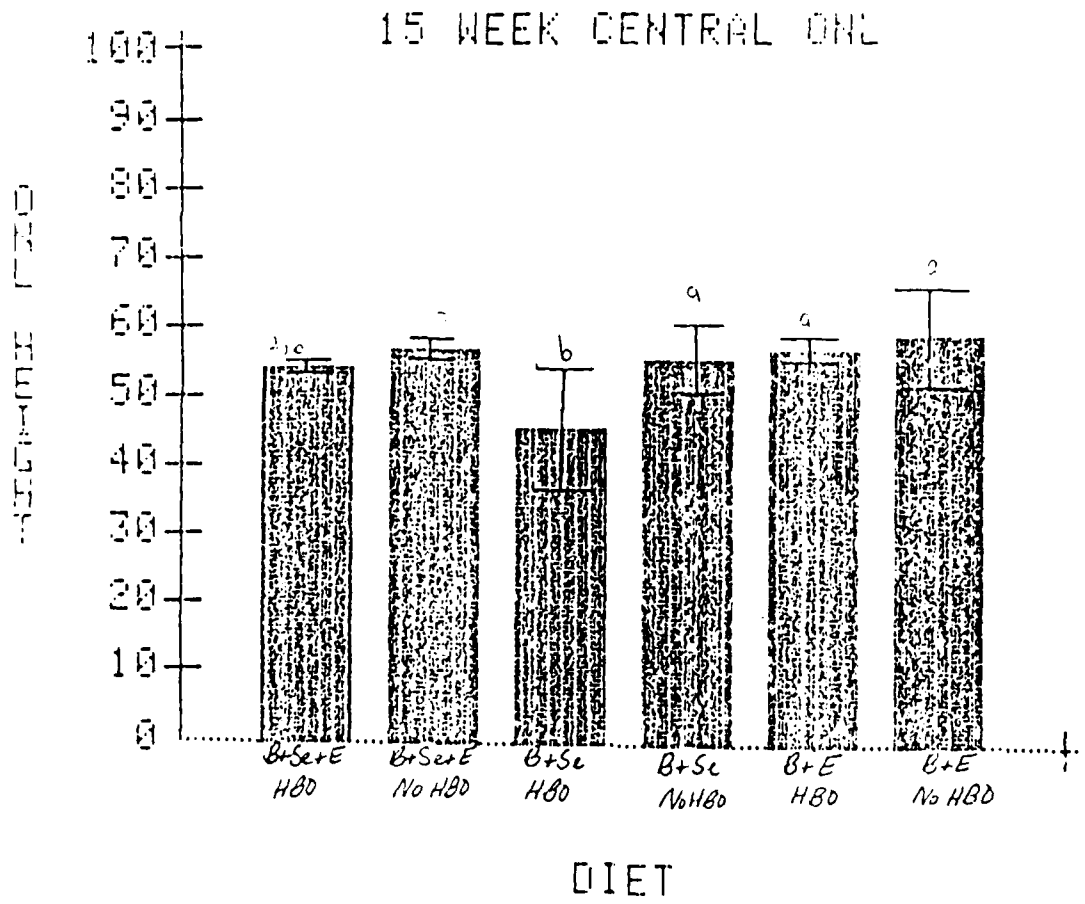

Figure 6

Liver lipid peroxidation as measured by malondialdehyde (MDA) content in rats fed diets deficient or supplemented with vitamin E and /or selenium and either treated (HBO) or not treated (nonHBO) with hyperbaric oxygen for 4 wks.

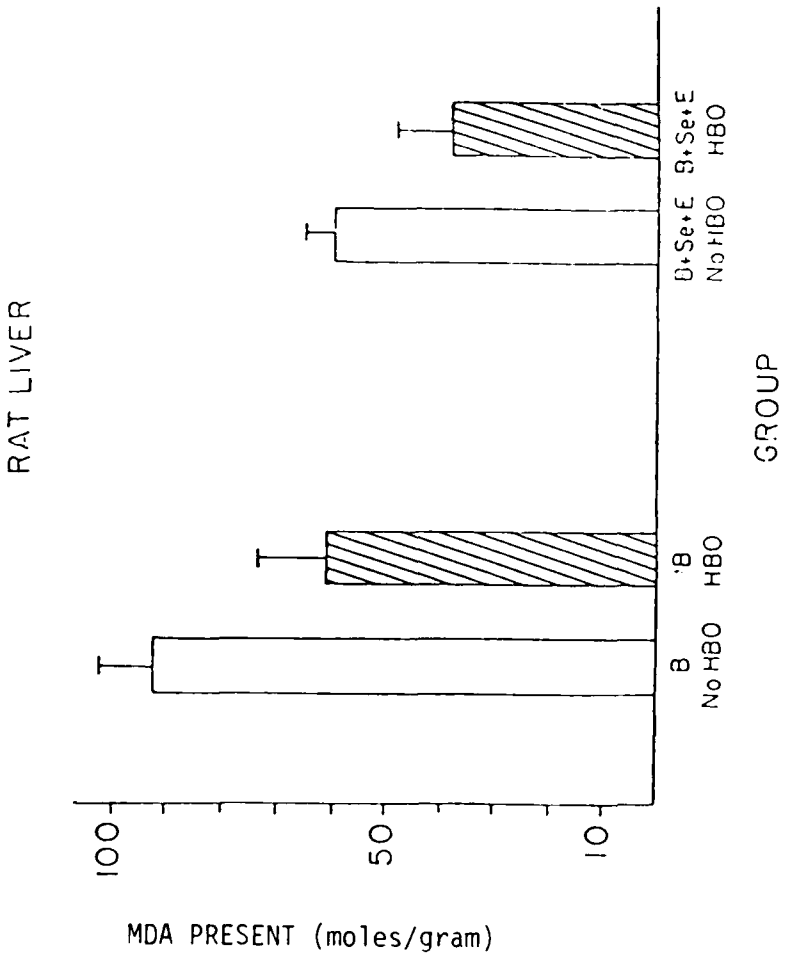
RAT LIVER
MDA PRESENT (moles/gram)
100
50
10
B
No HBO
B
HBO
D+Se+E
No HBO
B+Se+E
HBO
GROUP

Figure 7

Plasma lipid peroxidation as measured by malondialdehyde (MDA) content in rats fed diets supplemented or deficient in vitamin E and/or selenium and either treated (HBO) or not treated (nonHBO) with hyperbaric oxygen for 4 wks.

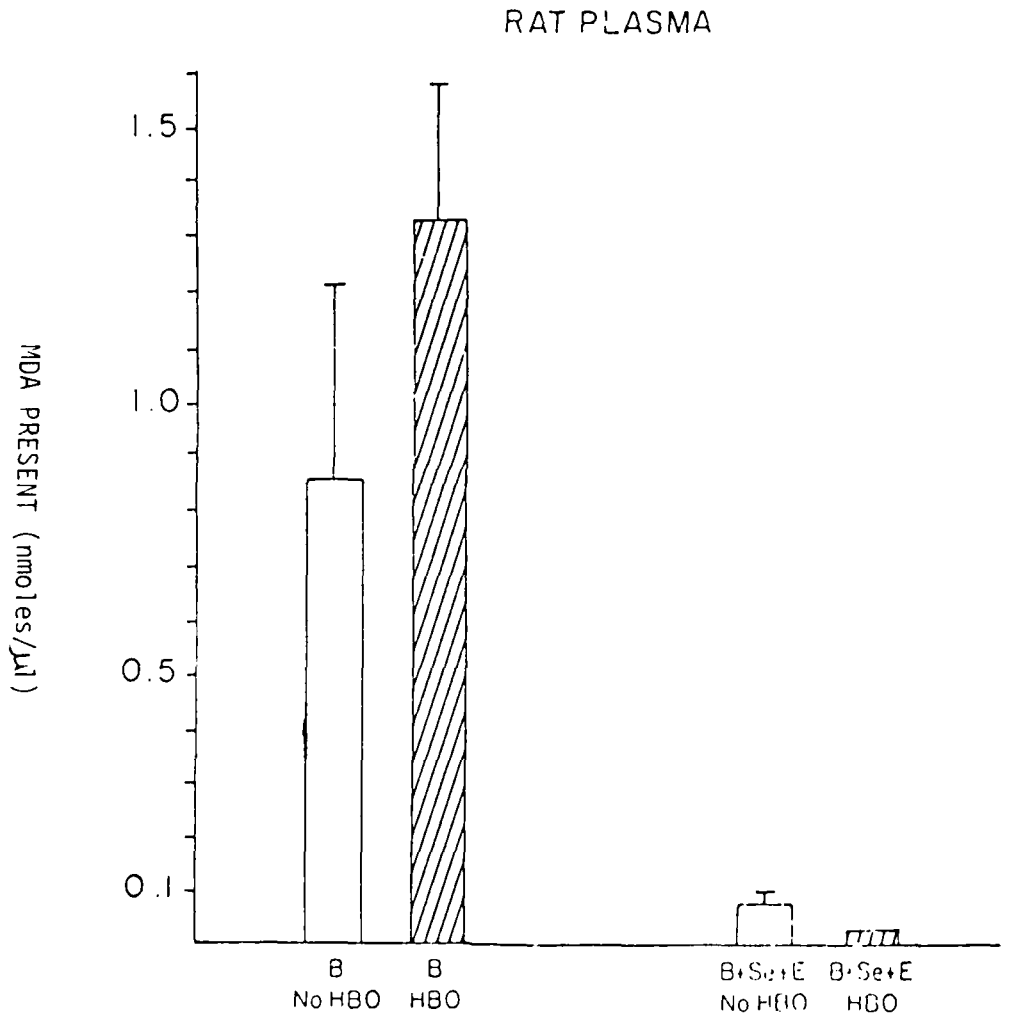
RAT PLASMA
MDA PRESENT (nmoles/µl)
1.5
1.0
0.5
0.1
B
No HBO
B
HBO
B+Se+E
No HBO
B+Se+E
HBO

1986 USAF MINI-GRANT

Sponsored by the

AIR FORCE OFFICE OF SCIENTIFIC RESEARCH

Conducted by

UNIVERSAL ENERGY SYSTEMS, INC.

FINAL REPORT

REPRESENTATION AND PROPAGATION IN HIERARCHIAL DOMAINS

Prepared By:	Dr. Thomas Sudkamp
Academic Rank:	Assistant Professor
Department:	Department of Computer Science
University:	Wright State University
Research Location:	Department of Computer Science Wright State University Dayton, Ohio
USAF Researcher:	Mr. Rudy Shaw Avionics Laboratory Wright-Patterson AFB, Ohio

Subcontract No.: S-760-0MG-022

Representation and Propagation in Hierarchical Domains

Thomas Sudkamp

Department of Computer Science
Wright State University
Dayton, Ohio 45435

Abstract : Evidential representations and inference techniques are constructed for reasoning in a hierarchical domain. Propagation of evidential support requires the capability of combining evidence on each level of the hierarchy. Probablistic reasoning with Bayesian updating, Dempster-Shafer evidential reasoning, inference networks and endorsement based reasoning are used to combine evidence within a single hierarchical level. Rules are constructed to generate evidence on the higher level from the result of lower level inferences. The evidential structures, interlevel transition techniques and support combination functions of each of the resulting hierarchical inference systems are compared.

This research was supported by the Air Force Office of Scientific Research/AFSC under contract number F49620-85-C0013 SB5851-0360.

1. Introduction.

Classification systems utilize information acquired by the system to determine the identity of an object from a set of possibilities. The information is interpreted to construct evidence for the reasoning component of the system. The resulting evidence may be incomplete, inaccurate or both. The representation and combination of evidence provides the reasoning capabilities of the classification system. This paper examines the suitability of several reasoning techniques for the propagation of evidential support in a hierarchical domain. These techniques include probabilisitic reasoning with Bayesian updating, the Dempster-Shafer theory of evidential reasoning and endorsement based reasoning.

A hierarchical domain requires the capability of reasoning with uncertain information on each level of the hierarchy. The result of the combination of evidence on a lower level must be interpreted to provide information for the higher level. To avoid the combinatorial difficulties inherent in hierarchical propagation, a transfer function compatible with the evidential structures of each level is defined to facilitate interlevel propagation of support.

2. Problem definition.

The objective of a classification system is to use the information acquired to determine the identity of an unknown object. Following the notation of Shafer [13], the set consisting of all the possible identifications is denoted Θ and called the frame of discernment. The hierarchical relationships

considered in this paper will be defined by set inclusion. The hierarchy consists of two sets; the set G of ground elements and Θ of possibilities. The ground elements are the basic, indecomposable elements of the domain. A member of Θ is a set of ground elements, hence $\Theta \subseteq 2^G$. Elements of Θ will be referred to as systems or possibilities. Figure 1 illustrates a hierarchy S defined by set inclusion.

Information is obtained concerning the identity of ground elements. The information must be interpreted and represented in a manner which is compatible with the reasoning techniques employed. The result of this interpretation is referred to as ground level evidence. As additional information is acquired and processed, the evidence must be combined to develop an assessment of the ground elements present.

Evidence for ground elements is used to generate evidence for the identity of the unknown system. The transformation of ground level evidence to system level is an essential feature of hierarchical reasoning. Even when no uncertainty exists on the ground level, system level reasoning is still required. Determining the presence of ground element b removes only two possibilities from the hierarchy in Figure 1. This type of system level uncertainty is referred to as ambiguity by Sullivan and Cohen [16].

A reasoning system can be described as having three components; an evidential structure, an evaluation configuration (or simply a configuration) and a combining function. A configuration consists of each system level object which may

receive evidential support and an assessment of the total support for that object. It should be noted that some reasoning strategies require the set of objects in a configuration to be a superset of the frame of discernment.

The combining function is used to pool evidence to construct a configuration which represents an assessment based on all the acquired information. The input to the combining function consists of a configuration and evidence, the result is a new configuration.

Sections 3 and 4 will compare the suitability of several generic inference techniques for reasoning in a hierarchical domain. Each system will be analyzed in terms of the

i) expressiveness of the evidential representation

ii) transformation of ground level to system level support

iii) complexity of the evaluation configuration

iv) properties and assumptions of the combining function.

Properties ii) and iii) present considerations which are unique to hierarchical reasoning while items i) and iv) represent topics relevant to the capabilities of all inference systems.

3. Evidence with singleton support.

In this section the evidence provided to the reasoning systems will be restricted to supporting or refuting the presence of a single ground element. This assumption simplifies the transfer from ground to system level evidence since the amount of analysis needed on the ground level is reduced. Ground level reasoning is not avoided, however, since the evidential

structure may still require a distribution of support prior to the construction of the system configuration. Due to the restricted form of information, this section concentrates on the generation of system level evidence and reasoning.

The hierarchy in Figure 1 will be used in the examples throughout this paper. Information will be presented concerning the identity a system consisting of three unidentified ground elements x, y and z. There is no a priori assumption on the number of ground elements present, this is determined as the evidence is accumulated and processed. There is, however, an assumption that evidence refering to the identity of x can be distinguished from that refering to y or z, etc.

The use of sets to define the elements of Θ implicitly imposes the restriction that no system will contain multiple instances of a ground element. When the identity of one of the elements is determined, this domain knowledge could be used to restrict the possibilities of the other elements. This domain dependent knowledge will not be employed, allowing the inference techniques presented to be used for hierarchical domains without this restriction.

The information pertaining to element x, y and z will be denoted e_x, e_y and e_z respectively.

e_x : supports with a 50% likelihood the proposition that x is ground element b

e_y : supports with complete certainty the proposition that y is ground element c

e_z : supports with complete certainty the proposition that z is

not ground element a

The previous statements attempt to express the information content in a manner which is neutral with repect to the evidential structures of the various reasoning systems. The use of the numeric value, however, is readily translated to probabilistic systems and may require reinterpretation for endorsement based systems.

3.1. Probablistic reasoning.

A reasoning system which uses subjective conditional probabilities as the evidential structure will be referred to as a probablistic reasoning system. By subjective probability we mean one in which the values assigned are not necessarily defined by the limit of a relative frequency. These values may represent odds, or an expert opinion, that the proposition is true.

The interpretation of information e_x will determine the evidential structure using the natural interpretation $P_x(b|e_x)$, the probability that the ground element x is b given evidence e_x. The definition of e_x results in assigning the value .5 to this conditional probability. Similarly, $P_y(c|e_y) = 1$ and $P_z(a|e_z) = 0$ are the structures constructed from the remaining information.

When the evidence is obtained and combined with the conditional probabilities, support is generated for ground elements, not systems. The transfer of support from ground elements to system evidence utilizes the "principle of indifference". This principle can be stated as follows: when evidence supports a number of objects, distribute that support

equally among each of the objects. For example, the support associated with evidence which asserts that ground element c is present is distributed equally to each system which contains c. Utilizing the principle of indifference, evidence produces a probability distribution over θ.

The evidential structure constructed by the processing of e_y will assign values of .5 to both s_3 and s_6. The use of indifference to transfer support form the ground level of the hierarchy to the system level infers a relationship which is not inherent in the information. Shafer [13], among others, argues against the propriety of this extra-evidential assumption.

The configuration in a probabilistic system is simply a probability distribution over θ. Bayes' theorem is used to update the current configuration whenever additional evidence is obtained. Implicit in the use of Bayes' theorem as a combining function is the assumption that θ is a mutually exclusive and exhaustive compilation of the possibilities.

Assume that the current configuration has been consturcted from evidence e_1, e_2 ..., e_{n-1}. When evidence e_n is obtained, Bayes' theorem is used to construct a new configuration which represents the totality of the evidence. The values in the current configuration are referred to as prior probabilities since they represent the assessment prior to the acquistion of the new evidence. The prior probabilities are combined with the conditional probabilities which represent the likelihood of the total evidence given each of the systems. The value $P(s_i \mid e_1 \,\&\, \ldots \,\&\, e_n)$ which incorporates e_n into the configuration is

computed by

$$\frac{P(e_1 \ \& \ \ldots \ \& \ e_n \mid s_i)*P(s_i)}{\sum_{j=1}^{n} P(s_j)*P(e_1 \ \& \ \ldots \ \& \ e_n \mid s_j)} \quad .$$

The denominator of this expression implies that conditional probabilities must be defined of all combinations of evidence for all elements in the frame of discernment. Apart from the likelihood that such information is unavailable, this requirement introduces combinatorial difficulties to the pooling procedure. Szolovits and Pauker [15] have shown that for a problem with 10 hypotheses and 5 queries with binary output there are 2420 conditional probabilities required for the computation of the denominator of Bayes' theorem.

To limit the combinatorial difficulties the conditional independence of evidence is often assumed. This assumption can be expressed by relationship

$$P(e_i \ \& \ e_j \mid s) = P(e_i \mid s)*P(e_j \mid s).$$

This assumption, used in the Prospector system [3], reduces the information requirements and simplifies the computation. Szolovits and Pauker, however, claim that in a classification system "The assumption of conditional independence is usually false". Moreover, Pednault et al. [10] exhibit conditions under which this assumption cannot hold.

Besides the use of conditional independence and the principle of indifference, there are several other objections to using probablistic techniques for reasoning with uncertainty.

These objections are not restricted to probablistic reasoning in a hierarchy, but refer to its general suitability as a method for evidential representation and combination. A more detailed exposition of the problems of probablistic reasoning in classification can be found in [2], [11] and [13].

One difficulty is the lack of flexibility inherent in the use of a single numeric value as a measure of likelihood. It is impossible to determine if the value assigned to a possibility is attributed to supporting evidence or ignorance. The interpretation of $P(s|e) = .5$ could represent either $.5 \pm .01$ or $.5 \pm .3$. The single value .5 is used to represent two clearly different types of information.

Another objection is the combination of supporting and refuting evidence into a single measure. The value $P(s|e_1 \& e_2) = .5$ can be obtained by the combination of evidence which supports and refutes s to equal degrees. This measure could also result from the combination of two pieces of evidence, both of which support s.

3.2 Evidential reasoning.

The theory of evidential reasoning (Shafer [13]) addresses two of the objections to the probablistic approach. The generation of evidence assigns values to sets rather than to elements of Θ. This avoids the use of a principle of indifference since evidence which supports several possibilities need not be distributed to the individual possibilities. This flexibilty is acquired at the expense of increasing the

complexity of the evidential structure and the configuration.

Evidence supports subsets of the frame of discernment and is represented by a basic probability assignment which is a function $m : 2^{\Theta} \rightarrow [0, 1]$ satisfying

i) $m(\emptyset) = 0$

ii) $\sum_{A \subseteq 2^{\Theta}} m(A) = 1$.

m(A) represents the total support committed to the proposition that the object is a member of A which cannot be distributed to individual members of A.

The basic probability assignment generated by evidence e_i will be denoted m_i. The transition from ground to system level uses set inclusion to distribute the support. m_x, generated from e_x, assigns its support to the set which consists of all systems containing b. Since evidence often provides support to a subset of 2^{Θ}, only those sets which receive support will be listed when defining a basic probability assignment. Hence m_x assigns the value .5 to $\{s_3, s_4, s_5, s_6\}$. Since the evidence does not favor any other systems, the remainder of the support is assigned to Θ. Basic probability assigments are positive support representations, information which denies a possibility is transformed into support for the alternatives. The interpretation of e_z generates the probability assignment which assigns 1 to $\{s_5, s_6\}$.

The measure of support in an evidential reasoning environment is a two valued system known as an evidential interval. The evidential interval is defined in terms of a

belief function BEL which is constructed from a basic probability assignment m. BEL is a function with domain 2^{Θ} defined by

$$BEL(A) = \sum_{B \subseteq A} m(B) \quad .$$

BEL(A) represents the total support in m for all the members of the set A. PLS(A), defined by 1 - BEL($\bar{A}$) where $\bar{A}$ is the complement of A in 2^{Θ}, is the plausibility of A. PLS(A) represents the total measure of the evidence in m which does not support the refutation of A. The evidential interval, the measure by which the alternatives are evaluated in a evidential reasoning system, is defined as [BEL(A), PLS(A)].

An evidential reasoning configuration consists of an evidential interval for each subset of 2^{Θ}. Hence the size of a configuration has increased from $|\Theta|$ in the probabilistic system to $|2^{\Theta}|$.

Dempster's rule is used to combine basic probability assignments and hence update configurations. This rule implicitly assumes the independence of evidence. Like the probablisitic system, it also requires the frame of discernment to be mutually exclusive and exhaustive.

Let m_1 and m_2 be two basic probability assignments over 2^{Θ}. A basic probability assignment m, the orthogonal sum of m_1 and m_2 denoted $m_1 \oplus m_2$, is defined as follows:

i) $m(\emptyset) = 0$

ii) $$m(A) = \sum_{A_i \cap B_j = A} (m_1(A_i) * m_2(B_j)) / (1-k)$$

where k is the total support given to incompatible sets by m_1 and m_2. That is, $k = \sum m_1(A_i) * m_2(B_j)$ where the sum is taken over all sets A_i and B_j such that $A_i \; B_j = \emptyset$. The evidence is inconsistent if the sum of the support for incompatible sets totals 1.

3.3. Inference networks.

Inference networks, also known as dependency graphs, are used to represent hierarchical relationships as a directed graph [7]. A network contains two types of nodes; nodes corresponding to elements in the hierarchy and nodes whose sole purpose is to assist in the propagation of support. The arcs of the graph indicate the relationships among the nodes and define the propagation rules.

Each node has a measure which indicates the support accumulated by the node. These measures may be probabilities, evidential intervals or other representations which indicate possibility. For nodes corresponding to elements of the hierarchy, this measure represents the support for that particular system.

The "minimal assumption" inference network of Quinlan [11], [12] will be used to illustrate the propagation of support in a hierarchy. The flexibility of this system results from the variety of relationships which may be specified. Each relationship has an associated set of propagation rules. Evidential indepence and the mutually exclusive and exhaustive

nature of Θ can be incorporated into the graph if desired but, unlike the previous two strategies, are not required.

The measure of support in this system is an evidential interval. The interval for a node A is defined by two values, t(A) and f(A). t(A) is the accumulated support for A and f(A) is the measure of evidence refuting A. Initially both t(A) and f(A) are set to 0. The propagation of evidence can increase, but never decrease, these values. The evidential interval is defined as [t(A), 1-f(A)]. The evidence indicates an inconsistency whenever f(A) + t(A) > 1 for any node A in the graph.

The t and f values are increased as support is propagated via the rules corresponding to the relationships which define the network. If node A is related to nodes B_1 and B_2 the propagation rules have the form

$t(A) \leftarrow \text{maximum}\ \{\ t(A),\ F_1(t(B_1),\ f(B_1),\ t(B_2),\ f(B_2))\ \}$

$f(A) \leftarrow \text{maximum}\ \{\ f(A),\ F_2(t(B_1),\ f(B_1),\ t(B_2),\ f(B_2))\ \}$

where F_1 and F_2 are functions which are defined to numerically represent the relationship among A, B_1 and B_2. Whenever one of the values in a function on the righthand side is changed, that function is evaluated. t(A) is then assigned the maximum of its current value and the value computed by F_1. Similarly a new f value is assigned if F_2 is greater f(A). Of course, if A is related to B_i then each of the B_i's are related to A. Hence the relationship also requires rules with B_i on the lefthand side. The choice of the maximum in the propagation rules enforces the increasing nature of support in the network.

The flexibility of the inference network is illustrated by

considering the inference rules corresponding to the relationship that the node A is the exclusive disjunction of B_1 and B_2.

$t(A) \leftarrow \text{maximum}\ (\ t(A),\ t(B_1) + t(B_2)\ )$

$f(A) \leftarrow \text{maximum}\ (\ f(A),\ 1 - (\ 1-f(B_1) + 1-f(B_2)\ )\ )$

$t(B_i) \leftarrow \text{maximum}\ (\ t(B_i),\ t(A) - (\ 1-f(B_j)\ )\ )$ where $i \neq j$

$f(B_i) \leftarrow \text{maximum}\ (\ f(B_i),\ f(A) + t(B_j)\ )$ where $i \neq j$

The t(A) rule indicates that A receives support when either B_1 or B_2 does. The exclusive nature of the disjunction is illustrated by the rule $t(B_i)$. If $t(A) = 1$ and $f(B_2) = 1$, the disjunction has been shown to be true and the B_2 component false, the value $t(B_1)$ is assigned 1 even though B_1 may have received no direct support.

Other relations for disjunction include disjoins-independent which assumes evidential independence and disjoins which makes assumptions on the relationship between evidence. Similary conjoins and conjoins-independent are conjunction relationships. A complete set of relations and corresponding propagation rules can be found in [11] and [16].

Since evidence directly supports ground elements, the network must accumulate the information and propagate to systems. Nodes a_i, b_i, c_i and d_i are introduced to accumulate the evidence for the identity of element i (Figure 2). Nodes labelled a, b, c and d represent the total support for the presence of the corresponding ground element in the system. The disjunction of support for the a_i's generates the total support for a. The interpretations of e_x, e_y and e_z will yield $t(b_x) = .5$, $t(c_y) = 1$

and $f(a_z) = 1$, respectively.

The use of the rule disjoins assures the evidence referring to different elements will not generate an inconsistency in the network. The f value of the system level node b will not increase unless evidence is obtained increasing the f values of each of the b_i's. Positive support is transmitted immediately, negative only when it is present in each ground level node.

Using the variety of relationships, the inference network can be designed to make tentative identifications and update them as additional evidence is processed. A system is identified when its t value is assigned 1. The processing of evidence in the network in Figure 2 will identify a system as soon as the existence of each element in the system is established. For example, evidence which establishes the existence of ground element a will identify system s_1, although additional information may ultimately determine the system to be s_2, s_3 or s_4.

In a network which makes tentative identifications, the determination of systems is not mutually exclusive. If $t(s_i) = 1$ the t value of any system whose elements are contained in s_i will also be 1. The inference system in Figure 2 does not make the assumption that Θ is exhaustive. Evidence establishing the existence of ground elements a, c and d will identify systems s_1 and s_2 without indicating an inconsistency.

The network in Figure 3 will make a deterministic identification. The rule A conjoins (a, not b) is an abbreviation for the rules X negates b and A conjoins (a, X).

The negation is indicated in Figure 3 by placing a circle in the arc which connects A and b. If $s_i \subseteq s_j$ then $t(s_i)$ is assigned 1 only if it has been established that all the elements of s_i are present and an element of s_j absent. This network does not assume Θ to be exhaustive but identification is exclusive for elements of Θ. Evidence supporting a set of ground elements X which is not in Θ will be assigned to the maximal systems s_i which are contained in X. Support for a and b or a and c will be attributed to system s_1. Similary, evidence which establishes the presence of all the ground elements will result in $t(s_3) = t(s_4) = t(s_6) = 1$.

3.4. Endorsement based reasoning.

Cohen [2] introduced endorsement based reasoning systems as an alternative to the numerical systems like the ones previously examined. Rather than representing information by a single number or a pair of numbers, evidence is interpreted and manipulated symbolically. This symbolic representation permits the use of information itself, rather than a numeric value, when combining evidence. Cohen asserts that the use of the information as in input to the combination function results in "reasoning about uncertainty" rather than "reasoning with uncertainty".

Endorsements are represented as propositions which offer positive or negative support for a system. Table 2 lists a set of endorsements for reasoning in the hierarchy S. The signs + and - indicate positive and negative endorsements respectively. When the presence of element a is established, the endorsement

$E_2(a,s_2)$ will be assigned to s_2. The total support for a system is indicated by its set of endorsements.

This representation contains two types of endorsements; evidential endorsements which result directly from ground element information and higher level endorsements. E_2, E_3, E_4 and E_5 are examples of the former type of endorsement. Processing e_2 will generate the endorsements $E_2(c,s_3)$ and $E_2(c,s_6)$. Endorsement E_3 is generated by e_1 which offers partial support for the presence of element b. e_3 generates negative endorsements $E_4(a,s_5)$ and $E_4(a,s_6)$.

E_0, E_1 and E_6 are higher level endorsements. They are not generated by evidence but rather by combinations of existing endorsements. The endorsement $E_0(s_i)$ is generated only when s_i is endorsed by E_1 and the endorsements assigned to each of the other systems indicate an inconsistency.

A configuration in an endorsement based system consists of a set of endorsements for every member of Θ. Processing of evidence generates endorsements and augments the existing sets. The combining function is defined by a set of rules for updating endorsements. The symbol -> is used to indicate replacement, the set of endorsements on the lefthand side is replaced by the righthand side. The rule $E_1(s_i)$, $E_4(s_i)$ -> $E_4(s_i)$ indicates that when an inconsistency occurs, the endorsement E_1 is removed from system s_i. Similarly, E_3, E_2 -> E indicates that there is no need to retain an endorsement when a stronger one has been obtained.

The generation of higher level endorsements will be

indicated by the notation =>. When the condition on the lefthand side is satisfied the endorsement on the righthand side is generated. Like the rules in an inference network, the generation rules must be evaluated whenever a value on the lefthand side is altered.

The assignment of endorsements makes no extra-evidentional assumptions nor any assumptions on the frame of discernment. Support for a combination of ground elements X which does not constitute a system will generate positive endorsements for systems containing X. Processing evidence which establishes the presence of all four ground elements will assign one negative and three positive endorsements of each system s_3, s_4 and s_6.

It has been mistakenly claimed that an endorsement based system maintains a history of the information processed. Replacement rules provide the capability of removing previously established endorsements. This behaviour was also exhibited by the endorsement based planner described in [16]. In that system, combinations of corroborating positive evidence were used to remove negative endorsements. The power of endorsement based reasoning is that it constructs a nonmontonic support system in which each of the components, the interpretation of evidence and combination rule, is definable to reflect the properties of the specific domain.

4. Ground level reasoning.

In the previous section, evidence was restricted to supporting or refuting the presence of a single ground element. With this restriction, the processing of ground level information was limited to the translating it into a form compatible with the system level inference rules. Relaxing this restriction allows evidence to support a several ground elements. e_1 and e_2 provide examples of this type of information.

e_1 : supports the proposition with a 50% likelihood that x is either ground element a or b

e_2 : supports the proposition with a 50% likelihood that x is either ground element b or c

The information contained in e_1 offers support for both a and b. Neither e_1 nor e_2 provide definitive support for the presence of a particular element. Combining this ground level evidence may produce better estimate of the identity of the ground element.

Identification in a hierarchical domain may require two levels of reasoning. Evidence may be combined to hypothesize the ground element present. We will refer to this as ground level reasoning. Hypotheses of the ground elements are used to generate evidence to be used in determining the system. The construction of system level evidence from ground level hypotheses will be referred to as the transition or transfer. After the transition occurs, the inference techniques of section 3 can be used to pool the system level evidence.

4.1. Probabilistic reasoning.

The interpretation of evidence in a probablistic system results in the assignment of value to elements of G. The transition to the system level utilized the principle of indifference to distribute the support for ground elements to support for systems. When evidence supports several ground elements, another application of indifference can distribute the support to individual elements.

With the generation of evidence defined using indifference, the proposition in e_1 generates the conditional probabilities $P_x(a|e_1) = .25$ and $P_x(b|e_x) = .25$. When e_1 is processed, the resulting ground level probabilities $P_x(a) = .25$ and $P_x(b) = .25$ are used to generate system level evidence. The transfer is implemented as in section 3.1. The distribution of support to ground elements and then to systems causes the interpretation to generate evidence which seems to have litte relation to the original information. For example, the system level evidence generated by e_1 includes $P(s_1) = .0675$.

A more sophisticated application of probablistic reasoning which combines Bayesian updating with a network representation has been developed by Pearl [8] [9]. A hierarchical inference network is constructed which employs additional relations to simplify the computations required by Bayes' theorem. Pearl also established that conditional independence is compatible with Θ being mutually exclusive and exhaustive in this extended domain.

4.2. Evidential reasoning.

Processing evidence which distributes its support to a set

of ground elements injects a computational complication into the use of evidential reasoning as an inference technique. Evidence for determining the identity of a single ground element generates a basic probability assignment whose domain is 2^G. These basic probability assignments must be interpreted to provide evidence for the determination of systems. Combining ground level evidence, which supports elements of 2^G, with Dempster's rule requires the frame of discernment to consist of subsets of 2^G.

Barnett [1] shows that when the evidence in a hierarchical system supports singleton sets or their complements that Dempster's rule can be computed in polynomial time. Gordon and Shortliffe [6] present a variation of the combination rule which can be used when the system relationships form a tree. Unfortunately, these restrictions are usually not satisified in the general hierarchic framework and alternative methods must be employed to avoid the combinatorial difficulties.

One possible solution is to immediately transform ground level evidence to system level evidence, thereby requiring the use of a combining rule on only one level. The evidential interpretations of e_1 and e_2 generate the basic probability assignments

$m_1 = [\ \{a, b\}, .5\ ;\ \Theta, .5\ ]$

$m_2 = [\ \{b, c\}, .5\ ;\ \Theta, .5\ ]$

respectively. Extrapolating the transfer technique presented in section 3.2 will attribute the support for the set {a, b} to all systems which contain either element a or b. Transfering m_1 to

system level will result in assigning all the support to Θ. The information contained in the ground level evidence is lost by this simple transfer method. This indicates that a combination of the evidence is required on the ground level prior to the transformation to the system level.

Dempster's rule can be used to combine this information to update the ground level estimate, resulting in the probability assignment

$$m_1 \oplus m_2 = [\ \{b\},\ .25\ ;\ \{a, b\},\ .25\ ;\ \{b, c\},\ .25\ ;\ \Theta,\ .25\ ]\ .$$

This represents the ground level estimate of the element x. Similarly, estimates of the other ground elements are constructed from the combination of evidence.

The assumptions that Θ is exhaustive and mutually exclusive can be used to limit the number of possibilities which must be considered when transfering evidence from the ground level. Employing the previous transition technique to $m_1 \oplus m_2$ results in the system level probability assignment

$$[\ \{s_3,s_4,s_5,s_6\},\ .25\ ;\ \{s_3,s_5,s_6\},\ .25\ ;\ \Theta,\ .5\ ]\ .$$

Support is transferred only to the subsets of 2^G which are systems, limiting the size of the resulting probability assignments to $|2^{\Theta}|$.

When evidence is acquired pertaining to n ground elements, the transfer of the support to systems will generate n system level probability assignments. Dempster's rule can be employed on the system level to combine this data to obtain the system level configuration. This process of directly transfering the results of ground level combinations to system level support is

essentially the technique presented by Garvey et al. [4] [5].

A more flexible transformation which analyzes the ground level evidence prior to the generation of system level evidence is presented in [15]. The evidence for the ground elements is combined to construct propositions concerning the combinations of ground elements which receive support. For example, assume

m_x = [(a), .5 ; (a,c), .5]

m_y = [(a,d), .5 ; (d), .5]

result from the combining the ground level evidence refering to x and y respectively. Since m_x and m_y contain information concerning different ground elements, they can be combined as conjunctions. The support for x being a and y being d combines to generate support for a system which contains both a and d. Utilizing this observation, probabilities are assigned to the sets of conjunctions.

The generation of system level evidence can use the exact combinations supported by the ground level evidence. The support for a conjunction is distributed to all systems containing those elements. Due to the exhaustive domain assumption, conjunctions which are not subsets of any system can be considered to result from inaccurate data. Following the technique of Dempster's rule, the support attributed to these conjunctions is distributed to the remaining, consistent possibilities. The conjuctions resulting from the combination of m_x and m_y and the system level interpretation is gvien below.

(a&a, a&d) -> .25	(s_2, s_4) -> .25
(a&a, a&d, c&a, c&d) -> .25	(s_2, s_3, s_4, s_6) -> .25

(a&d) -> .25	$\{ s_2, s_4 \}$ -> .25
(a&d, c&d) -> .25	$\{ s_2, s_3, s_6 \}$ -> .25

The intermediate analysis increases the flexibility available in the interlevel transition. The use of the conjunction eliminates the need for the assumption of at most one instance of a ground element in a system. Evidence supporting both x and y being a generates support for the conjunction a&a.

Utilizing the intermediate step, the transfer can be defined to distribute support based upon the domain, the confidence in the evidence and the type of ientification desired. Transition functions which yield tentative and deterministic identification have been constructed in [15].

4.3. Inference networks.

In section 3.3, networks were constructed to propagate system level information. The necessity of combining of ground level evidence indicates the need for another network. The rules of an inference network provide a straightforward representation for the relationships required for the combination of ground level evidence.

Evidence is assigned directly to nodes in the network. The combination of evidence and the transfer of support from the ground level to the system level is accomplished by the propagation rules corresponding to the arcs in the network. The network must contain nodes for each set of ground elements which may receive evidential support. In the worst case, this would

require $|2^G|$ nodes in a ground level network.

A ground level network must be constructed to identify each ground element present. A single ground level network will not suffice due to the possibility of interplay between evidence refering to different elements. The ground level network for determining the identity of an element x must contain nodes representing each of the possibilities (the members of G) and nodes to receive the evidence. The possible identifications are represented by nodes labelled a_x, b_x, c_x and d_x. Figure 4 shows the tentative identification network constructed in section 3.3 augmented with nodes capable of processing the information in e_1 and e_2. Figure 4 contains two ground level networks, $network_x$ and $network_y$, indicating that evidence has been obtained refering to two distinct ground elements.

The transfer to support from the ground level to the system level occurs whenever any of the elements a_i, b_i, c_i and d_i receive support. The use of the rule disjoins assures the evidence referring to different elements will not generate an inconsistency in the network. The f value of the system level node b will not increase unless evidence is obtained increasing the f values of each of the b_i's. Positive support is transmitted immediately, negative only when it is present in all ground level networks.

4.4 Endorsement based reasoning.

Like the evidential reasoning and network approaches, the use of endorsements requires a separate level to combine ground level data. Endorsements are assigned to elements of G as

information is received and interpreted. Endorsements of the form

$G_1(a,x)$, + x being a is moderately supported

$G_2(b,x)$, + x being b is moderately supported

may be generated by the interpretation of e_1. Terms such as weakly, moderately, strongly or with certainty can be used to indicate the level of support. The use of numeric ratings can be combined with endorsements to indicate the strength of the endorsement. The interpretation of e_1 using numeric values may be expressed by the endorsements

$G_1(a,x)$, + x being a is cosupported with degree .5

$G_2(b,x)$, + x being b is cosupported with degree .5 .

The form of this endorsement utilizes no extra-evidential assumption to distribute the support to the ground elements.

Replacement and generation rules must be constructed to combine the ground level endorsements. If numerical values are included in the endorsements, these can be used in the definition of the rules. Following the propagation techniques of the inference network, a rule combining endorsements

$G_i(a,x)$, + x being a is supported with degree n

$G_j(a,x)$, + x being a is supported with degree m

may be defined by

$G_i(a,x)$, $G_j(a,x)$ => $G_k(a,x)$, + x being a is supported with degree max(n, m).

Assumptions concerning the distribution of support or indepence of evidence can be incorporated into these combining rules.

The use of the numeric values in endorsements does not limit

the propagation rules to manipulating the values. A generation rule may utilize the endorsements, both positive and negative, assigned to all the ground level elements.

The difficulties presented by the transition to system level endorsements are the same whether support is indicated by the use of a numeric scale or terms like weakly, moderately and strongly. At what point does support for x being the element a generate the system level endorsement

$E_3(a,s_j)$ a, whose presence is supported, is in s_j ?

A rule which generates system level endorsements directly from the ground level endorsement G_1 will result in endorsements containing minimal information. It would be advantageous to generate fewer, more meaningful system endorsements. This requires the construction of endorsement generating rules whose conditions depend upon the strength of the ground level endrosement.

The transition of support can be accomplished by assigning a ground level endorsement to every system level endorsement which is generated directly by evidence. For example,

$G_k(a,x)$, + x being a is supported with degree m

corresponds to the system level endorsement

$E_3(a,s_j)$ a, whose presence is supported, is in s_j .

Whenever the ground level support for a reaches the predefined threshold m, the system level endorsement is generated. The correspondence between ground level and system level endorsements allows the evidence to be combined on the ground level where the endorsements and rules are specifically designed for that purpose.

5. Conclusions.

The evidential structures and inference techniques of the reasoning systems are summarized in Table 2. The interval [0, 1] is denoted by I, hence an evidential interval is an element of I X I. The minimal assumption inference network and endorsement based reasoning provide the greatest flexibility in the representation and propagation of evidence. The definability of the propagation rules in these systems removes the necessity of employing extra-evidential assumptions.

The increased expressiveness is obtained at the expense of more complicated ground level reasoning techniques and interlevel transition. The inference network requires an additional network for each ground element present and the transition occurs by connecting these networks to the system level network. The endorsement system requires ground level endorsements and rules to generate system level endorsements.

REFERENCES

1. Barnett, J. A. (1981). "Computational methods for a mathematical theory of evidence", Proc. 7th IJCAI, Vancouver, pp. 868-875.

2. Cohen, P. R. (1985). Heuristic Reasoning about Uncertainty: An Artificial Intelligence Approach, Boston, MA: Pitman Publishing Co.

3. Duda, R. O., Hart, P. E. and Nilsson, N. (1976). Subjective Bayesian Methods for Rule-based Inference Systems, Technical Note 124, Artificial Intelligence Center, SRI International.

4. Garvey, T. A., Lowrance, J. D. and Fischler, M. A. (1981). "An inference technique for integrating knowledge from disparate sources", Proc. 7th IJCAI, pp. 319-325.

5. Garvey, T. A. and Lowrance, J. D. (1983). Machine Intelligence for Electronic Warfare Applications, AFWAL Technical Report, 83-1168.

6. Gordon, J. and Shortliffe, E. H. (1985). "A method for managing evidential reasoning in a hierarchical hypothesis space", Artificial Intelligence, Vol. 26, July, pp. 323-357.

7. Lowrance, J. D. (1982). Dependency-Graph Models of Evidential Support, Ph. D. dissertation, Department of Computer Science, University of Massachusetts at Amherst.

8. Pearl, J. (1982). Distributed Bayesian Processing for Belief Maintenance in Hierarchical Inference Systems, Cognitive Systems Laboratory, UCLA, Technical Report ENG-CSL-81-11.

9. Pearl, J. (1985). A Constrain-Propagation Approach to Probablisitic Reasoning, Computer Science Department, UCLA Technical Report, CSD-85002.

10. Pednault, E. D. P., Zucker, S. W. and Muresan, L. V. (1981). "On the independence assumption underlying subjective Bayesian inference", Artificial Intelligence, Vol. 16, pp. 213-222.

11. Quinlan, J. R. (1983). "INFERNO: A cautious approach to uncertain inference", The Computer Journal, Vol. 26, No. 3, pp. 255-269.

12. Quinlan, J. R. (1985). "Internal consistency in plausible reasoning systems", New Generation Computing, Vol. 3, pp. 157-180.

13. Shafer, G. (1976). A Mathematical Theory of Evidence, Princeton: Princeton University Press.

14. Szolovits, P. S. and Pauker, S. G. (1978). "Categorical and probablisitic reasoning in medical analysis", Artificial Intelligence, Vol. 11, pp. 115-148.

15. Sudkamp, T. A. (1986). "Inference propagation in emitter, system hierarchies", AFWAL Technical Report, awaiting publication.

16. Sullivan, M. and Cohen, P. R. (1985). "An endorsement-based plan recognition program", Proc. 9th IJCAI,pp. 475-479.

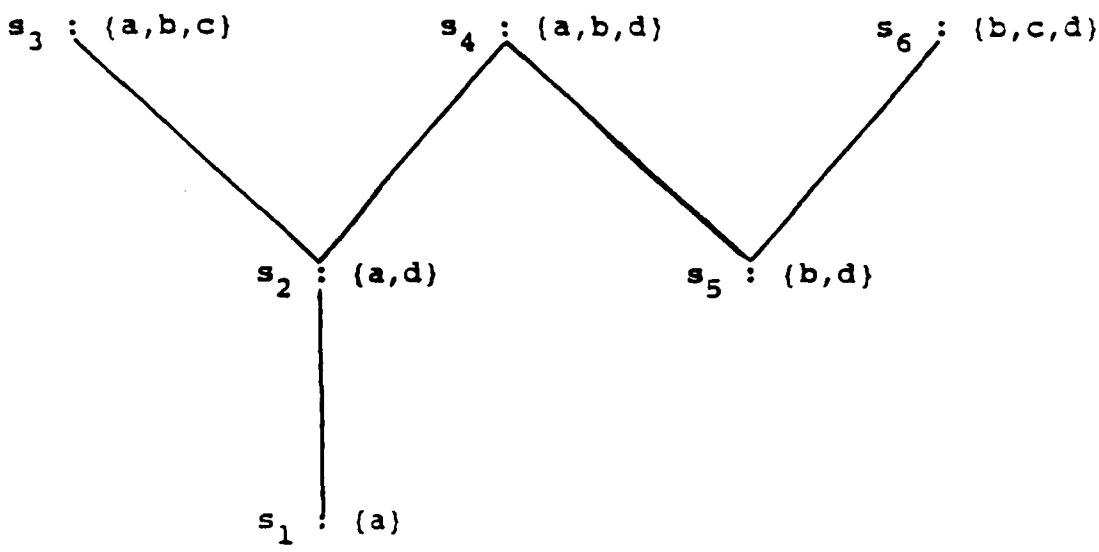

$G = \{ a, b, c, d \}$

$\Theta = \{ \{a\}, \{a,d\}, \{a,b,c\}, \{a,b,d\}, \{b,d\}, \{b,c,d\} \}$

Figure 1. Sample hierarchy S.

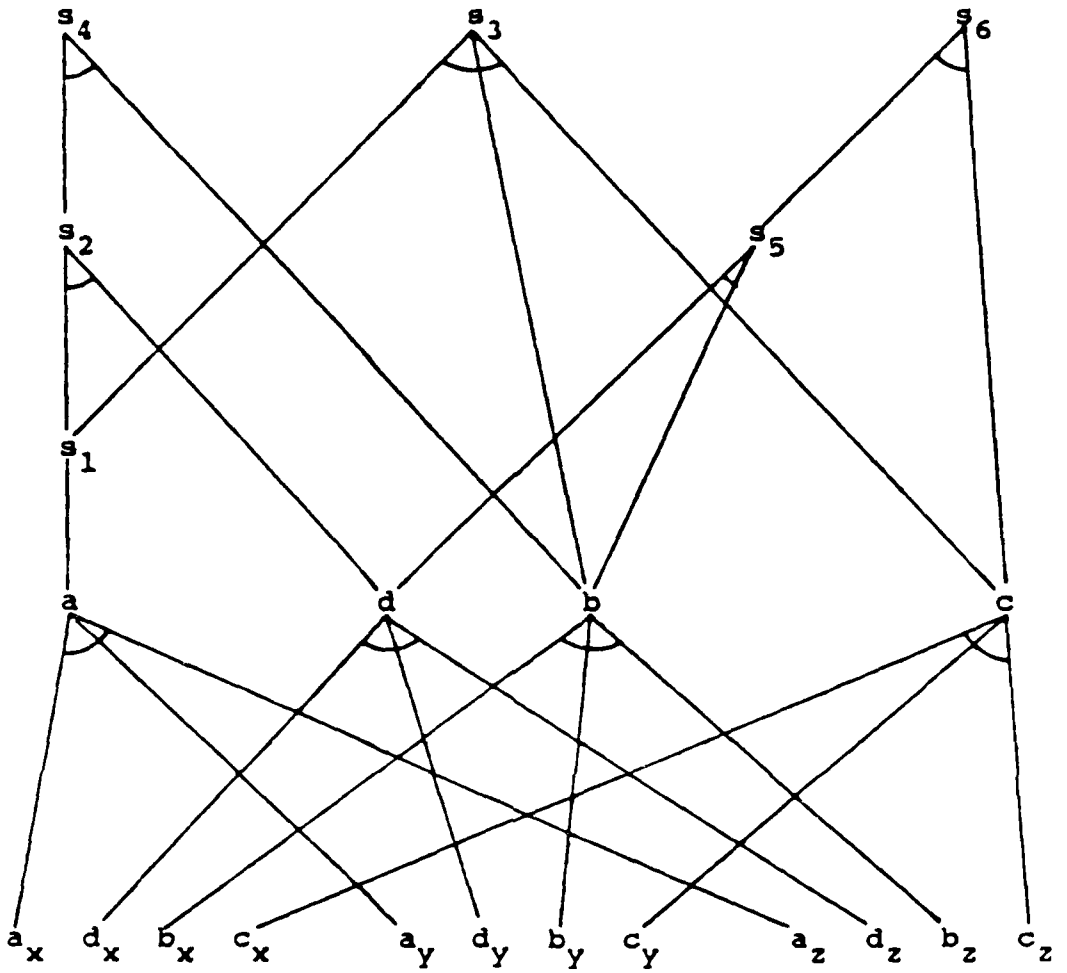

a enables s_1

s_2 conjoins (s_1, d)

s_4 conjoins (s_2, b)

s_3 conjoins (s_1, b, c)

s_5 conjoins (b, d)

s_6 conjoins (s_5, c)

a disjoins (a_x, a_y, a_z)

b disjoins (b_x, b_y, b_z)

c disjoins (c_x, c_y, c_z)

Figure 2. Inference network for tentative identification.

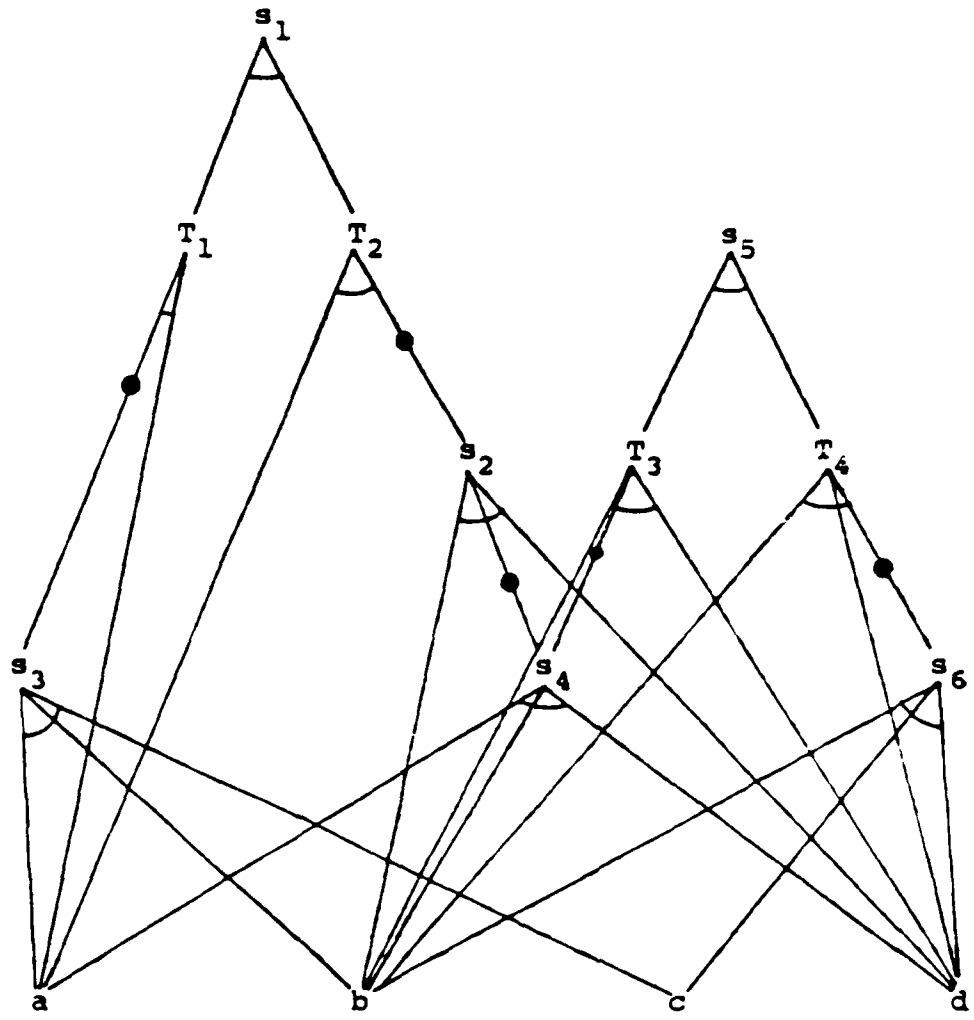

s_3 conjoins (a, b, c)

s_4 conjoins (a, b, d)

s_6 conjoins (b, c, d)

s_2 conjoins (a, d, not s_4)

T_1 conjoins (a, not s_3)

T_2 conjoins (a, not s_2)

T_3 conjoins (b, d, not s_4)

T_4 conjoins (b, d, not s_6)

s_1 disjoins (T_1, T_2)

s_2 disjoins (T_3, T_4)

Figure 3. Inference network for deterministic identification.

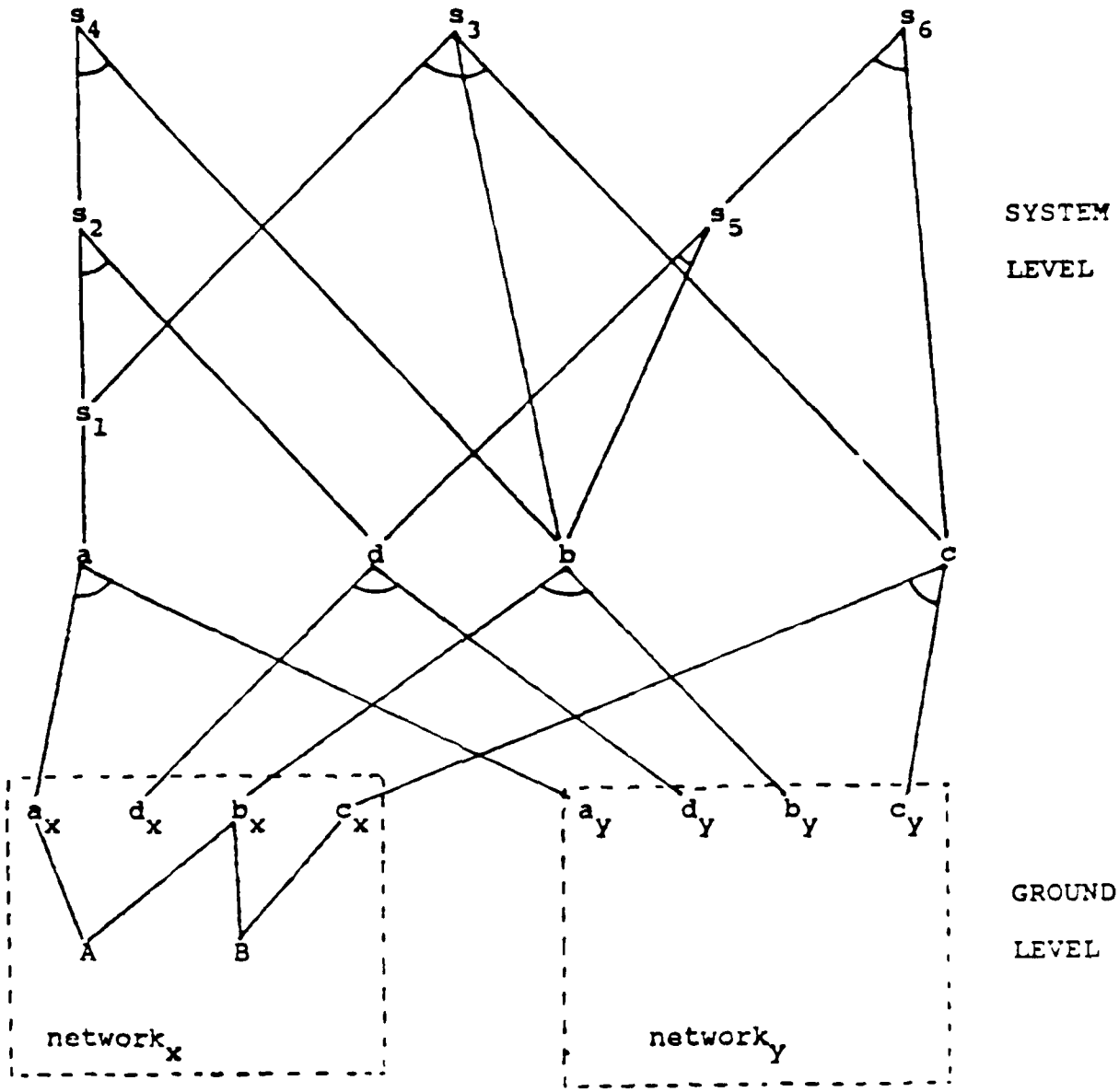

A disjoins-exclusive (a_x, b_x)

B disjoins-exclusive (b_x, c_x)

a disjoins (a_x, a_y)

b disjoins (b_x, b_y)

c disjoins (c_x, c_y)

d disjoins (d_x, d_y)

Figure 4. Ground level network.

Endorsements		Interpretation
$E_0(s_j)$,	+	only consistent possibility
$E_1(s_j)$,	+	is consistent with data
$E_2(x,s_j)$,	+	x, whose presence is established, is in s_j
$E_3(x,s_j)$,	+	x, whose presence is supported, is in s_j
$E_4(x,s_j)$,	-	x, whose presence is denied, is a member of s_j
$E_5(x,s_j)$,	-	x, whose presence is established, is not in s_j
$E_6(s_j)$,	-	other consistent possibilities

Replacement Rules

$E_i(s_j)$, $E_i(s_j)$ -> $E_i(s_j)$

$E_0(s_j)$, $E_1(s_j)$ -> $E_0(s_j)$

$E_3(s_j)$, $E_2(s_j)$ -> $E_2(s_j)$

$E_1(s_j)$, $E_4(s_j)$ -> $E_4(s_j)$

$E_1(s_j)$, $E_5(s_j)$ -> $E_5(s_j)$

$E_0(s_j)$, $E_4(s_j)$ -> $E_4(s_j)$

$E_0(s_j)$, $E_5(s_j)$ -> $E_5(s_j)$

Generation Rules

$$\forall (x)\ -E_4(x,s_j)\ \&\ -E_5(x,s_j) \Rightarrow E_1(s_j)$$

$$E_1(s_j)\ \&\ \underset{i\neq j}{\forall}\ (s_i)\ -E_1(s_i) \Rightarrow E_0(s_j)$$

$$E_1(s_j)\ \&\ \underset{i\neq j}{\exists}\ (s_i)\ E_1(s_i) \Rightarrow E_6(s_j)$$

Table 1. Endorsement system for hierarchy S.

Reasoning system	Configuration	Combining function	Assumptions
Probabilistic reasoning	$\theta \times I$	Bayes' theorem	principle of indifference, conditional independence, θ mutually exclusive, θ exhaustive
Evidential reasoning	$2^{\theta} \times I \times I$	Dempster's rule	independence, θ mutually exclusive, θ exhaustive
Influence nets	$\theta' \times I \times I$	definable	
Endorsements	$\theta \times 2^{E}$	definable	

Table 2. Summary of reasoning systems.

FINAL REPORT NUMBER 71
REPORT NOT RECEIVED IN TIME
WILL BE PROVIDED WHEN AVAILABLE
Dr. William Holt Sutton
760-OMG-091

FINAL REPORT NUMBER 72
REPORT NOT RECEIVED IN TIME
WILL BE PROVIDED WHEN AVAILABLE
Dr. Robert Swanson
760-OMG-067

1985-1986 RESEARCH INITIATION PROGRAM

Sponsored by the

AIR FORCE OFFICE OF SCIENTIFIC RESEARCH

Conducted by the

UNIVERSAL ENERGY SYSTEMS, INC.

FINAL REPORT

ANALYSIS OF LAYERED STRUCTURES TO RESIST BLAST EFFECTS OF CONVENTIONAL WEAPONS

Prepared by:	Joseph W. Tedesco
Academic Rank:	Assistant Professor
Department and University:	Department of Civil Engineering Auburn University

Date:	April 1987
Contract No.:	F49620-85-C-0013/SB5851-0360
Subcontract No.:	S-760-0MG-007

ABSTRACT

Protective military structures are typically constructed of massive, monolithic reinforced concrete slabs. This practice is considered necessary in order to protect personnel and/or vital equipment within the structure from the harmful effects of conventional weaponry. Recent studies have indicated, however, that "layered structures" may provide a viable alternative to conventionally hardened structures in certain environments.

This report presents the results of a preliminary finite element method (FEM) analysis of blast loading on layered structures. Both two-dimensional, linear and nonlinear, and three-dimensional, linear analyses were conducted on three different types of layered structures. The results indicate that layered structures show good promise as a viable alternative to conventional designs of hardened or semi-hardened facilities.

However, due to the limited scope of this study, further, more comprehensive numerical analyses are recommended. Subsequent experimental testing of some of the most promising layered structures is also recommended.

Chapter 1

INTRODUCTION

1.1 Background

Protective military structures are designed to house vital functions or equipment of extreme value. Consequently, survivability takes precedence over appearance and the structures are usually massive, with soil and concrete as the main building materials. Damage to protective shelters resulting from non-nuclear weapons occurs as a result of one or more of the following effects: penetration, fragmentation, and blast [1,2]. Penetration is a consideration only in the case of a direct hit, and fragmentation in cases of direct hits or near misses.

The conventional design of an underground (Fig. 1a) or aboveground (Fig. 1b) structure against a direct hit from an artillery shell or air bomb consists of providing protective layers above the structure [3]. A penetration layer (burster layer), usually constructed of concrete or rock, is employed at the outer surface to impede penetration of the weapon and induce its explosion. An absorption layer, existing between the penetration layer and the protective shelter, usually consists of soil and is intended to absorb the energy released by the weapon's explosion. The conventional design of an underground (Fig. 2a) or aboveground (Fig. 2b) structure against a near miss of an airbomb or artillery shell consists simply of a hardened structure with monolithic walls and roof.

The conventional design of an above-ground structure against a direct hit of a shaped-charge projectile consists of one of the following solution

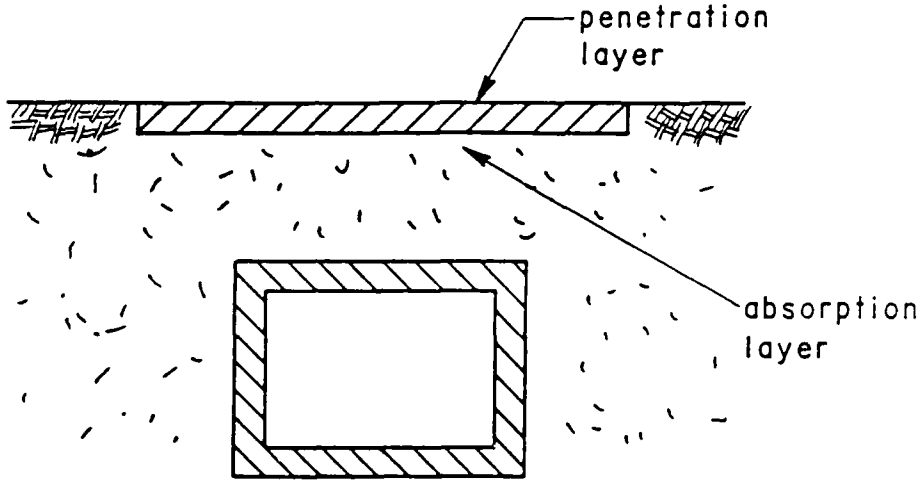

a) Underground hardened structure

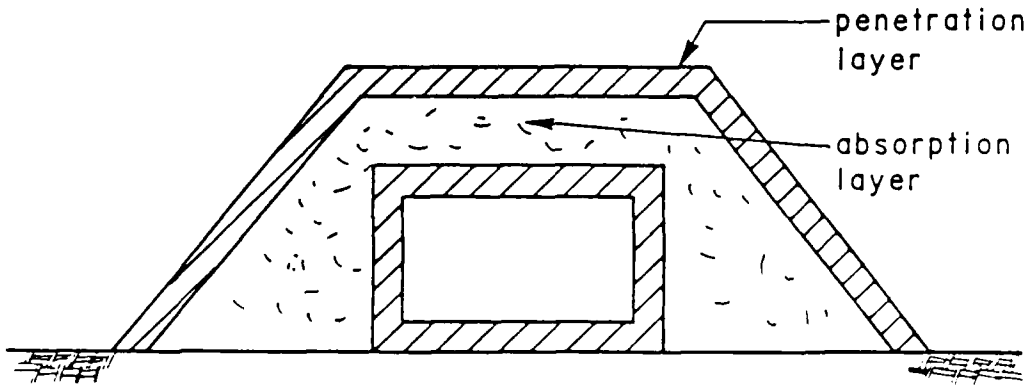

b) Aboveground hardened structure

Fig. 1. Conventional designs against direct hits of air bombs and artillery shells.

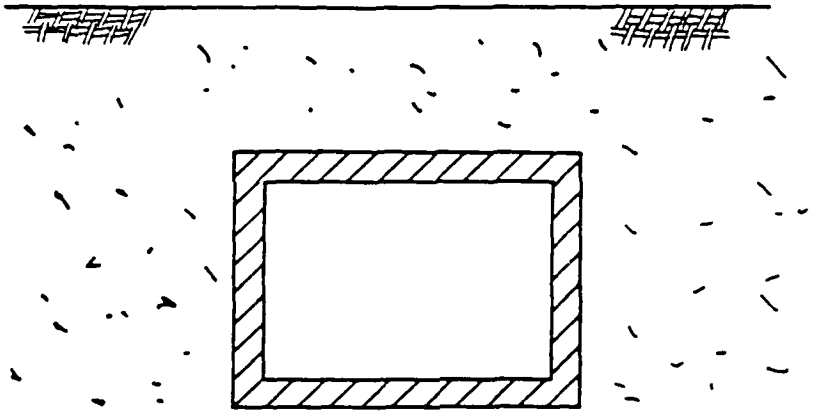

a) Underground hardened structure

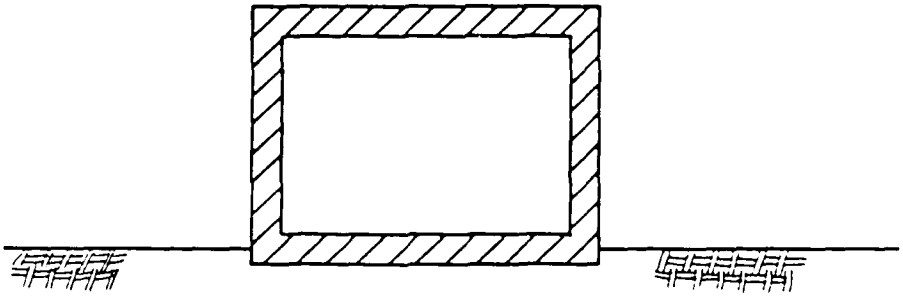

b) Aboveground hardened structure

Fig. 2. Conventional designs against near misses of air bombs and artillery shells.

schemes: (1) the provision of a thick monolithic structure capable of absorbing fully the jet effects (Fig. 3a), or (2) the provision of an "activator" element at a certain distance in front of the monolithic structure (Fig. 3b), intended to induce explosion of the projectile.

In each of the conventional designs discussed in the foregoing, the primary protective structure is invariably constructed of massive, monolithic concrete slabs. This practice is considered necessary in order to protect the personnel and/or equipment within the structure from the harmful effects of overpressure and interior spalling of the concrete walls. Recent studies [3,4] however, have indicated that, in certain situations, "layered structures" may provide a viable alternative to conventionally hardened structures.

1.2 Objectives

The use of layered structures in the building industry of the civilian sector is well established [5,6,7,8]. However, applications of layered structures for protective military shelters have received little attention. This report presents the results of a preliminary numerical investigation to evaluate the effectiveness of layered structures to resist the blast effects of conventional weaponry. The primary objective is to ascertain the capability of layered structures to substantially reduce or eliminate the incidence of spalling on the interior of the concrete shelter walls by diminishing the intensity of the blast-induced, compression stress wave which propagates through the wall.

A comprehensive numerical analysis was conducted on several different types of layered structures subject to blast loading in order to understand and evaluate the propagation of the blast wave through the various layers

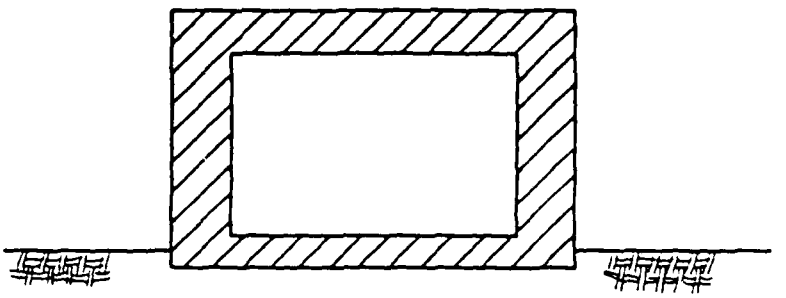

a) Single monolithic structure

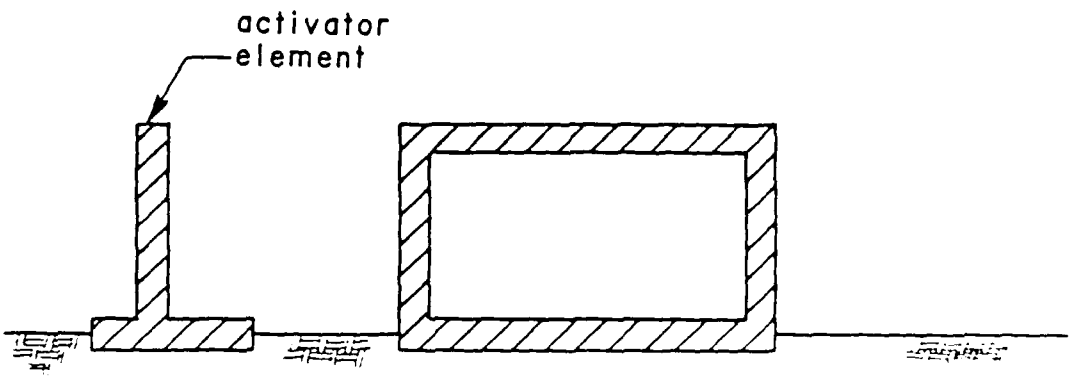

b) Activator element in front of the structure

Fig. 3. Conventional designs against direct hits of shaped-charge projectiles.

of the structure, and to determine the states of stress which develop in each layer. The results of this preliminary analysis indicate that layered structures, under certain circumstances, have the potential to be an adequate, cost-effective alternative to conventional hardened structures.

1.3 Scope of Study

Three different types of layered structures were examined. Details of the layered structures considered are depicted in Fig. 4. A brief description of each layered structure is presented in the following subsections.

1.3.1 Type I: Concrete-Air-Concrete

A typical detail of the Type I layered system is presented in Fig. 4a. The outer reinforced concrete layer is intended to fully or partially withstand the blast effects. The air gap is intended to prevent direct shock transfer to the inner reinforced concrete layer. The inner reinforced concrete layer will withstand the remaining blast effects passing through the outer layer and absorb all secondary concrete fragments of the outer layer.

1.3.2 Type II: Concrete-Polystyrene-Concrete

A typical detail of the Type II layered system is presented in Fig. 4b. The outer concrete layer will partially withstand the blast effects. The polystyrene layer will partially absorb the shock transferred from the outer layer. The inner concrete layer will withstand the remaining shock effects transferred through the polystyrene and stop the secondary concrete fragments of the outer layer.

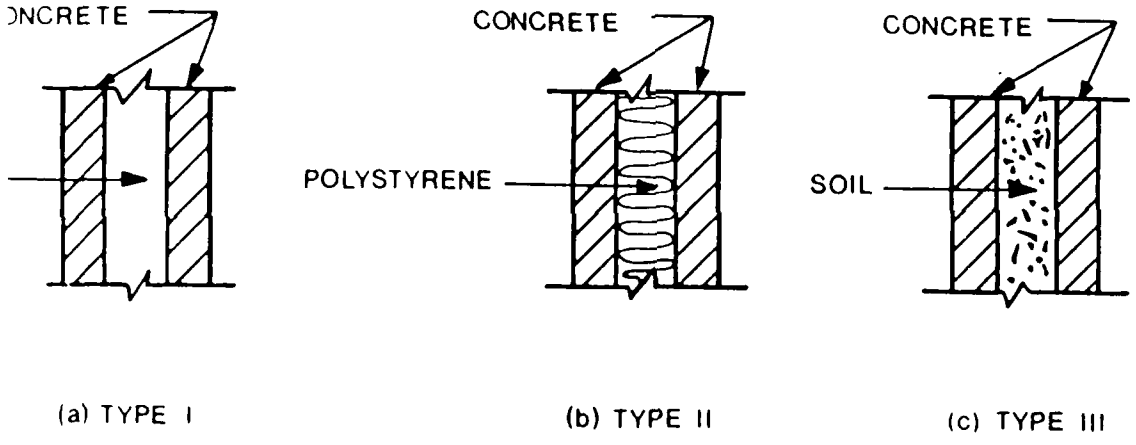

Fig. 4. Details of layered structures.

1.3.3 Type III: Concrete-Soil-Concrete

A typical detail of the type III layered system is presented in Fig. 4c. The outer concrete layer will partially withstand the blast effects. The soil will stop the secondary concrete fragments of the outer layer and partially absorb the shock transferred from the outer layer. The inner concrete layer will withstand the remaining shock effects transferred through the soil fill.

Due to the dynamic nature of the blast loading, and the highly nonlinear behavior of the materials used in the layered structures, the finite element method of analysis (FEM) was employed in this study through implementation of the ADINA computer programs. Two sets of analyses were conducted. The first series of analyses were performed on an axisymmetric structure comprised of 8-node isoparametric finite elements. The second series of analyses were conducted on a three-dimensional model comprised of 20-node isoparametric finite elements.

Chapter 2

DESCRIPTION OF STUDY

2.1 Compression Wave Propagation and Concrete Spalling

Spalling is defined [9] as fracturing caused when a high intensity transient stress wave reflects from a free surface. In the specific case of a blast, the compressive longitudinal wave strikes the exterior surface of the wall and is transmitted through the wall until it reaches a free surface (the interior face of the wall). At this instant, continuity of stress and continuity of particle velocity will be preserved only if the wave is reflected as a tensile longitudinal wave of equal strength. It is this reflected tensile wave which causes the concrete to spall at the interior face. Current procedures to minimize spalling in protective shelters include [10]: (1) the construction of earth berms on the exterior face of the shelter walls (Fig. 5a), (2) the installation of steel spall plates on the interior face of the shelter walls (Fig. 5b), and (3) increase the total wall thickness (Fig. 5c). All three methods exhibit some degree of effectiveness in reducing or eliminating spalling of the interior wall, with earth berms being the most effective, and increasing the wall thickness being the least effective. The results of this study will show layered structures to be a viable alternative to the above-mentioned practices for reducing and/or eliminating spalling in protective shelters.

When a plane elastic wave strikes a plane interface between two dissimilar materials (as would be the case in a layered structure), the interaction is regulated by the following boundary condition [11,12]:

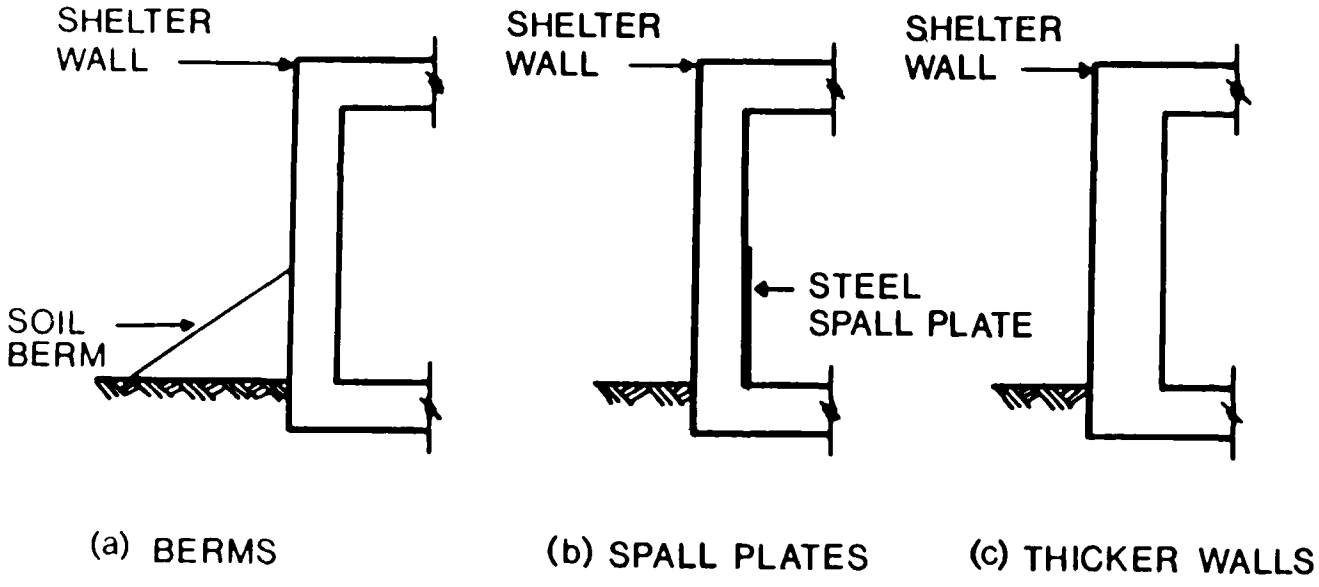

Fig. 5. Current spall protection methods used for protective shelters.

$$(\sigma_I)_1 + (\sigma_R)_1 = (\sigma_T)_2 \qquad (2\text{-}1)$$

where $(\sigma_I)_1$ and $(\sigma_R)_1$ are the instantaneous values of stress for the incident and reflected wave in medium one, respectively, and $(\sigma_T)_2$ is the instantaneous value of stress for the transmitted wave in medium two. The fundamental equations governing the portioning of stress at an abrupt change in media are given by [13]:

$$(\sigma_T)_2 = [2\rho_2 c_2/(\rho_2 c_2 + \rho_1 c_1)](\sigma_I)_1 \qquad (2\text{-}2)$$

and

$$(\sigma_R)_1 = [(\rho_2 c_2 - \rho_1 c_1)/(\rho_2 c_2 + \rho_1 c_1)](\sigma_I)_1 \qquad (2\text{-}3)$$

where ρ and c are the mass density of the material and velocity of propagation of the wave, respectively; the subscripts 1 and 2 denote the two different mediums. From Eqs. (2-2) and (2-3), the ratio of transmitted to reflected stress is given by:

$$(\sigma_T)_2/(\sigma_R)_1 = 2\rho_2 c_2/(\rho_2 c_2 - \rho_1 c_1) \qquad (2\text{-}4)$$

A number of important conclusions can be drawn from Eqs. (2-2), (2-3), and (2-4). When the two products $\rho_1 c_1$ and $\rho_2 c_2$ are equal, the ratio σ_R/σ_I is zero, and there is no reflected wave. The incident wave is transmitted at full intensity such as when the material is identical on both sides of the boundary. When $\rho_1 c_1 < \rho_2 c_2$ the ratio σ_R/σ_I is positive; implying that if σ_I is originally a compressive wave, the reflected wave will also be compressive. When $\rho_1 c_1 > \rho_2 c_2$ compressive waves will be reflected as tension waves, and vice versa. When $\rho_2 c_2$ is zero, the condition for a

free surface, $(\sigma_R)_I = -(\sigma_I)_1$, a compressive wave is reflected at full stress level as a tension wave, and vice versa. The transmitted stress (Eq. (2)) will always have the same sign as the incident stress, compression resulting in compression and tension in tension. For $\rho_1 c_1 < \rho_2 c_2$, σ_R is tension $\sigma_T < \sigma_I$: for $\rho_1 c_1 < \rho_2 c_2$, σ_R is compression and $\sigma_T > \sigma_I$.

2.2 Blast Loading

In general, an explosion is the result of a very rapid release of large amounts of energy within a limited space [1,14,15]. When an explosion takes place, the expansion of the hot gasses produces a pressure wave in the surrounding air (as illustrated by Fig. 6a). As this wave moves away from the center of the explosion, the inner part moves through the region that was previously compressed and is now heated by the leading part of the wave. As the pressure wave moves with the velocity of sound, the temperature and pressure of the air cause this velocity to increase. The inner part of the wave starts to move faster and gradually overtakes the leading part of the wave. After a short period of time the pressure wavefront becomes abrupt, thus forming a shock front somewhat similar to the one illustrated in Fig. 6b. The maximum overpressure occurs at the shock front and is called the peak overpressure. Behind the shock front, the overpressure drops very rapidly to about one-half the peak overpressure and remains almost uniform in the central region of the explosion.

As the expansion proceeds, the overpressure in the shock front decreases steadily; the pressure behind the front does not remain constant but, instead, falls off in a regular manner. After a short time, at a certain distance from the center of the explosion, the pressure behind the shock front becomes smaller than that of the surrounding atmosphere and

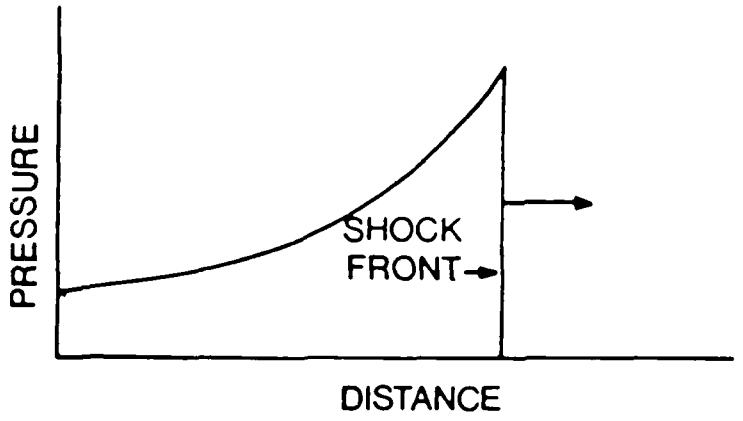

(a)

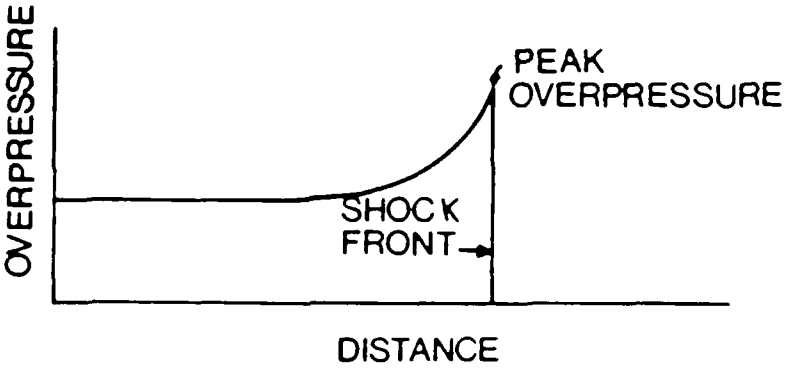

(b)

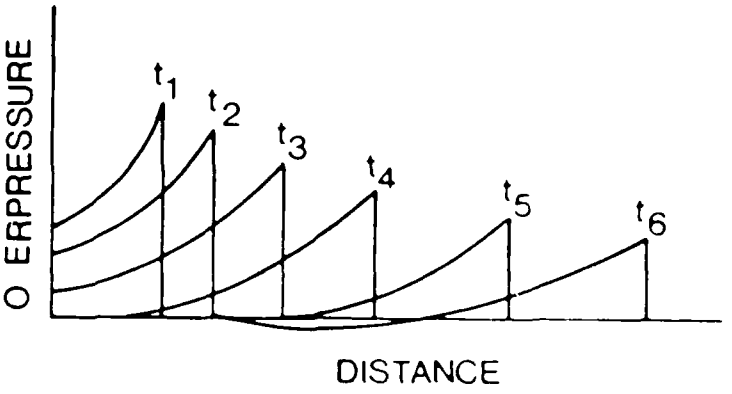

(c)

Fig. 6. (a) Variation of pressure with distance in shock wave; (b) Formation of shock front; (c) Variation of overpressure with distance from center of explosion at various times [14].

the so-called negative phase, or suction, develops. The front of the blast wave weakens as it progresses outward, and its velocity drops toward the velocity of sound in the undisturbed atmosphere. This sequence of events is shown in Fig. 6c. The overpressures at times t_1, t_2, ..., t_6 are indicated. In the curves marked t_1 through t_5, the pressure in the blast wave has not fallen below that of the atmosphere. In the curve marked t_6, at some distance behind the shock front, the overpressure becomes negative.

The time variation of the same blast wave at a given distance from the explosion is shown in Fig. 7. The shock front arrives at time t_A and, after the rise to the peak value, the incident pressure (P_{so}) decays to the ambient (P_a) value in the time t_o^+ which is the positive phase duration. This is followed by a negative phase with a duration t_o^- longer than the positive phase and characterized by a pressure below the preshot ambient pressure and a reversal of the particle flow [1]. (The negative phase is usually less important in a design than the positive phase and is generally neglected.)

If the shock wave impinges on a rigid surface oriented at an angle to the direction of propagation of the wave, a reflected pressure (P_r) is instantly developed on the surface, and the pressure is raised to a value in excess of the incident pressure. The reflected pressure is a function of the pressure in the incident wave and the angle formed between the rigid surface and the plane of the shock front. A typical reflected-pressure time history is illustrated in Fig. 8

The dynamic blast loadings used in the present study are the actual pressures measured in a series of tests conducted on one-half scale, reinforced concrete box structures [16]. Each box was designed to model the

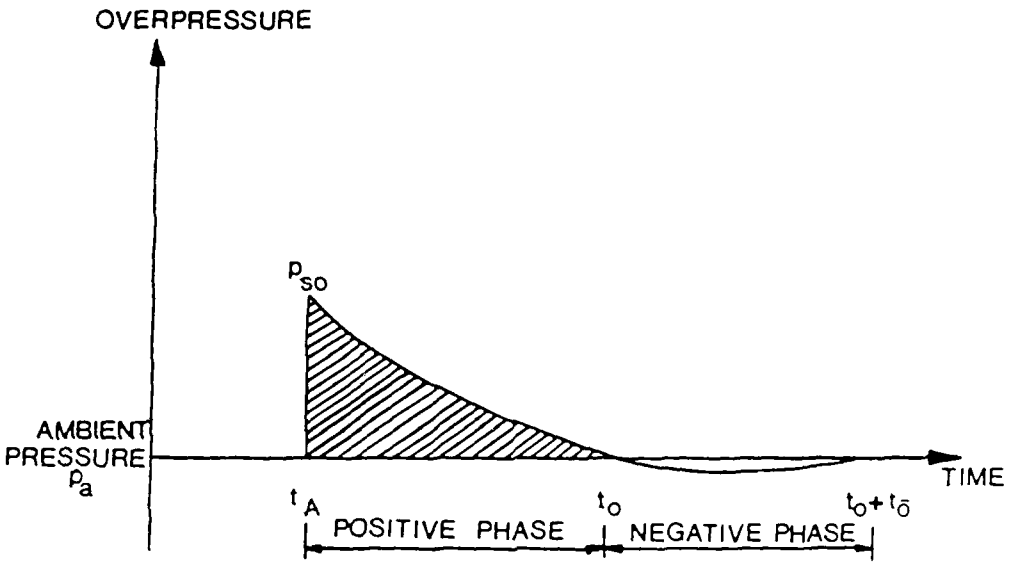

Fig. 7. Free-field pressure-time variation [1].

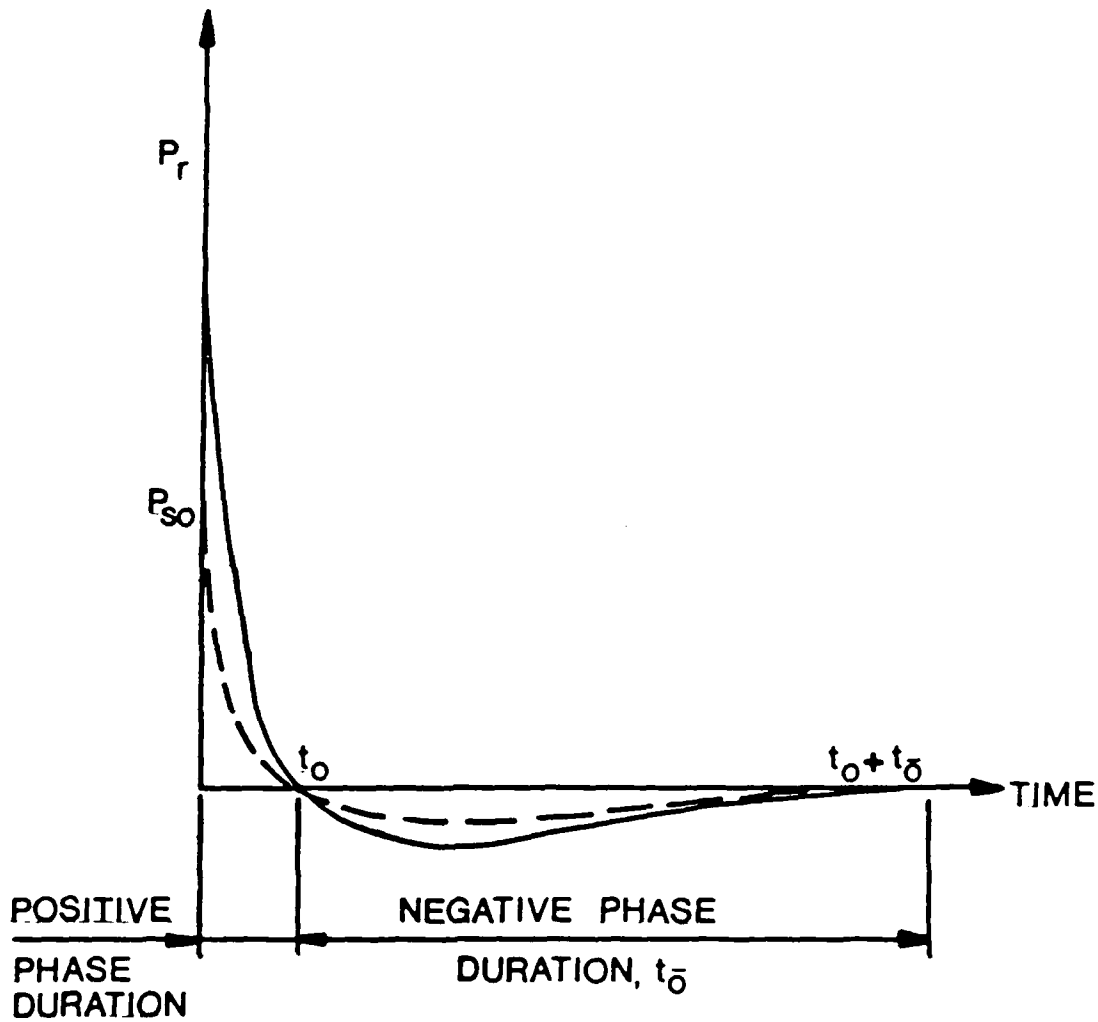

Fig. 8. Typical reflected pressure time history [1].

wall, roof, and floor sections of a large, single-story, above-ground building. A scaled, cased charge simulating the given weapon threat was detonated on the ground surface at the scaled criteria standoff from each of the test walls. The walls tested were 32 cm. thick. A schematic of the test structures is illustrated in Fig. 9.

Recordings of incident blast pressure vs. time were made at a position on the ground opposite the test wall at a distance from the charge equal to the charge standoff from the wall. A typical incident pressure trace is shown in Fig. 10a, where t_A indicates the arrival time, t_r is the rise time, and t_d is the time of positive duration. Similar recordings were made for the reflected dynamic pressures acting on the wall of the test structures.

In the present study the blast loads were represented with a simple triangular pulse illustrated in Fig. 10b. Two load cases were considered in the first series of analyses (two-dimensional FEM analysis): (a) load case 1 represents the incident blast pressure acting on the wall (P_o = 5.62 MP_a); (b) load case 2 represents the reflected dynamic wall pressure acting on the wall (P_o = 48.3 MP_a). In either case the duration of the load was 0.85 msec. In the second series of analyses (three-dimensional analysis), only load case 2 (P_o = 48.3 MP_a) was considered.

2.3 Two-Dimensional FEM Analysis

Due to the dynamic nature of the blast loading, and the highly non-linear behavior of the materials used in the layered structures, the finite element method of analysis (FEM) was employed in this study through implementation of the ADINA [17] computer programs. The analyses were conducted on an axisymmetric model comprised of two-dimensional, solid, 8-node

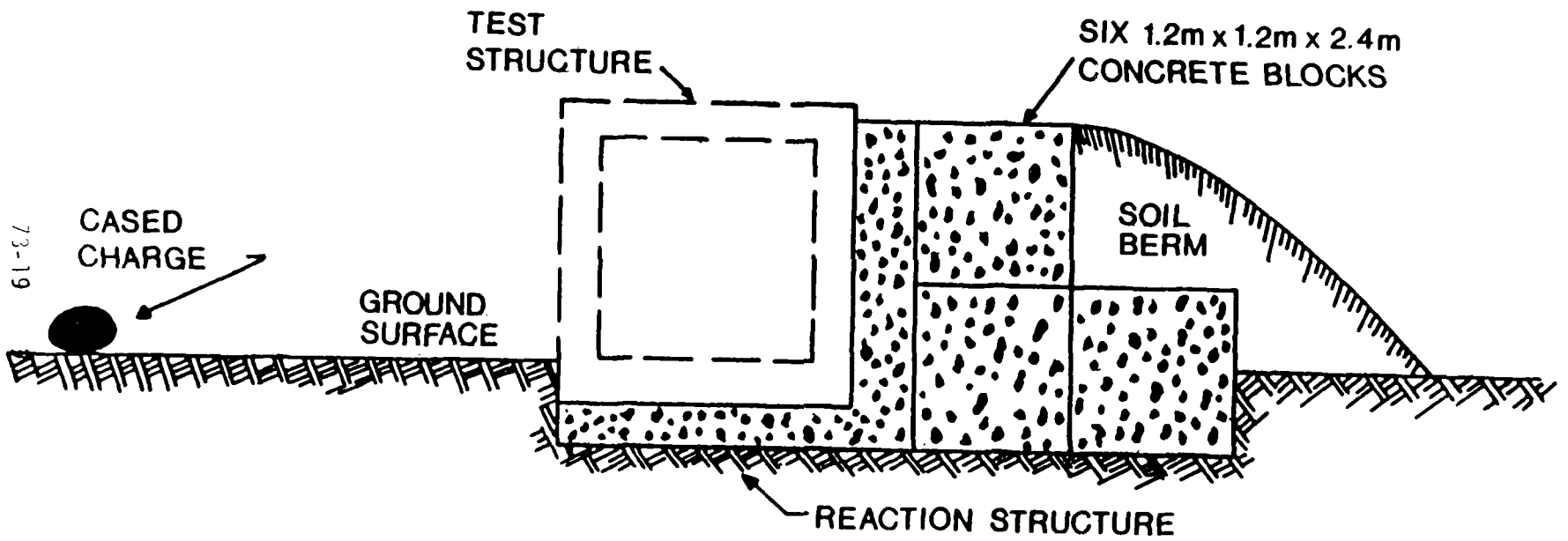

Fig. 9. Schematic of test structure [16].

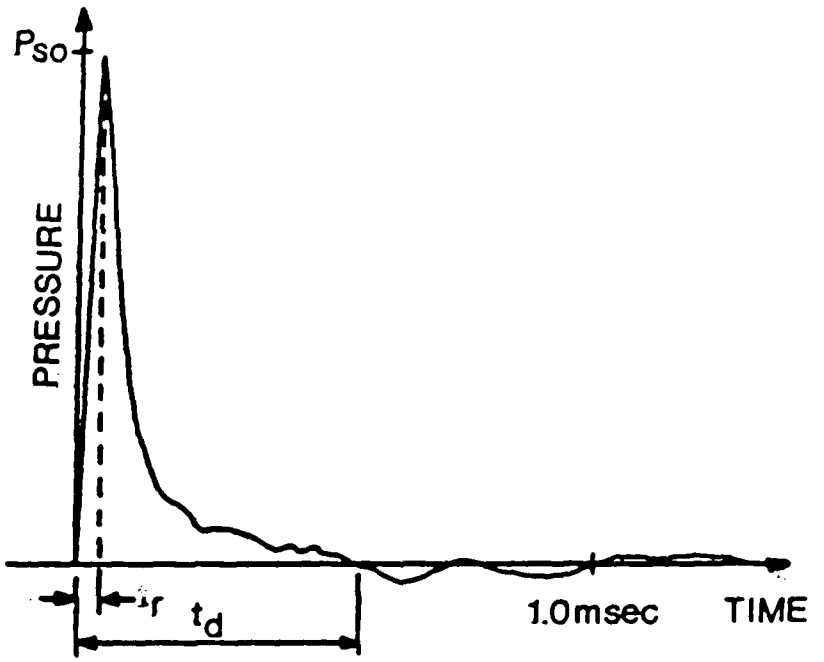

(a)

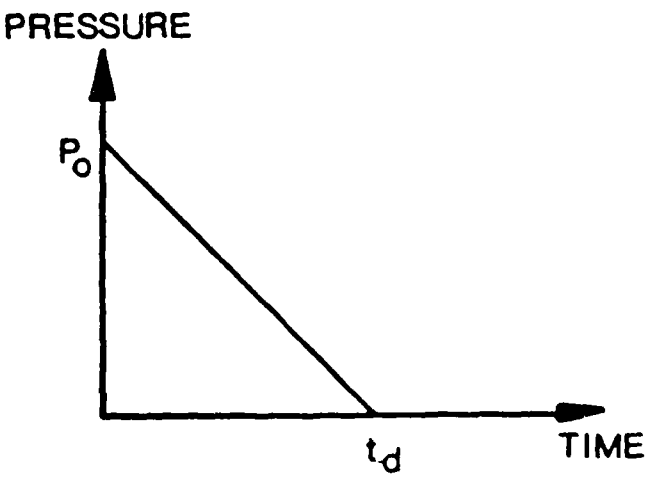

(b)

Fig. 10. (a) Incident pressure time history; (b) Simplified triangular pressure load representation.

isoparametric finite elements [18]. (For modeling the air layer in the Type I structure, two-dimensional fluid elements were used.)

The FEM model used in the present study was constructed to resemble as closely as possible (by an axisymmetric model) the walls tested in Ref. [16]. The benchmark case is a solid concrete wall 32 cm. thick, and having a diameter of 2.3 m. (This benchmark case will heretofore be referred to as the Prototype.)

For each layered structure (Type I, Type II, and Type III), two separate models were considered. Each model consisted of an outer layer (layer 1) and an inner layer (layer 3) of concrete having a thickness of 16 cm. The thickness of the middle layer, or absorption layer (layer 2), was 16 cm. for the "A" series of analyses, and 8 cm. for the "B" series of analyses. A typical axisymmetric FEM model mesh is presented in Fig. 11.

Both a linear and a nonlinear material representation of the absorption layer (layer 2) were considered for the Type III structure. A linear material law was utilized in the concrete layers (layer 1 and layer 3) for all structures. The physical properties for the linear material models are summarized in Table 1. For the nonlinear material representation of the absorption layers in the Type III structure, a linear elastic perfectly-plastic constitutive law was employed. In conjunction with this material model a Drucker-Prager [19,20] yield function with tension cut-off and hardening cap was specified. The pertinent parameters for the nonlinear material model are summarized in Table 2.

2.4 Three-Dimensional FEM Analysis

For this phase of the study, a three-dimensional FEM model was constructed to represent a one-quarter section of the structural walls tested

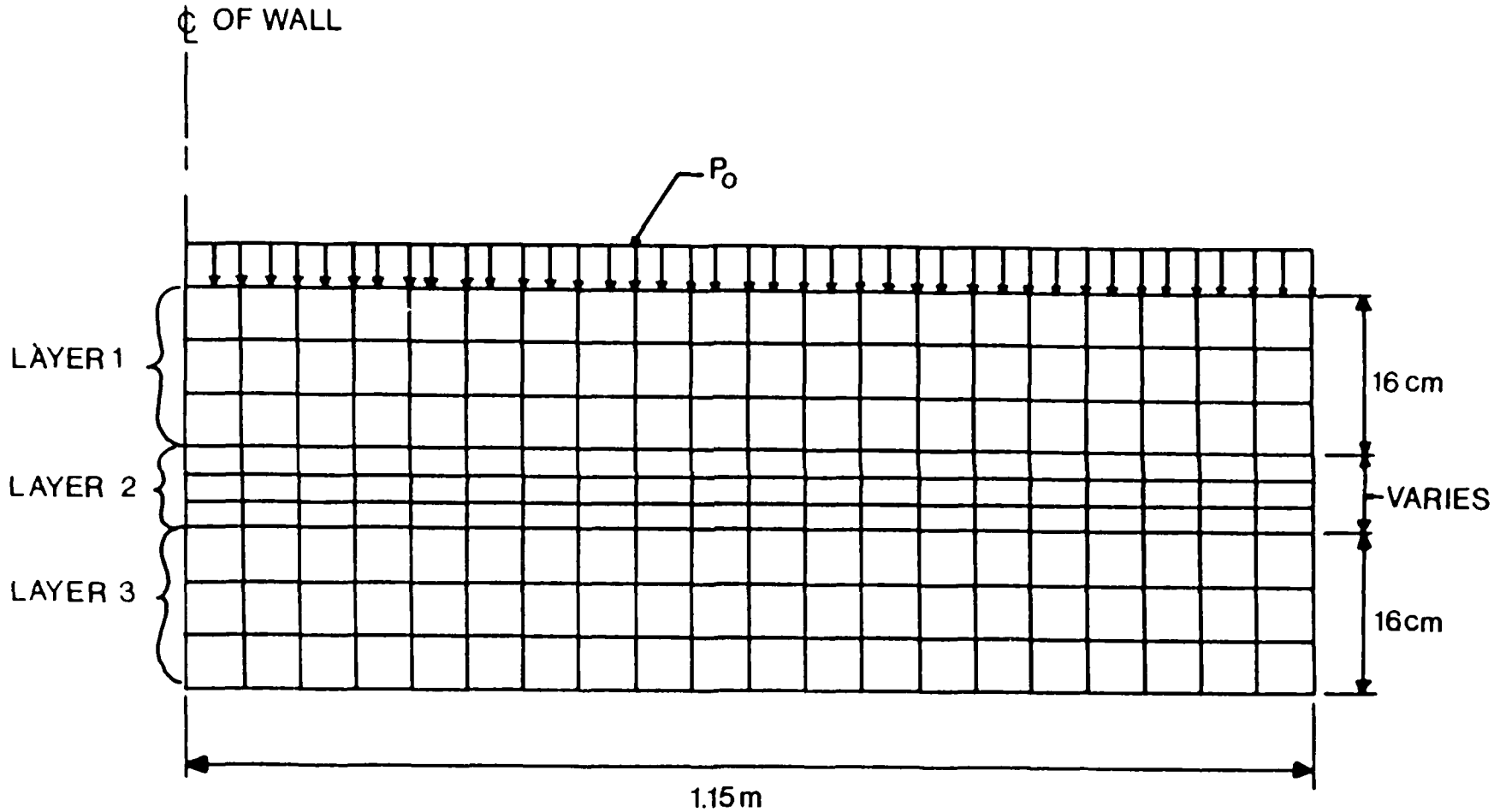

Fig. 11. Typical FEM mesh for layered structure.

Table 1. Physical properties for linear material models.

Material Parameters	Concrete	Sand	Polystyrene	Air
Mass density (kg/cm^3)	2.32×10^{-3}	1.76×10^{-3}	80.0×10^{-6}	1.225×10^{-6}
Young's Modulus (MP_a)	29600	690.0	6.9	----
Poisson's ratio	0.18	0.25	0.15	----
Bulk modulus (kg/cm^2)	----	----	----	7.05×10^{-4}

Table 2. Physical properties for nonlinear sand model.

Material Parameters	Sand (Drucker-Prager)
Young's modulus (MP_a)	690.0
Poisson's ratio	0.25
Yield function parameter, α	0.05
Yield function parameter, $k(MP_a)$	0.69
Cap hardening parameter, w	-0.066
Cap hardening parameter, $D(MP_a)^{-1}$	-0.1131
Tension cut-off limit (MP_a)	0.069
Initial cap position (MP_a)	0.0

in the experimental study reported in Ref. [9]. The FEM model was comprised entirely of three-dimensional, 20 node, isoparametric finite elements. An isometric view of the FEM model is depicted in Fig. 12, and a plan view is shown in Fig. 13.

Each FEM model representing the layered structures (Type II and Type III only) consisted of an outer layer (layer 1) and an inner layer (layer 3) of concrete having a thickness of 16 cm. The thickness of the middle absorption layer (layer 2) was 8 cm. A typical cross-section of the FEM mesh is presented in Fig. 14. The material properties used for the FEM models are summarized in Table 1. Linear elastic constitutive relations were assumed for all materials.

In this series of analyses, the blast loading was also delineated by a simple triangular pulse (Fig. 10b). The magnitude of the load was set equal to the recorded reflected dynamic wall pressure (P_o = 48.3 MP_a). The duration of the load, t_d, was 0.85 msec.

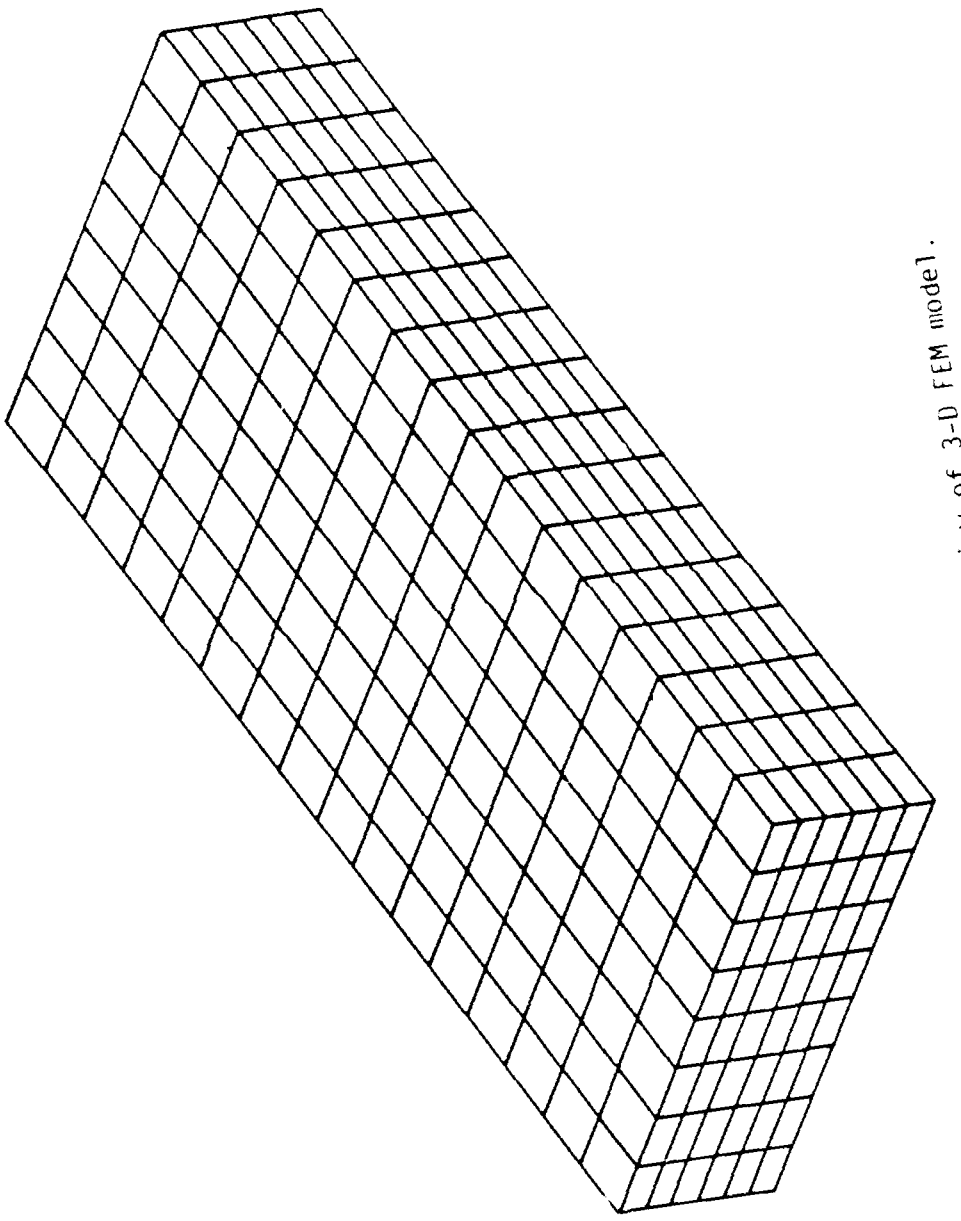

Fig. 12. Isometric view of 3-D FEM model.

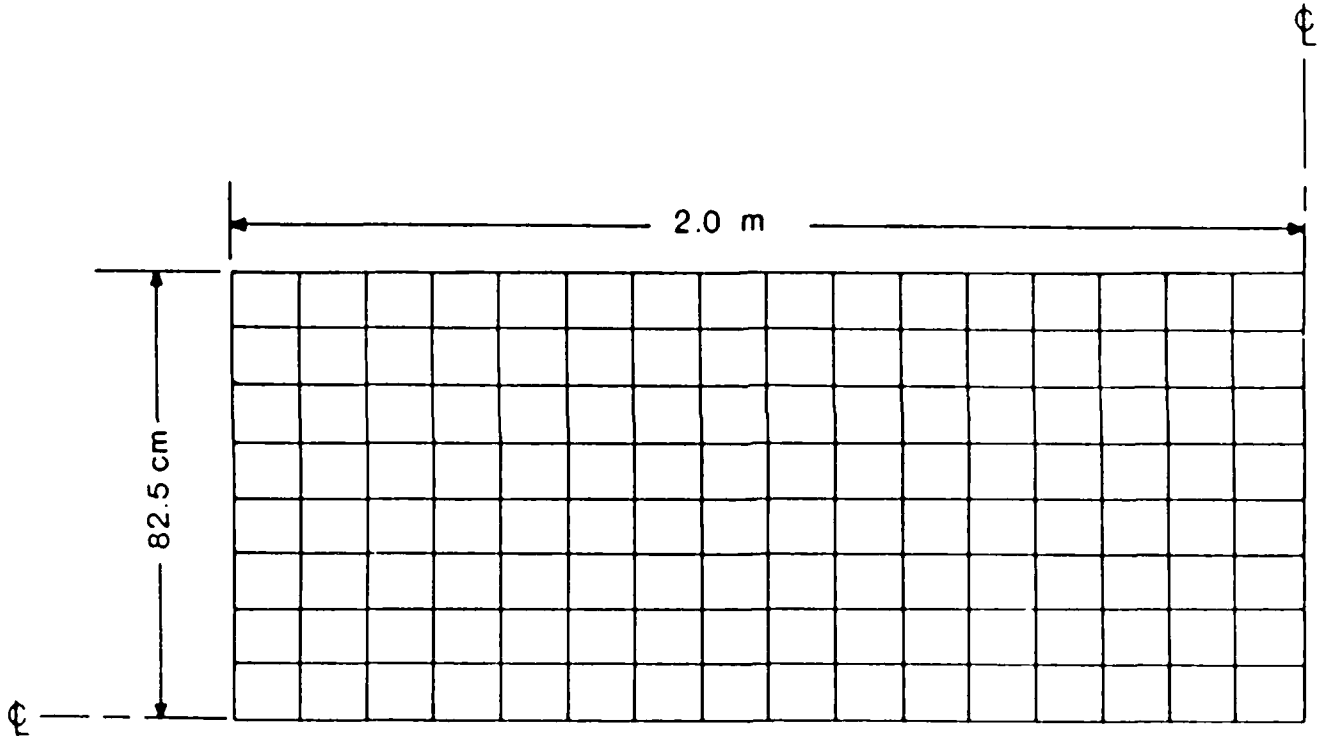

Fig. 13. Plan view of 3-D FEM model.

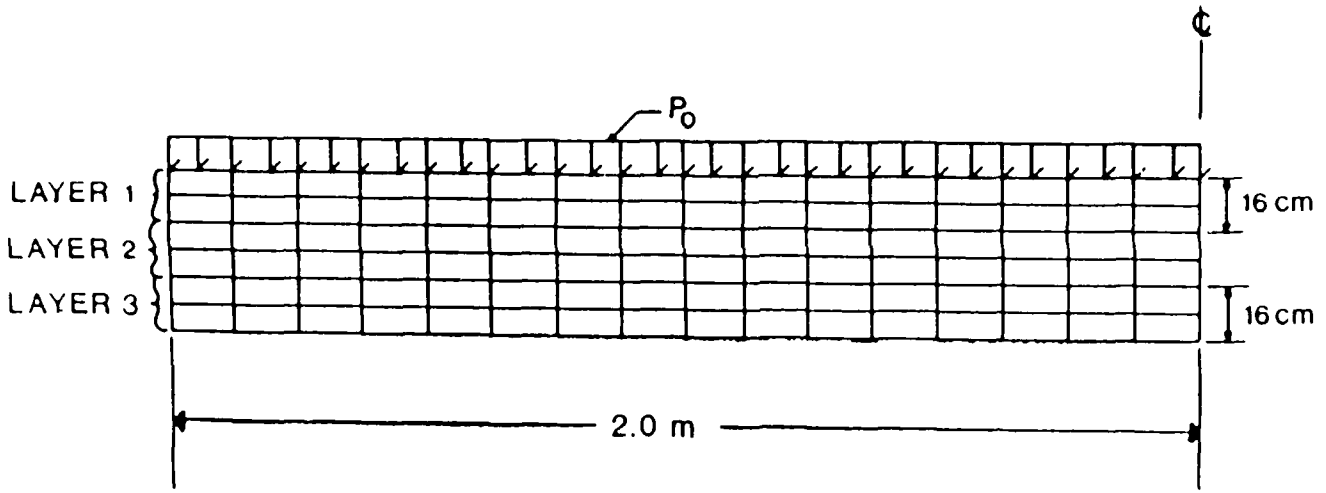

Fig. 14. Typical cross-section of 3-D FEM model.

Chapter 3

NUMERICAL ANALYSES

3.1 Wave Propagation Analysis

As was mentioned in Chapter 1, the primary objective of this study is to investigate the effectiveness of layered structures to minimize the intensity of blast-induced, compression stress wave propagation. To this end, a FEM parametric study was conducted in which the compression stress wave propagations through three different types of layered structures (Fig. 4) are compared to the compression stress wave propagation through a monolithic structure.

The major difference between a wave propagation problem and a structural dynamics problem is that in a wave propagation problem, a large number of frequencies are excited in the system, whereas in a structural dynamics problem only the lowest few modes (or only a few intermediate modes) are generally excited [21]. Therefore, in analyzing wave propagation problems, direct numerical integration procedures are preferable to modal analyses.

Dynamic integration operators are broadly classified as implicit or explicit. Explicit schemes obtain values for dynamic quantities at time $t + \Delta t$ based entirely on available results at time t. The stability of explicit schemes depends on the time step size in order to maintain numerical stability. Implicit schemes remove the upper bound on the time step size by basing the solution for dynamic quantities at time $t + \Delta t$ on both available results at time t and dynamic quantities at $t + \Delta t$.

AD-A186 493 UNITED STATES AIR FORCE RESEARCH INITIATION PROGRAM 5/ 8
1985 TECHNICAL REPORT VOLUME 3(U) UNIVERSAL ENERGY
SYSTEMS INC DAYTON OH R C DARRAH APR 87
UNCLASSIFIED AFOSR-TR-87-1719 F49620-85-C-0013 F/G 15/3 NL

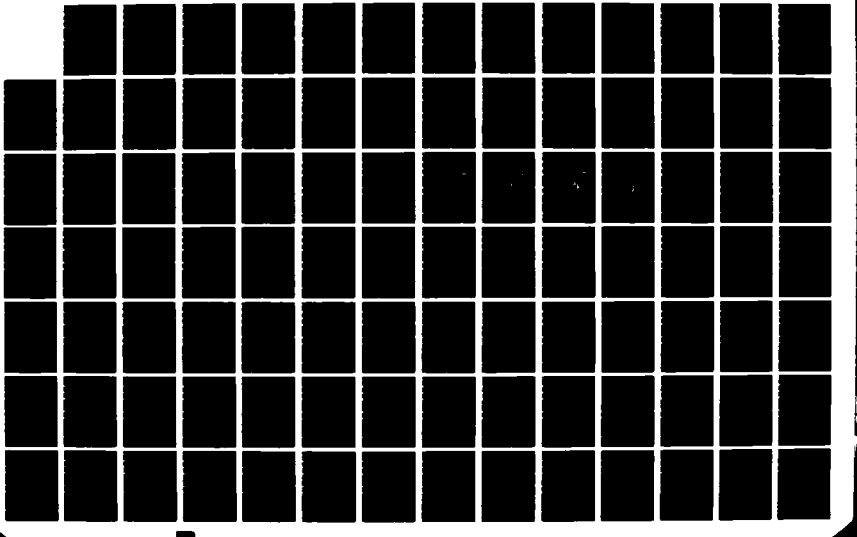

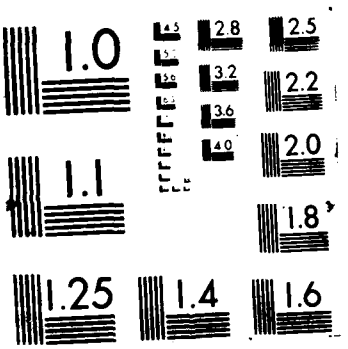
1.0
1.1
1.25
1.4
1.6
1.8
2.0
2.2
2.5
2.8
3.2
3.6
4.0

Explicit methods, such as the central difference method, have been used successfully in the past [22] for wave propagation problems. However, the method does have several significant shortcomings. Firstly, the method is only conditionally stable; for stability, the time step size Δt must be smaller than a critical time step, Δt_{cr}, which is equal to $\frac{T_n}{\pi}$, where T_n is the smallest period in the finite element system. Moreover, the most accurate solution is obtained by integrating with a time step equal to the stability limit and the solution is less accurate when a smaller time step is employed [21]. Secondly, the explicit central difference method is effective only when the mass matrix is diagonal [21], therefore, all degrees of freedom in the model must be mass degrees of freedom. If one of the diagonal elements in the mass matrix is zero, then $T_n = 0$ and $\Delta t_{cr} = 0$, and the central difference method cannot be used.

In the present study, the mass density of the materials comprising the absorption layers in the Type I and Type II structures are very small, which results in zero or near zero terms in the diagonal mass matrices. Therefore, the Newmark method of implicit time integration was used with a consistent mass formulation. The Newmark method is unconditionally stable, therefore, time step considerations were based entirely upon wave velocity and discretization. The time step criterion for wave propagation is given by [21]:

$$\Delta t = \frac{L_e}{c} \qquad (3\text{-}1)$$

where L_e is the distance between element integration points in the direction in which the wave is traveling, and c is the wave speed. In the present study, Δt is taken as 1μs.

3.2 Solution Strategy for Nonlinear Analyses

Because of the complexity of the material descriptions used for the sand and polystyrene in the two-dimensional FEM analyses, an appropriate strategy for solving the nonlinear finite element equations must be employed. For the present study, the Newton-Raphson iteration scheme was implemented. In the Newton-Raphson formulation, the equilibrium conditions at time $t + \Delta t$ are satisfied by successive approximations of the form (Ref. 16):

$$[K]^{i-1} \{\Delta U\}^{i} = \{R\} - \{F\}^{i-1} \tag{3-2}$$

in which $[K]^{i-1}$ is the tangent stiffness matrix at the iteration i-1 and time $t + \Delta t$; $\{\Delta U\}^{i}$ is the i^{th} correction to the current displacement vector; $\{F\}^{i-1}$ is the force vector that corresponds to the current element stresses. The displacement increment correction is used to obtain the next displacement approximation:

$$\{U\}^{i} = \{U\}^{i-1} + \{\Delta U\}^{i} \tag{3-3}$$

Equations (3-2) and (3-3) constitute the Newton-Raphson solution of the equilibrium equations. The iteration continues until appropriate convergence criteria are satisfied.

In nonlinear dynamic analysis, the solution of the governing differential equations is obtained by direct integration procedures. Of utmost concern in the selection of an appropriate time integration scheme is the stability of the solution technique and accuracy of the analysis. In the present study, the Newmark-Beta method of time integration was employed because it is unconditionally stable, regardless of the time step.

The dynamic equlibrium equations for the structure are written as:

$$[M]\{\ddot{U}(t)\} + [C]\{\dot{U}(t)\} + [K]\{U(t)\} = \{R(t)\} \qquad (3\text{-}4)$$

where [M], [C], [K] are the mass, damping, and stiffness matrices, respectively; {R} is the external load vector; and {U}, {$\dot{U}$}, and {$\ddot{U}$} are the displacement, velocity, and acceleration vectors of the finite element assemblage. In an implicit time integration scheme, equilibrium of the system [Eq. (3-4)) is considered at time t + Δt to obtain the solution at time t + Δt. In nonlinear analysis, this requires that an iteration be performed. Using the Newton-Raphson iteration, the governing equilibrium equations (neglecting the effects of a damping matrix) are:

$$[M]^{t+\Delta t}\{U\}^{i} + {}^{t}[K]\{\Delta U\}^{i} = {}^{t+\Delta t}\{R\} - {}^{t+\Delta t}\{F\}^{i-1} \qquad (3\text{-}5)$$

$$^{t+\Delta t}\{U\}^{i} = {}^{t+\Delta t}\{U\}^{i-1} + \{\Delta U\}^{i} \qquad (3\text{-}6)$$

In the Newmark-Beta integration scheme, the following assumptions are employed:

$$^{t+\Delta t}\{U\} = {}^{t}\{U\} + \frac{\Delta t}{2}\left({}^{t}\{\dot{U}\} + {}^{t+\Delta t}\{\dot{U}\}\right) \qquad (3\text{-}7)$$

$$^{t+\Delta t}\{\dot{U}\} = {}^{t}\{\dot{U}\} + \frac{\Delta t}{2}\left({}^{t}\{\ddot{U}\} + {}^{t+\Delta t}\{\ddot{U}\}\right) \qquad (3\text{-}8)$$

Using the relations in Eqs. (3-5), (3-6), (3-7), and (3-8) results in:

$$^{t+\Delta t}\{\ddot{U}\}^{i} = \frac{4}{\Delta t^{2}}\left({}^{t+\Delta t}\{U\}^{i-1} - {}^{t}\{U\} + \{\Delta U\}^{i}\right) - \frac{4}{\Delta t}\,{}^{t}\{\dot{U}\} - {}^{t}\{\ddot{U}\}, \qquad (3\text{-}9)$$

and substituting Eq. (3-9) into Eq. (3-5) yields:

$$ {}^{t}[\hat{K}]\{\Delta U\}^{i} = {}^{t+\Delta t}\{R\} - {}^{t+\Delta t}\{F\}^{i-1} $$

$$ - [M]\left(\frac{4}{\Delta t^{2}}\left({}^{t+\Delta t}\{U\}^{i-1} - {}^{t}\{U\}\right) - \frac{4}{\Delta t}\,{}^{t}\{\dot{U}\} - {}^{t}\{\ddot{U}\}\right), \tag{3-10} $$

where

$$ {}^{t}[\hat{K}] = {}^{t}[K] + \frac{4}{\Delta t^{2}}[M]. \tag{3-11} $$

3.3 Results of Two-Dimensional FEM Analyses

Several time histories for the compression longitudinal wave at the inside face of the Type I structure for load case 2 (48 MP_a) are presented in Fig. 15. The stresses are normalized with respect to the maximum stress occurring in the prototype structure (Fig. 15a). This figure illustrates the effectiveness of both the Type IA and Type IB layered structures in reducing the magnitude of the propagated compression longitudinal wave. The Type II and Type III layered structures exhibited similar behavior.

As was previously mentioned, spalling will occur when the compression longitudinal wave strikes a free surface (the inside face of the wall) and is reflected as a tension longitudinal wave of equal strength. The extent of spalling experienced by the wall is a function of the magnitude of the reflected tensile wave and the duration of the positive phase of the stress wave. The maximum reflected tensile stresses (normalized with respect to the maximum reflected tensile stress in the prototype structure) determined for the three layered structures are summarized in Table 3.

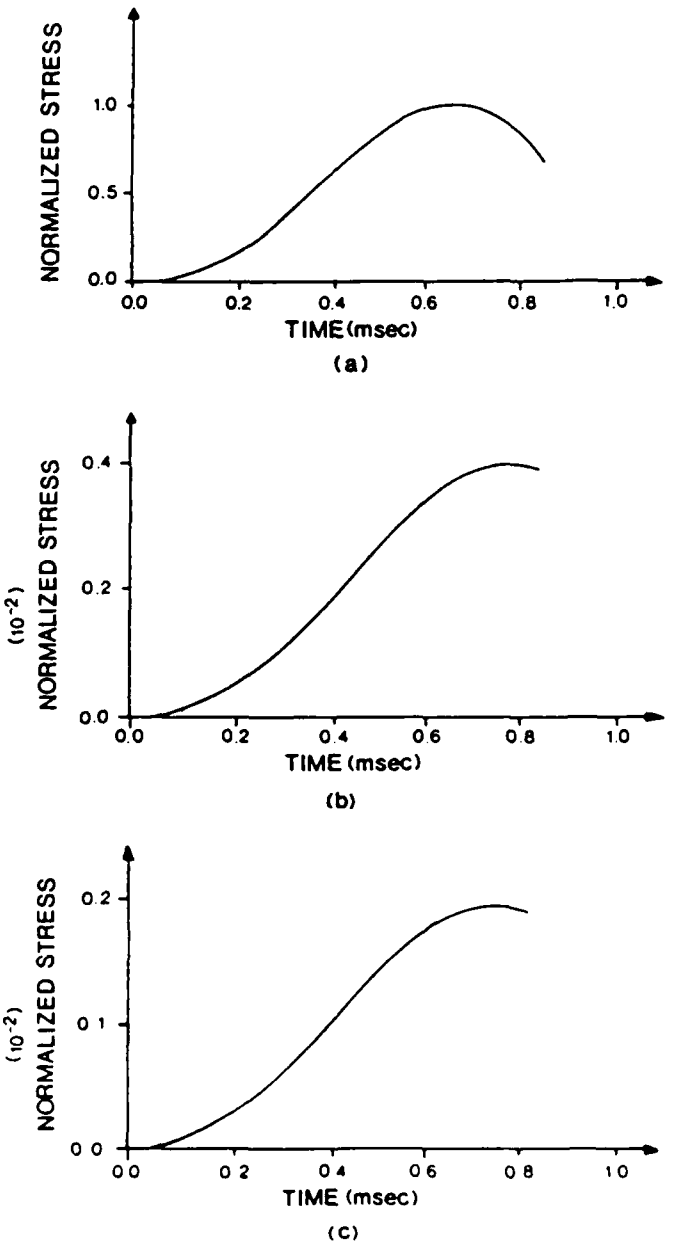

Fig. 15. Representative compression longitudinal wave time histories at inside face of layer 3. (a) Prototype; (b) Type IA; (c) Type IB.

Table 3. Summary of maximum normalized reflected tensile stresses on interior face of structure.

Structure Type (mid-layer thickness)	Loading	
	5.62 MP_a	48.3 MP_a
Type I(A)	0.383×10^{-2}	0.383×10^{-2}
Type I(B)	0.195×10^{-2}	0.195×10^{-2}
Type II(A)	0.6×10^{-3}	0.6×10^{-3}
Type II(B)	0.31×10^{-3}	0.31×10^{-3}
Type III(A)	0.482×10^{-2} (0.484×10^{-2})*	0.482×10^{-2} (0.484×10^{-2})*
Type III(B)	0.367×10^{-2} (0.372×10^{-2})*	0.367×10^{-2} (0.372×10^{-2})*

* nonlinear material model

The results indicate that all three layered structures are very effective in minimizing or eliminating the incidence of spalling.

3.4 Results of Three-Dimensional FEM Analyses

Several time histories for the compression longitudinal wave at the inside face of the Type II and Type III structures are presented in Fig. 16. The stresses are normalized with respect to the maximum stress occurring in the 32 cm. thick monolithic concrete wall structure (Fig. 16a). This figure illustrates the effectiveness of both the Type II and Type III layered structures in reducing the magnitude of the propagated compression longitudinal wave.

Spalling will occur when the compression longitudinal wave strikes a free surface (the inside face of the wall) and is reflected as a tension longitudinal wave of equal strength. The extent of spalling experienced by the wall is a function of the magnitude of the reflected tensile wave and the duration of the positive phase of the stress wave. The maximum reflected tensile stresses (normalized with respect to the maximum reflected tensile stress in the monolithic structure) determined for the two layered structures are summarized in Table 4. The results indicate that all three layered structures are very effective in minimizing or eliminating the incidence of spalling.

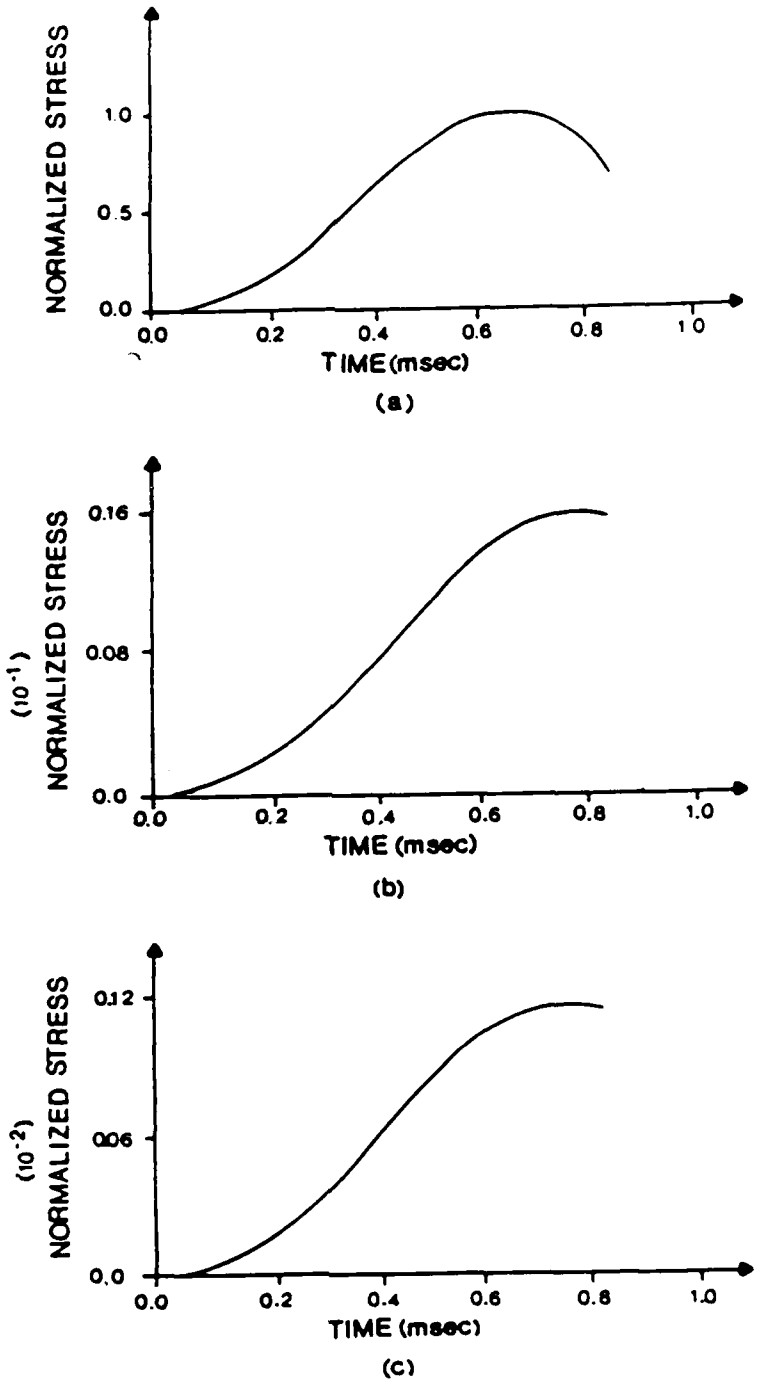

Fig. 16. Compression longitudinal wave time histories at inside face of layer 3. (a) Monolithic structure, (b) Type layered structure, (c) Type II layered structure.

Table 4. Normalized reflected tensile stresses at interior face of wall.

Structure	Normalized Reflected Tensile Stress
Monolithic concrete wall	1.0
Concrete-soil-concrete wall (Type III)	0.0149
Concrete-polystyrene-concrete wall (Type II)	0.00125

Chapter 4

SUMMARY

4.1 Type I Structure

The Type I structure of concrete-air-concrete appeared to be very effective in reducing the intensity of the longitudinal compression wave which propagated through to the wide face of layer 3 (see Fig. 12 and Table 3). However, there are several important shortcomings associated with the Type I structure which were not readily apparent from the results presented. The most noteworthy misgiving is that the outer concrete layer (layer 1) experienced extremely large flexural and shear stresses of sufficient magnitude to cause a break. The breaching action will expose the inner concrete layer to an increased overpressure as well as to some impact loads from fragmentation of layer 1. Future studies on layered systems must address this problem.

4.2 Type II Structure

Like the Type I structure, the Type II structure of concrete-polystyrene-concrete also appeared to be very effective in reducing the reflected tensile stress on the inside face of layer 3 (see Tables 3 and 4). However, the outer concrete layer of the Type II structure also experienced extremely high flexural and shear stresses, indicating a high likelihood for the development of a breach in layer 1. It is conceivable that the inner layer of polystyrene (layer 2) could absorb most of the impact due to fragmentation of layer 1 if sufficient thickness were provided. Determination of the optimal thickness for the absorption layer warrants further investigation.

4.3 Type III Structure

The Type III structure of concrete-sand-concrete, although apparently slightly less effective in reducing the intensity of the propagation of the longitudinal compression wave through the structure, appears to be the most effective structure overall. The soil in layer 2 would be more effective in stopping the secondary concrete fragments of the outer layer (layer 1), than the absorption layer of air in the Type I structure and polystyrene in the Type II structure. Moreover, the flexural and shear stresses in the inner concrete layer (layer 3) of the Type III structure were significantly less than those exhibited by the Type I and Type II structures. This indicates that the Type III structure is less likely to experience a breach in the inner concrete layer (layer 3), than the Type I and Type II structures.

4.4 Recommendations for Future Research

Structural designs for protective military structures have essentially not changed over the past 40 years. The majority of protective shelters are constructed of massive, monolithic, cast-in-place concrete slabs. This type of construction may not always be the best alternative, either in terms of safety or economy, or both.

The concept of a layered structure was presented and analyzed in this report. The results of the analyses indicate that layered structures are potentially a viable alternative in the construction of hardened or semi-hardened facilities. Although encouraging, the results of the present study are by no means conclusive. Additional studies in this area are required.

It is recommended that numerical studies similar to that reported herein be initiated to determine dimensions for the various layers of the layered systems in order to identify the most optimal and cost effective structures. It is also recommended that the most promising layered structure concepts be tested experimentally, first on a small scale in the laboratory, then at a much larger scale in the field.

REFERENCES

1. Robert E. Crawford, et al, Protection From Nonnuclear Weapons, Technical Report No. AFWL-TR-70-127, Air Force Weapons Laboratory, Kirtland Air Force Base, New Mexico, (1971).

2. Fundamentals of Protective Design for Conventional Weapons. Department of the Airmy, Waterways Experimentation Station, Corps of Engineers, Vicksburg, MS, (1984).

3. Reuben Eytan, Design of Layered Structures Against Conventional Weapons, Proceedings of the Second Symposium on the Interaction of Nonnuclear Munitions with Structures, Panama City Beach, FL, pp. 68-73, April 15-18, (1985).

4. P. Balags and B. Vretblad, Model Tests on Composite Slabs of Light Gauge Metal and Concrete Subjected to Blast Loading, Proceedings of the Second Symposium on the Interaction of Nonnuclear Munitions with Structures, Panama City Beach, FL, pp. 143-148, April 15-18, (1985).

5. K. P. Chong, K. A. Wang, and G. R. Griffith, Analysis of Continuous Sandwich Panels in Building Systems, Building and Environment, Vol. 44, pp. 125-130, (1979).

6. K. H. Ha, R. Hussein, and P. Fazio, Analytic Solutions for Continuous Sandwich Plates, ASCE, Journal of the Engineering Mechanics Division, Vol. 108, No. EM2, pp. 228-241, (1982).

7. F. J. Plantema, Sandwich Construction, John Wiley & Sons, Inc., New York, NY, (1966).

8. S. Rizzo and P. Fazio, Sandwich-Panel Assemblies: Analytical Model, ASCE, Journal of the Structural Division, Vol. 109, No. 11, pp. 2715-2732, (1983).

9. J. S. Rhinehart, Stress Transients in Solids, Santa Fe, New Mexico, Hyper Dynamics, (1975).

10. D. R. Colthorp, S. A. Kiger, K. P. Vitayaudom, and T. J. Hilferty, Blast Response Tests of Reinforced Concrete Box Structures, Proceedings of the Second Symposium on the Interaction of Non-Nuclear Munitions with Structures, Panama City Beach, FL, pp. 95-100, April 15-18, (1985).

11. R. J. Wasley, Stress Wave Propagation in Solids, New York, New York, Marcel Dekker, Inc., (1973).

12. H. Kolsky, Stress Waves in Solids, New York, New York, Dover Publications, Inc., (1963).

13. J. Zukas, T. Nicholas, H. Swift, L. Greszczuk, and D. Curran, Impact Dynamics, John Wiley and Sons, (1982).

14. D. G. Fertis, Dynamics and Vibrations of Structures, Krieger Publishing Company, pp. 427-463, (1984).

15. W. E. Baker, Explosions in Air, Southwest Research Institute, (1983).

16. D. R. Colthorp, K. P. Vitayaudom, and S. A. Kiger, NATO Semi-hardened Facility Design Criteria Improvement, Final Report, Air Force Engineering and Services Center, Tyndall Air Force Base, Florida, (1985).

17. ADINA - A Finite Element Computer Program for Automatic Dynamic Incremental Nonlinear Analysis, Report AE 81-1, ADINA Engineering, Inc., Watertown, MA, (1983).

18. ADINA System Verification Manual, Report AE 83-5, ADINA Engineering, Inc., Watertown, MA, (1983).

19. K. J. Bathe, On Some Current Procedures and Difficulties in Finite Element Analysis of Elastic Plastic Response, Computers and Structures, Vol. 12, pp. 607-624, (1980).

20. F. L. DiMaggio and I. S. Sandler, Material Model for Granular Soils, Journal of the Engineering Mechanics Division, ASCE, 97 (EMS), pp. 935-949, (1971).

21. K. J. Bathe, Finite Element Procedures in Engineering Analysis, Prentice Hall, Inc., Englewood Cliffs, NJ, (1981).

22. M. H. Klaus, Response of a Panel Wall Subjected to Blast Loading, Computers and Structures, Vol. 21, No. 1/2, pp. 129-135, (1985).

ACKNOWLEDGEMENTS

This work was sponsored by a research grant from the Air Force Office of Scientific Research. Special appreciation is extended to Mr. Jack Hayes, Senior Scientist, Engineering Research Division, Engineering and Services Laboratory, Tyndall AFB, for his assistance and fruitful discussions.

FINAL REPORT NUMBER 74
REPORT NOT RECEIVED IN TIME
WILL BE PROVIDED WHEN AVAILABLE
Dr. Walter E. Trafton
760-OMG-053

1986 USAF-UES MINI-GRANT

RESEARCH PROGRAM

Sponsored by the

AIR FORCE OFFICE OF SCIENTIFIC RESEARCH

Conducted by the

UNIVERSAL ENERGY SYSTEMS, INC.

FINAL REPORT

CASE STUDY ANALYSES

OF MILLIMETER WAVE LENGTH ATTENUATION

Prepared by: Dr. LARRY VARDIMAN

Academic Rank: Associate Professor

Department and University: Dept. of Physical Science
Christian Heritage College
El Cajon, CA 92021

Research Location: Christian Heritage College
El Cajon, CA 92021

Date: 31 December 1986

Contract No.: F49620-85-C-0013/SB5851-0360
Subcontract No.: S-760-0MG-010

CASE STUDY ANALYSES OF MILLIMETER WAVE LENGTH ATTENUATION

by

Larry Vardiman

ABSTRACT

Four cases on 9 January 1980 from Sierra Nevada storms were studied for attenuation of a 28 GHz (1.05 cm) signal through cloud and precipitation. A radiometer was positioned on the Sacramento Valley floor just upwind of the central Sierra. It measured the signal strength from a beacon on the COMSTAR satellite. Microphysics data from a cloud physics aircraft were used to calculate attenuation along the same path and compare with the radiometer.

Measured and calculated values of attenuation show poor correlation. Two reasons for the differences are apparent: 1) aircraft flights only slightly divergent from the path between the satellite beacon and radiometer produce significantly different results, even in relatively uniform precipitation and 2) the effects of melting hydrometeors on attenuation are highly variable compared to the simple algorithms used in these calculations.

It is recommended that future data acquisition of this type be made in such a way that microphysics data be more representative of conditions in the same path over which attenuation measurements are made. It is further recommended that the complex effects of hydrometeor melting on millimeter wave attenuation be more completely treated.

I. INTRODUCTION

The United States Air Force (USAF) is concerned about the effect of storms on the transmission of millimeter wave-length signals from satellite-to-ground and ground-to-ground systems. In the frequency band from 20 to 100 GHz the effect of rain and snow can be important. In this frequency band the wave length of the signal is on the same order as the size of the precipitation particles. A combination of Mie and Raleigh scattering theory applies and consideration of both ice and water phases must be made. Descriptions of the effects of hydrometeors on millimeter wave communication in the atmosphere have been reported by Hogg (1968), Hogg and Chu (1975), Tiffany (1983), and Ebersole et. al. (1985). Although the theory of attenuation of radio waves through a scattering medium has been fairly well developed, the simultaneous measurement of attenuation and in-situ particle distributions over long path lengths in precipitating events is relatively scarce.

As part of a summer appointment to the Air Force Geophysics Laboratory (AFGL) to study attenuation in 1985, I made use of measurements taken by the Sierra Cooperative Pilot Project (SCPP) during the winter of 1979-80 in northern California (See Fig. 1). The purpose of the original measurements was to develop a remote sensing technique for identifying supercooled liquid water in support of cloud-seeding experiments in the Sierra Nevada. Cloud liquid measurement by microwave sensors is described by Snider, Burdick, and Hogg (1980), Snider, Guiraud, and Hogg (1980), and

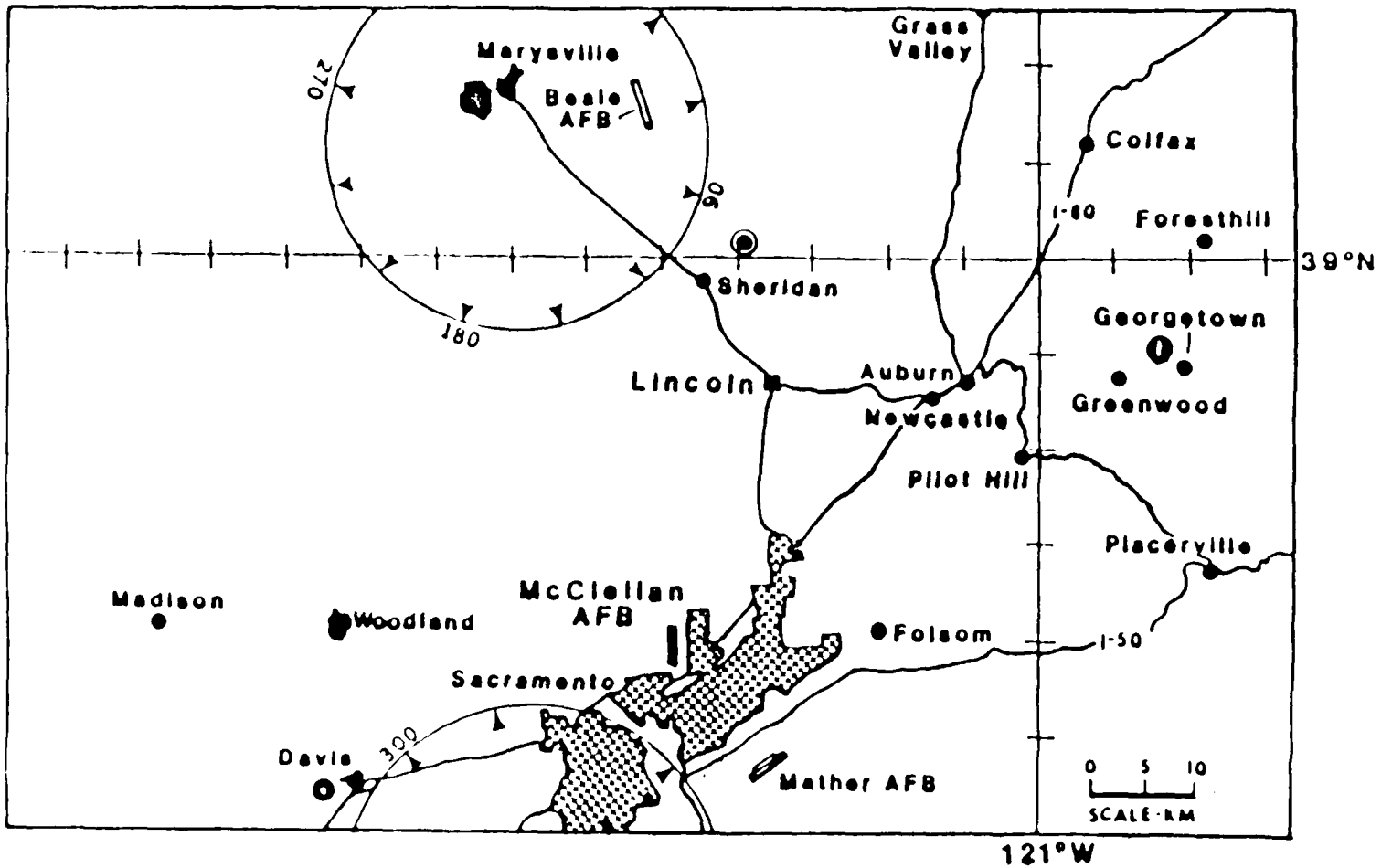

Figure 1. Map of SCPP research area near Sacramento, California. The research aircraft was hangared at McClellan AFB, the radar and radiometer located at Sheridan, California, and aircraft flights made southeastward from Sheridan over the foothills of the Sierra Nevada.

Hogg et. al. (1983). The description of the deployment and analysis of the radiometer system in the SCPP is given in Snider and Hogg (1981) and the SCPP Data Inventory (1979-80). In summary, the system was a dual channel radiometer which measured the signal strength of the 28.56 GHz beacon on the COMSTAR Satellite (see Cox, 1978) while simultaneously measuring the brightness temperature of the cloud and precipitation particles along the same path at the same frequency.

A full compliment of meteorological and cloud physics measurements were made in association with the radiometer data (see the SCPP data inventory 1979-80). The most important measurements for the purposes of this study were the microphysics measurements made with the University of Wyoming cloud Physics aircraft. Instrumentation flown on this aircraft are given in Appendix A and discussed in Cooper (1979) and Gordon and Marwitz (1984). Analysis and interpretation of data in support of the SCPP are reported in Stewart and Marwitz (1980), Pace (1980), Marwitz et. al. (1981), Stewart and Marwitz (1982), Bradford (1983), Stewart, Marwitz and Pace (1984), and Gordon and Marwitz (1985). The terrain and typical flight patterns flown in the SCPP are shown in Figures 2 and 3.

It was decided that these data sources should provide a unique opportunity to compare the direct measurement of signal attenuation through precipitating storms with the attenuation calculated from the particle distributions measured in situ. The conclusions from the study by Vardiman and Peterson (1985) were that measured and calculated values of attenuation in California

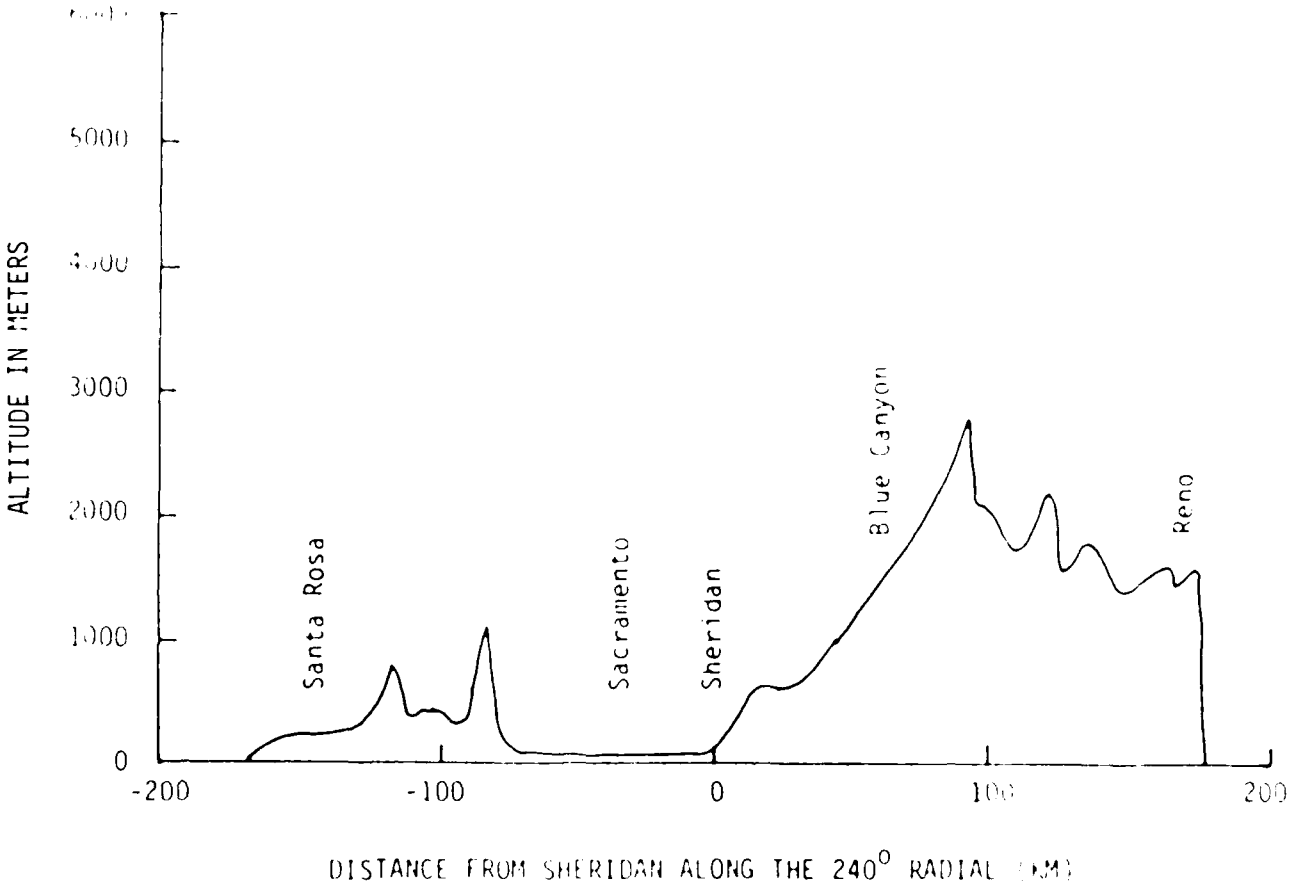

Figure 2. Terrian Profile near Sheridan, California

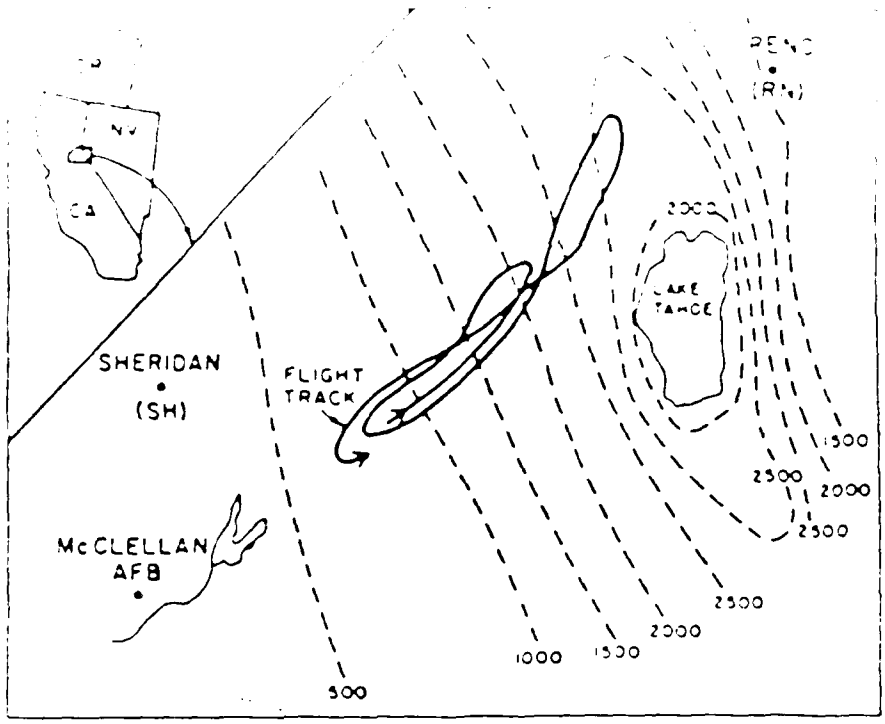

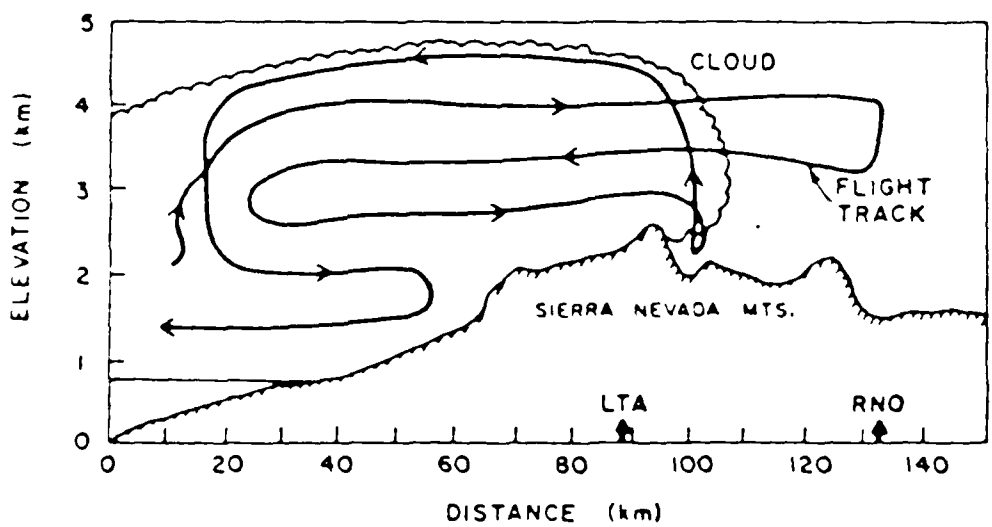

Figure 3. Typical flight patterns flown in the SCPP for research other than attenuation studies.

storms agreed well for the weak precipitation case. However, for two heavier cases the relative errors were large and of opposite sign. The explanation for these results was that the flight tracks for the two heavier cases were inadequate to characterize the hydrometeor distributions in the radiometer beam. In one case the track was flown in such a way that the rain was probably underestimated near the ground. In the other case, the vertical resolution was poor and the rain at lower levels was probably overestimated because of flight deviations to penetrate heavier precipitation regions.

The recommendations from Vardiman and Peterson (1985) included suggestions that two or three additional cases from the SCPP be analyzed with more severe constraints placed on case selection, particularly in regard to flight paths. In addition, precipitation rates calculated from the microphysics data should be calibrated by comparing with measured precipitation rates in the SCPP gage network.

These recommendations were recognized to be useful by the USAF and a follow-up contract awarded to pursue this line of research in 1986. This report describes the results of that additional work.

II. OBJECTIVES OF THE RESEARCH EFFORT

The objectives identified under this contract were that:

A. Precipitation gage data be used to calibrate the calculated precipitation rates.

B. Comparisons of measured and calculated attenuation be made for three time periods from 9 January 1980 using the SCPP data.

C. Travel be accomplished to Sacramento, California and Boston, Massachusetts to confer on similar research efforts.

D. An evaluation of the merits of analyzing the recent radiometer data from the SCPP for attenuation in snow above the melting level be made.

III. ANALYSIS

A. Identification of Case Studies

The case studies analyzed in the previous work led to the conclusion that flight paths must be as close as possible to the path between the satellite beacon and the radiometer. The assumption had been made earlier that the stratiform cloud conditions upwind of the Sierra Nevada were relatively uniform horizontally and a transect of the cloud close to the radiometer would be adquate. However, the results indicated otherwise. In addition, two of the three cases selected earlier did not have heavy precipitation or strong attenuation.

In reviewing the cases available in the SCPP, it was found that four transects occurred on 9 January 1980 which were oriented close to the beacon path, strong attenuation was observed by the radiometer, and relatively heavy precipitation fell. The meteorological conditions changed rapidly throughout the day so that the four transects represented unique situations.

Two of the cases occurred in the morning from 1938 to 1950 Z (Case 1) and from 1950 to 2006 Z (Case 2). These two cases are close in time because the microphysics aircraft flew up the beacon path and then immediately flew nearly back down the same path on a descent into McClellan AFB, where the plane was hangared. The other two cases occurred in the afternoon from 2208 to 2222 Z (Case 3) and from 2335 to 2345 Z (Case 4). The first of these was on climbout from McClellan AFB and the other up the beacon path. In reality, only Case 1 and Case 4 satisfy

the total criteria of this study. The other cases were included because they were the next best data available from the SCPP.

B. Meteorological Conditions

The meteorological conditions during the flights could be characterized by a general overcast condition in the morning with moderate, uniform precipitation covering the entire region. In the afternoon, precipitation was heavier but also more showery. The 0 degree Centigrade level was at about 2 km, winds were from the south/southeast at the surface veering to the southwest aloft, and embedded convection was present. The precipitation rate increased slowly throughout the day from less than 3 mm/hr in the morning to over 8 mm/hr near the end of the day. Convection became more prevalent in the afternoon with banded north/south precipitation features showing on the radar. A complete meteorological discussion with time cross sections, upper air and surface charts, satellite pictures, and soundings generated by Rhea et. al. (1980) may be found in Appendix B.

C. Reduction of Aircraft Data

The processing of aircraft microphysics data was a sizable task. Over 200 variables were available for each second of flight during the nearly 8 hours of archived aircraft data recorded on this day. This massive amount of data was reduced to selected variables and flight times of interest by several programs written previously on the CYBER computer at AFGL. These programs were transferred to the CRAY supercomputer at the University of California at San Diego (SDSC) where they were modified and run using the 9 January 1980 data. A Zenith Z-100

microcomputer was purchased and used on-site at Christian Heritage College to access the GDSC by local phone line.

Averages of many of the variables were made over time intervals determined by the aircraft flight patterns and sample volumes of the hydrometeor probes. The selection of appropriate averaging times was an integral part of the analysis. If the time interval is too short, an insufficient number of particles is sampled in the large size bins of the hydrometeor probes, causing a significant error. If the time interval is too long, the vertical resolution in computed variables is too great. An averaging interval of 30 seconds was selected for the 9 January case.

The end product desired from the aircraft microphysics data was a vertical distribution of cloud and hydrometeor equivalent water contents for the four cases. It was initially assumed during the previous study that the variables calculated by the University of Wyoming would be adequate, but after some effort to use their values it was realized that the particle spectra from the hydrometeor probes would have to be used to calculated our own. The first effort at calculating hydrometeor contents used only the 2DC PMS probe. This was an improvement, but the sample volume for the large bins was inadequate. Therefore, PMS-2DP size spectra were then included. With this inclusion of the 2DP probe, however, hydrometeor contents were only stable if bins which contained less than 10 particles in a sample were excluded. The University of Wyoming data provides two type of size spectra for each hydrometeor probe. The first rejects artifact images

caused by water "streaking" off the edges of the probes. The second rejects images, in addition to the "streakers", which do not have a certain degree of circularity. For a full discussion of the criteria for rejection of artifacts, see Cooper (1978). In looking at the particle images, we discovered that some of them were gigantic (up to 8 cm) and appeared to be either large, wet snowflakes or artifacts. By using the second type of spectra these peculiar particles were rejected, thus not affecting the calculation of water contents. Such particles, if they are real however, could have an important effect on attenuation because of their large size. The greatest degree of uncertainty in making these calculations occurs in the melting layer because of the difficulty in identifying particle type, shape, and size.

The calculation of liquid water content below the melting layer is quite straightforward since the particles are mostly spherical. In the melting layer and above, however, the particle shape and density are highly speculative causing a great degree of uncertainty in calculating equivalent water content. After several unsuccessful attempts to calculate water contents using the size to mass conversion equations of Nakaya (1954), we elected to use the conversion equations developed by Berthel (1981) at AFGL. We used his plate family equation for the 9 January 1980 cases. It is obvious when looking at the particle images that a mixture of particle types is present and no single equation will properly apply to any given case.

The assumption was made in these calculations that all

particles above the 0 degree Centigrade level were ice crystals and all particles below were water drops. In Sierra Nevada storms relatively few water drops occur above the 0 degree Centigrade level because of the abundance of ice crystals, which will quickly nucleate any supercooled drops. The assumption above the 0 degree Centigrade level is probably quite good. Below the 0 degree level, however, melting snow can take several hundreds of meters to completely melt, forming liquid drops. The assumption that all particles below the 0 degree Centigrade level are liquid probably overestimates the liquid water content. However, attenuation based on this inflated hydrometeor liquid water content may not be far from reality because an electromagnetic wave "sees" a water-coated ice particle, almost as if it were a spherical water drop of the same size. Therefore, this assumption should be appropriate for use in calculating attentuation even though the actual hydrometeor liquid water content would probably be less.

Cloud liquid water content was measured by the Particle Measuring System Forward Scattering Spectrometer Probe (FSSP) and is assumed to be liquid throughout the entire depth of the cloud. Because the cloud liquid water contents in Sierra Nevada storms are seldom greater than .1 gm/m , the integration of the FSSP spectra is considered to be more accurate than the Johnson-Williams liquid water content measurements.

D. Development of a Simple Attenuation Model

The attenuation of an electromagnetic signal in cloud and precipitation as a function of temperature and wavelength has

been reported by Gunn and East (1954). Snider, Burdick and Hogg (1982) fit a quadratic equation to this data to develop the attenuation coefficient for cloud water at 28.56 GHz as a function of temperature.

$$\alpha_W(T) = (43.164 - .287T + .000482T^2)LWC \qquad (1)$$

where: α_W = dB/km

LWC = gm/m^3

By fitting the data from Gunn and East (1954) or the data from Tiffany (1983) to a log-log plot the attenuation coefficent for rain at 28.56 GHz can be found.

$$\alpha_R = .21\ R_r^{.9666} \qquad (2)$$

where: α_R = dB/km

R_r = mm/hr

Although most investigators have discounted the contribution of snow on attenuation because of its low index of refraction, a recent analysis of data from the SNOW experiments by Ebersole et. al. (1985) has indicated that "attenuation due to falling snow will be significant at some frequencies if the path length is several kilometers." Fitting a straight line through the center of Ebersole's data gives the following equation for the attenuation coefficient of snow at 35 GHz.

$$\alpha_S = .6\ IWC^{.9445} \qquad (3)$$

where: α_S = dB/km

IWC = gm/m^3

Note, that Ebersole's attenuation coefficient for snow is in terms of a mass density rather than a precipitation rate. This formulation would seem to be more appropriate for rain as well, since the estimate of precipitation rates from aircraft or radar data introduce additional error due to uncertainties in fall velocity.

If we can now assume that we have accurate attenuation coefficients, we need only multiply the appropriate value of attenuation coefficient for cloud, rain, and snow by the thickness of each layer in the storm. The total vertical attenuation is then the sum of all layers. Since the radiometer was "looking" through the storm at an angle of 32.6 degrees from the horizontal, the actual attenuation along the beam is the vertical attenuation divided by the sine of 32.6 degrees. This model does not take into account the attenuation due to water vapor.

If γ is the attenuation in each layer due to the cloud water, rain, and snow, then the contribution of each layer to the brightness temperature seen by the radiometer is:

$$T_B = (1 - \exp(-\gamma/4.343)) T_M \qquad (4)$$

γ [illegible]

T_M [illegible]

T_M is the mass weighted temperature of each layer in the storm. The total brightness temperature seen by the radiometer is then the sum of the contributions from each layer.

A computerized model based upon the preceeding discussion was formulated to calculate the attenuation and brightness temperature in each layer and find the totals as "seen" by the radiometer. Listings of the programs used in the processing [illegible], VRTDIST, VRTPLT, FALL, SUM, SFSUM, SFRGPLT, FLPSUM, TIMESORT, ATTNPLT) are shown in Appendix C. Specific data used in various stages of the programs are shown in Appendix D.

E. Flight Paths and Radar Features

The flight paths taken by the aircraft during the four cases are shown in Figures 4-7. The flight paths are superimposed over plan position indicator (PPI) displays of the radar reflectivities seen from the Sheridan radar site coincident with the radiometer. In Case 1 the aircraft climbed as rapidly as possible (1000 feet/minute) along the direction of the beacon from about 3000 feet to 15,000 feet. In Case 2 the aircraft descended gradually from 15,000 feet to about 1000 feet over a path south of the beacon. In Case 3 the aircraft ascended from 1000 feet to about 14,000 feet on climbout from McClellan AFB. In this case the path was actually perpendicular to the beacon. In Case 4 the aircraft ascended from about 3000 feet to 15,000 feet, part way

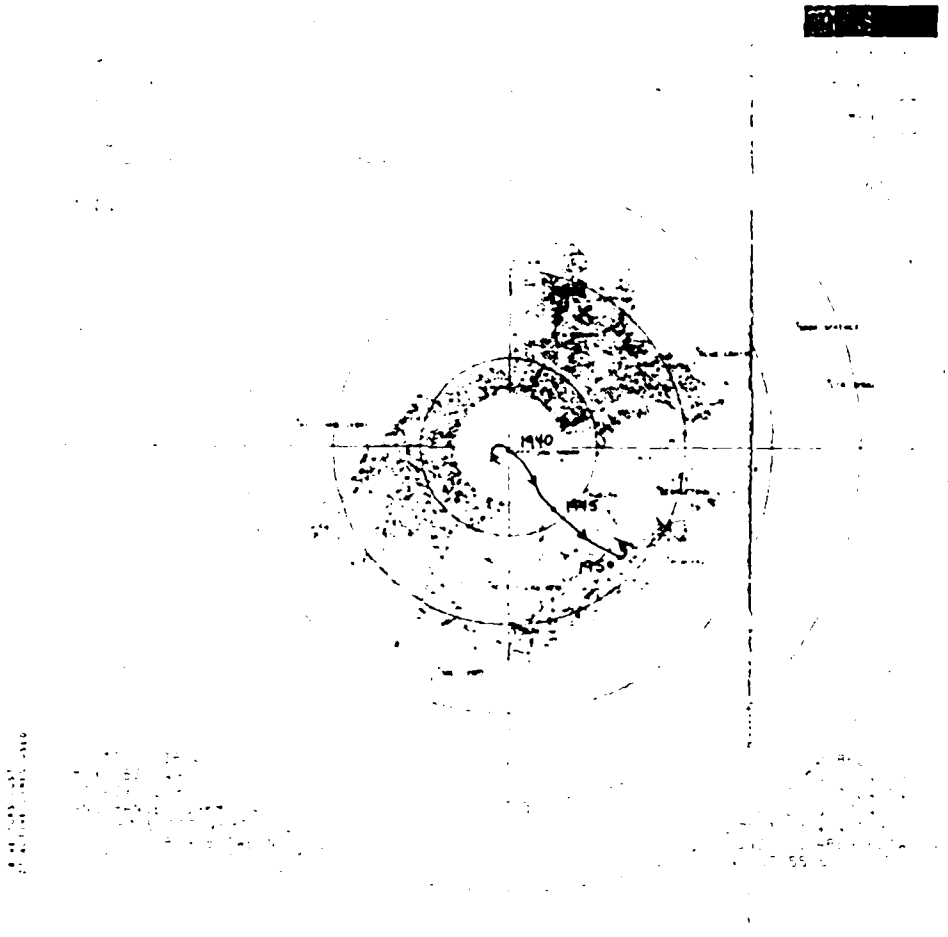

Figure 1. PPI display for 1946Z on 9Jan1980 (Case I). Elevation angle 1.6° and contour intervals of 50km. Intensities are in DBZ and displayed with symbols at the top of figure.

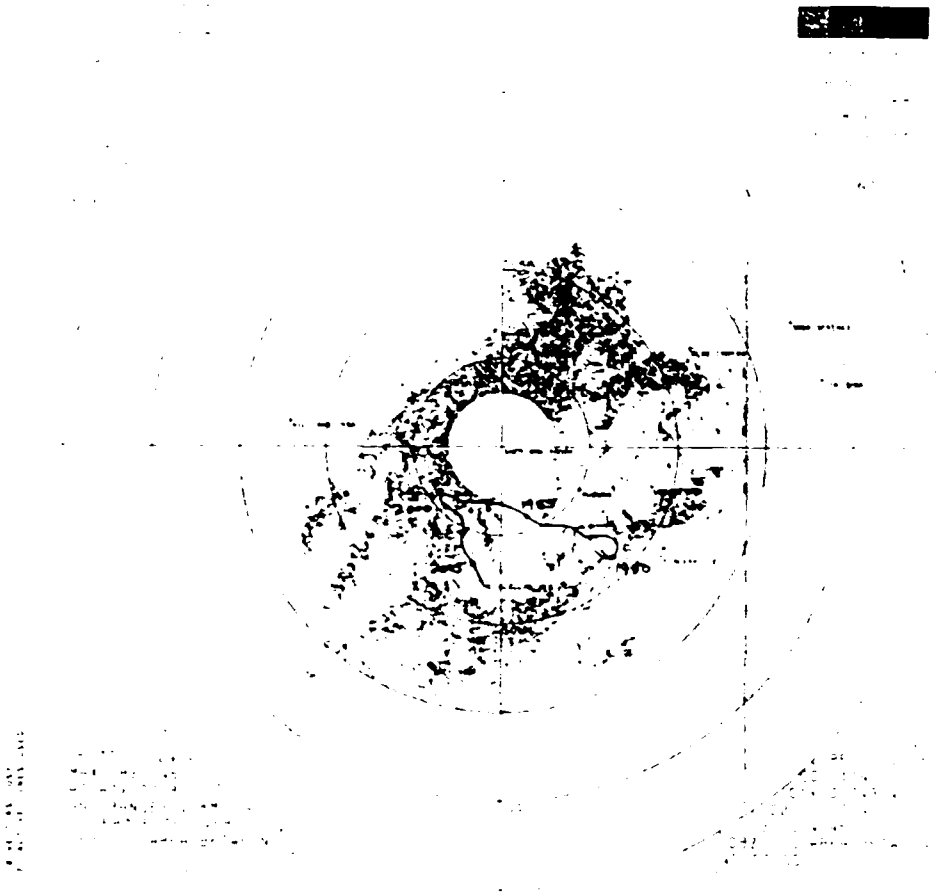

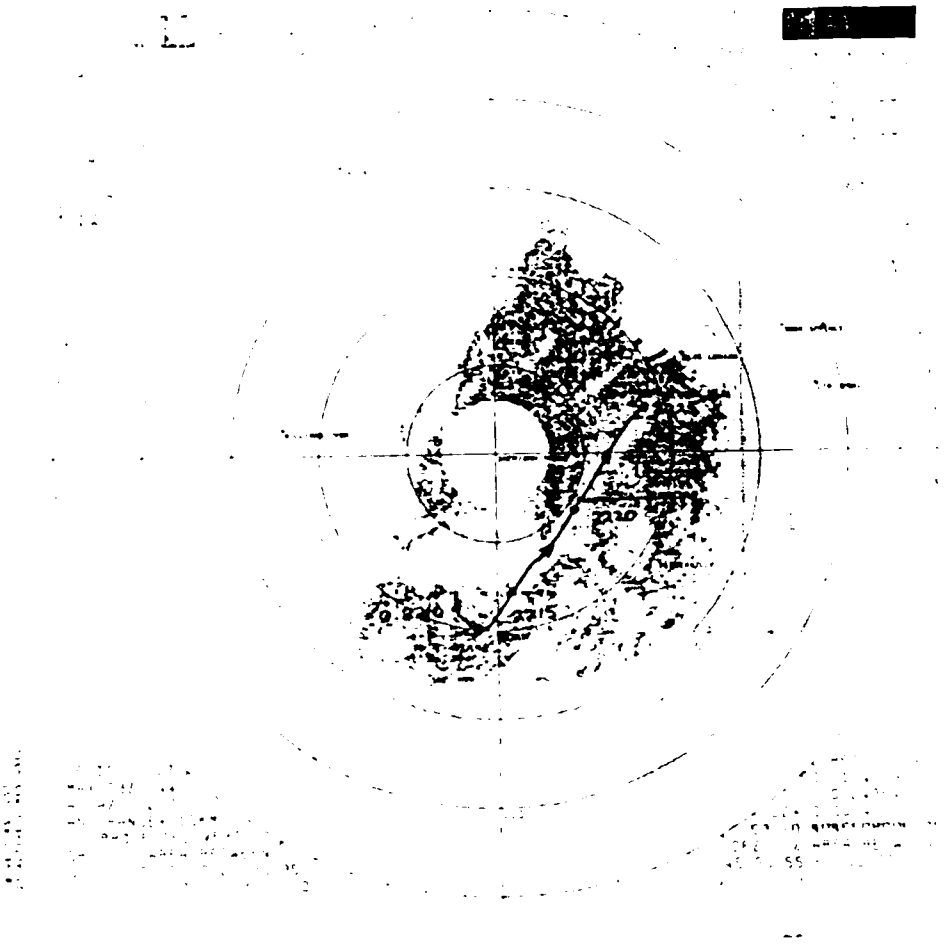

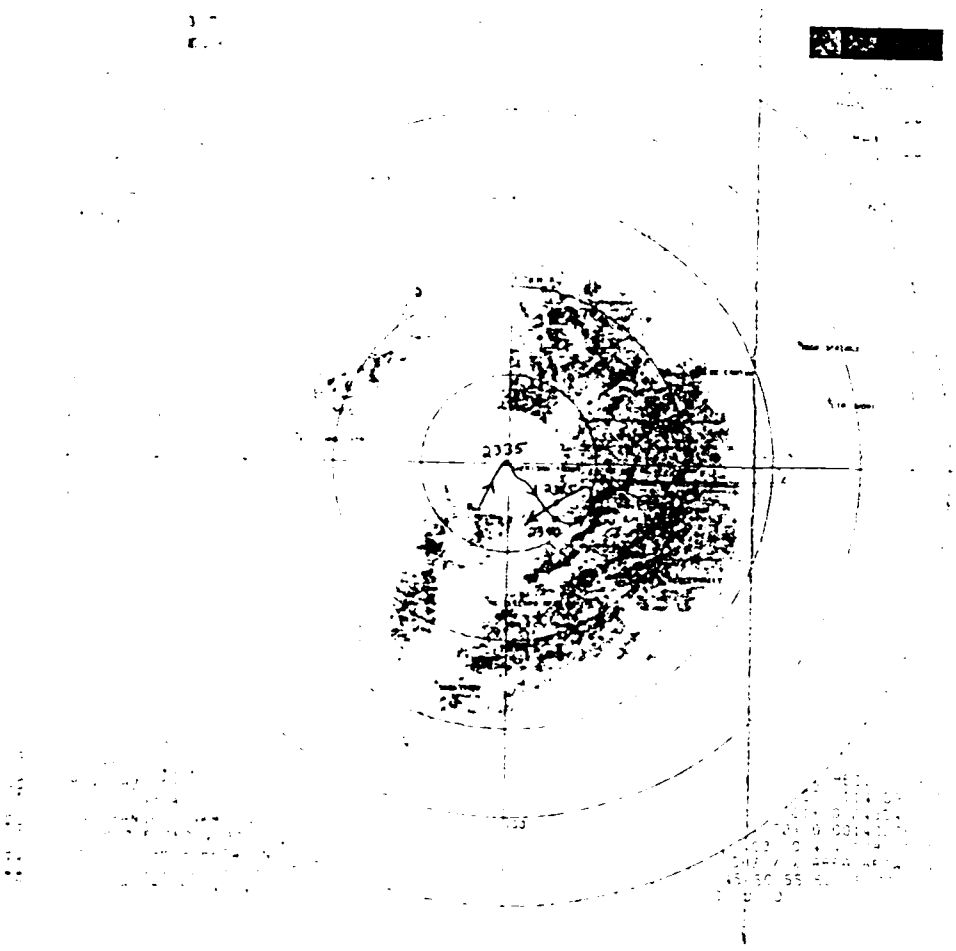

[illegible] display for 2312 on 90ant95b (Case 3).

[illegible] the upper part [illegible]

The path between the satellite and the radiometer was inclined at an angle of 22.5 degrees to the horizontal. This meant that the beacon path reached an altitude of 15,000 feet above the ground at a distance of about 8 kilometers from the Sheridan radar site. On the other hand, the aircraft typically took about 40 km of horizontal distance to climb to 15,000 feet altitude above the ground.

The reflectivities through which the aircraft flew in all four cases were generally 20 dBZ with some patches to 30 dBZ. In Case 4 the centers of some cells near the flight path exceeded 40 dBZ. Note that even though the precipitation was relatively uniform and no major features such as strong bands and intense cells were present in the PPI displays, considerable fine structure was evident. The convective instability in the time cross sections of Appendix B is evident in the weak, small-scale cells shown on the radar. This structure is important because the paths measured by the radiometer and the aircraftwere different. Since the precipitation is obviously not completely uniform, any differences in the two paths will be reflected in a comparison of measured and calculated attenuation. A more complete sequence of radar displays is given in Appendix E.

F. Particle Images and Distribution

Figure 8 shows typical particle images taken by the 2-D Knollenburg probes on the University of Wyoming aircraft. This particular display was from Case 1 when the aircraft was at an

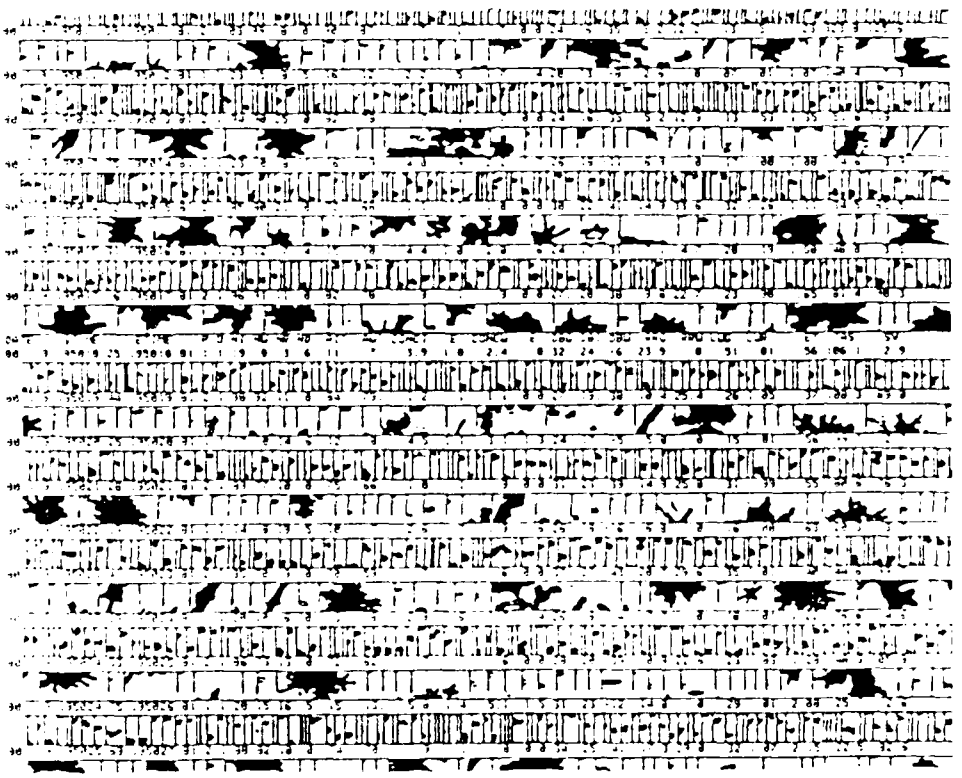

Figure 8. Typical hydrometeor images from Knollenberg 2D- and 2D-P probes at 1950Z on 22Jan1969. Ice crystals observed at an altitude of about 5000 [illegible] and a temperature of -17°

altitude of about 5000 feet and a temperature of -17 degrees centigrade. The small images are from the 2D-F probe and the larger from the 2D-C probe. Images were recorded electronically from alternate probes as the memory buffers were filled. The maximum lateral dimension of the 2D-C probe is 800 micrometers and the 2D-F probe 6.4 millimeters. The numbers shown between the images are date/time groups and value of variables calculated from the images such as particle concentrations, average sizes, and precipitation rates.

Appendix F contains several sets of images at different altitudes for each of the four cases. In addition, particle size distributions representative of the integrated path for each case are also displayed.

G. Radiometer Data

The attenuation measured by the radiometer and the precipitation observed at the Sheridan radar site are shown in Figure 7. The time period runs from 1600 to 2400 Z on 9 January 1980. Cases 1 and 2 occurred during the maximum attenuation event of 8.7 dB observed near 2000 Z. This attenuation means that less than 15% of the original signal from the beacon was received by the radiometer. A maximum in precipitation of 6 mm/hr was also observed near this time.

Cases 3 and 4 occurred when both the attenuation and the precipitation at the Sheridan site were less, although we will find later that the precipitation rate was actually greater on the slopes of the Sierra Nevada to the east. The fluctuations in the attenuation again attest to the showery nature of the

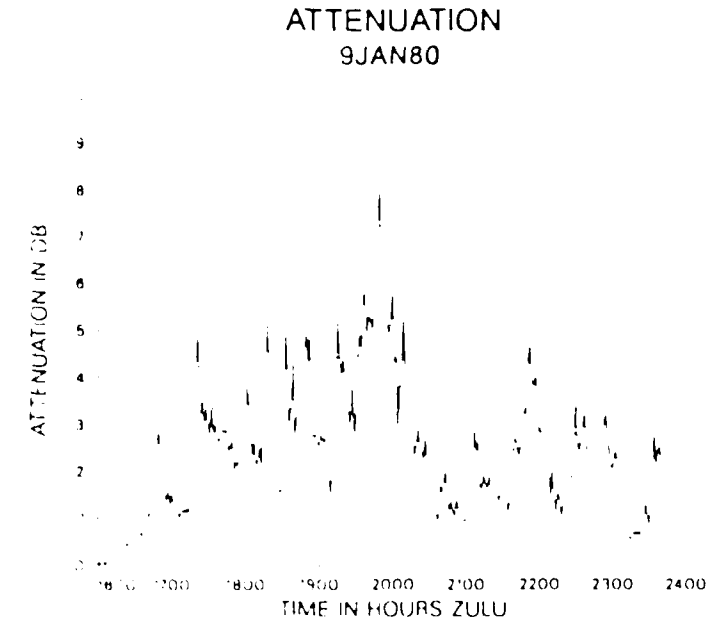

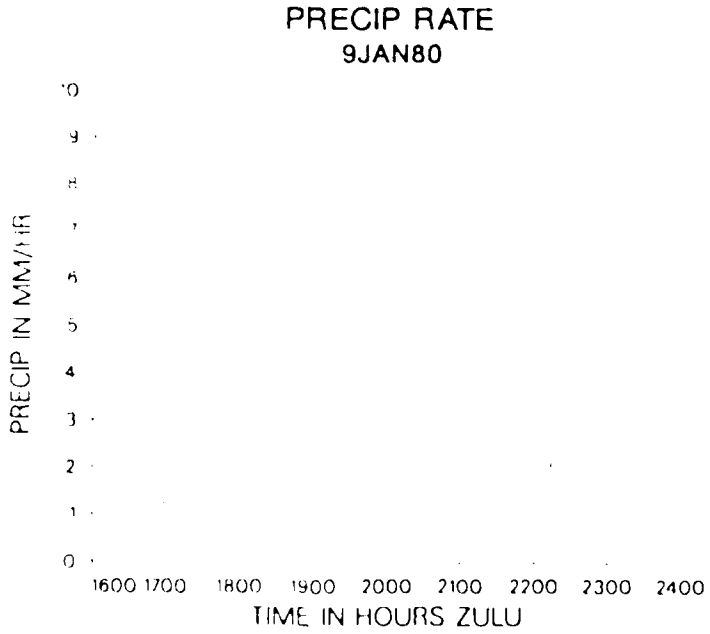

Figure 9. Attenuation of satellite beacon signal and precipitation rate observed at Sheridan, California on 9Jan1980.

precipitation.

H. Precipitation Data

Figures 10, 11, 12, and 13 show the horizontal distribution of average precipitation rates over the SCPP research area during the four cases. The average precipitation rate during an hour containing each case is shown for approximately 50 gage sites on the west side of the Sierra Nevada. The average value for gages in a small region under and downwind of the aircraft flight paths is shown with dashed lines. Notice that this average value increases throughout the day, from 1.3 mm/hr to 7.3 mm/hr.

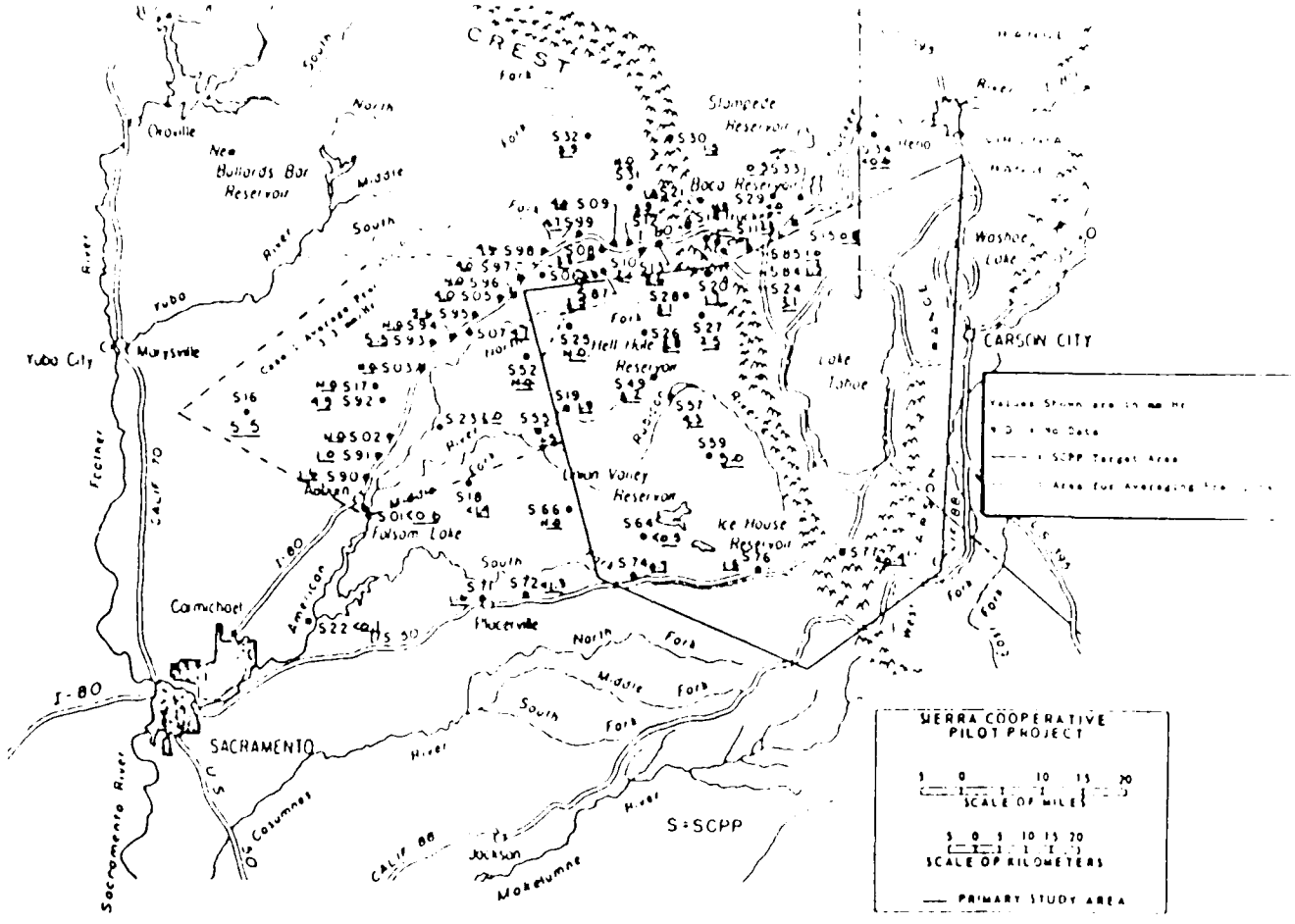
CREST
Stampede Reservoir
Boca Reservoir
Hell Hole Reservoir
Lake Tahoe
Loon Valley Reservoir
Ice House Reservoir
Folsom Lake
Auburn
Roseville
Carmichael
SACRAMENTO
Marysville
Yuba City
Oroville
New Bullards Bar Reservoir
Washoe Lake
CARSON CITY
I-80
Sacramento River
S=SCPP
SIERRA COOPERATIVE PILOT PROJECT
SCALE OF MILES
SCALE OF KILOMETERS
PRIMARY STUDY AREA

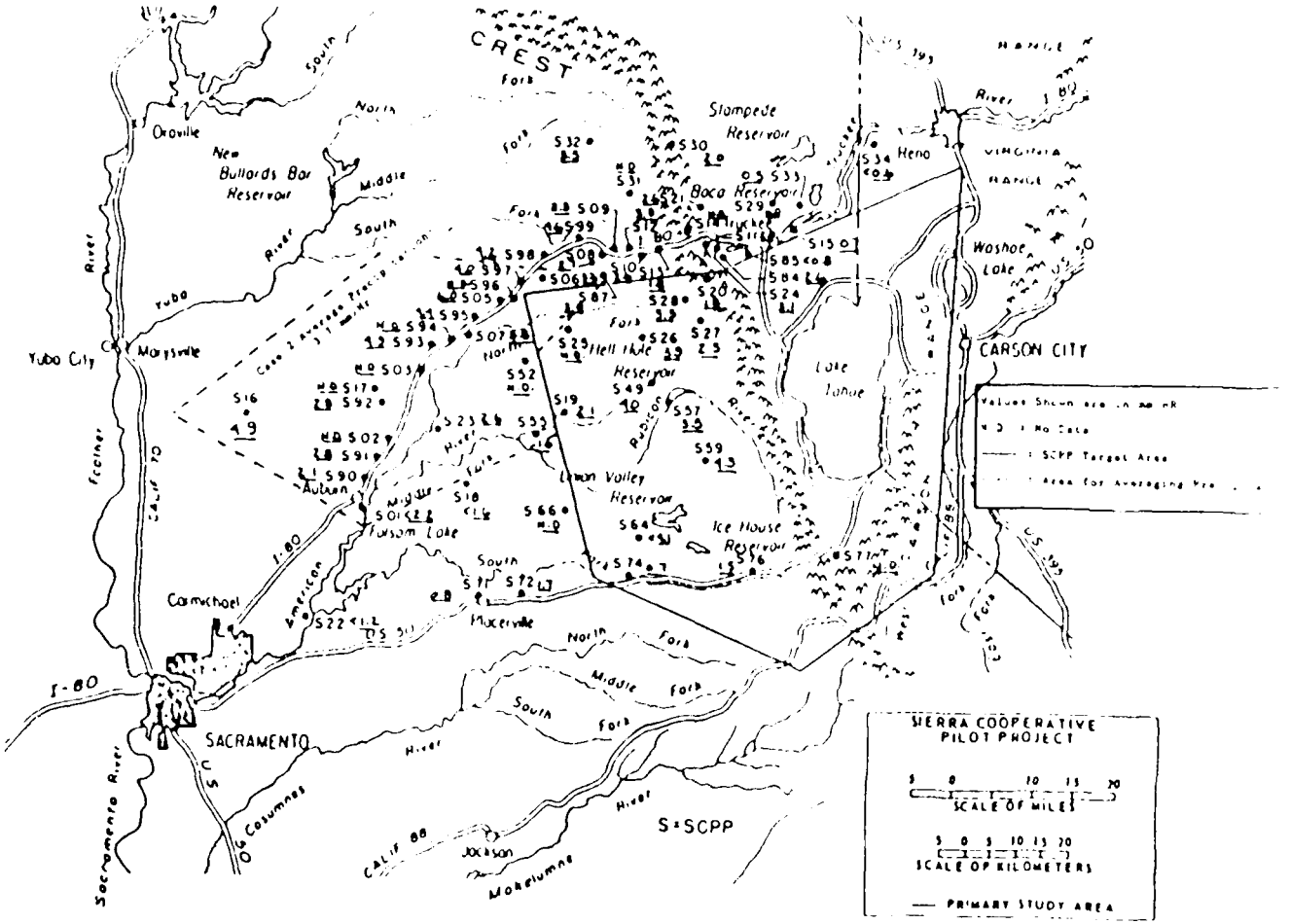

Figure 11

CASE 2 010980 1930Z TO 2030Z

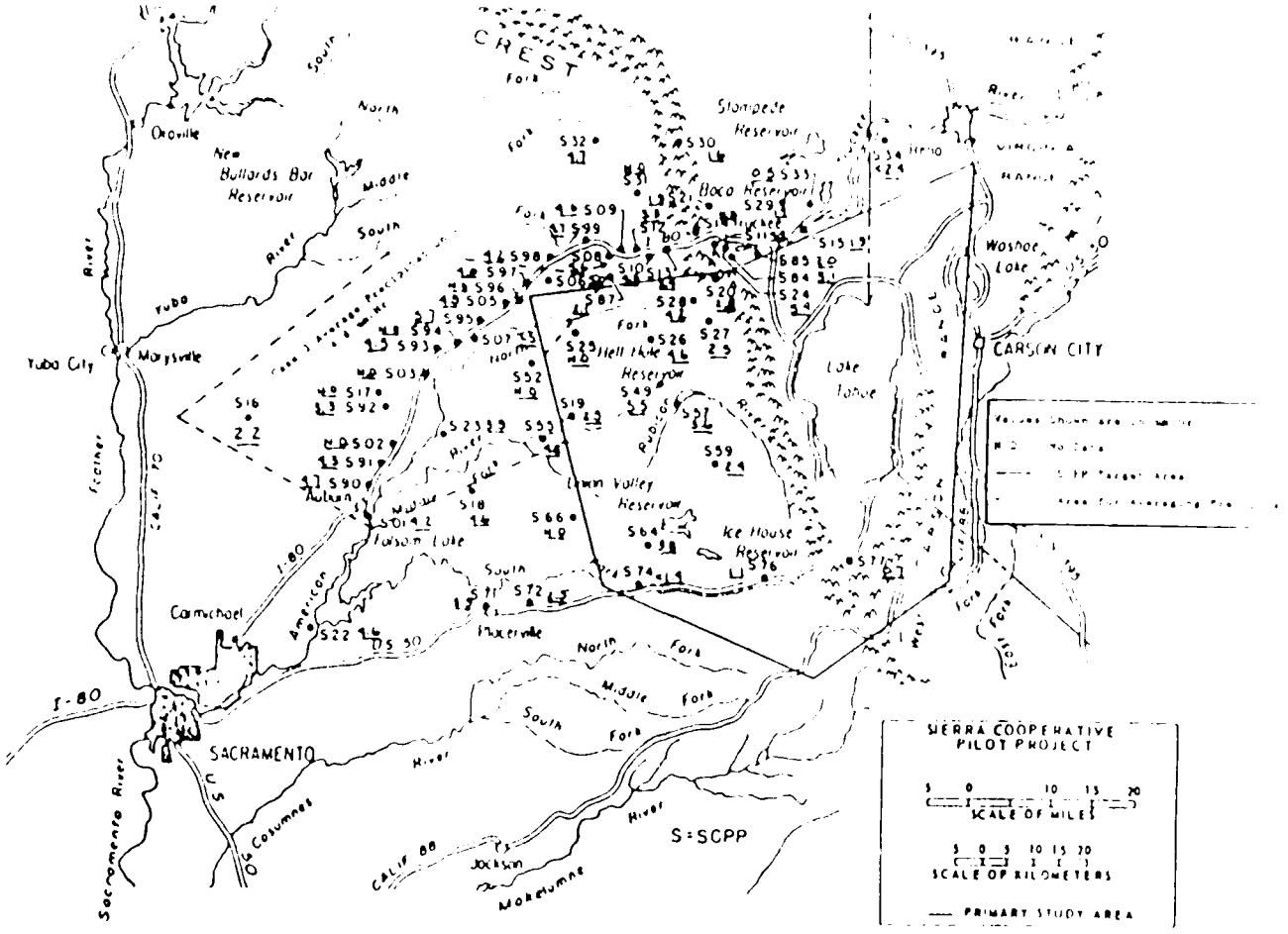

CASE 3 010980 2145Z TO 2245Z

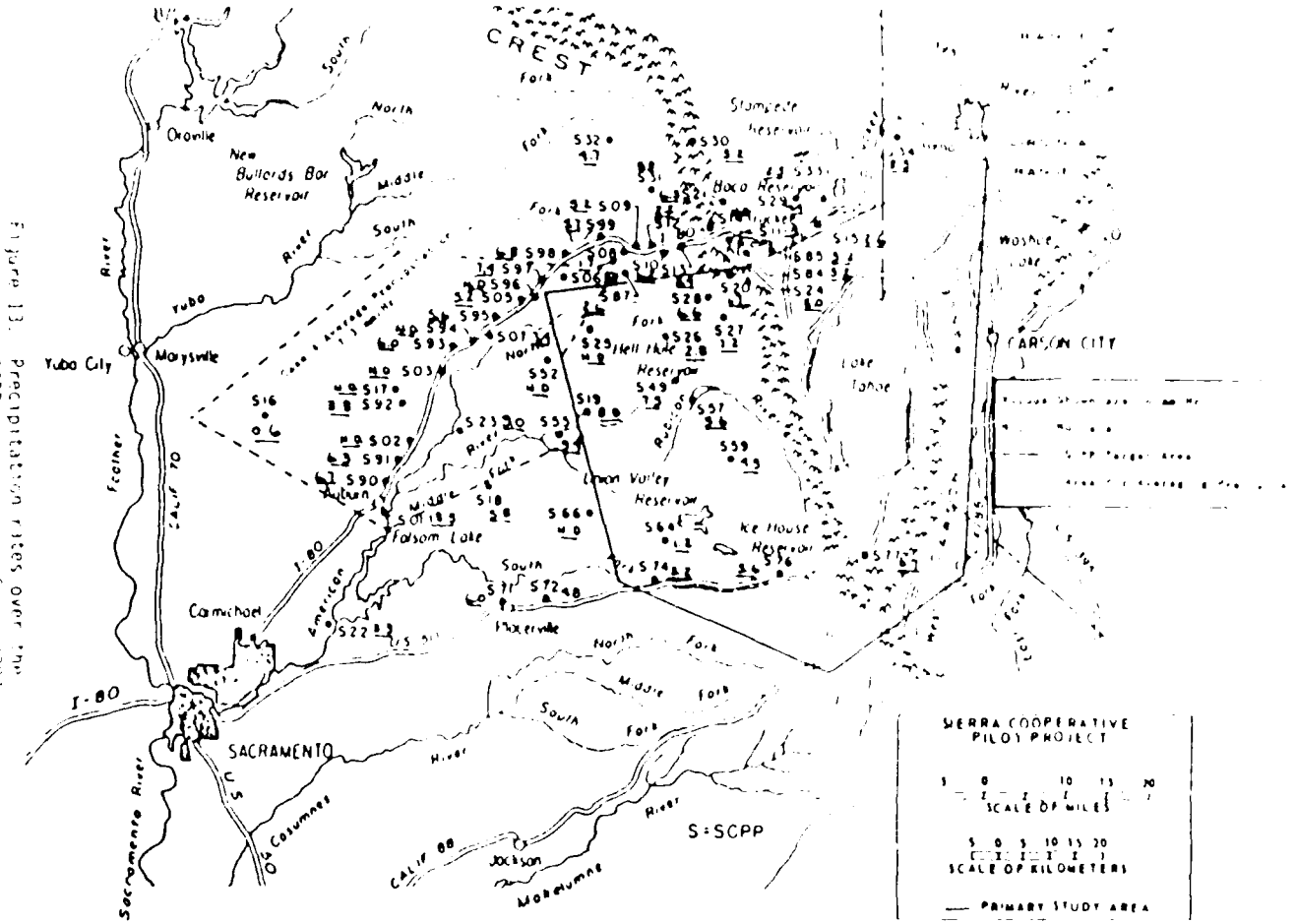

Figure 13. Precipitation rates over the SCPP research area from 1800Z to 2400Z on 9Jan1980 (Case 4)

CASE 4 - 010980 2300Z TO [illegible]

IV. RESULTS

A. Vertical Hydrometeor Distributions

Figures 14-21 show the vertical distributions of ice crystal concentration, cloud liquid water content, precipitation water content, and precipitation rate for each of the four cases. The ice crystal concentration is the total particle concentration observed by the 2D-C Knollenberg probe. The cloud liquid water content is the integrated mass concentration observed with the forward scattering spectrometer probe. The precipitation water content is the integrated mass concentration observed with the 2D-C and 2D-P probes combined, ignoring bins which contain fewer than 10 particles. The particles are assumed to be plate-like and have a mass/length relationship given by Berthel (1981). The precipitation rate was calculated from the precipitation water content and particle size distributions assuming standard fall velocity relations.

Ice crystal concentrations are typically less than 100/liter for the four cases except in shallow layers where concentrations can exceed 250/liter. The 2D-C probe observes some ice particle concentrations within and below the melting layer, although the magnitude decreases sharply below the 0 degree Centigrade level near 2.4 km. Note that Cases 3 and 4 appear to have higher concentrations of ice crystals and they seem to occur at higher altitudes. Size distributions of the ice crystals may be found in Appendix F.

Cloud liquid water contents are less than .3 gm/m for all four cases and is typically less than .1 gm/m except in shallow

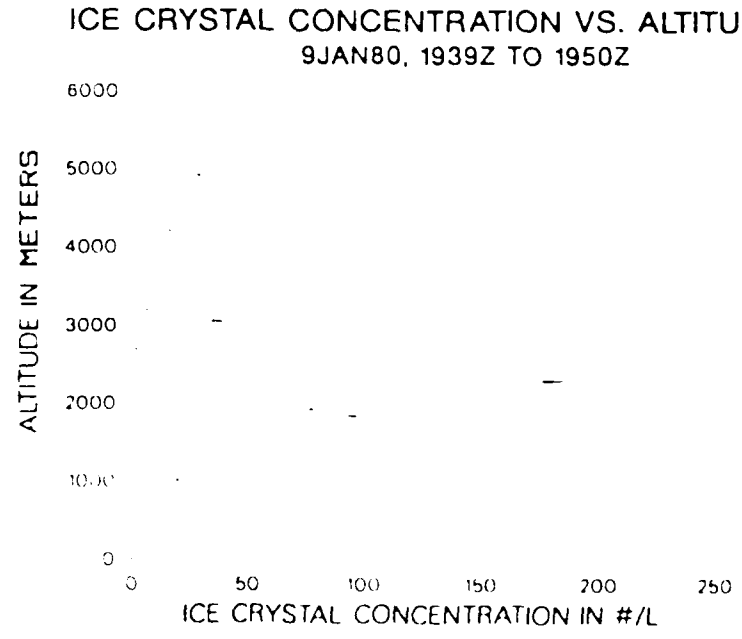

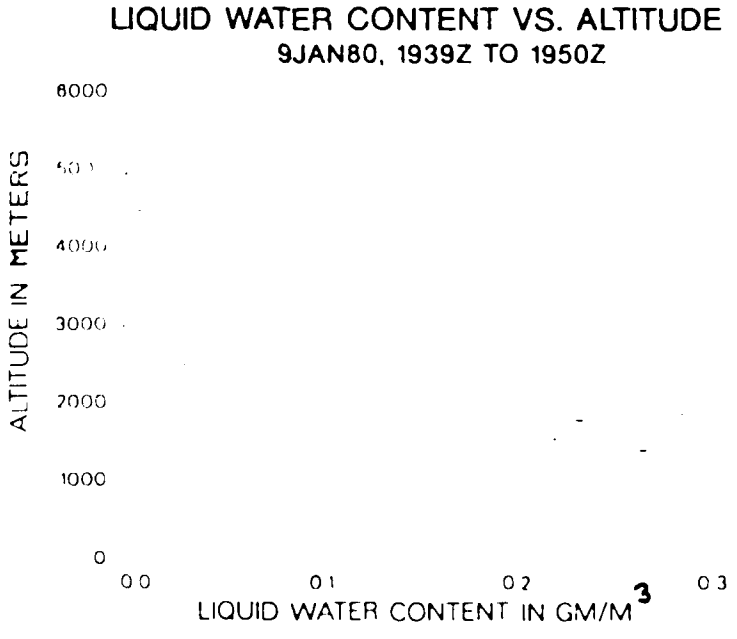

Figure 14. Vertical Distribution of Ice Crystal Concentration and Liquid Water Content for 1939-1950 Z (Case 1)

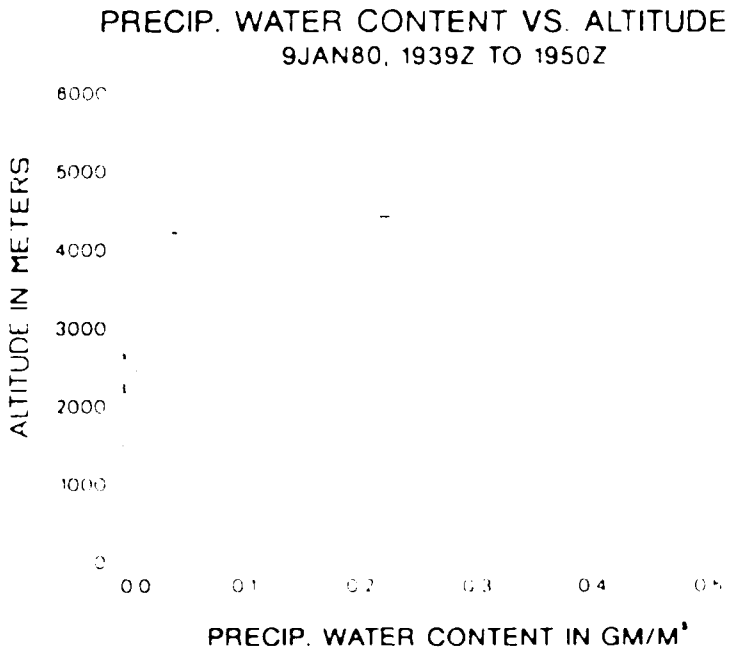

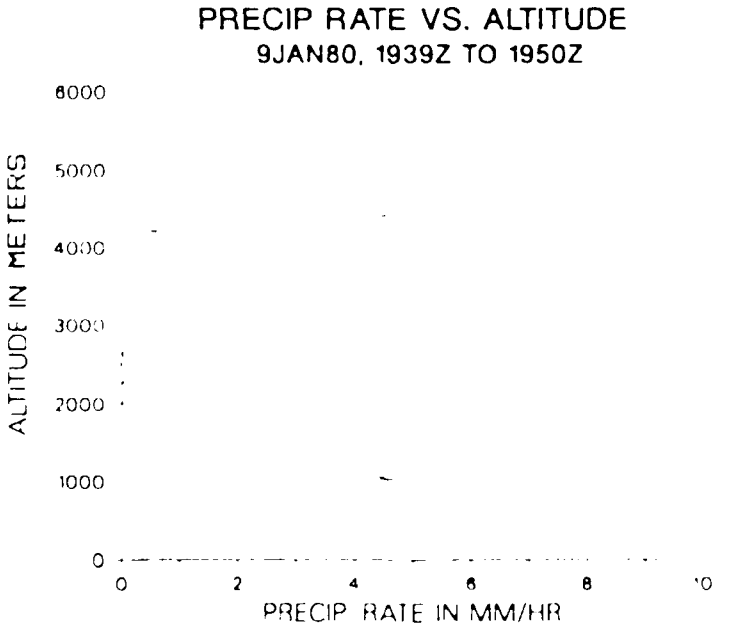

Figure 15. Vertical Distribution of Precipitation Water Content and Precipitation Rate for 1939-1950Z, Case 1

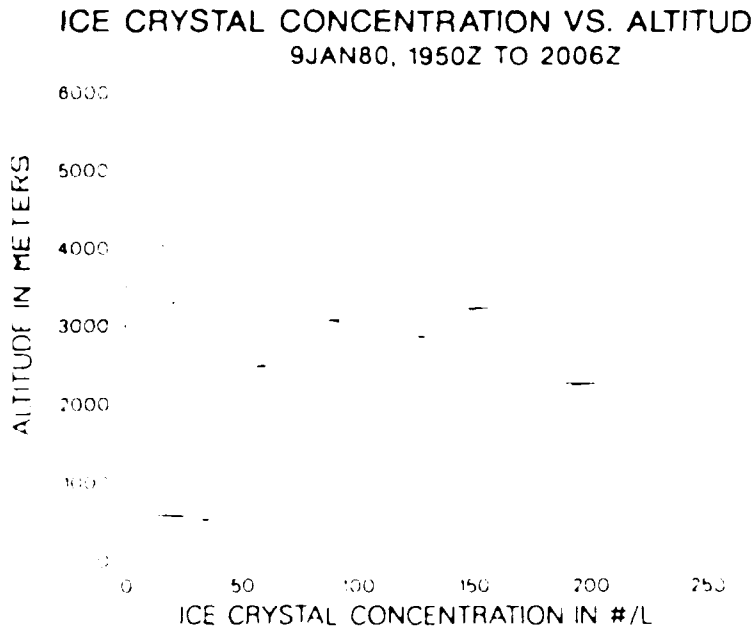

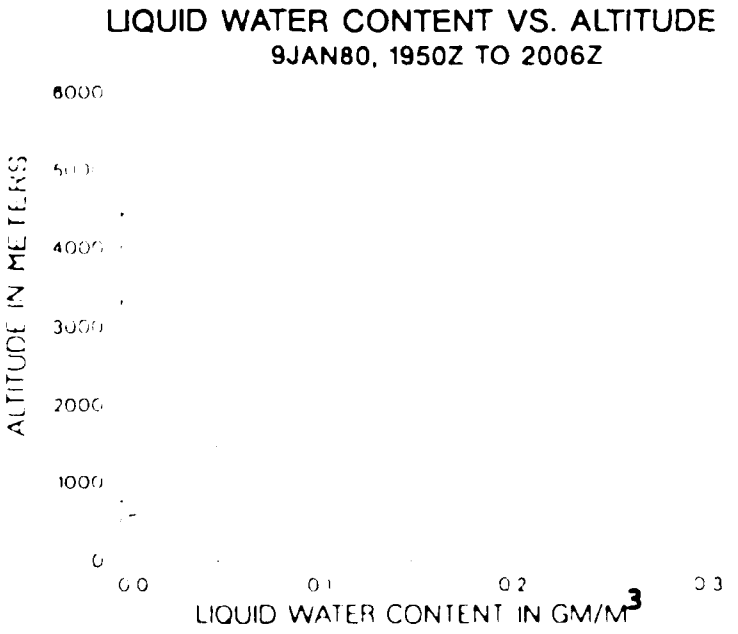

Figure 16. Vertical Distribution of Ice Crystal Concentration and Liquid Water Content for 1950-2006Z 9 January

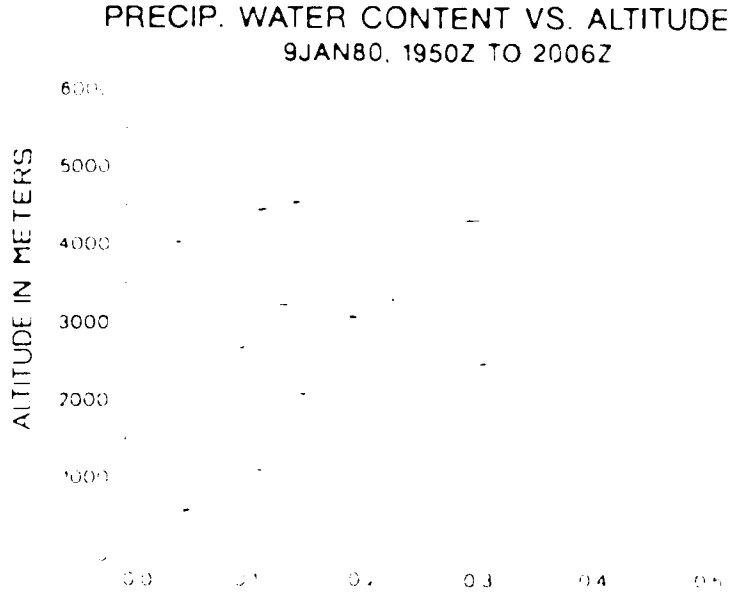

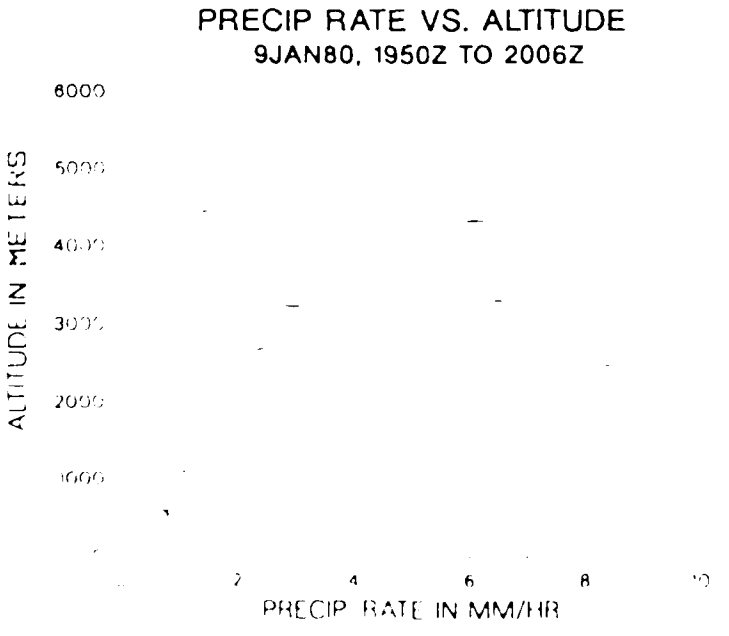

Figure 1. Vertical Distribution of Precipitation Water Content and Precipitation Rate for 1x-Band Radar

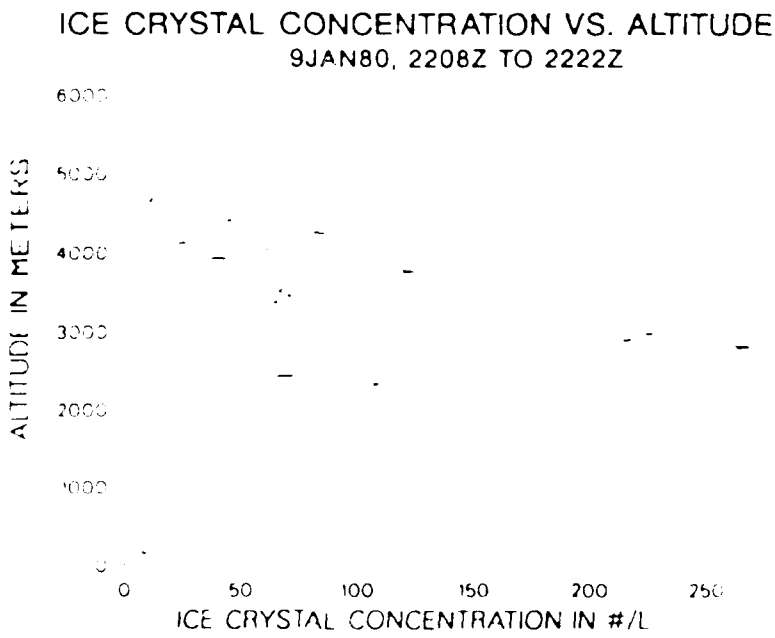

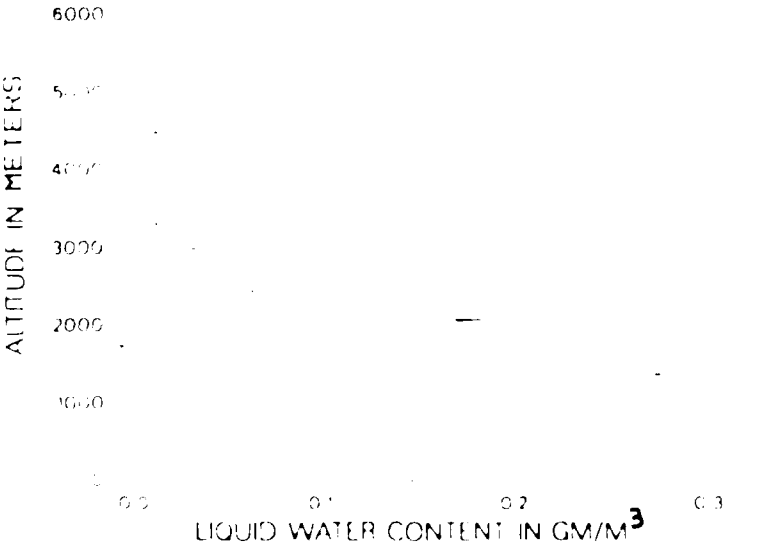

Figure [illegible] Vertical Distribution of Ice Crystal Concentration and Liquid Water Content for [illegible]

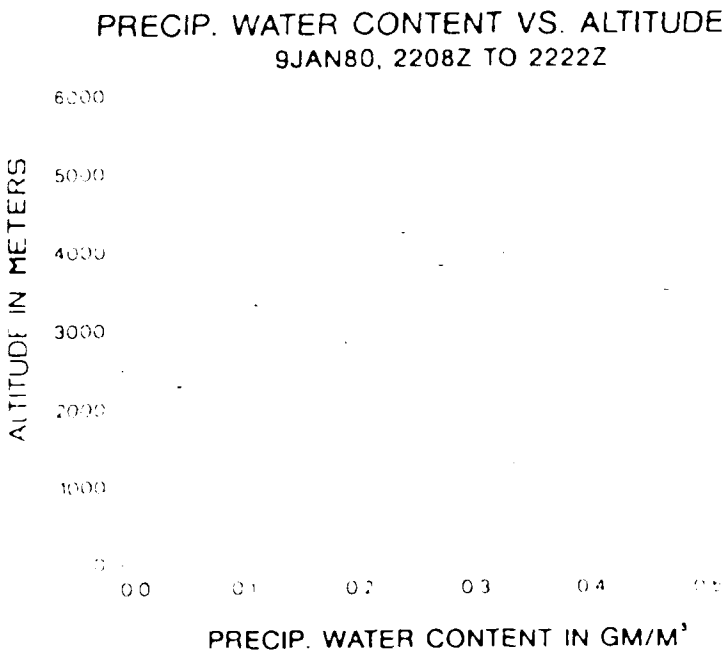

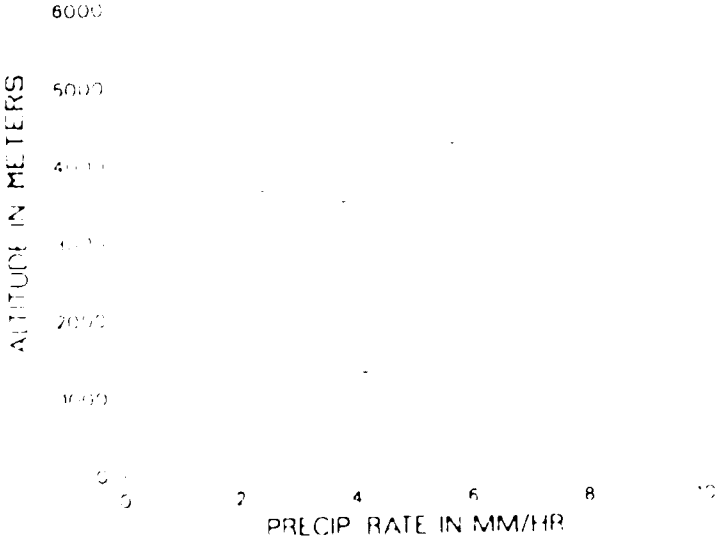

Figure 2. Vertical Distribution of Precipitation Water Content and Precipitation Rate for 2208-2222 Z (Case 3

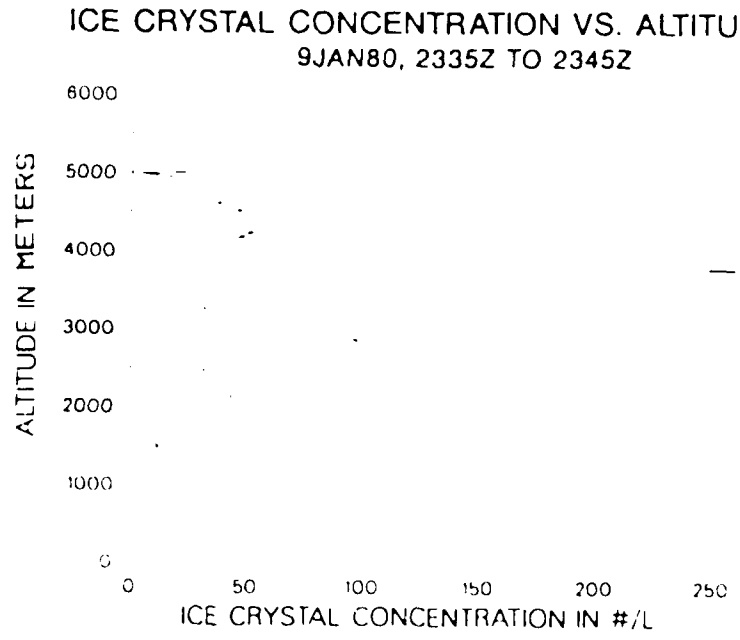

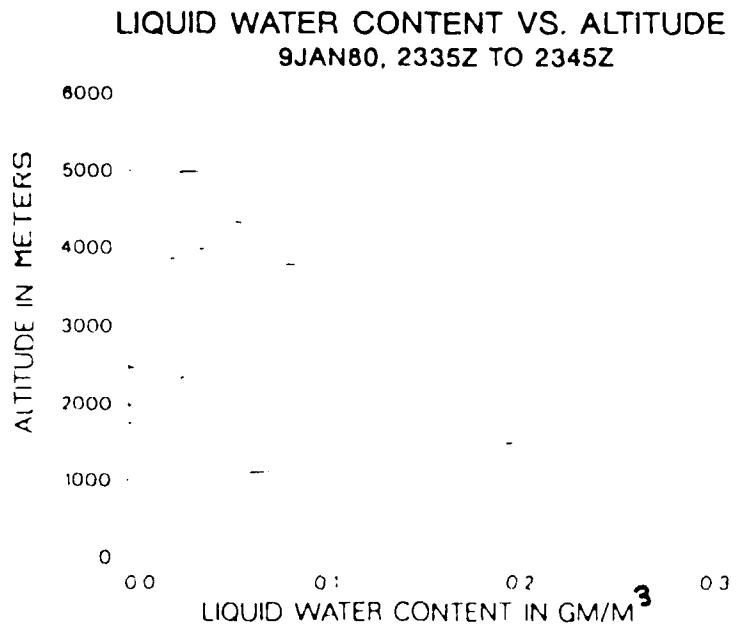

Figure 20. Vertical Distribution of Ice Crystal Concentration and Liquid Water Content for 2335-2345 Z (Case 4)

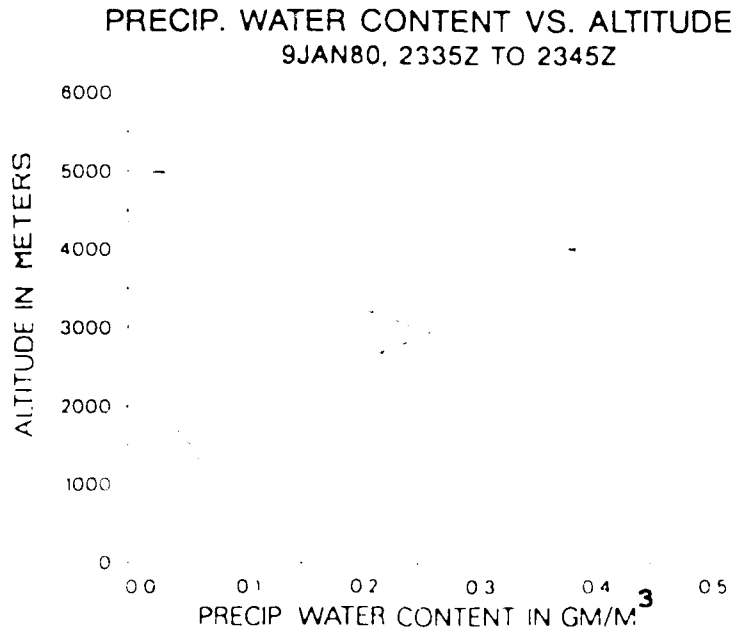

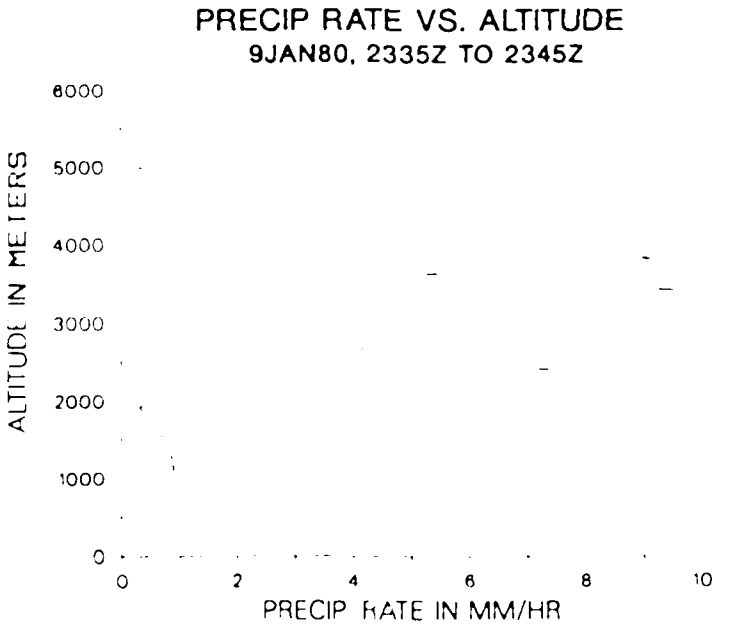

Figure 21. Vertical Distribution of Precipitation Water Content and Precipitation Rate for 2335-2345 Z (Case 4)

layers. Maximum liquid water contents occur near the 0 degree centigrade level at about 2 km. Relatively little liquid water is observed aloft due to the high concentrations of ice crystals present in Sierra Nevada storms. Case 1 has the greatest quantity of cloud liquid water but it is almost all concentrated at low levels. The cloud water is distributed to higher levels in the other three cases, although the magnitudes are quite low.

Precipitation water contents were on the order of .2 gm/m or less for the first three cases with what appears to be considerable variation in the vertical. However, this vertical variation is probably due to horizontal fluctuations as the aircraft flew in and out of embedded convection on its ascents and descents. A near vertical ascent might have seen a more uniform vertical distribution. Case 4 shows a much higher precipitation water content, frequently exceeding .5 gm/m . This case shows the increased activity to the east of the radiometer as the aircraft reached cloud tops near the end of its ascent. Unfortunately, the radiometer was probably not "seeing" this activity.

The average precipitation rate for all four cases, as calculated from the aircraft microphysics data, is 2.75 mm/hr. The rate typically shows an increase with altitude and an increase throughout the day. Like the precipitation water content the precipitation rate is highly variable in the vertical, and for the same reason. Table 1 gives a comparison of the aircraft-derived precipitation rate for the four cases compared to the average precipitation rate for a portion of the

Case	Aircraft Times	Gage Times	Aircraft Precipitation Rate (mm/hr)	Gage Precipitation Rate (mm/hr)
1	1938-1950 Z	1900-2000 Z	1.7	3.3
2	1950-2006 Z	1930-2030 Z	2.2	3.7
3	2203-2222 Z	2145-2245 Z	3.3	4.6
4	2335-2345 Z	2300-2400 Z	3.8	7.3

Table 1. Comparison of aircraft-derived precipitation rates versus average gage precipitation rates

cliff gage network. The average aircraft derived precipitation rate is about half of the average gage precipitation rate. The discrepancy in these two averages may be due to the following reasons: 1) Some precipitation is lost in the calculation of aircraft precipitation rates by the neglect of bins with fewer than 10 particles. This is more likely to affect larger bin sizes which have more mass and fall velocity. 2) Mass conversion and fall velocity assumptions could be affected strongly by crystal type, riming, aggregation, and melting, particularly in the melting layer. 3) Precipitation gradients in the foothill region of the Sierra Nevada could easily sway average values. 4) The low precipitation rates calculated at some levels in the vertical may be due to horizontal variations. However, averages, whether in the vertical or horizontal, should approach the same values, given enough data.

Since the aircraft-derived precipitation rate is too low, it is likely that the calculated attenuation is also low. Further work on this topic should explore which of the likely effects above caused the precipitation rate to be low and make appropriate corrections.

B. Vertical Attenuation Distributions

Figures 22-25 show the vertical distributions of calculated ice crystal attenuation, cloud water attenuation, and rain water attenuation for each of the four cases. Note that these values are given in dB/km in the vertical. That is, the values have not yet been corrected for the inclination through a precipitating cloud and integrated as a radiometer would obseve the satellite

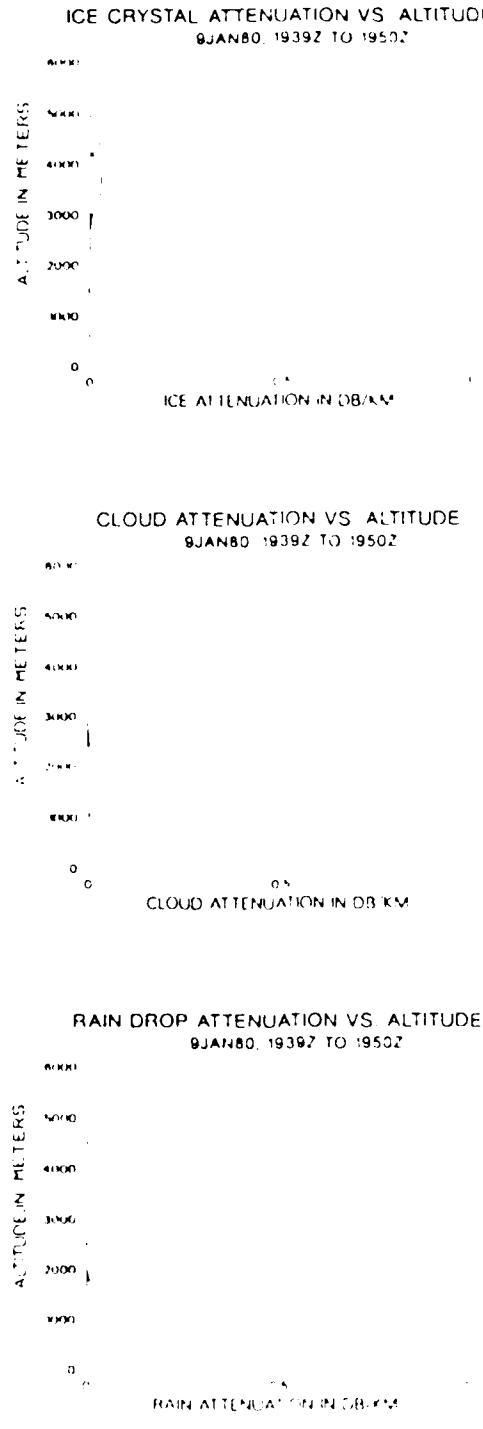

Figure 22. Vertical Distributions of Attenuation due to Ice Crystals, Cloud Water, and Rain (Case 1)

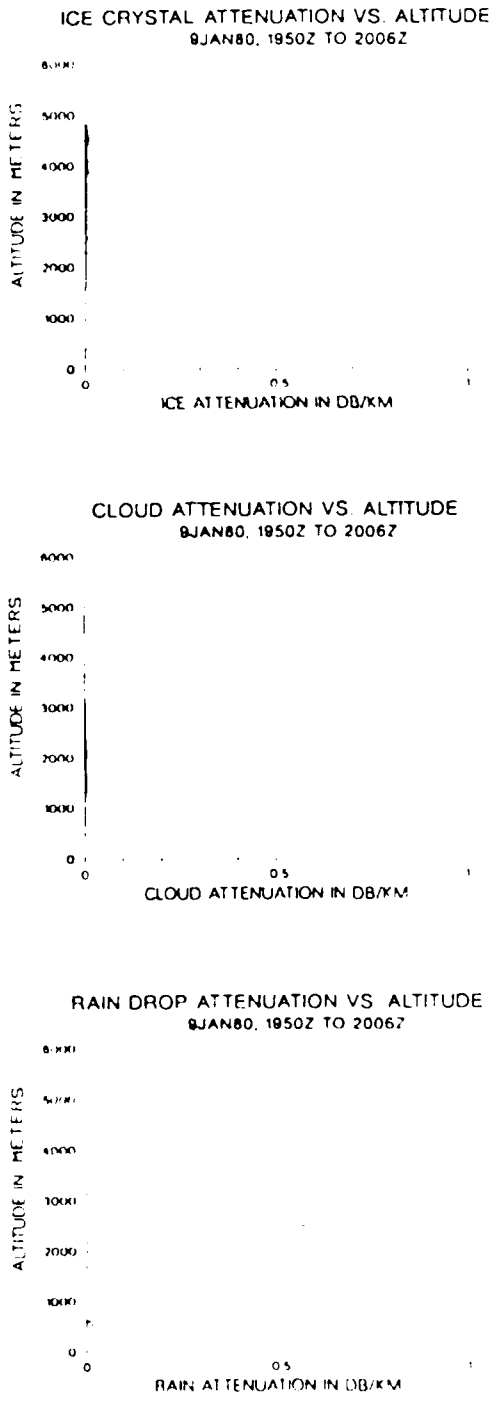

Figure 23. Vertical Distributions of Attenuation due to Ice Crystals, Cloud Water, and Rain (Case 2)

many years that melting hydrometeors produce a "bright band" for radars. The layer of liquid water which coats ice crystals and snow flakes below the 0 degree Centigrade level causes particles to scatter, absorb, and emit more microwave radiation than the same particles above the 0 degree Centigrade level. In addition, aggregation, riming, fracturing, and changes in fall velocities produce changes in particle distributions which also affect scattering, absorption, and emission. Millimeter wave length attenuation is similarly affected. Only elementary efforts to treat these effects were taken in this study.

It is recommended that the complex effects of hydrometeor melting on millimeter wave length attenuation be more completely treated. Such a study should explore the particle size distribution changes through the melting layer as a function of particle types and sizes falling into the melting layer. These changes could then be evaluated as to their effect on attenuation. Attenuation in the melting layer could easily be equal to or greater than the total attenuation through the remainder of the cloud combined.

VI. ACKNOWLEDGEMENTS

This research was accomplished under the sponsorship of the Air Force Office of Scientific Research, Bolling AFB, DC (Contract No. F49620-85-C-0013/SB5851-0360, Subcontract No. S-760-OMG-010). Appreciation is expressed to Dr. Arnold A. Barnes, Jr. for his encouragement and discussions during the effort. Several individuals and organizations provided data and advice for this study. John Marwitz of the University of Wyoming, provided microphysics data and guidance for its use. Jack Snider from the Wave Propagation Laboratory of the National Oceanic and Atmospheric Administration provided the radiometer data. The Office of Atmospheric Resources Research of the Bureau of Reclamation provided archived radar and aircraft data. Owen Rhea of Electronic Techniques, Inc. wrote the meteorological descriptions for the case studies. Morton Glass, Vernon Plank, and Robert Berthel of AFGL/LYC helped the effort with their discussions on crystal mass calculations and size spectra manipulations. Michael Birch and C. Roger Hall were of invaluable help in converting the programs to run on the CRAY and making the production runs. I wish to thank the San Diego Supercomputer Center for use of the CRAY and the excellent technical support I received. And finally, thanks to Rich Burt for typing the final report.

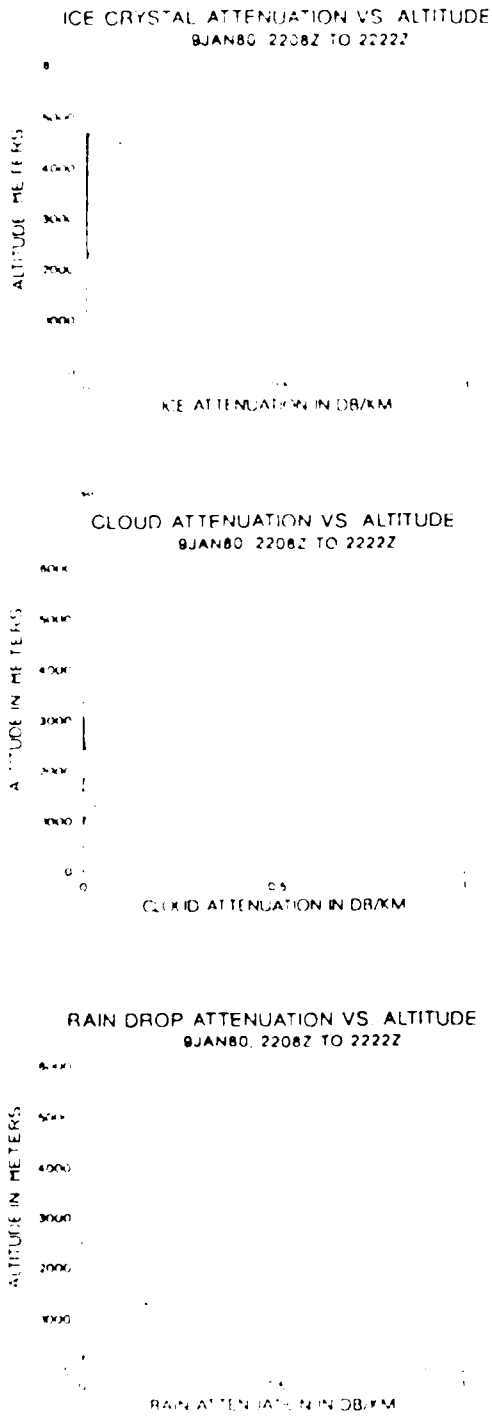

Figure 24. Vertical Distributions of Attenuation due to Ice Crystals, Cloud Water, and Rain (Case 3)

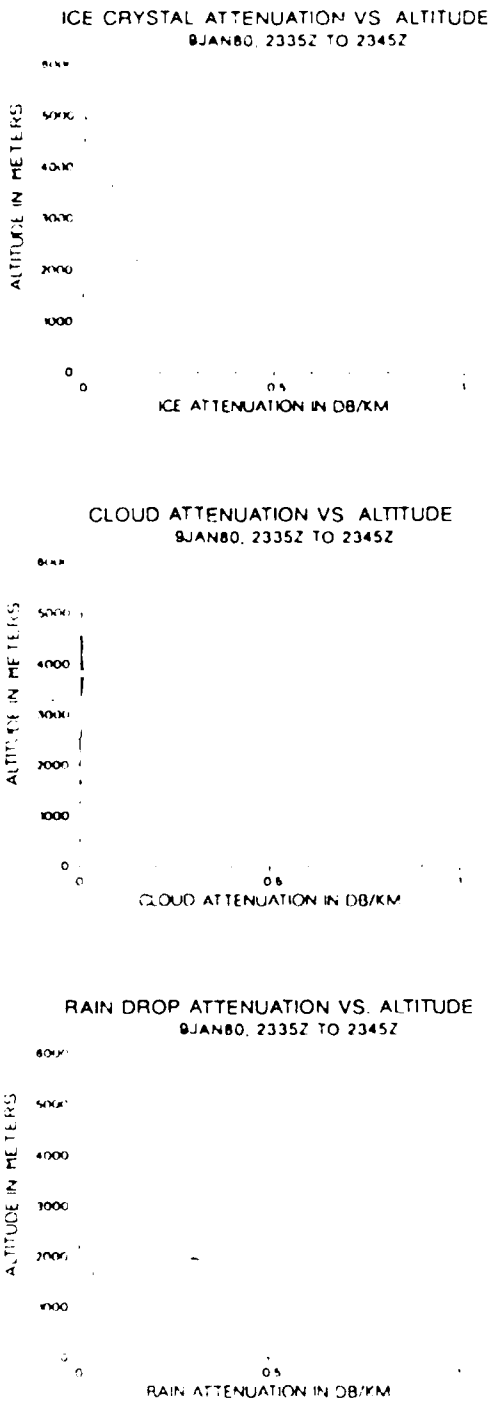

Figure 25. Vertical Distributions of Attenuation due to Ice Crystals, Cloud Water, and Rain (Case 4)

It is evident that the attenuation due to rain below the melting level contributes the greatest to the total attenuation, although it exceeds .5 dB/km only in Case 2. Cloud water contributes only neglibly to the attenuation. Ice crystals appear to make an important contribution in Case 4, consistently approaching .1 dB/km over the entire upper portion of the cloud.

In Case 1 and Case 4 the aircraft transects through the cloud were terminated at the bottom near 1000 meters. In none of the cases did the aircraft exit completely through the top of the cloud, although the major portion of the precipitation was evidently below the aircraft, as shown by the excursion of the attenuation traces back to near zero at 5000 meters. Missing data at the top and bottom of the cloud cause the integrated values of attenuation measured by the aircraft to appear too low.

C. Total Attenuation

Table 2 shows the integrated values of attenuation through the entire depth of the cloud for the four cases. These values have been corrected for the inclination of the radiometer observing the beacon at 32.5 degrees so that comparison can be made directly with observations by the radiometer.

Rain is the greatest contributor to attenuation for all four cases. In Case 1 and Case 4 additional attenuation due to rain should be considered because of missing data below 1000 meters. Case 4 shows an extremely high value due to rain. This particular value was primarily due to a single measurement in the melting layer at 1935 meters. The particle distribution was

Case	Ice (dB)	Cloud Water (dB)	Rain (dB)	Total (dB)
1	.362	.354	.378	1.09
2	.465	.116	1.364	1.95
3	.843	.262	1.091	2.20
4	1.711	.177	8.221	10.11

Table 2. Integrated attenuation through the depth of cloud for ice, cloud water, rain, and the total.

[illegible] resulted in an extreme value for attenuation. Exploration of these effects was beyond the scope of this effort.

Although cloud water contributed one third of the attenuation to the first case, it was a minor contributor to the other cases.

Ice crystals made substantial contribution to the attenuation for all four cases. Particularly in Case 4 the presence of high concentrations of precipitating ice particles in the upper part of the cloud contribute almost 2 dB to the attenuation of the beacon signal.

D. Comparisons of Measured and Calculated Attenuation

Table 1 shows the measured and calculated attenuation for the four cases. The measured values of attenuation are the averages observed by the radiometer over the same time interval that the aircraft data were tale. No adjustments have been made for water on the antenna. The calculated values of attenuation have not been adjusted for missing data below 1 km for Cases 1 and 4. In both these cases the total attenuation would probably be greater by about 1 dB if the rain below the 1 km level had been included in the data. Approximately 8 dB of the 10.11 dB calculated attenuation in Case 4 is due to a single extreme value of precipitation in the melting layer.

E. Travel to Confer on Similar Research

During the period of this contract I traveled to Sacramento, California and Boston, Massachusetts. The trip to Sacramento was made on January 27-29, 1986 in order to visit the Sierra

Case	Measured Attenuation (dB) from Radiometer	Calculated Attenuation (dB) from Aircraft
1	5.95	1.09
2	4.89	1.95
3	1.38	2.20
4	2.04	10.11

Table 3. Comparison of Measured and Calculated Attenuation

[illegible] project. Two major purposes were to obtain the [illegible] data for 9 January 1980 to be used in this [illegible] and to investigate the possibility of using data [illegible] by the SCPP radiometer at a new site higher in the [illegible]. I acquired the precipitation data and it has been incorporated in this report. However, the new location of the radiometer precluded using the data for the purposes of this contract. It is located at about 8000 feet in the Sierra Nevada near the height of the 0 degree Centigrade level in most storms. This location works well for the purposes of the SCPP in locating super cooled water, but its location prevents aircraft from approaching within about 3000-4000 feet vertically because of IFR and safety restrictions. This means only poor comparisons between the radiometer and aircraft measurements are possible. For these reasons use of recent SCPP data was not pursued further.

The trip to Boston, Massachusetts was made on August 19-23, 1980 to visit the Air Force Geophysics Laboratory. I reported on the preliminary results of my research to Dr. Arnold Barnes, who had suggested this study of millimeter wave attenuation under a previous summer research grant. He also provided an update to me on the results of a similar effort he is directing. My results were not surprising in light of his experience. The procedures he is using should help to avoid some of the meteorological uncertainty in path differences between radiometer and microphysics data. He encouraged me to consider investigations on the melting layer since this produces significant effects

which have not, as yet, been adequately treated. While in Boston I acquired some software needed on the microcomputer at Christian Heritage College to display graphical output and transfer files from the CRAY. These were subsequently installed and used operationally.

V. CONCLUSIONS AND RECOMMENDATIONS

Measured and calculated values of attenuation show poor correlation. Even if adjustments are made for a wet antenna and missing data below 1 km the attenuation measured by the radiometer is much greater than the calculated attenuation for Cases 1 and 2. In Cases 3 and 4 the measured attenuation is much less than the calculated attenuation. For Case 4 the calculated attenuation is strongly influenced by a single value in the melting layer.

By investigating the aircraft, radar, and precipitation gage data in some detail it is apparent that there are two reasons why the measured and calculated values of attenuation disagree: 1) aircraft flights only slightly divergent from the path between the satellite beacon and the radiometer produce significantly different results, even in relatively uniform precipitation, and 2) the effect of melting hydrometeors on attenuation are highly variable compared to the simple algorithms used in these calculations.

The expectation for this study was that the orographic precipitation upwind of the Sierra Nevada was sufficiently uniform in space and time that aircraft transects close to the radiometer would provide microphysics data characteristic of the path between the beacon and radiometer. It is now clear from this study and Vardiman and Peterson (1985) that the variation in hydrometeor concentration seen by the radiometer and aircraft is too great for a valid comparison. First, the aircraft path, even

[illegible] the radiometer [illegible], it is [illegible] to the radiometer path because the aircraft [illegible] climb or descend at an angle of 12.5 degrees. Second, time variations due to convection and drift of hydrometeors are so rapid that the aircraft cannot take measurements along a path of tens of kilometers which are characteristic of the radiometer path. When aircraft paths are taken which approximate the radiometer path, additional complications arise because of gradients in precipitation intensity up the foothills of the Sierra Nevada.

It is recommended that future data acquistion of this type be made in such a way that microphysics data be more representative of conditions in the same path over which attenuation measurements are made. This could be accomplished in either of two ways. The path over which the two measurements are made could be shortened and made more horizontal to allow faster, more parallel microphysics measurements to be taken. If uniformity in hydrometeor distributions could be assured in both space and time, the procedure used in this study could again be attempted. However, since heavy precipitation is needed for strong attenuation, and heavy precipitation is normally associated with non-uniform conditions, the first solution is probably the better of the two approaches.

In addition to the different hydrometeor concentrations observed in space and time, another reason for the poor correlation between measured and calculated values of attenuation is the effect of melting hydrometeors. It has been known for

REFERENCES

[illegible], [illegible], "[illegible] of Liquid Water Using Simulated Data", AFGL Environmental Research Paper No. 745, AFGL-TR-81-0173, 1981.

Bradford, M.L., "Hydrometeor Characteristics of Orographic Clouds and Rainbands in California", M.S. Thesis, Dept. of Atmospheric Science, University of Wyoming, 145pp, 1982.

Cooper, W.A., "Cloud Physics Investigations by the University of Wyoming in HIPLEX 1977", Annual Report to Water and Power Resources Service (formerly Bureau fo Reclamation), Contract No. 7-07-[illegible], Dept. of Atmospheric Science, Univ. of Wyoming, 320pp, 1978.

Cooper, W.A. and C.P.R. Saunders, "Winter Storms over the San Juan Mountains, Part II: Microphysical Processes", J. Appl. Meteor., 19(8) 927-941pp, 1980.

Cox, D.C., "An Overview of the Bell Laboratories 19- and 28- GHz COMSTAR Beacon Propagation Experiments", The Bell System Technical Journal, Vol. 57, No. 5, 1231-1255pp, 1978.

Ebersole, J.F., W.F. Cheng, J. Hallett, and R.G. Hohlfeld, "Effects of Hydrometeors on Electromagnetic Wave Propagaton", Final Report, AFGL-TR-84-0318, 74pp, 1985.

Falcone, V.J., L.W. Abreu, E.P. Shettle, "Atmospheric Attenuation in the 30 to 300 GHz region using RADTRAN and MWTRAN", Proceedings of SPIE, Vol. 337, 62-66pp, 1982.

Gordon, G.L. and J.D. Marwitz, "An Airborne Comparison of Three PMS Probes", J. of Atmos. and Ocean. Technol., 1, 22-27pp, 1984.

Gordon, G.L. and J.D. Marwitz, "Hydrometeor Evolution in Rainbands Over the California Valley", Manuscript submitted to J. Atm. Sci., 1985.

Gunn, K.L.S., and T.W.R. East, "The Microwave Properties of Precipitation Particles", Quart. J. Roy. Meteor. Soc., Vol. 80, 522-545pp, 1954.

Henderson, T.J. et. al., "SCPP Data Collection and Analysis for the period July 1, 1979 through June 30, 1980", Interim Progress Report, Atmospherics, Inc., Fresno, California, 1980.

Hogg, D.C., "Millimeter-Wave Communication through the Atmosphere", Science, Vol. 159, No. 3810, 39-46pp, 1968.

Hogg, D.C. and T. Chu, "The Role of Rain in Satellite Communications", Proceedings of the IEEE, Vol. 63, No. 9, 1308-1331pp, 1975.

Hogg, D.C., F.O. Guiraud, J.B. Snider, M.T. Decker and E.R. Westwater, "A Steerable Dual-Channel Microwave Radiometer for Measurement of Water Vapor and Liquid in the Troposphere", J. of Climate and Appl. Meteor., Vol. 22, 789-806pp, 1983.

[illegible], Cambridge, Harvard University [illegible], 19[illegible].

[illegible], John D., "Microphysical and Thermodynamic Characteristics through the Melting Layer", Report No. AS126 to the Water and Power Resources Service (formerly Bureau of Reclamation), Dept. of Atmospheric Science, Univ. of Wyoming, Contract No. 7-07-83-V0001, 204pp, 1980.

Parish, T.R., J.D. Marwitz, R.L. Lee, G.L. Gordon and A.R. Rodi, "Cloud Physics Studies in SCPP During 1980-81", Report No. AS132 to the Bureau of Reclamation, Dept. of Atmospheric Science, Univ. of Wyoming, Contract No. 7-07-83-V0001, 149pp, 1981.

Rhea, O.J., et.al., "Interim Progress Report, SCPP Forecasting Support for the period of July 1, 1979-June 30, 1980", Electronic Techniques, Inc., Fort Collins, Colorado, 1980.

Sierra Cooperative Pilot Project, "Operations Plan, 1979-80", Office of Atmospheric Resources Management, Bureau of Reclamtion, U.S. Dept. of Interior, Denver, Colorado, 1979.

Snider, J.B., F.O. Guiraud, and D.C. Hogg, "Comparison of Cloud Liquid Content Measured by Two Independent Ground-based Systems", J. Appl. Meteor., Vol. 19, 577-579pp, 1980.

Snider, J.B., H.M. Burdick, and D.C. Hogg, "Cloud Liquid Measurement with a Ground-based Microwave Instrument", Radio Science, Vol. 15, No. 3, 683-693pp, 1980.

Snider, J.B. and D.C. Hogg, "Ground-based Radiometric Observations of Cloud Liquid in the Sierra Nevada", NOAA Technical Memorandum ERL/WPL 72, Boulder, Colorado, 46pp, 1981.

Stewart, R.E. And J.D. Marwitz, "Cloud Physics Studies in SCPP During 1979-80", Report No. AS125 to the Water and Power Resources Service (formerly Bureau of Reclamation), Dept. of Atmospheric Science, Univ. of Wyoming, Contract No. 7-07-83-V0001, 96pp, 1980.

Stewart, R.E. and J.D. Marwitz, "Microphysical Effects of Seeding Winter-time Stratiform Cloud Near the Sierra Nevada Mountains", J. of Appl. Meteor., Vol. 21, 874-880pp, 1982.

Stewart, R.E., J.D. Marwitz, and J.C. Pace, "Characteristics through the Melting Layer of Stratiform Clouds", J. of Atmos. Sci., Vol. 41, No. 22, 3227-3237pp, 1984.

Tiffany, G.B., "Most Reliable Messenger: MM-Waves Get Through", Microwaves and R.F., 64pp, 1983.

Vardiman, L. and M. Peterson, "A Comparison of Measured and Calculated Attenuation of 28 GHz Beacon Signals in Three California Storms", Final Report, 1985 USAF-UES Summer Faculty Research Program/Graduate Student Summer Support Program, Contract No. F49620-85-C-0013, 20pp, 1985.

APPENDIX A

through

APPENDIX F

These are available from the author
or Universal Energy Systems, Inc.

FINAL REPORT NUMBER 76
REPORT NOT RECEIVED IN TIME
WILL BE PROVIDED WHEN AVAILABLE
Dr. Christian C. Wagner
760-OMG-030

1986 AFOSR-UES MINI-GRANT PROGRAM

Sponsored by the

AIR FORCE OFFICE OF SCIENTIFIC RESEARCH

Conducted by the

UNIVERSAL ENERGY SYSTEMS, INC.

FINAL REPORT

ASSESSMENT OF THE STABILITY AND CONTROL COMPUTER PROGRAM FOR CONCEPTUAL AIRCRAFT DESIGN

Prepared by	Dr. Richard C. Walker
Academic Rank:	Associate Professor
Department and University:	Department of Aeronautics Miami University, Oxford, Ohio
Research Location:	Flight Dynamics Laboratory, Office of Technology Assessment, Design Branch, Wright-Patterson AFB and Aeronautics Department, 219 Culler Hall, Miami University Oxford, Ohio
USAF Research:	Mr. Terry Smith
Date:	14 November 1986
Contract No:	Prime Contract No.: F49620-85-C-0013/ SB5851-0360 Sub Contract No.: S-760-OMG-045

ASSESSMENT OF THE STABILITY AND CONTROL COMPUTER PROGRAM FOR CONCEPTUAL AIRCRAFT DESIGN

By

Dr. Richard C. Walker

ABSTRACT

This report is concerned with the assessment and improvement of stability and methodology contained in a computer program being developed by the Design Branch of the Air Force Flight Dynamics Laboratory (AFWAL/FIAD). A comparison of stability derivatives obtained using the Stability and Control Conputer Program-SACP- and test data for the C-5A and F-4C is presented, as well as a comparison of results obtained by SACP and the Digital Datcom computer program for a wing-body-tail configuration. Excellent agreement with Digital Datcom was found; whereas in the case of the C-5A and F-4C, some of the stability derivatives predicted by SACP agreed very well with test data and some did not. Although the present accuracy level of SACP is sufficient for conceptual aircraft design, incorporation of the recommendations contained in this report should lead to improved stability and control estimates by SACP.

1.0 INTRODUCTION

The Stability and Control Program (SACP) is a computer program for predicting stability and control characteristics of aircraft at the conceptual design level. The program was developed as an in-house effort by the Design Branch (AFWAL/FIAD) to acquire the ability to analyze newly created aircraft designs comprehensively, yet in a rapid and efficient manner.

Documentation of SACP is contained in two volumes. Volume I documents methods used in the program, and Vol.II is a user's manual and computer program description of SACP.

This report contains the results of a preliminary investigation to assess the ability of SACP to provide credible stability and control parameter estimates in a conceptual design environment. The report also contains input files for several aircraft configurations, which should be useful to new users of SACP.

Complete aircraft investigated were of the transport type-C-5A, and the fighter type-F-4C. Motivation for selecting these aircraft was that comparison data for these aircraft was available in a widely referenced report by Heffley and Jewell (1). Data in Ref.(1) was based on a combination of wind tunnel, flight, and estimated data. Additional comparison data for the F-4C was also available in a report by Place, et al (2). These aircraft also demonstrate and exercise some of the features of the program such as accounting for the pronounced negative dihedral of the horizontal stabilizer on the F-4C.

Simple wing-body-tail and wing-body configurations were also investigated to provide a means of verifying methodology and program coding. These examples were taken from Digital Datcom (3), and Engineering Sciences Data Units-ESDU(4). Input data for these cases are quite straight forward and removes the factor of judgment, present for complex configurations, as a reason for non-correlation of results.

The report is organized in the following manner: first the results of the C-5A and F-4C test cases are discussed, next the results for the example test cases are presented, and finally conclusions and recommendations for improvement in the methodology for computing certain stability derivatives are listed.

2.0 C-5 AND F-4 TEST CASES

In addition to representing two different classes of aircraft, the C-5 and F-4 represent two very distinct configurations. The C-5's T-tail and high-wing configuration is a contrast to the F-4's fuselage-mounted-anhederal-horizontal tailplane, and low-wing configuration. These aircraft configurations should push the boundaries of the data base upon which many of the empirical methods in SACP are based and provide excellent test cases.

2.1 INPUT DATA

Configuration data for the C-5 and F-4 was obtained by scaling the three-view drawings contained in reference 1. Other pertinent data was obtained from Lockheed and McDonnell Douglas reports as well as other sources. Figure 1 contains the input data for the C-5 as well as an illustration of some of the input parameters. Input data for the F-4 is contained in figure 4.

Modeling of both configurations, aside from the inherent errors in scaling from a photocopy, was straight forward with the exception of the definition of the effective area of the vertical tail. One method of controlling the effective tail area is with the input parameter ZCREV, Z location of the vertical tail exposed root chord, along with the geometric parameters of the exposed vertical tail. The effect of ZCREV on the C-5 configuration is discussed in the results section.

2.2 RESULTS

Figures 2 and 3 contain C-5 stability derivatives calculated by SACP along with comparison values obtained from ref.1. Figure 2 contains stability derivatives obtained with the vertical tail of the C-5 modeled such that the effective area of the vertical tail is equal to the exposed area. Figure 3 illustrates the effect of using the theoretical vertical tail area (35% greater than the exposed area) as the effective area on the C-5 lateral stability derivatives. Longitudinal stability derivatives are only very slightly effected by the size of the vertical tail.

In addition to the stability derivatives for the F-4 calculated by SACP and the comparison values from ref.1, figure 5 contains stability derivatives estimated by a computer program, ref. 2--"Interactive Computer-Aided Design Aircraft Flying Qualities Program"--FQP--developed by the Convair Division of General Dynamics. The figure also contains comparison F-4 stability data extracted from ref.2. The source of this data, like that of ref.1, is from wind tunnel and flight test data and will certainly represent trends; howver, both references caution that discrepanies between actual and presented data may exist. It should be further be noted that the F-4 reference data from ref.2 is for a flight altitude of 55,000 ft, whereas the data from ref.1 is for 35,000 up to 45,000 ft. In general, the

reference data from both sources quite well, as is evident from figure 5.

The geometric references for the C-5 and F-4 comparison stability derivatives, taken from references 1 and 2, are shown in the input data (figures 1 and 4). Stability derivative reference data for the SACP calculated values are listed below:

C-5 Reference quantities:

Area	=	6200 sq ft
Longitudinal(MAC)	=	32.8 ft
Lateral(b)	=	223.5 ft

F-4 Reference quantities

Area	=	530 sq ft
Longitudinal(MAC)	=	14.9 ft
Lateral(b)	=	38.3 ft

Although the area can be input as a reference quantity, this in not the case for the longitudinal and lateral reference quantities. It would be useful to add to SACP the option of inputing the logitudinal and lateral reference parameters.

2.2.1 C-L-ALPHA

Derivative of the lift coefficient with respect to the angle of attack (C-L-ALPHA) for the C-5 and F-4 is shown in figures 2 and 5 respectively. F-4 C-L-ALPHA estimates by SACP and FQP agree with both references quite well. C-5 estimates for C-L-ALHPA by SACP is high for all Mach numbers but highest for Mach = .8. C-L-ALPHA = 8.12/rad at this Mach and the reference angle of attack of .1 degrees. At the same Mach, but at an angle of attack of 2.2 degrees, SACP estimates C-L-ALPHA = 3.67/rad. This large decrease in C-L-ALPHA is due to discontinuity between calculation "zones" in SACP. Removal of these large discontinuities across zones is an area in which SACP could be improved.

Theroretical wing area calculated for the C-5 by SACP is seven percent higher than the reference area for the C-5 which contributes to the higher value of C-L-ALPHA. Methods by which the theoretical wing is defined is another possible area in SACP where accuracy might be improved. Reference 4 contains an interesting method for defining an equivalent wing, which is similar the theoretical wing defined in SACP, is discussed in section 3.

2.2.2 C-M-ALPHA

Estimates of the derivative of the pitching-moment coefficient with respect to the angle of attack (C-M-ALPHA) by SACP and FQP for the F-4 show good agreement with the reference data as indicated in figure 5. Estimates for the C-5 for this

parameter are again shown to be of higher magnitude than the reference value in figure 2. This is not surprising since:

C-M-ALPHA=(C-L-ALPHA)*(XCG - XAC)/MAC

XCG = Distance of center of gravity from aircraft nose.
XAC = Distance of aerodynamic center from aircraft nose.
MAC = Mean aerodynamic chord.

This relationship illustrates that a high value of C-L-ALPHA, as well as a farther aft position of the aerodynamic center, will produce a higher magnitude of C-M-ALPHA.

2.2.3 C-M-Q and C-M-ALPHA DOT

Variation of moment coefficient with pitch rate (C-M-Q) and angle-of-attack rate (C-M-ALHPA DOT) are shown in figures 2 and 5 for the C-5 and F-4 respectively. The comparison between the estimated and reference data for the C-5 is quite good; however, both SACP and FQP tend to overestimate the magnitude of these derivatives for all Mach numbers for the F-4. SACP estimates for both derivates are much better than FQP for the F-4 except at Mach 1.2.

The methods in SACP for computing these derivatives for the C-4 and the F-4 consider them to be a function of the lift slope of the horizontal tail and the square of the horizontal tail arm. It would appear that the methodology overestimates the power of the horizontal tail, especially for the F-4.

2.2.4 C-N-BETA

The variation of yawing moment coefficient with side slip angle (C-N-BETA) is shown for the C-5 in figures 2 and 3, and for the F-4 in figure 5.

Data in figure 2 is for the C-5 with the vertical tail modeled such that the exposed area is the effective area. This modeling results in the C-N-BETA being substantially under estimated compared with the reference data for all Mach numbers except Mach .4. At Mach .4 the angle-of-attack is 9 degrees and wing contributes a significant amount to the total C-N-BETA. This is not the case for the higher Mach numbers and corresponding lower lift coefficients.

Figure 3 shows the effect of modeling the vertical tail such that the theoretical area of the tail is the effective area. Theoretical vertical tail area is computed by extending the vertical tail to the longitudinal axis of the aircraft. This results in an approximately 35% increase in the effective area for the C-5 and, as can be seen from figure 3, results in an overestimation of C-N-BETA by about the same amount as the exposed area modeling underestimated the parameter.

Size of the vertical tail is not the only factor that could account for the underestimation of C-N-BETA for the C-5 in figure 2. The effective aspect ratio used to compute the slope of the lift curve for the vertical tail is also a factor. SACP does not account for the variation of horizontal tail position on the vertical tail in computing the slope of the lift curve for the vertical tail. In the case of the T-tailed C-5, this would tend to underestimate the directional stabilizing power of the vertical tail in side slip.

Body and nacelle geometry are also factors in determining C-N-BETA. For the C-5 these components are destabilizing. Body side area is an important parameter in determining C-N-BETA. Body geometry input definition is another area where an improvement could be made in SACP. The better the side area definition for a configuration--the better the estimate for the body contribution to C-N-BETA.

Figure 5 indicates that for the F-4, both SACP and FQP do an excellent job of estimating C-N-BETA subsonically and SACP quite well supersonically; however, FQP over estimates the parameter dramatically at the higher supersonic Mach numbers.

2.2.5 C-N-R

Variation of yawing moment with yaw rate (C-N-R) is shown for the C-5 in figures 2 and 3 and for the F-4 in figure 5. Data shown in figure 2 is for the C-5 modeled with the effective vertical tail area based on the exposed area which yields good agreement with the comparison data for the C-N-R parameter. Whereas the data shown in figure 3 for the C-5 modeled with the larger theoretical vertical tail area, overestimates the magnitude of the parameter.

The method for determining the magnitude of C-N-R is essentially the same as for C-N-BETA, except that C-N-R does not contain a body or nacelle contribution. This would indicate that the magnitude for the body and nacelle contributions to C-N-BETA could be overestimated for the C-5.

Figure 5 indicates that FQP estimates C-N-R well for the F-4 for the subsonic Mach numbers, and not so well for the supersonic Mach numbers. SACP, on the other hand, underestimates C-N-R badly at all Mach numbers. This can be attributed, at least in part, to the fact that SACP does not include the contribution of the vertical component of the horizontal tail in the calculation of C-N-R as it does in the computation of C-N-BETA. Inclusion of the vertical component of the horizontal tail in the computation of C-N-R should lead to a better estimate of this parameter for the F-4 as well as other configurations with a horizontal tail of pronouced anhedral or dihedral.

2.2.6 C-L-P

Variation of rolling moment with roll rate (C-L-P) is shown for the C-5 in figure 2 and for the F-4 in figure 5. For the C-5, SACP overestimates the magnitude of C-L-P, and for the F-4, both SACP and FQP agree very well with the reference data for subsonic Mach numbers. Although SACP indicates the proper trend at supersonic speeds, the magnitude of C-L-P is high compared to the reference values. At Mach numbers 1.5 and 2.15, SACP and FQP agree quite well in the esitmates for C-L-P.

2.2.7 C-L-BETA

Variation of the rolling moment coefficient with side slip (C-L-BETA) is given in figures 2 and 3 for the C-5, and in figure 5 for the F-4. The data in figure 2 indicates that SACP underestimates the magnitude of C-L-BETA for the C-5, while the data in figure 5 shows SACP overestimates the magnitude C-L-BETA for the F-4 at all Mach numbers. Although modeling the C-5's vertical tail with a larger effective area leads to a closer agreement with the reference data for C-L-BETA, as shown in figure 3, C-L-BETA is still low in magnitude. Accounting for the effect of the horizontal tail on the vertical tail in the case of the T-tailed C-5, could increase the vertical moment arm of the vertical tail and increase its effectiveness in roll power thereby increasing the magnitude of C-L-BETA.

The C-5 and F-4 aircraft investigated in this section represent fairly complex configurations. Inaccuracies in scaling the small drawings to obtain the input data must also be considered when comparing the computed and test stability derivatives presented in this section. The next section contains the application of SACP to the solution of some example configurations which appear in Digital Datcom (3) amd ESDU (4).

3.0 Example Problems

This section contains the results of SACP applied to example problems taken from Digital Datcom (3) and ESDU(4). The example problems involve a wing-body-tail, and a wing-body configuration.

3.1 Wing-Body-Tail

The first example problem is a wing-body-tail problem taken from Digital Datcom. In this example, stability derivatives calculated by SACP are compared with those calculated by the Digital Datcom computer program.

3.1.1 Input

Input data for the wing-body-tail configruation, example problem 3 in Digital Datcom, is shown in figure 6. As can be seen from the figure it is a relatively simple mid-wing configuration.

3.1.2 Results

Comparison of the values of stability derivatives obtained by SACP and the Digital Datcom computer program for the wing-body-tail configuration is shown in figure 7. The symbols for the stability derivatives are the same as those defined in section 2. As is shown in figure 7, excellent agreement exists between SACP and Digital Datcom for each of the stability derivatives.

3.2 Wing-Body combination

An example problem concerning a wing-body combination from ESDU is presented to compare the aerodynamic center computed by SACP, with those computed by methods contained in ESDU.

The wing of the wing-body problem is of the type which can be modeled by three panels in the SACP. This allows a comparison of the theoretical wing defined by the various options in SACP with the theoretical wing defined by ESDU methods.

3.2.1 Input

Input data for the wing-body problem is shown in figure 8.

3.2.2 Results

Figure 9 contains graphical output by SACP of the actual wing and theoretical wing, for the theoretical wing defined by panels 1, 2, 3, and an average of all three panels. This figure indicates that the theoretical wing defined by wing panel 3 and the average of all wing three panels represent the actual wing best of the options available.

Table 1 contains the wing parameters for the theoretical wing defined by panel 3 and the average of all panels. Wing parameters for the wing defined by ESDU methods are also included in table 1. The ESDU theoretical wing, or equivalent wing as it is called in ESDU, is defined as an equivalent tapered wing with the same tip chord, span, and exposed area as the actual wing. The root chord at the center line of the aircraft is computed to define the equivalent wing according to the above constraints.

Theoretical wing definition is important in the computation of stability derivative coefficients for two reasons. First, theoretical wing parameters are used to compute the slope of the lift curve C-L-ALPHA, in SACP. And second, if the theoretical wing area is selected to be the reference area, then the relative effectiveness of all other surfaces as well as all stability coefficients will be effected. If the theoretical wing area, is not chosen as the reference area, wing parameters such as C-L-ALPHA and C-M-ALPHA will be effected. These parameters will be effected by an amount directly proportional to the ratio of the calculated theoretical wing area to reference area.

One of the most striking differences between SACP and ESDU wing parameters shown in table I, is the 40% difference in aerodynamic center location in percent mean aerodynamic chord. It should be noted that SACP does not calculate the aerodynamic center from the theoretical wing but from a weighted average of the individual panels of the actual wing (three in this example) and then refers the aerodynamic center to the mean aerodynamic chord of the calculated theoretical wing.

Data in table 2 shows that the body correction to the wing aerodynamic center is about the same for each method of defining the theoretical surface, when the size of the mean aerodynamic chord is considered. The data also shows that, although there is a difference in aerodynamic center location when referred to the mean areodynamic chord for the two theoretical wings defined by SACP, there is no difference when referred to the nose of the fuselage. The data in table 2 also shows that the aerodynamic center estimated by SACP for the three-panel wing-body combination is 2.2 ft farther aft than that estimated by ESDU methods. Accuracy of ESDU methods are claimed to be within plus or minus 0.5 ft for this configuration. A potential area of improvement in SACP is in the method of computing the aerodynamic center of multi-panel wings.

4.0 Conclusions and Recommendations

Based on the data presented in this report and experience gained using the Stability and Control Program (SACP) during the course of this study, the following conclusions and recommendations are made:

4.1. Conclusions

1). The SACP is a flexible and easy to use computer program which estimates stability derivatives quickly for a wide range of configurations over a wide range of flight conditions. The program structure is well designed. Graphical output options are extensive and excellent data graphs are produced.

2). Comparison of the stability derivatives estimated by SACP for the F-4C agree well with test data at most Mach numbers except for the yaw-damping, C-N-R, and the roll due to side-slip, C-L-BETA, derivatives. (Section 2.0)

3). Stability data estimates by SACP for the C-5A compared with test data indicate good agreement for the pitch damping, C-M-Q, yaw damping, C-N-R, and roll damping, C-L-P, derivatives; only fair agreement for the longitudinal derivatives C-L-ALPHA and C-M-ALPHA; and poor agreement for the yaw due to side-slip, C-N-BETA, and roll due to side-slip, C-L-BETA, derivatives. (Section 2.0)

4). Agreement of SACP estimates of stability derivatives with those computed by Digital Datcom for a wing-body-tail example configuration is excellent. (Section 3.0)

4.2. Recommendations

Recommendations for possible areas of methodology improvement are based on observations from using the Stability and Control Program (SACP) over the course of this investigation.

1). Add the option to SACP of using the ESDU Ref.(4) method of defining an equivalent wing. This could lead to a better definition of the theoretical wing area of a multi-panel wing, and thus give a better estimate of C-L-ALPHA.

2). Check the present method in SACP of calculating the aerodynamic center of a multi-panel surface. The present method appears to predict the aerodynamic center too far aft for multi-panel surfaces effecting the level of accuracy of C-M-ALPHA.

3). Include the vertical component of the horizontal tail in the computation of the yaw damping derivative, C-N-R. This would improve the estimate of C-N-R for the F-4 and other aircraft with a pronounced anhedral or dihedral of the horizontal tail.

4). Include the effect of the horizontal tail plane position on the stabilizing and rolling power of the vertical tail. This would improve the accuracy of C-N-BETA and C-L-BETA predictions for a T-tail configuration like the C-5.

5) Consider refining body geometry input definition so that more accurate body side area and body surface area values are available for all configurations. An increase in accuracy in the estimation of C-N-BETA should result from a more accurate body side area definition.

The Stability and Control Program is an excellent computer program which fulfills a need for rapid, efficient estimation of stability derivatives of flight vehicles at the conceptual design stage. Although the current predicton accuracy is sufficient for this level of design, further use and testing of the program will continue to improve its accuracy.

REFERENCES

1. Heffley, Robert K. and Wayne F. Jewell, "Aircraft Handling Qualities Data," NASA Contractor Report, NASA CR-2144, December 1972; National Aeronautics and Space Administration, Washington D.C.

2. Place, G., et al, "Interactive Computer-Aided Design Aircraft Flying Qualities Program," Vol.IV, ASD/XR 74-17, Wright Patterson Air Force Base, August 1974.

3. William, John E. and Steven K. Vukelicha, "USAF Stability and Control Digital Datcom," Vol.II. AFFDA-TR-79-3032, Wright Patterson Air Force Base, April 1979.

4. Chapell,P.D., et al, "Aerodynamic Centre of Wing-Fuselage Combinations," Engineering Sciences Data Item Number 76015, Engineering Sciences Data Unit, 251-259 Regent Street, London W1R 7AD, October 1981.

FIGURE 1. C-5A TEST CASE

REFERENCE CONDITIONS S = 6200 ft², b = 219.2 ft, $\bar{c}$ = 30.1 ft, c.g. = 99.7 ft (from nose)			
Mach	.4	.6	.8
Altitude - ft	20,000	20,000	20,000
Alpha-degree	9.0	2.2	.10

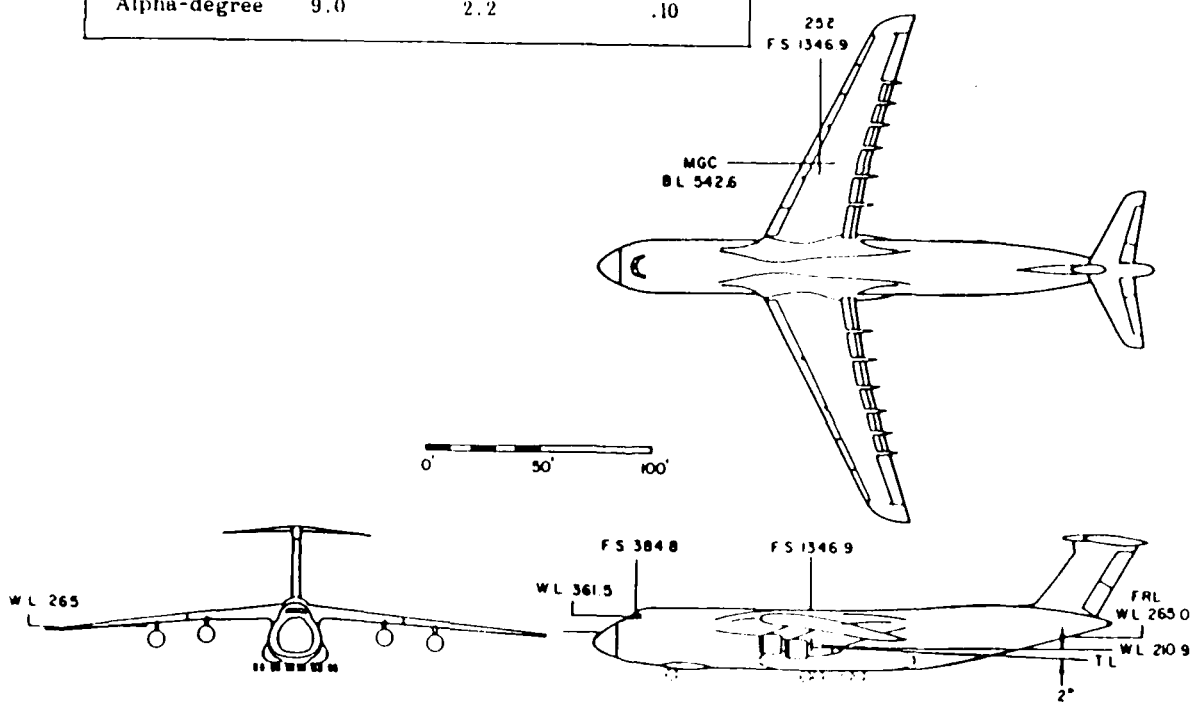

FIGURE 1.(continued) C-5A TEST CASE

C-5A SHOWING
SACP GEOMETRIC INPUTS

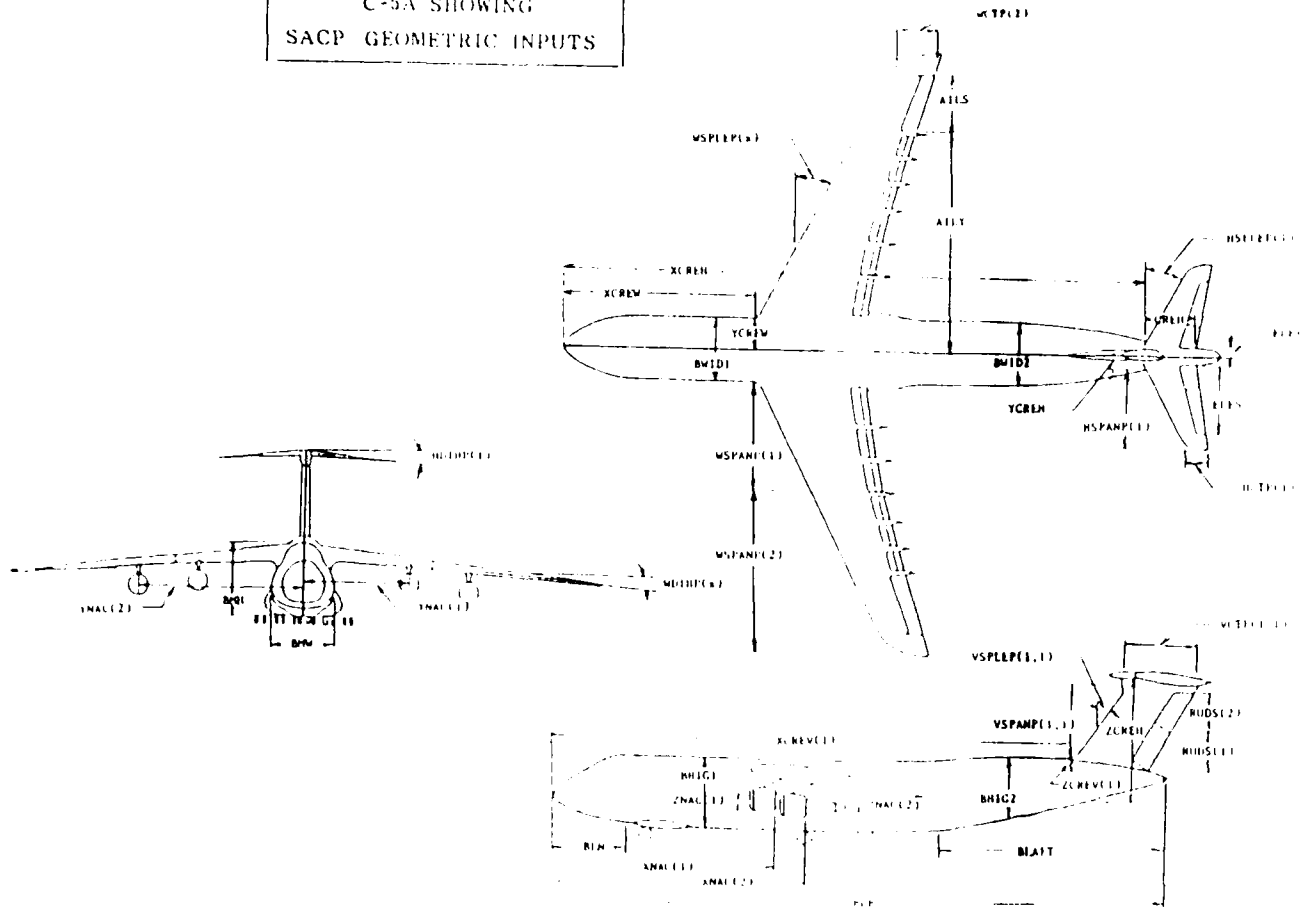

```
   C-5A  TEST CASE INPUT DATA
0100000000000000000100000000
 $CLASS  ICLASS=3,
 $END
 $WING    NATW=3,CREW=42.86,CSAW=638.28,XEXTW=00.00,WTFDD=00.00,
       XCREW=73.21,IWTED=0,BDW=25.31,IW=2.5,SEXTW=00.00,
       NPANSW=2,SLEXTW=00.00,NPTHW=0,XTCMW=.00,YCREW=11.88,
       TCREW=.125,WTFDU=00.00,AILY=207.5,WTFS=00.00,
       AILDD=15.00,ZCREW=11.25,AILC=5.94,IFLEXW=0,
       AILS=45.00,AILDU=-25.0,WTFC=00.00,WTFY=00.00,
       WTFA=00.00,AILA=252.79,WSPANP(1)=36.87,WSPANP(2)=63.0,
       WDIHP(1)=-5.08,WDIHP(2)=-5.08,WCTP(1)=29.13,
       WCTP(2)=15.34,WSPLEP(1)=28.0,WSPLEP(2)=28.0,WTOCP(1)=.10,
       WTOCP(2)=.097,
 $END
 $CANARD
 $END
 $HORZT  ELEY=2.50,TCREH=.10,ELEDU=-25.0,YCREH=5.0,NPTHH=0,
       ELEC=5.0,ELES=50.00,HTDD=-12.0,XCREH=217.86,HTDU=4.0,
       ELEDD=15.00,NATH=00,CSAH=24.89,SLEXTH=00.00,
       NPANSH=1,IFLEXH=0,ELEA=258.67,IHTED=3,IH=00.00,
       ZCREH=33.75,CREH=18.75,SEXTH=00.00,IHTAIL=1,
       BDH=5.63,XTCMH=.00,XEXTH=00.00,HSPANP(1)=29.36,
       HSPLEP(1)=30.0,HDIHP(1)=-5.0,HCTP(1)=7.71,HTOCP(1)=.10,
 $END
 $VERTT  IVTAIL=1,LVERT=1,NATV=00,RUDA(1)=127.08,RUDA(2)=99.58,VND(1)=1,
       XEXTV(1)=195.00,VCTP(1,1)=24.75,TCREV(1)=.10,YCREV(1)=0,
       VSPANP(1,1)=31.25,XCREV(1)=196.88,VSPLEP(1,1)=37.0,
       NPANSV(1)=1,RUDDEL(1)=35.0,RUDDEL(2)=35.0,RUDY(1)=2.0,
       RUDY(2)=16.25,ZCREV(1)=5.0,IVTED(1)=2,BDV(1)=11.13,
       CREV(1)=30.63,CSAV(1)=97.29,RUDS(1)=15.63,RUDS(2)=15.63,
       RUDC(1)=7.5,RUDC(2)=7.5,VTOCP(1,1)=.10,
 $END
 $FIN
 $END
 $FUSE    BBASE=00.00,IBODY=1,BHI62=20.00,BAMX=712.5,BLAFT=87.5,
       BABS=00.00,BWID2=21.63,BDNOSE=23.75,BMH=26.875,
       BLB=230.6,BWID1=23.75,BUSA=12.00,BLN=26.79,
       BNOSE=0.00,BWHU=1.08,BMW=23.75,BHI61=26.88,BHB=26.88,
 $END
 $NACELLE  ELEN(1)=25.9,EHI61(1)=8.75,EWID2(1)=4.38,ELBT(1)=15.0,
        EHI62(1)=4.38,LNAC(1)=1,EAMX(1)=50.0,EIN(1)=40.0,
        ELNS(1)=10.0,XNAC(1)=85.0,XNAC(2)=93.75,EMH(1)=8.75,
        ZNAC(1)=2.5,ZNAC(2)=-2.5,YNAC(1)=40.63,YNAC(2)=63.13,
        ENO(1)=4,EMW(1)=8.75,NNACS=1,EWID1(1)=8.75,
             IFN(1)=1.25,
 $END
 $MOMENT IXZ=2460000.,IXX=27800000.,IZZ=56200000.,IYY=31800000.,
 $END
 $AEROK  LCG=99.7,IXCD=0,NMAP=3,ITRIMD=0,SHK=00.00,
      ROUGHK=00.00,NTRIMD=0,FMISC=.15,XMEU=0.00,
      SREF=6200.,WEIGHT=654362.0,XCD=.00,AMC=40.00,
      XMG=.00,CDMG=0.00,ZGLCG=15.00,MACH(1)=.4,.6,.8,NLP=3,
        ALF(1)=.1,2.2,9.,
      ALT(1)=20000.,20000.,20000.,
 $END
 $PROP
 $END
 $SCRIT
 $END
 $HILIFT
 $END
 $OPTION
 $END
```

FIGURE 2

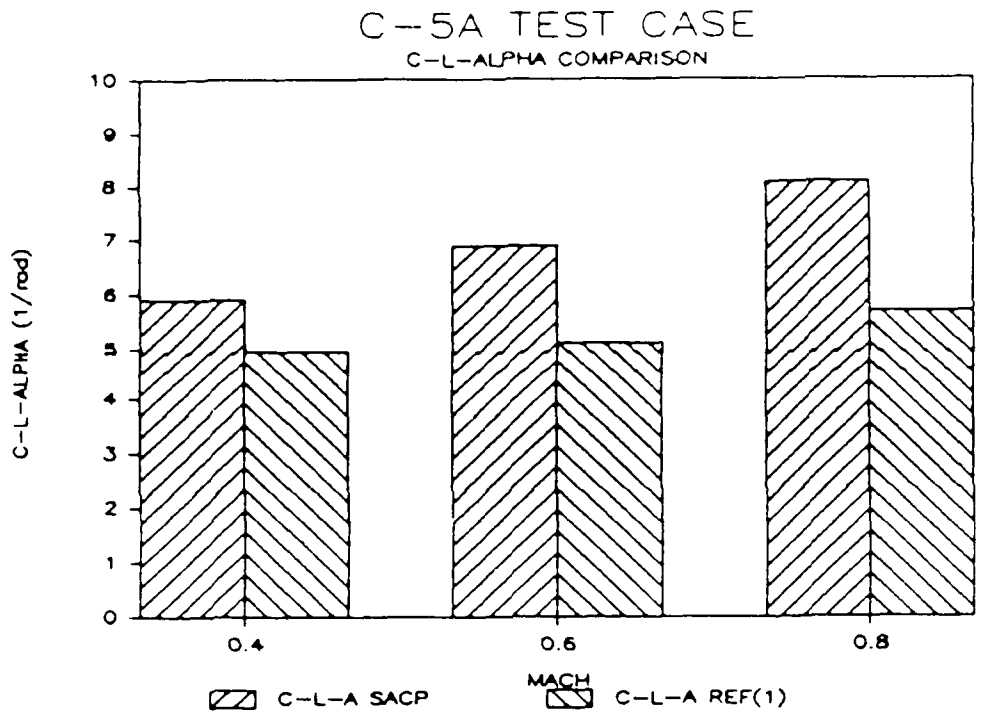
C-5A TEST CASE
C-L-ALPHA COMPARISON
C-L-ALPHA (1/rad)
10
9
8
7
6
5
4
3
2
1
0
0.4
0.6
0.8
MACH
C-L-A SACP
C-L-A REF(1)

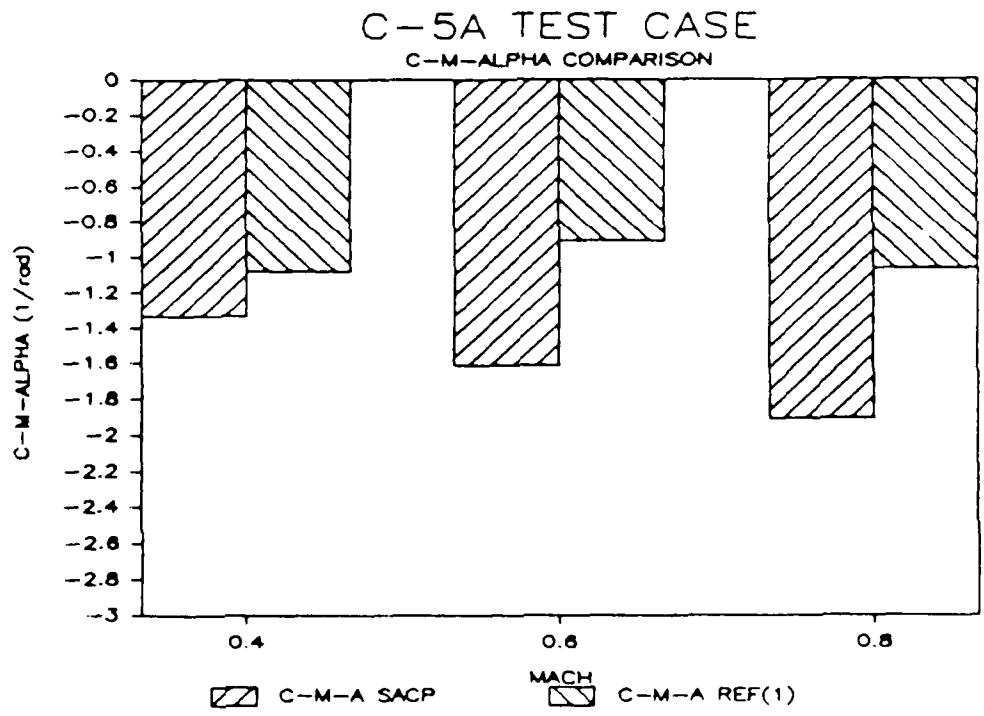
C-5A TEST CASE
C-M-ALPHA COMPARISON
C-M-ALPHA (1/rad)
0
-0.2
-0.4
-0.6
-0.8
-1
-1.2
-1.4
-1.6
-1.8
-2
-2.2
-2.4
-2.6
-2.8
-3
0.4
0.6
0.8
MACH
C-M-A SACP
C-M-A REF(1)

FIGURE 2(continued)

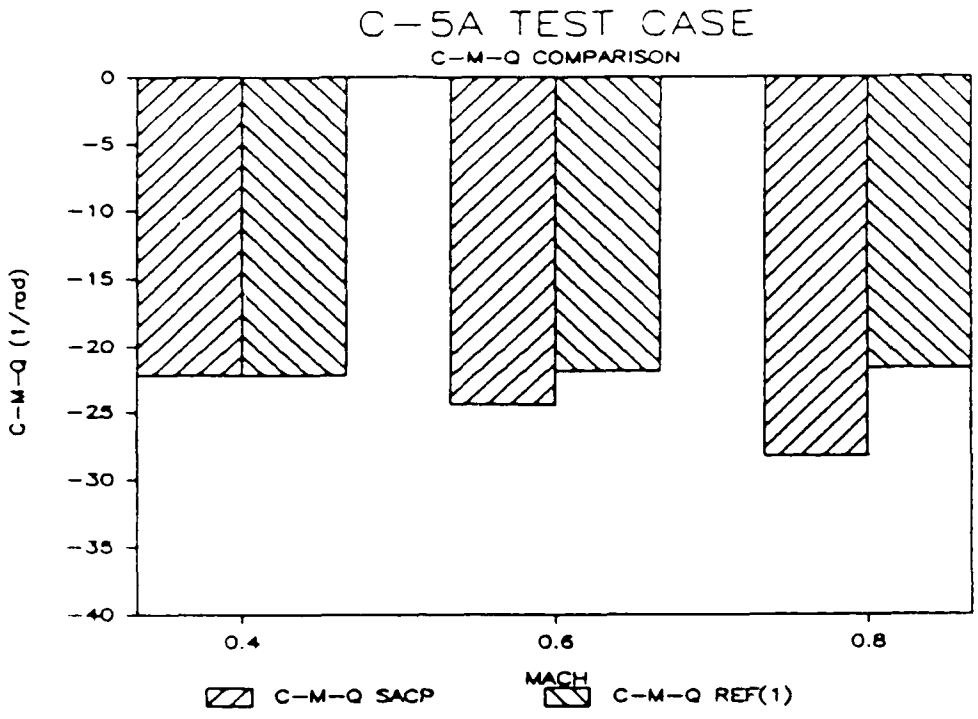

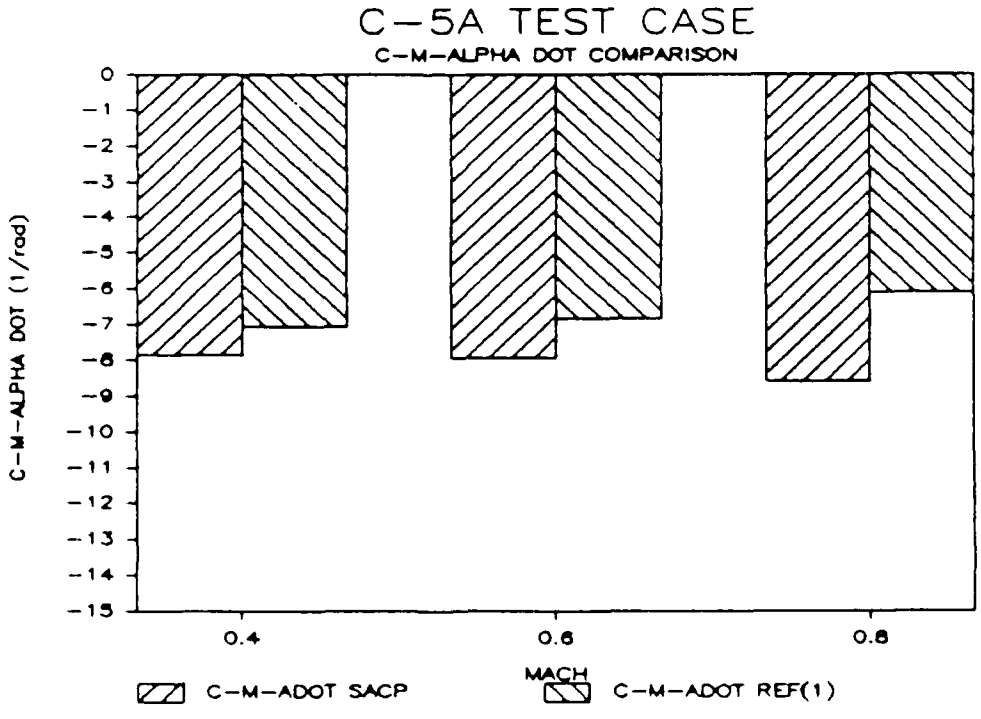

FIGURE 2(continued)

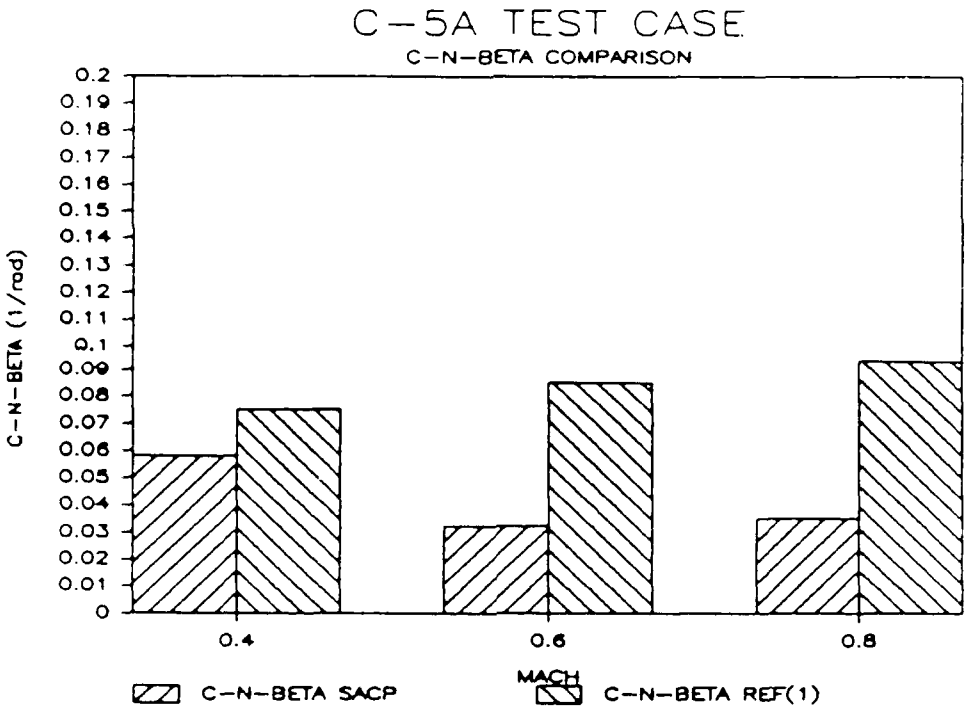

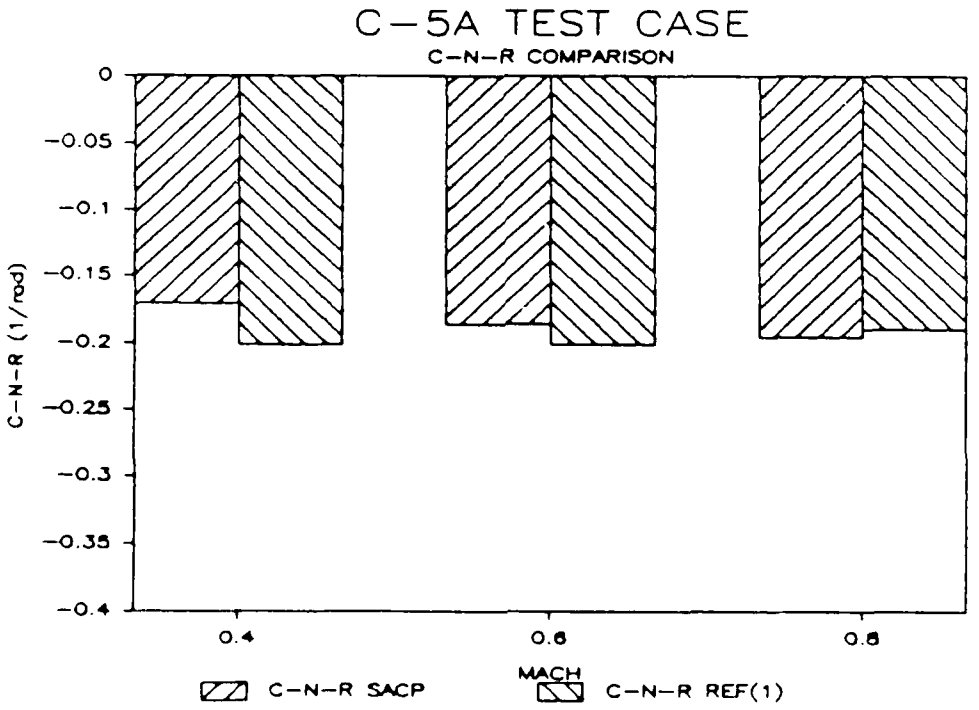

FIGURE 2(continued)

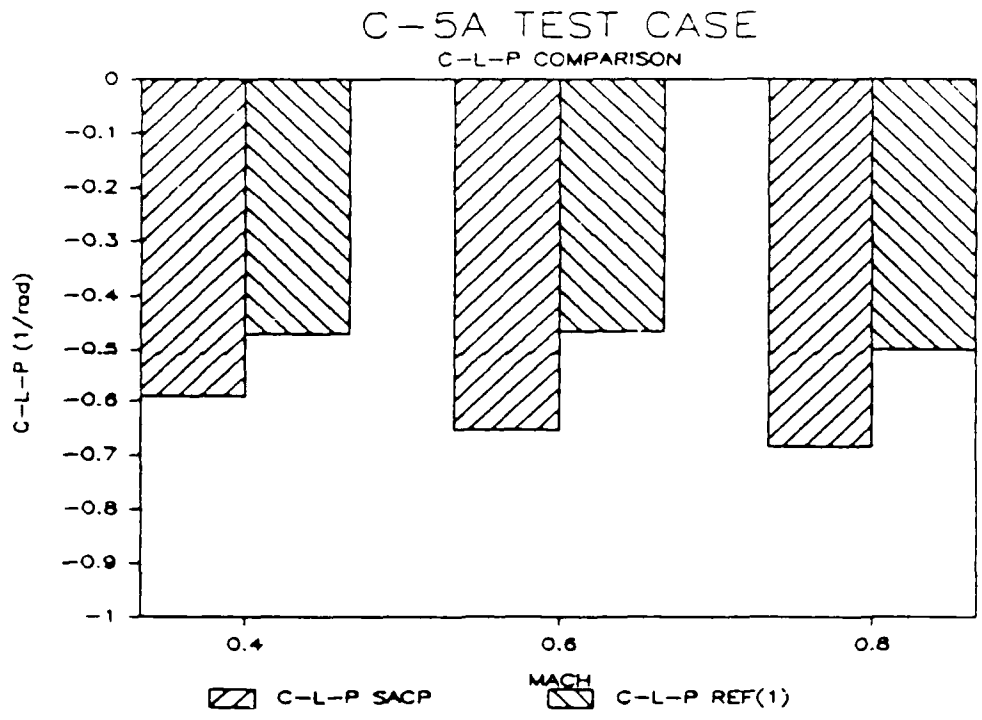

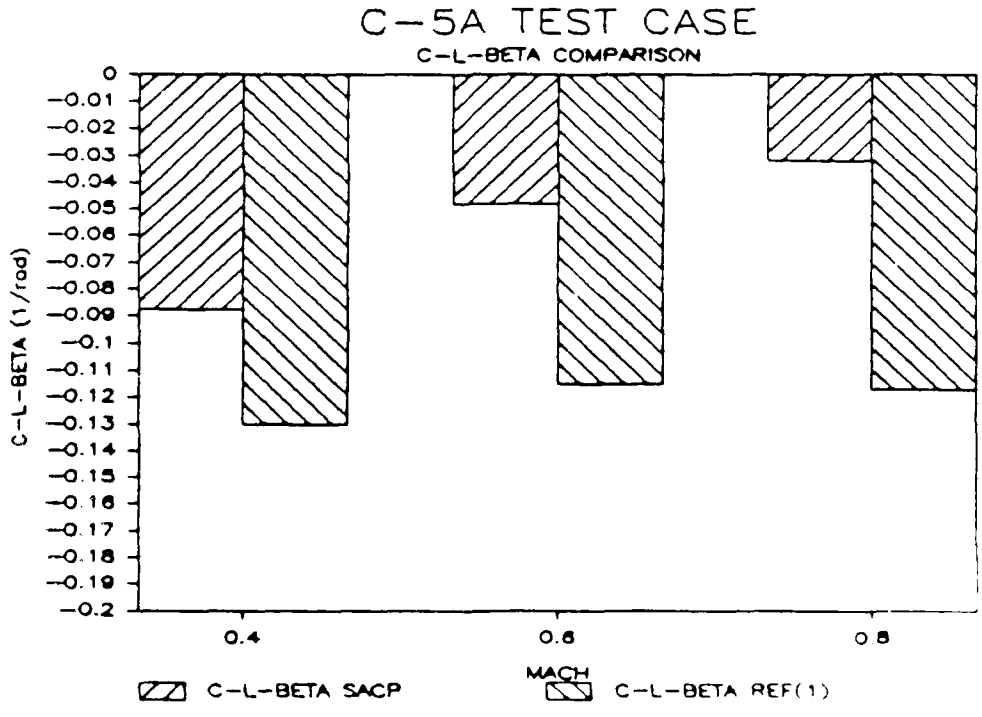

AD-A186 493 UNITED STATES AIR FORCE RESEARCH INITIATION PROGRAM 6/ 8
1985 TECHNICAL REPORT VOLUME 3(U) UNIVERSAL ENERGY
SYSTEMS INC DAYTON OH R C DARRAH APR 87
UNCLASSIFIED AFOSR-TR-87-1719 F49620-85-C-0013 F/G 15/3 NL

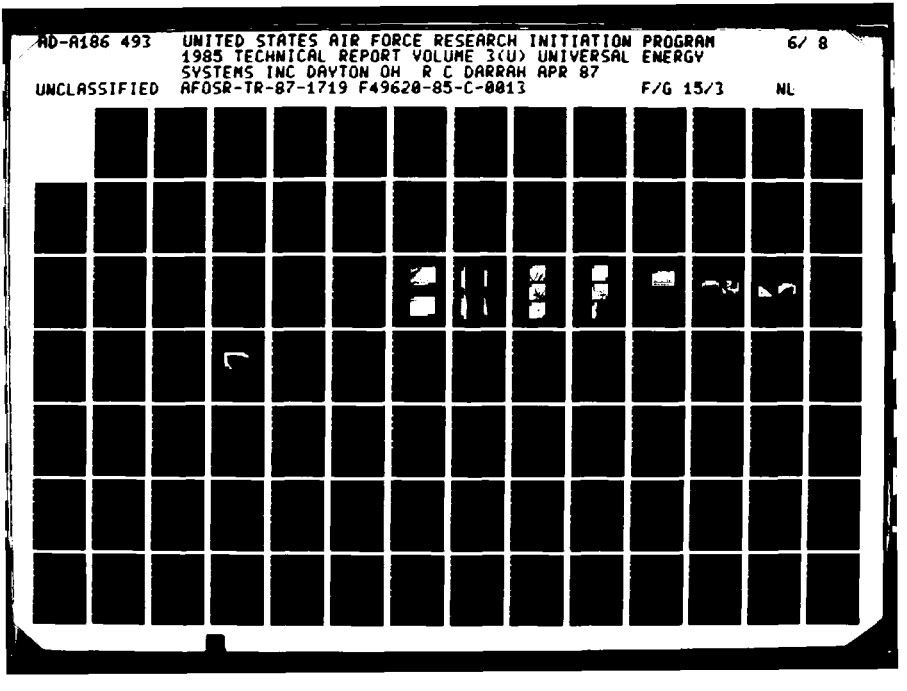

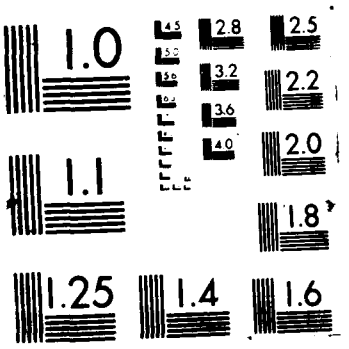
1.0
1.1
1.25
1.4
1.6
1.8
2.0
2.2
2.5
2.8
3.2
3.6
4.0
4.5
5.0
5.6
6.3

FIGURE 3

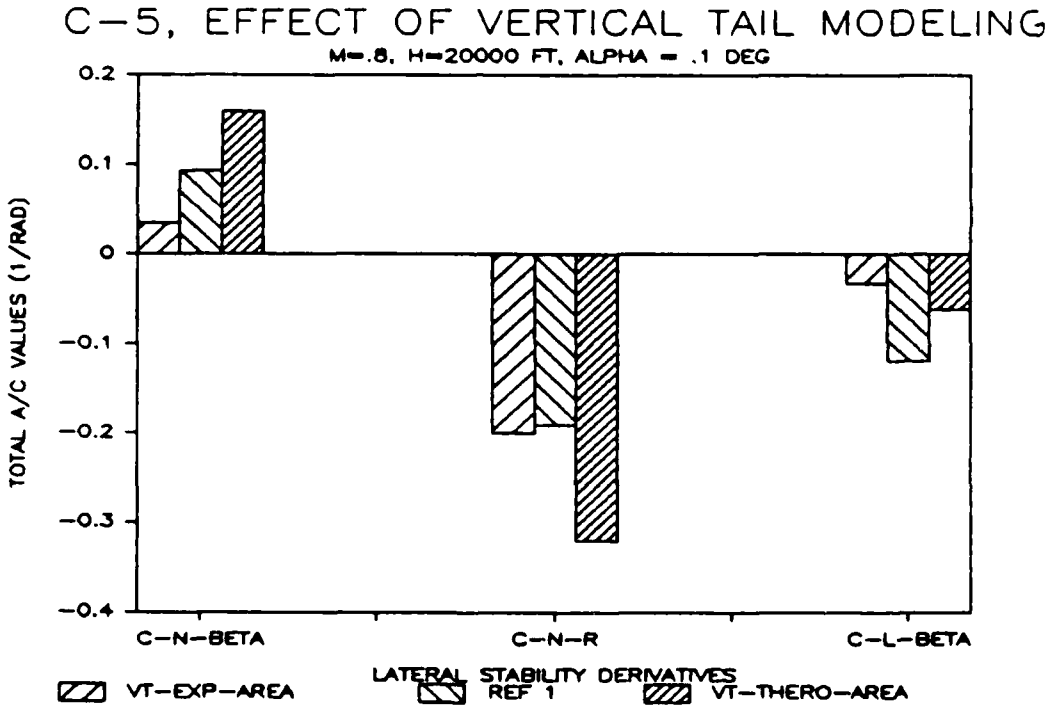
C-5, EFFECT OF VERTICAL TAIL MODELING
M=.8, H=20000 FT, ALPHA = .1 DEG
TOTAL A/C VALUES (1/RAD)
0.2
0.1
0
-0.1
-0.2
-0.3
-0.4
C-N-BETA
C-N-R
C-L-BETA
LATERAL STABILITY DERIVATIVES
VT-EXP-AREA
REF 1
VT-THERO-AREA

FIGURE 4. F-4C TEST CASE

REFERENCE CONDITIONS

S = 530 ft², b = 38.67 ft, $\bar{c}$ = 16.04 ft, c.g. = 27.63 ft (from nose)

Mach	.6	.9	1.2	1.5	2.15
Altitude - ft	35,000	35,000	35,000	45,000	45,000
Alpha-degree	9.4	2.6	1.6	2.6	1.4

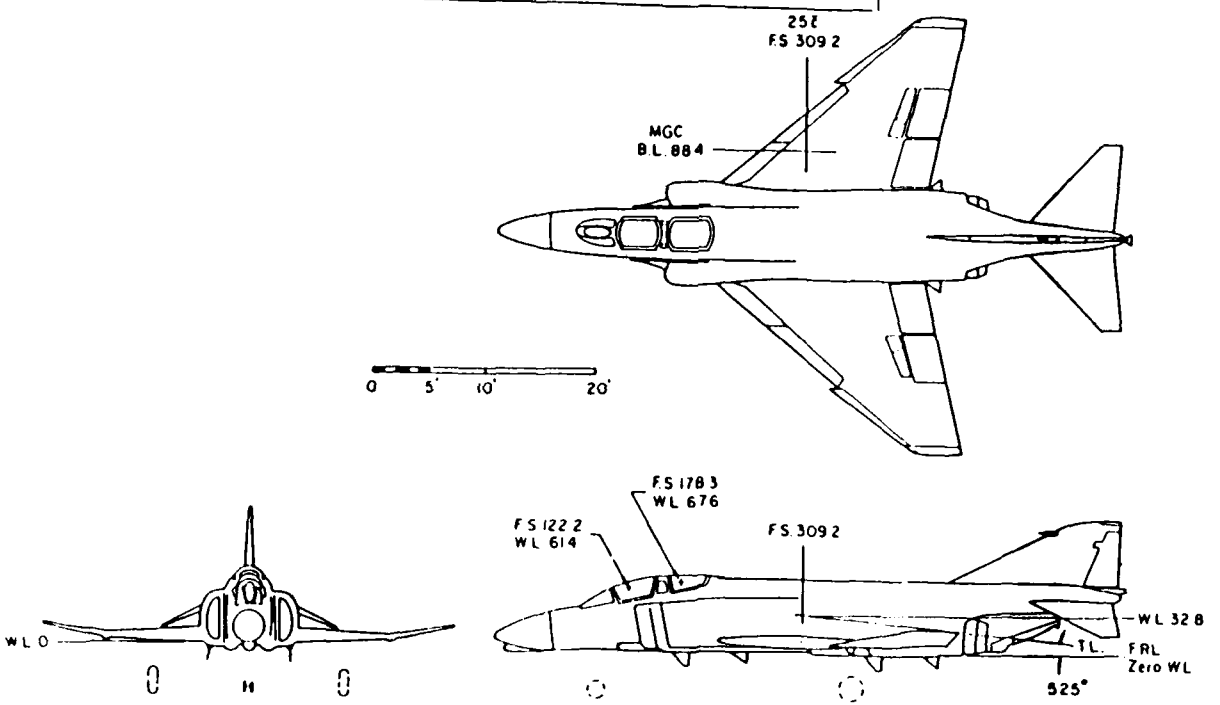

FIGURE 4. (continued) F-4C TEST CASE

F-4C SHOWING SOME
SACP GEOMETRIC INPUTS

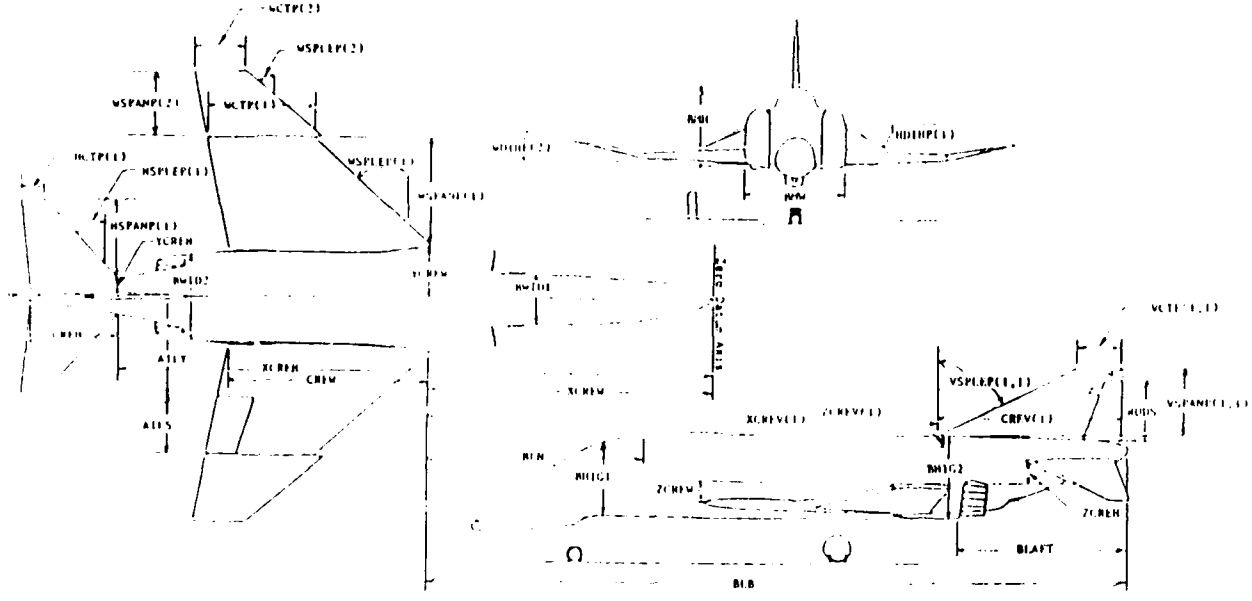

FIGURE 3 (continued)

F-4C INPUT DATA

```
   F-4 TEST CASE
0100000000000000000000000000000000
 $CLASS  ICLASS=4,
 $END
 $WING    NATW=3,CREW=18.2,CSAW=45.13,
       XCREW=19.60,IWTED=1,BDW=5.70,
       NPANSW=2,NPTHW=0,XTCMW=.40,YCREW=4.44,
       TCREW=.064,AILY=9.94,
       AILDO=20.0,ZCREW=1.68,AILC=2.76,IFLEXW=1,
       AILS=9.0,AILDU=-20.0,
       WSPANP(2)=5.46,WDIHP(2)=12.,
       WCTP(1)=8.70,WCTP(2)=4.25,WSPLEP(1)=51.41,WSPLEP(2)=51.41,
       AILA=12.42,WSPANP(1)=9.24,WTOCP(1)=.04,WTOCP(2)=.03,
       WOFFP(2)=.72,
 $END
 $CANARD
 $END
 $HORIZT  ELEV=00.00,TCREH=.064,ELEDU=00.00,YCREH=1.20,NPTHH=0,
       HTDO=-20.0,ZCREH=47.1,HTDU=20.0,
       NATH=3,CSAH=4.80,
       NPANSH=1,IFLEXH=1,IHTED=3,
       ZCREH=1.67,CREH=7.19,IHTAIL=1,
       BDH=2.2,XTCMH=.40,HSPANP(1)=7.79,
       HSPLEP(1)=42.0,HDIHP(1)=-23.0,HCTP(1)=2.16,HTOCP(1)=.03,
 $END
 $VERTT  IVTAIL=1,LVERT=1,NATV=3,RUDA=11.72,VNO(1)=1,VCTP(1,1)=3.83,
       NPTHV(1)=1,YCREV(1)=0.0,VSPANP(1,1)=6.10,XCREV(1)=40.,
       VSPLEP(1,1)=62.0,NPANSV(1)=1,IVTED(1)=2,BDV(1)=4.2,
       CREV(1)=5.57,CSAV(1)=21.0,RODS(1)=5.03,RUDC(1)=2.33,
       RUDY(1)=3.8,ZCREV(1)=.72,IVTED(1)=2,TCREV(1)=.064,
       VTOCP(1,1)=.03,XTCMV(1)=.40,RUDDEL(1)=20.0,IFLEXV(1)=1,
 $END
 $FIN
 $END
 $FUSE    BBASE=.1,BHIB2=6.90,BAMI=47.01,BLAFT=13.9,
       BABS=49.59,BWID2=7.42,BONOSE=8.74,SMH=7.79,
       BLB=56.,BWID1=4.13,BUSA=21.0,BLN=15.,BHB=7.79,
       BNOSE=00.00,IBODY=1,BWHU=.60,BNW=8.74,BHIG1=5.75,
 $END
 $NACELLE
 $END
 $MOMENT IXZ=2177.0,IXX=25001.0,IZZ=139759.0,IYY=122186.0,
 $END
 $AEROK  LCG=27.63,IXCD=0,NMAP=5,SHK=00.00,
       ROUGHK=00.00,NTRIMD=0,FMISC=.00,IMEU=0.00,
       SREF=530.0,WEIGHT=38924.0,  XCD=.00,AMC=40.00,
        ZGLCG=8.,MACH(1)=.6,.9,1.2,1.5,2.15,
     NLP=4,ALF(1)=1.4,1.6,2.6,9.4,
      ALT(1)=35000.,35000.,35000.,45000.,45000.,
 $END
 $PROP
 $END
 $SCRIT
 $END
 $HILIFT DS2L=00.00,CPF1T=1.00,DS2T=00.00,CPF1L=1.00,
       CPS1T=1.00,CPS1L=1.00,CPF2L=0.00,DS1T=00.00,
       BS10=0.71,CPF2T=1.00,CPS2L=1.00,CS1=0.00,
       CS2=0.00,BF1T=.230,DS1L=00.00,BS20=0.96,
       IHLS=0,BF10=.450,BF2I=0.00,CPS2T=0.00,BF20=0.00,
       BS1T=0.37,BS2I=0.71,DF1T(1)=40.0,NFLAP(1)=1,
 $END
 $OPTION
 $END
OK,
```

FIGURE 5

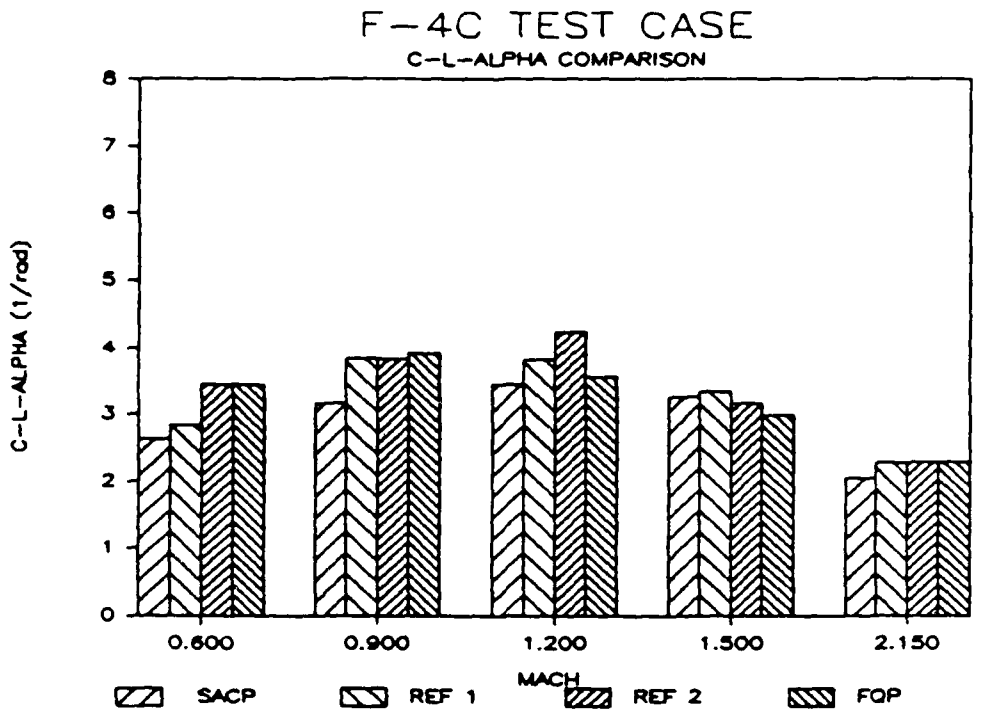
F-4C TEST CASE
C-L-ALPHA COMPARISON
C-L-ALPHA (1/rad)
8
7
6
5
4
3
2
1
0
0.600
0.900
1.200
1.500
2.150
MACH
SACP
REF 1
REF 2
FQP

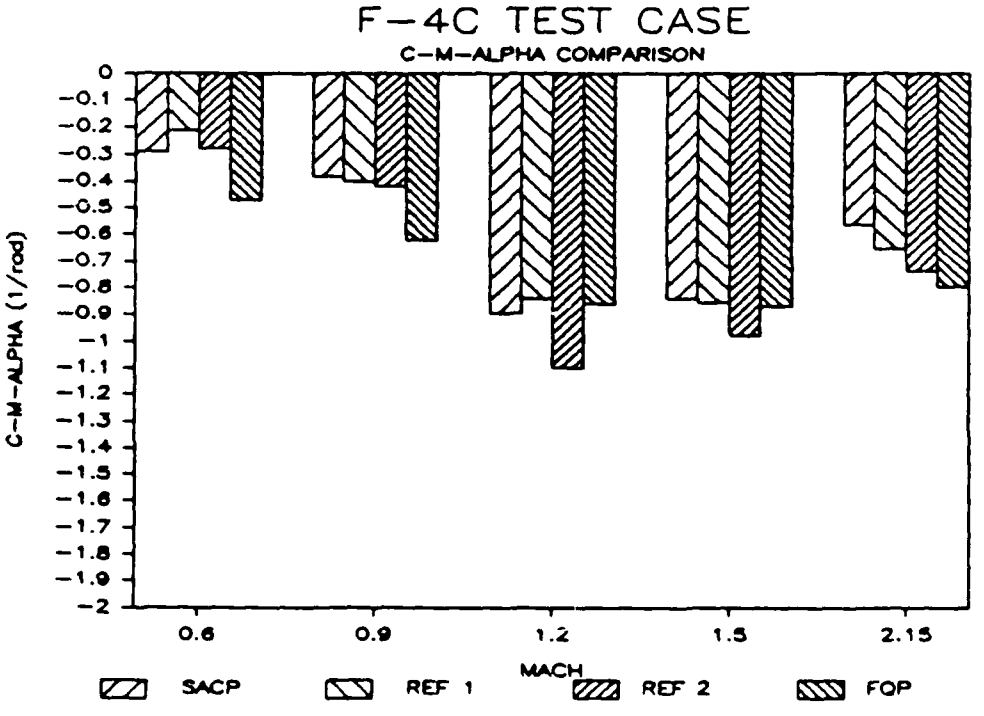
F-4C TEST CASE
C-M-ALPHA COMPARISON
C-M-ALPHA (1/rad)
0
-0.1
-0.2
-0.3
-0.4
-0.5
-0.6
-0.7
-0.8
-0.9
-1
-1.1
-1.2
-1.3
-1.4
-1.5
-1.6
-1.7
-1.8
-1.9
-2
0.6
0.9
1.2
1.5
2.15
MACH
SACP
REF 1
REF 2
FQP

FIGURE 5(continued)

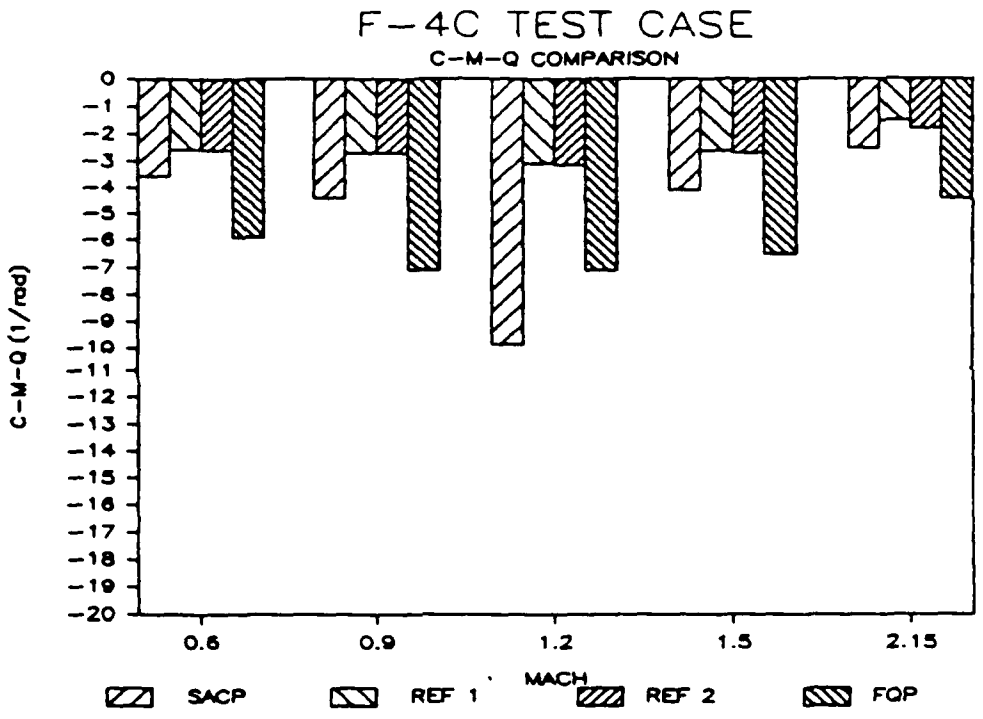

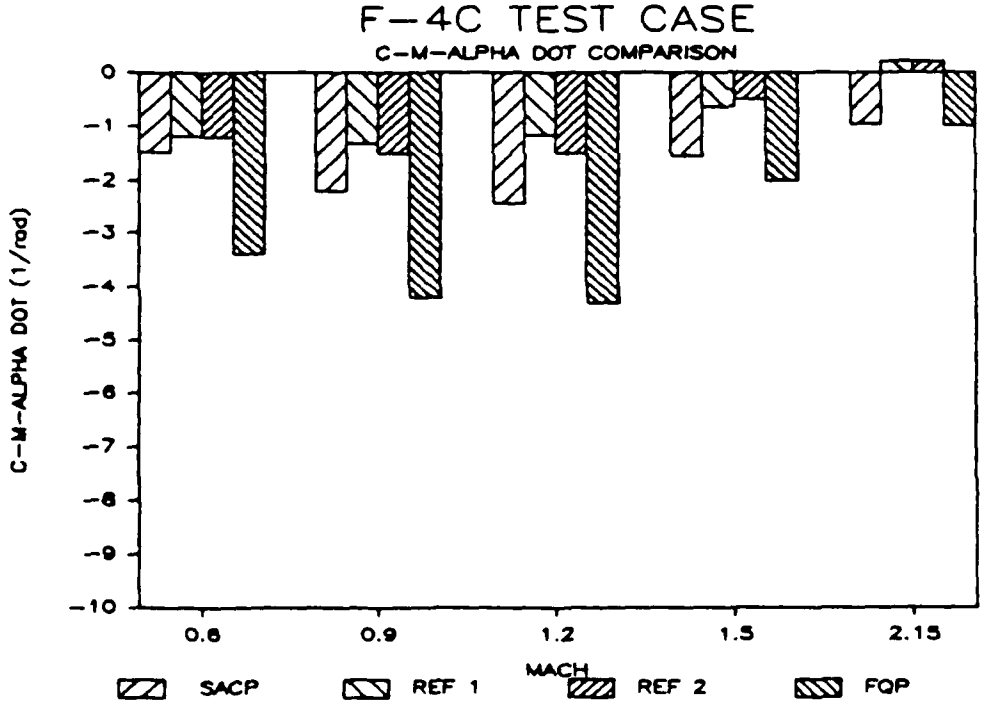

FIGURE 5(continued)

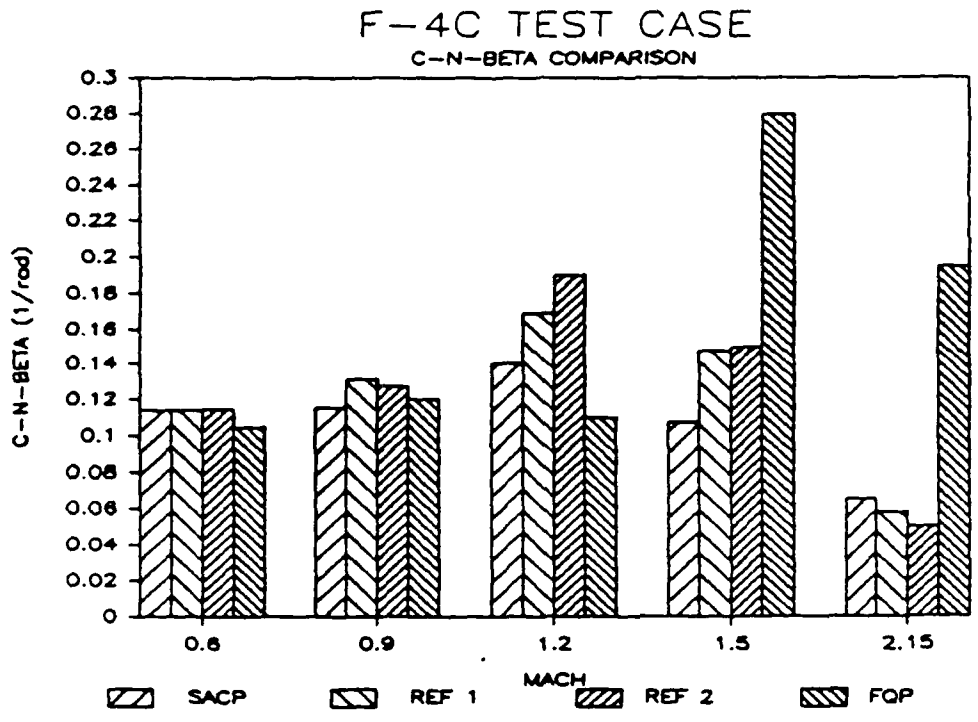

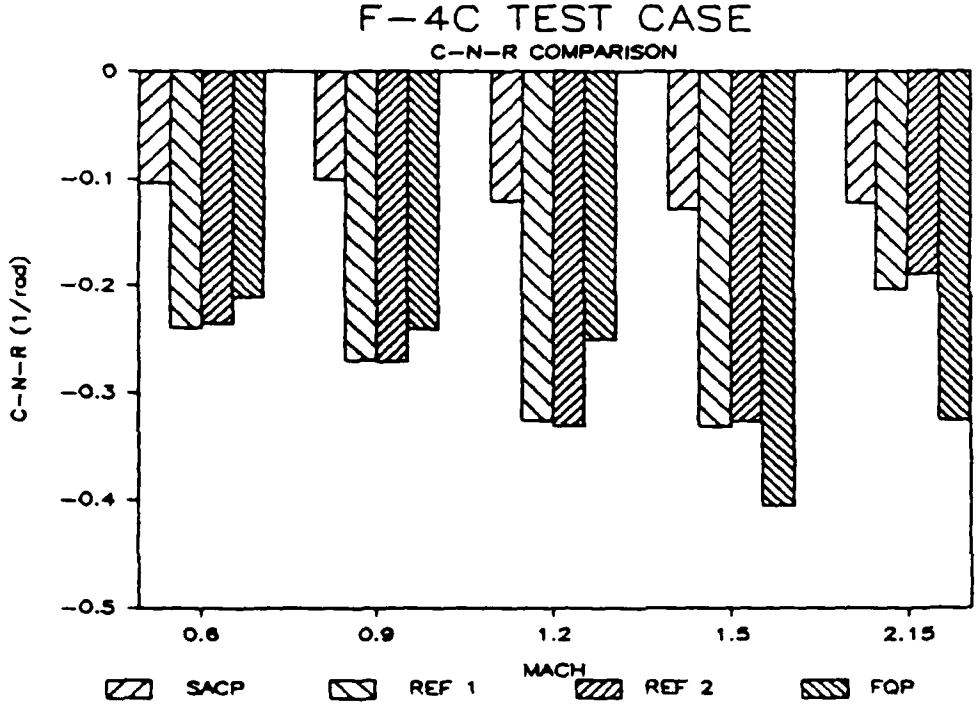

FIGURE 5(continued)

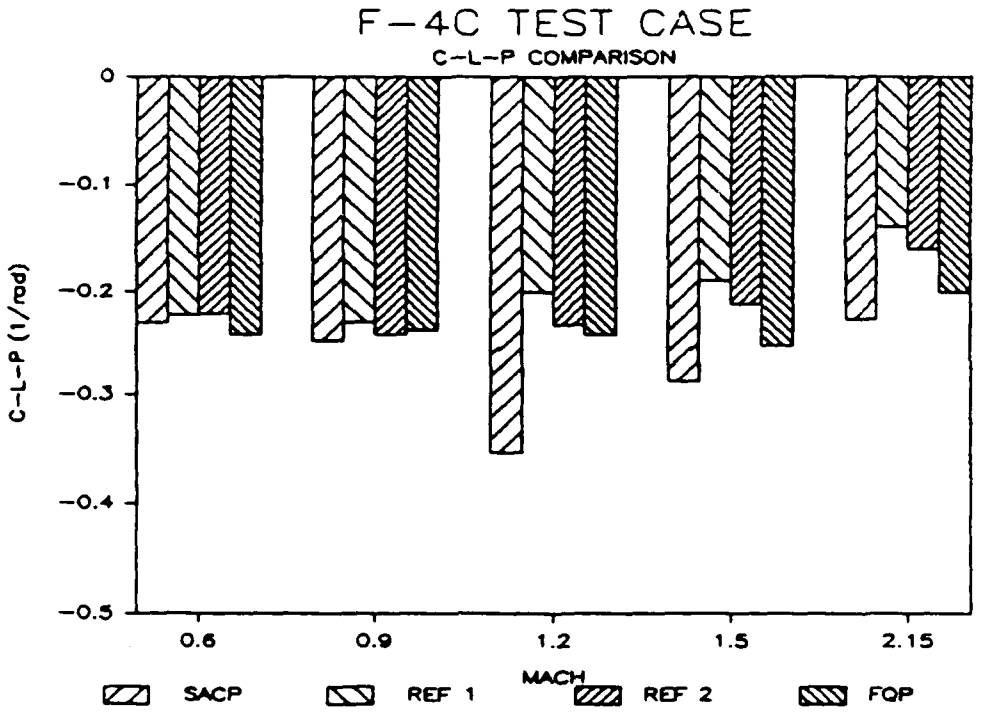

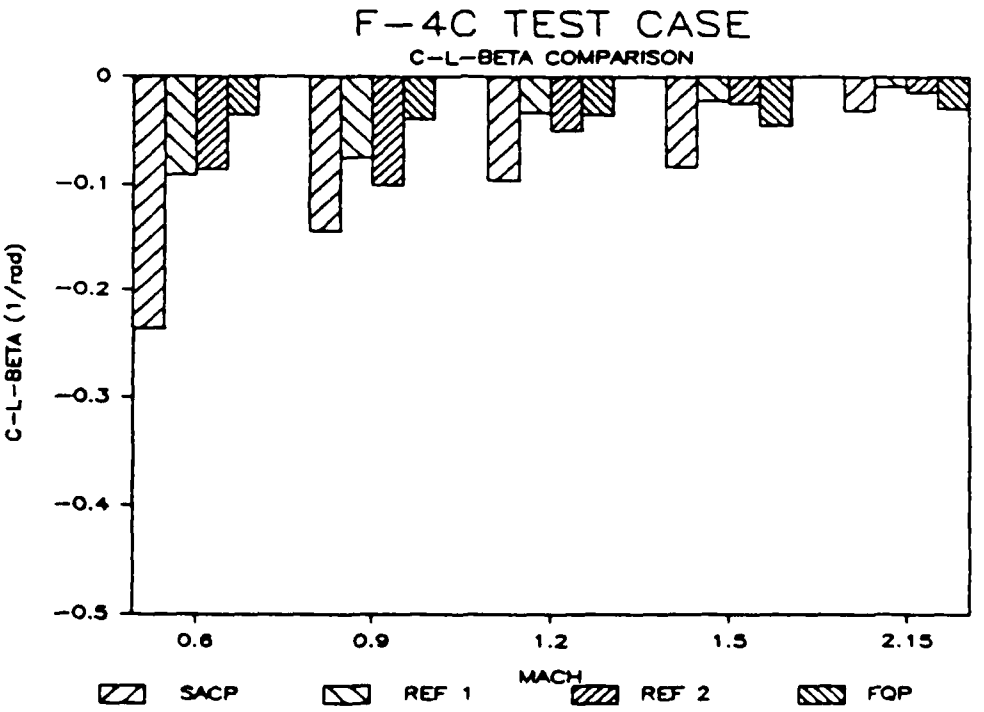

FIGURE 6

DIGITAL DATCOM
WING-BODY-TAIL EXAMPLE

FLIGHT CONDITIONS: MACH NUMBERS = 0.60, 0.80
REYNOLDS NUMBERS PER FT = 2.28×10^6, 3.04×10^6
SCHEDULED ANGLES OF ATTACK = -2.0, 0.0, 2.0, 4.0, 8.0, 12.0, 16.0, 20.0, 24.0

REFERENCE PARAMETERS: REFERENCE AREA = 2.25
LONG. REF. LENGTH = 0.822
LATERAL REF LENGTH = 3.00

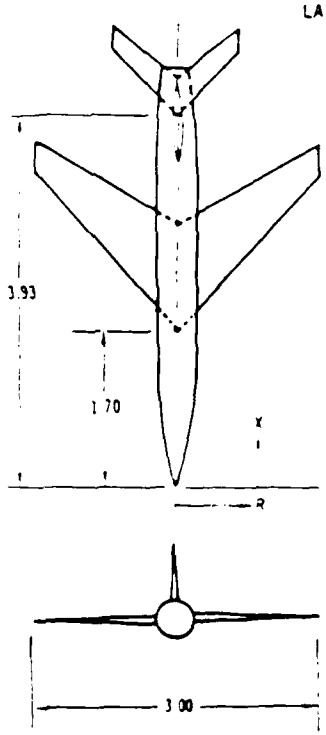

	WING	HORIZONTAL TAIL	VERTICAL TAIL
SEMISPAN	1.50	0.67	0.849
EXPOSED SEMISPAN	1.29	0.52	0.630
c_t	0.346	0.253	0.42
c_R	1.16	0.420	1.02
$\Lambda_{c/4}$	45°	45°	28.1
AIRFOIL	NACA 65A006	NACA 65A006	NACA 63A009

REFER TO INPUT DATA FOR BODY AND PROPELLER POWER DATA.

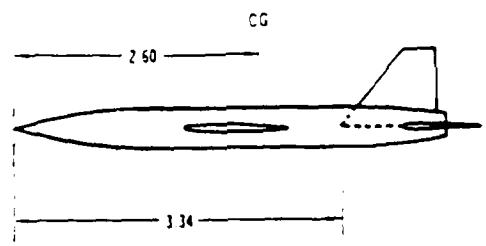

FIGURE 6(continued)

```
        INPUT FOR EXAMPLE PROBLEM 3 FROM DIGITAL DATCOM REF(3)

 DIGITAL DATCOM EX PROB 3       PAGE 115 VOL I
0100000000000000000000000
 $CLASS ICLASS=4,$END
 $WING NATW=7,NPTHW=1,NPANSW=1,CSAW=.136,BDW=.416,XTCMW=.40,IW=0.,IFLEXW=0,
       CREW=1.05,TCREW=.06,XCREW=1.938,YCREW=.208,ZCREW=0,
       WSPLEP(1)=48.6,WTOCP(1)=.06,WSPANP(1)=1.29,WCTP(1)=.346,WCAMP(1)=.0,
       WTWISTP(1)=0.,WDIHP(1)=0.,
       IWTED=0,
 $END
 $CANARD ICAN=0,
 $END
 $HORZT IHTAIL=1,
        NATH=7,NPTHH=1,NPANSH=1,
        CSAH=.07955,BDH=.3,XTCMH=.40,IH=0.,IFLEXH=0,
        CREH=.38,TCREH=.06,XCREH=4.119,YCREH=.15,ZCREH=0.,
       HSPLEP(1)=47.,HTOCP(1)=.06,HSPANP(1)=.52,HCTP(1)=.253,HCAMP(1)=0.,
       HTWISTP(1)=0.,HDIHP(1)=0.,
       IHTED=3,
      HTDU=25.,HTDD=-25.,
 $END
 $VERTT IVTAIL=1,LVERT=1,
        NATV(1)=5,VNO(1)=1,NPANSV(1)=1,NPTHV(1)=1,
        CSAV(1)=.1,BDV(1)=.356,XTCMV(1)=.40,
        CREV(1)=.85,TCREV(1)=.05,
        IV(1)=0.0,
        XCREV(1)=3.51,YCREV(1)=0.,ZCREV(1)=.22,
       VSPLEP(1,1)=35.,VTOCP(1,1)=.09,VSPANP(1,1)=.630,
       VCTP(1,1)=.42,VCAMP(1,1)=0.0,
       VTWISTP(1,1)=0.0,VDIHP(1,1)=0.,
       IVTED(1)=0,
 $END
 $FIN IFINS=0,$END
 $FUSE BLB=4.57,
       BNOSE=0.,BLN=1.46,BDNOSE=.416,BBASE=.0598,BAMX=.136,BABS=0.,
       BMW=.416,BMH=.416,BHIG1=.416,BWID1=.416,BHIG2=.416,BWID2=.416,
  BLAFT=.0,IBODY=1,BHB=.4,
 $END
 $NACELLE NNACS=0,
 $END
 $MOMENT IXX=25459.,IYY=166792.,IZZ=187083.,IXZ=-1001.,$END
 $AEROK
       NMAP=2,MACH(1)=.6,.8,
   ALT(1)=10000.,NLP=15,
      ALF(1)=.01,2.,4.,6.,8.,10.,12.,14.,16.,18.,20.,22.,24.,26.,28.,
      SREF=2.25,WEIGHT=1.,CDMG=.00145,LCG=2.60,ZGLCG=7.4167,AMC=40.,
      XMG=.418,XMEU=.04,
      IXCD=0,SHK=0.0,XCD=.9,FMISC=10.,ROUGHK=.001,NTRIMD=1,
      ITRIMD(1)=4,
      PTRIMD(1)=1.0,  $END
 $PROP NPDATA=0,
      $END
 $SCRIT $END
 $HILIFT IHLS=0, $END
 $OPTION $END
```

FIGURE 7

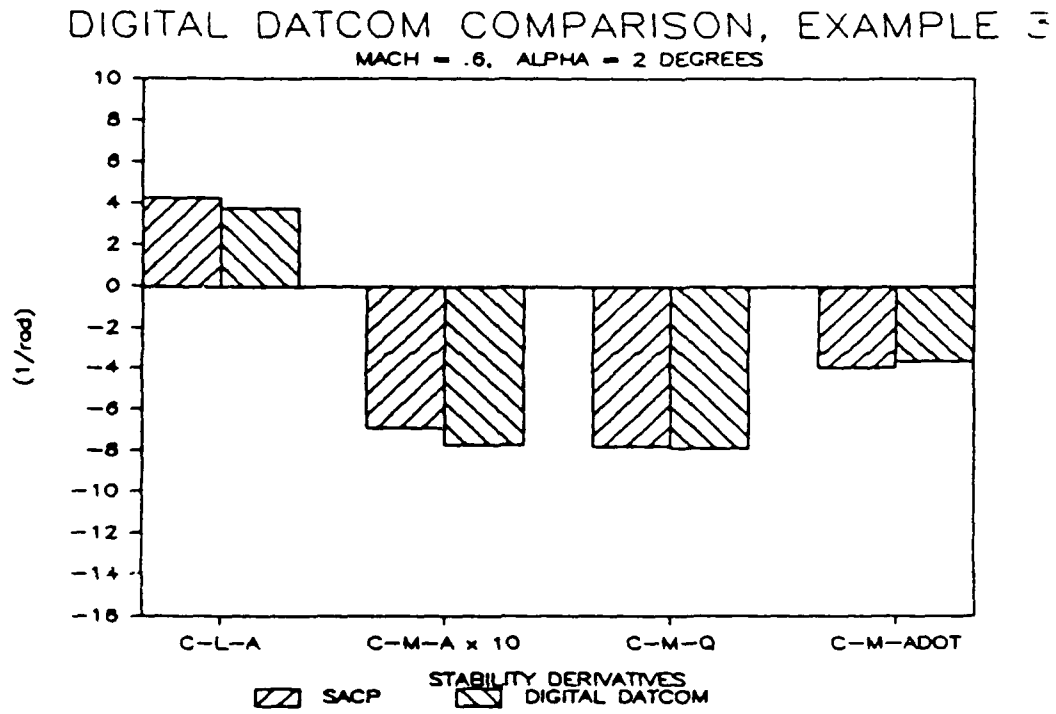
DIGITAL DATCOM COMPARISON, EXAMPLE 3
MACH = .6, ALPHA = 2 DEGREES
10
8
6
4
2
0
−2
−4
−6
−8
−10
−12
−14
−16
(1/rad)
C−L−A
C−M−A x 10
C−M−Q
C−M−ADOT
STABILITY DERIVATIVES
SACP
DIGITAL DATCOM

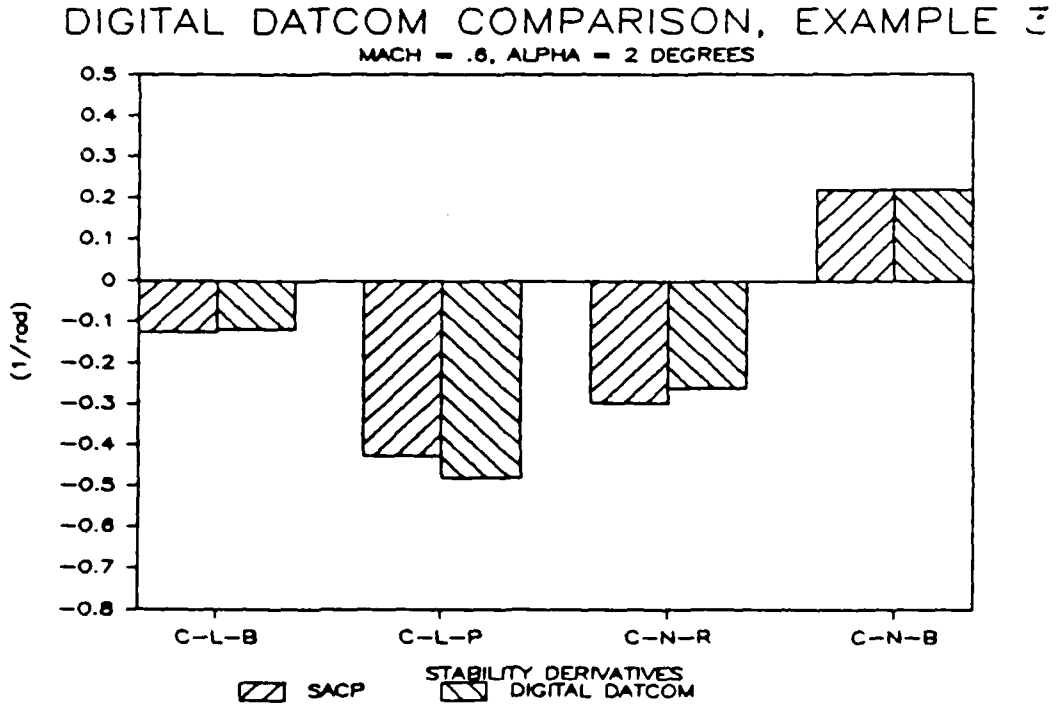
DIGITAL DATCOM COMPARISON, EXAMPLE 3
MACH = .6, ALPHA = 2 DEGREES
0.5
0.4
0.3
0.2
0.1
0
−0.1
−0.2
−0.3
−0.4
−0.5
−0.6
−0.7
−0.8
(1/rad)
C−L−B
C−L−P
C−N−R
C−N−B
STABILITY DERIVATIVES
SACP
DIGITAL DATCOM

ESDU

WING-BODY EXAMPLE

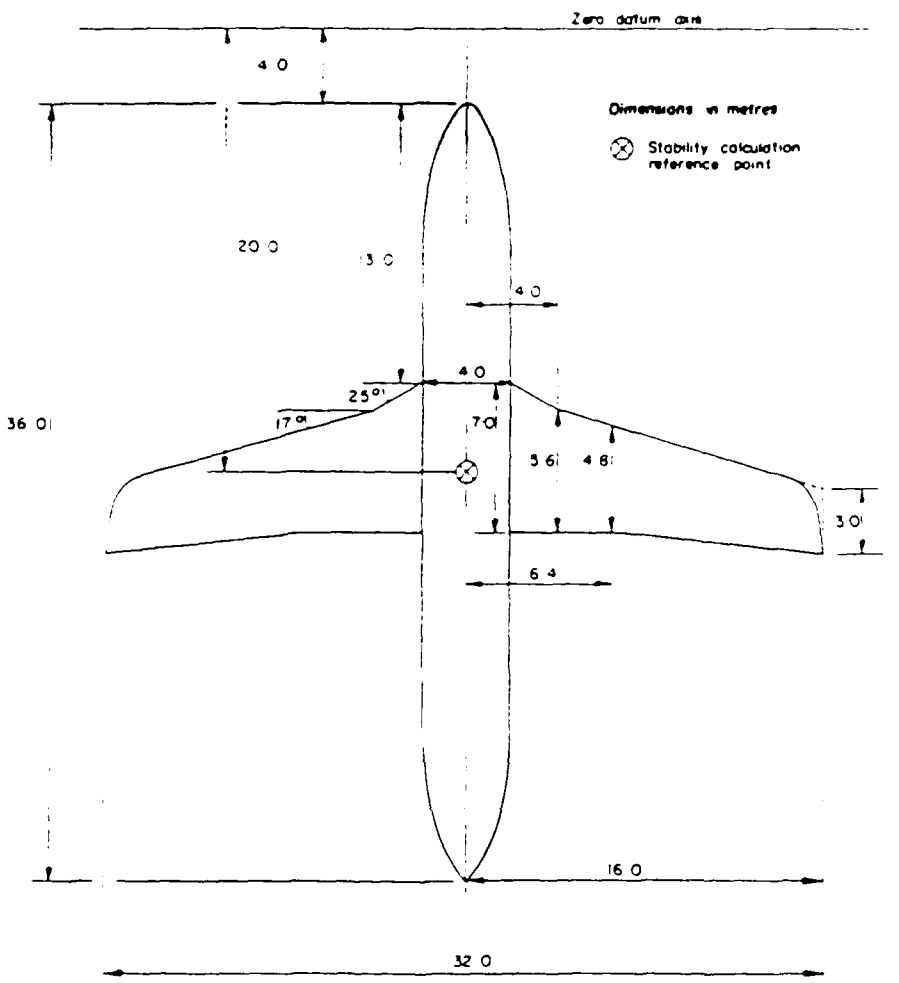

Fuselage height h = 5 0m

FIGURE 8(continued)

ESDU WING-BODY EXAMPLE SHOWING SACP GEOMETRIC INPUTS

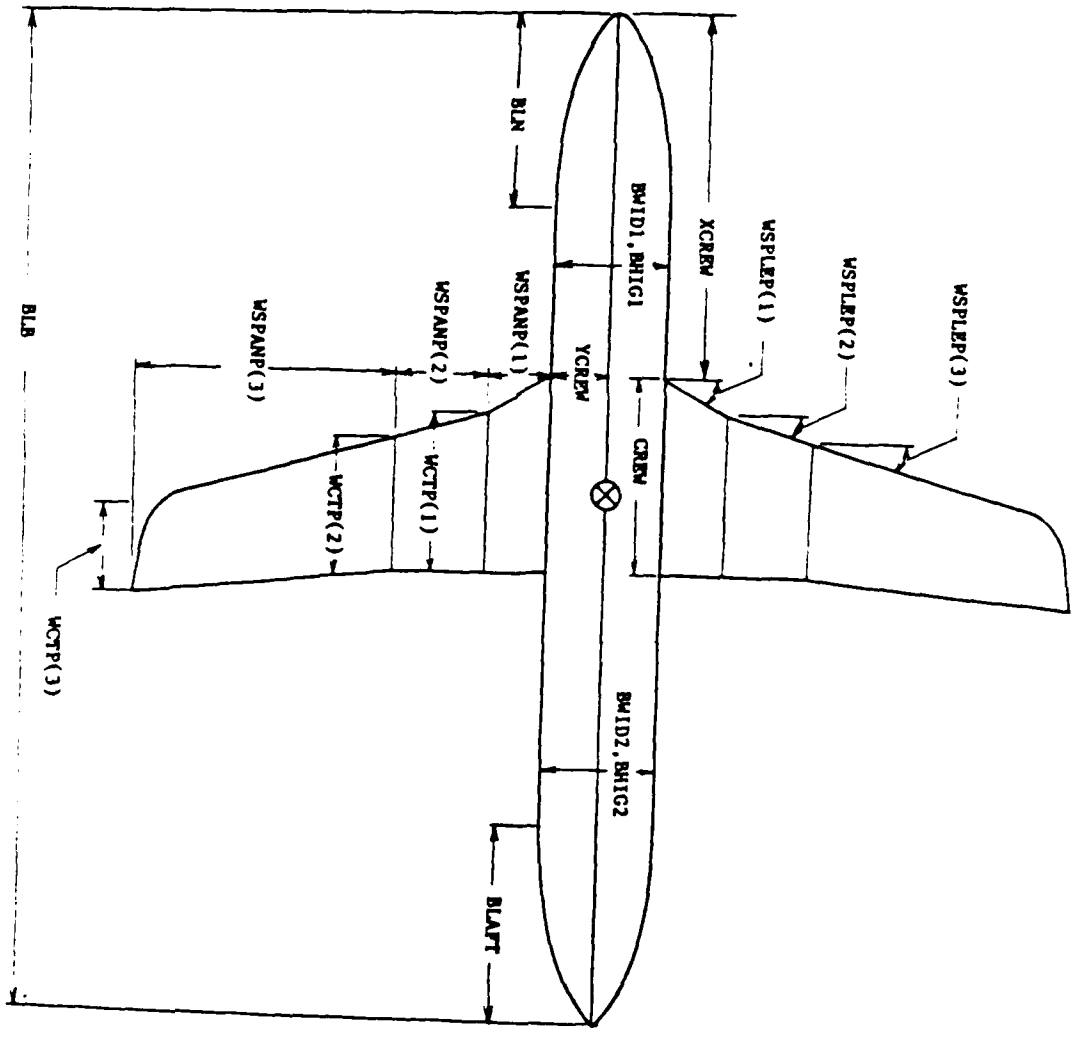

FIGURE 5 (continued)

```
      ESDU WING-BODY INPUT
0100000000000001000000000000
 $CLASS ICLASS=3,
 $END
 $WING NATW=6,NPTHW=0,NPANSW=3,CSAW=135.256,BDW=13.123,ITCMW=.50,
       CREW=22.966,TCREW=.06,ICREW=42.651,YCREW=6.562,ZCREW=0.,
       WTOCP(1)=.06,WSPANP(1)=6.562,WCTP(1)=18.373,
       WSPANP(2)=7.874,WCTP(2)=15.748,WSPLEP(1)=25.,WSPLEP(2)=17.,
       WSPANP(3)=31.496,WCTP(3)=9.843,WSPLEP(3)=17.,WTOCP(2)=.06,
       WTOCP(3)=.06,
 $END
 $CANARD
 $END
 $HORZT
 $END
 $VERTT
 $END
 $FIN
 $END
 $FUSE
      BAMX=135.256,IBODY=1,BLB=118.11,BDNOSE=13.123,BWI62=13.123,
      BMW=13.123,BMH=13.123,BHI61=13.123,BWID2=13.123,BWID1=13.123,
      BABS=.001,BLN=22.966,BLAFT=22.966,
 $END
 $NACELLE
 $END
 $MOMENT
 $END
 $AEROK
       NMAP=1,MACH=.1,ALT(1)=0.,NLP=2,
    ALF(1)=.01,6.,
       SREF=0.,LCG=1.25,AMC=40.,NTRIMD=0,WEIGHT=1.,ZGLCG=10.,
 $END
 $PROP
 $END
 $SCRIT
 $END
 $HILIFT
 $END
 $OPTION
 $END
```

FIGURE 9. SACP THEORETICAL WING DEFINITION

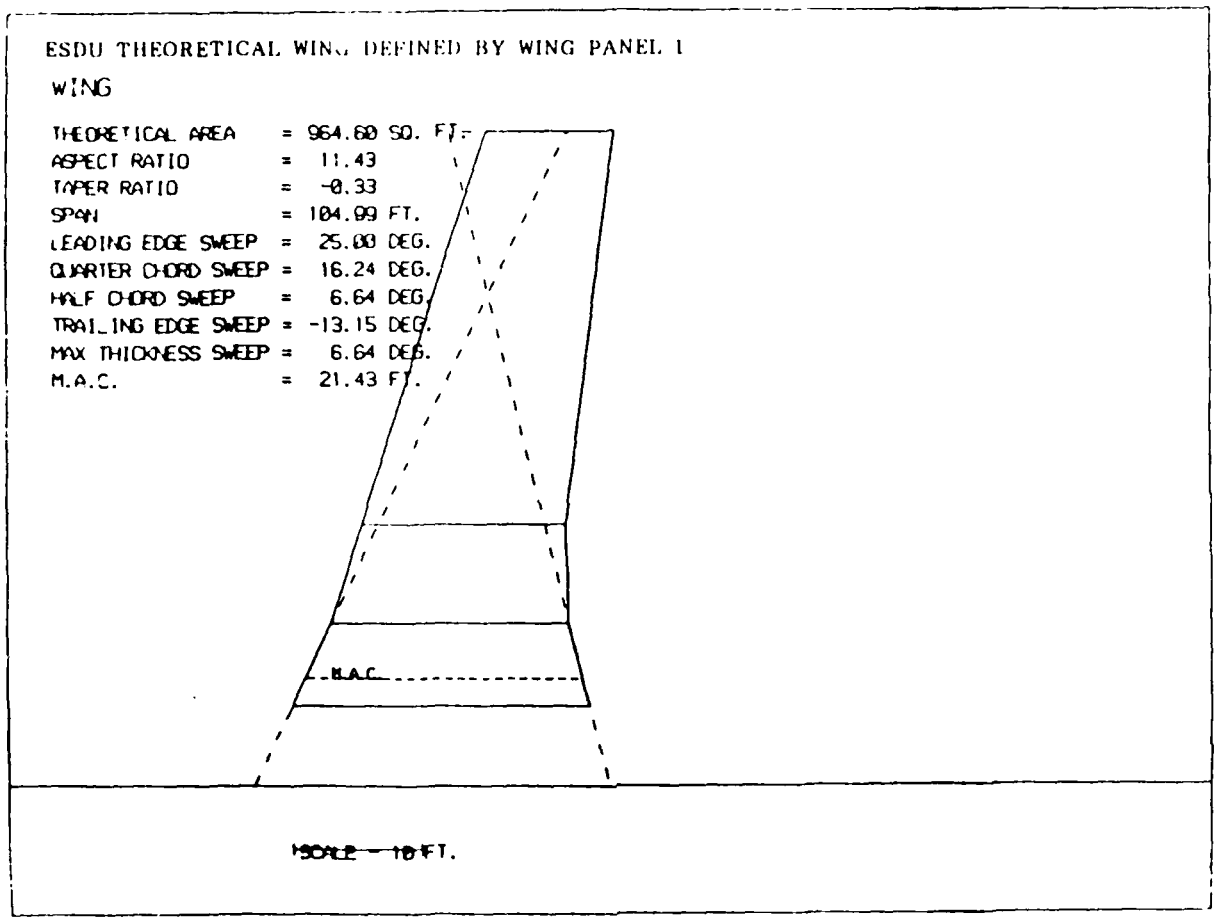

FIGURE 9(continued) SACP THEORETICAL WING DEFINITION

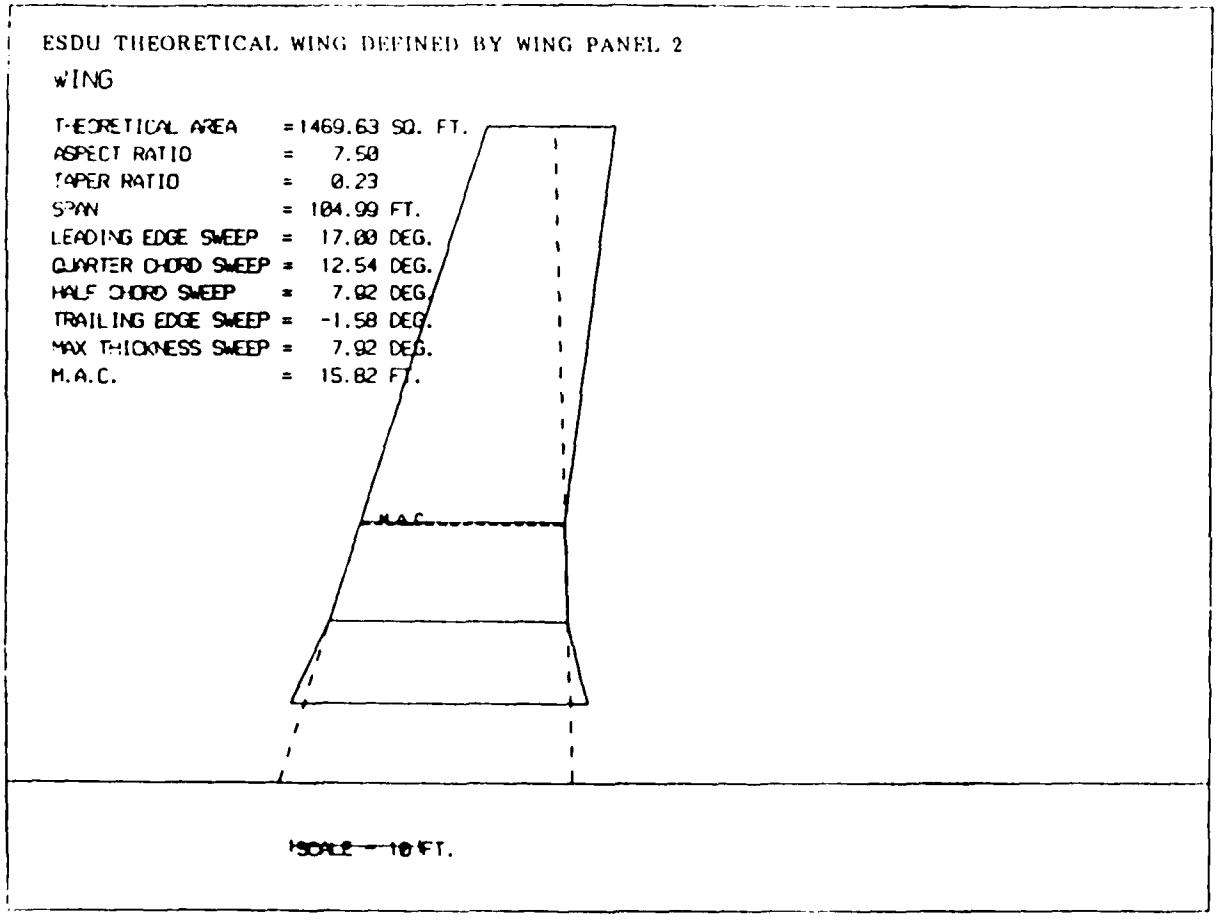

FIGURE 9(continued) SACP THEORETICAL WING DEFINITION

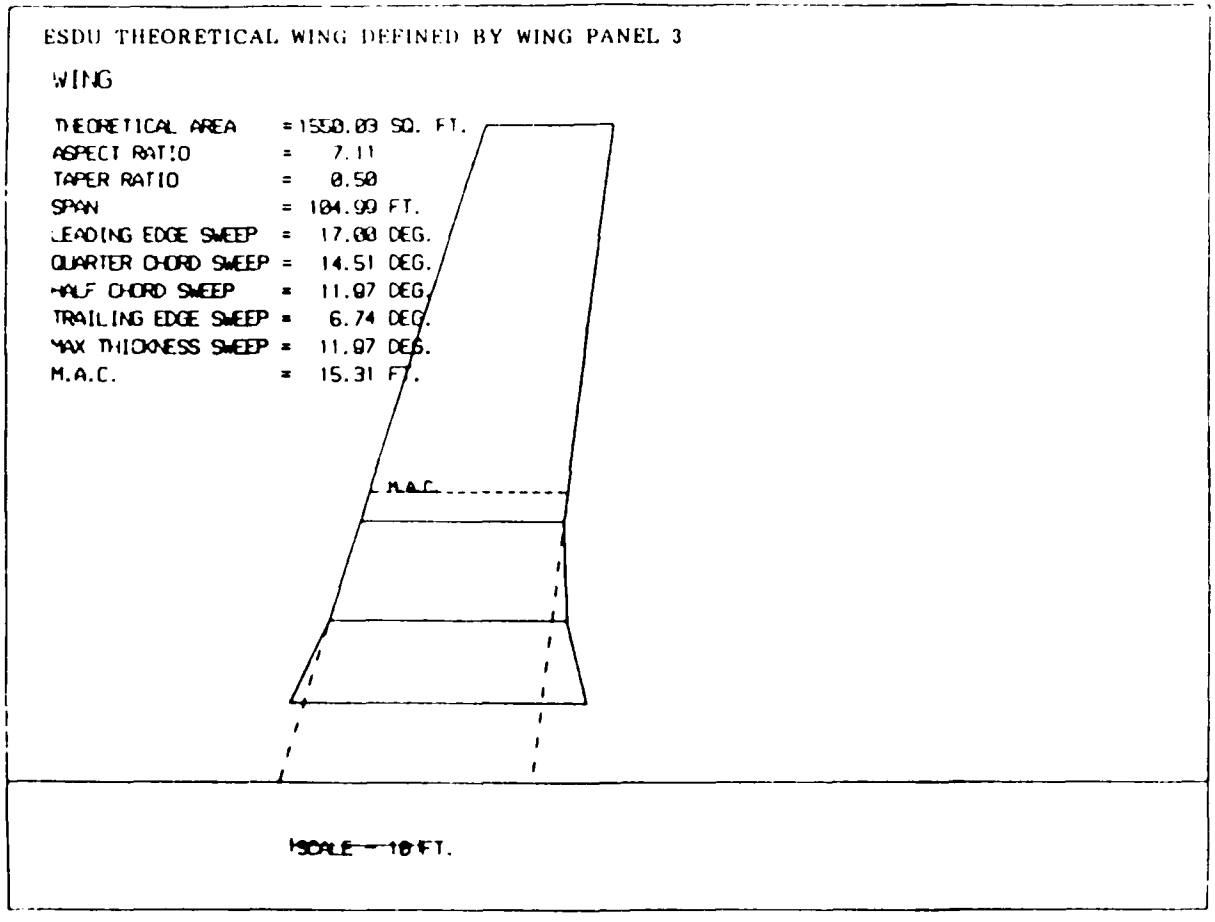

FIGURE 9(continued) SACP THEORETICAL WING DEFINITION

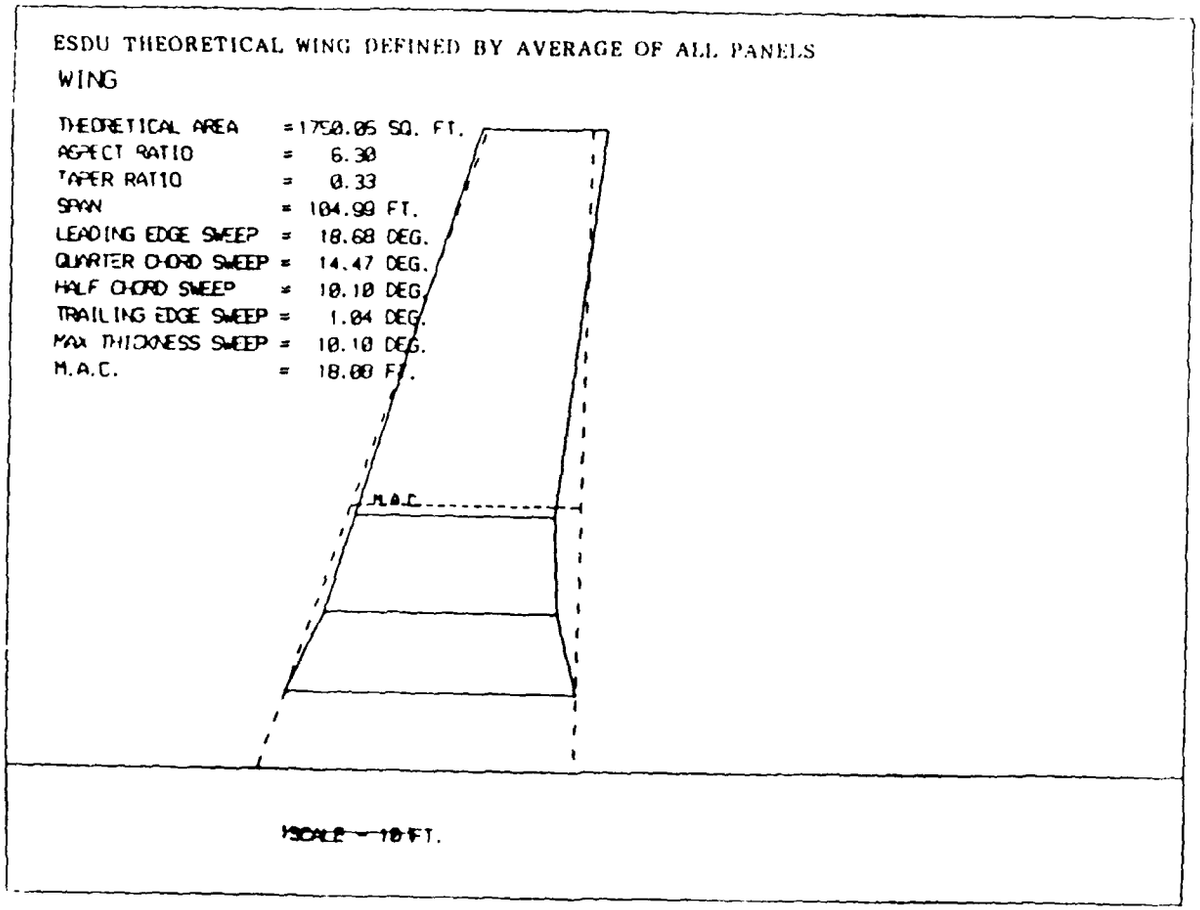

TABLE 1

EFFECT OF THEORETICAL SURFACE DEFINITION ON WING PARAMETERS

	SACP 3	SACP AVE	ESDU- REF 4
AREA -SQ FT	1550	1750	1610
L.E. SWEEP -DEG	17	18.7	17.2
ROOT CHORD -FT	19.7	23.1	20.8
TIP CHORD -FT	9.84	8.27	9.84
M.A.C -FT	15.3	18.8	16
TAPER RATIO	0.5	0.33	0.47
ASPECT RATIO	7.11	6.3	6.845
A.C.-% M.A.C	0.343	0.347	0.243

TABLE 2

EFFECT OF THEORETICAL SURFACE DEFINITION ON
WING-BODY PARAMETERS

	SACP 3	SACP AVE	ESDU- REF 4
BODY CORRECTION FORWARD -% M.A.C	-0.12	-0.102	-0.127
A.C. -% M.A.C	0.223	0.245	0.116
A.C. FROM NOSE -FT	52.3	52.3	50.3
C.G. FROM NOSE -FT	52.5	52.5	52.5
C-L-ALPHA (1/RAD)	6.6	6.7	4.87
C-M-ALPHA (1/RAD)	0.04	0.042	0.65

FINAL REPORT NUMBER 78
REPORT NOT RECEIVED IN TIME
WILL BE PROVIDED WHEN AVAILABLE
Dr. Yin-min Wei
760-OMG-071

Development of High Strength Beta Titanium Alloys Via Rapid Solidification Processing - The Coarsening of Erbium Oxide in Ti-15V-3Al-3Sn-3Cr Beta Titanium Alloy

by

I. Weiss

Associate Professor

Materials Science and Engineering

Wright State University, Dayton, Ohio 45435

Final Report Dec. 85 - Dec. 86

ABSTRACT

Coarsening of erbium oxide was studied in the metastable beta titanium alloy Ti-15V-3Al-3Sn-3Cr during isothermal annealing. Large erbium oxide dispersoids (mean particle size of 78 nm) were observed in the surface laser melted and rapidly solidified condition. Fine erbium oxide particles were formed on annealing at 870°C (1600°F) for times up to 24 hrs. after laser surface melting (rapid solidification). The fine erbium oxide dispersion with a mean particle size of 187 nm was formed during the first 2 hrs. of annealing at 870°C (1600°F). Both the fine ($\bar{d}$ = 18 nm) and large ($\bar{d}$ = 78 nm) erbium oxide particles undergo coarsening during annealing at 870°C (1600°F). Annealing for 24 hrs. at 870°C (1600°F) coarsen the small particles producing a dispersion with a mean size of 29 nm, with a smaller change in particle size for the larger erbium oxide particles (mean particle size of 95 nm). The results indicate that the coarsening process is an Ostwald-ripening process which follows an r^3 growth law.

INTRODUCTION

THE HIGH STRENGTH-TO-DENSITY ratio and the good corrosion resistance of titanium alloys make these alloys an attractive material for aerospace application. Further enhancement of this ratio beyond current alloys such as Ti-6Al-4V can be achieved by either an increase in strength or by a reduction in density [1].

Development of titanium alloys with improved strength by the ingot metallurgy route has been only partially successful because additions of large amounts of dispersoid-forming elements resulted in the formation of segregated phases which result in reduced ductility and fracture related properties [2].

Rapid solidification processing (RSP) provides a way to overcome the above limitation. By applying high solidification rates, metastable supersaturation of dispersoid-forming elements in titanium can be achieved. Subsequent isothermal annealing result in large volume fraction of fine dispersoids which will strengthen the alloy [3]. This approach can be carried out for dispersoid forming elements with quite large solubility levels (e.g., Ni, Cu, Si) or small levels (e.g., Er, Nd, Gd). Recent invesatigations on rapid solidification of alpha titanium alloys have shown that small additions or erbium resulted in the formation of uniform dispersion of erbium oxide [4-7], which is fine enough to produce strengthening [4-5]. Erbium oxide particles were found to be quite stable in the alpha phase and display a low rate of coarsening following isothermal annealing at 800°C (1470°F) for 16 hrs. [4]. Dispersoids containing other rare earth elements such as yttrium, gadolinium, etc. are larger in size than erbium oxide and exhibit a higher coarsening rate [4].

The present work is part of a larger program aimed at developing high

strength beta titanium alloys containing rare earth dispersoids and compound metalloids via rapid solidification processing. The thermal stability of the dispersoids and precipitates during RSP and post-RSP heat treatment is essential for retaining strength. However, little information is available on the thermal stability and coarsening behavior of dispersoids such as erbium oxide in the beta phase. It is the purpose of the present work to provide such information.

EXPERIMENTAL PROCEDURE

The commercial metastable beta alloy Ti-15V-3Al-3Sn-3Cr and erbium oxide powder were vacuum arc melted into a cigar-shaped button. The alloy button was remelted and solidified five times to increase homogeneity, annealed at 980°C (1800°F) for 24 hrs. and then swaged at 1040°C (1900°F) through successive dies to a final diameter of 6.5 mm. Disks 6.5 mm. in diameter and 3 mm thick with chemical composition given in Table 1 were sectioned transversely from the swaged and homogenized rod. Laser surface melting was performed using a 500 watt CO_2 laser in a continuous mode. A high speed, computer-controlled traversing system provided a uniform melt zone with argon shielding, minimizing contamination of the melt zone. Cooling rates between 10^3 to 10^{4}°C/s and 10^4 to 10^{5}°C/s were obtained for laser power of 500 wats and traversing speeds of 0.4 and 4.0 mm/s, respectively. Following laser melting, specimens were heat treated at 870°C (1600°F) for times ranging between 2 and 24 hrs. The microstructures of the heat treated specimens were examined by optical, SEM, and TEM microscopy. The composition of precipitates were semi-quantitatively determined by x-ray energy dispersive spectroscopy.

RESULTS AND DISCUSSION

A transverse section microstructure of the as-cast material is shown in Figure 1a. The dark field micrograph display elongated grains and coarse erbium oxide particles. Following swaging at 1040°C (1900°F) and homogenization at 980°C (1800°F) for 24 hrs., the cast material undergoes recrystallization and equiaxed beta grains are produced (Figure 1b). Large erbium oxide particles are also visible along the grain boundaries as well as in the grain interior, the result of low solubility of erbium in beta titanium [4,8].

Figure 2 illustrates short transverse sections of the rapidly solidified zone observed in material laser melted at traversing speeds of 0.4 and 4.0 mm/s. Larger melt pool (Figure 2a) and coarser structural features (Figure 2c) are observed for laser melting at a speed of 0.4 mm/s. Conversely, faster cooling rates (10^4 - 10^5°C/s) and finer structural details are obtained for the laser melting speed of 4.0 mm/s (Figure 2b and 2d).

SEM micrographs of the melt zone reveal a columnar structure which originated at the solid/liquid interface (Figure 3a) and extended towards the specimen surface as shown in Figures 3b and 3c. As indicated earlier, faster melting speeds resulted in finer structure as observed in Figures 4a and 4b. Larger erbium oxide particles are also detected in the as-laser melted conditions and are associated with the intercolumnar boundaries as shown in Figure 4c. These particles probably nucleated in the later stages of the solidification process at a cooling rate (and solidification velocity) much lower than the 10^3 to 10^4°C/s cooling rate estimated for the initial stages of the solidification process and grew in the solid state, and thus were present before annealing.

During annealing at 870°C (1600°F) for 2 hrs., a fine dispersion of erbium oxide was formed in the region which had been laser melted. Larger particles are also observed, and are better resolved near the melt zone/base metal interface (Figure 5a). Those particles which are associated with the intercolumnar liquid and formed during the later stages of the solidification process, are stable and show little change in size during annealing at 870°C (1600°F) for 2 hrs. Energy dispersive spectroscopy (EDS) analysis of the large precipitates reveals erbium rich particles (shown in Figure 5a) which are assumed to be the stable sesquioxide Er_2O_3 [9, 10].

Similar results were obtained for samples surface laser melted at a traversing speed of 4.0 mm/s. TEM micrographs of both fine and coarse dispersoids formed following 2 and 24 hr. annealing at 870°C (1600°F) are shown in Figures 6 and 7. The coarse hexagonal shaped particles are observed to be aligned along the intercolumnar boundaries as shown in Figure 6a. The fine dispersoids formed after 2 hrs. of annealing at 870°C (1600°F) coarsened to a larger degree than the coarse particles during a further 22 hrs. of annealing at 870°C (1600°F) as shown in Figure 7a. Nevertheless, both fine and coarse particles are small enough to interact with single dislocations as shown in (Figures 6b and 7a). Size distribution of the dispersoids was evaluated in the as-laser melted condition and after annealing at 870°C (1600°F). The changes in the size distribution during annealing allow the process of erbium oxide precipitation and coarsening to be followed.

Specimens in the as-laser melted condition contain large particles (up to 200 nm) with a mean particle size of 78 nm (Figure 8a). A fine erbium oxide dispersion (up to 40 nm) with a mean particle size of 18 nm was formed during the first 2 hrs. of annealing at 870°C (1600°F). This time is sufficient to

allow most of the oxide particles to precipitate out. However, little change in particle size was detected for the larger erbium oxide particles (mean size of 82 nm) as shown in Figure 8b. Annealing for 24 hrs. at 870°C (1600°F) coarsens both the fine and large particles and a bi-model dispersion with mean sizes of 29 nm and 95 nm, respectively, is observed as shown in Figure 8c. The change in the mean particle size ($\bar{d} = 2\bar{r}$) with increasing annealing time (t) for the fine and coarse dispersoids is shown in Figure 9.

The Lifshitz, Slyozov, and Wagner (LSW) model for particle coarsening [11, 12] was used in an attempt to explain the coarsening behavior of the erbium oxide dispersoids, during annealing in the beta phase. This model assumes a cube relationship between particle size ($\bar{r}$) and coarsening time (t) as shown in the following equation:

$$\bar{r}^3 - \bar{r}_o^3 = K\,(T)\,(t - t_o)$$

$$K\,(T) = 8/9\,\frac{C_s\,D\,\gamma\,Vm}{RT}$$

where: $\bar{r}_o$ and $\bar{r}$ are the average particle radii at the initial and final stages of particle coarsening, C_s-equilibrium solubility of solute in the matrix at a given temperature, D-diffusion coefficient, γ-interfacial energy of particles, V-molar volume of precipitate, t_o and t are the initial and final time of particle coarsening, R-gas constant and T-temperature. Modification of K(T) incorporates the effect of solute concentration in the matrix (C) and the volume fraction of the dispersoids (ϕ), leading to a new constant $F(T) = K(T)\ f\ (C, \phi)$ [13]. However, the cube relationship between $\bar{r}^3$

r_o^{-3} and $(t - t_o)$ is maintained. The mean particle size of 18 nm obtained following annealing at 870°C (1600°F) for 2 hrs. was taken as the equilibrium particle size for the fine dispersion prior to the coarsening process.

The cube relationship between $\bar{r}^{-3} - \bar{r}_o^{-3}$ and t for both the fine and large particles is shown in Figures 10 and 11 respectively. The results obtained in this work indicate that the coarsening process of erbium oxide during isothermal annealing in the beta phase is an Ostwald-ripening process obeying the LSW model. Erbium oxide particles coarsen more rapidly in a matrix containing an excess of erbium than in a matrix containing an excess of oxygen [10, 14]. The alloy composition studies in the present work (see Table 1) are excess oxygen, resulting in a low rate of coarsening and relatively small mean particle size following 24 hrs. of annealing at 870°C (1600°F), for both the fine and coarse oxide dispersions (29 nm and 95 nm, respectively). Similar behavior was observed during annealing of erbium containing alloys in the alpha phase [14, 15] and for yttrium-tin containing alloys isothermally annealed in the beta phase [16]. It was also suggested that in addition to bulk diffusion of oxygen and erbium in beta titanium, coarsening of the erbium oxide particles can take place by interaction of migrating grain boundaries and oxide dispersoids during processing and post-processing heat treatment [5]. Accelerated dispersoid coarsening was found during high temperature annealing of consolidated material especially in the vicinity of the grain boundaries, where large depletion zones were observed [5, 17].

Diffusion coefficient of the solute in beta titanium was not calculated from the data given in Figures 10 and 11 because the lack of accurate values for the interfacial energy (γ) and volume fraction of dispersoids (ϕ) make this calculation only a rough estimate. However, the rate of coarsening of the fine erbium oxide dispersoids at 870°C (1600°F) was estimated to be around 100 nm^3/hr.

CONCLUSIONS

1. Laser surface melting can be used to study the solidification and subsequent annealing behavior of a Ti-15V-3Al-3Sn-3Cr alloy containing erbium.

2. As-rapidly solidified coarse erbium oxide particles (78 nm) were present in intercolumnar regions with no evidence of any finer dispersoids within the interior of the columnar regions.

3. Fine erbium (Er_2O_3) oxide dispersoids with a mean particle size of 18 nm precipitate during the first 2 hr of annealing at 870°C (1600°F). These dispersoids coarsen during annealing for 24 hr at 870°C (1600°F) to attain a mean particle size of 29 nm.

4. The large erbium oxide disperoids (mean particle size of 78 nm) coarsen slightly and display a mean particle size of 95 nm following annealing at 870°C (1600°F) for 24 hr.

5. Both small and large erbium oxide disperoids coarsen by the Ostwald-ripening process following the LSW cube relationship with time. The coarsening is controlled by volume diffusion of oxygen and erbium in beta titanium and by the alloy composition, particularly the oxygen and erbium levels in the matrix.

6. Coarsening rate of the fine erbium oxide dispersoids at 870°C (1600°F) was estimated to be around 100 nm^3/hr.

REFERENCES

1. Titanium Technology Present Status and Future Trends, ed. by, F.H. Froes, D. Eylon, and H. Bomberger, TDA, Dayton, OH, 1985.
2. F.H. Froes and H. Bomberger, J. of Metals, 37, 7, 28, 1985.
3. S. Krishnamorthy and F.H. Froes, to be published 1987
4. Sastry, S. M. L., P.J. Meschter, and J.E. O'Neal, Met. Trans., 15A, 1451, (1984)
5. R. G. Rowe and F. H. Froes, this proceedings.
6. Sastry, S. M. L., Sastry, and J. E. O'Neal, R. J. Mater. Sci., 14, 66, (1979)
7. Sankaran, K. K., S. M. L. Sastry, and J. E. O'Neal, Met. Trans., 11A, 198, (1980)
8. S. A. Court, J. T. Stanley, D. G. Konitzer, M. H. Loretto, and H. L. Fraser, in "Titanium, Rapid Solidification Technology," edited by F. H. Froes and D. Eylon, p. 165, TMS Publications, Warrendale, PA (1986)
9. J. P. A. Lofvander, S. A. Court, R. Wheeler, J. W. Sears, D. A. Watson, and H. L. Fraser, in "Titanium, Rapid Solidification Technology," edited by F. H. Froes and D. Eylon, p. 77, TMS Publications, Warrendale, PA (1986)
10. D. B. Snow and A.F. Giamei, in "Titanium, Rapid Solidification Technology," edited by F.H. Froes and D. Eylon, p. 153, TMS Publications, Warrendale, PA (1986)
11. Lifshitz, I.M. and V.V. Slyozov, J. Phys. Chem. Solids, 19, 35, (1961)
12. Wagner, C., A. Electro Chem, 65, 581, (1961)
13. Davis, C.K.L., Acta Met., 28, 175, (1980)
14. D.G. Konitzer, B.C. Muddle, R. Kirchheim, and H.L. Fraser, in "Rapidly Quenched Metals," edited by S. Steb and H. Warlimont, p. 953, North-Holland, Amsterdam (1985)

15. R.G. Rowe, T.F. Broderick, E.F. Koch, and F.H. Froes, in "Rapidly Solidified Materials," edited by P.W. Lee and R.S. Carbonara, p. 107, American Society for Metals, Metals Park, OH (1985)

16. Y.D. Hahn, D. Vujic, and S.H. Whang, in "Titanium, Rapid Solidification Technology," edited by F.H. Froes and D. Eylon, p. 201, TMS Publications, Warrendale, PA (1986)

17. R.G. Rowe, J.A. Sutliff, and E.F. Koch, in "Titanium, Rapid Solidification Technology," edited by F.H. Froes and D. Eylon, p. 239, TMS Publications, Warrendale, PA (1986)

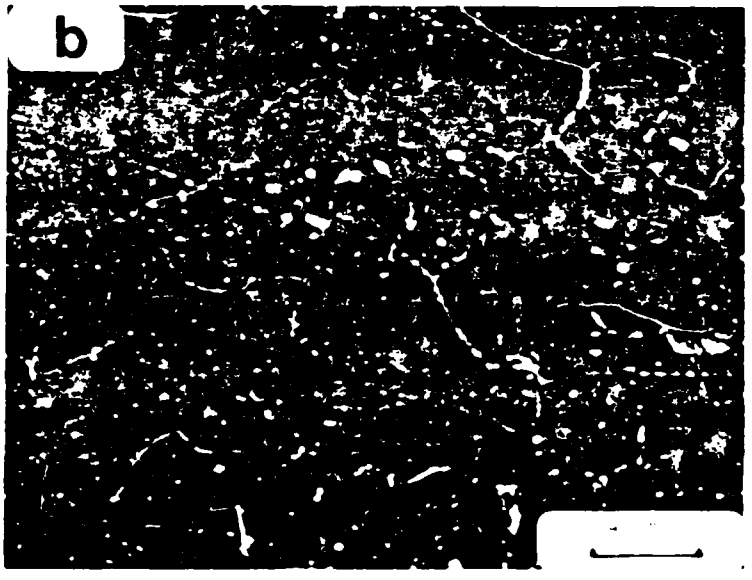

Figure 1
79-12

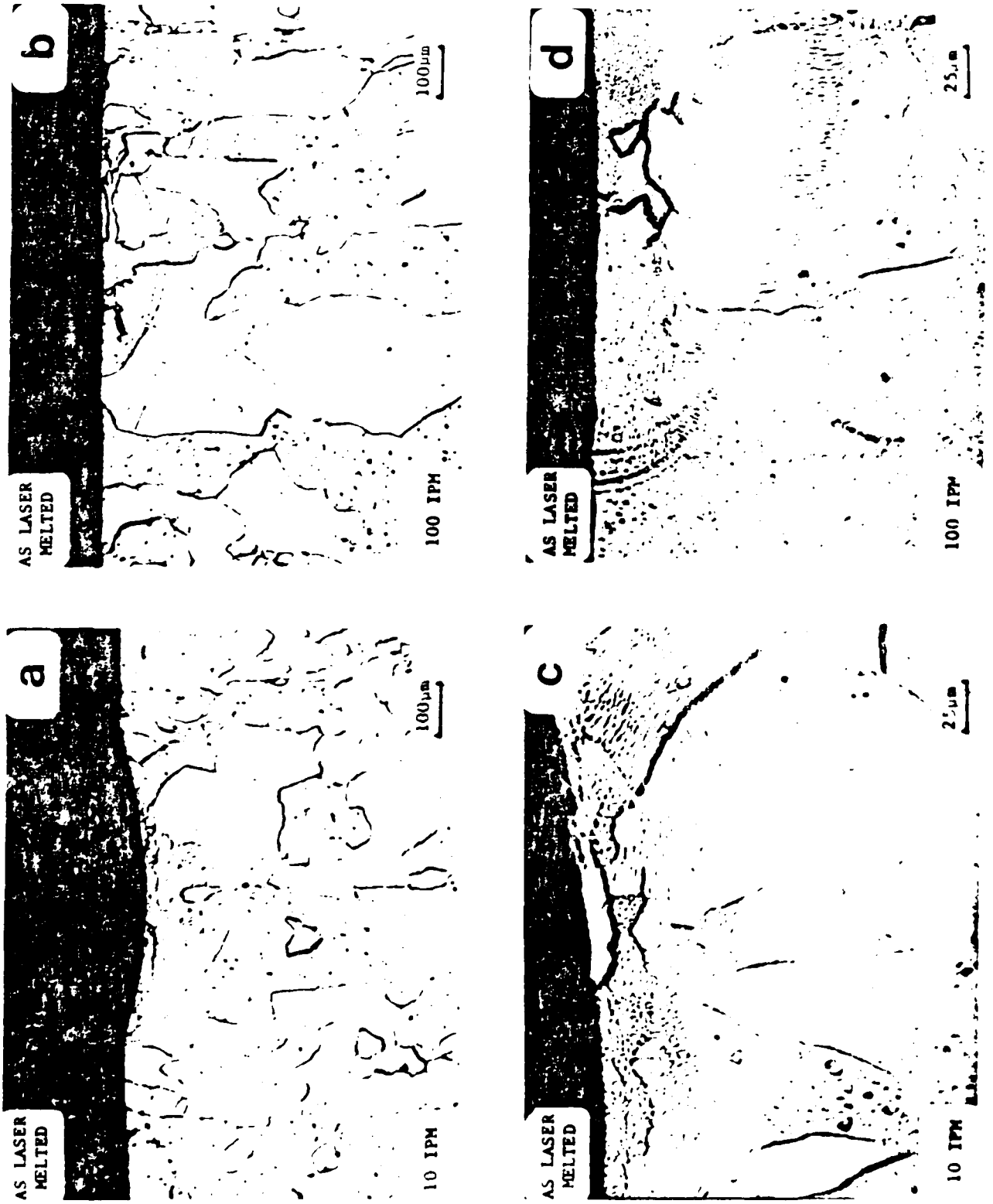
a
AS LASER MELTED
100μm
10 IPM
b
AS LASER MELTED
100μm
100 IPM
c
AS LASER MELTED
10 IPM
d
AS LASER MELTED
25μm
100 IPM

Figure 2

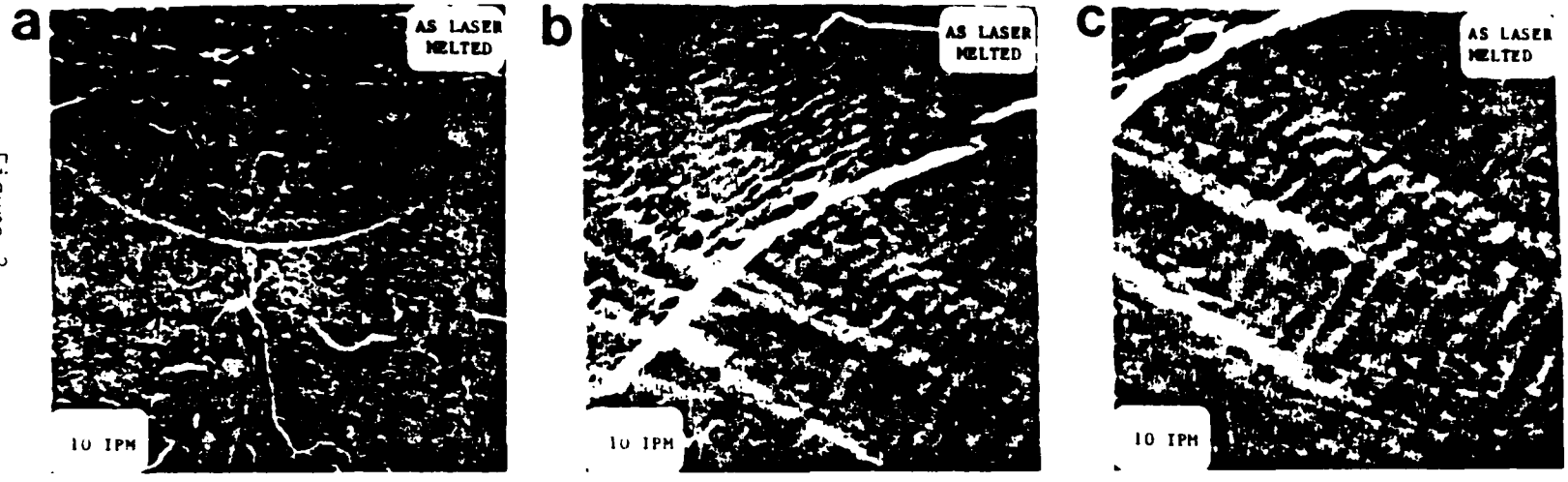
a
AS LASER MELTED
10 IPM
b
AS LASER MELTED
10 IPM
c
AS LASER MELTED
10 IPM

Figure 3

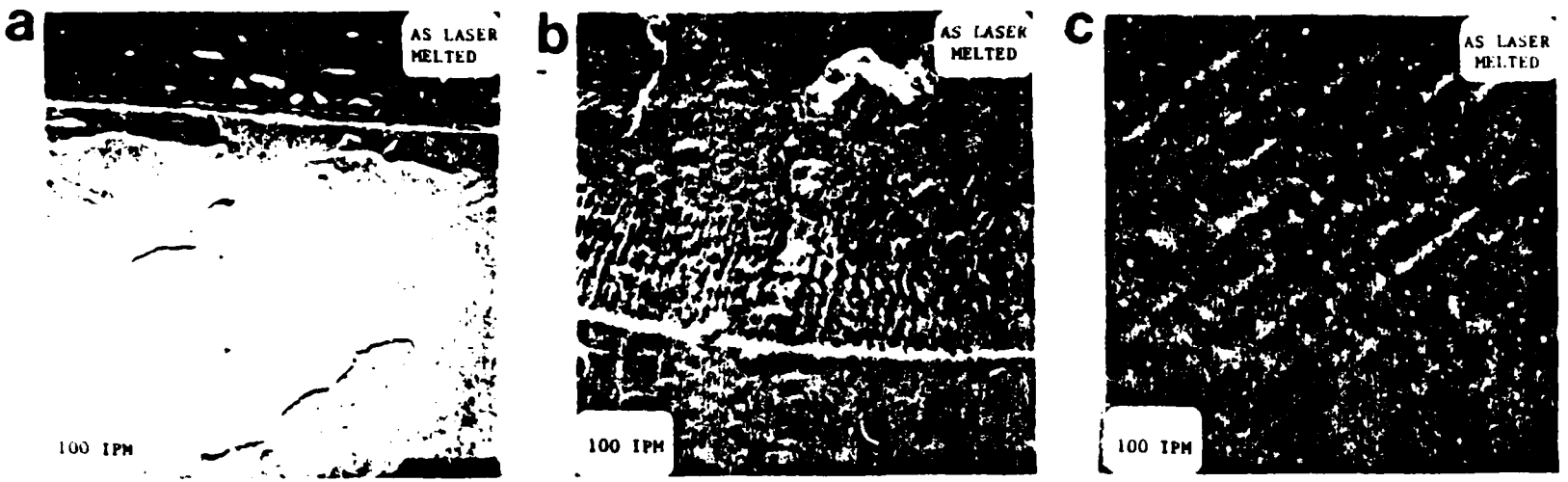

Figure 4
79-15

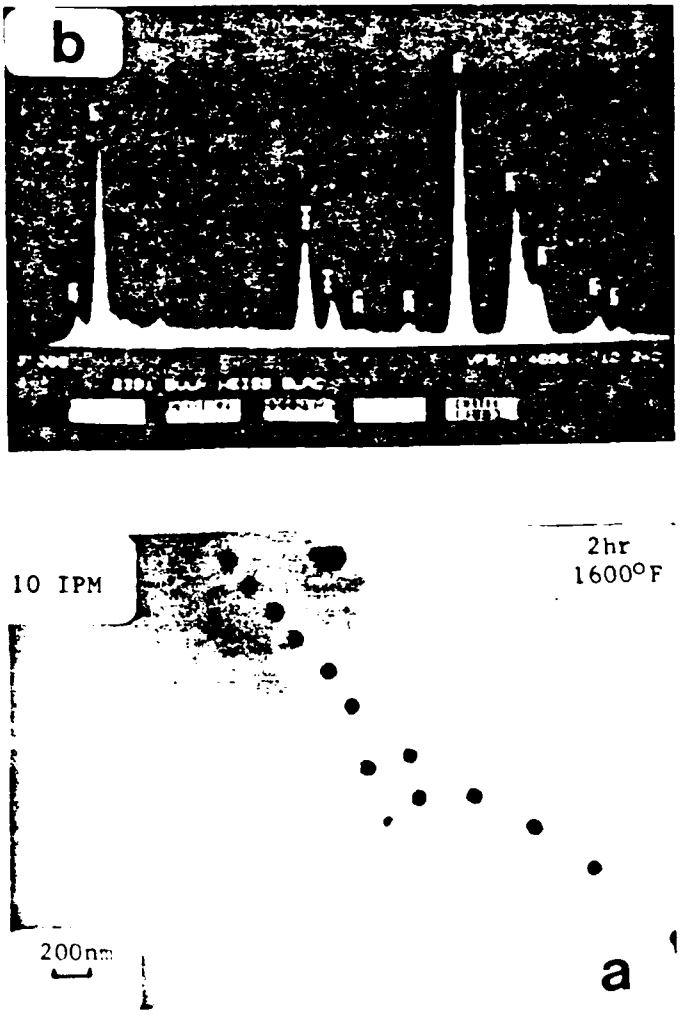

Figure 5
79-16

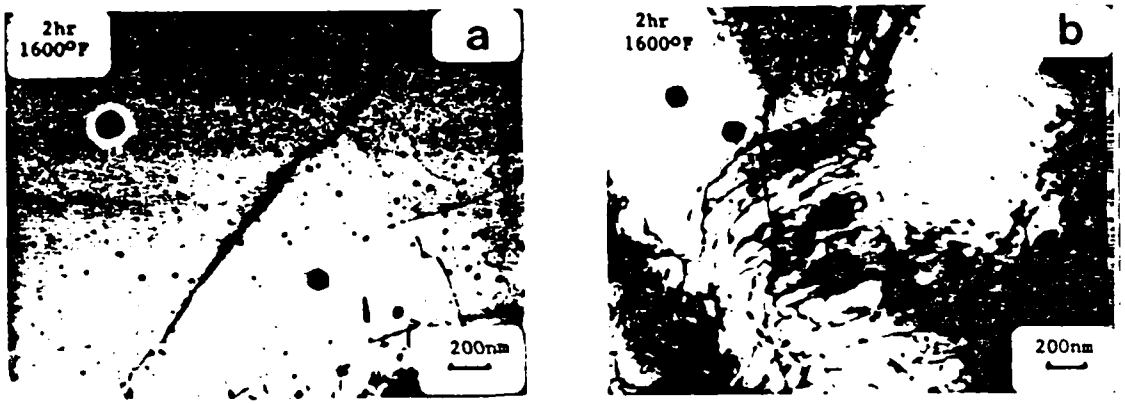

Figure 6

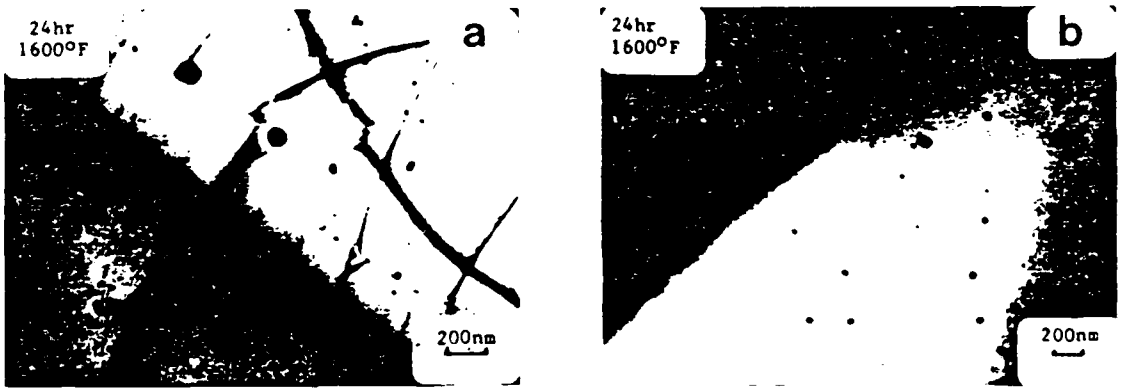

Figure 7

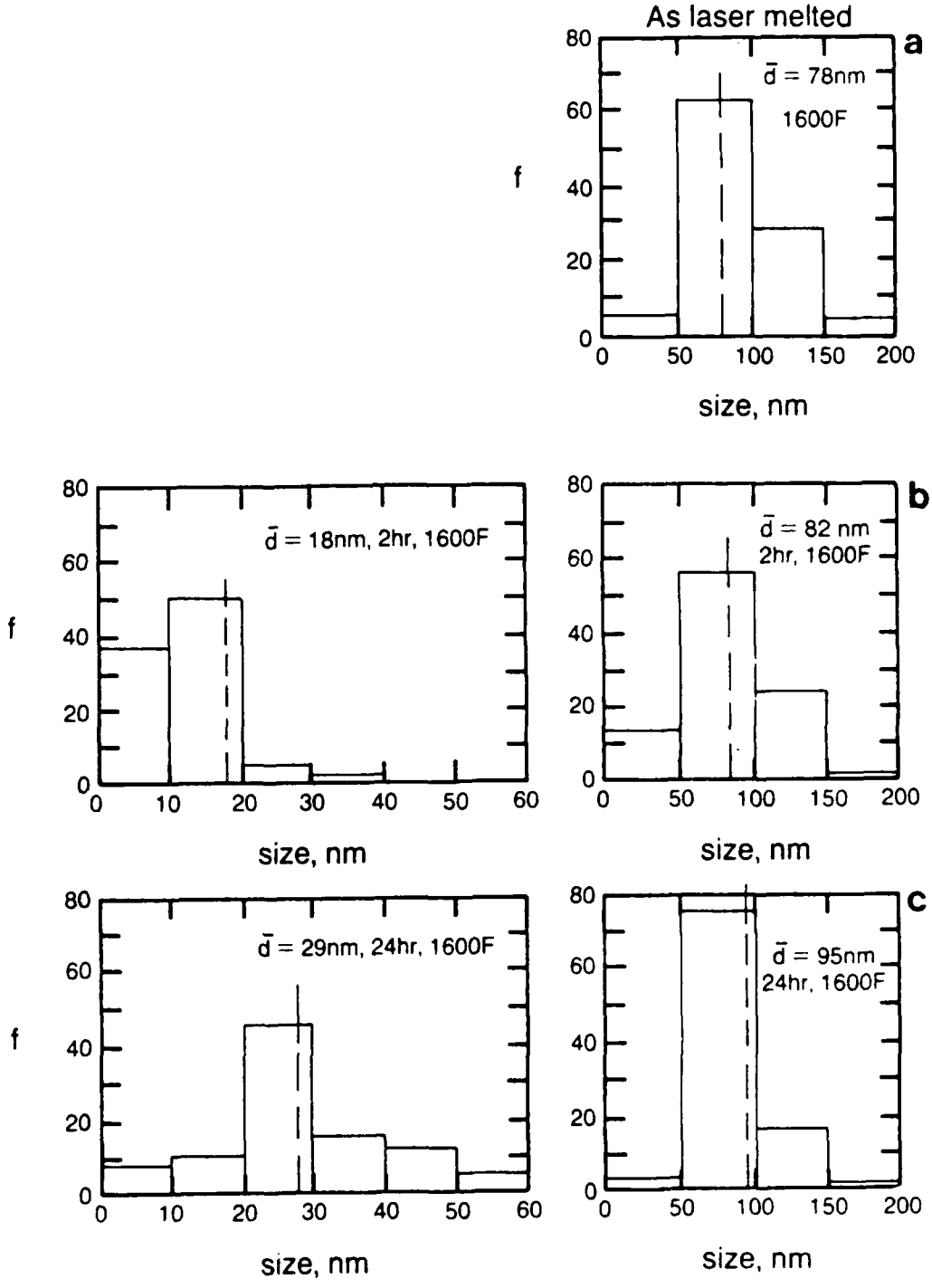

Figure 8
79-19

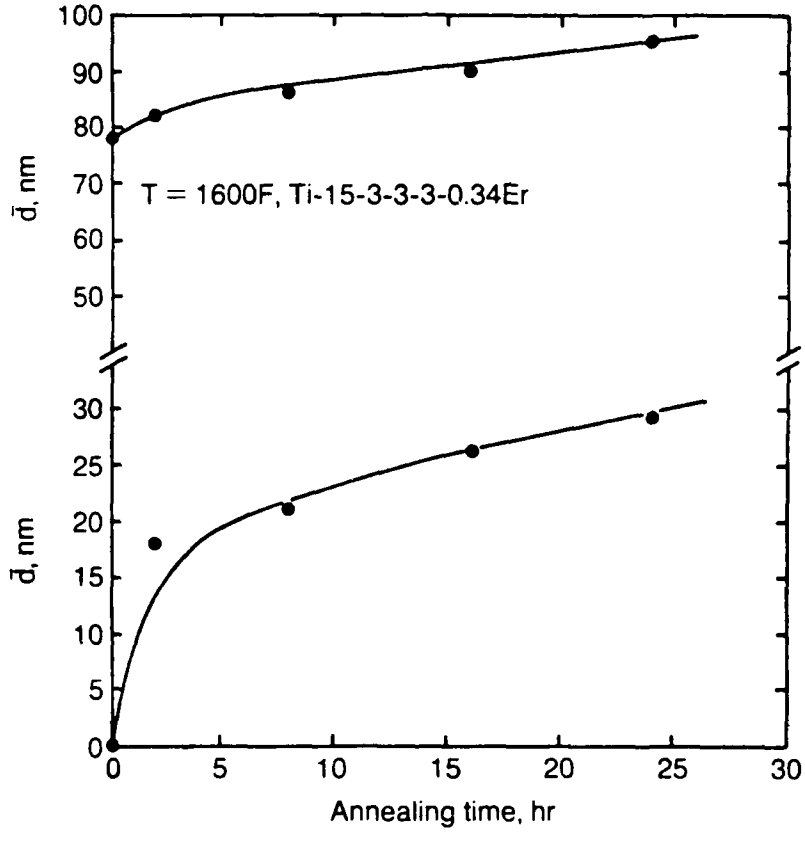
T = 1600F, Ti-15-3-3-3-0.34Er
d̄, nm
d̄, nm
Annealing time, hr
100
90
80
70
60
50
30
25
20
15
10
5
0
0
5
10
15
20
25
30

Figure 9

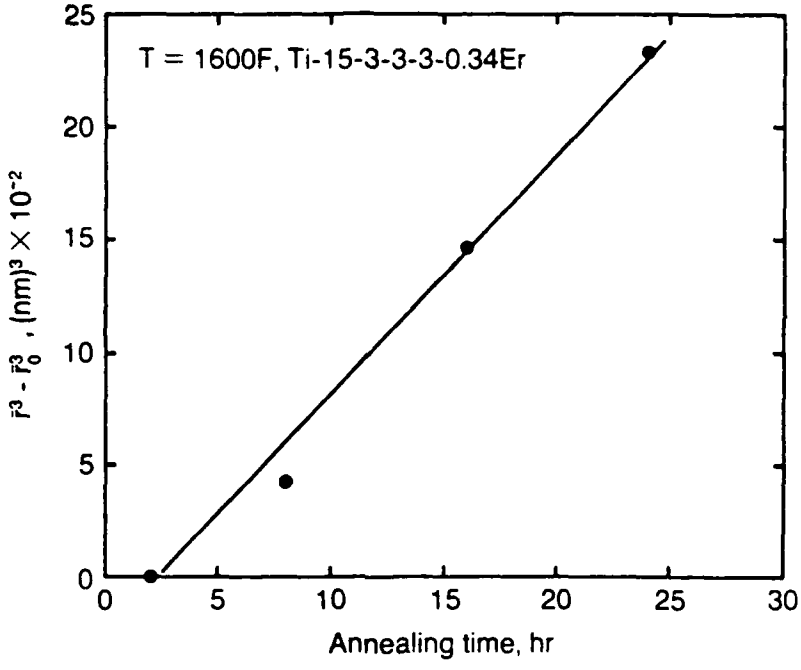
T = 1600F, Ti-15-3-3-3-0.34Er
$\bar{r}^3 - \bar{r}_0^3$, $(nm)^3 \times 10^{-2}$
Annealing time, hr
0
5
10
15
20
25
30

Figure 10

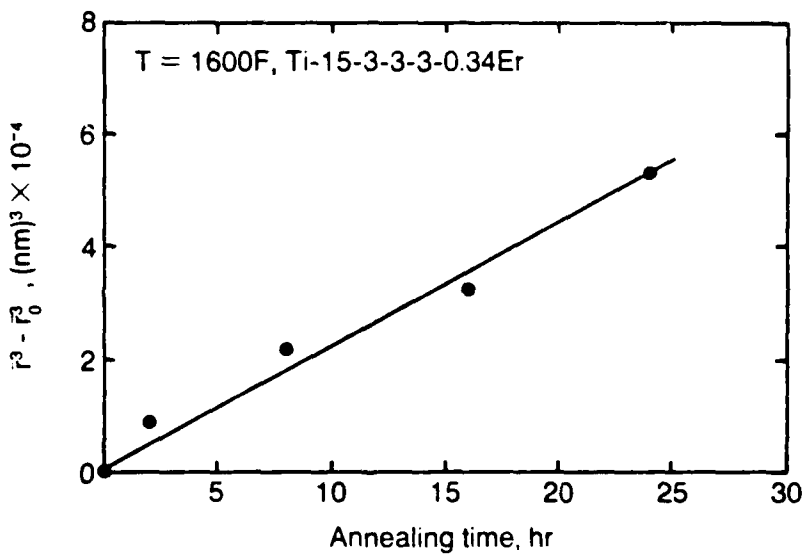
T = 1600F, Ti-15-3-3-3-0.34Er
$\bar{r}^3 - \bar{r}_0^3$, $(nm)^3 \times 10^{-4}$
0
2
4
6
8
5
10
15
20
25
30
Annealing time, hr

Figure 11

Figure 12

FINAL REPORT NUMBER 80
REPORT NOT RECEIVED IN TIME
WILL BE PROVIDED WHEN AVAILABLE
Dr. Jesse Williams
760-OMG-038

LABELING THE TOPOGRAPHIC FEATURES OF AN INFRARED IMAGE

by

David C. Wilson

Mathematics Department

University of Florida

Gainesville, Florida 32611

October 1986

Abstract: A method is described which labels the topographic features of a gray-level image. Regions of interest are identified through a segmentation technique based on edge detection, pixel value, and local geometric information. The local geometric information is determined by methods similar to the simplicial techniques employed by T. Banchoff to calculate the local index and Gauss curvature at a point. By combining the local topographic characteristics of the component's pixels together with various shape, size, and height tests, a region is labeled a peak, a crest, a ridge, a cliff, or a mesa. These region labelings are designed to provide a first step in the understanding of a low resolution digitized image. The algorithm was succesfully tested against 199 infrared images of buildings, bridges, petroleum tanks, and runways. A variety of target detection techniques have also been developed.

I. Introduction. The main goal of this report is to describe a method for labeling the topographic features of a gray-level image. The features considered include peaks, crests, ridges, cliffs, mesas, and ridge-peak systems. This approach is designed to provide a first step in the understanding of a low resolution digitized image. The methods were developed while investigating 199 120x360 digitized infrared images of such high-value targets as bridges, buildings, petroleum tanks, and runways provided by Eglin AFB. The motivation behind this project was to develop a systematic and general approach to image understanding that will useful in the detection of a wide variety of targets under a wide range of natural conditions and viewing angles. The four types of images mentioned above served as a guide in this study.

We feel the main contributions of the approach presented here is a new approach to segmentation and labeling. In most circumstances the segmentation of an image is accomplished by forming the connected components of certain identified points of interest. While it has been popular to select points by edge detection techniques such as the Kirsh or Sobel or by considering all pixels one or two standard deviations above the mean, we have chosen both local geometry and height as our criterion for a point to be considered important. The reason height is important in the images we investigated is that manmade objects such as buildings, bridges, petroleum tanks, and runways tend to appear "hot" in infrared images. Thus, their pixel values tend to be one or two standard deviations above the mean. However, in many of the images the centroid of the target is only slightly above the mean. In some of the bridge and petroleum tank images the centroid is even below the mean. Thus, if we centered our attention exclusively on the hot pixels, we would miss the target completely. While edge detection techniques are an attempt to locate where rapid change is occuring in the image irrespective of height, the images we are studying exhibit such a wide variety of different contours that we decided to take the view that a gray-level image is a digitized surface in 3-dimensional space. Regions of interest are identified through a segmentation technique based on local geometric information as well as edge detection and height. Techniques similar to those developed by Banchoff [2] are used to determine whether a pixel in an image should be considered a peak point, a ridge point, a flat point, a top-of-cliff point, a steep slope point, a gentle slope point, a flat point, a bottom of cliff point, a ravine point, or a sink point. The peak, ridge, flat, ravine, and sink points can be thought of as ideas borrowed from Differential Geometry. The top-of-cliff, steep slope, gentle slope, and bottom-of-cliff points can be thought of as measures of local steepness. Each of these last four groups of points can be thought of as a type of edge detector. In our first segmentation procedure the peak points and top-of-cliff points were combined with pixels two standard deviations above the mean. The buildings and petroleum tanks were usually found among the connected components of this set of pixels. In our second segmentation procedure the peak points, the ridge points, and the top-of-cliff points were combined with pixels one standard deviation above the mean. The bridges and runways were usually identified as the large connected components of this second set of pixels.

By combining the local topographic information together with certain height and length data we can make decisions whether a connected component in either segmentation step should be labeled a

peak, a crest, a ridge, a cliff, a mesa, or a ridge-peak system. We can also determine whether it should be considered small, medium, or large and whether it should be thought of as long or very long. The details for both segmentation and labeling are presented in Section III.

The topographic approach is proving to be very effective in the investigation of high value targets. Not only are we are able to label peaks, crests, ridges, mesas, and cliffs in an image, but we are also able to determine whether a peak is prominent, whether a ridge is long or very long, whether a mesa is large, etc. We also were able to make comparisons to determine which peak is highest, which ridge is longest, or which mesa is largest, etc. The preferred direction (or directions) of the long ridges and cliffs can be determined with the Hough transform. This topographic information tabulates the most important features appearing in the image and provides the user with an excellent idea of what type of scene is represented.

The components representing bridges and runways are not only large, but they also have a very distinctive topographic character because they frequently appear as long ridges and crests. The buildings are frequently represented as small peaks and the petroleum tanks as clusters of peaks and crests. However, one must be very careful when making general statements about these images. One reason for this caution is that in the data we studied sequences of 30-50 images were collected for each target. These images were taken at distances between 3,000 and 30,000 feet and altitudes between 960 and 1,300 feet. A building which appears as a small peak at 5 miles might appear as a ridge or crest at two miles, and as a prominent ridge at one mile. Thus, general statements of this type must be made with extreme caution. However, the advantage of the methods we have developed is that they are flexible enough to provide useful (though varying) information for each of these different situations.

An algorithm representing the ideas discussed above was coded into FORTRAN and used in the investigation of 63 bridge images, 61 building images, 50 petroleum tank images, and 25 runway images. The results of the labeling were excellent. The algorithm successfully identified virtually all the important topographic features in the images. We also found that when the output of the algorithm was compared with the range data provided with each image, we discovered that we could get a good approximation of the centroid of the target in over 80% of the images. A detailed discussion of this target location problem is given in Section IV. Additional general observations concerning the topographic features observed in the different types of images are also discussed in this section. Additional possible directions for future research are presented in Section V. A detailed discussion of each bridge image studied is given in Appendix A. The building images are discussed in Appendix B. The petroleum tank images are discussed in Appendix C. The runway images are discussed in Appendix D.

The ideas and results presented in this paper can be thought of as a continuation of the study begun in the paper by Davidson and Wilson [8]. Key portions of the details of the source code were also presented in [8].

II. History and Background. The interest in locating maxima and minima points (i.e. peaks and sinks) dates back at least to the early days of Calculus. Newton and Leibniz certainly understood critical points and their applications to extrema problems. In the nineteenth century Arthur Cayley [6] and James Clerk Maxwell [26] investigated critical points and slope lines to label regions of a surface as hills and dales. While laying the foundations for modern Differential Topology, they couched their works in the language of the earth's topography. During the twentieth century Marston Morse developed a completely modern treatment of critical point theory. The book by Morse and Cairns [27] probably gives the most complete exposition of this work. More recently, L. Nackman [29] and Nackman and Pizer [28] have combined Morse theory with the idea of a critical point configuration graph to partition a surface into a finite number of "slope districts". These districts are the regions where all the slope lines descend to a single pit (a dale) or ascend to a single peak (a hill). Using minimal cycles of the graph and the number of peaks, pits, and passes inside each cycle the surface can be reconstructed almost exactly. Thus, the configuration graph together with the information concerning the slope districts can be thought of as a recipe for reconstructing the surface. Two important theorems concerning these graphs are discussed: First, only eight types of critical points are possible: peaks, pits, and six types of passes. Second, only four types of slope districts are possible. All surfaces have a well-defined characterization as the union of slope-district regions, where each region belongs to one of four basic slope-district types. Nackman also mentions curvature districts determined by the sign of the Mean and Gauss curvature of the surface.

P. J. Besl and R. C. Jain [3-5] used the Mean curvature and Gaussian curvature in their work. These local shape descriptors from classical Differential Geometry are used to group the points of an image into eight different types. These shapes include, peak surface, flat surface, pit surface, minimal surface, ridge surface, saddle ridge, valley surface, and saddle valley. These shapes are determined by the Mean and Gauss curvatures. They not only indicate how the transition is to be made from the smooth theory to the numerical setting, but they also apply these methods to range data taken of a coffee cup, a keyboard, and a torus. A particularly attractive feature of the Gauss and Mean curvatures is that they are invariant under rotations and translations. Besl and Jain refer to this property as viewpoint independence.

T. Banchoff [2] developed a piecewise linear rather than a differential versions of Morse's Critcal Point Theorem and the Gauss-Bonnet Theorem. (Recall that the Critical Point Theorem equates the sum of the indices of the points of a surface with the Euler Characteristic, while the Gauss-Bonnet Theorem equates the integral of the Gauss curvature with Euler Characteristic.) Following the lead of Morse, Banchoff also defined the index at each vertex in the surface. However, since a piecewise linear surface is made up of vertices, edges, and triangles and since derivatives do not exist at every point, he defined the index at a vertex to be 1 - (1/2)*N, where the integer N equals the number of times the link of the vertex meets a fixed plane. (See reference [2] for more details.) For both the Banchoff and Morse definitions peak points and sink points have index +1, while saddle points have an index of -1. Since he had no need for ridge and valley points the way Besl

and Jain did, he did not consider these two possibilities. Our definitions of ridge and ravine points are in the spirit of Banchoff's definitions of index and curvature. Additional remarks on these similarities are given in Section III.

The Topographic Primal Sketch developed by Haralick [17], et. al. identifies each pixel of an image with one of ten possible labels: peak, pit, ridge, ravine (valley), saddle, convex hillside, concave hillside, saddle hillside, slope, or none. By first making a local approximation at a pixel with bicubic splines, the standard methods from Freshman Calculus can be used to calculate first and second derivatives, gradients, and Hessians. These calculations can then be used to label a pixel as a peak, pit, etc. These dervatives can also be used to calculate the Mean and Gauss curvatures at a point. (See for example Besl and Jain [3].) An attractive feature of the Haralick approach is that the derivatives can all be calculated locally by computing linear convolutions with various 5x5 masks. While our methods for identifying pixels as peak points, ridge points, etc. are also local, they are not simply linear convolutions. For more details on the Haralick approach see references 11 - 17.

Others who have taken a topographic point of view include Crowley and Parker [7], Hsu, Mundy, and Beaudet [18], Johnston and Rosenfeld [22], Lantuejoul [24], and Warntz [37]. Crowley and Parker define a multiple resolution representation (i.e. a partition of the image) by detecting peaks and ridges in the difference of low-pass (DOLP) transform. A pixel is declared a "peak point" if it is higher than its eight nearest neighbors. Ridge points are defined similarly. Hsu, Mundy, and Beaudet follow a line of thought very similar to that of Haralick. However, they not only label pixels as "peak points", etc., they also link ridges and valleys together in what they refer to as a "web network". From a mathematical view this network forms a partition (or segmentation) of the image. Johnston and Rosenfeld define a pixel to be a "peak point" if it is higher than all the points in some nxn neighborhood. Ridge points, ravine points, and sinks are defined in a similarly natural way. Lantuejoul borrows the idea of watershed from the area of physical geography to detect bubbles in radiogragrhic plates and fractures in steel. Additional references to the topographic approach are given in Haralick [17].

III. Description of the Method. While there are many aspects to the algorithm, the two main ideas are the "probe" and the "slice". The slice can be thought of as a convenient method for locating those pixels with the highest and lowest values. These pixels will usually be the ones of most interest. For our purposes, the pixels either one or two standard deviations above the mean were given special attention. The "probe", on the other hand, is a way of identifying the local topographic and geometric information at each pixel. For example, we would like to know if a pixel is on a ridge, in a ravine, or in a flat region.

The dimensions of the images studied are 120x360. The pixel values lie between 0 and 255. When the data from one of these images is read, it is first filtered by a mean filter which averages the values in a 3x3 window about each pixel. The mean and standard deviation (and all subsequent operations) are calculated for the filtered matrix. To estimate the local topographic character at each pixel, a "probe" or "sample" is made of nearby pixels to determine whether the pixel is above or below its neighbors. Since the data is of a natural scene, it is not of particularly high quality. Thus, while it is customary to consider the immediate eight neighbors as the most important, we felt that more information could be learned by reaching out five units in each direction. By comparing a pixel with its non-immediate neighbors we gain a second filtering of local irregularities. By selecting only eight points, we keep allow the algorithm to progress at a more rapid rate than it otherwise might.

The rules for the probe are as follows. The parameters ALPHA and L are declared. For most of the data we analysed, we let ALPHA = 7 and L = 5. We like to think of ALPHA as a measure of the "rise" or "drop" that takes place near each pixel and L as a measure of the distance "reached" out in each direction from the center pixel.

The probe at a pixel is computed in the following fashion. First, the value of the pixel A(I,J) is compared with each of its neighbors. The values V(I1,J1) are assigned to each non-immediate neighbor according to the following three rules:

1. If A(I1,J1) > A(I,J) + BETA, then V(I1,J1) = +1;

2. If A(I,J) + BETA > A(I1,J1) > A(I,J) - BETA, then V(I1,J1) = 0;

3. If A(I,J) - BETA > A(I1,J1), then V(I1,J1) = -1;

where BETA = ALPHA if ABS(I-I1) = ABS(J-J1) and BETA = SQRT(2.0) * ALPHA if ABS(I-I1) differs from ABS(J-J1). Thus, if A(I1,J1) is "significantly above" A(I,J), then V(I1,J1) = +1; if A(I1,J1) is "about the same height" as A(I,J), then V(I1,J1) = 0; and if A(I1,J1) is "significantly below" A(I,J), then V(I1,J1) = -1. The factor of SQRT(2.0) is obviously included to compensate for the greater distance along a diagonal rather than along a vertical or horizontal direction. The diagrams in Figure 1 indicate typical configurations.

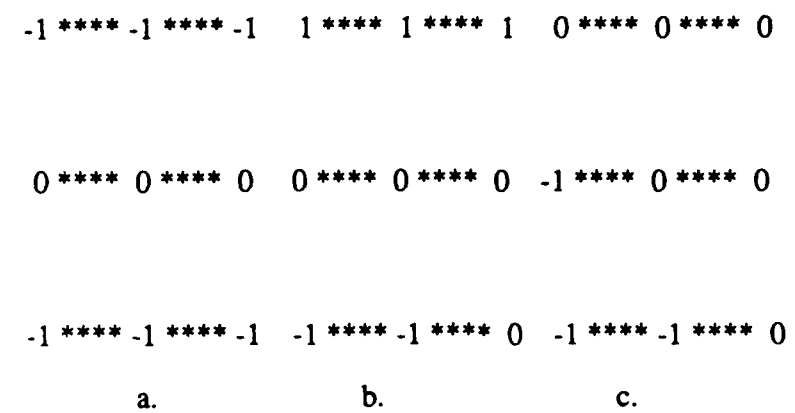

Figure 1. Typical Configurations

Three of the rules are now easy to state. First, if V(I1,J1) = -1 for each of the eight neighbors selected, then the pixel is declared a peak point. Banchoff would assign an index of +1 to such a point. Second, if V(I1,J1) = 0 for each of the eight neighbors, then the pixel is declared a flat point. Since the curvatures and indices of a flat point could only be assigned a value of zero, Banchoff ignored this group of points. Third, if V(I1,J1) = +1 for all eight neighbors, then the pixel is declared a sink point. Again, the index of a sink point is +1. These examples are indicated in Figure 2.

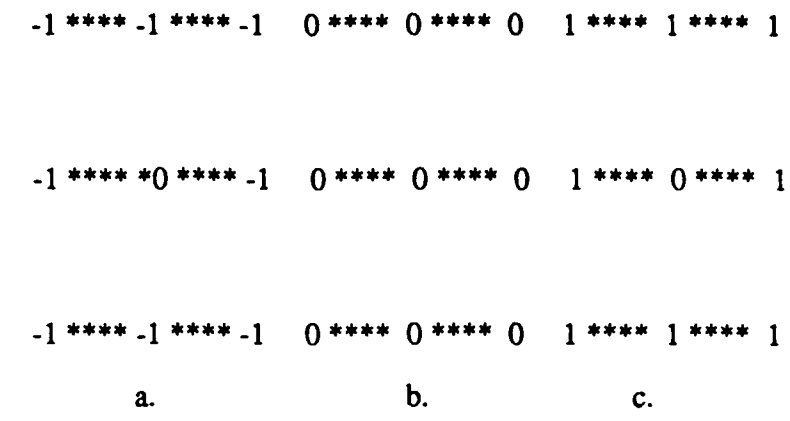

Figure 2. Typical Peak, Flat, and Sink Points

The three configurations indicated in Figure 1 represent a typical ridge, steep slope, and gentle slope points, respectively. The ridge points can be thought of as locations where the surface is level through the middle and drops off sharply on each side. Before we can give the precise description of the rules for a pixel to be considered a ridge point, we must count the number of value changes that occur in the eight neighbors. Note in Figure 1a that there are two groups of -1's with three elements in each group and two groups of zeroes with one element in each. Thus, there are four different groupings with only values of -1 or 0 in each group. Intuitively, there are two regions at about the same level as the center pixel and two groups each significantly below the center pixel. The rules for a pixel to be designated a ravine point are the same except that there will be only values of +1 and 0 in each group. Examples are indicated in Figure 3. Banchoff set up his definitions so that these cases never occured. Thus, he never assigned an index or curvature to such a point. However, if he had, he would have agreed that the Gauss curvature should be zero and the Mean curvature should be negative just the way it is described in [3].

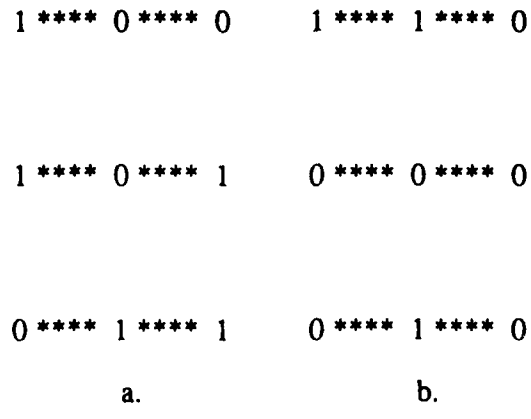

Figure 3. Ravine Points

A pixel will be designated a top-of-cliff point if there are

exactly two groupings of -1 values and 0 values and at least two of the neighbors satisfy the inequality A(I1,J1) < A(I,J) - 3 * BETA. Thus, these pixels will be the same as the gentle slope pixels except that the amount of drop will be much more significant. The rules for a bottom-of-cliff point are the same as those for a top-of-cliff point except that the values are now +1 and 0 and two of the neighbors must satisfy A(I1,J1) > A(I,J) + 3 * BETA. Examples are indicated in Figure 4. Note that we have placed 3 or -3 where there is a large rise or drop. Note also that these points would be detected by either the Kirsch or Sobel edge detector. Thus, we can think of the identification of a pixel as a top-of-cliff point as a location where very rapid change is occuring.

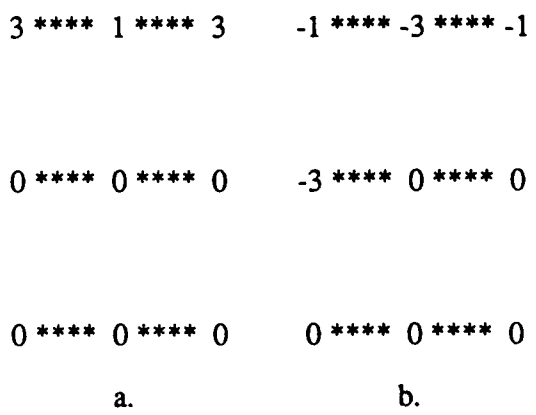

Figure 4. Bottom-of-cliff and Top-of-cliff Points

A pixel is to be designated as a steep slope point if its neighbors take on both the values +1 and -1 (and possibly zero) and the number of groupings is no more than three or if there are exactly four groupings and each of the values -1, 0, and +1 are assumed by some neighbor. Examples of steep slope pixels are indicated in Figure 5. As in the case of the top-of-cliff points these points would be identified by most edge detectors. However, note that the local change at a steep slope point is not quite as rapid as the change at a top-of-cliff or bottom-of-cliff point.

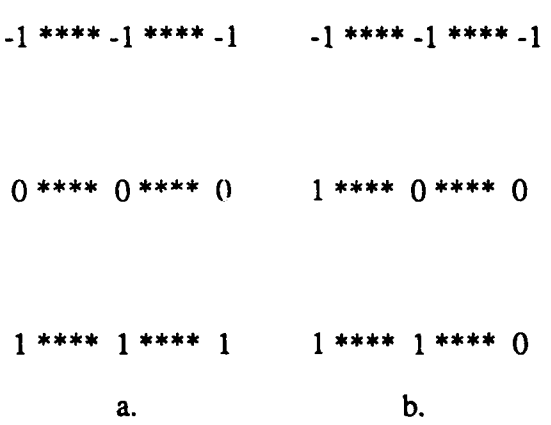

Figure 5. Steep Slope Points

A pixel will be designated a gentle slope point if there are exactly two groupings, where one group has all zeroes. Examples are indicated in Figure 6. (See Figure 1c for third example.) These types of points can be thought of as locations where a moderate rather than rapid change is occuring.

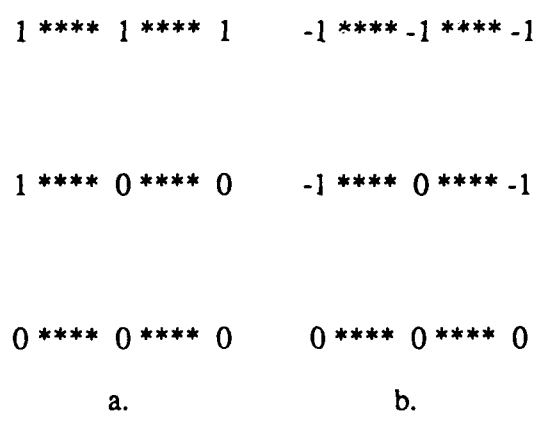

Figure 6. Gentle Slope Points

The algorithm is based on two segmentation procedures. The first identifies all connected components of those pixels which are either two standard deviations above the mean or are designated as top-of-cliff points or peak points. The second procedure identifies

all connected components of those pixels which are at least one standard deviation above the mean or are designated as top-of-cliff points, ridge points, or peak points. In addition, in the second segmentation procedure it was found that the introduction of a dilation and erosion helped to keep long narrow ridges representing runways from fragmenting.

Note that both segmentation procedures depend on pixel values, local geometry, and edge detection. This segmentation technique was developed when it was found that the pixels representing runways frequently were lower than one standard deviation above the mean. Thus, even though the runway was clearly visible in printouts of the data, the sigma-slice was not sensitive enough to identify these pixels. By introducing geometric considerations the results improved dramatically. A similar observation is true for the building images because the target in a building image was frequently found to be represented by pixels below two standard deviations above the mean. By including peak points in the segmentation process these buildings were usually located.

Once the two segmentation processes have been completed for an image, the next step is to label the connected components by their topographic features. The original idea was that a component with a large number of its pixels identified as peak points should be labeled a peak, a component with a large number of its pixels identified as ridge points should be labeled a ridge, and a component with a large number of its pixels identified as flat points should be labeled a mesa. However, we found that the above rules needed to be modified to ensure accurate.

The four separate criteria used to test whether a component should be labeled a peak are height, percentage of peak points, curvature, and shape. These properties are integrated into a single confidence factor, CFPEAK. The first calculation sets CFPEAK equal to the fraction of pixels three standard deviations above the mean. The second set of adjustments to CFPEAK is based on two tests for the percentage of peak points in a component. If the percentage of peak points is above 10%, then CFPEAK is replaced by .33 + .67 * CFPEAK. If the percentage of peak points is above 25%, then CFPEAK is replaced by .33 + .67 * CFPEAK. The third set of adjustments to CFPEAK is based on the curvature of the image at the pixel. Three curvature tests are made to determine the steepness of the drop on the sides of the peak. The curvature at a peak point is computed as the minimum of the absolute values of the curvatures in four different directions. The curvature of a component is the maximum of the curvatures at all the peak points in a component. Each time the curvature passes a test CFPEAK is updated to .33 + .67*CFPEAK. The fourth adjustment of CFPEAK consists of three ratio tests to determine whether or not the component is rounded or elongated. Each time the component passes a particular test the confidence factor CFPEAK is replaced by .20 + .80 * CFPEAK. If the component is excessively elongated, then CFPEAK is reduced by .20. Finally, if CFPEAK is greater than or equal to .60, then the component is labeled a peak.

The confidence factor, CFRIDGE, is used to decide whether or not a component is to be labeled a ridge. Its computation is very similar to the calculation of CFPEAK described above. The first computation in calculating CFRIDGE is to set CFRIDGE equal to the fraction of ridge pixels in the component. If this fraction is at least .30 or the sum of ridge points, top-of-cliff points, steep slope points together with one half of the gentle slope points is at least one half the pixels in the component, then a series of five ratio

tests are performed to determine the shape. Each time one of these tests is passed, CFRIDGE is replaced by .20 + .80 * CFRIDGE. If CFRIDGE is at least .60, then the component is declared a ridge. If the minimum of CFPEAK and CFRIDGE is at least .50, then it is labeled a crest.

If a component has at least 40% of its pixels identified as flat points or gentle slope points, then the component is labeled a mesa. Concern might be expressed that the presence of a large percentage of gentle slope points could lead to a large variation in height in different regions of the component. This problem is largely avoided because most of the pixels will be two standard deviations above the mean so that the variation between any two pixels in the component will not be large. Thus, the combination of these two factors will tend to ensure that a mesa will appear flat. The large components representing the land masses in the bridge images were frequently represented by mesas.

While studying the bridge images it was discovered that two different types of ridges were occurring. The first type had a high percentage of ridge points. The second consisted of 70 - 80% (sometimes even 100%) top-of-cliff points. Upon inspection of the data it was discovered that the ridges with a high percentage of ridge points usually represented the bridge or the road leading to the bridge, while the other type represented a cliff where the land met the water. Thus, we decided that it is worthwhile to distinguish between these two different types of components. A component is labeled a cliff if CFRIDGE was at least .60 and at least 75% of its pixels were top-of-cliff points.

Not only were components labeled as peaks, ridges, crests, mesas, and cliffs, but they were also ranked by size, length and prominence. For example, if the number of pixels in a peak, crest or mesa component comprise one half percent of all the pixels in the image, then it is labeled medium-sized; if 1%, then large. If a ridge or cliff satisfies certain elongation conditions, then it is labeled long or very long.

The study of the components generated by the second segmentation process is very similar to the first. The rules for labeling a component a peak, ridge or mesa is the same as before. Two modifications include the elimination of the crest label and the inclusion of the ridge-peak system label. A component is labeled a ridge-peak system if it contains at least two components from the first segmentation step and has at least 300 pixels. The criteria for determining the size of a component have been increased to 3% for a medium-sized component and 6% for a large component. A new size category of massive (such as in a massive ridge-peak system) has also been added. A component is massive if it contains 12% of all the pixels in the image. In the bridge images components representing land sometimes are labeled as massive ridge-peak systems.

While the target frequently appears as the most prominent peak in a building image, this is not always the case. Thus, we felt it was important to develop a test to measure the prominence of a peak. To estimate the prominence of a peak or crest we compute the fraction of pixels at least 3 standard deviations above the mean. The higher the fraction, the more prominent the peak or crest. In this way we can pick out the target from among the prominent and not so prominent peaks.

IV. Summary of Data Analysis. When we tested our methods on the 199 infrared images supplied by Eglin AFB, we concerned ourselves with four major questions. First, was the topographic labeling accurate? Second, were there general observations that could be made about the bridge images, the building images, etc.? Third, could patterns be detected in the topographic labeling of a chosen sequence of images of a particular target? Fourth, given the centroid of the target (or targets) in an image, could the topographic features be used to pinpoint this location?

After studying 199 images we have come to the conclusion that the topographic labeling is extremely accurate. While we assigned labels to several thousand components, only a few were clearly in error. (It was frequently the case that we left more complicated components unlabeled.) If a component was labeled a small peak, it was a small peak; if a component was labeled a long ridge it was a long ridge, etc. The results were excellent.

While the component representing the target in a bridge image is usually labeled a long ridge, there are a variety of other observations we can make. For example, it is frequently the case that the centroid of the target is represented by a cluster of ridge points appearing as a subset of a long ridge. Thus, we can pinpoint the target location more precisely. This precision is important when we want to distinguish between the road leading to the bridge and the bridge itself. Another observation to be noted is that the pixels representing the road tend to be hotter than those representing the bridge. This situation occurs when the sensor is 4-6 miles from the target and seems to be caused by the cooling effect of the water on the concrete and steel forming the bridge. Geometrically, the target appears as a saddle in a long ridge. In some cases the pixels representing the bridge are below one standard deviation above the mean (and are not identified as peak, ridge, or top-of-cliff points) so that the road is represented by a long narrow ridge with a gap in the middle. In some cases the target is represented by as few as six pixels so the gap is not very large.

Since we have developed two segmentation proceedures in our algorithm, we can combine information from both to pinpoint the target. For example, it can happen that the first segmentation step will identify six or seven ridges. The obvious question is which ridge represents the bridge? If a large ridge-peak system is found in the second segmentation step which represents both the land and the bridge, then sometimes this ridge-peak system will contain only one or two ridges from the first segmentation step. Thus, the possible choices are reduced. We refer to the above technique as "nested targeting" because a component from the first segmentation step will be contained (or nested) in a component from the second. It should be remarked, however, that in most of the bridge images the first segmentation proceedure did not provide nearly the useful information that the second one did.

An indication of the wide variability of the bridge images is the fact that the standard deviations ranged between five and seventy. The images with high standard deviations had a large amount of water represented in the image and extremely sharp drops between the pixels representing the land and those representing the water. These images are taken at a range of one to three miles. Some of these images are so clear that even the pilings stand out. The images with low standard deviations are so bland that when intensity level pictures were made, it was almost impossible to

detect any recognizable features. (One can only conjecture that there was a dense fog around the bridge at the time the image was taken.) However, even with these images, some useful information was obtained.

While the results of the topographic labeling were excellent, our ability to find the targets was also very good. In 58 of 63 bridge images studied some useful information was found which would help locate the target. Enough topographic information was generated in 53 of 63 images to obtain a good approximation of the centroid of the target.

A discussion of the grading system together with the details of the output of each bridge image studied are presented in Appendix A. A brief summary of the target grades is as follows.

Target Grade	Number
Excellent	2
Very Good	7
Good	44
Marginal Pass	5
Poor	5
Total	63

As mentioned in the introduction, the targets in the building images were usually represented by peaks or crests in the first segmentation process. However, the distance between the sensor and the target varied from one to six miles. Thus, while the labeling of the image taken at six miles might identify a small peak or crest at the centroid of the target, the labeling might change to prominent ridge when the sensor was only one or two miles away. Such progressions depended on the features in the images, but were usually natural.

Sometimes the target can be located as a small peak at the end of a very long ridge. Sometimes the centroid of the target is located among a cluster of three small peaks. Sometimes the target may be represented by a peak, which is not the most prominent one. However, the other labeled topographic features near the target can be used to confirm which component represents the target. Sometimes the target was found in the first segmentation process but not the second. In eight of the 59 images the target was not located at all. In these cases the pixels at the centroid of the target were only about one standard deviation above the mean. While these pixels formed a rather low-lying peak, it was rather small and dome-like so that it did not have any peak points. Thus, none of its pixels were even considered in the first segmentation process. In the second segmentation step the component was too small (less than 100 pixels) to be considered.

Despite the various problems mentioned above, we managed to find pixels representing at least 30% of the target in 51 of 59 images studied. A good approximation of the target was achieved in 43 of the 59 images. Some useful information was found in 51 of the 61 images. The following table grades our ability to pinpoint the target. A grade of excellent indicates that 80% of the pixels in the target were formed by one or two components. A grade of very good means that 60% of the pixels in the target were found. A grade of good indicates that 50% of the pixels in the target were found. A grade of marginal pass indicates that about 30% were found. A

grade of poor indicates no component was found near the centroid of the target. Note that since most of the targets in the building images are represented by a small number of pixels , even the low grade of marginal pass indicates the location of the target. The details of the data analysis of the building images studied are included in Appendix B.

Target Grade	Number
Excellent	15
Very Good	13
Good	15
Marginal Pass	8
Poor	8
Not Rated	2
Total	61

The petroleum tank images are much more complicated than the other three groups of images studied. Not only are there many more components generated in the two segmentation proceedures, but they are also more irregular in shape. One explanation for this complication is that there are as many as 23 targets in any one image. Moreover, these targets can be grouped tightly together so that one peak or ridge can be at the centroid of two or three different targets. Another complication is that the number of pixels representing a target can vary from less than one hundred to above several thousand. As in the situation with the bridge and building images the target (or targets) may not be the most prominent feature in the image. In fact, some large targets had pixel values below the mean at the centroid and very high values away from the centroid. This type of situation makes it very difficult to pinpoint the target exactly. Despite the complications indicated above, we obtained some useful information in 43 of 50 images studied. While a detailed discussion of the petroleum tank images is given in Appendix C, a summary of the target grades is as follows.

Target Grade	Number
Excellent	8
Very Good	18
Good	12
Marginal Pass	5
Poor	7
Total	50

In our study of the runway images we found the targets to represented by ridges and ridge-peak systems. The complexity of these images was much less than that for the petroleum tank images. While the first segmentation step provided some useful information, the target was usually identified as a long or very long ridge in the second segmentation step. The Hough transform was used to determine the preferred directions of these long ridges. If the image was taken close to the target, the component representing the target would be too wide to give useful information concerning a

preferred direction. In these cases we would apply the Hough transform to the bounday of the component. Since the data on the 25 runway images was the first group studied and since a variety of modifications were made on the algorithm since the data was run, the results are not directly comparable with the other three groups. Even though we did not develop a grading system for locating the target until after the data was run, we found the runway clearly visible in 13 of 25 images. We found part of the runway in 24 of 25 images. The details of the results of our study of the runway images is presented in Appendix D.

V. Possible Directions for Future Research. There seem to be a number of natural directions for future research. First, while the sinks and ravines have always been considered a part of the topographic labeling effort, we have discussed these features very little in this report. The primary reasons for this neglect is that the higher pixel values are more important and that the scope of the project was already sufficiently broad. In the future though these additional features should be considered to see what new information can be learned.

The second more important direction should be to develop and perfect a mathematical structure designed specifically to meet the needs of image processing. Our view is that this structure could very well evolve from a blend of the topographic and Differential Geometric approaches discussed earlier. Each of these approaches considers a gray-level image to be a digitized surface embedded in 3-dimensional Euclidean space. When one visualizes such a surface, it has the appearance of a topographic relief map of a geographic landmass. Features such as peaks, ridges, plains, valleys, ravines, and sinks become readily apparent. The foundation for this approach has already been laid by Haralick [11-18] and Davidson and Wilson [8]. The techniques of Mathematical Morphology are based on the Minkowski geometry. It seems worthwhile that these ideas should also be incorporated into any general theory.

The main reason for our interest in this approach is to develop techniques which will identify as many important features in an image as possible. Rather than rush to such standard methods as edge detection, thinning, the medial axis transform, and the like, it seems that consideration of the three dimensional character of the image at each stage of the analysis would provide for a more accurate understanding of the image.

The third direction we would like to begin exploring is the development of a complexity measure (or sequence of measures) based on the topographic and geometric information in the image. This phase of the project should be analogous to the initial developments in the area of Algebraic Topology when algebraic invariants were first being discovered. The history of these invariants proceeded approximately as follows. First, the Euler characteristic was used (by Euler) to show that the tetrahedron, the cube, the octahedron, the dodecahedron, and the icosahedron are the only regular polyhedra in 3-space. In 1895 Poincare made use of the Betti numbers to quantify the dual structure of triangulated manifolds. This theory was a natural extension of the duality observed earlier for the regular polyhedra. In 1911 Poincare utilized the Fundamental Group to show the existence of a homology 3-sphere which is not homeomorphic to a 3-sphere. Veblen introduced the idea of homology groups (with Z_2 coefficients) about the same time. Noether suggested the idea of homology groups with arbitrary coefficients about 1925. Lefschetz pointed out in the 1930's that the cohomology groups provide the proper setting for Poincare's duality theory developed some 30 years before. While this discussion of the history of Algebraic Topology could be continued at great length, the point is that it was not sufficient to consider only the Euler characteristic. The proper mathematical setting ultimately turned out to be much more complicated and took many years to develop. Our view is that the development of a complexity measure for an image could possibly proceed along a similar path.

While we are still unclear at the moment how the complexity of an image should be measured, it seems reasonable to base any such

metric on geometric considerations. However, the situation does not seem to be so simple. For example, if we were to follow the topographic approach, we might add up the number of peaks, sinks, ridges, ravines, etc. However, is an image with forty small peaks forty times as complex as an image with one peak. We think not. If we were to follow Nackman's approach, we might count up the number and type of slope districts present in an image. If we were to follow the Differential Geometric approach of Besl and Jain, we might sum the curvatures over all the pixels in the image. However, the classical theorem of Gauss-Bonnett relates the Gauss curvature, the surface area, and the Euler characteristic. A careful statement is as follows. (This theorem can be found on page 358 of Kobayashi and Nomizu [19].)

Gauss-Bonnet Theorem: If M is a closed orientable surface, then

$$\int_M KdA = 2* PI*X(M), \text{ where}$$

PI = 3.1415..., K is the Gaussian curvature of the surface M, dA denotes the area element of M, and X(M) denotes the Euler characteristic of M.

Note that this theorem states that the integral of the curvature is a constant which depends only on the Euler characteristic. Note further, that as stated above the theorem will have no applications to image processing because the assumption that the surface is closed is to restrictive. In image processing the surfaces will always be equivalent to the unit disk D in E^2 whose boundary C is equivalent to S^1. In this setting the Gauss-Bonnett theorem can be reformulated as follows [19].

Theorem. If D is an embedded disk in Euclidean space with boundary C, then

$$\int_C kds + \sum_{i=1}^{m}(PI - b_i) + \int_D KdA = 2*PI \quad , \text{where}$$

k is the geodesic curvature of C and $b_1,..., b_m$ denote the inner angles at the points where C is not differentiable. The consequence of this last theorem is that the integral of Gaussian curvature is determined by the constant 2*PI together with the sums of two numbers determined by the boundary. For the purposes of image processing this result is not very satisfying because the boundary is the least interesting part of the image. While the integral of the Gauss curvature will not be a useful measure of complexity, the integral of the mean curvature could very well be important. The mean curvature is an extrinsic property (the Gauss curvature is intrinsic) and does depend on the embedding. Thus, different images could very well have different total Mean curvatures. It might be possible to relate this number to the complexity of the image in some useful way. Other possible approaches include computing the sum of the minimum or maximum of the absolute values of the two principal curvatures.

In order to apply Nackman's approach we must first assume that we have a smooth surface which approximates the data. While this approximation may be possible in some situations, it is doubtfull the infrared data that we have been using would be easily smoothed in a way that the essential character of the image is retained. In particular, a large number of small innocuous false summits could appear making the image seem more complicated than it is. While a similar objection to the work of Besl and Jain might also be

raised, they have confronted the numerical aspects in considerable detail [3,5]. Polya [31] and Banchoff [1] and [2] have shown that the Critcal Point Theorem of Morse and the Gauss-Bonnett theorems can be phrased in the piecewise linear category. This result implies that the difficulties of approximating the data by a smooth function can be bypassed and there should be no problem in making the transition from the smooth category to the discrete setting of image processing. Thus, the work of Fenchel [9], Kuiper [20,21], Massey [25], Otsuki [30], and Wilson [39] can also be incorporated into our investigation.

References

1. T. Banchoff, "Critical points and curvature For embedded polyhedra," Journal of Differential Geometry, vol. 1, pp. 245-256, 1967.

2. T. Banchoff, "Critical points and curvature for embedded polyhedral surfaces", Math Monthly, vol. 77, 1970, pp. 475-585.

3. P. J. Besl and R. C. Jain, "Invariant surface characteristics for 3D object recognition in range images," Computer Vision, Graphics, and Image Processing, vol. 33, 1986, pp. 33-80.

4. P. J. Besl and R. C. Jain, "Three-dimensional object recognition," Computing Surveys, vol. 17, 1985, pp. 75-145.

5. P. Besl and R. Jain, "Surface characterization for three-dimensional object recognition in depth maps," Center for Research on Integrated Manufacturing, 1984.

6. A. Cayley, "On contour and slope lines," London, Edinburgh, and Dublin Philosophical Mag. and J. Sci. vol. 18, 1859, pp. 264-268.

7. J. L. Crowley and A. C. Parker, "A representation for shape based on peaks and ridges in the difference of low-pass transform," T-PAMI, vol. 6, pp. 156-170.

8. J. L. Davidson and D. C. Wilson, "Labeling the topographic features of a gray-level image", Proceedings from the Conference on Intellegent Systems and Machines, Oakland University, April 29-30, 1986, (to appear).

9. W. Fenchel, "On total curvatures of Riemannian Manifolds", J. London Math. Soc. 15 (1940), pp. 15-22.

10. S. B. Gray, "Local properties of binary images in two dimensions," Transactions on Computers, vol. 20, 1971, pp. 551-562.

11. R. M. Haralick, "Ridges and valleys on digital images," Computer Vision, Graphics, and Image Processing, vol. 22, 1983, pp. 28-38.

12. R. Haralick, "Author's reply," IEEE Transactions on Pattersn Analysis and Machine Intelligence, PAMI-7, 1985, pp. 127-129.

13. R. Haralick, "Digital step edges from zero crossing of second directional derivatives," IEEE Transactions on Pattern Analysis and Machine Intelligence, PAMI, vol. 6, 1984, pp. 58-68.

14. R. M. Haralick, "Edge and region analysis for digital image data," Comput. Graphics Image Processing, vol. 12, pp. 60-73, 1980.

15. R. M. Haralick and L. G. Shapiro, "Image segmentation techniques," Computer Vision, Graphics, and Image Processing, vol. 29, 1985, pp. 100-132.

16. R. M. Haralick, "Ridges and valleys on digital images," Computer Vision, Graphics, and Image Processing," vol. 22, 1983, pp. 28-38.

17. R. M. Haralick, L. T. Watson, and T. J. Laffey, "The topographic primal sketch," International Journal of Robotics Research, vol. 2, 1983, pp. 50-72.

18. S. Hsu, J. L. Mundy, and P. R. Beaudet, "Web representation of image data," Fourth International Joint Conference on Pattern Recognition, Kyoto, Japan, 1978, pp. 675-680.

19. S. Kobayashi and K. Nomizu, Foundations of Differential Geometry II, Interscience Publisher, 1969.

20. N. H. Kuiper, "On surfaces in Euclidean space," Bull Soc. Math Belg., vol. 12, 1960, pp. 5-22.

21. N. H. Kuiper, "Convex immersions of closed surfaces in E^3 , Non-orientable closed surfaces in E^3 with minimal total absolute Gauss-curvature", Comment. Math. Helv., vol. 35, 1961, pp. 85-92.

22. E. G. Johnston and A. Rosenfeld, "Digital detection of pits, peaks, ridges, and ravines," IEEE Transactions on Systems, Man and Cybernetics, vol. 5, 1974, pp. 472-480.

23. T. J. Laffey, R. M. Haralick, and L. T. Watson, "Topographic classification of digital image intensity surfaces," present-ed at the IEEE workshop on Computer Vision, Representation, and Control, Rindge, New Hampshire, 1982, pp. 171-177.

24. C. Lantuejoul, "Detection automatique de lignes de defauts dans les systemes eutectiques lamellaires," Rapport interne, Centre de Morphologie Mathematique Fontainebleau, France, 1978.

25. W. S. Massey, "Surfaces of Gaussian curvature zero on Euclidean 3-space, Tohoku Math. J., vol. 14, 1962, pp. 73-79.

26. J. C. Maxwell, "On hills and dales," London, Edinburgh, and Dublin Philosophical Mag. and J. Sci., 4th Series, vol. 40, 1870, pp. 421-425.

27. M. Morse and S. S. Cairns, Critical Point Theory in Global Analysis and Differential Topology, New York, Academic Press, 1969.

28. L. R. Nackman and S. M. Pizer, "Three-Dimensional shape description using the symmetric axis transform 1: theory," T-PAMI, vol. 7, 1982, pp. 187-202.

29. L. R. Nackman, "Two-dimensional critical point configuration graphs," T-PAMI, vol. 6, 1984, pp. 442-450.

30. T. Otsuki, "On the total curvature of surfaces in Euclidean spaces," Japan J. Math., vol. 35, 1966, pp. 61-71.

31. G. Polya, "An elementary analogue to the Gauss-Bonnet theorem," Amer. Math Monthly, vol. 61, 1954, pp. 601-603.

32. T. Pong, L. Shapiro, and R. Haralick, "Shape estimation from topographic primal sketch," Pattern Recognition, vol. 18, 1985, pp.

333-347.

33. T. Pavlidis, "A review of algorithms for shape analysis," Computer Graphics and Image Processing," vol. 7, 1978, pp. 243-258.

34. G. X. Ritter and P. D. Gader, "Image algebra implementation on cellular array computers", IEEE Computer Society Workshop on "Computer Architecture for Pattern Analysis and Image Database Management", Miami Beach Florida, 1985, pp. 430-437.

35. J. Serra, Image Analysis and Mathematical Morphology, New York, New York, Academic Press Inc., 1982.

36. E. Spanier, Algebraic Topology, New York, New York, McGraw-Hill, 1966.

37. W. Warntz, "The topology of a socio-economic terrain and spatial flows," Regional Sci. Ass. Papers, vol. 17, 1966, pp. 47-61.

38. L. Watson, T. Laffey, and R. Haralick, "Topographic classification of digital image intensity surfaces using generalized splines and the discrete cosine transformation," Computer Vision, Graphics, and Image Processing, vol. 29, 1985, pp. 143-167.

39. J. P. Wilson, "The total absolute curvature of an immersed manifold", J. London Math. Soc 40, 1965, pp. 362-366.

Appendix A. The purpose of this appendix is to summarize the results of our study of 63 bridge images selected from the Eglin AFB IRHVTA image library. The principal tool used in this analysis was the Topographic Labeling Algorithm. A glance at the results summarized below indicates that the algorithm proved to be an effective tool in locating targets. In particular, the algorithm provided some useful information in 58 of 63 images studied. Better yet, it provided a good approximation of the target location in 53 of 63 images. The results of the algorithm have been checked against outputs of the range data, probe values, level slices, and raw data. Mr. Paul Gader has kindly lent me the pictures he used in his 1984 bridge study. I have included as many of these as were available. Note, however, since we ran our data before learning of Mr. Gader's collection, the bridge numbers do not always correspond exactly between picture and output.

Observations made while analyzing the bridge data include the following. A new topographic feature, the cliff, should be introduced. The reason for this addition is that a distinction between a very long ridge with a high percentage of ridge points and one with a high percentage of top-of-cliff points (and thus a low percentage of ridge points) would help us differentiate between components which represent the conjunction of land and water and those which represent a bridge. The bridges were frequently represented by very long ridges which had a very high percentage of ridge points. Note that the ridge points replace the idea of "reverse parallel" and "antiparallel" lines used by Navatia and Babu and Davidson and Gader. A second observation is that sometimes a long ridge would represent the bridge together with a portion of the land at one or both ends of the bridge. Even though this component would contain many more pixels than the target, the ridge points in the

component would corgregate at the centroid of the target. We refer to this welcome event as "nested targeting" because the bridge can be pinpointed as one set nested inside another. Other observations include the fact that landmasses are frequently represented by flat ridges and mesas as well as cliffs. Also, while the VERY HIGH points were very important in the building images and somewhat important in the runway images, they provided very little useful information in these bridge images. Thus, the output from this part of the algorithm has not been emphasized. A final observation is that it was not uncommon in these images to identify the road and land leading up to the bridge but then to have the bridge itself disappear. Upon examination of the raw data, we realized that sometimes the pixel values at the bridge would be lower than those of the nearby land. The reason for this would seem to be the cooling effect that the water has on the bridge. If the bridge is small, the pixels representing the target have the appearance of a "saddle". At some future time in the project we may want to introduce saddle points as a new local topographic label. Haralick has already done this in his work.

Since the principal interest in this project is to find targets, the focus of the summary presented here is on the application of the topographic features to locate the bridge. The algorithm was tested on the 63 bridge images discussed below. Range data indicating the size and placement of the target was available for all of these images. If the algorithm labeled one or two components that contained 80% of the pixels in the target, then we assigned a grade of EXCELLENT. If the bridge together with adjacent land is represented by a long ridge (for example) and the number of ridge points approximates the number of pixels in the

target, then we assigned a grade of VERY GOOD. If the bridge together with adjacent land is represented by a long ridge, then we assigned a grade of GOOD. If no component is found at the centroid of the target, but a significant ridge is found which points in the direction of the target, then MARGINAL PASS. If the target was not found, then POOR. The following list gives a summary of the results.

GRADE	NUMBER
Excellent	2
Very good	7
Good	44
Marginal pass	5
Poor	5
Total	63

The following tables and subsequent remarks give a summary of the study of the bridge images investigated so far. Note that there is only one target and one object in each image. Note further that all images with the same first three numbers are of the same target. All images are 115x355 and thus contain 40,825 pixels. In the following chart the distance (in feet) from the sensor to the target is listed in the column headed by DIST. The coordinates of the center of the target in the image appear in the column headed by CENTROID. The dimensions of the smallest rectangle containing the target is listed in the column headed by DIM. The number of pixels in the target is in the column PIXELS. The mean and standard deviation of the entire image are listed under MEAN and STAND. Note that the column ALT, present in Report Two has been deleted. The reason for this omission is that every altitude of every runway, building, and bridge investigated so far has been between 1,000 and 1,360 feet. The slight differences in these heights did not seem worth recording.

DBRG201**

IMAGE	DIST	CENTROID	DIM	PIXELS	MEAN	STAND
BRG20101	25,220	(51,180)	(2,8)	16	130.85	36.29
BRG20112	19,021	(57,167)	(2,11)	22	123.57	41.81
BRG20117	13,893	(54,173)	(3,15)	30	120.74	44.81
BRG20123	8,760	(49,178)	(6,23)	67	107.03	42.11
BRG20131	1,902	(57,177)	(38,123)	1,040	124.74	41.02

Remarks:

BRG20101 contains 8 ridges (4 of these are very long) and 3 small and very small peaks among the very high points. The target is in an isolated, small ridge which has 78 pixels.

The image contains two very long ridges and one massive ridge- peak system among the high points. The ridge containing the target has 21% of its 1,112 pixels identified as ridge points. The other ridge has 48% of its 726 pixels identified as ridge points. These two ridges have 752 and 352 top-of-cliff points respectively. This high percentage of top-of-cliff points indicates these ridges represent a region where the land meets the water.

Target grade: good

BRG20112 contains six ridges among the very high points. Three of the ridges are very long and one is long. The target is between two unlabeled components which contain 63 and 39 pixels, respectively.

The image contains one massive ridge-peak system with 11,257 pixels among the high points. This ridge-peak system represents the causeway, bridge, and land. Ten percent of its pixels are ridge points, which are concentrated at the centroid of the target. Since the target contains only 22 pixels, we assign a target grade of poor.

Target grade: poor

BRG20117 contains 8 ridges and three peaks among the very high points. One of the ridges is long and the peaks are all small or very small.

The image contains one massive ridge-peak system and one large ridge-peak system among the high points. The larger component has 63% of its 10,138 pixels identified as flat points and represents both the land and bridge. The target is also near the end of the large ridge-peak system which has 11% of its 2,663 pixels identified as ridge points. These ridge points tend to be concentrated near the target.

Target grade: good

BRG20123 contains 6 peaks and 4 ridges. The peaks are small o very small. Three of the ridges are very long and one is long.

Located among the high points are one large mesa, one small ridge, one long ridge, one very long ridge, and one large ridge- peak system. The mesa is parallel to the bridge and represents land. The target is located at the point where the large ridge-peak system containing 3,381 pixels and a very long ridge containing 759 pixels come into the closest contact. The ridge-peak system has [5% of its pixels identified as ridge points, while the very long ridge has 26% of its pixels identified as ridge points.

Target grade: good

BRG20131 contains 6 ridges among the very high points. One or ridges is very long and two are long. The target contains a ver long ridge with 676 pixels.

The image contains two very long ridges among the high points. The target is located in a massive ridge which contains 8,384 pixels. This ridge clearly contains the roadway and the target. The pilings are even visible in the output. While this ridge has 797 ridge points (which is approximately the number of pixels in the target), there does not seem to be a concentration at the centroid of the target.

Target grade: good

DBRG206**

IMAGE	DIST	CENTROID	DIM	PIXELS	MEAN	STAND
BRG20611	20,409	(52,162)	(2,55)	110	107.97	26.72
BRG20616	18,330	(59,179)	(2,63)	126	107.45	28.08
BRG20620	14,832	(60,180)	(3,79)	197	106.61	29.53
BRG20631	6,271	(46,180)	(8,224)	561	104.35	19.27
BRG20636	2,029	(71,180)	(74,360)	19,620	148.71	22.15

Remarks:

BRG20611 contains 11 ridges and one small peak among the very high points. Five of the ridges are very long and one is long. The target is located in a very long ridge that contains 191 pixels.

The image contains 5 ridges and one small mesa among the high points. Two of the ridges are very long and one of the ridges is a massive high flat ridge containing 8,161 pixels. The land is represented by the massive high flat ridge and is parallel to a very long ridge containing 825 pixels. A spit of land is represented by a long (but not very long) ridge with 40% of its pixels identified as ridge points. The target is at the end of a ridge with 37% of its 1,138 pixels identified as ridge points. When the raw data of the image was examined in the vicinity of the centroid of the target, the bridge did not stand out.

Target grade: good

BRG20616 contains 10 ridges among the very high points. Six of these ridges are very long. The target is located in a ve long ridge which contains 166 pixels. One component, containing 39 pixels, is not labeled and is lined up towards the target.

The image contains 4 ridges among the high points. One of the ridges is very long, one is massive and flat, and one is small and flat. The target is located near the two smaller ridges which have 1,134 and 926 pixels, respectively. The massive ridge has 8,369 pixels and represents the land. The ridges are distinctive because 27% and 39% of their pixels, respectively, are identified as ridge points.

Target grade: good

BRG20620 contains 8 ridges and 4 small peaks among the very high points. Three of the ridges are very long. A very long rid with 189 pixels represents land and is near the target.

The image contains 4 ridges among the high points. Two are small, one is very long, and one is massive. The very long ridge with 57% of its 1,024 pixels identified as ridge points represents the bridge together with the causeway. Another small ridge with 84% of its 173 pixels identified as ridge points represents the road on the other side of the bridge. There was a concentration of ridge points at the centroid of the target. The massive flat ridge with 9,432 pixels represents the land.

Target grade: good

BRG20631 contains 5 ridges among the very high points. Three of the ridges are long and one is very long. A small ridge containing 86 pixels and a very long ridge containing 120 pixels together form a line. Those ridges contain only top-of-cliff points. The centroid of the target is on the small ridge.

The image contains two ridges among the high points. One ridge is long and has 10% of its 2,610 pixels identified as ridge points. The other is very long and has 51% of its 3,631 pixels identified as ridge points. The ridges are parallel and clearly represent the bridge and causeway. Even the superstructure of the bridge is visible. There is also a concentration of ridge points at the target.

Target grade: very good

BRG20636 contains 10 ridges, 5 peaks and 6 unlabeled components among the very high points. Two of the ridges are very long and two are long. Four of the peaks are very small. A very long ridge containing 1,165 pixels is parallel to a component containing 60 pixels that is not labeled.

The image contains 5 ridges and one small mesa among the high points. Two of the ridges are very long and two are long. All the components except possibly one very long ridge are contained in the target. The total of all the pixels in these components in the target is 7,978. Note that the target is represented by 19,620.

Target grade: good

DBRG207**

IMAGE	DIST	CENTROID	DIM	PIXELS	MEAN	STAND
BRG20711	23,544	(62,167)	(2,49)	73	117.64	26.05
BRG20715	17,471	(53,170)	(5,57)	115	116.14	30.20
BRG20720	13,775	(53,177)	(7,67)	145	108.02	38.10
BRG20724	11,376	(52,171)	(11,84)	187	95.99	38.70
BRG20730	6,779	(56,181)	(27,156)	690	86.67	25.57

Remarks:

BRG20711 contains 7 ridges and 6 unlabeled components among the very high points. Five of the ridges are very long while two are long. A very long ridge with 225 pixels contains the target.

The image contains 8 ridges and two small mesas among the high points. Three of the ridges are very long, three are long and two are small. Two long ridges containing 308 and 279 pixels, respectively, are parallel to a very long ridge containing 896 pixels. This very long ridge is at the target and contains the bridge and one piece of the land leading up to the bridge. The ridge is also distinctive because it has 61% of its pixels identified as ridge points. All the other ridges have a much lower percentage of ridge points. They would be more accurately labeled as cliffs. There is a concentration of ridge points at the target.

Target grade: good

BRG20715 contains nine ridges among the very high points.

Three of these are very long.

The image contains 9 ridges among the high points. Six of these are very long and one is small and flat. A very long ridge containing 1,228 pixels contains the centroid of the target and is parallel to a very long ridge containing 878 pixels. There is a concentration of ridge pixels at the target.

Target grade: good

BRG20720 contains five ridges, one small crest, and one small peak among the very high points. Two of the ridges are very long.

The image contains 7 ridges and one massive ridge-peak system among the high points. Four of the ridges are very long. The target is located in the middle of a very long ridge which has 56% of its 1,660 pixels identified as ridge points. This ridge is parallel to another very long ridge containing 210 pixels. A massive flat ridge-peak system with 6,536 pixels represents a major portion of the land.

Target grade: good

BRG20724 contains three small ridges and one small peak among the very high points.

The image contains two ridges and a massive ridge-peak system containing 5,923 pixels among the high points. One of the ridges is very long and represents a narrow spit of land. The massive ridge-peak system connects the bridge to the land and contains the target. Most of its 1,024 ridge points form a line which contain the target. Note that the target contains 187 pixels. There is a concentration of ridge points at the target.

Target grade: good

BRG20730 contains 5 small ridges and 4 very long ridges amon the very high points.

The image contains one small peak and a massive ridge among the high points. The ridge has 1,304 of its 6,351 pixels identified as ridge points. Since the target contains 690 pixels, we have a fairly good approximation.

Target grade: good

DBRG208**

IMAGE	DIST	CENTROID	DIM	PIXELS	MEAN	STA
BRG20801	21,605	(43,209)	(2,3)	6	142.36	21.20
BRG20806	24,118	(58,183)	(4,4)	16	148.51	21.67
BRG20821	12,158	(56,176)	(11,14)	117	148.18	36.68
BRG20825	8,079	(48,172)	(20,20)	390	133.02	42.92
BRG20831	3,603	(57,167)	(114,48)	4,743	123.16	23.09

Remarks: Note that the orientation of the last two images in this group is rotated 90 degrees from the first three.

BRG20801 contains 13 ridges among the very high points. Six of these ridges are very long. The target is located near two parallel, unlabeled components as well as two very long parallel ridges.

The image contains 10 ridges and one medium-sized ridge-peak system among the high points. The target is found at the end of a very long ridge containing 772 pixels. This ridge is parallel to a very long ridge containing 676 pixels and a long ridge containing 744 pixels and is colinear with another very long ridge containing 430 pixels. All of these ridges have a low percentage of ridge points and would probably be more accurately labeled cliffs.

Target grade: good

BRG20806 contains four peaks and 7 ridges among the very high points. The peaks are small and very small. Two of the ridges are long and two are very long.

The image contains 7 ridges among the high points. Two of these are very long and three are long. The target is located on a very long ridge with 30% of its 1,481 pixels identified as ridge points Most of the ridge points are near the target. This ridge is parallel to two ridges containing 294 pixels and 538 pixels, respectively.

Target grade: good

BRG20821 contains three small ridges and 10 small and very small peaks among the very high points. A component that is not labeled contains 74 pixels is located near the target. An isolated small peak containing 38 pixels is also located near the target.

The image contains 11 ridges and two small peaks among the high points. Two of the ridges are very long. The target is located near the very long ridge with 52% of its 514 pixels identified as ridge points. The target is also near two small, parallel ridges. The closer one contains 166 pixels, while the further one contains 104 pixels. These last two ridges contain 52% and 26% ridge points, respectively.

Target grade: good

BRG20825 contains 5 small and very small peaks among the very high points. A small ridge containing 32 pixels is located near the target.

The image contains one massive ridge-peak system containing 5,048 pixels and one small ridge among the high points. The target is between where this ridge-peak system and an unlabeled component with 5,030 come in closest contact. Since the target contains only 390 pixels, this information would not be of much use. ,However, a very distinct concentration of the ridge-peak system s 791 ridge points appears near the centroid of the target.

Target grade: good

BRG20831 contains a small ridge and very long ridge among the very high points. The very long ridge containing 440 pixels and the small ridge containing 187 pixels are near the target. The centroid of the target is located on a small crest containing 1,9 pixels.

The image contains one massive ridge-peak system among the hig points. It contains 6,271 pixels and covers everything near the target. Forty percent of its points are flat. Note that the target has 4,743 pixels.

Target grade: good

DBRG215**

IMAGE	DIST	CENTROID	DIM	PIXELS	MEAN	STAND
BRG21504	20,065	(45,167)	(2,14)	28	117.53	39.06
BRG21511	20,029	(57,177)	(2,17)	34	121.11	39.91
BRG21516	15,423	(52,175)	(3,22)	44	119.11	44.15
BRG21520	13,262	(56,173)	(2,28)	56	144.00	46.69
BRG21534	3,795	(64,175)	(33,192)	2,186	142.80	39.19

Remarks:

BRG21504 contains 9 ridges and three peaks among the very high points. Four of the ridges are very long and one is long. A ver long ridge containing 228 pixels is located at the target. A small ridge containing 43 pixels is also near the target and colli to the very long ridge mentioned above.

The image contains three ridges, one small mesa and one large ridge-peak system among the high points. The small ridge with 12 pixels is flat. A very long ridge with 407 of its 2,056 pixels identified as ridge pixels contains the target.

Target grade: good

BRG21511 contains 8 ridges and 3 small and very small peaks among the very high points. Two of the ridges are very long. lw small ridges containing 30 pixels and 42 pixels, respectively are near the target. The ridge containing 42 pixels is at the target and is one pixel wide.

The image contains one massive ridge-peak system, one ridge, and one very long ridge among the high points. The target is nea each of these three components. The ridge-peak system represents large portion of the land. The pixel values which represent the bridge itself are somewhat lower than the road and land leading u to it. Thus, it has a somewhat "saddle" shape. The ridge has 71 of its pixels identified as ridge points.

Target grade: good

BRG21516 contains 5 ridges and 5 peaks among the very high points. Three of the ridges are very long. The peaks are small and very small. A very long ridge containing 470 pixels is located near the target.

The image contains three ridges and one ridge-peak system amon the high points. A very long ridge containing 892 pixels is located near the target and points at it. The massive range-peak system with 60% of its 10,137 pixels identified as flat and gentl slope points is next to the target.

Target grade: marginal pass

BRG21520 contains 5 small and very small peaks and 5 ridges among the very high points. A very small peak containing 15 pixels is near the target. A component that is not labeled is near the target and contains 39 pixels.

The image contains 4 ridges and one massive ridge-peak system among the high points. One of the ridges is very long, one is long, and one is flat. The massive ridge-peak system is nearest the centroid of the target and contains 7,578 pixels. The small flat ridge contains 334 pixels and is parallel to the massive ridge-peak system. The very long ridge containing 729 pixels as well as a branch of the massive ridge-peak system points directly at the target. A small component of ridge points in the ridge- peak system is at the centroid of the target.

Target grade: good

BRG21534 contains 5 ridges and and one small peak among the very high points. One of the ridges is very long and has the property that one third of its pixels are ridge points. More importantly, 1,209 of its 1,591 pixels are within a half a standa deviation of the maximum value of the image. Thus, this ridge is very prominant.

The image has a massive ridge and a medium sized mesa among th high points. The ridge is very prominent and has the property th 1,170 of its 7,050 pixels are identified as ridge points. While the ridge engulfs the target, the ridge points are near the centroid of the target. The medium sized mesa has 1,861 pixels a represents a part of the land Note that the target contains 2,18 pixels.

Target grade: very good

DBRG216**

IMAGE	DIST	CENTROID	DIM	PIXELS	MEAN	STAND
BRG21601	24,162	(52,175)	(2,3)	6	112.59	39.06
BRG21606	21,080	(53,176)	(2,3)	6	102.73	24.39
BRG21610	19,186	(57,178)	(3,4)	12	100.60	26.68
BRG21621	10,298	(47,188)	(6,3)	18	98.26	49.00
BRG21623	9,685	(61,171)	(7,3)	21	74.12	43.73

Remarks: In this set of images the target is very small and is oriented at a right angle from the directions of the very long ridges found nearby. Moreover, the pixel values exactly on the bridge are somewhat lower than the nearby road and land. (These lower values are probably caused by the proximity to the bridge.)

BRG21601 contains 7 ridges and one very small peak among the very high points. Three of the ridges are very long. A very lon ridge containing 502 pixels points at the target, as does a small ridge with 204 pixels. One end of a small ridge containing 45 pixels is almost at the centroid of the target.

The image contains 11 ridges and two small mesas among the high points. A very long ridge containing 662 pixels and a small ridge containing 102 pixels are parallel to a very long ridge containing 2,119 pixels. The very long ridge with 662 pixels and the small ridge are near the target. The very long ridge with 37% of its 2,119 pixels identified as ridge points contains the target. Sev of its 10 peak point.s in this ridge are near the target. Another small ridge with 105 pixels is also near the target.

Target grade: good

BRG21606 contains 15 ridges among the very high points. Five of the ridges are very long. All but two components have every pixel identified as a top-of-cliff point.

The image contains 12 ridges and one medium-sized mesa among the high points. Nine of the ridges are very long. None of the components have more than a few pixels higher than the mean. The target is near the ends of two very long ridges with 15% of 352 a 44% of 734 pixels, respectively, identified as peak points. Howe since ther are 9 very long ridges in the image, these ridges are very distinctive.

Target grade. good (but not great)

BRG21610 contains 18 ridges among the very high points. Ten of the ridges are very long. Every component has the property that every pixel is a top-of-cliff point.

The image contains 13 ridges among the high points. Seven of the ridges are very long and one is long. The centroid of the target is at the end of a very long ridge with 21% of its 887 pixels identified as ridge pixels. The target is also at the end of another very long ridge with 60% of 887 pixels identified as ridge points. However, there are other very long ridges in the image with a high percentage of ridge points.

Target grade: good (but not great)

BRG21621 contains 6 peaks and 4 ridges among the very high points. The peaks are small and very small. Two of the ridges ar very long and one is long.

The image contains three small mesas, 11 ridges and one small peak among the high points. The small peak has 190 pixels and is near the target. A very long ridge with 85% of its 208 pixels points directly at the target. A ridge with 20% of its 933 pixels represents the land and road leading up to the target.

Target grade: good

BRG21623 contains 7 ridges and 7 small and very small peaks among the very high points. One ridge is very long and one is long. The centroid of the target is located on a ridge containing 99 pixels.

The image contains a massive ridge-peak system. The ridge-peak system contains 9,499 pixels and engulfs the target. While the target is very clearly delineated by the ridge-peak system, there seems to be no way to locate the 21 pixels representing the bridge

Target grade: marginal pass

DBRG227**

IMAGE	DIST	CENTROID	DIM	PIXELS	MEAN	STAND
BRG22703	38,505	(66,282)	(2,3)	6	101.54	23.17
BRG22706	27,453	(56,298)	(3,4)	9	118.05	22.08
BRG22710	24,124	(57,283)	(4,5)	12	119.33	20.57
BRG22741	15,882	(67,282)	(7,19)	88	111.24	34.78
BRG22745	9,595	(50,290)	(15,34)	258	100.93	46.34
BRG22753	2,199	(61,205)	(119,180)	8,211	125.51	35.10

Remarks:

BRG22703 contains 8 ridges, 7 small and very small peaks, one crest, and one small mesa among the very high points. Four of the ridges are very long and one is long.

The image contains 7 ridges and one small peak among the high points. Three of the ridges are very long and one is long. The peak containing 3,395 pixels is located near the target. The pixels representing the target itself are missing because they hav somewhat lower values than the surrounding land. (This situation can probably be attributed to the influence of the surrounding water.)

Target grade: poor

BRG22706 contains 8 ridges, 6 small and very small peaks, and two small crests among the very high points. Two of the ridges ar very long and one is long.

The image contains 11 ridges among the high points. Five of the ridges are very long and three are long. A very long ridge with 61% of its 272 pixels identified as ridge points is located the centroid of the target. The pixels representing the bridge a between this ridge and another.

Target grade: marginal pass

BRG22710 contains 17 peaks and 5 ridges among the very high points. Three of the ridges are very long.

The image contains 9 ridges, one prominant peak, and one small ridge-peak system among the high points. Four of the ridges are very long. The peak, two very long ridges, and a small ridge are near the target. The peak has 2,223 pixels and is probably miss- labeled. The ridges have only 15% and 13% of their pixels identified as ridge points.

Target grade: marginal pass

BRG22741 contains 32 small and very small peaks as well as two small ridges among the very high points. One small peak was near the target.

The image has 17 ridges and 3 small peaks among the high points. Two of the ridges are very long and three are long. A ridge with 133 pixels is at the centroid of the target. This ridge has 60% of its pixels identified as ridge points. Another ridge with 30% of its 737 pixels identified as ridge points is located near the centroid of the target. However, there are many other ridges that are more distinctive than the ones near the target.

Target grade: good (but not great)

BRG22745 contains 19 small and very small peaks among the very high points. One small unlabeled component with 37 pixels is near the centroid of the target.

The image contains 10 ridges and two small peaks among the high points. Two of the ridges are long. The centroid of the target is on a ridge with 3,378 pixels. Twenty one percent of the pixels on this ridge are ridge points. These ridge points are concentrated at the target.

Target grade: very good

BRG22753 contains 6 ridges and one small peak among the very high points. Two of the ridges are very long.

The image contains one massive ridge-peak system and one ridge among the high points. The ridge-peak system contains 7,176 pixel and is located at the centroid of the target. Note that the targe contains 8,211 pixels.

Target grade: very good

DBRG229**

IMAGE	DIST	CENTROID	DIM	PIXELS	MEAN	STAND
BRG22911	17,506	(56,271)	(5,49)	122	116.41	30.56
BRG22916	15,025	(68,280)	(8,58)	120	108.63	36.35
BRG22920	15,085	(65,275)	(9,62)	132	111.72	36.01
BRG22927	8,270	(69,254)	(20,107)	424	106.72	35.99

Remarks:

BRG22911 contains 11 ridges and 6 small and very small peaks among the very high points. Six of the ridges are very long.

The image contains 18 ridges and one small mesa among the high points. Seven of the ridges are very long and two are long. A very long ridge with 71% of its 480 pixels identified as ridge points is located at the target. All the other very long ridges have fewer than 30% ridge points. (All but one below 21%.)

Target grade: good

BRG22916 contains 5 ridges and 7 small and very small peaks among the very high points. Four of the ridges are very long and one is long.

The image contains 9 ridges, one small mesa, and one small ridge-peak system among the high points. Five of the ridges are very long. A very long ridge with 90% of its 3,853 pixels identified as ridge points contains the target and a portion of the land. The ridge pixels are concentrated at the target. A very long ridge containing 433 pixels is parallel and near the ridge that is located at the target.

Target grade: good

BRG22920 contains 11 ridges among the high points. Seven of the ridges are very long. Very long ridges containing 513 and 315 pixels, respectively, are located near the target. A small ridge containing 107 pixels is also located near the target.

Target grade: good

BRG22927 contains 5 ridges and 5 peaks among the very high points. One of the ridges is very long and one is long.

The image contains three ridges among the high points. A massive ridge with 16% of its 5,828 pixels identified as ridge points runs through the target.

Target grade: good

DBRG234**

IMAGE	DIST	CENTROID	DIM	PIXELS	MEAN	STAND
BRG23411	23,028	(66,245)	(3,3)	6	147.27	5.78
BRG23415	20,666	(76,242)	(3,2)	6	151.90	5.24
BRG23420	16,433	(94,177)	(4,2)	8	149.08	5.31
BRG23423	16,185	(118,177)	(4,2)	8	154.98	5.75
BRG23429	4,564	(53,118)	(57,8)	342	141.42	19.35
BRG23432	2,851	(63,135)	(115,20)	748	121.74	17.15

Remarks: Note the extremely low standard deviation in the first four images in this group. While it was very difficult to discern any features in these images when inspected visually, the labeling algorithm performed reasonably well.

BRG23411 contains three small and very small peaks, one small mesa and one ridge among the very high points.

The image contains one medium-sized mesa, one large ridge-peak system containing 4,344 pixels, and three ridges among the high points. The target was not found.

Target grade: poor

BRG23415 contains two ridges, one very small peak, one small crest and one small mesa among the very high points. One of the ridges was very long.

The image contains 5 ridges, one medium-sized mesa, and one large ridge-peak system among the high points. Three of the ridges are very long and one is long and flat. The small ridge with 149 pixals is at the centroid of the target. The long flat ridge and the ridge-peak system are near. Two of the very long ridges are parallel and point towards the target. Fifty-nine percent of the pixels in the ridge-peak system are flat or gently sloping points. Thus, while the target has only 6 pixels and is not represented by any particular component, its location can be pinpointed almost exactly. Note the incredible blandness of the CCGRAY picture of this image.

Target grade: good

BRG23420 contains 5 ridges, two small peaks, and a medium- sized crest among the high points. An unlabeled component with 55 pixels is near the centroid of the target.

The image contains 10 ridges and one small mesa among the high points. Three of the ridges are very long and one is long. One of the very long ridges is also flat. A small ridge with 258 pixels is at the centroid of the target. The small mesa is also close to the target. The long ridge has a high percentage of steep slope points and top of cliff points and represents part of the land. One very long ridge has 872 pixels of which 65% are ridge points. The centroid of the target is near where this last ridge and the flat ridge come together. Thus, while the target only contains 8 pixels and is not represented by any particular component, its location can be pinpointed almost exactly.

Target grade: good

BRG23423 contains three ridges, a medium-sized crest, and a very small peak among the very high points. One of the ridges is very long.

The image contains 10 ridges, one large ridge-peak system, and a small mesa among the high points. Two of the ridges are very long and three are long. The ridge-peak system contains 68% flat and gentle-slope points and represents the land. A long ridge with 1,153 pixels also represents part of the land. This last ridge is an example of a phenomenon that has appeared frequently with the bridge images. In particular, while this last component is labeled a ridge, it would be more accurate to label it a cliff The reason for this modification is that this component contains only 15% ridge points, while containing 65% steep slope and top- of-cliff points. Moreover, this component really does represent the edge of a level region, which drops off sharply into the water. The road leading to the bridge also is represented by a component labeled a ridge. However, these components typically have 55-65% ridge points. The very long ridge that repesents the road in this image contains 63% ridge points. The target is next to a small ridge with 193 pixels.

Target grade: good

BRG 3429 contains three small ridges and one small peak among the very high points. None of these components is near the target.

The image contains three ridges and four mesas among the high points. Two of the mesas are medium-sized and one of the ridges is long. The mesas clearly represent part of the land, while the ridge with 730 pixels contains the target. (The ridge points in this ridge are concentrated at the target.) The long ridge with 316 pixels points at the target. This long ridge has 69% of its pixels identified as ridge points. However, this ridge represents a small narrow island next to the bridge instead of the bridge itself. The two other ridges represent the two spans of the bridge together with the road leading up to them. Note the orientation of this image is rotated 90 degrees from BRG24323.

Target grade: very good

DBRG235**

IMAGE	DIST	CENTROID	DIM	PIXELS	MEAN	STAND
BRG23521	13,504	(61,168)	(5,26)	30	154.48	8.68
BRG23526	8,322	(56,185)	(17,57)	89	154.06	14.45
BRG23530	4,531	(58,205)	(60,114)	431	143.28	20.05
BRG23534	1,767	(61,156)	(119,77)	1,130	134.21	21.27

Remarks:

BRG23521 contains two very long ridges among the very high points.

The image contains 5 ridges and two mesas among the high points. One of the ridges is very long, one is small and flat, and one is long. The mesas are medium-sized and small. The target was not found.

Target grade: poor

BRG23526 contains one small peak and one very long ridge among the very high points. The very long ridge is located near the target.

The image contains two mesas and 4 ridges among the high points. One ridge is very long and two are long. A ridge with 85% of its 108 pixels is located at the target. From the best I can determine, this ridge represents an island in the river which is next to the bridge. A very long ridge with 206 pixels is nearby. However, this last ridge has only 2% of its pixels identified as ridge points and thus would be more accurately labeled a cliff. This cliff represents where the land meets the water.

Target grade: good

BRG23530 contains 6 ridges and two small peaks among the very high points.

The image contains one massive ridge-peak system, two small mesas, and one very long ridge among the high points. The massiv ridge-peak system contains 7,136 pixels and represents both the, land and the bridge. However, 1,262 of the ridge-peak system s pixels are ridge points and clearly represent the spans of the bridge.

Target grade: good

BRG23534 contains 8 ridges, three peaks, and one medium-sized mesa among the very high points.

The image contains two ridges and one large ridge-peak system amont the high points. A very long ridge with 699 of its 4,551 pixels identified as ridge points engulfs the target. This ridge contains part of a small island as well as the lower support span under the bridge. The other ridge and the ridge-peak system clearly delineate the two elevated spans of the bridge.

Target grade: good

DBRG271**

IMAGE	DIST	CENTROID	DIM	PIXELS	MEAN	STAND
BRG27121	5,831	(59,175)	(15,24)	71	134.04	1.06
BRG27124	5,556	(51,190)	(28,39)	216	134.73	3.97
BRG27128	5,347	(47,164)	(91,37)	2,574	137.57	5.31

Remarks: Note the low standard deviation of the images in this group.

BRG27121 contains one ridge and one large mesa among the very high points.

The image contains two small mesas, one large ridge-peak system, and three ridges among the high points. One of the ridges is very long and one is long. The target is at the end of the ridge-peak system. Another unlabeled component with 27% of ite 12 pixels is also near the target. (This component narrowly missed being labeled a ridge.)

Target grade: good

BRG27124 contains one small peak among the very high points. The image contains two small mesas and one long ridge among the high points. An unlabeled component containing 4,618 pixels runs through the target. The region around the target was extremely bland since almost every pixel was identified as a flat point or a gentle slope point.

Target grade: poor (but not surprising)

BRG27128 contains 5 peaks and one small mesa among the very high points.

The image contains one small flat ridge and one massive ridge- peak system among the high points. The ridge-peak system with 53% of its 7,312 pixels identified as flat and gentle slope points engulfs the target.

Target grade: good

DRBG272**

IMAGE	DIST	CENTROID	DIM	PIXELS	MEAN	STAND
BRG27202	13,580	(51,241)	(9,239)	832	134.05	3.88
BRG27206	10,531	(61,180)	(28,360)	1,440	135.41	4.30
BRG27210	5,915	(52,180)	(44,360)	1,800	133.38	4.34

Remarks: Note the unusually low standard deviations for the images in this group.

BRG27202 contains one small mesa and one ridge among the very high points.

The image contains one large ridge-peak system, one small mesa, and one very long ridge among the high points. The very long ridge containing 274 pixels is located at the target. The ridge- peak system containing 3,338 pixels is near the target.

Target grade: good

BRG27206 contains three mesas among the very high points. Two of the mesas are small and one is large.

The image contains one small mesa, three ridges, and one large ridge-peak system among the high points. One of the ridges is very long. The very long ridge containing 731 pixels is located at the centroid of the target.

Target grade: good

BRG27210 contains one ridge among the very high points. The image contains two small mesas and one very long ridge among the high points. The ridge is very distinctive with 59% of its 1,446 pixels identified as ridge points. Note that the target has 1,800 pixels.

Target grade: very good

DBRG273**

IMAGE	DIST	CENTROID	DIM	PIXELS	MEAN	STAND
BRG27321	13,219	(75,138)	(4,28)	76	139.53	4.05
BRG27331	4,190	(44,86)	(21,171)	1,454	143.46	7.21

Remarks:

BRG27321 contains no components of any interest among the very high points.

The image has three ridges and two small mesas among the high points. One of the ridges is labeled very long and contains 3,888 pixels. This very long ridge clearly represents both the land as well as the bridge. More important, however, is the fact that this ridge contains 635 ridge points which form a line which ends at the centroid of the target. The mesas represent portions of the land.

Target grade: good

BRG27331 contains two small peaks, one medium-sized crest, and two ridges among the very high points. One ridge is very long ano has 28% of its pixels identified as ridge points.

The image has two very long ridges and one massive high flat ridge among the high points. The two ridges are long thin, parallel, and together contain 1,248 pixels. (Note that the target contains 1,454 pixels!) The ridges have 94% and 37%, respectively, of their pixels identified as ridge points.

Target grade: excellent

DRBG274**

IMAGE	DIST	CENTROID	DIM	PIXELS	MEAN	STAND
BRG27405	19,148	(54,197)	(5,31)	65	136.65	4.36
BRG27411	18,671	(69,189)	(8,52)	125	137.07	4.04
BRG27421	10,661	(64,210)	(28,131)	773	139.25	4.04
BRG27424	8,333	(65,201)	(56,210)	2,175	140.76	4.83

Remarks: Note the unusually low standard deviations of the images in this group.

BRG27405 contains four mesas among the very high points. Two of these are small and two are medium-sized. None of these components are near the target.

The image has three ridges, one large ridge-peak system, and one large mesa among the high points. One of the ridges is very long. A small ridge with 108 pixels is at the centroid of the target. this ridge has 76% of its pixels identified as ridge points. The very long ridge contains 213 pixels, has 66% of its pixels identified as ridge points, and is near the target.

Target grade: excellent

BRG27411 contains a large and a medium-sized mesa among the very high points. Neither of these components is near the target They represent portions of the land.

The image has three mesas and two ridges among the high points One of the ridges is very long. This very long ridge has 75% of its 211 pixels identified as ridge points and is lined up towards the centroid of the target. However, it is not very close to the centroid of the target. The mesas represent portions of the land

Target grade: marginal pass

BRG27421 contains three ridges and two small peaks among the very high points. One of the ridges is very long. None of these components is near the target.

The image has six ridges and one small mesa among the high points. One of the ridges is very long and one is small and flat The ridge with 2,935 pixels contains the target. Note that 20% or pixels are identified as ridge points. Note that this number is very close to the number of pixels in the target. An unlabeled component with 1,467 represents a portion of the land.

Target grade: good

BRG27424 contains two very small peaks, one large peak, and one ridge among the very high points. None of these components is near the target.

The image a large peak and a ridge among the high points. The peak has 3,209 pixels and contains the target which has 2,175 pixels. The labeling of the component as a peak is one of the few examples of poor labeling that I have found.

Target grade: good (except for the label)

DRBG275**

IMAGE	DIST	CENTROID	DIM	PIXELS	MEAN	STAND
BRG27521	15,855	(79,170)	(51,15)	211	142.58	4.15
BRG27527	7,291	(84,168)	(72,19)	613	143.63	3.28

Remarks: Note the extremely low standard deviations of the images in this group.

BRG27521 contains one large mesa with 1,307 pixels among the very high points. This mesa represents a portion of the land and is not near the target.

The image has four ridges and one large mesa among the very high points. Two of the ridges are flat. The mesa represents a portion of the land. The target is reprsented by two small ridges which have a total of 280 pixels. (Note that the target has 211. These ridges have 63% and 67% ridge points respetively.

Target grade: very good

BRG27527 contains one very small peak with 12 pixels among the very high points. This peak is near the centroid of the target.

The image has four ridges and one large mesa among the high points. One of the ridges is long and one is flat. The long ridge has 60% of its 131 pixels identified as ridge points but is not particularly near the target. A ridge with 37% of its 162 pixels is at the centroid of the target. The mesa represents the land.

Target grade: good

Appendix B. The purpose of this appendix is to summarize the results of a study of 61 building images. The principal tool used in this analysis was the Topographic Labeling Algorithm. While very small peaks were not of any particular importance in the bridge and runway images, they are very important in the building images. The reason for this interest in very small peaks is that the target in a building image frequently will have fewer than 30 pixels. Thus, the threshold for ignoring components had to be reduced from 29 to 9. However, to avoid the problem of dealing with scores of insignificant components, we require a very small component to contain at least 10 peak points. As noted below the results proved to be quite satisfactory.

The algorithm was tested on the 61 building images discussed below. Range data indicating the size and placement of the target was available for 59 of these images. One group of images proved defective and is not included in the discussion given below. If the algorithm labeled one or two components that had about 90% of the pixels in the target, then we assigned a grade of excellent. If the algorithm found 80% of the target, then we graded very good. If 50%, then good. If 30%, then marginal pass. If the target was not found, then poor. The following list gives a summary of the results.

GRADE	NUMBER
Excellent	15
Very good	13
Good	15
Marginal pass	8
Poor	8
Not rated	2
Total	61

The groups of images that gave the best results were BLD223**, BLD224**, BLD245**, and BLD247**. Four of the five images in the group BLD243** were rated good to excellent. Four of the 6 images in the group BLD246** were rated good or very good. While we graded the results of the target detection as poor in 10 images, none of these images had prominent small peaks as targets. These 10 images had neither enough pixels two standard deviations above the mean nor more than a few scattered peak points near the target so that the target was completly missed. However, if the target is not found, the grade must be: poor. If a local version of the standard deviation had been used instead of one global standard deviation, these peaks might have been identified. The image BLD25701 was so bland that that even when the original data was examined, there seemed to be little evidence of a target at all.

The following table gives a summary of the results of all the building images studied. In the following charts the distance (in feet) to the target is given in the column headed by DIST; the altitude (in feet) at which the image was taken is in the column headed by ALT. The dimensions of the smallest rectangle containing the target is listed in the column headed by DIM. The number of pixels in the target is in the column PIXELS. The mean and standard deviation of the entire image are listed under MEAN and STAND.

IMAGE	DIST	ALT	DIM	PIXELS	MEAN	STAND	TARGET GRADE
BLD22301	22,697	1,000	(6,23)	123	122.14	26.53	excell
BLD22302	24,233	1,000	(5,24)	109	120.34	27.31	excell
BLD22305	22,419	1,000	(6,27)	137	128.64	25.31	good
BLD22308	20,237	1,000	(8,30)	189	135.65	24.52	good
BLD22310	18,990	1,000	(9,33)	233	139.94	24.11	good
BLD22403	31,033	1,000	(3,7)	17	163.97	30.92	excell
BLD22404	33,413	1,000	(3,7)	21	126.26	32.00	excell
BLD22405	27,034	1,000	(3,6)	18	100.32	35.12	excell
BLD22406	26,508	1,000	(3,8)	24	113.90	26.93	excell
BLD22408	25,396	1,000	(4,8)	28	116.26	26.55	excell
BLD22409	24,930	1,000	(4,10)	35	119.66	26.64	excell
BLD22410	21,236	1,000	(4,11)	38	126.63	22.20	excell
BLD22521	8,396	1,170	(26,80)	1,399	128.96	39.94	good
BLD22522	7,126	1,170	(32,90)	1,808	138.16	42.93	m pass
BLD22525	4,648	1,170	(63,160)	6,171	150.79	44.39	v good
BLD22601	31,034	1,160	(2,29)	58	87.74	33.02	m pass
BLD22606	19,951	1,160	(6,45)	178	107.30	25.07	m pass
BLD22611	15,738	1,160	(6,44)	132	116.73	22.12	m pass
BLD22614	12,534	1,160	(8,55)	219	129.31	24.41	good
BLD22620	10,076	1,160	(10,89)	485	135.27	24.73	good
BLD22627	2,962	1,160	(65,311)	12,574	147.49	76.09	m pass
BLD24201	24,609	1,060	(4,7)	19	120.62	20.57	poor
BLD24209	22,640	1,160	(4,15)	46	122.03	19.42	poor
BLD24215	13,274	1,160	(6,21)	94	141.51	11.30	poor
BLD24221	9,875	1,360	(13,37)	335	153.66	13.55	m pass
BLD24301	30,414	1,260	(3,9)	22	121.20	21.43	poor
BLD24316	15,308	1,260	(6,14)	61	136.27	11.58	excell
BLD24320	11,986	1,260	(7,20)	97	140.46	11.77	[illegible]
BLD24321	10,326	1,260	(7,25)	127	142.03	12.70	[illegible]
BLD24331	1,142	1,160	(69,130)	5,606	198.72	25.51	[illegible]
BLD24403	23,907	1,26	(2,5)	10	112.85	[illegible]	
BLD24410	18,677	1,16	(3,9)	27	111.44	[illegible]	
BLD24415	15,154	1,060	(4,11)	44	[illegible]		
BLD24420	10,049	1,060	(6,15)	83	[illegible]		
BLD24431	635	1,060	(51,64)	2,684	[illegible]		
BLD24502	23,192	1,360	(4,11)	[illegible]			
BLD24509	17,895	1,160	(6,18)	[illegible]			
BLD24518	10,899	1,160	[illegible]				
BLD24525	5,745	960	[illegible]				
BLD24530	682	1,360	[illegible]				

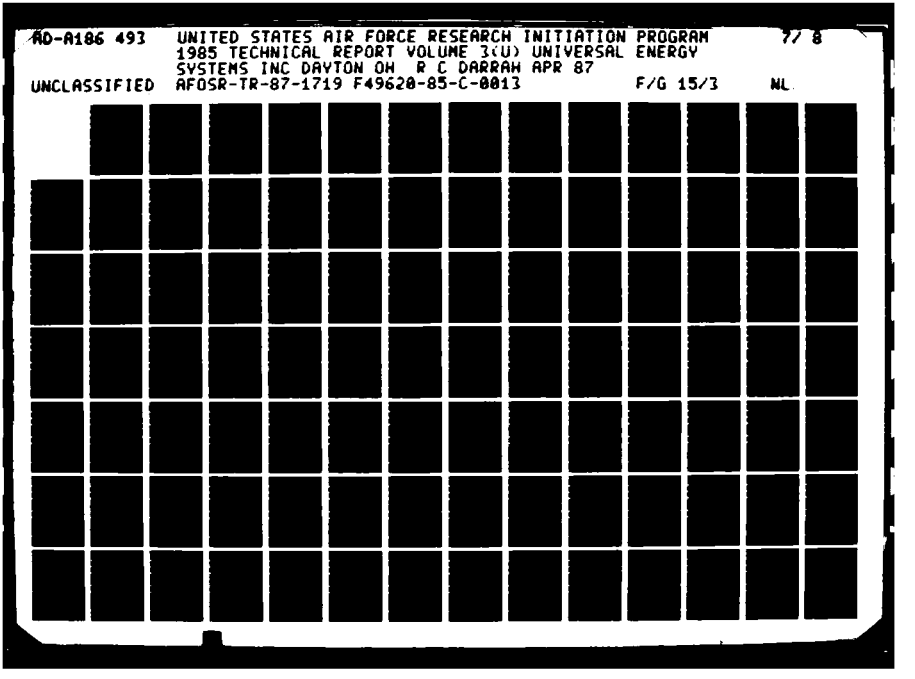
AD-A186 493 UNITED STATES AIR FORCE RESEARCH INITIATION PROGRAM 7/ 8
1985 TECHNICAL REPORT VOLUME 3(U) UNIVERSAL ENERGY
SYSTEMS INC DAYTON OH R C DARRAH APR 87
UNCLASSIFIED AFOSR-TR-87-1719 F49620-85-C-0013 F/G 15/3 NL

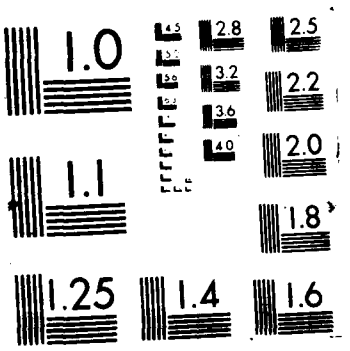
1.0
1.1
1.25
1.4
1.6
2.8
3.2
3.6
4.0
2.5
2.2
2.0
1.8

BLD24611	13,363	1,160	(7,24)	130	115.35	13.96	v good
BLD24612	12,807	1,160	(8,28)	180	118.86	13.43	good
BLD24615	9,968	1,160	(9,36)	241	128.70	16.64	good
BLD24619	6,185	1,160	(16,54)	564	142.56	21.72	good
BLD24620	5,269	1,160	(20,68)	880	145.81	23.71	v good
BLD24625	1,582	1,160	(107,200)	12,959	145.95	36.95	good
BLD24701	28,832	1,360	(3,10)	29	99.45	21.76	poor
BLD24705	24,921	1,360	(4,11)	35	105.26	18.23	v good
BLD24710	20,841	1,360	(5,13)	58	111.30	15.40	v good
BLD24715	16,603	1,260	(6,16)	72	117.62	13.83	excell
BLD24721	12,146	1,260	(7,22)	132	124.61	18.04	excell
BLD24731	3,409	1,160	(107,139)	12,017	167.11	39.50	v good
BLD25411	14,089	1,360	(8,41)	159	134.07	14.03	good
BLD25414	12,649	1,260	(16,63)	320	135.69	15.14	good
BLD25501	19,405	1,260	(6,37)	99	124.34	18.47	good
BLD25511	19,018	1,260	(11,85)	359	154.99	17.38	excell
BLD25611	19,622	1,300	(5,32)	97	138.76	14.50	m pass
BLD25623	4,982	1,200	(59,120)	3,981	140.03	37.08	m pass
BLD25701	25,990	1,260	(3,35)	70	96.87	18.96	poor
BLD25721	(Range data not available.)				147.74	15.43	nr
BLD26019	(Range data not available.)				142.81	12.80	nr

The following summaries give more details of the study of the building images listed above. Note that there is only one target and one object in each image. Note further that all images with the same first three numbers are of the same target. All images are 115x355 and thus contain 40,825 pixels. The coordinates of the center of the target in the image appear in the column headed by CENTROID.

DBLD223**

IMAGE	DIST	ALT	CENTROID	DIM	PIXELS	MEAN	STAND
BLD22301	22,697	1,000	(45,138)	(6,23)	123	122.14	26.53
BLD22302	24,233	1,000	(50,179)	(5,24)	109	120.34	27.31
BLD22305	22,419	1,000	(50,180)	(6,27)	137	128.64	25.31
BLD22308	20,237	1,000	(49,180)	(8,30)	189	135.65	24.52
BLD22310	18,990	1,000	(49,182)	(9,33)	233	139.94	24.11

Remarks:

BLD22301 has two small peaks and 4 very small peaks among the very high points. One of these peaks together with another unlabeled component form the target. (The confidence factor CFPEAK of this unlabeled component lacks 0.01 of the threshold for declaring it to be a peak.) The total number of pixels in these two components is 111. Note that the target consists of 123 pixels so that it has been located almost exactly.

The image contains 8 ridges among the high points. Two of these are very long and one is long. The target is contained in one of the ridges.

Target grade: excellent

BLD22302 has three small peaks and 6 very small peaks among the very high points. The union of two of these peaks contain 102 of the 109 pixels in the target.

The image contains 6 ridges among the high points. Two of the ridges are very long and one is long. The target is a subset of the long ridge.

Target grade: excellent

BLD22305 has 12 small and very small peaks and one ridge among the very high points. The target is contained in the ridge. This ridge contains 220 pixels compared with 137 in the target.

The image contains 4 ridges among the high points. Two of the ridge are very long and one is long. The target is contained in one of the very long ridges.

Target grade: good

BLD22308 has 12 peaks among the very high points. One of these is medium-sized, while the rest are either small or very small. While the component containing the target is made up of 299 pixels, the target itself has 189 pixels. Unfortunately, the target is left unlabeled. However, it does have a rather box-like shape that could be detected by other methods.

The image contains 6 ridges and one peak among the high points. One of the ridges is very long and two are long. The target is contained in the very long ridge.

Target grade: good

BLD22310 has 14 peaks among the very high points. One of these is medium-sized while the remainder are either small or very small. The component representing the target contains 390 pixels while the target itself has 233. Unfortunately, even though this key component almost passes enough tests to be labeled a ridge, it is left unlabeled.

The image contains one large ridge-peak system and 4 ridges among the high points. Two of the small ridges are long. The target is contained in the ridge with 1,338 pixels.

Target grade: good

DBLD224**

IMAGE	DIST	ALT	CENTROID	DIM	PIXELS	MEAN	STAND
BLD22403	31,033	1,000	(67,224)	(3,7)	17	163.97	30.92
BLD22404	33,413	1,000	(72,214)	(3,7)	21	126.26	32.00
BLD22405	27,034	1,000	(78,206)	(3,6)	18	100.32	35.12
BLD22406	26,508	1,000	(66,218)	(3,8)	24	113.90	26.93
BLD22408	25,396	1,000	(69,206)	(4,8)	28	116.26	26.55
BLD22409	24,930	1,000	(71,280)	(4,10)	35	119.66	26.64
BLD22410	21,236	1,000	(65,262)	(4,11)	38	126.63	22.20

Remarks:

BLD22403 contains 6 very small peaks among the very high points. The target is almost exactly represented by a very small peak containing 14 peak points. This peak has one close neighbor.

The image contains 8 ridges and one small mesa among the high points. Two of the ridges are very long and one is long. The target is contained in the end of the long ridge. Another small ridge is nearby.

Target grade: excellent

BLD22404 contains 5 very small peaks among the very high points. The peak containing 17 pixels is the target. Note that the target contains 21 pixels.

The image contains 4 ridges among the high points and one mesa. One of the ridges is very long and one is flat. The target is contained in the end of the very long ridge.

Target grade: excellent

BLD22405 contains 9 very small peaks and one very low lying very long ridge. There is a cluster of three very small peaks near the target. The peak at the centroid of the target contains 17 pixels, while the target contains 18. The most prominent peak is not near the target.

The image contains 6 ridges and two small peaks among the high points. Two of the ridges are very long. One of these long ridges contains the target.

Target grade: excellent

BLD22406 contains one small peak and 9 very small peaks among the very high points. There is a cluster of three peaks very small peaks at the target. The peak containing 23 pixels is at the centroid of the target. Note that the target contains 24 pixels. The most prominent peak is not near the target.

The image contains 7 ridges, one mesa, and one peak among the high points. Two of the ridges are very long and two are flat. The target is at the end of the small ridge.

Target grade: excellent

BLD22408 contains 13 peaks (11 of which are very small) and one small ridge among the very high points. There is a cluster of three very small peaks near the target. Component number 11 contains 27 pixels and is the target exactly.

The image contains 7 ridges and three peaks among the high points. Three of the ridges are long and one is very long. The target is in the small peak with almost 1/3 of its pixels designated as peak points. There is a cluster of 5 components at the target including one very long ridge.

Target grade: excellent

BLD22409 contains 13 peaks among the very high points. Eight of these peaks are very small. ,The peak at the centroid of the target contains 31 of the target s 35 pixels. Again there is a cluster of three peaks at the target.

The image contains 3 peaks, 8 ridges, and one mesa among the high points. One of the ridges is very long, one is long, and one is flat. Component number 7 is a small peak with 132 pixels and contains the target. This peak has 5 close neighbors.

Target grade: excellent

BLD22410 contains 15 peaks and one small ridge among the very high points. The target is a small peak containing 35 pixels. There is a cluster of 3 small peaks at the target.

The image contains 7 ridges, two small peaks, and two small mesas among the high points. The target is contained in a small ridge which has two close neighbors.

Target grade: excellent

DBLD225**

IMAGE	DIST	ALT	CENTROID	DIM	PIXELS	MEAN	STAND
BLD22521	8,396	1,170	(52,207)	(26,80)	1,399	128.96	39.94
BLD22522	7,126	1,170	(44,188)	(32,90)	1,808	138.16	42.93
BLD22525	4,648	1,170	(73,219)	(63,160)	6,171	150.79	44.39

Remarks:

BLD22521 has 17 small peaks, 16 very small peaks, 4 ridges, and one crest among the very high points. Component number 11 is at the centroid of the target. There is a cluster of 4 or 5 small peaks and ridges near this component which probably make up the rest of the target. Note that the target contains 1,399 pixels so that it would be unlikely to uncover the target on this first slice.

The image contains 11 ridges and one ridge-peak system among the high points. Components 5 and 12 contain 1247 pixels and seem to make up the target.

Target grade: good

BLD22522 has 32 small and very small peaks, two ridges, and three crests among the very high points. Several of these components including a long ridge appear along the edge of the target.

The image contains 15 ridges and one small peak among the hig points. Six of the ridges are long. The centroid of the targe is contained in a ridge with 565 pixels. Two other ridges are nearby. One of these close ridges contains 873 pixels while another contains 1871 pixels. While no information is availabl concerning the shape of the target, a reasonable guess is that it contains these two smaller ridges.

Target grade: marginal pass

BLD22525 has 51 components among the very high points. Most of these components are small and very small peaks. A large very prominent crest with 735 of its 741 pixels within a half a standard deviation of the maximum is contained in the target.

The image contains 7 ridges, one small peak, and one medium- sized ridge-peak system among the high points. A long very prominent ridge with 3,980 pixels contains most of the target.

Target grade: Very good

DBLD226**

IMAGE	DIST	ALT	CENTROID	DIM	PIXELS	MEAN	STAND
BLD22601	31,034	1,160	(63,196)	(2,29)	58	87.74	33.02
BLD22606	19,951	1,160	(47,147)	(6,45)	178	107.30	25.07
BLD22611	15,738	1,160	(41,149)	(6,44)	132	116.73	22.12
BLD22614	12,534	1,160	(38,192)	(8,55)	219	129.31	24.41
BLD22620	10,076	1,160	(62,158)	(10,89)	485	135.27	24.73
BLD22627	2,962	1,160	(41,188)	(65,311)	12,574	147.49	76.09

Remarks:

BLD22601 contains three small crests and two ridges among the very high points. One of the ridges is very long. A very long ridge with 424 pixels and a ridge with 106 pixels is located near the target.

The image contains 8 ridges among the high points. Five of the ridges are very long and two are long. A very long ridge with 2,027 pixels is located near the target. A very long ridge with 495 pixels is located near the target. A long ridge with 320 pixels is located at the centroid of the target.

The target is located on a long ridge (in high) with 94% of its 320 pixels identified as ridge points. However, there are 7 long and very long ridges with a high percentage of ridge points. Thus, the target is not well located.

Target grade: marginal pass

BLD22606 contains 7 ridges and 4 small and very small peaks among the very high points. One of the ridges is very long. Two components that are neither prominent nor labeled, one with 74 pixels and another with 52 pixels, are located at the target.

The image contains 7 ridges among the high points. Five are very long and one is massive. A very long ridge with 55% of its 547 pixels identified as ridge points is located at the target. A small ridge with 82% of its 114 pixels identified as ridge points is near the target. A very long ridge with 58% of its 472 pixels identified as ridge points is also near the target.

The target grade is "marginal pass" because of the ambiguity incurred by the large number of ridges.

Target grade: marginal pass

BLD22611 contains 8 ridges and two small and very small peaks among the very high points. Four of the ridges are very long and one is long. A very long ridge with 287 pixels is located near the centroid of the target. Another very long ridge with 171 pixels is also located near the centroid of the target.

The image contains 11 ridges and one small peak among the high points. Five of the ridges are very long and 4 are long. Five of the very long ridges are near the target. They have 231, 402, 381, 2,310, and 1,090 pixels, respectively.

Since the target is contained in a very long ridge with 402 pixels and since there are 9 very long and long ridges, it is impossible to pinpoint the target.

Target grade: marginal pass

BLD22614 contains 11 peaks and 6 ridges among the very high points. Two of the ridges are very long. A ridge is near the target, which contains 219 pixels.

The image contains 10 ridges, one small peak, and one small ridge-peak system. Four of the ridges are very long and two are long. A very long ridge wiht 712 pixels is located at the target. Another very long ridge is located near the target. A very long ridge with 3,053 pixels is located near the target.

Target grade: good

BLD22620 contains a very prominent unlabeled component with 67 pixels which is near the centroid of the target among the very high points. It also contains another unlabeled component with 43 pixels that is near the target.

The image contains 6 ridges and one massive ridge-peak system among the high points. Two of the ridges are very long and two are long. A massive ridge-peak system with 6,269 pixels and a ridge with 40% of its 191 pixels labeled as ridge points are located at the target. An unlabeled component (almost a ridge) with 31% of its 161 pixels identified as ridge points is also at the target.

Target grade: good

BLD22627 contains 60 components among the very high points. Most are small and very small peaks, though a number were crests.

The image contains 9 ridges and two small peaks among the high points. Three of the ridges are very long, three are long. A very long ridge located near the centroid of target contains 1,033 pixels. Another very long ridge located near the target contains 784 pixels.

Note that the target contains 12,574 pixels.

Target grade: marginal pass

DBLD242**

IMAGE	DIST	ALT	CENTROID	DIM	PIXELS	MEAN	STAND
BLD24201	24,609	1,060	(49,180)	(4,7)	19	120.62	20.57
BLD24202	25,110	1,060	(53,179)	(4,7)	20		
BLD24203	24,514	1,060	(54,177)	(4,8)	22		
BLD24204	24,515	1,060	(57,178)	(5,11)	35		
BLD24205	24,424	1,060	(60,176)	(4,12)	32		
BLD24206	23,910	1,060	(62,177)	(6,13)	44		
BLD24207	23,610	1,060	(65,177)	(5,12)	39		
BLD24208	24,118	1,160	(71,177)	(4,10)	31		
BLD24209	22,640	1,160	(71,176)	(4,15)	46	122.03	19.42
BLD24210	20,465	1,160	(68,177)	(6,15)	64		
BLD24211	20,700	1,160	(69,177)	(8,17)	84		
BLD24212	19,538	1,160	(70,181)	(8,19)	101		
BLD24213	17,284	1,160	(65,181)	(10,19)	118		
BLD24214	15,761	1,160	(63,172)	(8,20)	98		
BLD24215	13,274	1,160	(51,173)	(6,21)	94	141.51	11.30
BLD24216	13,277	1,160	(62,173)	(7,24)	122		
BLD24217	12,107	1,260	(62,175)	(8,26)	148		
BLD24218	10,677	1,260	(58,176)	(8,28)	168		
BLD24219	9,028	1,260	(47,177)	(11,32)	244		
BLD24220	9,535	1,360	(82,188)	(12,38)	316		
BLD24221	9,875	1,360	(83,183)	(13,37)	335	153.66	13.55

Remarks:

BLD24201 contains 4 very small peaks among the very high points. Unfortunately, the target was not found. The reason for this problem can be explained by the fact that the target is represented by a very small peak with values only one standard deviation above the mean. Moreover, this peak is rounded or dome shaped so that it contains no peak points. Thus, it is nor prominent enough to be detected by our methods.

The image contains one large mesa (3,465 pixels) and one small ridge among the high points. The target was also not found at this level.

Target grade: poor

BLD24209 contains one small peak and one small mesa among the very high points. As in the case of the previous image, the target was not found. The reasons are similar to those mentioned in the previous image. However, this image also had the problem that there were many pixels near the target that were just as high. Thus, the target did not stand out at all.

The image contains three ridges and one mesa among the high points. One of the ridges is long. The target is contained in a large component containing 2099 pixels. While this component was left unlabeled, it narrowly missed being labeled a mesa.

Target grade: poor

BLD24215 contains 7 small and very small peaks, one crest, three ridges, and two crests among the very high points. Unfortunately, the target was again not found in this slice because it did not have enough pixels two standard deviations above the mean.

The image contains one small peak, 4 small ridges, and two mesas among the high points. The target is contained in an unlabeled component with 577 pixels. While this component has an odd horseshoe type shape, it was almost labeled a ridge.

Target grade: poor

BLD24221 contains 15 small peaks, 4 small ridges, two small crests, and two mesas among the high points. The crest with 84 pixels is at the centroid of the target. Two small peaks with 44 and 28 pixels, respectively were not far from the centroid. These three components make up about one third of the target.

The image has three ridges, one medium-sized peak, and one small mesa among the high points. One of the ridges is very long. The target is contained in the peak. While the peak contains 1,894 pixels and thus is not a very good approximation of the target, it almost disconnects into two pieces one of which would contain about 700 pixels. Note that the target contains 335 pixels.

Target grade: marginal pass

DBLD243**

IMAGE	DIST	ALT	CENTROID	DIM	PIXELS	MEAN	STAND
BLD24301	30,414	1,260	(58,121)	(3,9)	22	121.20	21.43
BLD24302	30,558	1,360	(60,94)	(3,8)	19		
BLD24303	28,372	1,360	(58,94)	(4,10)	34		
BLD24304	29,430	1,360	(62,95)	(3,9)	22		
BLD24316	15,308	1,260	(51,139)	(6,14)	61	136.27	11.58
BLD24317	14,938	1,260	(55,146)	(6,16)	73		
BLD24318	14,868	1,260	(62,153)	(8,17)	93		
BLD24320	11,986	1,260	(56,167)	(7,20)	97	140.46	11.77
BLD24321	10,326	1,260	(48,167)	(7,25)	127	142.03	12.70
BLD24322	9,858	1,160	(56,172)	(8,25)	147		
BLD24323	8,642	1,160	(53,176)	(9,28)	181		
BLD24324	7,922	1,160	(61,172)	(10,29)	211		
BLD24326	6,442	1,160	(49,207)	(12,39)	327		
BLD24327	5,514	1,160	(54,168)	(15,41)	431		
BLD24328	4,546	1,160	(62,174)	(18,51)	655		
BLD24329	3,404	1,160	(61,163)	(25,64)	1,053		
BLD24330	2,336	1,160	(75,157)	(37,90)	2,196		
BLD24331	1,142	1,160	(57,166)	(69,130)	5,606	198.72	25.61

Remarks:

BLD24301 contains one very small peak and one very long ridge among the very high points. Unfortunately, the target was not found. The reason for this problem was that values of the pixels in the two very small peaks representing the target had values approximately one standard deviation above the mean. Thus, the peaks were not prominent enough to be detected in the first slice.

The image contains 5 ridges among the high points. One of these is very long. The target was too small to be detected in this second slice.

Target grade: poor

BLD24316 contains 17 small and very small peaks, one small mesa, and two ridges among the very high points. One ridge is very long. The target is represented by two small peaks, which contain 31 and 34 pixels, respectively. Note that the target contains 61 pixels so that the fit is almost exact.

The image contains 11 ridges, one small peak, one massive ridge-peak system, and one small mesa among the high points. Four of the ridges are very long. The target is contained in the small peak with 113 pixels. Two small ridges are nearby.

Target grade: excellent

BLD24320 contains 15 small peaks 4 small ridges, and one small mesa among the very high points. A very prominent small peak with 56 pixels is at the centroid of the target. Another prominent small peak with 59 pixels is close to the first. Note that the target contains 97 pixels, which is only slightly less than the the total in these two peaks.

The image contains 7 ridges, one small peak, and one large ridge-peak system among the high points. The peak has 298 pixels and is very prominent. Two ridges and the ridge-peak system are near.

Target grade: very good

BLD24321 contains 11 small and very small peaks among the very high points. A cluster of two small peaks with a total of 134 pixels are at the centroid of the target. One of these is the highest and steepest peak in the image. Note that the target consists of 127 pixels.

The image has 7 ridges and one small peak among the high points. The target is contained in a small peak which has 246 pixels. A very long flat ridge containing 4267 pixels is near the target. A small ridge is also near the target.

Target grade: excellent

BLD24331 contains 7 peaks and two large crests among the very high points. One large peak (containing 2,948 pixels) is contained in the target. This peak is extremely prominent since its average height is 254.27!

The image has 9 ridges, one small peak, and one large mesa among the high points. Two of the ridges are long. The target is represented by the large mesa, which contains 3,547 pixels. Note that the target contains 5,606 pixels.

Target grade: good

DBLD244**

IMAGE	DIST	ALT	CENTROID	DIM	PIXELS	MEAN	STAND
BLD24403	23,907	1,260	(51,177)	(2,5)	10	112.85	20.16
BLD24410	18,677	1,160	(54,176)	(3,9)	27	117.44	13.94
BLD24415	15,154	1,060	(54,181)	(4,11)	44	123.84	12.07
BLD24420	10,049	1,060	(54,177)	(6,15)	83	138.21	14.82
BLD24431	635	1,060	(52,173)	(51,64)	2,684	170.65	30.40

Remarks:

BLD24403 contains three small and very small peaks among the very high points.

The image contains two mesas and three ridges among the high points. One of the mesas is small, one is medium-sized. One or the ridges is long. The target is found in neither the high points nor the very high points.

Target grade: poor

BLD24410 contains 10 small and very small peaks and one small crest among the very high points. A small peak with 23% of its 52 pixels identified as ridge points is located at the target. The target has 27 pixels.

The image contains 5 ridges among the high points. Two of the ridges are very long and two are long. A small ridge with 49% of its 116 pixels identified as ridge points is located near the target.

Target grade: good

BLD24415 contains 12 small peaks, small ridges, and one small crest among the very high points. A small peak with the highest average height and 92 pixels contains the target. Note that the target has 44 pixels.

The image contains 12 ridges, one small mesa, and two small peaks among the high points. Two of the ridges are very long and two are long.

Target grade: very good

BLD24420 contains 9 small and very small peaks, three ridges, one medium-sized mesas, and one small crest among the very high points. The very prominent small crest with 144 of its 185 pixels three standard deviations above the mean contains the target.

The image contains 7 ridges, three small peaks, and one large ridge-peak system among the very high points. Three of the ridges are very long and one is long.

Target grade very good

BLD24431 contains 14 peaks, one ridge, and one large crest among the very high points. One of the peaks is large and the rest are small and very small. A very large peak with 2,253 pixels is located at the centroid of the target. A very small peak with 26 pixels is located near the target.

The image contains 9 ridges, one large mesa, and one small peak. One of the ridges is long. A large mesa with 2,860 pixels is located at the centroid of the target. A long ridge with 1,534 pixels is located near the target. A ridge with 225 pixels is located near the target.

The very large peak with 2,253 pixels is contained in the target. Since the target contains 2,684 pixels, the target grade is excellent.

Target grade: excellent

DBLD245**

IMAGE	DIST	ALT	CENTROID	DIM	PIXELS	MEAN	STAND
BLD24502	23,192	1,360	(52,169)	(4,11)	34	112.56	18.73
BLD24509	17,895	1,160	(53,174)	(6,18)	69	116.96	13.75
BLD24518	10,899	1,160	(53,174)	(8,26)	127	127.57	13.44
BLD24525	5,745	960	(57,171)	(15,45)	509	139.12	15.41
BLD24530	682	1,060	(42,169)	(57,139)	6,571	166.76	25.10

Remarks:

BLD24502 contains two very small peaks and three ridges among the very high points. Two of the ridges are very long. A very small peak with 85% of its 14 pixels identified as peak points is located at the target; the target has 34 pixels.

The image contains 4 ridges, one large ridge-peak system, and one small mesa among the high points. Two of the ridges are very long and two are long. The target is not found in the high points.

Target grade: very good

BLD24509 contains 5 small and very small peaks, two ridges, and one small crest among the very high points. The target is not foung among the very high points.

The image contains 6 ridges, one medium-sized mesa, and one medium-sized ridge-peak system. Three of the ridges are very long and two are long. Each ridge contains at least 65% ridge points. The target is at the end of a very long ridge with 569 pixels.

Target grade: poor

BLD24518 contains 5 small and very small peaks, two small crests, and two small mesas among the very high points. A prominent small peak with 96 pixels is located at the target. This peak has the highest average height. The target has 509 pixels.

The image has 10 ridges, three small peaks, two small mesas, and one medium-sized ridge-peak system among the high points. Six of the ridges are very long including one incredibly long ridge. One of the peaks is very steep. A component with 136 pixels is located at the target. Two components, one with 1,137 pixels and another with 2,268 pixels, are located near the target.

Target grade: very good

BLD24525 contains 8 peaks, one large crest, and one very long ridge among the very high points. A medium-sized peak with 307 pixels is located at the target. The large crest is very prominent and has 412 pixels.

The image contains 7 ridges, one small mesa, and one small peak. Four of the ridges are long and two are long. A very long ridge with 2,682 pixels contains the target.

Target grade: very good

BLD24530 contains 6 small and very small peaks, two ridges, an one small crest among the very high points. One ridge is long. The long ridge is very prominent and has 27% of its 1,893 pixels identified as ridge points. This ridge represents the target.

The image contains 9 ridges and one small peak among the high points. A very prominent massive high ridge with 26% of its 5,171 pixels represents the target.

Target grade: very good

DBLD246**

IMAGE	DIST	ALT	CENTROID	DIM	PIXELS	MEAN	STAND
BLD24611	13,363	1,160	(53,225)	(7,24)	130	115.35	13.96
BLD24612	12,807	1,160	(56,231)	(8,28)	180	118.86	13.43
BLD24613	11,888	1,160	(56,235)	(8,31)	191		
BLD24614	11,123	1,160	(58,240)	(9,34)	238		
BLD24615	9,968	1,160	(55,247)	(9,36)	241	128.70	16.64
BLD24616	9,209	1,160	(58,242)	(9,40)	283		
BLD24617	8,159	1,160	(56,242)	(10,46)	340		
BLD24618	6,948	1,160	(48,207)	(12,46)	385		
BLD24619	6,185	1,160	(53,181)	(16,54)	564	142.56	21.72
BLD24620	5,269	1,160	(54,185)	(20,68)	880	145.81	23.71
BLD24621	5,420	1,160	(54,185)	(20,66)	850		
BLD24622	4,458	1,160	(53,187)	(25,80)	1,285		
BLD24623	3,507	1,160	(53,191)	(34,100)	2,140		
BLD24624	2,557	1,160	(55,204)	(55,136)	4,514		
BLD24625	1,582	1,160	(55,227)	(107,200)	12,959	145.95	36.95

Remarks:

BLD24611 contains three peaks, three ridges, and two crests among the very high points. One of the ridges is very long. The target is represented by a small isolated peak which contains 109 pixels. Note that the target contains 130 pixels.

The image has 13 ridges and one small mesa among the high points. Eight of these ridges are very long. The target is contained in a very long ridge. Three other ridges (including two very long ones) are near the target.

Target grade: very good

BLD24612 contains 5 peaks and 5 ridges among the very high points. Two of the peaks are medium-sized and one of the ridge is very long. A prominent (but not the most prominent) small peak represents 128 of the 180 pixels in the target.

The image has 12 ridges among the high points. Seven of thes ridges are very long. The target is contained in a ridge with 916 pixels. Three other ridges are nearby. Two of these ridge are very long.

Target grade: good

BLD24615 contains 6 small peaks, 4 ridges, and one medium- sized crest among the very high points. Two of the ridges are very long. A prominent peak with 185 pixels is at the centroid of the target. (Note that the target has 241 pixels) The longest very long ridge is near the target.

The image has 12 ridges and one small peak among the high points. Five of the ridges are very long and three are long. One of the very long ridges is at the centroid of the target. Another very long ridge is close by and parallel to the first.

Target grade: good

BLD24619 contains 8 peaks and three ridges among the very high points. One of the peaks is large and one is medium-sized. On of the ridges is very long. The medium-sized peak with 151 of 322 pixels at least three standard deviations above the mean. This peak is a subset of the target, which has 564 pixels.

The image has 9 ridges, two small peaks, and one small mesa among the high points. Four of the ridges are very long and on is long. The target is an unlabeled component with 633 pixels, which narrowly missed the thresholds for both ridge and peak designation. This component was very prominent since it had 151 pixels at least three standard deviations above the mean.

Target gz.ade: good

BLD24620 contains 10 peaks, two ridges, and one large crest among the very high points. Nine of the peaks are small or very small. The large peak has 430 pixels and is very prominent. Moreover, this peak is at the centroid of the target. Two small peaks with a total of 66 pixels are near this large peak.

The image has 8 ridges, one small ridge-peak system, and one small mesa among the high points. Three of the ridges are very long and one is long. The ridge-peak system contains 800 pixels and is very prominent. This component is almost exactly the target. (Note that the target contains 880 pixels.) A small ridge and a long ridge are near the target.

Target grade: very good

BLD24625 contains 10 peaks, two ridges, and three crests among the very high points. The longest component is a crest containing 2,519 pixels. The target contains this long crest.

The image has 6 small ridges and one massive ridge-peak system among the high points. The ridge-peak system contains 4,962 pixels and is a subset of the target, which has 12,959 pixels.

Target grade: good

DBLD247**

IMAGE	DIST	ALT	CENTROID	DIM	PIXELS	MEAN	STAND
BLD24701	28,832	1,360	(56,192)	(3,10)	29	99.45	21.76
BLD24705	24,921	1,360	(55,187)	(4,11)	35	105.26	18.23
BLD24710	20,841	1,360	(56,179)	(5,13)	58	111.30	15.40
BLD24715	16,603	1,260	(53,174)	(6,16)	72	117.62	13.83
BLD24721	12,146	1,260	(55,178)	(7,22)	132	124.61	18.04
BLD24731	3,409	1,160	(60,171)	(107,139)	12,017	167.11	39.50

Remarks:

BLD24701 contains Two small and very small peaks among the very high points. A small peak with 30 pixels is locatd near the target. An unlabeled component with 64 pixels is located near the target.

The image contains one small ridge and two mesas among the high points. One of the mesas is large and one is medium-sized A large mesa with 3,244 pixels is located near the target. A medium-sized mesa with 1,822 pixels is located near the target.

The target is not found in either the high points or the very high points.

Target grade: poor

BLD24705 contains 6 small and very small peaks and one small ridge among the very high points. A very small peak with 22 pixels is located at the target. A small peak with 33 pixels i located near the target.

The image contains 5 ridges and one large mesa among the high points. One of the ridges is long and one is small and flat. The target is not found among the high points.

Target grade: very good

BLD24710 contains 15 small and very small peaks among the very high points. A peak with 29 pixels is at the target. A peak with 51 pixels is near the target.

The image contains three ridges, one small peak, and two medium-sized mesa among the high points. One of the ridges is very long and one is small and flat. The target is not found in the high points.

Target grade: very good

BLD24715 contains 14 small and very small peaks and two ridges among the very high points. A moderately prominent small peak with 79 pixels is located at the target. A small peak with 31 pixels is near the target.

The image contains one small mesa, three small peaks, and 6 ridges. Two are flat, one is very long, and one is long. A small peak is at the target. The most prominent small peak with 462 pixels is located near the target.

Target grade: excellent

BLD24721 contains one medium sized crest and 12 small and very small peaks among the very high points. A small peak with 118 pixels is at the target. A prominent small peak with 74 pixels and a small peak with 30 pixels are near the target. Note that the target has 132 pixels.

The image contains two peaks, 5 ridges, and one small ridge- peak system among the high points. One of the ridges is very long. A moderately prominent small ridge-peak system contains the target, which has 361 pixels. A ridge with 14% of its 2620 pixels identified as ridge points is located near the target. ridge with 76% of its 131 pixels identified as ridge points is located near the target.

The target is "excellent" because of nesting and size of small peak in very high.

Target grade: excellent

BLD24731 contains 13 small and very small peaks, two ridges, and two large crests among the very high points. An unlabeled component with 35 pixels is located near the centroid of the target.

The image contains 8 ridges and two small peaks among the high points. A very prominent component with 1,692 pixels is locate near the centroid of the target.

Target grade: very good

DBLD254**

IMAGE	DIST	ALT	CENTROID	DIM	PIXELS	MEAN	STAND
BLD25411	14,089	1,360	(49,137)	(8,41)	159	134.07	14.03
BLD25412	13,576	1,260	(54,164)	(10,46)	206		
BLD25414	12,649	1,260	(70,291)	(16,63)	320	135.69	15.14

Remarks:

BLD25411 contains three small mesas, two very small peaks, and one small ridge among the very high points. The target is represented by a small unlabeled isolated component containing 48 pixels. (This component was almost labeled a ridge.)

The image has 11 ridges and one massive ridge-peak system among the high points. Four of the ridges are very long and two are long. The target is a subset of a small ridge, which contains 225 pixels. This ridge is parallel to three other ridges near the target. Note that the target contains 159 pixels.

Target grade: good

BLD25414 has a cluster of 4 small components with a total of 232 pixels. Two of these components are small ridges. There is also a large mesa among the very high points.

The image has 9 ridges and one large mesa among the high points. Four of the ridges are very long and two are long. The target is represented by the long ridge containing 279 pixels. A very long ridge is near the target. Note that the target contains 320 pixels.

Target grade: good

DBLD255**

IMAGE	DIST	ALT	CENTROID	DIM	PIXELS	MEAN	STAND
BLD25501	19,405	1,260	(55,282)	(6,37)	99	124.34	18.47
BLD25502	18,104	1,260	(49,283)	(5,40)	86		
BLD25511	19,018	1,260	(55,307)	(11,85)	359	154.99	17.38

Remarks:

BLD25501 has only one very long ridge among the very high points. The target was not found.

The image has 6 ridges and two mesas among the high points. Two of the ridges are long. One mesa is medium-sized. The target is represented by a small flat ridge with 148 pixels. Another small ridge and a long ridge are near the target. Note that the target contains 99 pixels.

Target grade: good

BLD25511 has three ridges, three peaks, and one crest among the very high points.

The image contains 4 ridges and one ridge-peak system among the high points. Two of the ridges are very long and one is long. The target is almost exactly represented by a very long ridge which contains 376 pixels.

Target grade: excellent

DBLD256**

IMAGE	DIST	ALT	CENTROID	DIM	PIXELS	MEAN	STAND
BLD25611	19,622	1,300	(61,313)	(5,32)	97	138.76	14.50
BLD25621	7,236	1,200	(51,288)	(23,97)	1,389		
BLD25623	4,982	1,200	(58,275)	(59,120)	3,981	140.03	37.08

Remarks:

BLD25611 contains one small ridge and one medium-sized mesa among the very high points. The small ridge contains 33 pixels and is a subset of the target. Note that the target has 97 pixels.

The image has 6 ridges and two medium-sized mesas among the high points. One of the ridges is very long, one is long, and two are flat. The target is contained in a small ridge with 410 pixels. Another component with 336 pixels is near.

Target grade: marginal pass

BLD25623 has 4 small peaks and three ridges among the very high points. One of the ridges is long and one is very long. Two small ridges and a peak are near the centroid of the target.

The image contains 10 ridges and one small mesa among the high points. Three ridges are very long and two are long. A number of these long and very long ridges are in the target area. Together they seem to make up about 30% of the target. Since the target is so large and spread out, it is difficult to determine what it is. The shape and direction of some of the very long ridges in the target area are more indicative of runway images than building images.

Target grade: marginal pass

DBLD257**

IMAGE	DIST	ALT	CENTROID	DIM	PIXELS	MEAN	STAND
BLD25701	25,990	1,260	(49,228)	(3,35)	70	96.87	18.96
BLD25721	(Range data not available.)					147.74	15.43

Remarks:

BLD25701 contains one small mesa among the very high points. Unfortunately, the target was not located. However, upon inspection of the data it was noticed that the pixel values in the image were very bland in the region around the target.

The image contains 6 ridges among the high points. Four of these ridges are very long and one is long.

Target grade: poor

BLD25721 contains two ridges, one mesa, and one small peak among the very high points.

The image has 4 ridges and two small mesas among the high points. One of the ridges is massive and one is very long.

DBLD260**

IMAGE	DIST	ALT	CENTROID	DIM	PIXELS	MEAN	STAND
BLD26019	(Range data not available.)					142.81	12.80

Remarks:

BLD26019 contains 6 peaks, 6 ridges, one small mesa, and one small crest among the very high points.

The image has 7 ridges, one mesa, and one medium-sized ridge-peak system among the high points. One of the ridges is very long and three are long.

Appendix C. The purpose of this appendix is to summarize the results of a study of 50 petroleum tank images. Since the petroleum tank images contain as many as 23 targets in a single image, they are much more complicated than the bridge, building, or runway images. Thus, the target grading system was modified from that used for the buildings and bridges. In particular, if virtually all the targets were found, then we assigned a grade of excellent. If 75% of the targets were found, then we assigned a grade of very good. If 50% of the targets were found, then we assigned a grade of good. If a few of the targets were found, then we assigned a grade of marginal pass. If none, then we assigned a grade of poor. As noted in the summaries given below, the petroleum images are much more complicated than the runway, building, and bridge images studied before. However, in most cases the algorithm was able to generate useful information.

The following table summarizes the results of all the petroleum tank images studied. In the following charts the distance (in feet) from the sensor to the target is given in the column headed by DIST, while the mean and standard deviation of the entire image are listed under MEAN and STAND.

GRADE	NUMBER
Excellent	8
Very good	18
Good	12
Marginal pass	5
Poor	7
Total	50

IMAGE	DIST	MEAN	STAND	NUMBER OF TARGETS	TARGET GRADE
POL24811	15,093	155.35	8.64	6	good
POL24812	14,228	157.57	9.19	6	very good
POL24813	13,314	158.84	9.95	6	very good
POL24815	10,861	168.00	12.34	6	good
POL24817	8,814	175.93	15.07	7	good
POL24820	5,670	147.76	18.01	22	good
POL24912	16,094	146.33	9.45	7	good
POL24914	14,142	146.44	12.00	7	good
POL24917	10,580	163.35	15.57	15	very good
POL24919	8,361	154.69	11.41	19	very good
POL24921	7,141	158.79	13.55	19	very good
POL24924	3,693	190.71	21.57	11	marginal pass
POL24925	2,431	152.80	25.32	8	marginal pass
POL25003	20,450	140.47	10.44	1	excellent
POL25005	20,798	140.13	10.32	1	poor
POL25007	19,046	142.84	9.26	1	very good
POL25009	18,466	141.26	8.85	1	excellent
POL25011	18,663	141.34	9.27	1	excellent

POL25013	14,724	146.09	7.99	1	excellent
POL25015	11,591	145.90	8.57	1	excellent
POL25021	7,167	133.39	9.09	10	very good
POL25023	5,069	141.01	13.52	22	very good
POL26301	30,639	96.70	16.98	1	poor
POL26304	25,133	120.23	14.23	1	marginal pass
POL26306	24,809	119.26	15.82	1	marginal pass
POL26308	19,097	127.67	11.58	1	good
POL26310	19,146	128.86	13.74	1	marginal pass
POL26311	18,976	130.32	13.15	1	very good
POL26313	14,530	137.59	12.70	6	good
POL26321	7,854	141.58	10.39	12	very good
POL26323	5,244	152.78	12.66	12	very good
POL26324	4,199	144.55	13.76	9	good
POL26326	1,931	121.80	6.52	1	poor
POL26421	17,194	95.65	13.71	5	very good
POL26423	13,016	103.89	12.50	18	good
POL26424	12,713	103.71	12.94	20	very good
POL26426	9,749	110.50	13.27	23	very good
POL26427	8,620	114.12	13.24	23	very good
POL26430	4,681	136.10	14.07	13	good
POL26431	5,261	129.57	12.84	17	very good
POL26432	4,330	139.11	14.71	10	very good
POL26434	2,101	153.03	22.75	4	good
POL32401	26,511	118.83	15.06	4	poor
POL32402	27,140	117.50	15.89	2	poor
POL32403	27,654	117.68	14.87	2	poor
POL32404	21,139	125.75	12.34	4	poor
POL32411	13,269	134.04	8.03	5	excellent
POL32414	10,544	133.56	9.81	6	excellent
POL32415	8,980	138.24	10.18	8	excellent
POL32416	7,618	134.46	9.52	15	very good

A summary of the observations of the output of the labeling algorithm is given below.

DPOL248**

IMAGE	DIST	MEAN	STAND	NUMBER OF TARGETS	TARGET GRADE
POL24811	15,093	155.35	8.64	6	good
POL24812	14,228	157.57	9.19	6	very good
POL24813	13,314	158.84	9.95	6	very good
POL24815	10,861	168.00	12.34	6	good
POL24817	8,814	175.93	15.07	7	good
POL24820	5,670	147.76	18.01	22	good

Remarks:

POL24811 contains 9 peaks, two ridges, and one small crest among the very high points. The peaks are small and very small. One of the ridges is long. There is a very small peak with 29 pixels at the centroid of target 3 and a small peak with 119 pixels at the centroid of target 4. These targets contain 160 and 94 pixels, respectively. A long ridge with 40% of its 467 pixels identified as ridge points contains targets 5 and 6. Targets 1 and 2 were not found.

The image contains 6 ridges, one small peak, and one massive ridge among the high points. One of the ridges is massive and one is very long. Five of the six ridges have a very high percentage of ridge points. The massive ridge has 5,795 pixels and contains all targets.

POL24812 contains 10 peaks, 7 ridges, and one small mesa among the very high points. One of the ridges is very long and one is long. A small mesa with 72 pixels and a very small peak with 27 pixels represent target 4. Note that target 4 has 91 pixels. A very small peak with 27 pixels is at the location of target 5.

The image contains 5 ridges among the high points. Two of the ridges are very long, one is long, and one is a massive, flat ridge. The long ridge with 73% of its 272 pixels is almost exactly the length, width, and size of target 3.

POL24813 contains 9 peaks, 5 ridges, and one small mesa among the very high points. One of the peaks is medium sized. One of the ridges is long and one is very long. The small mesa represents target 4. Two very small peaks represent targets 5 and 6.

The image contains 6 ridges and one small mesa among the high points. Three of the ridges are long and one is a massive, flat ridge. One of the long ridges with 65% of its 329 pixels represents target 3. Target 3 has 403 pixels.

Targets 1 and 2 were not found.

POL24815 contains 10 small and very small peaks and three small ridges among the very high points. A very small peak represents target 5. A small peak with 129 pixels represents target 6 and is near target 4.

The image contains 6 ridges and one massive ridge-peak system among the high points. The ridges have a high percentage of ridge points. Three of the ridges are very long. The ridge-peak system contains 7,017 pixels. A ridge with 60% of its 130 pixels represents target 1. Note that target 1 has 104 pixels.

Targets 2 and 3 were not found.

POL24817 contains 14 peaks and two small ridges among the very high points. Ten of the peaks are very small. A small cliff with 35 pixels is at the centroid of target 1. A small peak with 28 pixels almost exactly represents target 6. Two small peaks are at the centroid of target 7.

The image contains 9 ridges and one large ridge-peak system among the high points. Two of the ridges are very long, one is long, and one is flat.

Targets 2-5 were not located.

POL24820 contains 12 small and very small peaks and two small ridges among the very high points. Small and very small peaks represent 6 of the 22 targets. A small ridge and two unlabeled components are at or near 6 other targets.

The image contains 9 ridges and two small mesas among the high points. Two of the ridges are long and one is flat. Four ridges (3 with at least 73% ridge points) are near a number of the targets. A prominent ridge with 21% ridge points contains 3 or 4 targets. While many of the 22 targets are represented, this image is very complicated. The output from the labeling algorithm reflects this complexity.

DPOL249**

IMAGE	DIST	NUMBER OF MEAN	STAND	TARGET TARGETS	GRADE
POL24912	16,094	146.33	9.45	7	good
POL24914	14,142	146.44	12.00	7	good
POL24917	10,580	163.35	15.57	15	very good
POL24919	8,361	154.69	11.41	19	very good
POL24921	7,141	158.79	13.55	19	very good
POL24924	3,693	190.71	21.57	11	poor
POL24925	2,431	152.80	25.32	8	marginal pass

Remarks:

POL24912 contains one small crest, three small and very small peaks, and one very long ridge among the very high points. The ridge contains 2,169 pixels. Three of the targets are represented by small and very small peaks.

The image contains seven ridges and two small mesas among the high points. Two of the ridges are very long and one is long. One of the very long ridges dominates the image. The long ridge with 53% of its 128 pixels represents a target.

Targets 1-3 were not found.

POL24914 contains three small and very small peaks and two ridges among the very high points. One of the ridges is very long and has very few ridge points and a large number of flat points. The very long ridge has 3,390 pixels and dominates the image.

The image contains 7 ridges among the high points. One ridge with 4,709 pixels has many top-of-cliff and flat points. Another ridge has 18 percent of its points being peak points. The rest of the ridges have a very high percentage of ridge points.

POL24917 contains four small and very small peaks, two mesas, and one ridge among the very high points. One of the mesas is large. Three of the small and very small peaks represent targets.

The image contains three ridges and one massive ridge-peak system among the high points. Two of the ridges are long. Seven of the 15 targets are contained in a long ridge with 57% of its 661 pixels identified as ridge points. Two other targets are contained in the other long ridge.

POL24919 contains 7 peaks, two small crests, and three ridges among the very high points. One of the peaks is medium-sized, while the rest are small and very small. One of the ridges is very long. Another has all top of cliff points. Target 6 is represented by a very small peak. Target 7 is represented by a small ridge. Targets 8-10 are contained in a medium-sized peak. Targets 11-12 are represented by a small crest.

The image contains 4 ridges among the high points. One of the ridges is massive with 22% of its 6,076 pixels identified as ridge points. This massive ridge contains targets 5-17. A small ridge with 89% of its 109 pixels represents targets 18 and 19. A ridge with 24% of its 609 pixels contains targets 1-4.

POL24921 contains 5 peaks and one very long ridge among the very high points. One of the peaks is medium-sized. Ten of the 19 targets are represented by components in very high. A small peak with 82 pixels represents target 5, a medium-sized peak with 324 pixels represents targets 9-11, a small peak with 123 pixels represent targets 12-14, and a very long ridge with 227 pixels represents targets 15-17.

The image contains three ridges, one small peak, and one medium-sized mesa among the high points. One of the ridges is long. A large ridge with 25% of its 3,709 pixels identified as ridge points contains targets 5-17.

Targets 1-4 and 18-19 are not found.

POL24924 contains 12 small and very small peaks, one medium- sized peak, one medium-sized crest, and one ridge among the very high points.

The image contains 8 small peaks, one small ridge-peak system, one small mesa, and 8 ridges among the high pints.

The targets did not correspond to the topographic features in either level.

POL24925 contains 10 peaks and two ridges among the very high points. Two of the peaks are medium-sized. One medium-sized peak is very prominent, but not near any target.

The image contains two small peaks, one small mesa, two small ridge-peak systems, and three ridges among the high points. One ridge with 27% of its 1,162 pixels identified as ridge-points represents target 4 almost exactly. Some of the other targets were represented by small peaks, but the results were somewhat disappointing.

DPOI250**

IMAGE	DIST	MEAN	STAND	NUMBER OF TARGETS	TARGET GRADE
POL25003	20,450	140.47	10.44	1	excellent
POI25005	20,798	140.13	10.32	1	poor
POI25007	19,046	142.84	9.26	1	very good
POL25009	18,466	141.26	8.85	1	excellent
POI25011	18,663	141.34	9.27	1	excellent
POL25013	14,724	146.09	7.99	1	excellent
POI25015	11,591	145.90	8.57	1	excellent
POI25021	7,167	133.39	9.09	10	very good
POL25023	5,069	141.01	13.52	22	very good

Remarks:

POI25003 contains two peaks and two ridges among the very high points. One of the ridges is very long.

The image contains two ridges and three mesas among the high points. One of the ridges is long, one is flat. One of the mesas is large and contains 3,315 pixels. A small ridge among the high points with 69 percent of its 116 pixels identified as ridge points represents the target almost exactly.

POI25005 contains two ridges and one peak among the high points. A long ridge has 75 percent of its 337 pixels identified as ridge points. Another long ridge has 81 percent of its 597 pixels identified as ridge points.

The image contains one small ridge and one long ridge among the high points. Ninety-four percent of the 185 pixels on the small ridge are identified as ridge points.

The target is not found in either the very high points or the high points.

POL25007 contains two very small peaks, two ridges, and one small mesa among the very high points. One of the ridges is long.

The image contains 4 ridges, one large ridge-peak system, and three small mesas among the high points. One of the ridges is long, one is very long.

The target is represented in the high points by a small ridge with 103 pixels. This component has 35 percent ridge points and 17 percent peak points. Another small ridge with 92% of its 115 pixels is also near the target. The long ridge among the high points is much more prominent with 279 of 751 pixels three standard deviations above the mean.

POL25009 contains 10 small and very small peaks, one medium- sized crest, and one small ridge among the very high points. There is a very small peak with 21 pixels at the target. There is a prominent medium-sized crest a distance from the target.

The image contains 4 ridges, one medium-sized mesa, and one large ridge-peak system among the high points. One of the ridges is long. The ridges all have a high percentage of ridge points.

There is a small ridge among the high points with 29% of its 151 pixels at the centroid of the target. Since the target has 163 pixels, the target grade is excellent. A small ridge with 80% of its 110 pixels is also near the target.

POL25011 contains 9 small and very small peaks, one small ridge, and one small crest among the very high points. The small crest has 278 of its 470 pixels three standard deviations above the mean. In the very high points two small peaks with a total of 100 pixels are at the target, which contains 144 pixels. A prominent small crest is far from the target.

The image contains three ridges, one small mesa, and one large ridge-peak system among the high points. The two ridges away from the target have 50% and 65% ridge points respectively. A long ridge with 18% of its 296 pixels identified as ridge points is located at the target.

POL25013 contains 14 peaks and one small crest among the very high points. One of the peaks is large, the rest are small and very small. A small crest containing 153 pixels is located at the centroid of the target. A long ridge with 289 pixels contains the target which has 217 pixels.

The image contains 8 ridges, one small peak, and one large ridge-peak system. A long ridge with 289 pixels is located at the target. This ridge has 47 ridge points and 50 peak points. A long ridge with 55% of its 134 pixels identified as ridge points is near the target. A large ridge-peak system with 14% of its 2,933 pixels identified as ridge points is near the target.

POL25015 contains 8 small and very small peaks, two ridges, one medium-sized crest, and one small crest among the very high points. A very prominent, medium-sized crest with 14% of its 327 pixels identified as ridge points is located at the target which contains 392 pixels. Note that this crest also is prominent since 109 of its pixels are three standard deviations above the mean.

The image contains 9 ridges and one medium-sized ridge peak system among the high points. A prominent ridge with 9% of its 405 pixels identified as ridge points is near the target.

POI25021 contains 8 small and very small peaks and 4 small ridges among the very high points. A small peak with 35 pixels is located at target 3. A large peak with 810 pixels is located at target 4. A small peak with 188 pixels and a small peak with 31 pixels are located at target 8. A small peak with 188 pixels is near targets 3 and 5. A small peak with 53 pixels is located at target 7. An unlabeled component with 42 pixels is located at target 9. A very small peak with 29 pixels is located at target 10. Targets 1,2 and 5 are not found among the very high points.

The image contains 6 ridges among the high points. Three are very long and one is long. A small ridge with 104 pixels is near targets 1 and 2. A very prominent, very long ridge with 18% of its 3,394 pixels identified as ridge points is located at targets 3-4 and 6-10. Targets 1, 2, and 5 are not found among the high points.

POI25023 contains 8 peaks, two large crests, and one small ridge among the very high points. One of the peaks is medium- sized, the rest are small. A prominent, medium-sized peak with the highest average height and 256 pixels is located at target 4. An unlabeled component with 14 pixels is located near targets 5- 6. A prominent, large crest with 478 pixels is at targets 8, 10, and 13. The prominent, large crest with 545 pixels is located at targets 15-17. The small peak with 31 pixels is located at target 11. The ridge with 63% of its 47 pixels identified as ridge points is near target 19. Targets 2-3, 7, 12, 18, and 20- 22 are not found among the very high points.

The image contains 9 ridges and one small peak among the high points. One of the ridges is very long, one is long. A small ridge with 86% of its 135 pixels identified as ridge points is located at target 1 which has 232 pixels. A long ridge with 3,674 pixels contains targets 12-21. A small peak with 151 of its 474 pixels three standard deviations above the mean contains targets 4 and 5. A very long ridge with 216 pixels contains target 22. A small, flat ridge with 318 pixels contains target 18. A small ridge with 84% of its 1,138 pixels identified as ridge points is located at target 3. A small ridge with 57% of its 110 pixels identified as ridge points is located at target 2.

DPOL263** IMAGE	DIST	MEAN	STAND	NUMBER OF TARGETS	TARGET GRADE
POL26301	30,639	96.70	16.98	1	poor
POL26304	25,133	120.23	14.23	1	marginal pass
POL26306	24,809	119.26	15.82	1	marginal pass
POL26308	19,097	127.67	11.58	1	good
POL26310	19,146	128.86	13.74	1	marginal pass
POL26311	18,976	130.32	13.15	1	very good
POL26313	14,530	137.59	12.70	6	good
POL26321	7,854	141.58	10.39	12	very good
POL26323	5,244	152.78	12.66	12	very good
POL26324	4,199	144.55	13.76	9	good
POL26326	1,931	121.80	6.52	1	poor

Remarks:

POL26301 contains one ridge with 68% of its 170 pixels identified as ridge points among the very high points. No components are at the target at this level.

The image contains one large mesa and two ridges among the high points. One ridge has 85% of its 119 pixels identified as ridge points. The other has 24% of its 2,360 pixels identified as ridge points. The target is near the mesa which has 3,092 pixels.

POL26304 contains one ridge among the high points. This ridge has 56% of its 67 pixels identified as ridge points.

The image contains three mesas and two ridges among the high points. One of the mesas is small, one is medium-sized, and one is large. The target is near the large mesa which has 4,064 pixels. The target has 847 pixels.

POL26306 contians one ridge and one small mesa among the very high points. The ridge has 60% of its 255 pixels identified as ridge points. The mesa has 82% of its 88 pixels identified as flat points.

The image contains three ridges and one small mesa, and one large ridge-peak system with 4,183 pixels among the high points. One of the ridges is flat, two are very long. The ridges have 27%, 72%, and 36% ridge points. The target is next to the ridge- peak system. The target has 820 pixels.

POL26308 contains two small peaks, three ridges, and one small mesa among the very high points. Two of the ridges are very long. All of the components are near the target. A very long ridge has 86% of its 186 pixels identified as ridge points. Another very long ridge has 30% of its 810 pixels identified as ridge points. There are over 1,000 pixels total in all the components.

The image contains three ridges, two small mesas, and one large ridge peak system among the high points. The ridge-peak system has 20% of its 822 pixels identified as ridge points. The target is contained in the ridge-peak system. The target contains 1,097 pixels.

POI25021 contains 8 small and very small peaks and 1 small ridges among the very high points. A small peak with 35 pixels is located at target 3. A large peak with 810 pixels is located at target 4. A small peak with 188 pixels and a small peak with 31 pixels are located at target 8. A small peak with 188 pixels is near targets 3 and 5. A small peak with 53 pixels is located at target 7. An unlabeled component with 42 pixels is located at target 9. A very small peak with 29 pixels is located at target 10. Targets 1,2 and 5 are not found among the very high points.

The image contains 6 ridges among the high points. Three are very long and one is long. A small ridge with 104 pixels is near targets 1 and 2. A very prominent, very long ridge with 18% of its 3,394 pixels identified as ridge points is located at targets 3-4 and 6-10. Targets 1, 2, and 5 are not found among the high points.

POI25023 contains 8 peaks, two large crests, and one small ridge among the very high points. One of the peaks is medium- sized, the rest are small. A prominent, medium-sized peak with the highest average height and 256 pixels is located at target 4. An unlabeled component with 14 pixels is located near targets 5- 6. A prominent, large crest with 478 pixels is at targets 8, 10, and 13. The prominent, large crest with 545 pixels is located at targets 15-17. The small peak with 31 pixels is located at target 11. The ridge with 63% of its 47 pixels identified as ridge points is near target 19. Targets 2-3, 7, 12, 18, and 20- 22 are not found among the very high points.

The image contains 9 ridges and one small peak among the high points. One of the ridges is very long, one is long. A small ridge with 86% of its 135 pixels identified as ridge points is located at target 1 which has 232 pixels. A long ridge with 3,674 pixels contains targets 12-21. A small peak with 151 of its 474 pixels three standard deviations above the mean contains targets 4 and 5. A very long ridge with 216 pixels contains target 22. A small, flat ridge with 318 pixels contains target 18. A small ridge with 84% of its 1,138 pixels identified as ridge points is located at target 3. A small ridge with 57% of its 110 pixels identified as ridge points is located at target 2.

DPOL263** IMAGE	DIST	MEAN	STAND	NUMBER OF TARGETS	TARGET GRADE
POL26301	30,639	96.70	16.98	1	poor
POL26304	25,133	120.23	14.23	1	marginal pass
POL26306	24,809	119.26	15.82	1	marginal pass
POL26308	19,097	127.67	11.58	1	good
POL26310	19,146	128.86	13.74	1	marginal pass
POL26311	18,976	130.32	13.15	1	very good
POL26313	14,530	137.59	12.70	6	good
POL26321	7,854	141.58	10.39	12	very good
POL26323	5,244	152.78	12.66	12	very good
POL26324	4,199	144.55	13.76	9	good
POL26326	1,931	121.80	6.52	1	poor

Remarks:

POL26301 contains one ridge with 68% of its 170 pixels identified as ridge points among the very high points. No components are at the target at this level.

The image contains one large mesa and two ridges among the high points. One ridge has 85% of its 119 pixels identified as ridge points. The other has 24% of its 2,360 pixels identified as ridge points. The target is near the mesa which has 3,092 pixels.

POL26304 contains one ridge among the high points. This ridge has 56% of its 67 pixels identified as ridge points.

The image contains three mesas and two ridges among the high points. One of the mesas is small, one is medium sized, and one is large. The target is near the large mesa which has 4,064 pixels. The target has 847 pixels.

POL26306 contians one ridge and one small mesa among the very high points. The ridge has 60% of its 255 pixels identified as ridge points. The mesa has 82% of its 88 pixels identified as flat points.

The image contains three ridges and one small mesa, and one large ridge-peak system with 4,183 pixels among the high points. One of the ridges is flat, two are very long. The ridges have 27%, 72%, and 36% ridge points. The target is next to the ridge- peak system. The target has 820 pixels.

POL26308 contains two small peaks, three ridges, and one small mesa among the very high points. Two of the ridges are very long. All of the components are near the target. A very long ridge has 86% of its 186 pixels identified as ridge points. Another very long ridge has 30% of its 810 pixels identified as ridge points. There are over 1,000 pixels total in all the components.

The image contains three ridges, two small mesas, and one large ridge peak system among the high points. The ridge-peak system has 20% of its 822 pixels identified as ridge points. The target is contained in the ridge-peak system. The target contains 1,097 pixels.

P01 26310 contains two small peaks, one ridge, and one large mesa among the very high points. There are no components at the centroid of the target.

The image contains 5 ridges, one massive ridge peak system, and one medium-sized mesa. Three of the ridges are long. A ridge with 17% of its 196 pixels identified as ridge points and a massive ridge-peak system with 13% of its 5,050 pixels identified as ridge points are located at the target. The target has 1,486 pixels.

P01 26311 contains two small peaks and one very long ridge among the very high points. The ridge has 21% of its pixels identified as ridge points and 75% of its pixels identified as flat points. A small peak is located near the centroid of the target.

The image contains three small ridges, one massive ridge-peak system, and one small mesa among the high points. All of the ridges have over 80% ridge points. A massive ridge-peak system with 63% of its 5,508 pixels identified as flat points is located at the target. The target contains 1,557 pixels. The target grade is very good because inside the ridge-peak system there is a small peak at the centroid of the target.

P01 26313 contains two peaks, one small ridge, and one large mesa among the very high points. A small peak with 79 pixels is located at target 3. A very small peak with 42 pixels is located at target 4. Targets 1-2 and targets 5-6 are not found.

The image contains three ridges and two mesas among the high points. One of the ridges is long and one is long and flat. One of the mesas is small and one is large. The long, flat ridge with 1,661 pixels contains targets 5-6. Target 1-4 are not found among the high points.

P01 26321 contains 6 peaks, one small crest, and two small ridges among the very high points. One of the peaks is large and the rest are small and very small. A prominent, small peak with 131 pixels is located at target 5 and at target 6. A small peak with 24 pixels is located at target 1. A very prominent, large peak with 522 pixels is located at target 7, target 8, and target 9. The number of pixels in these targets is 741. A small peak with 111 pixels is located at targets 11 and 12. The total number of pixels in these two targets is 299. Targets 2-4 and target 10 are not found among the very high points.

The image contains two ridges, three mesas, and one medium- sized ridge-peak system among the high points. A ridge with 40% of its 446 pixels identified as ridge points is located at targets 1-4. A prominent, medium-sized ridge-peak system with 15% of its 1,580 pixels identified as ridge points is located at targets 5-12.

POL26323 contains 6 peaks, one small ridge, and one large mesa. Two of the peaks are medium-sized. A small peak with 30 pixels is located at target 3 which has 489 pixels. A medium sized peak with 358 pixels is located at targets 5-8 which together have 926 pixels. A prominent, large mesa with 1,160 pixels is located at targets 10-12. Targets not found among the very high points are 1,2,4, and 9.

The image contains 8 ridges, one large ridge-peak system, and one small mesa among the high points. Two of the ridges are very long and one is long. A very long ridge with 76% of its 223 pixels identified as ridge points is located at target 1 which contains 580 pixels. A small ridge with 80% of its 132 pixels identified as ridge points is located at target 2 which has 608 pixels. A ridge with 39% of its 1,168 pixels identified as ridge points is located at target 3 and target 4 which together contain 534 pixels. A prominent, large ridge-peak system with 2,650 pixels is located at targets 5-8 and 10-12. Target 9 is not found.

POL26324 contains 5 small and very small peaks, one large mesa, and one long ridge among the very high points. A very prominent long ridge with 670 pixels is located at target 2 which contains 105 pixels. A prominent large mesa with 759 pixels is located at targets 6 and 7. These targets have 684 and 589 pixels, respectively. Targets 1, 3-5, and 8 are not found among the very high points.

The image contains 8 ridges and two mesas. One of the ridges is long and one is flat. One of the mesas is small, one is medium-sized. A very prominent long ridge with 23% of its 1,785 pixels identified as ridge points is located at target 2. A medium sized mesa with 2,046 pixels engulfs targets 6 and 7. It is near target 9 which contains 203 pixels. Targets 1, 3, and 5 are not found among the high points.

POL26326 contains 4 mesas and one small ridge among the very high points. One of the mesas is medium-sized. The target is not found, all components are small.

The image contains two large ridge-peak systems, one long ridge, and one small ridge among the high points. Since the target contains 7,739 pixels and the total number of pixels in these components is less than 1,000, a target grade of poor is assigned.

DPOL264**

IMAGE	DIST	MEAN	STAND	NUMBER OF TARGETS	TARGET GRADE
POL26421	17,194	95.65	13.71	5	very good
POL26423	13,016	103.89	12.50	18	good
POL26424	12,713	103.71	12.94	20	very good
POL26426	9,749	110.50	13.27	23	very good
POL26427	8,620	114.12	13.24	23	very good
POL26430	4,681	136.10	14.07	13	good
POL26431	5,261	129.57	12.84	17	very good
POL26432	4,330	139.11	14.71	10	very good
POL26434	2,101	153.03	22.75	4	good

Remarks:

POL26421 contains 5 peaks among the very high points. Three are small, one is very small, and one is medium-sized. A small peak with 84 pixels is located at targets 2 and 3. A small peak with 31 pixels is located at target 4. Targets 1 and 5 are not found.

The image contains three ridges, one large mesa, and one large ridge-peak system among the high points. A long ridge with 84% of its 125 pixels identified as ridge points is located at target 1. A large ridge-peak system with 4,739 pixels is located at targets 2, 3, 4, and 5. A very long ridge with 93% ridge points is near the large ridge-peak system.

POL26423 contains 7 peaks among the very high points. One of the peaks is large, two are small, and 4 are very small. One small peak is prominent and has 150 pixels while another small peak has 50 pixels.

The image contains 4 ridges, one massive ridge-peak system, and one medium-sized mesa among the high points. Two of the ridges are long; one is small and flat. A ridge with 81% of its 117 pixels identified as ridge points is located near targets 4 and 5. A massive ridge-peak system with 14% of its 5,024 pixels identified as ridge points engulfs targets 6-18.

POL26424 contains 10 small and very small peaks among the very high points. A moderately prominent peak with 109 pixels is located at targets 5 and 6. A moderately prominent peak with 65 pixels is located at targets 7-12. A moderately prominent peak with 77 pixels is located at targets 13-15. A peak with 35 pixels is located at targets 16-18. Targets 1-4, 19, and 20 are not found among the very high points.

The image contains one large mesa, 4 ridges, and one large ridge-peak system among the high points. Two of the ridges are very long. A ridge-peak system with craters has 13% of its 4,350 pixels identified as ridge points. This ridge-peak system contains target 5.

Note that target 5 can be pinpointed almost exactly as first a subset of the ridge-peak system and second near a moderately prominent peak contained in the ridge-peak system. We refer to this technique as "nested targeting".

POL26426 contains 6 small and very small peaks and one very long ridge among the very high points. Three of the peaks are moderately prominent. A peak with 157 pixels is located at targets 6-9. A peak with 98 pixels is located at targets 10-14. A peak with 107 pixels is located at targets 15-18. A peak with 62 pixels is located at targets 19-21.

The image contains 7 ridges and two mesas among the high points. Three of the ridges are very long; one is long. One of the mesas is small and one is medium-sized. A long ridge with 16% of its 4,273 pixels identified as ridge points and 42% identified as mesa points is located at targets 2-23.

POL26427 contains three peaks and two ridges among the very high points. One of the peaks is medium-sized; two are small. One of the ridges is very long. A prominent, medium-sized peak with 231 pixels is located at targets 6-9. A small peak with 148 pixels is located at targets 10-13. A prominent ridge with 21% of its 388 pixels identified as ridge points is located at targets 14-20 and is near targets 21 and 23. Targets 1-5 and 22 are not found among the very high points.

The image contains 9 ridges and one small mesa among the high points. One of the ridges is long, two are very long, one is very long and flat, and one is flat. A very long flat ridge with 4,584 pixels contains targets 3-23. Target 1 is not found.

POL26430 contains 6 ridges and three peaks among the very high points. One of the peaks is medium-sized. A very high ridge has 70% of its 30 pixels identified as ridge points. Another ridge has all of its 39 pixels identified as top-of-cliff points. An unlabeled component with 49 pixels is located at target 1. A medium-sized peak with 320 pixels is located at target 2. An unlabeled component with 21% of its 151 pixels identified as ridge points is located at target 6. A very high ridge with 53% of its 133 pixels identified as ridge points is located at target 11.

The image contains 9 ridges, one small peak, and one small mesa among the high points.

Note that 5 unlabeled components were at targets. All but two targets were located almost exactly.

POL26431 contains 7 peaks and five ridges among the very high points. A prominent medium-sized peak with 19% of its 286 pixels identified as ridge points is located at target 4. A small peak with 28% of its 78 pixels identified as ridge points is located at target 5. A small peak with 15% of its 180 pixels identified as ridge points is located at target 8. A small peak with 17% of its 143 pixels identified as ridge points is located at target 11. A prominent ridge with 14% of its 172 pixels identified as ridge points is located at targets 14 and 15. A long ridge is located at target 16.

The image contains 4 ridges and two small mesas among the high points. One of the ridges is massive; one is small and flat.

POL26432 contains 5 ridges and 3 peaks among the very high points. A prominent ridge with 380 pixels is located at target 1. An unlabeled component with 153 pixels is located at target 2. A small peak with 33 pixels is located at target 5. A ridge with 109 pixels is located at target 8.

The image contains 6 ridges and one small mesa among the high points. A prominent ridge with with 4,581 pixels is located at targets 1, 2, 5, and 8; it is near targets 7 and 9.

POL26434 contains one small peak, 7 ridges, and one small mesa among the very high points. Three of the ridges are very long and two are long. Three very long ridges and one ridge are located at target 1. One small ridge and two long ridges are located at target 3. Targets 2 and 4 are not found among the very high points.

The image contains 10 ridges among the high points. One is small and flat; three are long. A ridge with 1,189 pixels and an unlabeled component with 453 pixels are at target 1. A long ridge with 37% ridge points, a component with 102 pixels, and a long ridge with 170 of its 172 pixels identified as top-of-cliff points are located at target 3. Targets 2 and 4 are not clearly defined among the high points. Target 1 has 4,036 pixels, target 2 has 1,512, target 3 has 2,288, and target 4 has 1,292 pixels.

DPOL324**

IMAGE	DIST	MEAN	STAND	NUMBER OF TARGETS	TARGET GRADE
POL32401	26,511	118.83	15.06	4	poor
POL32402	27,140	117.50	15.89	2	poor
POL32403	27,654	117.68	14.87	2	poor
POL32404	21,139	125.75	12.34	4	poor
POL32411	13,269	134.04	8.03	5	excellent
POL32414	10,544	133.56	9.81	6	excellent
POL32415	8,980	138.24	10.18	8	excellent
POL32416	7,618	134.46	9.52	5	very good

Remarks:

POL32401 contains two small mesas among the very high points. Neither of the mesas are near the target.

The image contains one massive ridge-peak system and one small mesa among the high points. The ridge-peak system has 76% of its 5,081 pixels identified as mesa points. The target is not found.

POL32402 contains one small mesa, one large mesa, and one small ridge among the very high points. None of the components are near either target.

The image contains one large ridge-peak system, two small mesas, and one long ridge among the high points. The ridge-peak system has 1,477 pixels. The target is not found.

POL32403 contains one small mesa among the very high points. All of the mesa's 103 pixels are flat points. An unlabeled component with 566 pixels is near the boundry of the target.

The image contains one large mesa, one small flat ridge, and one small mesa among the high points. Neither of the two targets is found in either the high or very high points.

POL32404 contains one unlabeled component with 1,644 pixels among the very high points.

The image contains three mesas and one small ridge among the high points. Two of the mesas are small and one is large. Target 4 is near the large mesa with 4,258 pixels.

POL32411 contains 5 peaks and two small ridges among the very high points. Three of the peaks are small and two are very small. A small peak with 33 pixels is located at target 1. A small peak with 46 pixels is located at targets 2 and 3. A small peak with 92 pixels is located at targets 4 and 5.

The image contains 11 ridges, one ridge-peak system, one small mesa, and one medium-sized mesa among the high points. The medium-sized ridge-peak system has 44% of its 2,354 pixels identified as mesa points and 17% identified as ridge points. It contains all 5 targets.

POL32414 contains 6 small and very small peaks as well as one prominent ridge among the very high points. A small peak with 59 pixels is located at target 1. A small peak with 82 pixels is located at targets 2 and 3. A small peak with 101 pixels is near targets 4-6.

The image contains 7 ridges, 4 mesas, and one small peak. Four of the ridges are very long, one is long, and one is flat. A small peak with 130 pixels contains targets 2 and 3. A small mesa with 19% of its 948 pixels identified as ridge points and 40% as flat points contains targets 4-5. A very long ridge with 89% of its 197 pixels identified as ridge points is parallel to the small mesa with 948 pixels. A very long ridge with 95% of its 270 pixels identified as ridge points is also parallel to the small mesa with 948 pixels. Target 1 has 144 pixels, target 2 has 24, target 3 has 126, target 4 has 98, target 5 has 28, and target 6 has 150.

POL32415 contains three small peaks and 5 very small peaks among the very high points. The three small peaks are identified as targets. A prominent small peak with 68 pixels is located at targets 1 and 2. A prominent, small peak with 108 pixels is located at targets 3 and 4. A prominent, small peak with 135 pixels is located at targets 5-6 and is near target 8. An unlabeled component has 27% of its 499 pixels identified as ridge points; this component is the most prominent.

The image contains two prominent small peaks and one prominent ridge among the high points. The small peak with 103 pixels is located at targets 1 and 2 which together have 132 pixels. The small peak with 159 pixels is located at targets 3 and 4 which together contain 198 pixels. The ridge with 837 pixels is located at targets 5-8 which together have 331 pixels.

All targets are located.

POI32416 contains 9 peaks among the very high points. One is medium-sized, three are small, and 5 are very small. A small peak with 20% of its 97 pixels identified as ridge points is located at targets 1 and 2 while it is close to 3 and not far from 4. A small peak with 21% of its 156 pixels identified as ridge points is located at targets 5-8 and 15. A medium-sized peak with 14% of its 216 pixels identified as ridge points is located at targets 9-11. Targets 12-14 are not found.

The image contains two small peaks, 6 ridges, and two mesas among the high points. One of the ridges is long and one is very long. One of the mesas is medium-sized; one is small. A small peak with 15% of its 132 pixels identified as ridge points is located at targets 1 and 2; it is close to target 3 and not far from target 4. A small peak with 14% of its 221 pixels identified as ridge points is located at targets 5-8 and 15 which together have 454 pixels. An unlabeled component with 20% of its 1,006 pixels identified as ridge points is located at targets 9- 14 which have a total of 300 pixels. This component missed being labeled a ridge by .01. The ridge with 113 pixels is parallel to the unlabeled component.

Appendix D. The purpose of this appendix is to indicate how the Topographic Labeling Algorithm is proving useful in runway analysis.

The most important change implemented while studying these images was an improved segmentation process. Previously, the regions to be labeled were chosen to be the connected components of those pixels either one or two standard deviations above the mean of the entire image. However, several difficulties emerged with this method when applied to images taken 4 to 6 miles from the target. First, the images were so "bland" that pixels representing the landing strip had values below one standard deviation above the mean. Thus, in the segmentation process the pixels representing the target were never considered. The first step towards correcting this problem was to include "ridge" and "top of cliff" pixels when computing the connected components. While this technique helped, the runways still tended to appear in fragments instead of one connected whole. The addition of one dilation and one erosion before segmenting improved results considerably.

The second problem to be confronted with these distant images was that they were so bland that the standard deviations tended to be extremely low-sometimes below 6. This situation meant that the "drop parameter" alpha was disproportionately large. Consequently, the local topographic content of most points was determined to be "flat". Thus, the local topographic content of the image was lost. The solution to this problem was to set alpha equal to 7 if the standard deviation is at least 14 and one half the standard deviation, if not.

The Hough Transform has been added to the algorithm to determine how many straight-line directions are present in a long ridge. The number of directions will be important in deciding whether or not a paticular ridge matches with a particular runway.

While we have over 90 runway images in our data set, only 11 different targets are represented. (We have as many as 30 images of the same runway taken at distances varying between 3,000 and 35,000 feet.) Where possible, at least three images of each runway have been discussed below. In the cases where more than one image is available, the nearest and farthest images will always be considered.

The following list gives a summary of the study of the runway images investigated so far. Note that there is only one target and one object in each image. Note further that all images with the same first three numbers are of the same target.

RWY22002

Range Data:

Distance to target	31,960
Altitude	3,160
Centroid	(62,173)
Height, width	(32,9)
Pixels in target	256

Image Data:

Size	115x355
Mean	128.06
Standard Deviation	18.38
Min Value, Max Value	46, 255

Remarks:

The labeling algorithm identified one medium-sized crest among the very high points in the image.

Six ridges were identified among the high points. Three of these six ridges were long. One very long ridge was left unlabeled because it was close to the boundary so that it failed to satisfy a technical condition for the ratio tests to apply. The runway was formed from one of the very long ridges.

RWY22011

Range Data:

Distance to target	19,676
Altitude	3,160
Centroid	(72,174)
Height, width	(97,15)
Pixels in target	1259

Image Data:

Size	115x355
Mean	149.49
Standard Deviation	21.30
Min Value, Max Value	63, 255

Remarks:

The algorithm labeled two crests among the very high points. One of these crests was large and one was small. The large crest was unusually prominant because almost half of its points were at least three standard deviations above the mean. Moreover, its steepness factor was 1119 which is unusually large.

The algorithm labeled 10 ridges among the high points. One of these was labeled a massive ridge-peak system, while three were very long and one was long. Most of the runway was made up of th massive ridge-peak system and one of the very long ridges.

RWY22021

Range Data:

Distance to target	8,905
Altitude	3,160
Centroid	(61,165)
Height, width	(119,25)
Pixels in target	2,559

Image Data:

Size	115x355
Mean	138.20
Standard Deviation	31.42
Min Value, Max Value	70, 238

Remarks:

The algorithm labeled two ridges and two small peaks among the very high points. One of the ridges was very long and is part of the runway.

The algorithm labeled 7 ridges among the high points. Two of these ridges were very long. A massive component containing 7085 points was left unlabeled. It would have been labeled a massive ridge if its ridge confidence factor, CFRIDGE, had been .01 higher. This component had an unusually amorphous shape so that while it was more like a ridge than anything else, it was not as clearly a ridge as a number of the other components. The Hough Transform gave a very clear indication that one of the very long ridges had a preferred direction. The runway was clearly formed from the two very long ridges and two other shorter ridges.

RWY22101

Range Data:

Distance to target	17,969
Altitude	3,160
Centroid	(62,199)
Height, width	(18,322)
Pixels in target	985

Image Data:

Size	115x355
Mean	160.74
Standard Deviation	14.62
Min Value, Max Value	115, 255

Remarks:

The algorithm labeled 4 of the components of the very high points as peaks and 4 as ridges. One of the ridges was very long. The Hough Transform gave a very strong indication of a preferred direction in this very long ridge. This last ridge was part of the runway.

The algorithm labeled 8 ridges, one peak, and one mesa among the components of the high points. One ridge was a massive ridge-peak system, one was a small ridge-peak system, and two were very long. The runway was clearly delineated as the massive ridge-peak system.

Rwy22102

Range Data:

Distance to target	18,209
Altitude	3,160
Centroid	(65,175)
Height, width	(22,339)
Pixels in target	1,201

Image Data:

Size	115x355
Mean	161.58
Standard Deviation	15.08
Min Value, Max Value	115, 255

Remarks:

The algorithm labeled two peaks and 4 ridges among the very high points. One of the ridges was very long. This very long ridge was part of the runway.

The algorithm labeled 11 ridges and two small peaks in the high points of the image. The one component labeled a massive ridge-peak system clearly delineated the runway.

RWY22111

Range Data:

Distance to target	18,131
Altitude	3,160
Centroid	(64,180)
Height, width	(14,360)
Pixels in target	1,260

Image Data:

Size	115x355
Mean	164.82
Standard Deviation	21.11
Min Value, Max Value	57, 255

Remarks:

The algorithm labeled 7 peaks and 8 ridges among the very high points. One peak was small but very prominant. None of the ridges were very long, but the runway was made up of 4 or 5 of the smaller ridges.

The algorithm identified 12 ridges among the high points. Two of these ridges were long, while two more were very long. The runway was clearly delineated by a massive ridge-peak system which contains 5356 pixels together with one of the very long ridges. The Hough Transform indicated a preferred direction in the very long ridge.

RWY23013

Range Data:

Distance to target	23,559
Altitude	2,870
Centroid	(22,154)
Height, width	(44,200)
Pixels in target	625

Image Data:

Size	115x355
Mean	126.77
Standard Deviation	9.12
Min Value, Max Value	97, 187

Remarks:

The algorithm located two small ridges and one small mesa among the very high points.

The algorithm identified 4 ridges, one medium-sized mesa, and a massive ridge-peak system among the high points. One of the 4 ridges was the centroid of the runway.

RWY23023

Range Data:

Distance to target	11,368
Altitude	2,970
Centroid	(51,195)
Height, width	(102,239)
Pixels in target	1,766

Image Data:

Size	115x355
Mean	129.35
Standard Deviation	11.82
Min Value, Max Value	87, 176

Remarks:

The algorithm identified two small peaks, one crest, and 5 small ridges among the very high points. The 5 ridges were fragments of the runway.

The algorithm identified two large ridge-peak systems and a small mesa among the high points. The runway was clearly represented by the smaller of the two ridge-peak systems.

RWY23211

Range Data:

Distance to target	21,996
Altitude	3,220
Centroid	(58,256)
Height, width	(5,164)
Pixels in target	490

Image Data:

Size	115x355
Mean	123.61
Standard Deviation	5.81
Min Value, Max Value	102, 255

Remarks:

The algorithm identified three ridges among the very high points. One was fairly large.

The algorithm identified 4 ridges and two mesas among the high points. Three of the ridges were very long. The runway was partly formed from the larger mesa and two of the very long ridges.

RWY23222

Range Data:

Distance to target	12,544
Altitude	3,220
Centroid	(53,150)
Height, width	(27,299)
Pixels in target	1,020

Image Data:

Size	115x355
Mean	135.92
Standard Deviation	9.55
Min Value, Max Value	107, 181

Remarks:

The algorithm labeled 4 ridges and one small peak among the very high points.

The algorithm labeled 11 ridges among the high points. Three of these ridges were very long and one was a large ridge-peak system. The runway was clearly delineated by two of the very long ridges.

RWY23229

Range Data:

Distance to target	5,763
Altitude	3,220
Centroid	(29,180)
Height, width	(58,360)
Pixels in target	6,918

Image Data:

Size	115x355
Mean	145.38
Standard Deviation	15.94
Min Value, Max Value	102, 199

Remarks:

The algorithm labeled one small ridge and one small mesa among the very high points.

The algorithm identified only one component among the high points. This component was a massive ridge-peak system containing 9879 pixels. This ridge-peak system clearly formed the runway.

RWY23311

Range Data:

Distance to target	18,029
Altitude	2,970
Centroid	(64,177)
Height, width	(43,12)
Pixels in target	407

Image Data:

Size	115x355
Mean	134.48
Standard Deviation	5.98
Min Value, Max Value	106, 172

Remarks:

The algorithm identified 4 small ridges, one small peak, and one small mesa among the very high points.

The algorithm identified one massive ridge-peak system, 6 ridges, and two small mesas among the high points. While a small ridge was displayed at the centroid, the runway was not clearly visible.

RWY23317

Range Data:

Distance to target	10,414
Altitude	2,970
Centroid	(71,170)
Height, width	(99,19)
Pixels in target	1,284

Image Data:

Size	115x355
Mean	139.16
Standard Deviation	8.57
Min Value, Max Value	112, 171

Remarks:

The algorithm identified three ridges and a small mesa among the very high points. One of the ridges was long.

The algorithm identified one large ridge-peak system, three ridges, and 5 mesas among the high points. One of the ridges was long and narrow. Even though this long ridge was far from the centroid (71,170) of the target, it seemed to be a part of the runway. A somewhat larger but less elongated ridge appeared at the centroid.

RWY23322

Range Data:

Distance to target	5,142
Altitude	2,970
Centroid	(62,170)
Height, width	(116,20)
Pixels in target	2,146

Image Data:

Size	115x355
Mean	143.14
Standard Deviation	11.44
Min Value, Max Value	111, 187

Remarks:

The algorithm identified 6 ridges and two medium-sized mesas among the very high points. One ridge was long and one was very long.

The algorithm identified one massive ridge-peak system and one long ridge among the high points. The ridge-peak system clearly contained the runway. The runway seemed to have three parallel landing strips, which cut across the middle of the image. The Hough Transform indicated these different directions.

RWY23703

Range Data:

Distance to target	32,568
Altitude	2,460
Centroid	(58,166)
Height, width	(19,100)
Pixels in target	316

Image Data:

Size	115x355
Mean	114.71
Standard Deviation	10.00
Min Value, Max Value	81, 159

Remarks:

The algorithm indicated one small mesa among the very high points. The other two components, both unlabeled, were near the boundary of the image, where our methods frequently fail.

The algorithm identified 6 ridges and two mesas among the high points. A very long narrow ridge was colinear with another long ridge at the centroid of the target. More than likely these components formed part of the runway.

RWY23715

Range Data:

Distance to target	21,023
Altitude	2,460
Centroid	(75,289)
Height, width	(90,50)
Pixels in target	1,395

Image Data:

Mean	136.49
Standard Deviation	10.14
Min Value, Max Value	98, 183

Remarks:

The algorithm identified two small peaks, one small ridge, and one large mesa among the components of the very high points. The mesa is at the centroid of the target.

The algorithm identified one large ridge-peak system and three ridges among the high points. The ridge-peak system was located at the centroid of the target. The Hough Transform indicated several of the straight-line directions in the landing strip.

RWY23724

Range Data:

Distance to target	9,151
Altitude	2,360
Centroid	(60,305)
Height, width	(120,78)
Pixels in target	2,880

Image Data:

Size	115x355
Mean	165.10
Standard Deviation	15.41
Min Value, Max Value	114, 228

Remarks:

The algorithm identified two small peaks, a small ridge, and three mesas among the very high points.

The algorithm identified a large and a medium sized ridge-peak system, two ridges, and two small mesas among the high points. The two ridges, one small and one large (with 4472 pixels), were close together and clearly delineated the target. The Hough Transform very clearly indicated two preferred directions in the target.

RWY23901

Range Data:

Distance to target	29,737
Altitude	3,060
Centroid	(57,201)
Height, width	(32,277)
Pixels in target	582

Image Data:

Size	115x355
Mean	130.48
Standard Deviation	9.56
Min Value, Max Value	94, 198

Remarks:

The algorithm identified 5 small peaks, two small ridges, and one medium sized mesa among the very high points.

The algorithm identified two ridge-peak systems, 8 ridges, and two mesas among the high points. Two of the ridges were very long. The runway was pieced together from the two ridge-peak systems and several of the ridges.

RWY23915

Range Data:

Distance to target	16,875
Altitude	3,060
Centroid	(51,180)
Height, width	(21,358)
Pixels in target	1,432

Image Data:

Size	115x355
Mean	144.42
Standard Deviation	15.60
Min Value, Max Value	62, 255

Remarks:

The algorithm identified 3 small peaks and 4 ridges among the very high points. None of the peaks were particularly prominant. Three of the ridges were long or very long and fit together to makeup the runway.

The algorithm identified one massive ridge-peak system, 4 ridges, and one mesa among the high points. The ridge-peak system clearly delineated the target. The Hough Transform indicated several preferred directions.

RWY23930

Range Data:

Distance to target	3,357
Altitude	3,060
Centroid	(52,180)
Height, width	(82,358)
Pixels in target	10,203

Image Data:

Size	115x355
Mean	190.75
Standard Deviation	30.13
Min Value, Max Value	113, 255

Remarks:

The algorithm identified two medium sized peaks and two ridges among the very high points. The peaks were very prominant and appeared much higher than any other pixels in the image. The ridges were fragments of the runway.

The algorithm identified two ridge-peak systems, 4 ridges, and a small mesa among the high points. These components made up about 65% of the target. (Note that there were 10,203 pixels in the target.)

RWY24024

Range Data:

Distance to target	16,244
Altitude	3,060
Centroid	(60,198)
Height, width	(104,323)
Pixels in target	1,909

Image Data:

Size	115x355
Mean	172.36
Standard Deviation	17.30
Min Value, Max Value	123, 244

Remarks:

The algorithm identified two small peaks, one medium-sized crest, and 13 ridges among the very high points. Five of the ridges were very long. This image was unusual because the 13 ridges and crest almost fit together to form the runway.

The algorithm identified one massive ridge-peak system, one small ridge, one small peak, and one small mesa among the high points. The runway was clearly displayed in the ridge-peak system. The Hough Transform indicated several preferred directions.

RWY24030

Range Data:

Distance to target	10,897
Altitude	3,060
Centroid	(61,174)
Height, width	(119,346)
Pixels in target	3,489

Image Data:

Size	115x355
Mean	163.28
Standard Deviation	22.01
Min Value, Max Value	125, 236

Remarks:

The algorithm identified three small peaks and 5 small ridges among the very high points.

The algorithm identified one massive ridge-peak system and one small ridge among the high points. The ridge-peak system contained 6,870 pixels and clearly represented the runway.

RWY24035

Range Data:

Distance to target	7,238
Altitude	3,060
Centroid	(61,181)
Height, width	(119,277)
Pixels in target	3,993

Image Data:

Size	115x355
Mean	176.56
Standard Deviation	29.00
Min Value, Max Value	120, 255

Remarks:

The algorithm identified one small peak and 7 ridges among the very high points. All these components were fragments of the runway which were to appear in the next slice.

The algorithm identified one massive (8580 pixels) and one large ridge-peak system among the high points. The one massive component by itself clearly delineated the runway. The Hough Transform indicated 4 different lines appearing in the boundary of this component.

RWY25217

Range Data:

Distance to target	
Altitude	(not available)
Centroid	
Height, width	
Pixels in target	

Image Data:

Size	115x355
Mean	155.37
Standard Deviation	13.68
Min Value, Max Value	129, 213

Remarks:

The algorithm identified one small peak and two ridges among the very high points. While the peak was small, it was unusually distinct. One ridge was very long. This long ridge clearly outlined the runway. The Hough Transform clearly indicated the two preferred directions of the runway.

The algorithm identified three ridges, one small peak, and one small mesa among the high points. The peak was the same as the one mentioned above. One of the ridges was very long and flat and contained the long ridge mentioned above. The Hough Transform indicated several preferred directions.

RWY26713

Range Data:

Distance to target	
Altitude	(not available)
Centroid	
Height, width	
Pixels in target	

Image Data:

Size	115x355
Mean	139.90
Standard Deviation	10.54
Min Value, Max Value	116, 193

Remarks:

The algorithm identified two small peaks and one very long ridge among the very high points. The ridge clearly delineated the runway. The Hough Transform indicated the two preferred directions of the runway.

The algorithm identified one large ridge-peak system, two ridges, and two small mesas among the high points. The runway was contained in the ridge-peak system. The shape of the runway was not as well represented by this ridge-peak system as it was by the long ridge mentioned above.

RWY63903

Range Data:

Distance to target	
Altitude	(available)
Centroid	
Height, width	
Pixels in target	

Image Data:

Size	115x355
Mean	127.56
Standard Deviation	28.42
Min Value, Max Value	14, 243

Remarks:

The algorithm identified three peaks and 5 ridges among the very high points. One peak was medium sized and was very prominant since almost one third of its pixels were at least three standard deviations above the mean. Two of the ridges were very long.

The algorithm identified one massive ridge-peak system and one long ridge among the high points. The runway was clearly contained in the ridge-peak system. The Hough Transform indicated two of the three preferred directions.

Bridge - DBRG20123

Image Data:

Distance of sensor to target: .....8,760 Feet
Dimensions of image: .....120 x 360
Dimensions of smallest rectangle
containing target: .....6 x 23
Number of pixels in target: 67
Mean of image: 107.03
Standard deviation of image: 41.02

Output of Second Segmentation:

The labeled regions include one large mesa, one small ridge, one long ridge, and one large ridge-peak system. The very long ridge has 26% of its pixels identified as ridge points.

Target Grade: .....Good

Bridge - DBRG20616

Image Data:

Distance of sensor to target: .....18,330 Feet
Dimensions of image: .....120 x 360
Dimensions of smallest rectangle
containing target: .....2 x 63
Number of pixels in target: 126
Mean of image: 107.45
Standard deviation of image: 28.08

Output of Second Segmentation:

The image contains four ridges. One ridge is very long, one is massive and flat, and two are small. The massive ridge represents the land. The two smaller ridges are distinctive because 27% and 39% of their pixels, respectively, are identified as ridge points. The road to the bridge is represented by one of the small ridges.

Target Grade: .....Good

Bridge - DBRG23429

Image Data:

Distance of sensor to target: .....4,564 Feet
Dimensions of image: .....120 x 360
Dimensions of smallest rectangle
containing target: .....57 X 8
Number of pixels in target: 342
Mean of image: 141.42
Standard deviation of image: 19.35

Output of Second Segmentation:

The image contains three ridges and four mesas. Two of the mesas are medium sized and one ridge is long. The ridge contains 730 pixels and contains the target. The mesas represent the land. The long ridge represents the island near the bridge.

Target Grade: .....Very Good

Bridge - DBRG27210

Image Data:

Distance of sensor to target: .....5,915 Feet
Dimensions of image: .....120 x 360
Dimensions of smallest rectangle
containing target: .....44 x 360
Number of pixels in target: 1,800
Mean of image: 133.38
Standard deviation of image: 4.34

Output of Second Segmentation:

The image contains two small mesas and one very long ridge. The ridge is very distinctive with 59% of its 1,446 pixels identified as ridge points.

Target Grade: .....Very Good

Bridge - DBRG27521

Image Data:

Distance of sensor to target: .....15,855 Feet
Dimensions of image: .....120 x 360
Dimensions of smallest rectangle
containing target: .....51 x 15
Number of pixels in target: 211
Mean of image: 142.58
Standard deviation of image: 4.45

Output of Second Segmentation:

The image contains four ridges and one large mesa among the very high points. Two of the ridges are flat. The mesa represents a portion of the land. The target is represented by two small ridges which have a total of 280 pixels. These ridges have a total of 63% and 67% ridge points respectively.

Target Grade: .....Very Good

Building - DBLD22301

Image Data:

Distance of sensor to target: .....22,697 Feet
Dimensions of image: .....120 x 360
Dimensions of smallest rectangle
containing target: .....6 x 23
Number of pixels in target: 123
Mean of image: 122.14
Standard deviation of image: 26.53

Output of First Segmentation:

The image contains two small peaks and four very small peaks. One of these peaks together with another unlabeled component form the target. (The confidence factor of this unlabeled component lacks .01 of the threshold for declaring it to be a peak.) The total number of pixels in these two components is one hundred eleven (111).

Target Grade: .....Excellent

Building - DBLD22310

Image Data:

Distance of sensor to target: .....18,990 Feet
Dimensions of image: .....120 x 360
Dimensions of smallest rectangle
containing target: .....9 x 33
Number of pixels in target: 233
Mean of image: 139.94
Standard deviation of image: 24.11

Output of First Segmentation:

The image contains fourteen peaks. One of these peaks is medium-sized, while the remainder are small or very small. The component representing the target has 390 pixels. This component is almost labeled a ridge.

Target Grade: .....Good

Building - DBLD22403

Image Data:

Distance of sensor to target: .....31,033 Feet
Dimensions of image: .....120 x 360
Dimensions of smallest rectangle
containing target: .....3 x 7
Number of pixels in target: 17
Mean of image: 163.97
Standard deviation of image: 30.92

Output of First Segmentation:

The image contains six very small peaks. The target is almost exactly represented by a peak containing fourteen pixels. This peak has one close neighbor. The most prominent peaks do not represent the target.

Target Grade: .....Excellent

Building - DBLD22410

Image Data:

Distance of sensor to target: .....21,236 Feet
Dimensions of image: .....120 x 360
Dimensions of smallest rectangle
containing target: .....4 x 11
Number of pixels in target: 38
Mean of image: 126.63
Standard deviation of image: 22.20

Output of First Segmentation:

The image contains 15 peaks and one small ridge. The target is almost exactly represented by a peak containing 35 pixels. There is a cluster of three small peaks at the target.

Target Grade: .....Excellent

Building - DBLD24316

Image Data:

Distance of sensor to target: .....15,308 Feet
Dimensions of image: .....120 x 360
Dimensions of smallest rectangle
containing target: .....6 x 14
Number of pixels in target: 61
Mean of image: 136.27
Standard deviation of image: 11.58

Output of First Segmentation:

The image contains seventeen small and very small peaks, one small mesa, and two ridges among the very high points. One ridge is very long. The target represented by two small peaks which contain thirty-one (31) and thirty four (34) pixels respectively. While there are many peaks, this pair is the most prominent.

Target Grade: .....Excellent

Building - DBLD24321

Image Data:

Distance of sensor to target: .....10,326 Feet
Dimensions of image: .....120 x 360
Dimensions of smallest rectangle
containing target: .....7 x 25
Number of pixels in target: 127
Mean of image: 142.03
Standard deviation of image: 12.70

Output of First Segmentation:

The image contains eleven small and very small peaks. A cluster of two small peaks with a total of 134 pixels are at the centroid of the target. One of these peaks is the highest in the image.

Target Grade: .....Excellent

Building - DBLD24715

Image Data:

Distance of sensor to target: .....16,603 feet
Dimensions of image: .....120 x 360
Dimensions of smallest rectangle
containing target: .....6 x 16
Number of pixels in target: 72
Mean of image: 117.62
Standard deviation of image: 13.83

Output of First Segmentation:

The image contains fourteen small and very small peaks as well as two ridges. A moderately prominent small peak with seventy nine (79) pixels is located at the target. Two small peaks are near the target.

Target Grade: .....Excellent

Petroleum Tank - DPOL26311

Image Data:

Distance of sensor to target: .....18,976 Feet
Dimensions of image: .....120 x 360
Number of targets: 1
Mean of image: 130.32
Standard deviation of image: 13.15

Output of First Segmentation:

The image contains two small peaks and one very long ridge among the very high points. The ridge has 21% of its pixels identified as ridge points and 75% of its pixels identified as flat points. A small peak is identified at the centroid of the target.

Output of Second Segmentation:

A massive ridge-peak system with 63% of its 5,508 pixels identified as flat points contains the target. The target contains 1,557 pixels.

Target Grade: .....Very Good

Petroleum Tank - DPOL26421

Image Data:

Distance of sensor to target: .....17,194 Feet
Dimensions of image: .....120 x 360
Number of targets: 5
Mean of image: 95.65
Standard deviation of image: 13.71

Output of First Segmentation:

The image contains five peaks. Three of the peaks are small, one is very small, and one is medium-sized. A small peak is located at targets two and three. A second small peak is located at target four.

Output of Second Segmentation:

The image contains three ridges, one large mesa, and one large ridge-peak system among the high points. A long ridge with 84% of its 125 pixels identified as ridge points is located at target one. A large ridge-peak system contains the others.

Target Grade: .....Very Good

Runway - DRWY22101

Image Data:

Distance of sensor to target: .....17,969 Feet
Dimensions of image: .....120 x 360
Dimensi ns of smallest rectangle
containing target: .....18 x 322
Number of pixels in target: 985
Mean of image: 160.74
Standard deviation of image: 14.64

Output of Second Segmentation:

The algorithm labeled eight ridges, one peak, and one mesa. One ridge was massive and two were very long. The runway was clearly delinated as the massive ridge.

Target Grade: .....Very Good

Runway - DRWY23915

Image Data:

Distance of sensor to target: .....16,875 Feet
Dimensions of image: .....120 x 360
Dimensions of smallest rectangle
containing target: .....21 x 358
Number of pixels in target: 1,432
Mean of image: 144.42
Standard deviation of image: 15.60

Output of Second Segmentation:

The algorithm identified one massive ridge-peak system, four ridges, and one mesa. The ridge-peak system clearly delineated the runway. The Hough transform indicated several preferred directions.

Target Grade: .....Very Good

1986 USAF-USE MINI-GRANT

Sponsored by the

AIR FORCE OFFICE OF SCIENTIFIC RESEARCH

Conducted by the

UNIVERSAL ENERGY SYSTEMS, INC.

FINAL REPORT

RADIATION FROM FLYING THROUGH NUCLEAR DEBRIS CLOUDS

Prepared by:	Dr. Arthur Woodrum
Academic Rank:	Professor and Head
Department:	Department of Physics
University:	Georgia Southern College
Research Location:	Department of Physics Georgia Southern College Statesboro, Georgia

Date:	March 24, 1987
Contract No:	F49620-85-C-0013/SB5851-0360
Subcontract No:	S-760-OMG-035

RADIATION FROM FLYING THROUGH NUCLEAR DEBRIS CLOUDS

by

Arthur Woodrum
Professor of Physics
Georgia Southern College

ABSTRACT

A simple mathematical model for calculating the estimated radiation dose of an aircrew in an aircraft flying through a debris cloud from a single nuclear detonation was developed. This work has been reported by presentation, governmental report and has been presented for journal publication. Work was begun on creating a computer model for the growth of clouds from nuclear multiburst.

I. INTRODUCTION

My research background involves much work on the study of wave motions in the upper atmosphere. Experimental data on winds, pressure, density and temperature variations in the atmosphere around 100 kilometers were obtained from artificial clouds put into the atmosphere with rockets. These data were analyzed to discover the systematic wave motions in each of the variables.

Other research work involving the creation of a worldwide computer model of the atmosphere depicting representative values of winds, pressure, density, temperature, and their variations for any latitude, longitude, day of year, time of day and any height from surface up to about 200 kilometers was performed in the mid-1970's. This work was done for NASA in connection with the Space Shuttle program. It resulted in a computer model named GRAMS which is still being used.

The most recent work was done through the Summer Faculty Research Program with Brooks AFB during 1985. The Air Force was interested in modeling the clouds of nuclear bursts in the atmosphere for the purpose of studying radiation doses of objects penetrating the clouds. Continuation of this work led to the present study.

II. OBJECTIVE OF THE RESEARCH EFFORT

The objectives of the present research were:

1. Continue reporting the results of work on the radiation doses of aircrews from flying through nuclear debris clouds from single nuclear bursts.
2. Develop a computer model for nuclear debris clouds arising from the simultaneous bursting of many densely spaced nuclear detonations.

III. PROCEDURE

Objective one required a close working association with Lt. Peter Vanden Bosch of Brooks AFB to complete the work which was begun in the Summer of 1985. After work was completed, the results were to be reported both orally and by journal publication.

The procedure for fulfilling objective two involved transferring a computer program known as "CASSIE" simulating the growth of a single nuclear cloud from the Brooks AFB computer to the computer at Georgia Southern College. Then by using this model as a basis, one would develop a new model for calculating the cloud growth of a multiburst and check its applicability.

IV. RESULTS

The work for objective one was completed with very good results. The research was successfully accomplished by Fall of 1985. A presentation was made to the Weapons Research Lab, Kirkland AFB, Albuquerque, New Mexico, during Fall of 1985. The results were well received. In addition, a Technical Report displaying the research and results was developed and was published by Brooks AFB in April, 1986. This technical report is included as Appendix I. Furthermore, this research work is being presented to the Journal of Geophysical Research for publication. This preparation is included as Appendix II.

The work for objective two was partially completed before time expired. The computer program for calculating nuclear cloud growth was very long and complicated. Although the source tape from the Air Force was from a CDC 830 computer and the computer at Georgia Southern College was also a CDC 830, there were still serious incompatibility problems. These problems were overcome but there was little time to check any multiburst theories.

V. RECOMMENDATIONS

The work for objective one was completed and a useable real time method for rapidly calculating the radiation doses of aircrews from flying through nuclear debris clouds was developed. However, the development of a computer model of the nuclear debris cloud originating from multibursts needs much more work. It is a very complicated problem but can probably be accomplished by thermodynamic considerations as opposed to hydrodynamic techniques.

VI. ACKNOWLEDGEMENTS

I would like to extend a special thanks to Lt. Peter Vanden Bosch for his friendship and technical assistance. It has been an honor to work with him on the research.

The research was made possible by funds from the Air Force Systems Command, Air Force Office of Scientific Research under contract F 4962-85-C-0013. The management of the program was by Universal Energy System, Inc. under the leadership of Mr. Rodney Darrah and Ms. Sue Espey. Thanks go to them for the opportunity to do this work.

VII. REFERENCE

1. Showers, R. L., and C. Crisco. User's manual for CASSANDRA: Cloud snapshots of dust raised aloft, Report ARBL-TR-2116, 169 pp, Ballistic Research Laboratory, Aberdeen Proving Ground,, Md., 1979.

2. Vanden Bosch, P. M., and Arthur Woodrum, Radiation doses from flying through nuclear debris clouds, USAFSAM-TR-85-86, 18 pp, USAF School of Aerospace Medicine, Brooks AB, Texas, April, 1986.

Appendix I

RADIATION DOSES FROM FLYING THROUGH NUCLEAR DEBRIS CLOUDS

INTRODUCTION

Estimates of radiation doses to aircrews flying through nuclear debris clouds are of critical interest to USAF mission planners. The probability of such an event occurring is high following a nuclear attack. Since real data are lacking, prediction must depend upon mathematical modeling of the cloud environment and flythrough.

Taboada et al. (1) recently developed a computer model which predicts doses from flythroughs. The model, which will be called CASSIE in this report, is based upon the dust environment model CASSANDRA (2), which in turn uses the benchmark DELFIC (3) code as the basis of its cloud rise and fallout dynamics. The CASSIE model is user friendly; it supplies default values and descriptions of parameters when requested and has all the input flexibilities of the DELFIC and CASSANDRA codes.

The CASSIE model uses the CASSANDRA code to calculate the dust density at various points along the trajectory of an aircraft flying through a nuclear debris cloud. A gamma-radiation dose rate is calculated from the dust densities and integrated over time to obtain the total radiation dose that an aircrew would experience.

The total radiation dose is assumed to originate from 2 sources: (1) the immersion radiation dose, which is a result of the aircraft being immersed in a radioactive cloud, and (2) the onboard radiation dose, which results from radiation exposure of the aircrews to dust particles trapped inside the aircraft cabin and filtering system. The immersion rate exists only while the aircraft is inside the radioactive debris cloud, whereas the onboard radiation is a continuing hazard.

The purpose of this report is to use the CASSIE model to calculate the radiation doses to aircrewmembers for various conditions of flythrough. Due to the long program running time, the model would have little use in an operational setting. The intent of this report is to supply results of the model in a form which will allow planners to estimate in advance realistic and worst case doses for flythrough scenarios.

FLYTHROUGH MODEL

CASSIE provides for changing flight and aircraft parameters easily. A scenario is needed which will allow an analysis of radiation dose dependence on [illegible] of flythrough, time of flight, and detonation yield. For the purposes of this report, the following flight scenario was used.

An aircraft flies from a point 40 km (24 mi) from ground zero on one side [illegible] to 40 km on the opposite side, passing directly over ground [illegible] flight duration is 500 s, which corresponds to a velocity of 311 [illegible] is maintained throughout the flight and the aircraft passes

over ground zero at t seconds after detonation. This path is expressed in the form (-40 km, O, H, t-250) - (40 km, O, H, t+250).

The aircraft parameters are chosen to resemble those of a KC-135 aircraft. The model approximates the cabin as a cylinder, chosen to be 32.05 m (107 ft) in length and 2.74 m (9 ft) in radius. The filtration system is arbitrarily chosen to allow 50% of the dust particles taken onboard to enter the cabin, with the remainder staying on the filter. Once aboard, the dust particles do not exit. The distance from the crewmembers to the filter is arbitrarily chosen to be 250 cm (100 in.). The air-mass flow into the aircraft is 67.5 kg/min (150 lb/min). The dose received by aircrewmembers will be dependent on the choice of these parameters, which are discussed in Appendix A. If cloud penetration is unavoidable, Figure 3 shows that it is most advantageous to fly through as high in the cloud as possible. This will allow the aircraft to be exposed to the lowest possible dose within the cloud. A flythrough beneath the cloud may result in a lower dose, but there is the danger of the aircraft encountering large particles.

CLOUD DIMENSIONS

The size of the nuclear debris cloud depends on a number of factors. The parameters used in the analysis include:

(1) A surface burst, with 50% of the available energy expended in fission.

(2) Ground zero at 670 m (2211 ft) above mean sea level.

(3) No wind.

(4) Soil type is siliceous.

The debris cloud is modeled throughout its creation, expansion, and cooling. At some point the model considers the turbulence, upward rise, and expansion to be negligible and stabilizes the cloud dimensions at current values. These calculations are reported in Table 1 and the cloud dimensions are shown in Figures 1 and 2. Stabilization is relative; in actuality, the cloud will continue to grow slowly as a result of buoyancy, turbulence, and wind patterns.

TABLE 1. CLOUD DIMENSION DATA AT STABILIZATION

Yield (MT)	Stab. Time(s)	Cloud Base(m)	Cloud Top	Cloud Radius
0.003	312	3700	5200	1100
0.01	423	5300	7400	1800
0.03	661	6700	10500	2900
0.1	611	8400	12400	5400
0.3	720	9500	14900	8500
1.	783	11300	18000	13800
3.	785	13500	22000	20300
10.	787	17700	29000	31000
30.	852	21000	37200	52400

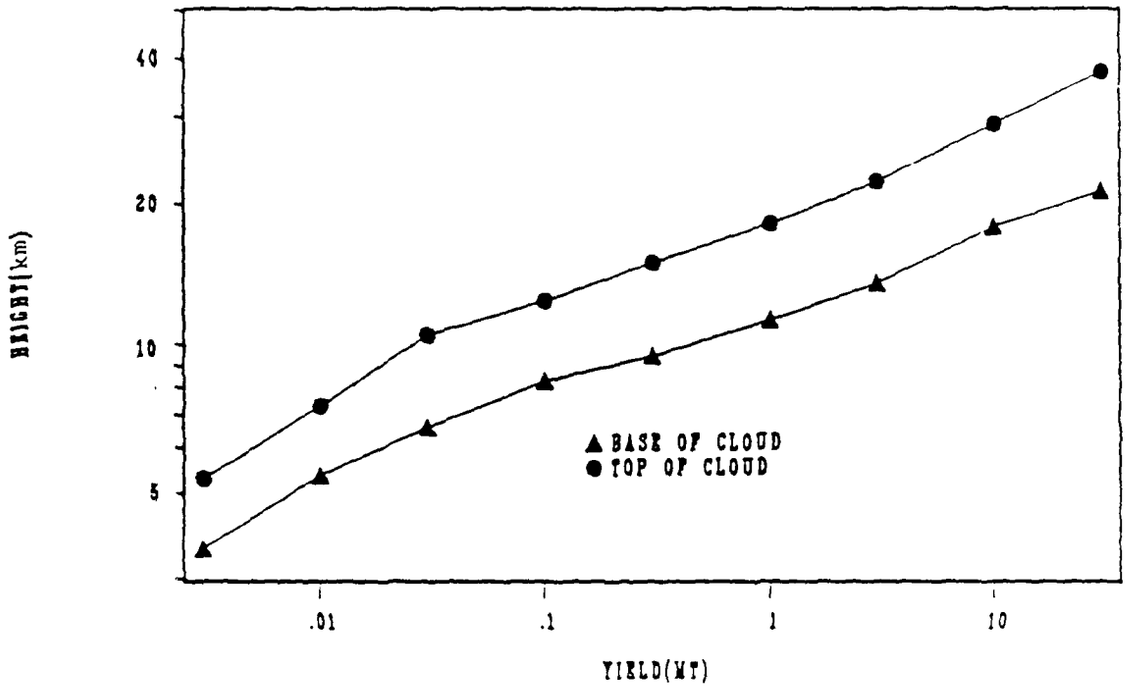

Figure 1. Base and top heights of clouds vs. yield.

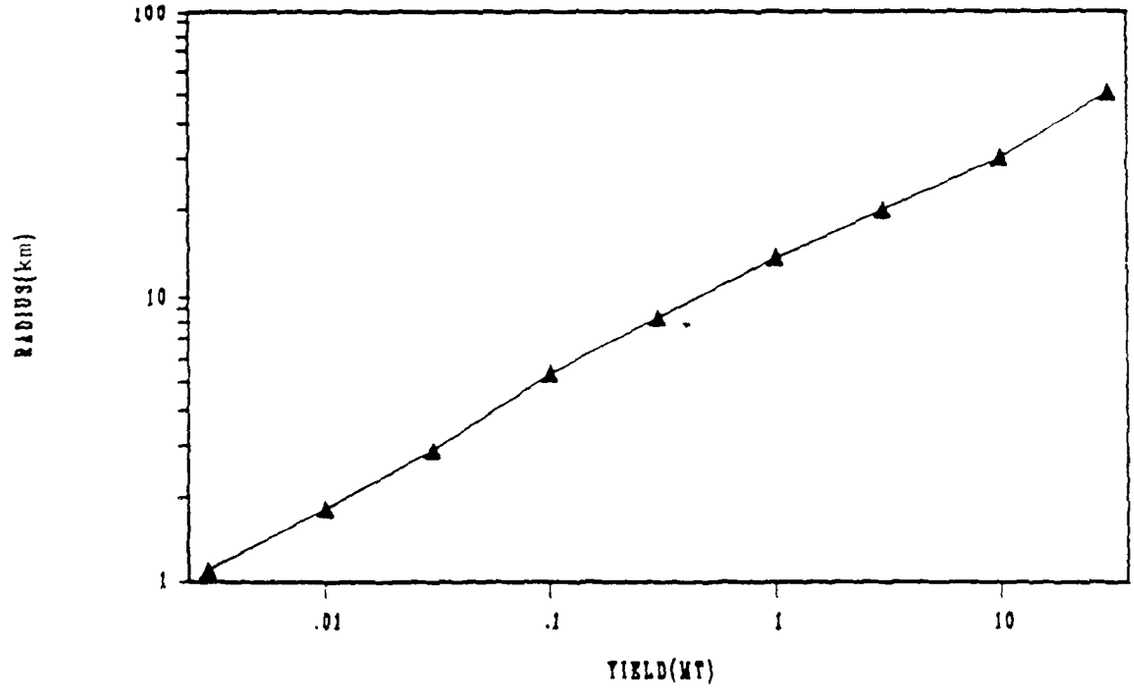

Figure 2. Radius of cloud vs. yield.

These calculations are based on the DELFIC and CASSANDRA portions of the model. The cloud top and bottom heights agree well with values reported by Glasstone and Dolan (4). Cloud radii appear to be larger by as much as a factor of 1.4 than those reported. Part of the disagreement may be explained by the ambiguous nature of the cloud dimensions. Part may be explained by the fact that DELFIC was intended as a ground fallout code, and ground fallout is relatively insensitive to cloud radius or base height choices (7). This is a drawback since flythrough dose is approximately inversely proportional to cloud radius in this model.

DUST CLOUD CHARACTERISTICS

In the model, the mass of soil entrained by the burst is dependent on the height of burst above ground, type of soil, and explosive yield. A log-normal distribution of particle sizes is assumed, and the dust is partitioned into 100 size classes. At initial time the soil burden is distributed uniformly throughout the cloud. As the cloud grows with time, the soil debris will be lofted with the cloud at a rate dependent on particle size. The gamma-radiation rate at each point in the cloud is proportional to the dust mass concentration at that point. The latter assumption is considered in detail in Appendix B.

One way of looking at the vertical distribution of dust is to conduct flythroughs at various heights. Figure 3 shows the dependence of total dose accumulated during the flythrough scenario as height is varied for 3 different times. For T=500 s the flythrough starts 250 s and ends 750 s after burst. The aircraft passes through the entire cloud (radius = 13.8 km (8.4 mi)) before stabilization is reached at 783 s (Table 1). The dose is nearly constant for flythroughs passing through the cloud. As the aircraft flies at heights lower than the cloud base, the dose received is relatively much lower; only large particles have fallen out to those levels. At later times, the dust activity has decayed as well as fallen. The dose received during flights below the cloud base is relatively more substantial.

The flythrough at the cloud base receives the largest dose. In the following analyses, this will be considered as the worst case scenario.

DOSE AT THE END OF FLYTHROUGH

The dose from a flythrough is strongly dependent on the time of flythrough and the yield of the detonation. Figure 4 shows the dose accumulated by the end of the flythrough at the cloud base vs. yield at 1000 s. Although the data on this graph (Fig. 4) do not all lie on a straight line, the data with yields greater than 0.1 MT strongly suggest a power relationship.

Figure 5 shows the dependence of dose at the end of flythrough on time of flythrough. The time plotted is the time after detonation that the aircraft passes over ground zero. Regression lines to these data are also shown. The

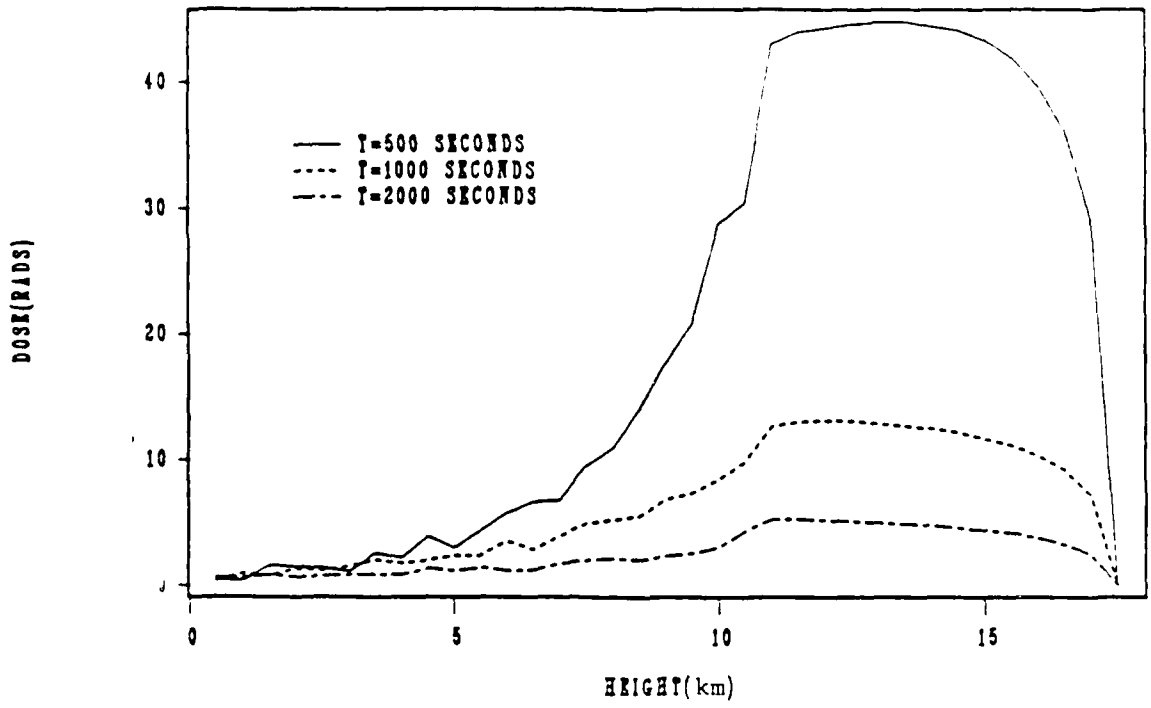

Figure 3. Dose vs. height for a 1 MT yield flythrough.
(-40 km, 0, H, t-250)-(40 km, 0, H, t+250).

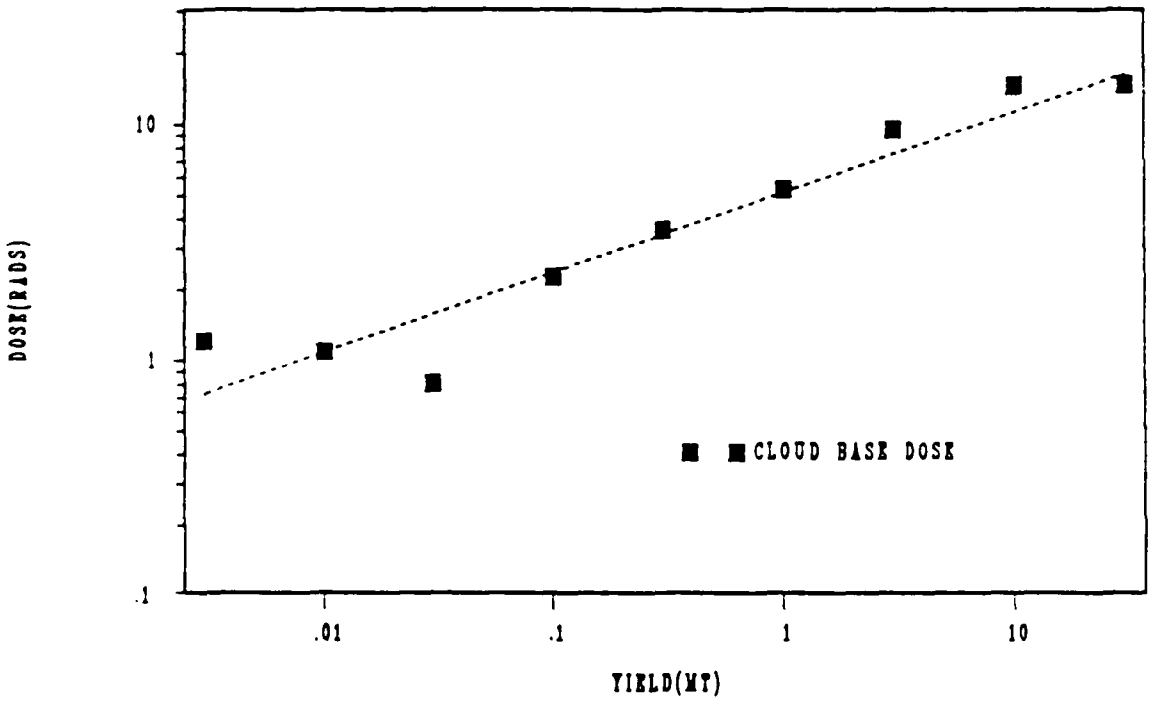

Figure 4. Dose vs. yield.
Flythrough (-40 km, 0, H, 1750)-(40 km, 0, H, 2250).

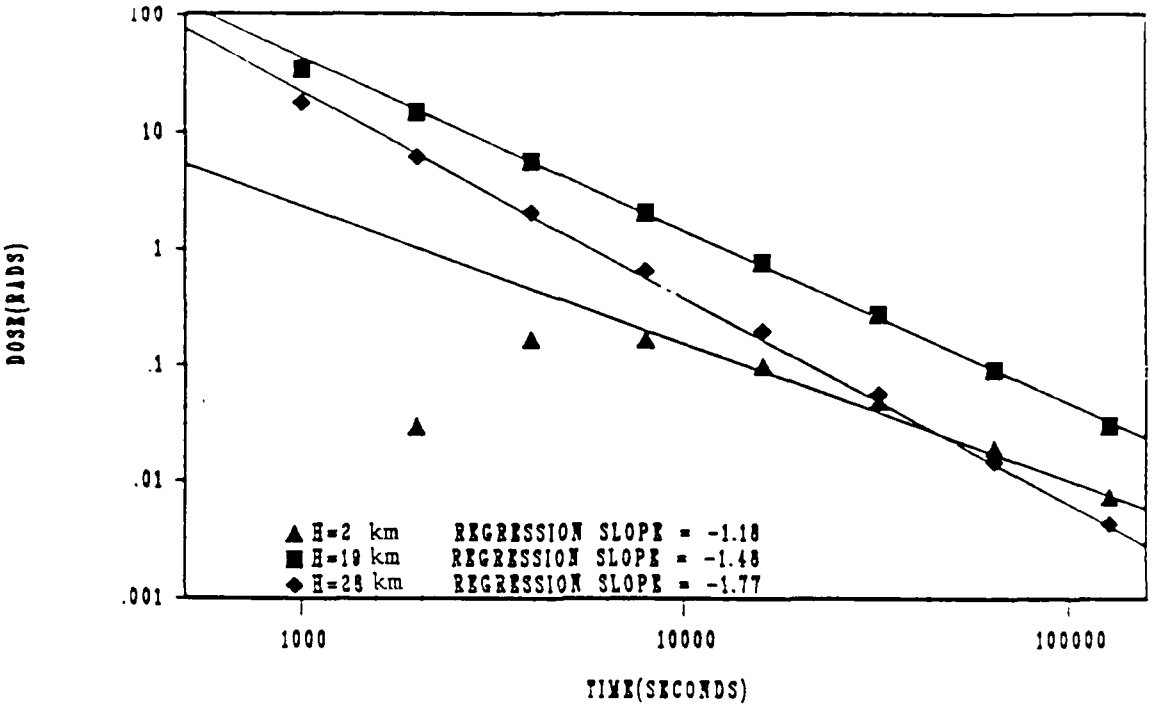

Figure 5. Dose vs. time for a 10 MT yield.
Flythrough (-40km, 0, H, t-250)-(40km, 0, H, t+250)

regression fit to the flythrough at an altitude of 2 km (1.2 mi) does not include the data for the four earliest times. The flythrough at 19-km (11.6 mi) altitude represents a flight through the base of the cloud while the flythrough at 28-km (17.1 mi) altitude is close to the top of the cloud. The power dependence of dose on time is greater than the $t^{-1.2}$ (Way-Wigner (5)) dependence built into the model. This is a result of the dust "falling out" to lower levels.

Figures 6 and 7 show the dependence of dose on time for flythroughs near the cloud top and bottom, respectively. These graphs show that the exponent in the time dependence is nearly independent of yield. A multiple regression on data for times between .5 h and 3 days, for yields above .1 MT, and for flythroughs near the cloud base produces the approximate relationship

$$\text{Dose} = 2.34\ W^{.48}\ t^{-1.53} \qquad (1)$$

where W is in megatons and t is in hours. This time dependence compares favorably with the $t^{-1.6}$ dependency observed in actual flythroughs (6).

POST FLYTHROUGH DOSE

The radiation from onboard sources is insignificant (3% of immersion dose) while the aircraft is immersed in the cloud. However, since the onboard dust

particles are carried with the aircraft, the radiation from this source can become significant for extended missions. The gamma-radiation rate decays as:

$$R(t) = R_1 \, t^{-1.2} \tag{2}$$

where R(t) is the radiation dose rate in rads/hour at time t hours after detonation and R_1 is the dose rate constant, equal to the dose rate at one hour after detonation (5). The evaluation of R_1 is based on the actual values of the total onboard dose rates at the corresponding cloud exit times of the aircraft. The calculated dose rate constants for trajectories near the cloud base and near the cloud top are given in Figures 8 and 9. A multiple regression fit to the data shows that the dose rate constant can be approximated by

$$R_1 = 1.44 \, W^{.55} \, t^{-.33} \tag{3}$$

where W is yield (megatons) and t is time (hours) after detonation that the plane reaches ground zero.

The total onboard radiation dose can be obtained by integrating equation (2) over the total time of the mission:

$$D(t) = \int_{t_a}^{t} R_1 \, t^{-1.2} \, dt = 5R_1 \, (t_a^{-0.2} - t^{-0.2}) \tag{4}$$

where D(t) is the dose in rads for the mission at time t hours after detonation and t_a is the time after detonation that the aircraft exits the debris cloud.

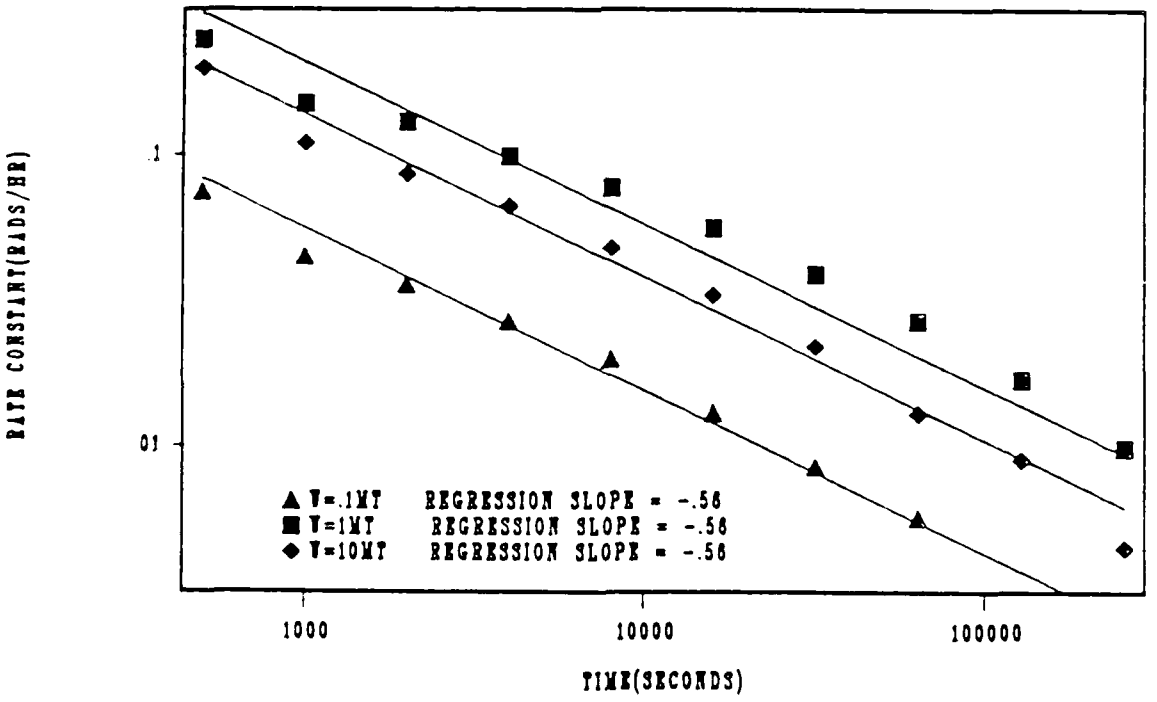

Figure 8. Rate constant vs. time near cloud top.
Flythrough (-40 km, 0, Ht, t-250)-(40 km, 0, Ht, t+250).

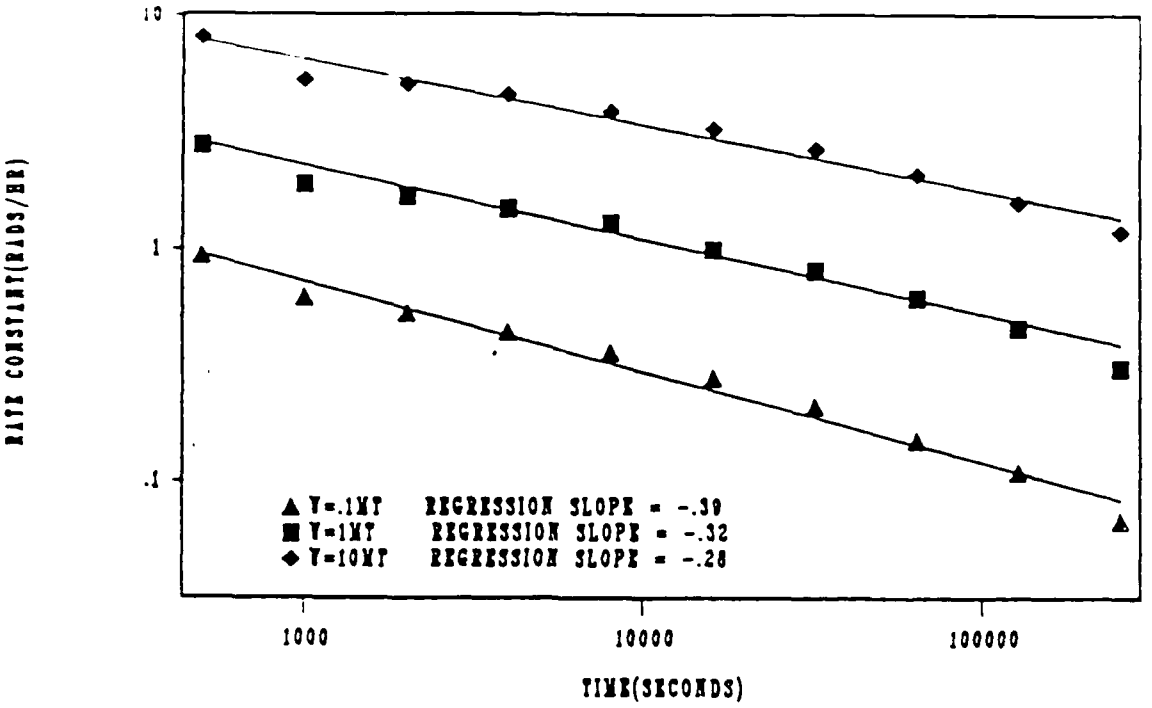

Figure 9. Rate constant vs. time near cloud base. Flythrough (-40 km, Hb, t-250)-(40 km, 0, Hb, t+250).

CONCLUSIONS

The problem of radiation exposure to aircrews during or immediately after a nuclear attack is critical for USAF mission planners. The best way to reduce radiation exposure is for the aircraft to avoid the nuclear debris clouds. However, the size of the cloud or the number of clouds may preclude this option.

The CASSIE model will calculate the radiation doses to aircrews flying through the debris clouds from a few seconds after detonation to time of cloud disbursement. However, the residual nuclear radiation will not be the major concern for early times. The initial radiation, thermal effects, and the problems of flying through clouds of large debris particle sizes will be the major considerations. Thus, the results of this report should not be considered as feasible for flythrough times before cloud stabilization.

Radiation doses of aircrews flying through the nuclear debris clouds under various conditions have been calculated by the use of the CASSIE model for an aircraft moving with a constant speed of about 311 knots. The radiation dose for an aircraft moving at a different speed will change in an essentially inverse relationship with the speed of the aircraft. If an aircraft penetrates the cloud at a slower speed, the aircraft will be exposed to the radiation for a longer time and thus, the dose will increase. The adjusted dose, D_1, is calculated by the equation:

$$D_1 = (311/v)\ D \qquad (5)$$

where V is the actual speed of the aircraft in knots and D is the predicted dose that the aircraft would have had if it traveled at a speed of 311 knots. The error introduced by this approximation is less than 6% for a range of speeds of 200 to 700 knots at a flythrough time of 1 h. For later times or for speeds closer to 311 knots, this approximation is even better.

To illustrate the application of the results of this study, consider the following problem. An estimate of the radiation dose is desired for an aircraft flying through the middle of a debris cloud at the cloud base from a 0.5-MT surface burst with a flythrough speed of 250 knots at a time of 2000 s after detonation enroute to a target that requires 12 h for mission completion. The steps for this calculation are as follows:

(1) For the moment, consider the aircraft as having a speed of 311 knots. Calculate the radiation dose while immersed in the debris cloud from equation (1):

$$D = (2.34)\ (.5)^{0.48}\ (2000/3600)^{-1.53} \qquad (6)$$

$$D = 4.1 \text{ rads}$$

(2) Find the onboard radiation dose rate constant from equation (3):

$$R_1 = (1.44)\ (.5)^{.55}\ (2000/3600)^{-0.33} \qquad (7)$$

$$R_1 = 1.2 \text{ rads/hour}$$

(3) Find the onboard dose for a 12-h mission from equation (4):

$$D(12) = (5)\ (1.2)\ [(2000/3600)^{-.2} - (12)^{-.2}] \qquad (8)$$

$$= 3.1 \text{ rads}$$

At this point multiply by the aircraft correction factor if known; see Appendix A.

(4) Calculate the total dose that the aircrew would experience by adding the results of steps (1) and (3):

$$\text{Total dose} = 7.2 \text{ rads}$$

(5) Adjust the dose to account for the speed of the aircraft by using equation (5):

$$D_1 = (311/250)(7.2) = 9.0 \text{ rads}$$

Thus, the predicted gamma-radiation dose to the aircrew is 9.0 rads for the mission. For 50 runs in the range .1 MT<W<10 MT and 30 min<T< 1 day, the standard deviation of these predictions from the CASSIE predictions is 16%. Two runs deviated more than 30% from the CASSIE results.

If the aircraft flies through more than one cloud, the radiation dose of each cloud must be calculated separately. The total dose is the sum of all the individual doses.

ACKNOWLEDGMENTS

We gratefully acknowledge the encouragement and technical assistance of Colonel (Ret.) J. E. Pickering, chief of the Radiation Sciences Division of the USAF School of Aerospace Medicine, Brooks Air Force Base. Appreciation and thanks are also extended to Dr. R. A. Albanese, Mr. Earl Bell, ROTC Cadet William Berger, Dr. D. N. Farrer, and Dr. J. Taboada for their technical advice and support.

REFERENCES

1. Taboada, J., D. Hegedusich, and E. Bell. Interactive scenario computer model for dose rates to aircrew in flight through nuclear debris clouds. USAFSAM-TR-85-49, USAF School of Aerospace Medicine, Brooks AFB, Texas, July 1985.

2. Showers, R. L., and C. Crisco. User's manual for CASSANDRA: Cloud Snapshots of Dust Raised Aloft. Report ARBRL-TR-02116, Ballistic Research Laboratory, Aberdeen Proving Ground, MD, 1978.

3. Norment, H. G., DELFIC: Department of Defense fallout prediction system Vol I and II. Report DNA 5159F-1, Atmospheric Science Associates, MA, 1977.

4. Glasstone, S., and P. J. Dolan. The effects of nuclear weapons, 3d ed., p. 391. U.S. Government Printing Office, Washington D.C., 1977.

5. Way, K., and E. P. Wigner. The rate of decay of fission products. Phys Rev 73:1318 (1948).

6. Banks, J. E., Operation TEAPOT. Manned penetrations of atomic clouds, Project 2.8b. Report WT-1156 (EX), Air Force Special Weapons Center, Kirtland Air Force Base, NM, 1958.

7. Norment, H. G., Validation and Refinement of the DELFIC Cloud Rise Module. Report DNA 4320F, Atmospheric Science Associates, MA, 1977.

APPENDIX A

CORRECTION FOR AIRCRAFT PARAMETERS

To obtain the dose prediction outlined in the conclusions, the following aircraft parameters were arbitrarily chosen:

CL(cabin length) = 3205 cm (1300 in.)
CR(cabin radius) = 274 cm (110 in.)
DF(distance of crewmember to filter) = 250 cm (100 in.)
FR(air-flow rate into cabin) = 67.5 kg (150 lb)/min
PF(fraction of dust not trapped by filter) = .5

Given actual measurements of these 5 parameters, a correction factor for a particular type of aircraft may be calculated and the carryalong dose modified as follows:

1. Calculate the correction factor for cabin dimensions, C_{DM}:

$$C_{DM} = 147060[CL \cdot LOG(4CR^2+CL^2) + 4CR \cdot ATN(CL/2CR) - 2CL \cdot LOG(CL)]/(CL \cdot CR^2)$$

2. Calculate the correction factor for crew distance from the filter, C_F:

$$C_F = 62500/D^2$$

3. Calculate the correction factor for air flow into the cabin, C_{FR}:

$$C_{FR} = FR/150$$

4. Calculate the correction factors for the fraction of dust allowed to pass into the cabin through the filter, C_{PF1} and C_{PF2}:

$$C_{PF1} = 2PF$$

$$C_{PF2} = 2(1-PF)$$

5. Calculate the combined correction factor, C:

$$C = 0.3 \cdot C_{PF1}\ C_{DM}\ C_{FR} + 0.7 \cdot C_{PF2}\ C_{FR}\ C_F$$

The carryalong dose (result of step 3 in the conclusions) is multiplied by this combined correction factor to obtain the corrected carryalong dose. The correction factor is based on: (a) analytical considerations discussed by Taboada et al.(1), and (b) the empirical observation that, given the arbitrary parameters originally chosen, the CASSIE model calculates that 30.% of the carryalong dose is due to dust trapped in the cabin while 70.% is due to dust trapped in the filter. The correction factor thus contributes no deviation of hand calculated results from CASSIE results.

APPENDIX B

EVALUATION OF MODEL ASSUMPTIONS

In the CASSIE model, the dose rate for a flythrough is calculated by the following steps.

(1) Divide the flight path into a sequence of target points (x_1, y_1, z_1, t_1), (x_2, y_2, z_2, t_2),...(x_n, y_n, z_n, t_n), each 4 km apart.

(2) Calculate the dust concentration at each target point for each of 100 dust sizes using the CASSANDRA code.

(3) Calculate the dose rate at each target point assuming:

(a) The rate contributed by a volume of space is proportional to the mass of dust contained therein.

(b) When the dose rate is calculated at a particular target point, the dust concentration is uniform and equal to the concentration at the target point.

(c) The cloud is considered to be infinite in extent for the purpose of integrating the dose rate for a target point.

(4) Approximate the dose integration over the flight path by assuming:

(a) Constant velocity

(b) The dose rate varies linearly between target points.

Each of these operations contributes some error. An analysis of the extent of some of them follows.

Frequency of Target Points

A variety of flight paths were evaluated by taking points much closer together than 4 km (2.4 mi). The differences between these doses and the original dose were less than 5%. Thus, it was concluded that the 4 km (2.4 mi) interval for target points was a good compromise between accuracy and computer time.

Integration to get Gamma Rate

Taboada et al. (1) calculated the immersion dose rate D at a point (r_i) and time (t) by the following integral:

$$D(r_i) = t^{-1.2} K_1 \sum_{j=1}^{100} K(j) \int \frac{\rho(r,t,j) \exp(-K_3 |r - r_i|)\, dV}{4\pi |r - r_i|^2} \qquad \text{(B-1)}$$

The space independent portion of the gamma rate at [illegible] size category is

$$D(r_i,j) = \text{Constant} \int \frac{\rho(r,j) \exp(-K_3 |r - r_i|)\, dV}{4\pi |r - r_i|^2} \qquad (B-2)$$

where r_i is the i th target point location, $\rho(r)$ is the dust density at location r, $K_3 = 6.767 \times 10^{-3}$ meters^{-1} is the atmospheric absorption of a 1-MeV gamma photon, and j is the dust size category. The integral is taken over the volume of the cloud. If a coordinate transformation is made to put the origin at the target point and spherical coordinates are used, this equation becomes

$$D(r_i,j) = \text{Constant} \iiint \frac{\rho(s,j) \exp(-K_3 s)}{4\pi} \sin\theta \, d\theta d\phi ds \qquad (B-3)$$

If the assumptions in steps 3(b) and 3(c) are made, then $\rho(s) = \rho(r_i)$. Then, $\rho(s)$ is constant for purposes of evaluating the integral. Also, the cloud is spherically symmetric and infinite in size. Thus, the integral becomes

$$D(r_i,j) = \text{Constant } \rho(r_i,j) \int_0^\infty \exp(-K_3 s)\, ds \qquad (B-4)$$

$$D(r_i,j) = \text{Constant } \rho(r_i,j)/K_3 \qquad (B-5)$$

Two objections may occur at this point. First, the dust density does not continue indefinitely. This is not a serious problem because only 1% of the dose rate calculated by this approximation is due to any activity beyond a 680 m (2244 ft) sphere about r_i. That is,

$$\int_0^{680} \exp(-K_3 s)ds = .99 \int_0^\infty \exp(-K_3 s)ds \qquad (B-6)$$

A second objection is that $\rho(r)$ is not constant enough even within a 680 m (2244 ft) sphere to make a good approximation. To estimate the error incurred from the constant density approximation, an alternative integration scheme was performed, using the following symmetry argument. Consider the target point (x_i, y_i, z_i, t_i). Poll the dust concentrations at 7 points: (x_i, y_i, z_i, t_i), ($x_i \pm 200$m, y_i, z_i, t_i), (x_i, $y_i \pm 200$m, z_i, t_i) and (x_i, y_i, $z_i \pm 200$m, t_i). Assume the dust concentration is uniform within a 100 m (327 ft) sphere around the target point. This region would encompass one-half the dose rate in the previous scheme. Divide the remaining space into 6 "congruent" (infinite) regions, each with axis of symmetry about the line through (x_i, y_i, z_i) and the respective polling point. This can be pictured by imagining the 8 points of a cube, ($x_i \pm d$, $y_i \pm d$, $z_i \pm d$), on a hollow cantaloupe and slicing between them. Of course, this cantaloupe is infinite in radius. The intent of this division is to justify a weighting of the polled points. The dose rate due to one of the outside regions is one-twelfth of the rate calculated over all space if the dust concentration were uniformly equal to that of the polled point. In like manner, the interior sphere receives a one-half weighting.

The sequence of polling points $(x_1, y_1, z_1 + 200, t_1)$, ... $(x_n, y_n, z_n + 200, t_n)$ creates a flight path 200 m (660 ft) above the original. The dose received from the upper outside region can be evaluated by running the original program and taking one-twelfth of the resulting dose. The same is true of $(x_1, y_1 \pm 200, z_1, t_1)$ and $(x_1, y_1, z_1 - 200, t_1)$. The other 2 outside integration regions $(x_1 \pm 200, y_1, z_1, t_1)$ form flight paths along the original path but shifted in time by 200 m (660 ft)/velocity, which is a negligible amount. It is assumed that the starting and ending points are outside the cloud.

Thus, the dose from this integration scheme is a linear function of 5 runs of the original program:

New dose estimate

$$
\begin{aligned}
= \quad & (1/2 + 1/12 + 1/12)\ \text{Dose}\ [(x_1, y_1, z_1, t_1) \rightarrow (x_n, y_n, z_n, t_n)] \\
& + (1/12)\ \text{Dose}\ [(x_1, y_1 + 200, z_1, t_1) \rightarrow (x_n, y_n + 200, z_n, t_n)] \\
& + (1/12)\ \text{Dose}\ [(x_1, y_1 - 200, z_1, t_1) \rightarrow (x_n, y_n - 200, z_n, t_n)] \qquad (B\text{-}7) \\
& + (1/12)\ \text{Dose}\ [(x_1, y_1, z_1 + 200, t_1) \rightarrow (x_n, y_n, z_n + 200, t_n)] \\
& + (1/12)\ \text{Dose}\ [(x_1, y_1, z_1 - 200, t_1) \rightarrow (x_n, y_n, z_n - 200, t_n)]
\end{aligned}
$$

The doses predicted by CASSIE along the $(x_1, y_1 \pm 200, z_1, t_1)$ - $(x_n, y_n \pm 200, z_n, t_n)$ flight paths do not differ from the prediction along the original path. As can be seen from Figure 3, doses along the $(x_1, y_1, z_1 \pm 200, t_1)$-$(x_n, y_n, z_n \pm 200, t_n)$ paths may differ by 25% from the prediction along the original path but both will not differ in the same direction from the original. The choice of one flight path, to differ by 25% while the other agrees with the original is a worst case and results in 25/12 or about 2% error. We take this as evidence that the original integration scheme is sufficiently accurate.

Calculation of Dust Densities

Results of CASSANDRA agree well with dust concentrations measured in the Dial Pack tests using conventional explosives. There are no measurements of airborne dust from detonations in the megaton range with which to compare the model's results. The cloud size discrepancy in the megaton range has already been noted. The lack of experimental data and other models for comparison makes the sources and amounts of error difficult to assess.

Atmospheric Conditions

The atmospheric winds are assumed to be zero. If nonzero winds are injected horizontally, the cloud will be translated as a unit if the wind is uniform and distorted if a wind shear exists. A wind shear along the length of the flight path will cause little difference in dose while a cross wind shear will produce a lower dose.

The effects of precipitation and large vertical winds in a thunderstorm are not considered. Precipitation will cause particles to fall out earlier and thus, reduce doses from flights through

AD-A186 493 UNITED STATES AIR FORCE RESEARCH INITIATION PROGRAM 8/ 8
1985 TECHNICAL REPORT VOLUME 3(U) UNIVERSAL ENERGY
SYSTEMS INC DAYTON OH R C DARRAH APR 87
UNCLASSIFIED AFOSR-TR-87-1719 F49620-85-C-0013 F/G 15/3 NL

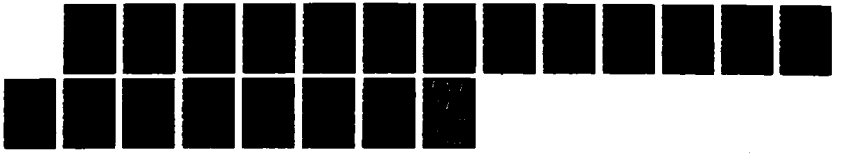

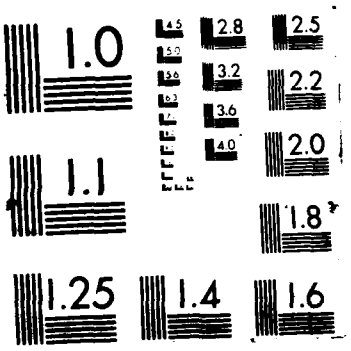
1.0
1.1
1.25
1.4
1.6
1.8
2.0
2.2
2.5
2.8
3.2
3.6
4.0

Flight Through Cloud Center

The trajectories of the aircraft are assumed to pass over ground zero. If the aircraft passes a distance from ground zero, the radiation dose will be reduced by virtue of the aircraft spending less time inside the cloud and going through a lower dust concentration.

Appendix II

Rapid Calculations of Radiation Doses From Flying Through Nuclear Debris Clouds

P. M. Vanden Bosch

School of Aerospace Medicine, Aerospace Medical Division,

Brooks Air Force Base, San Antonio, Texas

Arthur Woodrum

Department of Physics, Georgia Southern College, Statesboro, Georgia

Short title: Radiation Doses From Flying Through Nuclear Debris Clouds

Abstract

A procedure for five second calculation of gamma doses incurred by aircrew members flying through nuclear debris clouds is presented. The procedure is based on sensitivity studies of a recent flythrough model which has run times of up to fifteen minutes. Accuracy is acceptable using only a small subset of the original input variables for worst-case estimations.

Introduction

Estimates of radiation doses to aircrews flying through nuclear debris clouds are of critical interest to USAF mission planners. The probability of such an event occurring is high following a nuclear attack. Since real data are lacking, prediction must depend upon mathematical modeling of the cloud environment and flythrough.

Taboada et al [1985] developed a computer model which predicts doses from flythroughs. The model is based upon the dust environment model CASSANDRA [Showers and Crisco, 1978] which in turn uses the benchmark DELFIC [Norment, 1977] code as the basis of its cloud rise and fallout dynamics. Taboada's model uses the CASSANDRA code to calculate the dust density at various points along the trajectory of an aircraft flying through a nuclear debris cloud. A gamma-radiation dose rate is calculated from the dust densities and integrated over time to obtain the total radiation dose that an aircrew would experience.

The total radiation dose is assumed to originate from two sources: (1) the immersion radiation dose, which is a result of the aircraft being immersed in a radioactive cloud, and (2) the onboard radiation dose, which results from radiation exposure of the aircrews to dust particles trapped inside the aircraft cabin and filtering system. The immersion rate exists only while the aircraft is inside the radioactive debris cloud, whereas the onboard radiation is a continuing hazard.

Due to the long program running time, Taboada's model has little use in an operational setting. This report presents a method of obtaining worst-case radiation doses quickly, allowing planners to create complex scenarios with relative ease.

Flythrough Model

Taboada's model provides for changing flight and aircraft parameters easily. A scenario is needed which will allow an analysis of radiation dose dependence on height of flythrough, time of flight, and detonation yield. For the purposes of this report, the following flight scenario was used.

An aircraft flies from a point 40 km (24 mi) from ground zero on one side of a detonation to 40 km on the opposite side, passing directly over ground zero. The flight duration is 500 seconds, which corresponds to a velocity of 311 knots. A height H is maintained throughout the flight and the aircraft passes over ground zero at t seconds after detonation. This path is expressed in the form (-40 km, 0, H, t-250) - (40 km, 0, H, t+250).

The aircraft parameters are chosen to resemble those of a KC-135 aircraft. The model approximates the cabin as a cylinder, chosen to be 32.05 m (107 ft) in length and 2.74 m (9 ft) in radius. The filtration system is arbitrarily chosen to allow 50% of the dust particles taken onboard to enter the cabin, with the remainder staying on the filter. Once aboard, the dust particles do not exit. The distance from the crewmembers to the filter is arbitrarily chosen to be 250 cm out (100 in.). The air-mass flow into the aircraft is 67.5 kg/min (150 lb/min).

Cloud Dimensions

The size of the nuclear debris cloud depends on a number of factors. The parameters used in the analysis include:

(1) A surface burst, with 50% of the available energy expended in fission.

(2) Ground zero at 670 m (2211 ft) above mean sea level.

(3) No wind.

(4) Soil type is siliceous.

The debris cloud is modeled throughout its creation, expansion, and cooling. At some point the model considers the turbulence, upward rise, and expansion to be negligible and stabilizes the cloud dimensions at current values. These calculations are reported in Table 1. Stabilization is relative; in actuality, the cloud will continue to grow slowly as a result of buoyancy, turbulence, and wind patterns.

TABLE 1. Cloud Dimension Data at Stabilization

Yield (MT)	Stab. Time(s)	Cloud Base(m)	Cloud Top(m)	Cloud Radius(m)
0.003	312	3,700	5,200	1,100
0.010	423	5,300	7,400	1,800
0.030	661	6,700	10,500	2,900
0.100	611	8,400	12,400	5,400
0.300	720	9,500	14,900	8,500
1.000	783	11,300	18,000	13,800
3.000	785	13,500	22,000	20,300
10.000	787	17,700	29,000	31,000
30.000	852	21,000	37,200	52,400

These calculations are based on the DELFIC and CASSANDRA portions of the model. The cloud top and bottom heights agree well with value reported by Glasstone and Dolan [1977]. Cloud radii appear to be

larger by as much as a factor of 1.4 than those reported. Part of the disagreement may be explained by the ambiguous nature of the cloud dimensions. Part may be explained by the fact that DELFIC was intended as a ground fallout code, and ground fallout is relatively insensitive to cloud radius or base height choices [Norment, 1977]. Since the flythrough dose is approximately inversely proportional to cloud radius in this model, the inaccuracy in cloud size will cause the calculated dose to be underestimated.

Dust Cloud Characteristics

In the model, the mass of soil entrained by the burst is dependent on the height of burst above ground, type of soil, and explosive yield. A log-normal distribution of particle sizes is assumed, and the dust is partitioned into 100 size classes. At initial time the soil burden is distributed uniformly throughout the cloud. As the cloud grows with time, the soil debris will be lofted with the cloud at a rate dependent on particle size. The gamma-radiation rate at each point in the cloud is proportional to the dust mass concentration at that point.

One way of looking at the vertical distribution of dust is to conduct flythroughs at various heights. Figure 1 shows the dependence of total dose accumulated during the flythrough scenario as height is carried for 3 different times. For T=1,000 seconds the flythrough starts 750 seconds and ends 1,250 seconds after burst. The dose is nearly constant with respect to horizontal distances for flythroughs passing within 8 km of the center. As the aircraft flies at heights lower than the cloud base, the dose received is relatively much lower; only large particles have fallen out to those levels. At later times,

FIGURE #1. DOSE VS HEIGHT FOR A 1 MT YIELD
FLYTHROUGH (-40Km,0,H,T-250)-(40Km,0,H,T+250)

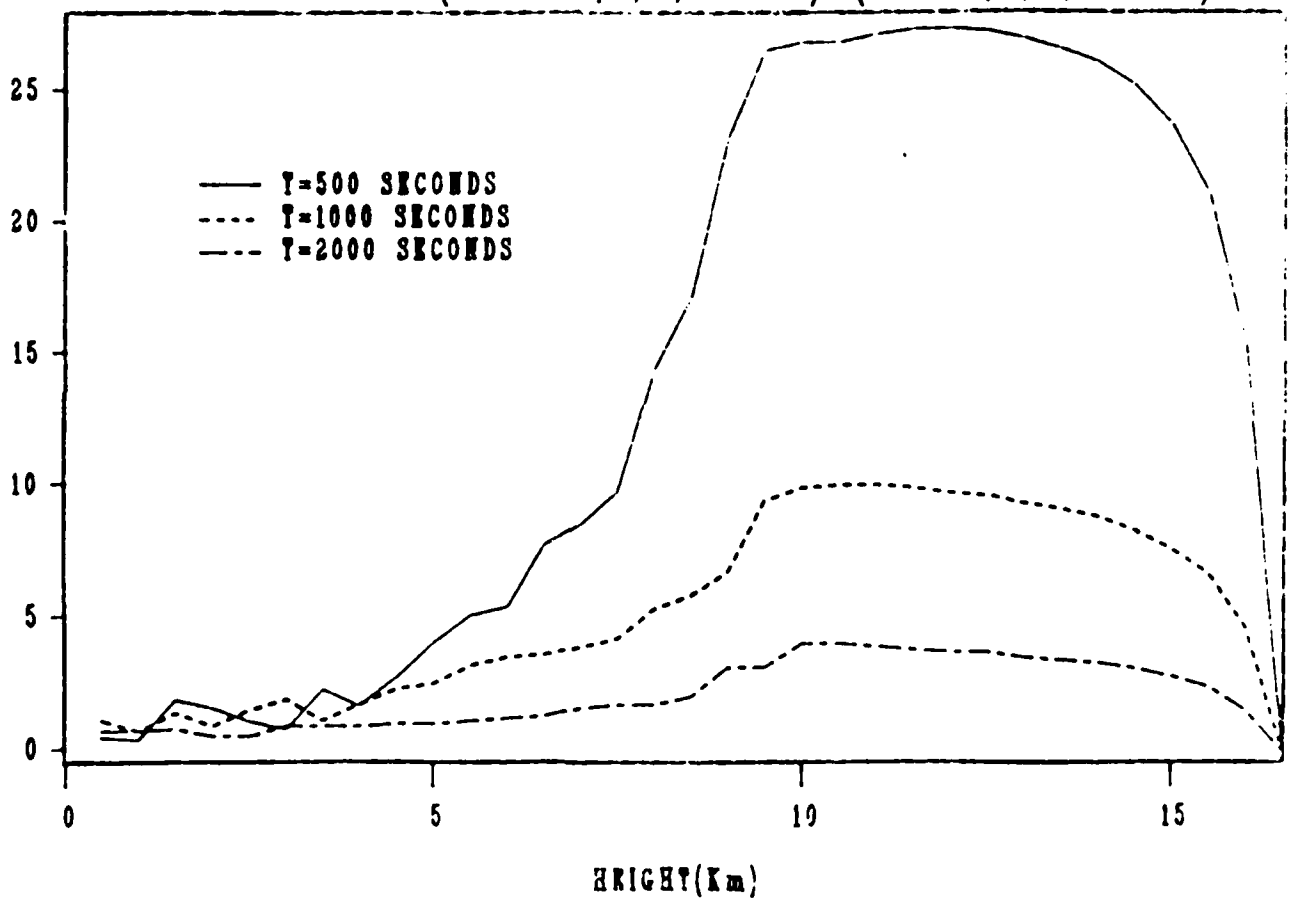

the dust activity has decayed as well as fallen. Thus the dose received during flights below the cloud base at these later times is relatively more substantial.

The flythrough at the cloud base receives the largest dose. In the following analyses, this will be considered as the worst case scenario.

Dose at the End of Flythrough

The dose from a flythrough is strongly dependent on the time of flythrough and the yield of the detonation. Figure 2 shows the dose accumulated by the end of the flythrough at the cloud base versus yield at 2000 seconds. Although the data on this graph do not all lie on a straight line, the data with yields greater than 0.1 MT strongly suggest a power relationship.

Figure 3 shows the dependence of dose at the end of flythrough on time of flythrough. The time plotted is the time after detonation that the aircraft passes over ground zero. Regression lines to these data are also shown. The regression fit to the flythrough at an altitude of 2 km (1.2 mi) does not include the data for the four earliest times. The flythrough at 19 km (11.6 mi) altitude represents a flight through the base of the cloud while the flythrough at 28-km (17.1 mi) altitude is close to the top of the cloud. The power dependence of dose on time is greater than the $t^{-1.2}$ dependence built into the model [Way and Wigner, 1948]. This is a result of the dust "falling out" to lower levels.

Figure 4 shows the dependence of dose on time for flythroughs near the cloud base. This graph shows that the exponent in the time dependence is nearly independent of yield. A multiple regression on

FIGURE 12. DOSE VS YIELD
FLYTHROUGH (-40Km,0,H,1750)-(40Km,0,H,2250)

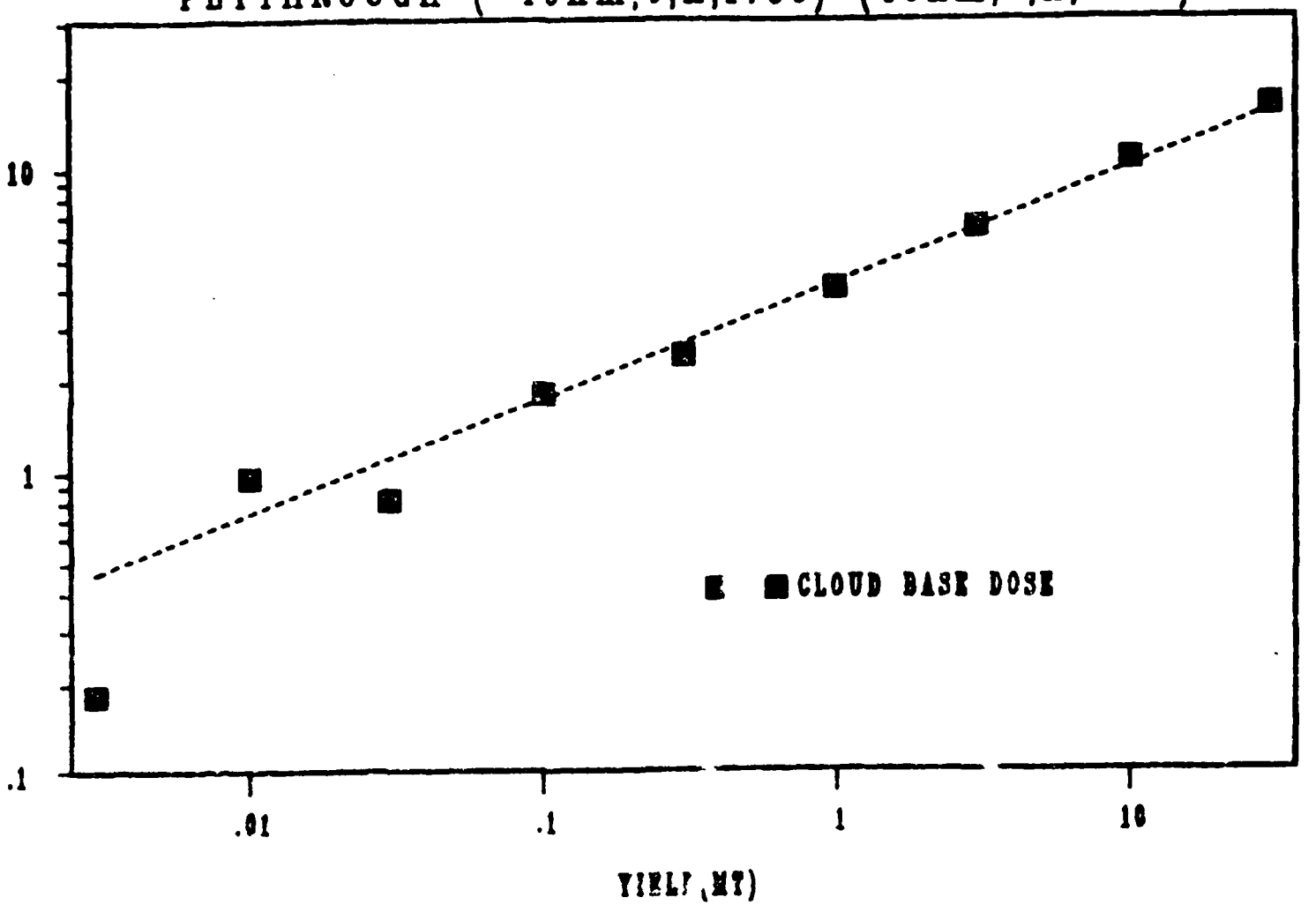

FIGURE 3. DOSE VS TIME FOR A 10 MT YIELD
FLYTHROUGH (-40Km,0,H,T-250)-(40Km,0,H,T+250)

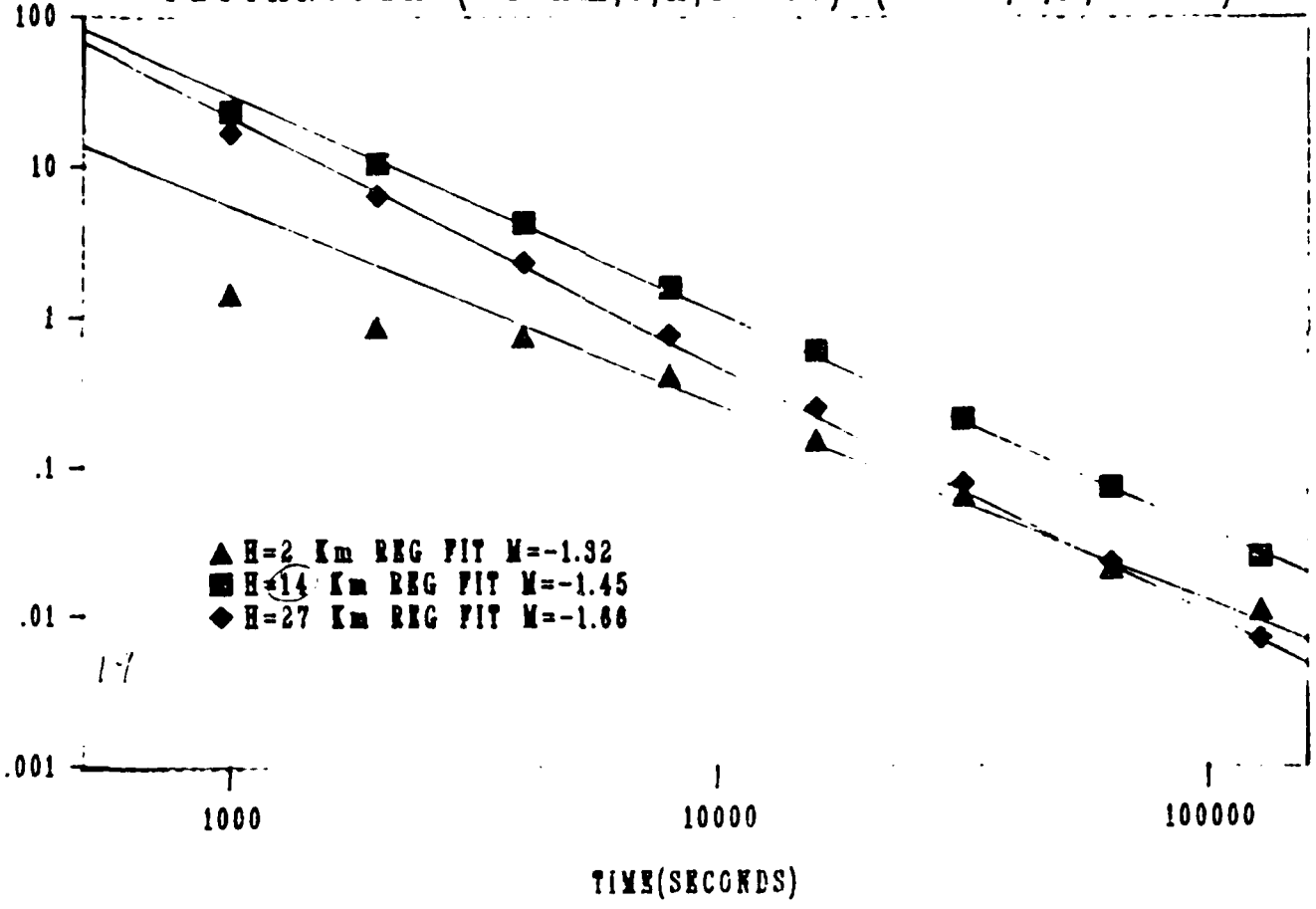

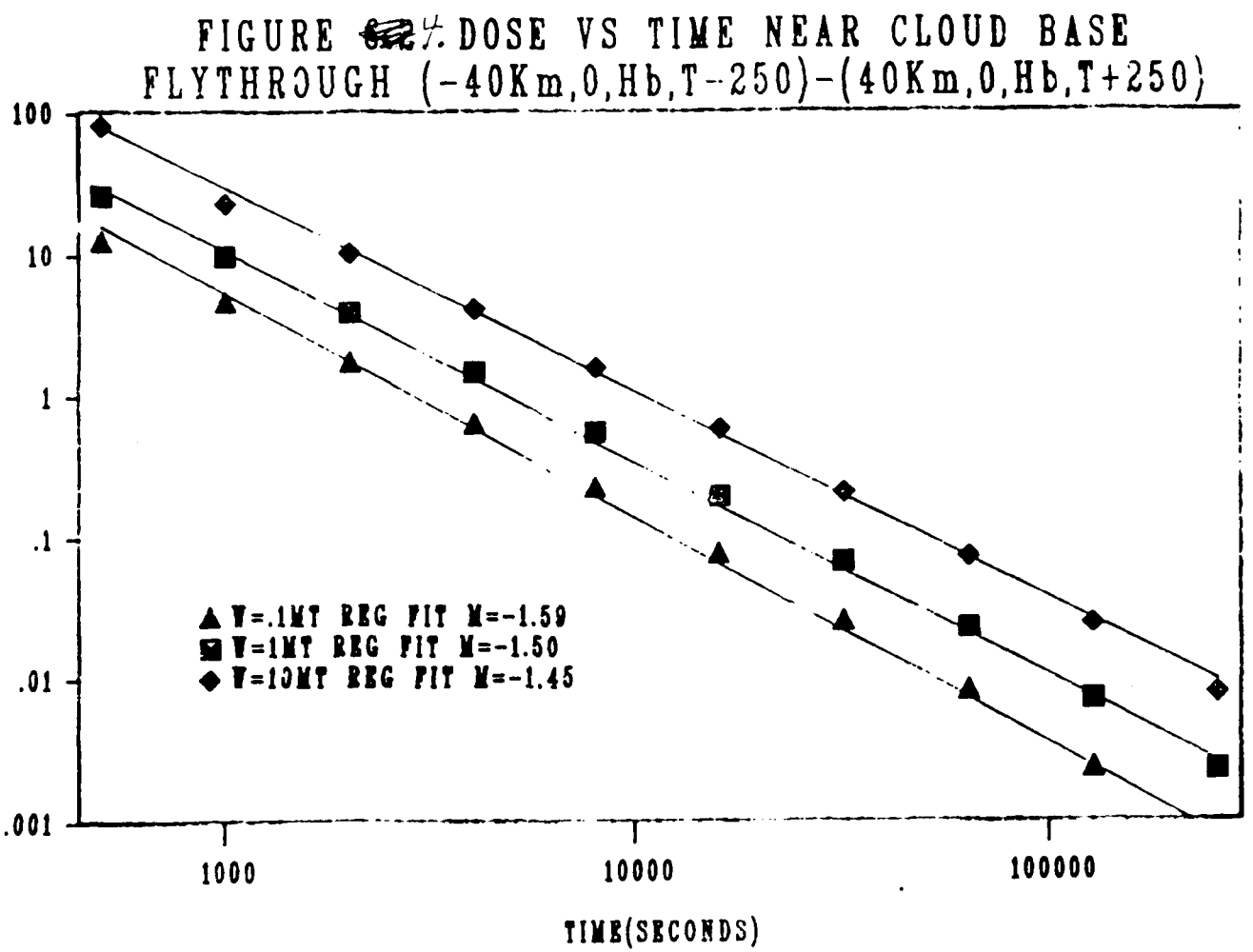
FIGURE 6a. DOSE VS TIME NEAR CLOUD BASE
FLYTHROUGH (-40Km,0,Hb,T-250)-(40Km,0,Hb,T+250)
100
10
1
.1
.01
.001
1000
10000
100000
TIME(SECONDS)
▲ W=.1MT REG FIT M=-1.59
■ W=1MT REG FIT M=-1.50
◆ W=10MT REG FIT M=-1.45

data for times between .5 h and 3 days, for yields above .1 MT, and for flythroughs near the cloud base produces the approximate relationship

$$\text{Dose} = 2.34\ W^{.48}\ t^{-1.53} \qquad (1)$$

where W is in megatons and t is in hours. This time dependence compares favorably with the $t^{-1.6}$ dependency observed in actual flythroughs [Banks, 1958].

Post Flythrough Dose

The radiation from onboard sources is insignificant (3% of immersion dose) while the aircraft is immersed in the cloud. However, since the onboard dust particles are carried with the aircraft, the radiation from this source can become significant for extended missions. The gamma-radiation rate decays as:

$$R(t) = R_1\ t^{-1.2} \qquad (2)$$

where R(t) is the radiation dose rate in rads/hour at time t hours after detonation and R_1 is the dose rate constant, equal to the dose rate at one hour after detonation [Way and Wigner, 1948]. The evaluation of R_1 is based on the actual values of the total onboard dose rates at the corresponding cloud exit times of the aircraft. The calculated dose rate constants for trajectories near the cloud base are given in Figure 5. A multiple regression fit to the data shows that the dose rate constant can be approximated by

FIGURE [illegible]. RATE CONSTANT VS TIME NEAR CLOUD BASE
FLYTHROUGH (-40Km,0,Hb,T-250) (40Km,0,Hb,T+250)

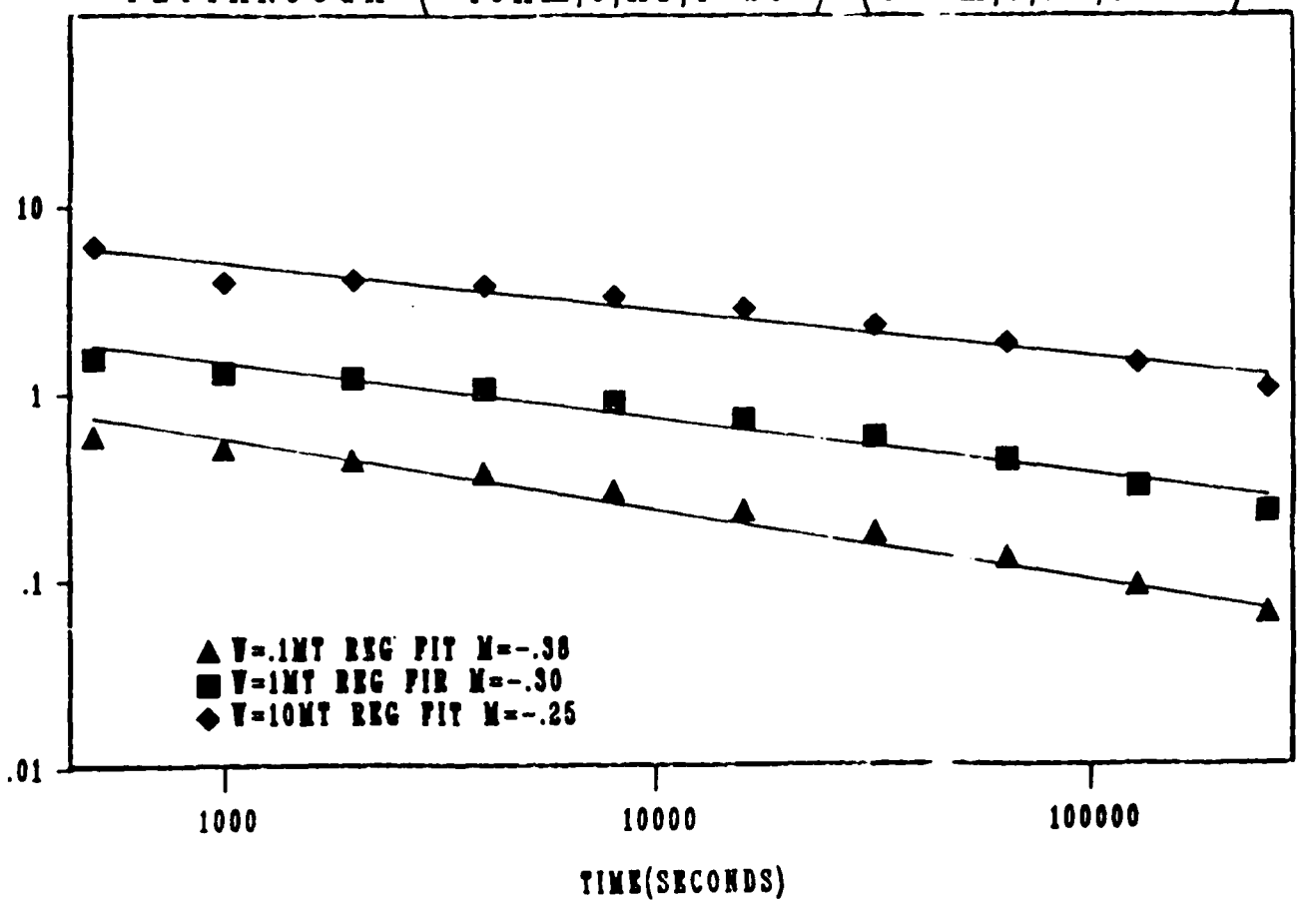

$$R_1 = 1.44\ W^{.55}\ t^{-.33} \qquad (3)$$

where W is yield (megatons) and t is time (hours) after detonation that the plane reaches ground zero.

The total onboard radiation dose can be obtained by integrating equation (2) over the total time of the mission:

$$D(t) = \int_{t_a}^{t} R_1\ t^{-1.2}\ dt = 5R_1\ (t_a^{-0.2} - t^{-0.2}) \qquad (4)$$

where D(t) is the dose in rads for the mission at time t hours after detonation and t_a is the time after detonation that the aircraft exits the debris cloud.

Conclusions

The problem of radiation exposure to aircrews during or immediately after a nuclear attack is critical for USAF mission planners. The best way to reduce radiation exposure is for the aircraft to avoid the nuclear debris clouds. However, the size of the cloud or the number of clouds may preclude this option.

The model will calculate the radiation doses to aircrews flying through the debris clouds from a few seconds after detonation to time of cloud disbursement. However, the residual nuclear radiation will not be the major concern for early times. The initial radiation, thermal effects, and the problems of flying through clouds of large debris particle sizes will be the major considerations. Thus, the results of this report should not be considered as feasible for flythrough times before cloud stabilization.

Approximate radiation doses of aircrews flying through the nuclear debris clouds under various conditions can be calculated rapidly with a small calculator using equations (1) and (4) for an aircraft moving with a constant speed of about 311 knots. The radiation dose for an aircraft moving at a different speed will change in an essentially inverse relationship with the speed of the aircraft. If an aircraft penetrates the cloud at a slower speed, the aircraft will be exposed to the radiation for a longer time and thus, the dose will increase. The adjusted dose, D_1, is calculated by the equation:

$$D_1 = (311/v)\ D \qquad (5)$$

where v is the actual speed of the aircraft in knots and D is the predicted dose that the aircraft would have had it traveled at a speed of 311 knots. The error introduced by this approximation is less than 6% for a range of speeds of 200 to 700 knots at a flythrough time of 1 h. For later times or for speeds close to 311 knots, this approximation is even better.

An illustration of the application of these results and an evaluation of many of the assumptions made is contained in Vanden Bosch and Woodrum [1986].

If the aircraft flies through more than one cloud, the radiation dose of each cloud must be calculated separately. The total dose is the sum of the individual doses.

Acknowledgments

We gratefully acknowledge the encouragement, technical assistance, and financial assistance of the Radiation Sciences Division of the USAF School of Aerospace Medicine, Brooks Air Force Base.

References

1. Way, K., and E. P. Wigner, The rate of decay of fission products, Phys. Rev., 73, 1318, 1948.

2. Banks, J. E., Operation TEAPOT. Manned penetrations of atomic clouds, project 2.8b, Report WT-1156 (EX), 51 pp, Air Force Special Weapons Center, Kirkland Air Force Base, N. M., 1958.

3. Glasstone, S., and P. J. Dolan, The Effects of Nuclear Weapons, 3d ed., 391 pp, U.S. Government Printing Office, Washington, D. C., 1977.

4. Norment, H. G., DELFIC: Department of Defense fallout prediction system Vol I and II, Report DNA 5159F-1, 328 pp, Atmospheric Science Associates, Mass., 1977.

5. Norment, H. G., Validation and refinement of the DELFIC cloud rise module, Report DNA 4320F, 125 pp, Atmospheric Science Associates, Mass., 1977.

6. Showers, R. L., and C. Crisco, User's manual for CASSANDRA: Cloud snapshots of dust raised aloft, Report ARBRL-TR-02116, 169 pp, Ballistic Research Laboratory, Aberdeen Proving Ground, Md., 1978.

7. Taboada, J., D. Hegedusich, and E. Bell, Interactive scenario computer model for dose rates to aircrew in flight through nuclear debris clouds, USAFSAM-TR-85-49, 15 pp, USAF School of Aerospace Medicine, Brooks AFB, Texas, July 1985.

8. Vanden Bosch, P. M., and Arthur Woodrum, Radiation doses from flying through nuclear debris clouds, USAFSAM-TR-85-86, 18 pp, USAF School of Aerospace Medicine, Brooks AFB, Texas, April 1986.

Figure 1. Dose vs height for a 1 MT yield.

Flythrough (-40 km, 0, H, T - 250) - (40 km, 0, H, T + 250)

Figure 2. Dose vs yield.

Flythrough (-40 km, 0, H, 1750) - (40 km, 0, H, 2250).

Figure 3. Dose vs time for a 10 MT yield.

Flythrough (-40 km, 0, H, T - 250) - (40 km, 0, H, T + 250).

Figure 4. Dose vs time near cloud base.

Flythrough (-40 km, 0, Hb, T - 250) - (40 km, 0, Hb, T + 250).

Figure 5. Rate constant vs time near cloud base.

Flythrough (-40 km, 0, Hb, T - 250) - (40 km, 0, Hb T + 250).

END

DATE

FILM

JAN

1988